

Olena Fesenko  
Leonid Yatsenko *Editors*

# Nanochemistry, Biotechnology, Nanomaterials, and Their Applications

Selected Proceedings of the  
5th International Conference  
Nanotechnology and Nanomaterials  
(NANO2017), August 23-26, 2017,  
Chernivtsi, Ukraine

# **Springer Proceedings in Physics**

Volume 214

The series Springer Proceedings in Physics, founded in 1984, is devoted to timely reports of state-of-the-art developments in physics and related sciences. Typically based on material presented at conferences, workshops and similar scientific meetings, volumes published in this series will constitute a comprehensive up-to-date source of reference on a field or subfield of relevance in contemporary physics. Proposals must include the following:

- name, place and date of the scientific meeting
- a link to the committees (local organization, international advisors etc.)
- scientific description of the meeting
- list of invited/plenary speakers
- an estimate of the planned proceedings book parameters (number of pages/articles, requested number of bulk copies, submission deadline).

More information about this series at <http://www.springer.com/series/361>

Olena Fesenko • Leonid Yatsenko  
Editors

# Nanochemistry, Biotechnology, Nanomaterials, and Their Applications

Selected Proceedings of the 5th International  
Conference Nanotechnology and  
Nanomaterials (NANO2017),  
August 23–26, 2017, Chernivtsi, Ukraine



Springer

*Editors*

Olena Fesenko  
National Academy of Sciences of Ukraine  
Institute of Physics  
Kyiv, Ukraine

Leonid Yatsenko  
National Academy of Sciences of Ukraine  
Institute of Physics  
Kyiv, Ukraine

ISSN 0930-8989

ISSN 1867-4941 (electronic)

Springer Proceedings in Physics

ISBN 978-3-319-92566-0

ISBN 978-3-319-92567-7 (eBook)

<https://doi.org/10.1007/978-3-319-92567-7>

Library of Congress Control Number: 2018948698

© Springer International Publishing AG, part of Springer Nature 2018

This work is subject to copyright. All rights are reserved by the Publisher, whether the whole or part of the material is concerned, specifically the rights of translation, reprinting, reuse of illustrations, recitation, broadcasting, reproduction on microfilms or in any other physical way, and transmission or information storage and retrieval, electronic adaptation, computer software, or by similar or dissimilar methodology now known or hereafter developed.

The use of general descriptive names, registered names, trademarks, service marks, etc. in this publication does not imply, even in the absence of a specific statement, that such names are exempt from the relevant protective laws and regulations and therefore free for general use.

The publisher, the authors and the editors are safe to assume that the advice and information in this book are believed to be true and accurate at the date of publication. Neither the publisher nor the authors or the editors give a warranty, express or implied, with respect to the material contained herein or for any errors or omissions that may have been made. The publisher remains neutral with regard to jurisdictional claims in published maps and institutional affiliations.

Printed on acid-free paper

This Springer imprint is published by the registered company Springer International Publishing AG part of Springer Nature.

The registered company address is: Gewerbestrasse 11, 6330 Cham, Switzerland

## Preface

This book highlights the most recent advances in nanoscience from leading researchers in Ukraine, Europe, and beyond. It features contributions from participants of the 5th International research and practice Conference “Nanotechnology and Nanomaterials” (NANO-2017), held in Chernivtsi, Ukraine on August 23–26, 2017. This event was organized jointly by the Institute of Physics of the National Academy of Sciences of Ukraine, Ivan Franko National Chernivtsi National University (Ukraine), University of Tartu (Estonia), University of Turin (Italy), and Pierre and Marie Curie University (France). Internationally recognized experts from a wide range of universities and research institutes shared their knowledge and key results in the areas of nanocomposites and nanomaterials, nanostructured surfaces, microscopy of nano-objects, nanooptics and nanophotonics, nanoplasmonics, nanochemistry, nanobiotechnology, and surface enhanced spectroscopy.

Nowadays nanotechnology is becoming the most actively developing and promising field of science. Numerous nanotechnology investigations are already producing practical results that can be applied in various areas of human life from science and technology to medicine and pharmacology. The aim of the present book is to highlight the latest investigations from different areas of nanoscience and to stimulate new interest in this field. Volume II of this two-volume work covers such important topics as nanocomposites, nanochemistry, nanobiotechnology, and enhanced vibrational spectroscopy.

This book is divided into two sections—Part I: *Nanochemistry and Biotechnology*; and Part II: *Nanocomposites and Nanomaterials*. Sections covering Nanoscale Physics, Nanooptics and Photonics, and Nanostructured Interfaces and Surfaces can be found in Volume I.

The papers published in these five sections fall under the broad categories of nanomaterial preparation and characterization, nanobiotechnology, nanodevices and

quantum structures, and spectroscopy and nanooptics. We hope that both volumes will be equally useful and interesting for young scientists or PhD students and mature scientists alike.

Kyiv, Ukraine

Olena Fesenko  
Leonid Yatsenko

# Contents

## Part I Nanochemistry and Biotechnology

- 1 Nanostructured Functional Coatings of Iron Family Metals with Refractory Elements** ..... 3  
 Maryna V. Ved', Nikolay D. Sakhnenko, Iryna Yu. Yermolenko, and Tatyana A. Nenastina
- 2 Multifunctional Magnetic Nanocomposites on the Base of Magnetite and Hydroxyapatite for Oncology Applications** ..... 35  
 Ie. V. Pylypchuk, M. V. Abramov, A. L. Petranovska, S. P. Turanksa, T. M. Budnyak, N. V. Kussyak, and P. P. Gorbyk
- 3 Structural Peculiarities and Properties of Silver-Containing Polymer Nanocomposites** ..... 49  
 V. Demchenko, S. Riabov, S. Kobylinskyi, L. Goncharenko, and N. Rybalchenko
- 4 Effect of Incorporated Inorganic Nanoparticles on Porous Structure and Functional Properties of Strongly and Weakly Acidic Ion Exchangers** ..... 63  
 Ludmila Ponomarova, Yuliya Dzyazko, Yurii Volkovich, Valentin Sosenkin, and Sergey Scherbakov
- 5 Peculiarities of the Crystal-Chemical Structure of Spinel Ferrites  $\text{Co}_x\text{Fe}_{3-x}\text{O}_4$  ( $0.25 \leq x \leq 1$ ) Obtained Under the Action of a Low-Temperature Contact Nonequilibrium Plasma** ..... 79  
 L. A. Frolova, O. A. Pivovarov, O. A. Kushnerov, and N. M. Tolstopalova
- 6 The Dynamics of Water Molecules Confined in the Interior of DMPC Phospholipid Reverse Micelle** ..... 89  
 D. Makiela, Przemyslaw Raczynski, and Zygmunt Gburski



<b>7 Applications Perspectives of Nanodispersed Chalcogenides of Transition Metals in Photocatalysis</b> .....	99
Iryna Ivanenko, Tetiana Dontsova, and Yurii Fedenko	
<b>8 Nanocomposites Based on Thermosetting Polyurethane Matrix and Chemically Modified Multiwalled Carbon Nanotubes</b> .....	115
L. V. Karabanova, R. L. Whitby, V. A. Bershtein, P. N. Yakushev, A. W. Lloyd, and S. V. Mikhalovsky	
<b>9 Polymeric Composite Films with Controlled Release of Natural Antioxidant Enoxil</b> .....	149
Roman Kozakevych, Yulia Bolbukh, Lucian Lupascu, Tudor Lupascu, and Valentin Tertykh	
<b>10 High-Temperature Electrochemical Synthesis of Nanostructured Coatings of Molybdenum (Tungsten)–Nickel (Cobalt) Alloys and Intermetallic Compounds</b> .....	165
Viktor Malyshev, Nataliia Uskova, Dmytro Shakhnin, Tetiana Lukashenko, Viktor Antsibor, and Zafer Ustundag	
<b>11 Structure and Electrical/Dielectric Properties of Ion-Conductive Polymer Composites Based on Aliphatic Epoxy Resin and Lithium Perchlorate Salt</b> .....	177
Liubov K. Matkovska, Maksym V. Iurzhenko, Yevgen P. Mamunya, Valeriy Demchenko, and Gisele Boiteux	
<b>12 Mechanical and Thermal Characteristics of Irradiation Cross-linked Hydrogels</b> .....	205
O. Nadtoka, N. Kutsevol, A. Onanko, and V. Neimash	
<b>13 Nanostructural and Nanochemical Processes in Peloid Sediments Aided with Biogeocenosis</b> .....	215
A. V. Panko, I. G. Kovzun, O. M. Nikipelova, V. A. Prokopenko, O. A. Tsyganovich, and V. O. Oliinyk	
<b>Part II Nanocomposites and Nanomaterials</b>	
<b>14 Directional Synthesis of SnO<sub>2</sub>-Based Nanostructures for Use in Gas Sensors</b> .....	233
Svitlana Nahirniak, Tetiana Dontsova, and Ihor Astrelin	
<b>15 “Polymer–Oxide” Micro-/Nanocomposites: Background and Promises</b> .....	247
S. G. Nedilko	
<b>16 Interactions Between Carbon-Based Nanostructures and Biomembranes: Computer Simulations Study</b> .....	277
Przemysław Raczyński, Mateusz Pabiszczak, and Zygmunt Gburski	

<b>17</b>	<b>Percolation Threshold of 5-Cyanobiphenyl Mesogene Phases Between Graphene Planes: Computer Simulation Study</b> .....	289
	Violetta Raczyńska, Krzysztof Górny, Przemysław Raczyński, and Zbigniew Dendzik	
<b>18</b>	<b>The Ultrasonic Treatment as a Promising Method of Nanosized Oxide CeO<sub>2</sub>-MoO<sub>3</sub> Composites Preparation</b> .....	297
	V. A. Zazhigalov, O. V. Sachuk, O. A. Diyuk, V. L. Starchevskyy, S. V. Kolotilov, Z. Sawlowicz, S. M. Shcherbakov, and O. I. Zakutevskyy	
<b>19</b>	<b>High-Temperature Electrochemical Synthesis of Nanopowders of Tungsten Carbide in Ionic Melts</b> .....	311
	Viktor Malyshev, Angelina Gab, Dmytro Shakhnin, Tetiana Lukashenko, Oleksandr Ishtvanik, and Marcelle Gaune-Escard	
<b>20</b>	<b>Magnetic Memory of Antitumor Magneto-sensitive Nanocomplex</b> ...	323
	V. Orel, A. Shevchenko, O. Rykhalskyi, A. Romanov, A. Burlaka, and S. Lukin	
<b>21</b>	<b>Nonlinear Optical Properties of Polymer Nanocomposites with a Random and Periodic Distribution of Silver Nanoparticles</b> .....	333
	T. N. Smirnova, V. I. Rudenko, V. O. Hryn	
<b>22</b>	<b>The Nanocomposite Diffusion Coating of Details Prepared of Boriding</b> .....	345
	Andrew Stetsko	
<b>23</b>	<b>Ni Addition Induced Changes in Structural, Magnetic, and Cationic Distribution of Zn<sub>0.75-x</sub>Ni<sub>x</sub>Mg<sub>0.15</sub> Cu<sub>0.1</sub>Fe<sub>2</sub>O<sub>4</sub> Nano-ferrite</b> .....	357
	Manvi Satalkar, Shashank Narayan Kane, Tetiana Tatarchuk, and João Pedro Araújo	
<b>24</b>	<b>Dielectric Properties and AC Conductivity of Epoxy/Hybrid Nanocarbon Filler Composites</b> .....	377
	Ludmila L. Vovchenko, Ludmila Yu. Matzui, Yulia S. Perets, and Yurii S. Milovanov	
<b>25</b>	<b>Obtaining of the Modified NH<sub>4</sub>NO<sub>3</sub> Granules with 3-D Nanoporous Structure: Impact of Humidifier Type on the Granule's Structure</b> .....	395
	A. E. Artyukhov, J. Gabrusenoks, and P. C. Rossi	
<b>26</b>	<b>Bifunctional Silicas with Immobilized Lignin</b> .....	407
	Yulia Bolbukh, Stanislav Sevostianov, Beata Podkoscielna, Dariusz Sternik, Panagiotis Klonos, Polycarpos Pissis, Barbara Gawdzik, and Valentin Tertykh	

<b>27</b>	<b>Cooperative Phenomena in Spin-Crossover Molecular Crystals</b> .....	427
	Iurii Gudyma, Artur Maksymov, and Kateryna Polonska	
<b>28</b>	<b>Copper Nucleation on Nickel from Pyrophosphate-Based Polyligand Electrolyte</b> .....	443
	Antonnia Maizelis and Boris Bairachnyi	
<b>29</b>	<b>Structural Study of the Modified <math>\text{Cu}_{0.4}\text{Co}_{0.4}\text{Ni}_{0.4}\text{Mn}_{1.8}\text{O}_4</math> and <math>\text{Cu}_{0.1}\text{Ni}_{0.8}\text{Co}_{0.2}\text{Mn}_{1.9}\text{O}_4</math> Ceramics Using Combined Methods</b> ...	459
	H. Klym, I. Hadzaman, A. Ingram, O. Shpotyuk, I. Karbovnyk, Yu. Kostiv, I. Vasylychshyn, and D. Chalyy	
<b>30</b>	<b>Effect of a Hydrogen Sulfide-Containing Atmosphere on the Physical and Mechanical Properties of Solid Oxide Fuel Cell Materials</b> .....	475
	B. D. Vasylyv, V. Ya. Podhurska, O. P. Ostash, and V. V. Vira	
<b>31</b>	<b>Influence of Annealing in Vacuum on Dispersion Kinetics of Titanium and Zirconium Nanofilms Deposited onto Oxide Materials</b> .....	487
	Y. V. Naidich, I. I. Gab, T. V. Stetsyuk, B. D. Kostyuk, O. M. Fesenko, and D. B. Shakhnin	
<b>32</b>	<b>Grain Porous Structure and Exploitation Properties of Humidity-Sensitive Magnesium Aluminate Spinel-Type Ceramics</b> .....	499
	H. Klym, I. Hadzaman, O. Shpotyuk, and A. Ingram	
	<b>Index</b> .....	521

## Contributors

**M. V. Abramov** Chuiko Institute of Surface Chemistry of National Academy of Sciences of Ukraine, Kyiv, Ukraine

**Viktor Antsibor** University “Ukraine”, Kyiv, Ukraine

Dumlupinar University, Kutahya, Turkey

**João Pedro Araújo** IFIMUP and IN-Institute of Nanoscience and Nanotechnology, Department of Physics and Astronomy, Faculty of Sciences, University of Porto, Porto, Portugal

**A. E. Artyukhov** Processes and Equipment of Chemical and Petroleum Refinery Department, Sumy State University, Sumy, Ukraine

**Ihor Astrelin** Department of Chemistry, National Technical University of Ukraine, “KPI”, Kyiv, Ukraine

**Boris Bairachniy** National Technical University “Kharkiv Polytechnic Institute”, Kharkiv, Ukraine

**V. A. Bershtein** Ioffe Institute, St. Petersburg, Russia

**Gisele Boiteux** Université de Lyon, Université Lyon 1, Ingénierie des Matériaux Polymères, UMR CNRS 5223, Villeurbanne, France

**Yulia Bolbukh** Chuiko Institute of Surface Chemistry, National Academy of Sciences of Ukraine, Kyiv, Ukraine

**T. M. Budnyak** Chuiko Institute of Surface Chemistry of National Academy of Sciences of Ukraine, Kyiv, Ukraine

**A. Burlaka** R.E. Kavetsky Institute of Experimental Pathology, Oncology and Radiobiology of the National Academy of Sciences of Ukraine, Kyiv, Ukraine

**D. Chalyy** Lviv State University of Life Safety, Lviv, Ukraine

**V. Demchenko** Institute of Macromolecular Chemistry, The National Academy of Sciences of Ukraine, Kyiv, Ukraine

**Zbigniew Dendzik** Institute of Physics, University of Silesia, Chorzow, Poland  
Silesian Center for Education and Interdisciplinary Research, University of Silesia, Chorzow, Poland

**O. A. Diyuk** Institute for Sorption and Problems of Endoecology, National Academy of Sciences of Ukraine, Kyiv, Ukraine

**Tetiana Dontsova** Department of Inorganic Substances Technology, Water Treatment and General Chemical Engineering, National Technical University of Ukraine “Igor Sikorsky Kyiv Polytechnic Institute”, Kyiv, Ukraine

**Yuliya Dzyazko** V. I. Vernadsky Institute of General and Inorganic Chemistry of the National Academy of Science of Ukraine, Kyiv, Ukraine

**Yurii Fedenko** Department of Inorganic Substances Technology, Water Treatment and General Chemical Engineering, National Technical University of Ukraine “Igor Sikorsky Kyiv Polytechnic Institute”, Kyiv, Ukraine

**O. M. Fesenko** Institute of Physics of National Academy Sciences of Ukraine, Kyiv, Ukraine

**L. A. Frolova** Ukrainian State Chemical Technology University, Dnipro, Ukraine

**Angelina Gab** University “Ukraine”, Kyiv, Ukraine

**I. I. Gab** Frantsevich Institute for Problems of Materials Science of National Academy Sciences of Ukraine, Kyiv, Ukraine

**J. Gabrusenoks** Institute of Solid State Physics, University of Latvia, Riga, Latvia

**Marcelle Gaune-Escard** Ecole Polytechnique, CNRS UMR 6595, Technopôle deChateau Gombert, Marseille Cedex 13, France

**Barbara Gawdzik** Faculty of Chemistry, Maria Curie-Sklodowska University, Lublin, Poland

**Zygmunt Gburski** Institute of Physics, University of Silesia, Katowice, Poland  
Silesian Centre of Education & Interdisciplinary Research, Chorzów, Poland

**L. Goncharenko** Institute of Macromolecular Chemistry, The National Academy of Sciences of Ukraine, Kyiv, Ukraine

**P. P. Gorbyk** Chuiko Institute of Surface Chemistry of National Academy of Sciences of Ukraine, Kyiv, Ukraine

**Krzysztof Górny** Institute of Physics, University of Silesia, Chorzow, Poland  
Silesian Center for Education and Interdisciplinary Research, University of Silesia, Chorzow, Poland

**Iurii Gudyma** Department of General Physics, Technical and Computer Sciences, Yuriy Fedkovych Chernivtsi National University, Chernivtsi, Ukraine

**I. Hadzaman** Drohobych State Pedagogical University, Drohobych, Ukraine

**V. O. Hryn** Institute of Physics, National Academy of Sciences of Ukraine, Kyiv, Ukraine

**A. Ingram** Opole University of Technology, Opole, Poland

**Oleksandr Ishtvanik** University “Ukraine”, Kyiv, Ukraine

**Maksym V. Iurzhenko** Institute of Macromolecular Chemistry of National Academy of Sciences, Kyiv, Ukraine

**Iryna Ivanenko** Department of Inorganic Substances Technology, Water Treatment and General Chemical Engineering, National Technical University of Ukraine “Igor Sikorsky Kyiv Polytechnic Institute”, Kyiv, Ukraine

**Shashank Narayan Kane** Magnetic Materials Laboratory, School of Physics, D. A. University, Indore, India

**L. V. Karabanova** Institute of Macromolecular Chemistry of National Academy of Sciences of Ukraine, Kyiv, Ukraine

**I. Karbovnyk** Ivan Franko National University of Lviv, Lviv, Ukraine

**Panagiotis Klonos** Department of Physics, National Technical University of Athens, Athens, Greece

**H. Klym** Lviv Polytechnic National University, Lviv, Ukraine

**S. Kobylinskyi** Institute of Macromolecular Chemistry, The National Academy of Sciences of Ukraine, Kyiv, Ukraine

**S. V. Kolotilov** L. V. Pisarzhevskii Institute of Physical Chemistry, National Academy of Sciences of Ukraine, Kyiv, Ukraine

**Yu. Kostiv** Lviv Polytechnic National University, Lviv, Ukraine

**B. D. Kostyuk** Frantsevich Institute for Problems of Materials Science of National Academy Sciences of Ukraine, Kyiv, Ukraine

**I. G. Kovzun** F. D. Ovcharenko Institute of Biocolloid Chemistry of National Academy of Sciences of Ukraine, Kyiv, Ukraine

**Roman Kozakevych** Chuiko Institute of Surface Chemistry, National Academy of Sciences of Ukraine, Kyiv, Ukraine

**O. A. Kushnerov** Oles Honchar Dnipropetrovsk National University, Dnipro, Ukraine

**N. V. Kusyak** Ivan Franko Zhytomyr State University, Zhytomyr, Ukraine

**N. Kutsevol** National Taras Shevchenko University of Kyiv, Kyiv, Ukraine

**A. W. Lloyd** University of Brighton, Brighton, UK

**Tetiana Lukashenko** University “Ukraine”, Kyiv, Ukraine

**S. Lukin** R.E. Kavetsky Institute of Experimental Pathology, Oncology and Radiobiology of the National Academy of Sciences of Ukraine, Kyiv, Ukraine

**Lucian Lupascu** Institute of Chemistry of the Academy of Sciences of Moldova, Chisinau, Republic of Moldova

**Tudor Lupascu** Institute of Chemistry of the Academy of Sciences of Moldova, Chisinau, Republic of Moldova

**Antonnia Maizelis** National Technical University “Kharkiv Polytechnic Institute”, Kharkiv, Ukraine

**D. Makiela** Institute of Physics, University of Silesia, Katowice, Poland  
Silesian Centre of Education & Interdisciplinary Research, Chorzów, Poland

**Artur Maksymov Marian** Smoluchowski Institute of Physics, Jagiellonian University, Krakow, Poland

**Viktor Malyshev** University “Ukraine”, Kyiv, Ukraine

**Yevgen P. Mamunya** Institute of Macromolecular Chemistry of National Academy of Sciences of Ukraine, Kyiv, Ukraine

**Liubov K. Matkovska** Institute of Macromolecular Chemistry of National Academy of Sciences of Ukraine, Kyiv, Ukraine  
Université de Lyon, Université Lyon 1, Ingénierie des Matériaux Polymères, UMR CNRS 5223, Villeurbanne, France

**Ludmila Yu. Matzui** Departments of Physics and Institute of High Technologies, Taras Shevchenko National University of Kyiv, Kyiv, Ukraine

**S. V. Mikhailovsky** University of Brighton, Brighton, UK

**Yurii S. Milovanov** Departments of Physics and Institute of High Technologies, Taras Shevchenko National University of Kyiv, Kyiv, Ukraine

**O. Nadтока** National Taras Shevchenko University of Kyiv, Kyiv, Ukraine

**Svitlana Nahirniak** Faculty of Chemical Technology, National Technical University of Ukraine “Igor Sikorsky Kyiv Polytechnic Institute”, Kyiv, Ukraine

**Y. V. Naidich** Frantsevich Institute for Problems of Materials Science of National Academy Sciences of Ukraine, Kyiv, Ukraine

**S. G. Nedilko** Taras Shevchenko National University of Kyiv, Kyiv, Ukraine

**V. Neimash** Institute of Physics of the National Academy of Sciences of Ukraine, Kyiv, Ukraine

**Tatyana A. Nenastina** National Technical University “Kharkiv Polytechnic Institute”, Kharkiv, Ukraine

**O. M. Nikipelova** State agency “Ukrainian Research Institute of Medical Rehabilitation and Balneology, Ministry of Health of Ukraine”, Odessa, Ukraine

**V. O. Oliinyk** F. D. Ovcharenko Institute of Biocolloid Chemistry of National Academy of Sciences of Ukraine, Kyiv, Ukraine

**A. Onanko** National Taras Shevchenko University of Kyiv, Kyiv, Ukraine

**V. Orel** National Cancer Institute, Kyiv, Ukraine

National Technical University of Ukraine “Igor Sikorsky Kyiv Polytechnic Institute”, Kyiv, Ukraine

**O. P. Ostash** Karpenko Physico-Mechanical Institute of the National Academy of Sciences of Ukraine, Lviv, Ukraine

**Mateusz Pabiszczak** Institute of Physics, University of Silesia, Katowice, Poland  
Silesian Centre of Education & Interdisciplinary Research, Chorzów, Poland

**A. V. Panko** F. D. Ovcharenko Institute of Biocolloid Chemistry of National Academy of Sciences of Ukraine, Kyiv, Ukraine

**Yulia S. Perets** Departments of Physics and Institute of High Technologies, Taras Shevchenko National University of Kyiv, Kyiv, Ukraine

**V. Ya. Podhurska** Karpenko Physico-Mechanical Institute of the National Academy of Sciences of Ukraine, Lviv, Ukraine

**A. L. Petranovska** Chuiko Institute of Surface Chemistry of National Academy of Sciences of Ukraine, Kyiv, Ukraine

**Polycarpus Pissis** Department of Physics, National Technical University of Athens, Athens, Greece

**O. A. Pivovarov** Ukrainian State Chemical Technology University, Dnipro, Ukraine

**Beata Podkoscielna** Faculty of Chemistry, Maria Curie-Skłodowska University, Lublin, Poland

**Kateryna Polonska** Department of General Physics, Institute of Physical, Technical and Computer Sciences, Yuriy Fedkovych Chernivtsi National University, Chernivtsi, Ukraine

**Ludmila Ponomarova** V. I. Vernadsky Institute of General and Inorganic Chemistry of the National Academy of Sciences of Ukraine, Kyiv, Ukraine

**V. A. Prokopenko** F. D. Ovcharenko Institute of Biocolloid Chemistry of National Academy of Sciences of Ukraine, Kyiv, Ukraine

National Technical University of Ukraine “KPI”, Kyiv, Ukraine



**Ie. V. Pylypchuk** Chuiko Institute of Surface Chemistry of National Academy of Sciences of Ukraine, Kyiv, Ukraine

**Violetta Raczyńska** Institute of Physics, University of Silesia, Chorzow, Poland

**Przemysław Raczyński** Institute of Physics, University of Silesia, Chorzow, Poland

Silesian Center for Education and Interdisciplinary Research, University of Silesia, Chorzow, Poland

**S. Riabov** Institute of Macromolecular Chemistry, The National Academy of Sciences of Ukraine, Kyiv, Ukraine

**A. Romanov** National Cancer Institute, Kyiv, Ukraine

**P. C. Rossi** Department of Chemical Technology, National University of Río Cuarto, Río Cuarto, Córdoba, Argentina

**V. I. Rudenko** Institute of Physics, National Academy of Sciences of Ukraine, Kyiv, Ukraine

**N. Rybalchenko** Zabolotny Institute of Microbiology and Virology, The National Academy of Sciences of Ukraine, Kyiv, Ukraine

**O. Rykhalskyi** National Cancer Institute, Kyiv, Ukraine

National Technical University of Ukraine “Igor Sikorsky Kyiv Polytechnic Institute”, Kyiv, Ukraine

**O. V. Sachuk** Institute for Sorption and Problems of Endoecology, National Academy of Sciences of Ukraine, Kyiv, Ukraine

**Nikolay D. Sakhnenko** National Technical University “Kharkiv Polytechnic Institute”, Kharkiv, Ukraine

**Manvi Satalkar** Magnetic Materials Laboratory, School of Physics, D. A. University, Indore, India

**Z. Sawlowicz** Institute of Geology, Jagiellonian University, Krakow, Poland

**Sergey Scherbakov** M. G. Kholodny Institute of Botany of the National Academy of Science of Ukraine, Kyiv, Ukraine

**Stanislav Sevostianov** Chuiko Institute of Surface Chemistry, National Academy of Sciences of Ukraine, Kyiv, Ukraine

**D. B. Shakhnin** V.I. Vernadsky Institute of General and Inorganic Chemistry of National Academy Sciences of Ukraine, Kyiv, Ukraine

**Dmytro Shakhnin** University “Ukraine”, Kyiv, Ukraine

**S. M. Shcherbakov** M. G. Kholodny Institute of Botany of the National Academy of Science of Ukraine, Kyiv, Ukraine

**A. Shevchenko** G.V. Kurdyumov Institute for Metal Physics of the National Academy of Sciences of Ukraine, Kyiv, Ukraine

**O. Shpotyuk** Vlokh Institute of Physical Optics, Lviv, Ukraine  
Jan Dlugosz University in Czestochowa, Czestochowa, Poland

**T. N. Smirnova** Institute of Physics, National Academy of Sciences of Ukraine, Kyiv, Ukraine

**Valentin Sosenkin** A.N. Frumkin Institute of Physical Chemistry and Electrochemistry of the Russian Academy of Science, Moscow, Russia

**V. L. Starchevskyy** National University “Lviv Polytechnic”, Lviv, Ukraine

**Dariusz Sternik** Faculty of Chemistry, Maria Curie-Sklodowska University, Lublin, Poland

**Andrew Stetsko** Faculty of computer engineering printing, Ukraine Academy of Printing, Lviv, Ukraine

**T. V. Stetsyuk** Frantsevich Institute for Problems of Materials Science of National Academy Sciences of Ukraine, Kyiv, Ukraine

**Tetiana Tatarchuk** Department of Pure and Applied Chemistry, Vasyl Stefanyk Precarpathian National University, Ivano-Frankivsk, Ukraine

Educational and Scientific Center of Chemical Materials Science and Nanotechnology, Vasyl Stefanyk Precarpathian National University, Ivano-Frankivsk, Ukraine

**Valentin Tertykh** Chuiko Institute of Surface Chemistry, National Academy of Sciences of Ukraine, Kyiv, Ukraine

**N. M. Tolstopalova** National Technical University of Ukraine “Igor Sikorsky Kyiv Polytechnic Institute”, Kyiv, Ukraine

**O. A. Tsyganovich** F. D. Ovcharenko Institute of Biocolloid Chemistry of National Academy of Sciences of Ukraine, Kyiv, Ukraine

**S. P. Turanksa** Chuiko Institute of Surface Chemistry of National Academy of Sciences of Ukraine, Kyiv, Ukraine

**Nataliia Uskova** University “Ukraine”, Kyiv, Ukraine  
Dumlupinar University, Kutahya, Turkey

**Zafer Ustundag** University “Ukraine”, Kyiv, Ukraine  
Dumlupinar University, Kutahya, Turkey

**I. Vasylyshyn** Lviv Polytechnic National University, Lviv, Ukraine

**B. D. Vasylyv** Karpenko Physico-Mechanical Institute of the National Academy of Sciences of Ukraine, Lviv, Ukraine

**Maryna V. Ved** National Technical University “Kharkiv Polytechnic Institute”, Kharkiv, Ukraine

**V. V. Vira** Lviv Polytechnic National University, Lviv, Ukraine

**Yurii Volfkovich** A.N. Frumkin Institute of Physical Chemistry and Electrochemistry of the Russian Academy of Science, Moscow, Russia

**Ludmila L. Vovchenko** Departments of Physics and Institute of High Technologies, Taras Shevchenko National University of Kyiv, Kyiv, Ukraine

**R. L. Whitby** University of Brighton, Brighton, UK

**P. N. Yakushev** Ioffe Institute, St. Petersburg, Russia

**Iryna Yu. Yermolenko** National Technical University “Kharkiv Polytechnic Institute”, Kharkiv, Ukraine

**O. I. Zakutevskyy** Institute for Sorption and Problems of Endoecology, National Academy of Sciences of Ukraine, Kyiv, Ukraine

**V. A. Zazhigalov** Institute for Sorption and Problems of Endoecology, National Academy of Sciences of Ukraine, Kyiv, Ukraine

**Part I**  
**Nanochemistry and Biotechnology**

# Chapter 1

## Nanostructured Functional Coatings of Iron Family Metals with Refractory Elements



Maryna V. Ved', Nikolay D. Sakhnenko, Iryna Yu. Yermolenko, and Tatyana A. Nenastina

Solving the applied problems in the development of new technologies and extending a range of functional materials predetermine the interest of researchers and technologists in the galvanic multicomponent alloys. Special attention is paid to the electrochemical synthesis of iron triad metal alloys with  $d^4$ -elements, namely, Fe(Ni, Co)–Mo(W) [1]. Such coatings are interesting by the possibility of combining functional properties that exceed alloying metals [2]. Comprehensive realization in the thin layers of improved microhardness, wear and corrosion resistance, and catalytic and magnetic properties makes it possible to significantly expand the scope of such coating usage [3].

Spheres of multicomponent coating application are replacement of electrolytic toxic chromium [4] and hardening of the surface [5, 6], corrosion protection [7, 8], and magnetic films with increased microhardness [9, 10].

Eco-friendly fuel cells (FC) and solar cells (SC) are among the promising renewable energy sources; however, the high cost of the noble metal electrodes prevents their dissemination and widespread use [11, 12]. Development of FC, SC, and various redox flow batteries (RFB) needs to create effective catalytically active electrodes on the basis of transition metal alloys [13, 14]. The presence in such alloys of metals with different affinity for oxygen and hydrogen opens up prospects for their use as the catalysts and electrode materials for current sources [15]. Also, it demonstrated the possibility of using multicomponent coatings as electrocatalytic materials for hydrogen synthesis [16] and active layers for detoxification of toxins [17].

Utilization of the electrochemical methods for thin alloy coating synthesis displays interactions in the chain “process parameters, composition and structure of the material, properties, functions, and application.” Of course, the advantage

---

M. V. Ved' · N. D. Sakhnenko · I. Y. Yermolenko (✉) · T. A. Nenastina  
National Technical University “Kharkiv Polytechnic Institute”, Kharkiv, Ukraine

of the above techniques for deposition of thin film multicomponent systems is the possibility to flexibly control the content of components, rate of deposition, and surface condition through the variation of the composition of electrolytes and regimes of polarization (static or pulse, reverse current, or a decrease in potential) [18, 19]. Because of this it is possible to fabricate the deposits of varied qualitative and quantitative composition and with desirable functional properties, such as microhardness; wear-, thermo-, chemical, and corrosion resistance; catalytic activity; etc. [20–22].

Most researchers note outstanding properties of synergistic metal alloys of the iron triad with d4-elements. Thus, the results of studies [4, 8, 23] show that the Fe-W, Co-W, and Co-W-Fe alloys successfully compete with galvanic chromium on wear and corrosion resistance. The hardness of the Co-W-Fe alloys with the content of tungsten  $\approx 30\%$  by mass is close to the hardness of chromium coatings, while the corrosion resistance is considerably higher. The Co-W coatings synthesized by the authors of [24] demonstrate microhardness of 550 HV. The represented results [15] demonstrate a considerable increase in the microhardness and corrosion resistance of Co-Mo-W coatings in comparison with the material of the substrate. Of practical interest are studies of the authors of [5, 6] on the electrosynthesis of the ternary Fe-Mo-W alloys with improved physical, mechanical, and anticorrosion properties. Improved electrocatalytic activity of the binary alloys Co-W was demonstrated for the model reaction of the electrolytic hydrogen evolution [8], catalytic oxidation of benzene [17], and catalytic methanol oxidation in acidic media [25].

It should be noted that most of the published results deal with the binary Fe(Ni, Co)-Mo(W) alloys. More to the point, the main attention is paid to the composition of electrolytes. The world scientific literature presents a significant number of positive results of the multicomponent alloy deposition from the gluconate-chloride [4], citrate and citrate-ammonia [23], pyrophosphate [26], and sulfate-citrate [27] electrolytes by galvanostatic and nonstationary mode. However, the main problem of the presented technologies remains the low content of refractory components and current efficiency.

It is obvious that the formation of coatings in each individual case depends first on the qualitative [28] and quantitative [29] composition of electrolyte. The variation in the electrolyte component concentration is an effective tool for leveling of the potential difference of alloying components, according to the theory of co-deposition of several metals in the alloy [30]. Therefore, not only the concentrations of alloying components and their ratios but also the content of the ligand in the electrolyte, namely, the lack or excess of citrate ion concentration relative to the total concentration of complexing agents, will affect the composition and morphology and, consequently, the properties of the coatings.

Secondly, the composition of electrolytic deposits, the ratio of components, and the phase composition of coatings are essentially affected by the synthesis conditions [31]. In turn, the structure of alloy predetermines the properties and areas of application of coatings.

**Table 1.1** Electrolytes for deposition of Fe-Co-W coating

Component concentration, mol/dm <sup>3</sup>	The ratio $c(\text{Fe}^{3+}): c(\text{Co}^{2+}): c(\text{WO}_4^{2-}): c(\text{Cit}^{3-})$		
	W1	W2	W3
	1: 1: 0.4: 2	1: 1.3: 0.6: 2.7	1: 1.3: 0.6: 3.3
Fe <sub>2</sub> (SO <sub>4</sub> ) <sub>3</sub> ·9H <sub>2</sub> O	0.075	0.075	0.075
CoSO <sub>4</sub> ·7H <sub>2</sub> O	0.15	0.2	0.2
Na <sub>2</sub> WO <sub>4</sub> ·2H <sub>2</sub> O	0.06	0.06	0.06
Na <sub>3</sub> Cit·2H <sub>2</sub> O	0.3	0.4	0.5
Na <sub>2</sub> SO <sub>4</sub>	0.15	0.15	0.15
H <sub>3</sub> BO <sub>3</sub>	0.1	0.1	0.1
pH	3.8	4.3	4.55

Given this, a detailed study is required of the influence of parameters of the pulse electrolysis on the composition, morphology, and, consequently, the properties of promising, in our opinion, Fe-Co-W, Fe-Co-Mo, and Co-Mo-Zr alloys.

## 1.1 Experimental

Ternary coatings were deposited onto planar samples out of two metals: copper and mild steel. Pretreatment of copper sample surface included mechanical polishing, degreasing, chemical etching in a mixture of the 50% nitric and 50% sulfuric acids, thorough washing with distilled water, and drying. Pretreatment of steel samples included grinding, degreasing in a solution of sodium carbonate at 50 °C, washing, etching in a mixture of hydrochloric acid and sulfuric acid at a temperature of 20 °C, and thoroughly washing in flowing water.

Coatings Fe-Co-W were formed from electrolytes of the composition provided in Table 1.1; the pH value was adjusted within the range of 3.8–4.6 by addition of sulfuric acid or sodium hydroxide.

Coatings Fe-Co-Mo were deposited from electrolytes with different ratio of alloying components as shown in Tables 1.2 and 1.3; the pH value was adjusted within the range of 4.0–4.9.

Coatings Co-Mo-Zr were deposited from complex bi-ligand citrate-pyrophosphate electrolyte of composition (mol/dm<sup>3</sup>): CoSO<sub>4</sub>·7H<sub>2</sub>O, 0.15; Na<sub>2</sub>MoO<sub>4</sub>·2H<sub>2</sub>O, 0.06; Zr(SO<sub>4</sub>)<sub>2</sub>·4H<sub>2</sub>O, 0.05; Na<sub>3</sub>C<sub>6</sub>H<sub>5</sub>O<sub>7</sub>·2H<sub>2</sub>O, 0.2; and K<sub>4</sub>P<sub>2</sub>O<sub>7</sub>, 0.1. The pH value of electrolytes was adjusted within the range of 8–9 by sodium hydroxide [15].

All electrolytes were prepared from analytically pure reagents, dissolved in a small amount of distilled water followed by solution mixture in a certain sequence, based on the ionic equilibrium study results [32]. The acidity of solutions was controlled by pH-meter pH -150 M with the glass electrode ESL-6307. Electrolyte temperature during deposition was varied in the range of 25–50 °C.

The Fe-Co-W(Mo) coatings were formed in two modes: (i) galvanostatic with the current density  $i$  of 2–7 A/dm<sup>2</sup> and (ii) unipolar pulsed with current amplitude

**Table 1.2** Electrolytes for deposition of Fe-Co-Mo coating

Component concentration, mol/dm <sup>3</sup>	Electrolyte $c(\text{Fe}^{3+}):c(\text{Co}^{2+}):c(\text{MoO}_4^{2-}):c(\text{Cit}^{3-}) = 1:1:0.5:2$				
	Mo1	Mo2	Mo3	Mo4	Mo5
$\text{Fe}_2(\text{SO}_4)_3 \cdot 9\text{H}_2\text{O}$	0.075	0.083	0.090	0.097	0.113
$\text{CoSO}_4 \cdot 7\text{H}_2\text{O}$	0.150	0.165	0.180	0.195	0.225
$\text{Na}_2\text{MoO}_4 \cdot 2\text{H}_2\text{O}$	0.080	0.088	0.096	0.104	0.120
$\text{Na}_3\text{Cit} \cdot 2\text{H}_2\text{O}$	0.3	0.33	0.36	0.39	0.45
$\text{Na}_2\text{SO}_4$	0.1	0.11	0.12	0.13	0.15
$\text{H}_3\text{BO}_3$	0.1	0.11	0.12	0.13	0.15
pH	4.85	4.65	4.50	4.30	4.45

**Table 1.3** Electrolytes for deposition of Fe-Co-Mo coating

Component concentration, mol/dm <sup>3</sup>	Electrolyte			
	Mo6	Mo7	Mo8	Mo9
	$c(\text{Fe}^{3+}):c(\text{Co}^{2+}):c(\text{MoO}_4^{2-}):c(\text{Cit}^{3-})$			
	1:1.3:0.4:2	1:1.3:0.4:2.7	1:1.3:0.4:3.3	1:2:0.6:5
$\text{Fe}_2(\text{SO}_4)_3 \cdot 9\text{H}_2\text{O}$	0.075	0.075	0.075	0.050
$\text{CoSO}_4 \cdot 7\text{H}_2\text{O}$	0.200	0.200	0.200	0.200
$\text{Na}_2\text{MoO}_4 \cdot 2\text{H}_2\text{O}$	0.06	0.06	0.06	0.06
$\text{Na}_3\text{Cit} \cdot 2\text{H}_2\text{O}$	0.3	0.4	0.5	0.4
$\text{Na}_2\text{SO}_4$	0.15	0.15	0.15	0.15
$\text{H}_3\text{BO}_3$	0.1	0.1	0.1	0.1
pH	4.2	4.8	5.15	4.85

$i$  of 2–6 A/dm<sup>2</sup> at an on-time (pulse duration)  $t_{\text{on}} = 1 \cdot 10^{-2}$ – $2 \cdot 10^{-2}$  s and off-time (pause duration)  $t_{\text{off}} = 1 \cdot 10^{-2}$ – $5 \cdot 10^{-2}$  s. As anode served plates of AISI 304 steel, the cathode-to-anode area ratio was 1: 5, and the volume current density was kept at the level of 2 A/dm<sup>3</sup>.

The Co-Mo-Zr deposits were formed in unipolar pulsed mode with current amplitude of 2–15 A·dm<sup>-2</sup> in the frequency  $f$  range of 19–910 Hz at a pulse duration  $t_{\text{on}} = 2$ –50 ms and pause time  $t_{\text{off}} = 5$ –50 ms; duty factor  $q = (t_{\text{on}} + t_{\text{off}})/t_{\text{on}}$  was 2–26. Coplanar cobalt plates were used as anodes; the cathode-to-anode area ratio was kept at 1: 5.

Both the galvanostatic and pulse electrolysis were performed using dc and pulse current supply unit (ZY-100 ± 12).

The electrode potentials were measured relative to an EVL-1 M1 silver chloride reference electrode connected to the working cell via a salt bridge filled with saturated potassium chloride solution jellied with Ceylon gelatin. The potentials presented in the paper are given relative to the standard hydrogen electrode (SHE).

The electrodeposition current efficiency  $C_e$  (%) was determined from the weight and chemical composition of the deposited alloys and the charge passed using the electrochemical equivalent of the alloy. The thickness of the deposits was calculated from a sample actual weight increase after the electrolysis.



The chemical composition of the coatings was determined by energy-dispersive X-ray spectroscopy (EDS) on an Oxford INCA Energy 350 electron probe micro-analysis integrated into the system of the SEM. The X-rays were excited by exposure of the samples to a beam of 15 keV electrons. The surface morphology of the deposits was studied with a Zeiss EVO 40XVP scanning electron microscope (SEM). Images were recorded by the registration of secondary electrons (SEs) via scanning with an electron beam; this mode made it possible to study the topography with a high resolution and contrast ratio.

The surface morphology of thin films was studied by an atomic force microscopy (AFM) using a NT-206 scanning probe microscope. The tapping mode was conducted to measure sample surface morphologies. Scanning was performed by using the contact probe CSC-37 with a cantilever lateral resolution of 3 nm [33]. The scan area sizes were fixed at different scopes, namely,  $39.9 \times 39.9 \mu\text{m}$ ,  $20.0 \times 20.0 \mu\text{m}$ ,  $10.0 \times 10.0 \mu\text{m}$ , and  $5.0 \times 5.0 \mu\text{m}$ , and the height of the surface relief was recorded at the resolution of  $256 \times 256$  pixels. For each sample, a variety of scans were obtained at random locations on the surface of thin films. In order to analyze the AFM images, all image data were converted into Surface Explorer software.

The structure of the deposits was examined by X-ray diffraction analysis using a diffractometer (DRON-2.0) in the emission of iron (cobalt) anode and  $\text{CuK}\alpha$  radiation. X-ray patterns were recorded in discrete mode with a step  $2\theta = 0.1^\circ$  with the exposure at each point for 20 s; the operating voltage was 35 kV and current, 20 mA.

Magnetic characteristics of the Fe-Co-W(Mo) thin films were measured using the vibration magnetometer for the fields up to  $1600 \text{ kA}\cdot\text{m}^{-2}$ . The coercive force  $H_c$  and the saturation field  $H_s$  were defined by hysteresis loops measured in the fields applied to the coating plane. The saturation magnetization  $I_s$  and the saturation induction  $B_s$  were estimated by hysteresis loops obtained for the magnetization of specimens by the film plane normal.

Corrosion tests of coated samples were carried out in a model media of 1 M sodium sulfate with the addition of sulfuric acid to pH 3 or potassium hydroxide to pH 11 and in 3% potassium chloride (pH 7). The corrosion current was determined by the polarization resistance technique using digital analysis of anodic and cathodic plots in Tafel coordinates within the range of 200–300 mV from open circuit potential [34]. The potentiostat IPC-Pro controlled by PC was used for voltammetry measurements with scan rate of 1 mV/s. Corrosion depth index  $k_h$  (mm per year) was converted from corrosion current:

$$k_h = (8.76k_e i_{\text{cor}}) / \rho,$$

where  $k_e$  is the electrochemical equivalent of alloy,  $\text{kg}\cdot\text{C}^{-1}$ ;  $i_{\text{cor}}$  the corrosion current density,  $\text{A}/\text{m}^2$ ; and  $\rho$  the density of the alloy,  $\text{kg}/\text{m}^3$ . Electrochemical equivalent  $k_e$  and density  $\rho$  of the alloys were determined considering their quantitative composition [35].

The results were verified by mass metric (gravimetric) tests and spectroscopy of electrode impedance.

Electrocatalytic properties of coatings were studied in model reaction of electrolytic hydrogen evolution from acidic and alkali media. The hydrogen exchange current density  $i_{\text{H}}^0$  is utilized as the criteria of electrochemical catalysis since this parameter is independent of the electrode potential. Experimentally  $i_{\text{H}}^0$  was determined at the point of intersection, the linear portion of the cathodic polarization dependence in Tafel coordinates at zero overvoltage [35].

The testing of catalytic properties was also carried out in the process of the carbon (II) oxide oxidation in a tubular flow reactor fabricated from quartz glass with the coaxially situated heating element. Initial mixture of CO (1 vol.%) and air was supplied to the reactor inlet at a rate of 0.025 dm<sup>3</sup>/min. Reactor temperature was increased gradually from 20 to 420 °C. Content of CO in the final mixture was analyzed using the indicator-analyzer "Dozor" [36].

### 1.1.1 FeCoW Alloy

The choice of the quantitative composition of electrolyte is based on accounting the competing reactions of iron (III) hydrolysis and citrate anion protonation that determined the ionic equilibrium in the solution and the solution pH. In addition, peculiarities of the electrochemical behavior of the electrolyte components were taken into account [32]. Increasing the concentration of citrate ions in solution at fixed Fe<sup>3+</sup> content expectedly increases the electrolyte pH (Table 1.1). The protonation of citrate anions decreases with pH, while the degree of Fe<sup>3+</sup> hydrolysis increases; therefore ionic forms of complexing agents and ligand in the electrolytes are different. Consequently, the composition of particles discharged at the electrode varies, which effects the composition of coatings.

Fe-Co-Mo alloy deposition occurs by competitive reduction of iron, cobalt, and tungsten. The form of competition depends on the ratio of electrolyte components and electrolysis parameters (Fig. 1.1). We observe a slight decrease in the cobalt content without changing the iron portion in the alloy at current densities of 2.0–3.0 A/dm<sup>2</sup> when components' concentration ratio in the electrolyte  $c(\text{Fe}^{3+}):c(\text{Co}^{2+}):c(\text{WO}_4^{2-}):c(\text{Cit}^{3-})$  is 1:1:0.4:2 (Fig. 1.1a). Coatings are enriched with cobalt at the expense of iron if increasing  $i_c$  up to 4 A/dm<sup>2</sup>, but higher current density contributes cobalt content decreasing to 40 at.%. The tungsten content in the deposits increases with current density, but does not exceed to 8 at.%.

Changing the ratio of alloying component content in the electrolyte in favor of cobalt with the simultaneous increase of the ligand concentration up to 0.4 mol/dm<sup>3</sup> (electrolyte Mo2, Table 1.1) leads to an inversion of the metal ratio in the alloy (Fig. 1.1b). This occurs as a result of a change in the composition of heteronuclear complexes discharged at the electrode. The cobalt content exceeds the iron portion in coatings deposited at current densities of 3–7 A/dm<sup>2</sup>. A trend to gradually decreasing the cobalt content is observed with increasing current density

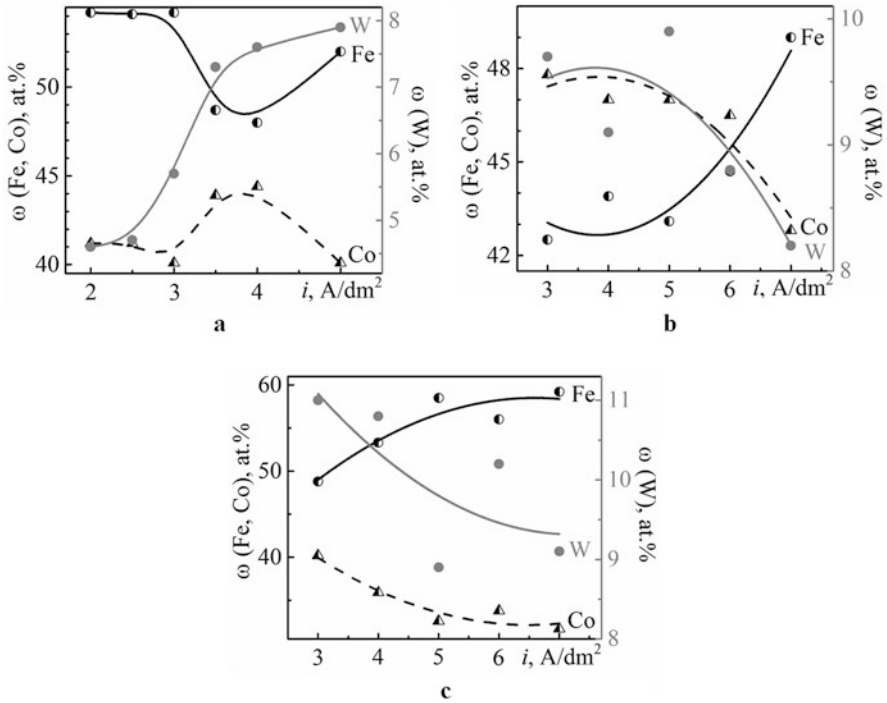


**Fig. 1.1** Current density effect on Fe-Co-W coating composition deposited from electrolytes: W1 (a), W2 (b), W3 (c)

(Fig. 1.1b). Iron and cobalt are co-deposited in the alloy in the ratio of 1:1 at a current density of 6 A/dm<sup>2</sup>. Further rising  $i_c$  promotes a significant increase in iron content at the expense of cobalt and tungsten. The refractory component content in the alloy varies within 8–10 at.% with a tendency to decrease at rising current density. It should be noted that iron, cobalt, and tungsten are co-deposited at the alloy in proportion to 4.5:5:1, respectively, at alloy components ratio in electrolyte  $c(\text{Fe}^{3+}):c(\text{Co}^{2+}):c(\text{WO}_4^{2-}) = 2.5:3:1$ . Thus soluble anodes can be recommended for continuous operation of the electrolyte [37].

Tungsten content increases slightly (9–11 at.%) if the citrate concentration in the solution is 0.5 mol/dm<sup>3</sup> at the other conditions being equal (Fig. 1.1c). However, the trend to tungsten content decreasing with rising current density is maintained. At the same time, the competitive reduction of iron and cobalt becomes more significant. The iron content in the coating increases to 59 at.% with a simultaneous decreasing in cobalt portion to 30 at.% when rising current density from 3 to 7 A/dm<sup>2</sup> as we can see from Fig 1.1c.

The efficiency of galvanostatic deposition does not exceed 45%, regardless of the electrolyte concentration. Increasing  $i_c$  to 7 A/dm<sup>2</sup> reduces the current efficiency to 27% due to side reaction of hydrogen evolution. Deposited in stationary mode, Fe-Co-W coatings have globular morphology of surface with a grain sizes of 2–6  $\mu\text{m}$  (Fig. 1.2a).

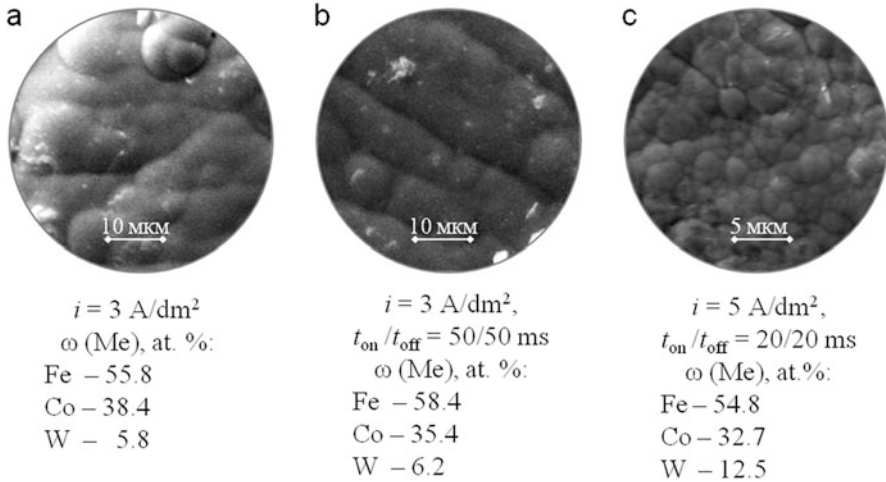


**Fig. 1.2** The morphology of Fe-Co-W coatings deposited in galvanostatic (a) and pulse (b, c) modes from electrolytes: W1 (a, b), W3 (c)

Coatings deposited in pulse mode contain expanded amount of refractory metals and are more uniform (Fig. 1.2b). The tungsten content in the coatings deposited by pulse current from electrolyte W3 (Table 1.1) is of 12.5 at.%. On more developed surface enriched with tungsten coatings, we can see agglomerates of spheroids (Fig. 1.2c).

Time parameters of pulsed electrolysis are an effective tool for controlling the composition and nature of the coating surface. Prolong pulse at a fixed pause time contributes an increasing of cobalt and tungsten content in the alloy at studied current densities (Fig. 1.3). At the same time, observed for the galvanostatic regime, a rising trend of iron content at the expense of cobalt and tungsten with increasing current density is preserved, as one can see in Fig. 1.3a, b.

The deposition efficiency increases almost twice when applying pulse current as compared with galvanostatic regime: at a current density of  $3 \text{ A/dm}^2$ , the current efficiency is 70–75%, and at  $4 \text{ A/dm}^2$   $\eta$  decreases to 63–68%, due to hydrogen evolution site reaction.

Traditionally in materials science, roughness is an indicator of surface quality and depends on the material processing. The roughness of galvanic coatings is the result of the alloy deposition and may serve as an additional indicator of the surface development as well as topography [38]. The coating samples Fe-Co-W containing refractory components of 10–12 at.% deposited on mild steel were studied by AFM analysis.

The substrate of mild steel is characterized by evenly surface (Fig. 1.4) with roughness  $R_a = 0.008$  and  $R_q = 0.011$ . However, the structure of surface is not ordered. The cross-sectional profile between markers 1 and 2 indicates that the grain sizes are in the range of 2–3  $\mu\text{m}$  as one can see from Fig. 1.4.

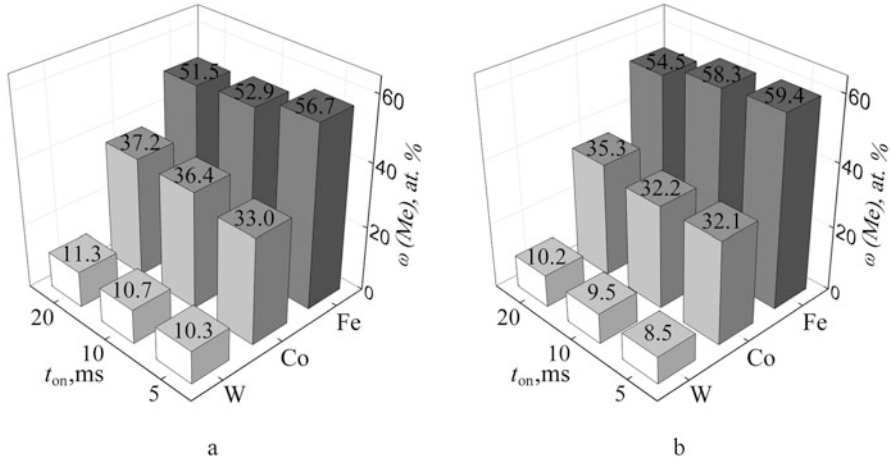


**Fig. 1.3** Pulse duration effect on the composition Fe-Co-W alloy deposited from electrolyte W2 at  $t_{\text{off}} = 10 \text{ ms}$ ; current density  $i$ ,  $\text{A/dm}^2$ : (a) 5, (b) 6

The data of the AFM analysis demonstrate the globular surface of the Fe-Co-W coatings, wherein larger spheroids of size of  $2.5\text{--}3.5 \mu\text{m}$  is formed with a smaller grains of sizes of  $0.2\text{--}0.5 \mu\text{m}$  as one can see from Fig. 1.5. It was found earlier [3] that globular structure of the surface is caused by the refractory metal incorporation into the alloy. Such composition and character of the surface are favorable for increasing microhardness, corrosion resistance, and catalytic activity of the material [4]. Surface roughness parameters for Fe-Co-W at scanning area  $5 \times 5 \mu\text{m}$  are defined as  $R_a = 0.06$  and  $R_q = 0.07$  that is much higher than those for the substrate and shows substantial development of the surface.

Figure 1.6 shows the results of X-ray diffraction analysis and phase structure for Fe-Co-W coatings of composition (in terms of metal) at.% (Fe, 54; Co, 36; W, 10), which is deposited on a copper substrate, and the thickness of the coating is of  $30 \mu\text{m}$ . The X-ray diffraction pattern indicates an amorphous-crystalline structure of the Fe-Co-W alloy (Fig. 1.6). We can see some lines of copper substrate, and lines corresponding to intermetallic phases  $\text{Co}_7\text{W}_6$  and  $\text{Fe}_7\text{W}_6$ , as well as  $\alpha\text{-Fe}$  and cementite  $\text{Fe}_3\text{C}$  at diffraction patterns. Besides, a low halo with width about  $10^\circ$  is detected at angles  $2\theta$   $50\text{--}55^\circ$  (Fig. 1.6), which corresponds to amorphous structure. The crystallite size of the amorphous part is  $L = 77 \text{ \AA}$ .

Phases  $\text{Co}_7\text{W}_6$ ,  $\text{Fe}_7\text{W}_6$ ,  $\alpha\text{-Fe}$ , and  $\text{Fe}_3\text{C}$  found in Fe-Co-W deposits reflect the competition of alloying metal reduction from hetero-nuclear complexes and confirm mechanism of co-deposition proposed in [32].

Thus ternary Fe-Co-W alloys with micro-globular surface of different composition were deposited by direct and pulse current from citrate Fe(III)-based electrolyte. Current density and time parameters of pulse electrolysis are shown to be affective tools to control the refractory metal content and electrolysis efficiency.

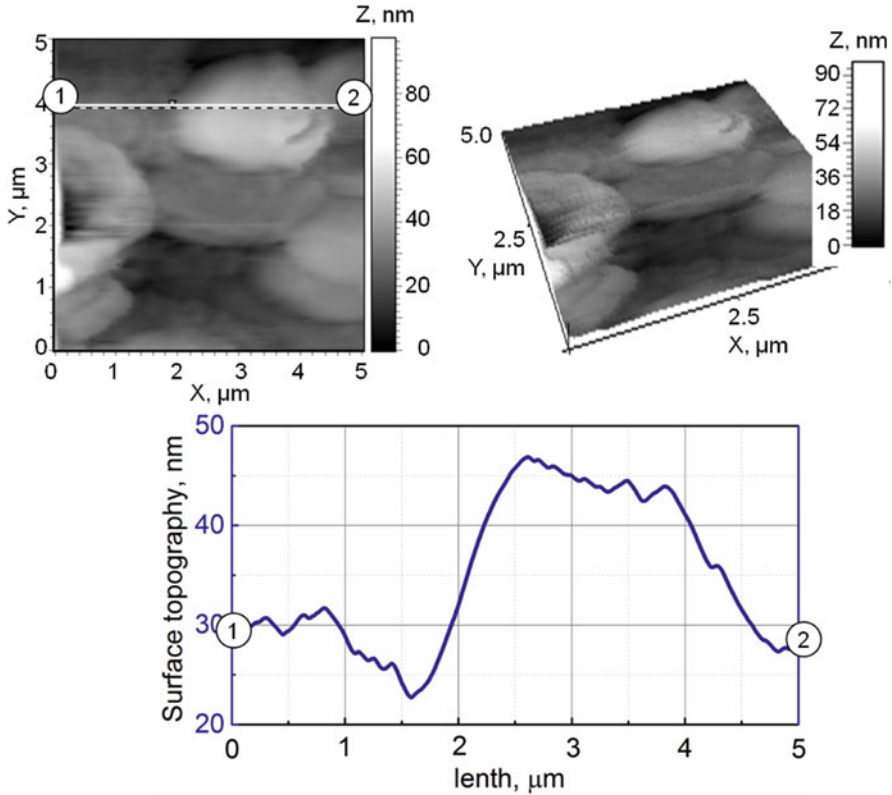


**Fig. 1.4** 2D and 3D maps of the surface and cross-sectional profile between markers 1 and 2 for mild steel substrate. Scan area AFM  $5.0 \times 5.0 \mu\text{m}$

### 1.1.2 FeCoMo Alloy

The elemental analysis of Fe-Co-Mo coatings deposited at direct current density of  $2 \text{ A/dm}^2$  from electrolytes Mo1–Mo5 shows that the metal content varies within 2 at.% (Fig. 1.7). The maximal molybdenum content was detected in the deposits obtained from the electrolyte Mo3 (Table. 1.2). Increasing the electrolyte concentration at a constant ratio of components promotes the alloy's enrichment with cobalt when deposited at current densities of  $3\text{--}6 \text{ A/dm}^2$ ; unfortunately, molybdenum portion decreases (Fig. 1.7a, b). Consequently, competitive reduction of cobalt and molybdenum in the alloy takes place that confirms involvement of particles of various natures in electrode reactions. On the contrary, we observe a trend to coating enrichment with molybdenum at the expense of cobalt when increasing current density in all electrolytes (Mo1–Mo5). Also, a gradual decreasing of iron portion by 5–6 at.% is noted with rising current density from 2 to  $6 \text{ A/dm}^2$  (Fig. 1.7c).

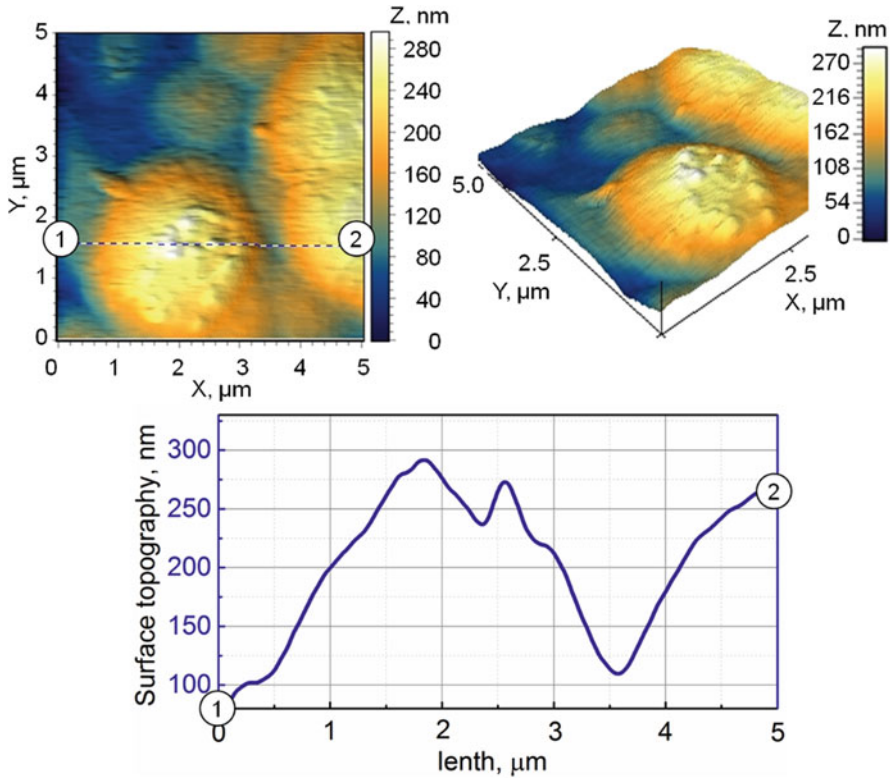


**Fig. 1.5** 2D and 3D map and cross-sectional profile of the surface Fe-Co-W between markers 1 and 2 deposited in pulse mode at current density  $4 \text{ A/dm}^2$ ;  $t_{\text{on}}/t_{\text{off}} = 10/10 \text{ ms}$ ;  $T = 25^\circ \text{C}$ ; pH 3.8; plated time 30 min. Scan area  $5.0 \times 5.0 \mu\text{m}$

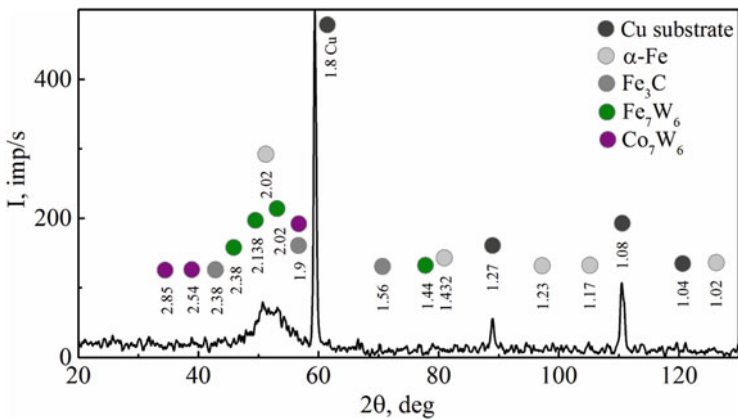


**Fig. 1.6** X-ray diffraction patterns for deposit Fe-Co-W, the composition is similar to Fig. 1.2c

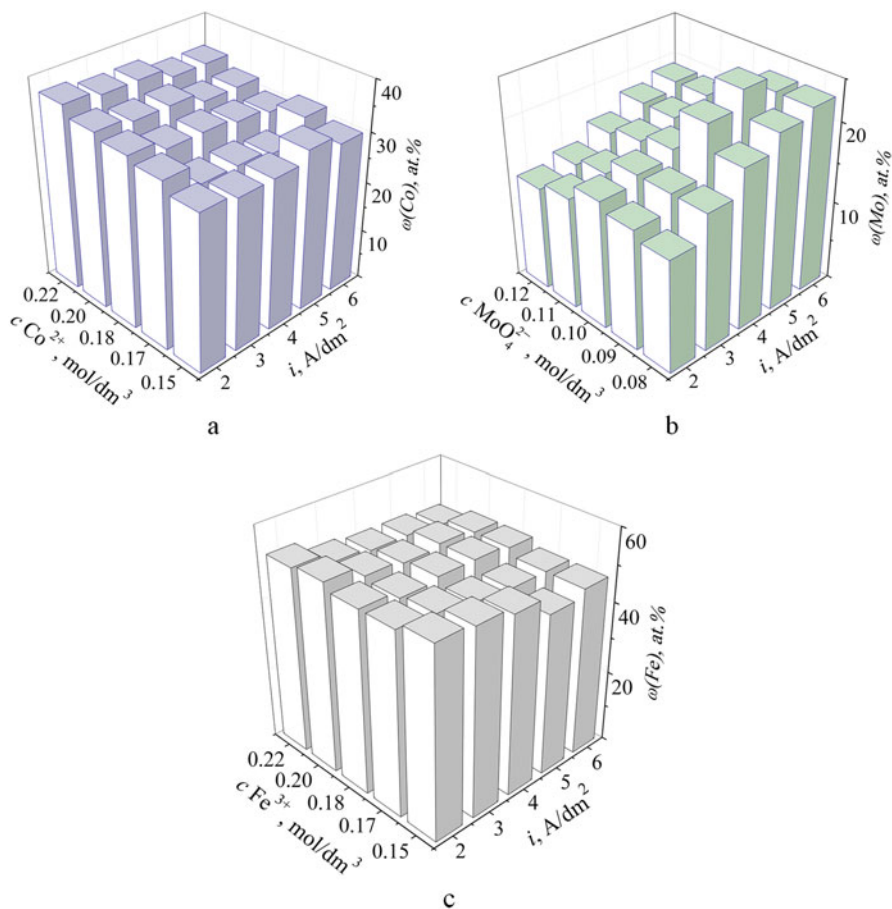


**Fig. 1.7** Effect of electrolyte concentration and current density on composition Fe-Co-Mo coating deposited from electrolytes Mo1–Mo5

Increasing the ligand concentration at fixed alloying component content in an electrolyte (Mo6–Mo8) promotes the coating enrichment with molybdenum at all else being equal electrolysis conditions. At the same time, the competitive reduction of iron and cobalt is more substantial. The cobalt content in the alloy regularly decreases to 27 at.% when citrate concentration rises to 0.5 mol/dm<sup>3</sup> (Fig. 1.8). The excess of citrate ions in the solution promotes formation of iron-citrate complexes  $[\text{FeHCit}]^+$  ( $\text{pK}_{\text{in}} = 6.3$ ), more stable than cobalt-citrate ones  $[\text{CoCit}]^-$  ( $\text{pK}_{\text{in}} = 4.8$ ), and the amount of hetero-nuclear complexes  $[\text{FeHCitMoO}_4]^-$  increases [32]. It is obvious that exactly  $[\text{FeHCit}]^+$  and  $[\text{FeHCitMoO}_4]^-$  particles discharge contributes more to the overall cathode process, which causes deposit enrichment with iron and molybdenum. At the same time, the concentration of hydrated cobalt (II) ions decreases with citrate ion excess, which also reduces the cobalt content in the alloy.



**Fig. 1.8** Effect of ligand concentration on composition Fe-Co-Mo coating deposited at direct current  $i = 4 \text{ A/dm}^2$

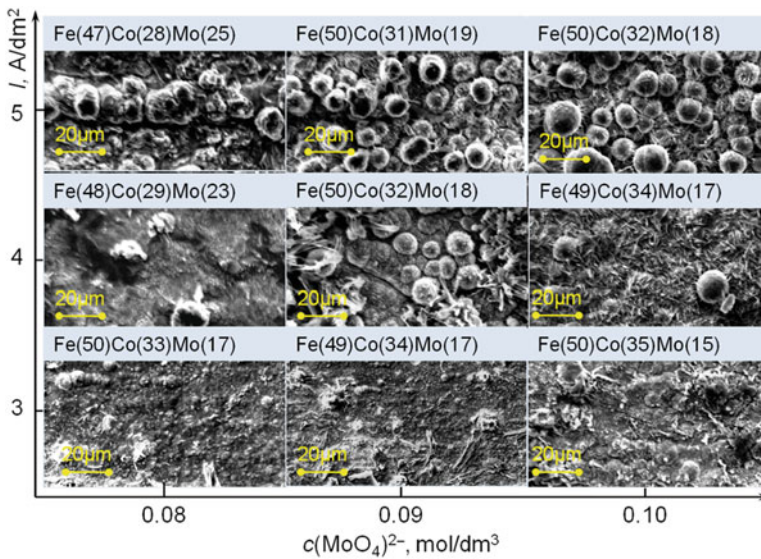
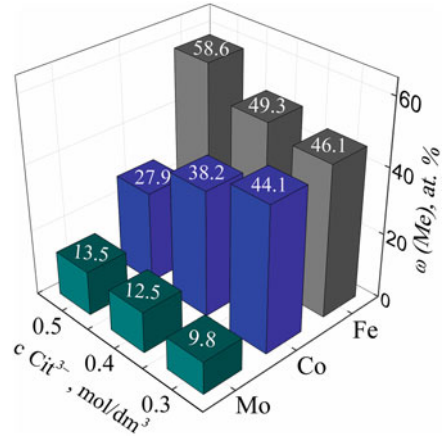


**Fig. 1.9** Composition  $\omega(M)$ , at.%, and morphology of Fe-Co-Mo coatings deposited in galvanostatic mode from electrolytes of varying concentration at component ratio in electrolyte  $c(\text{Fe}^{3+}):c(\text{Co}^{2+}):c(\text{MoO}_4)^{2-} = 2:2:1$

Morphology of Fe-Co-Mo deposits varies from fine crystalline to globular with increasing current density, due to the change in the ratio of alloying metal content in the alloy (Fig. 1.9). As it was shown earlier (Fig. 1.7), the cobalt and molybdenum ratio in the alloy changes toward increasing the refractory metal content with current density. It is established that globular surface appears for deposits with not higher than twice the prevalence of cobalt portion over molybdenum (Fig. 1.9).

The studies demonstrate that at current amplitude of 2–3 A/dm<sup>2</sup> and the fixed ratio of the on-/off-time  $t_{\text{on}}/t_{\text{off}} = 2 \text{ ms}/20 \text{ ms}$ , the composition of alloy is practically

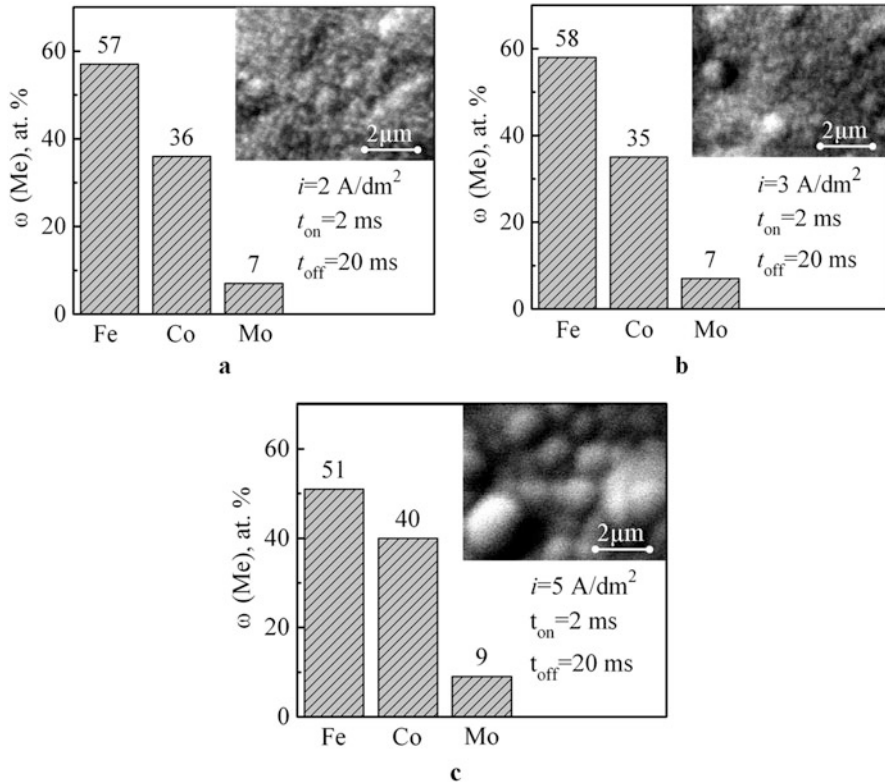


**Fig. 1.10** Composition and morphology of a Fe-Co-Mo coating deposited from electrolyte Mo6 at pulse current density, A/dm<sup>2</sup>: (a) 2, (b) 3, (c) 5

identical (Fig. 1.10a, b). Increasing current density to 5 A/dm<sup>2</sup> contributes rising cobalt and molybdenum content in coatings due to a decrease in the iron portion (Fig. 1.10c). Variation of current amplitude substantially influences the morphology of the deposited coatings. The deposits, obtained at current density of 2 A/dm<sup>2</sup>, possess fine-grained structure. Separate spheroids are formed on the surface when increasing  $i$  to 3 A/dm<sup>2</sup>, (Fig. 1.10b), and developed globular structure with the grain agglomerates of diameter  $\approx 2 \mu\text{m}$  appears at 5 A/dm<sup>2</sup> (Fig. 1.10c), which agrees with results obtained in [39].

At low current densities of 2–3 A/dm<sup>2</sup> and fixed off-time  $t_{\text{off}} = 10 \text{ ms}$ , an increase in on-time ambiguously affects the composition of a coating. Figure 1.11 shows that cobalt and iron content in the alloy changes in the range of 4–10 at. %. Maximum portion of molybdenum  $\omega(\text{Mo})$  of 12–14 at. % corresponds to  $t_{\text{on}}$  interval of 5–20 ms (Fig. 1.11a, b). However, at  $t_{\text{on}}/t_{\text{off}} = 50 \text{ ms}/10 \text{ ms}$ , there occurs a sharp reduction in the content of alloying components (cobalt and molybdenum) in the coating. Simultaneously, we observe an increase in the iron portion in the alloy up to 56 at.% (Fig. 1.11a, b).

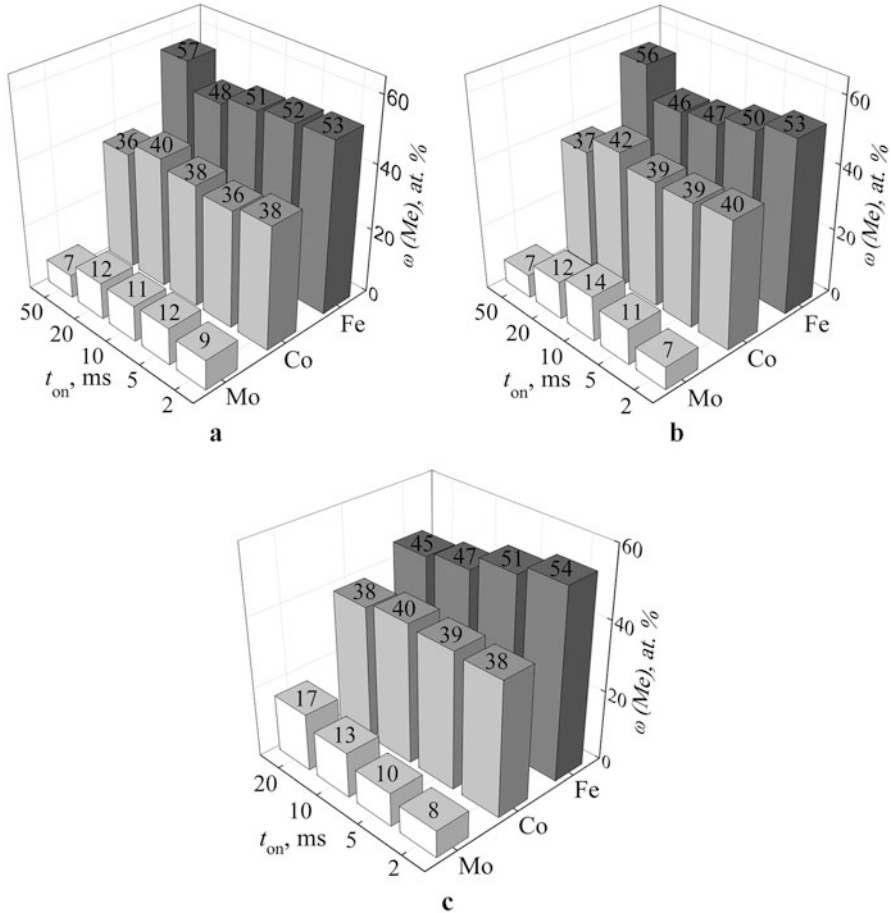


**Fig. 1.11** Effect of on-time on the composition Fe-Co-Mo alloy at  $t_{off} = 10$  ms; current density  $i$ , A/dm<sup>2</sup>: (a) 2, (b) 3, (c) 5

At current density of 5 A/dm<sup>2</sup>, the content of molybdenum grows proportional to the pulse duration. The maximum of the molybdenum content is registered at  $t_{on} = 20$  ms and is 17 at.%. The same path is followed by a reduction in the iron portion in the coating (Fig. 1.11c). Maximum total content of the alloying components ( $\geq 50$  at.%) is achieved at ratio  $t_{on}/t_{off} = 10$  ms/10 ms (20 ms/10 ms). At such coating composition, it is possible to expect that the obtained materials will possess improved microhardness in combination with the soft magnetic properties [40].

The surface of Fe-Co-Mo coatings (scanning area  $39.9 \times 39.9 \mu\text{m}$ ) is more developed and globular compared with the substrate as it follows from AFM 2D maps analysis [41]. Moreover one can observe the parts of different morphology (Fig. 1.12).

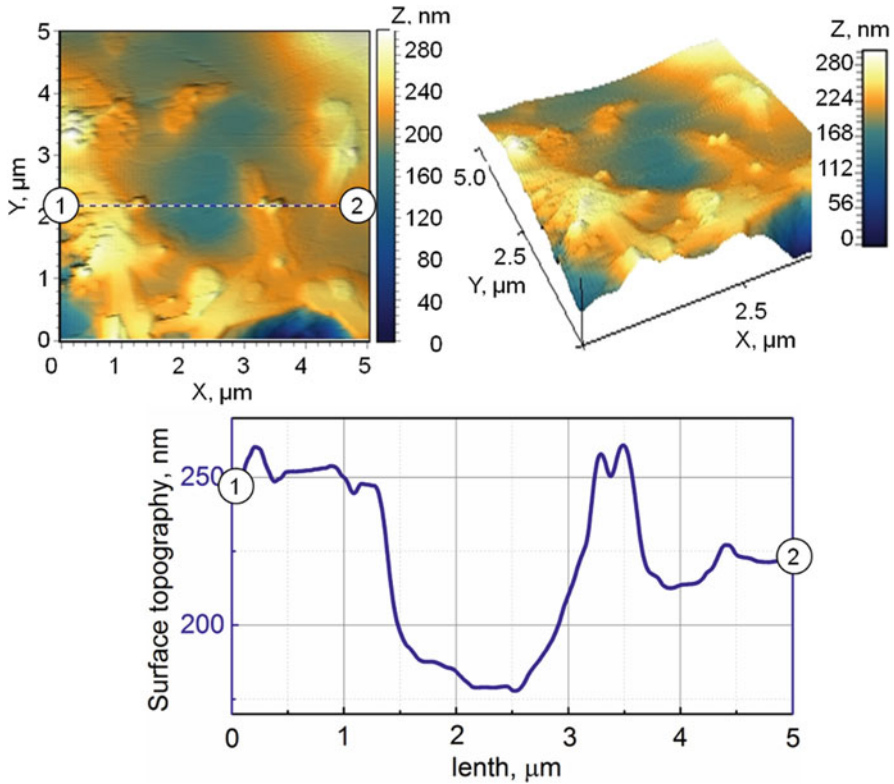


**Fig. 1.12** 2D and 3D map and cross-sectional profile of the surface Fe-Co-Mo between markers 1 and 2 deposited in pulse mode at current density  $4 \text{ A/dm}^2$ ;  $t_{\text{on}}/t_{\text{off}} = 10/10 \text{ ms}$ ;  $T = 25 \text{ }^\circ\text{C}$ ; pH 4.8; plated time 30 min. Scan area  $5.0 \times 5.0 \text{ } \mu\text{m}$

The structure of coatings Fe-Co-Mo with an iron content of 51 at.%, cobalt 36 at.%, and molybdenum 13 at.% (in terms of metal) formed on a copper substrate with a thickness of  $30 \text{ } \mu\text{m}$  was examined. The results of the X-ray diffraction analysis indicate an amorphous-crystalline structure as for Fe-Co-W alloy. Diffraction patterns for Fe-Co-Mo alloys are characterized by the lines of copper substrate and broad halo with a width of about  $18^\circ$  at angles  $2\theta$   $45\text{--}58^\circ$  as can be seen in Fig. 1.13. However, the Fe-Co-Mo deposit differs from Fe-Co-W films by some phases. We see lines for intermetallic phases  $\text{Fe}_7\text{Mo}$ ,  $\text{Fe}_7\text{Co}$ , and  $\text{FeCo}$  along with  $\alpha\text{-Fe}$  and  $\text{Fe}_3\text{C}$  but not any one corresponding to  $\text{CoMo}$  compounds (Fig. 1.13). The crystallite size of the amorphous part is  $L = 66 \text{ \AA}$ .

Phases  $\text{Fe}_7\text{Mo}$  and  $\text{Fe}_7\text{Co}$  found in Fe-Co-Mo deposits reflect the competition of alloying metal reduction from hetero-nuclear complexes and confirm mechanism of co-deposition proposed in [32], as for Fe-Co-W alloy.

Thus ternary Fe-Co-Mo alloys were deposited by direct and pulse current from citrate Fe(III)-based electrolyte. Variation in current density and time parameters

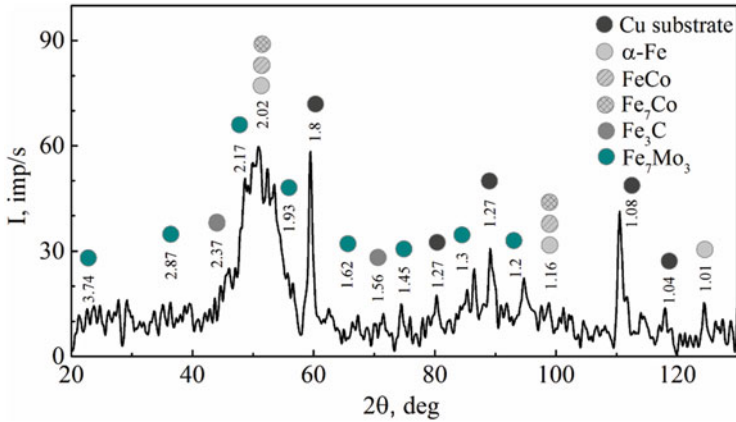


**Fig. 1.13** X-ray diffraction patterns for alloy Fe-Co-W deposited from electrolyte Mo9 at  $i = 2.5 \text{ A/dm}^2$

of pulse electrolysis favors changes in refractory metal content, and surface morphology with micro-globular surface and crystalline-amorphous structure of Fe-Co-Mo deposits differs by crystallite size of the amorphous part of 7 nm that is associated with nano-sized materials.

### 1.1.3 CoMoZr Alloy

Increasing the current density amplitude  $i$  by  $2\text{--}4 \text{ A}\cdot\text{dm}^{-2}$  rises the molybdenum content in the deposit Co-Mo-Zr up to  $\omega(\text{Mo}) = 24 \text{ at.}\%$  (Fig. 1.14a) reaching the concentration plateau at  $24\text{--}25 \text{ at.}\%$  at current densities of  $4\text{--}8 \text{ A/dm}^2$ . Coating enrichment by this alloying component with increasing current density is entirely predictable since the reduction of molybdate is at least a complex multistep process including chemical reduction of intermediate molybdenum oxides with hydrogen ad-atoms  $H_{\text{ad}}$  [36, 42]. As we see from (Fig. 1.14b), the potential of the cathode at electrodeposition of the coatings Co-Mo-Zr is in the range  $-(2.0\text{--}2.8) \text{ V}$ . Thus with increasing current density, electrode potential shifts in the negative direction resulting in faster parallel reaction of hydrogen reduction to form  $H_{\text{ad}}$  which are involved in a chemical step of intermediate molybdenum oxide reduction. Due to these processes, the Mo content in the deposits is increased. However, at current densities above  $8 \text{ A/dm}^2$ , reaction of hydrogen evolution becomes dominant as evidenced by the current efficiency (Fig. 1.14b) whereby the molybdenum content in the alloy decreases.

The dependence of the Zr content in the ternary coatings from current amplitude  $i$  has an extreme character with a maximum  $\omega(\text{Zr}) = 3.6\text{--}3.7 \text{ at.}\%$  at current densities of  $4 \text{ A/dm}^2$  (Fig. 1.14a). It should be stated that when the amplitude of the current is

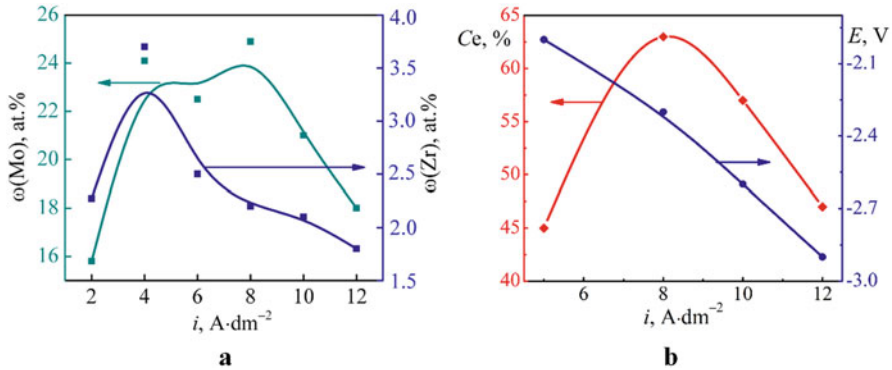


**Fig. 1.14** Pulse current density influence on the composition (a) and current efficiency (b) for Co-Mo-Zr coatings;  $t_{\text{on}}/t_{\text{off}} = 2/10$  ms;  $T$  20–25 °C; pH 8; plated time 30 min

higher than  $4/\text{dm}^2$ , there is a competitive deposition of molybdenum and zirconium in the coating, which is obviously due to the different mechanism of alloying metal reduction from polyligand electrolytes. Indeed, molybdenum reduction requires the transfer of six electrons accompanied by the removal of four coordinated oxygen atoms. Zirconium is likely included in the deposit in the form of oxygen compounds, which follows from the higher binding energy Zr-O [43] and confirmed by analysis of the composition of the surface layers.

A similar nonlinear relationship  $C_e$  vs  $i$  (Fig. 1.14b) was observed for current efficiency of the ternary alloy:  $C_e$  increases by 20% and reaches 63% with rising current density from 5 to  $8/\text{dm}^2$ ; however further increase in  $i$  reduces the current efficiency up to 47%. Such behavior may be attributed with acceleration of hydrogen evolution site reaction at more negative potentials.

Time parameters of pulsed electrolysis strongly affect the composition and current efficiency of multicomponent deposits. Increasing on-time of 0.5–2 ms at a constant current density  $i = 4/\text{dm}^2$  and off-time  $t_{\text{off}} = 10$  ms favors rising both Mo and Zr content in the deposits (Fig. 1.15a). This is due to an increase in active current at the expense of a full signal handling, thereby achieving potential of alloying metal reduction in the alloy. Increasing the on-time of more than 2 ms does not contribute to the significant change in the above metal content. Moreover, the zirconium content decreases with on-time exceeding 2 ms.

Prolong pause of 5–10 ms at a constant current density and on-time ( $t_{\text{on}} 2$  ms) provides rising of zirconium content in the alloy from 2.1 to 3.7 at.% which is followed by decreasing of  $\omega(\text{Zr})$  at larger  $t_{\text{off}}$  time (Fig. 1.15b). So the maximum Zr content is reached at the ratio  $t_{\text{on}}/t_{\text{off}} = 2/10$  ms (duty factor  $q = 10$ ,  $f = 85$  Hz). At the same time, the molybdenum portion in Co-Mo-Zr deposits regularly increases from 16.0 to 24.0 at.% with off-time due to more complete chemical reduction of intermediate oxides by  $H_{\text{ad}}$  (Fig. 1.15b). It also shows the different mechanism of zirconium and molybdenum reduction and confirms their competitive co-deposition in the coating.

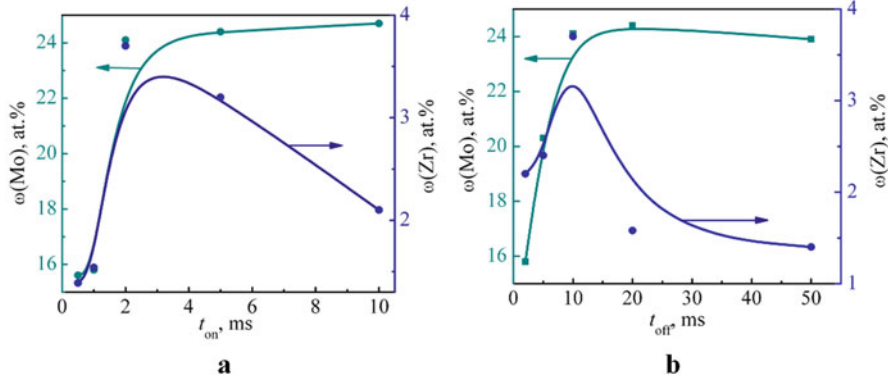


**Fig. 1.15** Dependence of Co-Mo-Zr coating composition on pulse time  $t_{on}$  (a) ( $t_{off}$  10 ms) and off-time  $t_{off}$  (b) ( $t_{on}$  2 ms);  $i = 4 \text{ A/dm}^2$ ;  $T = 20\text{--}25 \text{ }^\circ\text{C}$ ; pH 8; plated time 30 min

Current efficiency logically decreases from 60 to 36% with on-time increasing of  $4\text{--}10 \text{ A/dm}^2$  due to the hydrogen evolution site reaction. Prolong the pause positively affects the current efficiency as subsequent chemical reactions accompanying the alloying metals discharge are more fully; but a longer off-time reduces the efficiency of the process. Thus, current efficiency reaches 98% when  $t_{off} = 50 \text{ ms}$  and  $t_{on} = 2 \text{ ms}$ .

Increasing the current density changes the surface morphology and amplified internal stress that leads to fracture grid (Fig. 1.16). Figure 1.16 shows the surface becomes less smooth and more globular, and the crystallite sizes increase exactly due to the higher content of Mo in the deposits. Uniform distribution of the coating components on uneven relief should be emphasized sufficiently as one can see from EDS data (Fig. 1.17). Increasing on-time at a constant off-time promotes formation of spheroids on the surface, but increasing tension in the coating and micro-cracks become larger as observed for other coatings [44]. Furthermore, some pores appear in coatings when the on-time is 10 ms and the current density is  $6\text{--}8 \text{ A}\cdot\text{dm}^{-2}$ , apparently due to hydrogen evolution (Fig. 1.16b, c).

The AFM analysis of Co-Mo-Zr coatings shows that their surface includes the parts of different morphology (Fig. 1.18). The surface is characterized by a globular structure with an average size of grains and crystallites of  $100\text{--}200 \text{ nm}$  and singly located cone-shaped (Fig. 1.18a) or semi-spheroid (Fig. 1.18c) hills with a base diameter of  $1\text{--}3 \text{ }\mu\text{m}$  and a height of  $0.5\text{--}1.5 \text{ }\mu\text{m}$ . As appears from 2D and 3D maps of the surface, the cone-shaped hills are formed from the smaller spheroids (Fig. 1.18). Such globular surface is caused by the presence of molybdenum in the deposits as it was shown in [3, 34, 36]. Uniform distribution of alloying elements at picks and valleys of the surface with a slight predominance of Mo and Zr at picks (Fig. 1.18b, c) is specified in EDS data (Fig. 1.17). As the current density rises, the number of spheroids at the deposit surface also increases, but both their height and diameter diminish (Fig. 1.18c).

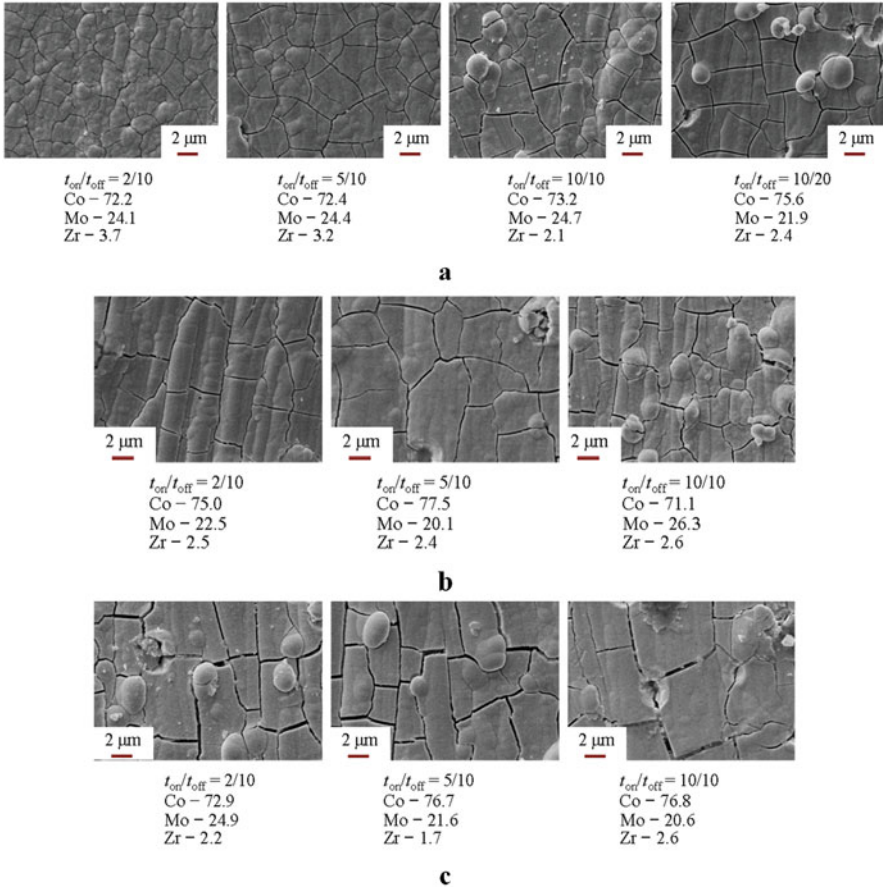
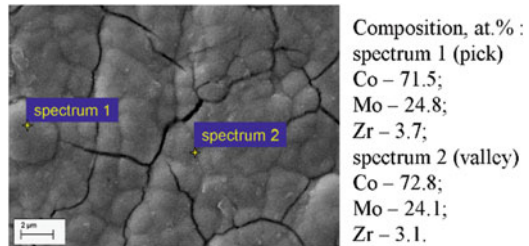


**Fig. 1.16** Morphology ( $\times 2000$ ) and composition (at.%) of Co-Mo-Zr coatings deposited in pulse mode at current density,  $A/dm^2$ : 4 (**a**), 6 (**b**), and 8 (**c**);  $T = 20-25^\circ C$ ; pH 8; plated time 30 min

**Fig. 1.17** Distribution of alloying elements at picks and valleys of coating Co-Mo-Zr deposited at 4  $A/dm^2$ ,  $t_{on}/t_{off} = 2/10$  ms



The parameters of surface roughness  $R_a = 0.29$  and  $R_q = 0.38$  for ternary coatings deposited at current density of 4  $A/dm^2$  do not differ from  $R_a = 0.29$  and  $R_q = 0.4$  for 6  $A/dm^2$  and exceed the parameters of the polished substrate  $R_a = 0.007$  and  $R_q = 0.01$ .



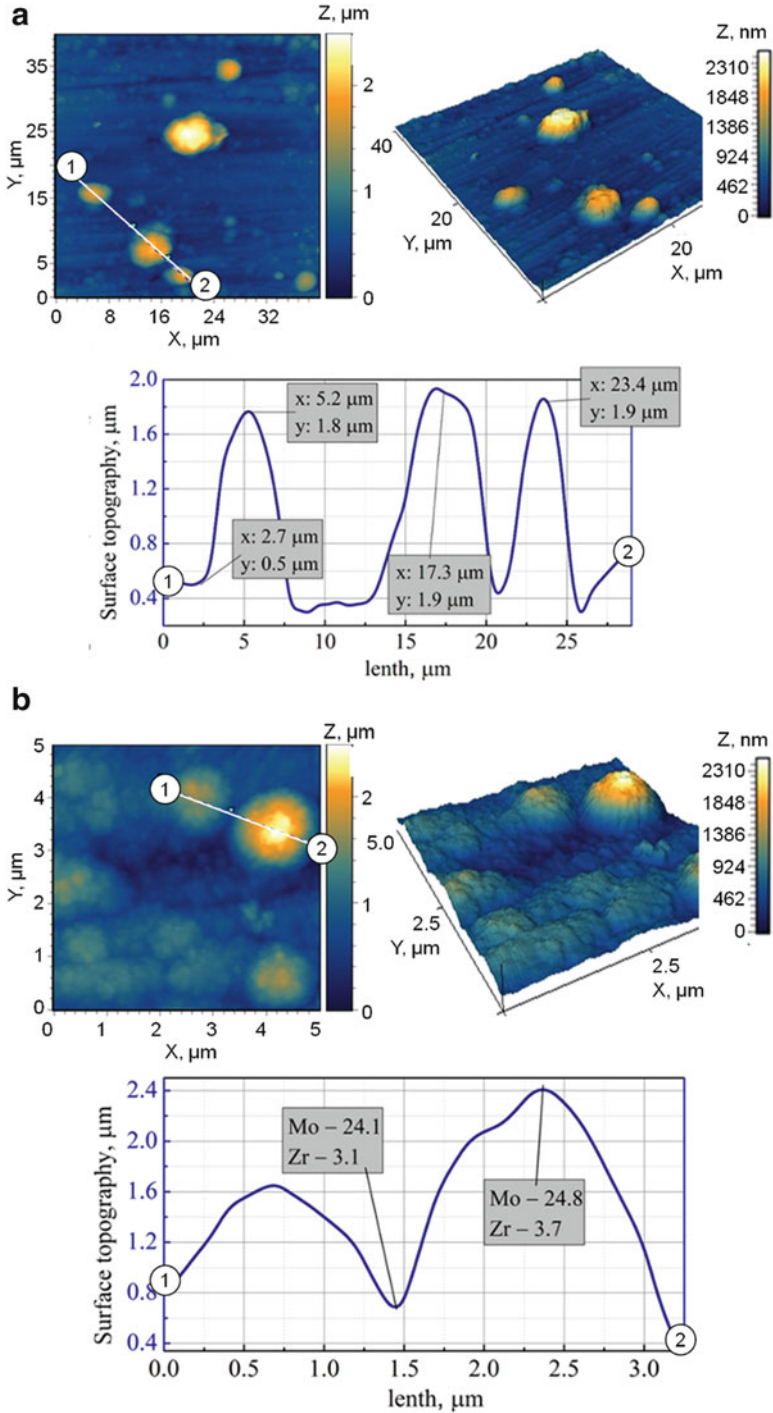


**Fig. 1.18** 3D and 2D map and cross-sectional profile of the surface Co-Mo-Zr between markers 1–2 deposited in pulse mode at current density 4 A/dm<sup>2</sup> (a, b) and 6 A/dm<sup>2</sup> (c);  $t_{\text{on}}/t_{\text{off}} = 2/10$  ms;  $T = 25^\circ\text{C}$ ; pH 8; plated time 30 min. Scan area AFM: (a) 40  $\times$  40  $\mu\text{m}$ ; (b) 5.0  $\times$  5.0  $\mu\text{m}$ ; (c) 10  $\times$  10  $\mu\text{m}$

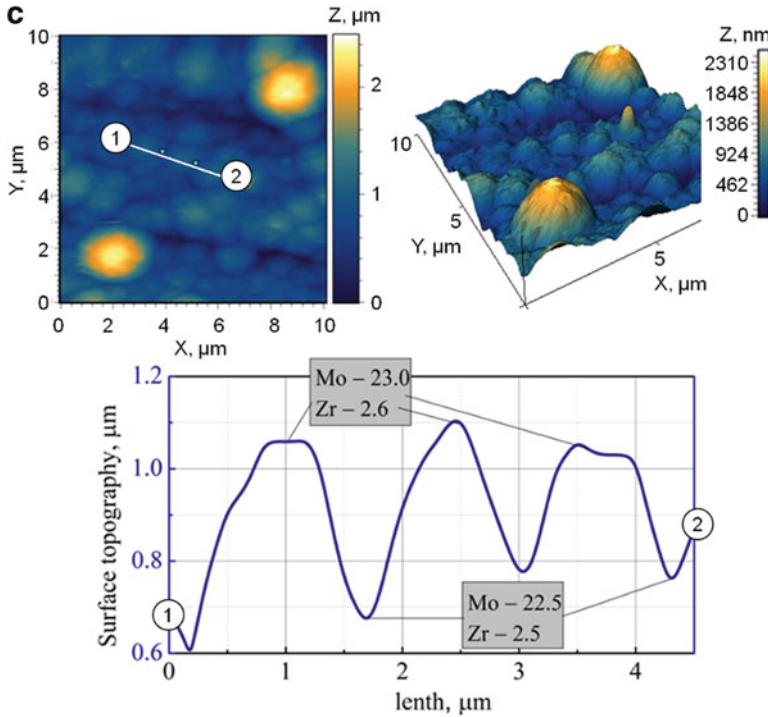
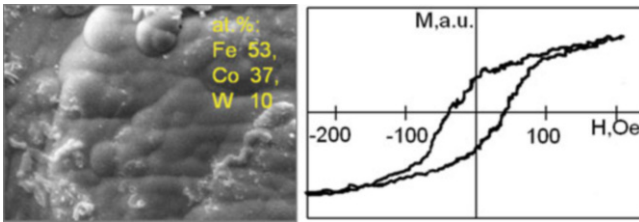
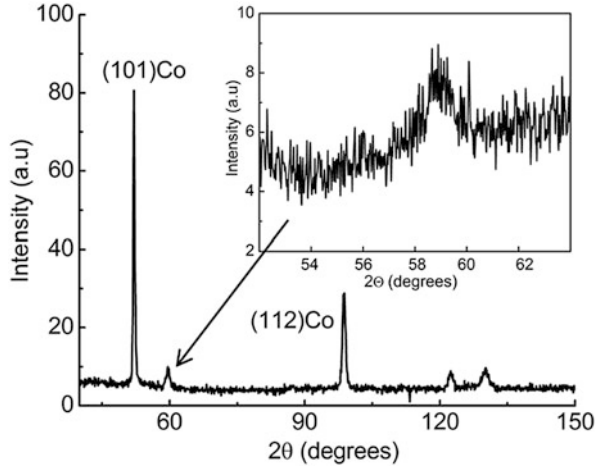


Fig. 1.18 (continued)

A series of diffraction lines for  $\alpha$ -Co on X-ray diffraction patterns for Co-Mo-Zr deposits on steel substrates was obtained (Fig. 1.19). No other phases including intermetallic compounds were found in the coating structure even after a 3-h annealing of the coated sample on the air at a temperature of 870 K. Furthermore, one can find a small halo with full width at half maximum about  $5^\circ$  at angles  $2\theta \sim 59^\circ$ , which indicates an XRD amorphous structure of above materials [45].

Thus content of the alloying metals in the coating Co-Mo-Zr deposited from polyligand citrate-pyrophosphate electrolyte depends on the current density and on-/off-times extremely, and maximum Mo and Zr content corresponds to the current density interval of  $4\text{--}6\text{ A/dm}^2$  and on-/off-time of  $2\text{--}10\text{ ms}$ . It was established the coating enrichment by molybdenum with current density increasing up to  $8\text{ A/dm}^2$  as well as the rising of on-time and off-time promotes the content of molybdenum because of subsequent chemical reduction of its intermediate oxides by hydrogen ad-atoms. Developed and globular surface of Co-Mo-Zr as well as composition of material may be associated with high catalytic activity.

**Fig. 1.19** X-ray diffraction patterns for deposit Co-Mo-Zr, the composition is similar to Fig. 1.16a ( $t_{\text{on}}/t_{\text{off}} = 2/10$  ms)



**Fig. 1.20** Surface morphology and hysteresis loop for Fe-Co-W coating. Substrate – copper M1

### 1.1.4 Functional Properties of Fe-Co-W, Fe-Co-Mo, and Co-Mo-Zr Coatings

#### 1.1.4.1 Magnetic Characteristics of Fe-Co-W and Fe-Co-Mo Coatings

The magnetic behavior of Fe-Co-W and Fe-Co-Mo deposits obtained in the same conditions varies in some way. As one can see from Fig. 1.4, the shape of hysteresis loop for both alloys in the saturation interval is smoothed that indicates the presence of an amorphous structure in the electrolytic deposits. At the same time, the effect of smoothing the hysteresis loop for the Fe-Co-W film is stronger than for the Fe-Co-Mo ones (Fig. 1.20). Concurrently, we observe the saturation of magnetization as well as demagnetization for the Fe-Co-Mo film which is stepwise that confirms the presence of two magnetic phases in the coating (Fig. 1.21).

It was found that the coercive force for synthesized Fe-Co-W and Fe-Co-Mo films is 50–60 Oe and 7–10 Oe, respectively. Coercive force is a structure-sensitive material characteristic. Therefore, we can assume that the main reason for higher coercive force values for Fe-Co-W films are the larger size of grains compared to size of grains of Fe-Co-Mo films.

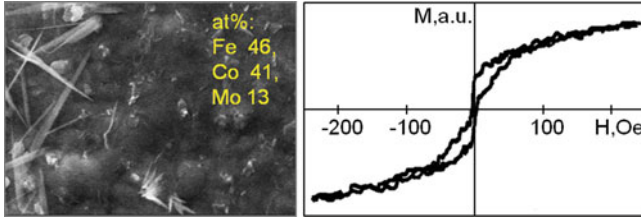


**Fig. 1.21** Surface morphology and hysteresis loop for Fe-Co-Mo coating. Substrate – copper M1

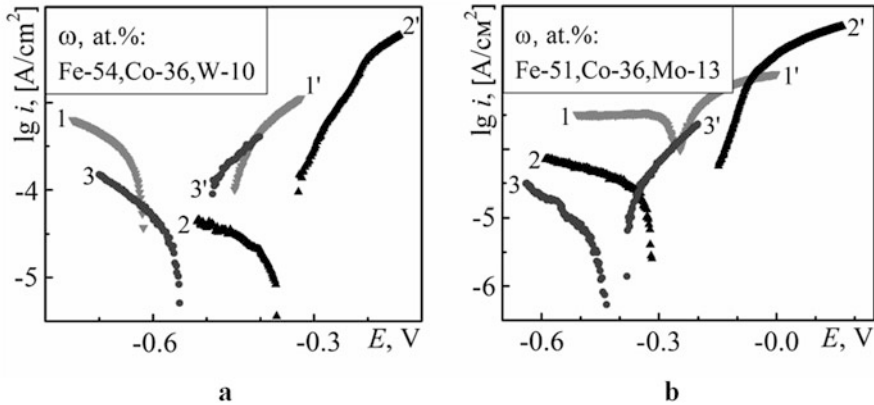


**Fig. 1.22** The cathodic (1, 2, 3) and anodic (1', 2', 3') polarization dependences of the coatings in corrosive environment with pH 3 (1, 1'), pH 5 (2, 2'), and pH 9.5 (3, 3')

#### 1.1.4.2 Corrosion Behavior of Ternary Alloys

Corrosion of cobalt-based electrolytic coatings as it follows from the nature of alloying components proceeds predominantly with hydrogen depolarization in an acidic medium (Fig. 1.23) and in neutral and alkaline under oxygen action.

The open circuit potential of Fe-Co-W coatings shifts to the negative side compared with the steel substrate at all solution pH, indicating cathodic control of the corrosion process (Fig. 1.22a). The cathode reaction is inhibited due to the depolarizer (oxygen) transport deceleration caused by acidic nonstoichiometric tungsten oxides. Thus, the coating enrichment with tungsten, which occurs predominantly at the expense of iron content, contributes to increasing the corrosion resistance in acidic media. Corrosion current decreasing in a neutral media indicates the formation and stability of alloying components' passive oxide film, even in the presence of activating  $\text{Cl}^-$  ions. In the alkaline media, on the contrary, the cathode reaction inhibition is ensured by insoluble iron hydroxides formed on the alloy surface, which prevent depolarizer transport to the substrate. The highest corrosion resistance in alkaline medium is observed for Fe-Co-W coatings with iron content 59 at. % and tungsten 8 at. % (Table 1.4).

**Table 1.4** Corrosion indexes of Fe-Co-Mo and Fe-Co-W coatings

Composition of alloy, $\omega$ , at. %	pH 3		pH 5		pH 9.5	
	$E_{cor}$ , V	$\lg i_{cor}$ , A/cm <sup>2</sup>	$E_{cor}$ , V	$\lg i_{cor}$ , A/cm <sup>2</sup>	$E_{cor}$ , V	$\lg i_{cor}$ , A/cm <sup>2</sup>
Сталь	-0.34	-2.8	-0.35	-3.0	-0.32	-2.8
Fe51Co36Mo13	-0.25	-3.7	-0.30	-4.9	-0.46	-5.5
Fe31Co31Mo38	-0.16	-4.5	-0.31	-4.8	-0.32	-5.1
Fe54Co36W10	-0.54	-4.7	-0.36	-5.1	-0.53	-5.2
Fe59Co33W8	-0.35	-4.1	-0.39	-4.8	-0.36	-5.5

The Fe-Co-Mo alloy corrosion mechanism in acidic and neutral media differs by open circuit potential shift to the positive side compared with substrate material (Fig. 1.22, b; Table 1.4). The corrosion rate decreases due to the formation of the dense film of acidic molybdenum oxide on the surface. On the contrary, the open circuit potential shifts toward the negative side in the alkaline environment, which is evidence of the cathode reaction inhibition by insoluble iron and cobalt hydroxides formed at the alloy surface. Accordingly, the coatings with a molybdenum content of 38 at. % and iron of 31 at. % are more resistant in acidic environments; and coatings containing molybdenum of 13 at. % and iron of 51 at. % are more resistant in alkaline media as one can see from Table 1.4.

Verification of polarization method results was carried out using electrode impedance spectroscopy (EIS) technique. It was found that in neutral environment the Nyquist plot for Fe-Co-Mo(W) alloy (Fig. 1.23) is a connection of two conjugate semicircles at high frequencies complicated by the diffusion Warburg impedance  $Z_W$  at low frequencies. The fact that semicircles are not overlapping is due, presumably, to near values of the time constants  $\tau = RC$  of parallel circuits, which reflect the kinetic nature of the charge transfer inhibition on parts of the surface with different composition. Indeed, part of the surface is covered with chemically stable neutral media oxides, which correspond to elements of the substitution scheme  $C_{OX}$  and  $R_{OX}$  (Fig. 1.24), while Faraday reactions on the other surface parts are visualized by the elements  $C_d$  and  $R_f$ . A conclusion on the inhibition of transport stages, the presence of which reflects Warburg impedance, is quite identical to the results of polarization measurements. The relatively near values of the corrosion current density, calculated from data of polarization resistance technique and EIS, are also evidence of correctness of both the parameters of the corrosion process determination and the validity of the electrochemical systems equivalent circuit. Parameter  $R_f$  for tested materials decreases in the range:

$$R_f(\text{Fe} - \text{Co} - \text{W}) > R_f(\text{Fe} - \text{Co} - \text{Mo}) \gg R_f(\text{steel substrate}).$$

Open circuit potential of coatings alloyed with zirconium becomes more negative in all environments (Figs. 1.25 and 1.26; Table 1.5). At the same time, the corrosion rate of a ternary alloy in the acidic and neutral chloride-containing environment

**Fig. 1.23** The Nyquist plots for steel electrode (1), Fe-Co-Mo (2), and Fe-Co-W (3) alloys in a neutral chloride-containing environment

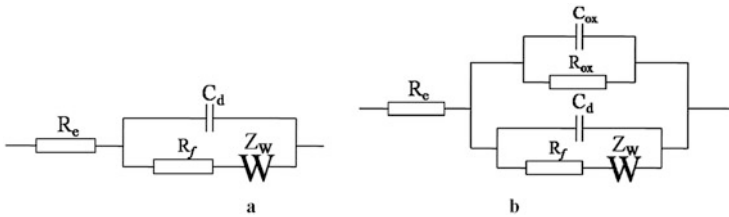
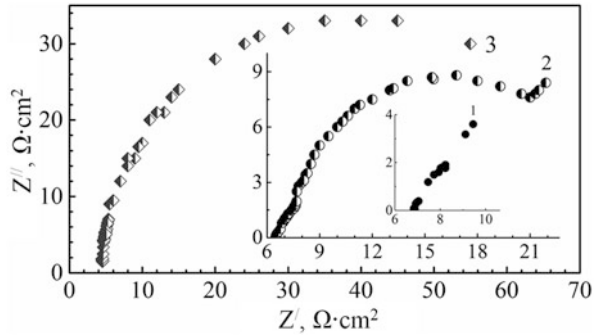
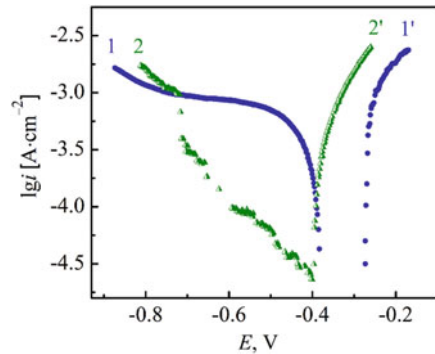


**Fig. 1.24** The equivalent circuits of corrosion processes in a neutral chloride-containing environment: (a) steel electrode, Fe-Co-W alloy, (b) Fe-Co-Mo alloy

**Fig. 1.25** Corrosion diagrams for coatings Co(76)-Mo(24) (1) and Co(72.2)-Mo(24.1)-Zr(3.7) (2) in 1 M Na<sub>2</sub>SO<sub>4</sub> (pH 3): cathodic plots (1, 2) and anodic plots (1', 2')



declines by almost an order of magnitude compared with the binary system (Table 1.5). It can be explained by an increased zirconium trend to passivity as can be seen from the corrosion plots (Fig. 1.25) and anodic polarization dependences (Fig. 1.26).

Also ternary alloy increases resistance to pitting corrosion as it was shown for other corrosion-resistant materials [46, 47]. The difference in corrosion rate of Co-Mo and Co-Mo-Zr coatings in an alkaline environment is not as great due to the acidic nature of passive oxides of molybdenum and zirconium.

**Fig. 1.26** Anodic polarization plots for coatings Co(72.2)-Mo(24.1)-Zr(3.7) (1, 2) and Co(76)-Mo(24) (3, 4) in media: 1 M Na<sub>2</sub>SO<sub>4</sub> pH 11 (1, 3) and 3% NaCl pH 7 (2, 4)

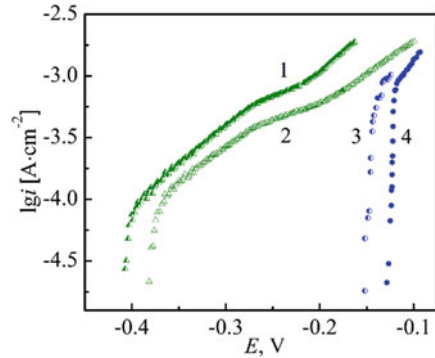


**Table 1.5** Corrosion indicators of testing materials in different media

Corrosion medium pH	Corrosion parameters	Electrolytic alloys	
		Co76-Mo24	Co72-Mo24-Zr4
3	$i_{cor}$ , A·cm <sup>-2</sup>	$2 \cdot 10^{-4}$	$3 \cdot 10^{-5}$
	$E_{cor}$ , V	-0.42	-0.46
	$k_h$ , mm·year <sup>-1</sup>	$2.3 \cdot 10^{-3}$	$3.1 \cdot 10^{-4}$
7 (3% NaCl)	$i_{cor}$ , A·cm <sup>-2</sup>	$2.5 \cdot 10^{-4}$	$2.1 \cdot 10^{-5}$
	$E_{cor}$ , V	-0.2	-0.5
	$k_h$ , mm·year <sup>-1</sup>	$2.9 \cdot 10^{-3}$	$2.2 \cdot 10^{-4}$
11	$i_{cor}$ , A·cm <sup>-2</sup>	$8 \cdot 10^{-5}$	$3 \cdot 10^{-5}$
	$E_{cor}$ , V	-0.43	-0.47
	$k_h$ , mm·year <sup>-1</sup>	$9.3 \cdot 10^{-4}$	$3.1 \cdot 10^{-4}$

**Table 1.6** The exchange current density of hydrogen at the platinum and ternary alloy coatings

Composition of alloy, ω, at. %	lg $i^0_H$ , A/cm <sup>2</sup>		
	pH 3	pH 5	pH 9.5
Pt	-3.3	-3.2	-3.1
Fe51Co36Mo13	-3.1	-2.8	-4.0
Fe31Co31Mo38	-3.1	-3.6	-3.4
Fe54Co36W10	-3.5	-3.4	-3.3
Fe59Co33W8	-3.3	-3.1	-3.5

### 1.1.4.3 The Catalytic Properties of Fe-Co-W, Fe-Co-Mo, and Co-Mo-Zr Coatings

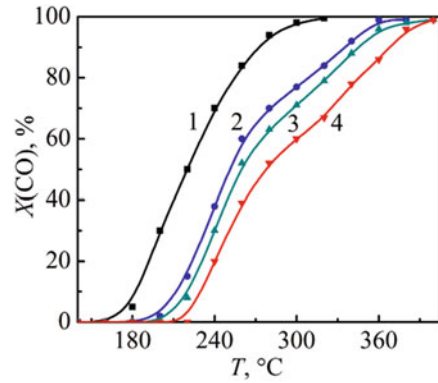
Results of testing the catalytic activity of Fe-Co-W, Fe-Co-Mo, and Co-Mo-Zr alloy coatings in the model reaction of hydrogen evolution from different media (Tables 1.6 and 1.7) indicate the synergistic nature of the electrolytic alloys.

The values of the hydrogen exchange current density are related to the analogous indices for platinum family metals, as one can see from Tables 1.6 and 1.7.

The exchange current density of hydrogen at binary and ternary alloys is higher than this parameter on alloying components which can be attributed obviously with the change in the mechanism of the process. From the literature [48], it is known

**Table 1.7** Exchange current density of hydrogen evolution  $\log i_{\text{H}}^0$  and coefficient  $b \lg i_{\text{H}}^0$  for different materials in acidic and alkali media

Material composition, at. %	Medium			
	acidic		Alkaline	
	$-\log i_{\text{H}}^0$ [ $\text{A}\cdot\text{cm}^{-2}$ ]	$-b$ , V	$-\log i_{\text{H}}^0$ [ $\text{A}\cdot\text{cm}^{-2}$ ]	$-b$ , V
Pt100	3.30	0.03	3.10	0.100
Co100	4.35	0.14	4.30	0.14
Mo100	8.25	0.08	4.80	0.14
Co76-Mo24	4.1	0.03	4.2	0.10
Co72-Mo-24-Zr4	4.0	0.1	3.9	0.03

**Fig. 1.27** Thermograms of CO conversion degree at Pt (1) and galvanic alloys Co-Mo-Zr of composition, at. %: Co, 72; Mo, 24; Zr, 4 (2); Co, 72.4; Mo, 24.4; Zr, 3.2 (3); Co, 73.2; Mo, 24.7; Zr, 2.1 (4)

that the hydrogen evolution on cobalt occurs by Volmer-Heyrovsky mechanism ( $b = -0.1$  V) with the limiting discharge stage (Volmer). As can be seen from the coefficient  $b = 0.03$  V (Table 1.7), hydrogen evolution both on the electrolytic Co-Mo alloy in an acidic medium and on Co-Mo-Zr coating in an alkali medium is limited by recombination stage, i.e., flows through the Tafel mechanism. The same mechanism is typical for platinum; this is evidence of the high catalytic activity of the materials studied.

Thus, the combination in the active layer of metals with different limiting stage of hydrogen evolution allows obtaining a material with catalytic activity close to platinum metals. Obtained results are evidenced to the competitiveness of the received coatings and allow recommending Fe-Co-W, Fe-Co-Mo, and Co-Mo-Zr systems as promising electrode materials for redox flow batteries.

Testing of the catalytic activity of the synthesized Co-Mo-Zr coatings was also performed in the model reaction of carbon (II) oxide conversion to carbon (IV) oxide. Quantitative characteristics of the oxidation are the carbon (II) oxide conversion degree  $X(\text{CO})$  and ignition temperature  $T_i$ . The catalytic properties of galvanic alloys were compared to platinum which is the most effective catalyst. As one can see from the temperature dependencies (Fig. 1.27, 1) at the platinum plate catalyst with  $\omega(\text{Pt}) = 100$  at.%, the oxidation of CO begins at 190 °C, while 100% conversion degree is achieved at 250 °C.



**Table 1.8** Parameters of CO oxidation model reaction at different catalytic materials

Catalyst composition (at.%)	Ignition temperature $T_i$ , °C	Temperature for 50% conversion	Temperature for 100% conversion
Pt <sub>100</sub>	190	220	250
Co(72)Mo(24)Zr(4)	230	260	370
Co(72.4)Mo(24.4)Zr(3.2)	240	270	375
Co(73.2)Mo(24.7)Zr(2.1)	230	280	400

As can be seen from Fig. 1.27, the thermograms of carbon (II) oxide conversion at the surface of catalyst coated with ternary alloys with various contents of zirconium (dependences 2–4) have two sections with different slopes. In the first plot within the temperature interval 200–270 °C, the kinetics of CO oxidation is not different from the platinum plate catalyst with  $\omega(\text{Pt}) = 100$  at.% although both the reaction initiation temperature  $T_{in}$  and temperature of 50% conversion are higher than on platinum by 40–50 °C (Table 1.8). In the second plot at a temperature above 270 °C, oxidation rate declines probably due to the formation of alloying metal oxides on the surface. The conversion degree rises by an average of 7–10% with the increase in zirconium content in the coating by 1 at.%, but the influence of zirconium weakens at the temperatures higher than 350 °C. Evidence of high catalytic activity of materials is the fact that 99% conversion is achieved at temperatures of 375–380 °C. Catalytic properties of the synthesized systems are caused by cobalt ability to form nonstoichiometry oxides with different thermal resistance as well as by high affinity for oxygen of molybdenum and especially zirconium.

The above results are conclusive evidence not only of Co-Mo-Zr high catalytic activity but gives every reason to replace platinum catalysts at a cheaper galvanic alloy cobalt-molybdenum-zirconium, an added benefit of which is a metallic substrate.

Thus, the obtained results allow us to consider the synthesized nano-sized ternary alloys as promising and effective materials and recommend them for use as anticorrosive coatings and active catalyst layers. The Fe-Co-Mo coatings are soft magnetic materials and are recommended for usage of such systems in the production of magnetic head elements for recording and reproducing information devices.

## References

1. Tsyntsaru N, Cesiulis H, Donten M, Sort J, Pellicer E, Podlaha-Murphy EJ (2012) Modern trends in tungsten alloys electrodeposition with iron group metals. *Surf Eng Appl Electrochem* 48(6):491–520
2. Podlaha EJ, Landolt D (1997) Induced codeposition: III. Molybdenum alloys with nickel, cobalt and iron. *J Electrochem Soc* 144(5):1672–1680
3. Yar-Mukhamedova G, Ved' M, Sakhnenko N, Karakurkchi A, Yermolenko I (2016) Iron binary and ternary coatings with molybdenum and tungsten. *Appl Surf Sci* 383:346–352. <https://doi.org/10.1016/j.apsusc.2016.04.046>

4. Capel H, Shipway PH, Harris SJ (2003) Sliding wear behaviour of electrodeposited cobalt–tungsten and cobalt–tungsten–iron alloys. *Wear* 255:917–923. [https://doi.org/10.1016/S0043-1648\(03\)00241-2](https://doi.org/10.1016/S0043-1648(03)00241-2)
5. Ved' MV, Sakhnenko MD, Karakurkchi HV, Ermolenko IY, Fomina LP (2016) Functional properties of Fe–Mo and Fe–Mo–W galvanic alloys. *Mater Sci* 51(5):701–710. <https://doi.org/10.1007/s11003-016-9893-5>
6. Feng-jiao H, Jing-tian L, Xin L, Yu-ning H (2004) Friction and wear behavior of electrodeposited amorphous Fe–Co–W alloy deposits. *Trans Nonferrous Met Soc China* 14(5):901–906
7. Tsyntsaru N, Dikuser A, Cesiulis H, Celis J-P, Bobanova Z, Sidel'nikova S, Belevskii S, Yu Y, Bersirova O, Kublanovskii V (2009) Tribological and corrosive characteristics of electrochemical coatings based on cobalt and iron superalloys. *Powder Metallurgy and Metal Ceramics* 48(7–8):419–428
8. Yaponseva YS, Dikuser AI, Kyblanovskii VS (2014) Study of the composition, corrosion, and catalytic properties of Co–W alloys electrodeposited from a citrate pyrophosphate electrolyte. *Surf Engin Appl Electrochem* 50:330. <https://doi.org/10.3103/S1068375514040139>
9. Gomez E, Pellicer E, Valles E (2001) Electrodeposited cobalt\_molybdenum magnetic materials. *J Electroanal Chem* 517:109–116
10. Gomez E, Kipervaser ZG, Pellicer E, Valles E (2004) Extracting deposition parameters for cobalt–molybdenum alloy from potentiostatic current transients. *Phys Chem Chem Phys* 6:1340–1344
11. Larminie J, Dicks A (2003) *Fuel cell systems explained*, 2nd edn. John Wiley & Sons Ltd, Chichester, pp 121–137
12. Tomantschger K, Kordesch KV (1989) Structural analysis of alkaline fuel cell electrodes and electrode materials. *J Power Sources*:25195–25214
13. Skyllas-Kazakos M, Chakrabarti MH, Hajimolana S et al (2011) Progress in flow battery research and development. *J Electrochem Soc* 158:R55–R79
14. Haile SM (2003) Fuel cell materials and components. *Acta Mater*:515981–516000
15. Sakhnenko ND, Ved MV, Hapon YK, Nenastina TA (2015) Functional coatings of ternary alloys of cobalt with refractory metals. *Russ J Appl Chem* 87:1941–1945. <https://doi.org/10.1134/S1070427215012006X>
16. Kublanovsky VS, Yaponseva YS (2014) Electrocatalytic properties of Co–Mo alloys electrodeposited from a citrate-pyrophosphate electrolyte. *Electrocatalysis* 5:372–378. <https://doi.org/10.1007/s12678-014-0197-y>
17. Glushkova M, Bairachna T, Ved M, Sakhnenko M (2013) Electrodeposited cobalt alloys as materials for energy technology. In: *MRS proceedings*, vol 1491. Cambridge University Press, pp mrsf12–mr1491
18. Ramanauskas R, Gudavičiūtė L, Juškėnas R (2008) Effect of pulse plating on the composition and corrosion properties of Zn–Co and Zn–Fe alloy coatings. *Chemija* 19:7–13
19. Ved' MV, Sakhnenko ND, Karakurkchi AV, Zyubanova SI (2014) Electrodeposition of iron–molybdenum coatings from citrate electrolyte. *Russ J Appl Chem* 87:276–282. <https://doi.org/10.1134/S1070427214030057>
20. Shao H, Vereecken PM, Chien CL, Cammarata RC, Searson PC (2003) Electrochemical deposition of FeCo and FeCoV alloys. *J Electrochem Soc* 150:C184–C188
21. Tsyntsaru N, Cesiulis H, Budreika A (2012) The effect of electrodeposition conditions and post-annealing on nanostructure of Co–W coatings. *Surf Coat Technol* 206:4262–4269
22. Grabco DZ, Dikuser IA, Petrenko VI, Harea EE (2007) Micromechanical properties of Co–W alloys electrodeposited under pulse conditions. *Surf Eng and Appl Electrochem* 43:11–17
23. Silkin SA, Gotelyak AV, Tsyntsaru N, Dikuser AI, Kreivaitis R, Padgurskas J (2016) Effect of bulk current density on tribological properties of Fe–W, Co–W and Ni–W coatings. In: *Proceedings of the 8th International Scientific Conference "BALTRIB 2015"*. Published online 25 February 2016 by Aleksandras Stulginskis University. Kaunas, Lithuania, 51–56. <https://doi.org/10.15544/baltrib.2015.10>
24. Ma SL, Xi X, Nie Z, Dong T, Mao Y (2017) Electrodeposition and characterization of co–W alloy from regenerated tungsten. *Int J Electrochem Sci* 12:1034–1051. <https://doi.org/10.20964/2017.02.37>

25. Vernickaite E, Tsyntsaru N, Cesiulis H (2016) Electrodeposited co-W alloys and their prospects as effective anode for methanol oxidation in acidic media. *Surf & Coatings Tech* <https://doi.org/10.1016/j.surfcoat.2016.07.049>
26. Elezović N, Grgur BN, Krstajić NV, Jović VD (2005) Electrodeposition and characterization of Fe–Mo alloys as cathodes for hydrogen evolution in the process of chlorate production. *J Serb. Chem Soc* 70(6):879–889
27. Gomez E, Pellicer E, Alcobe X, Valles E (2004) Properties of co-Mo coatings obtained by electrodeposition at pH 6.6. *J Solid State Electrochem* 8:497–504. <https://doi.org/10.1007/s10008-004-0495-z>
28. Danilov FI, Sknar IV, Sknar YE (2014) Electroplating of Ni-Fe alloys from methanesulfonate electrolytes. *Russ J Electrochem* 50:293–296
29. Weston DP, Harris SJ, Shipway PH, Weston NJ, Yap GN (2010) Establishing relationships between bath chemistry, electrodeposition and microstructure of Co-W alloy coatings produced from a gluconate bath. *Electrochim Acta* 55:5695–5708
30. Ved MV, Sakhnenko MD (2010) Katalitychni ta zakhysni pokryttia splavamy i skladnymy oksydamy: elektrokhimichniyi syntez, prohnozuvannia vlastyvoستي [Tekst]: monohrafiia. Kharkiv NTU “KhPI” 272
31. Ćirović N, Spasojević P, Ribić-Zelenović L, Mašković P, Spasojević M (2015) Synthesis, structure and properties of nickel-iron-tungsten alloy electrodeposits PART I: effect of synthesis parameters on chemical composition, microstructure and morphology. *Sci Sinter* 47:347–365. <https://doi.org/10.2298/SOS1503347C>
32. Yermolenko IY, Ved' MV, Karakurkchi AV, Sakhnenko ND, Kolupaieva ZI (2017) Electrochemical behavior of  $\text{Fe}^{3+}\text{-WO}_4^{2-}\text{-Cit}^{3-}$  and  $\text{Fe}^{3+}\text{-MoO}_4^{2-}\text{-WO}_4^{2-}\text{-Cit}^{3-}$  systems. *The Issues of Chemistry and Chemical Technology* 2(III):4–14
33. Labardi M, Allegrini M, Salerno M, Fredriani C, Ascoli C (1994) Dynamical friction coefficient map using a scanning force and friction force microscope. *Appl Phys* 59:3
34. Karakurkchi AV, Ved' MV, Sakhnenko ND et al (2015) Functional properties of multicomponent galvanic alloys of iron with molybdenum and tungsten. *Func Mater* 22:181–187. <https://doi.org/10.15407/fm22.02.181>
35. Glushkova MO, Ved MV, Sakhnenko MD (2013) Corrosion properties of cobalt–silver alloy electroplates. *Mater Sci* 49:292–297. <https://doi.org/10.1007/s11003-013-9613-3>
36. Ved' M, Glushkova M, Sakhnenko N (2013) Catalytic properties of binary and ternary alloys based on silver. *Func Mater* 2087–91. <https://doi.org/10.15407/fm20.01.087>
37. Yermolenko IY, Ved' MV, Zyubanova SI, Androshchuk DS (2011) Polilihandni elektrolity dlya anodnoho rozchynennya splaviv vol'framu [Poliligand electrolytes for anodic dissolution of tungsten alloys]. *The Issues of Chemistry and Chemical Technology* 4:192–195
38. Tabakovic I, Gong J, Riemer S, Kautzky M (2015) Influence of surface roughness and current efficiency on composition gradients of thin NiFe films obtained by electrodeposition electrochemical/electroless deposition. *J Electrochem Soc* 162:D102–D108
39. Gómez E, Pellicer E, Vallés E (2004) Electrodeposition of soft-magnetic cobalt–molybdenum coatings containing low molybdenum percentages. *J Electroanal Chem* 568:29–36 <https://doi.org/10.1016/j.jelechem.2003.12.032>
40. Ghaferi Z, Sharafi S, Bahrololoom ME (2016) The role of electrolyte pH on phase evolution and magnetic properties of CoFeW codeposited films. *Appl Surf Sci* 375(1):35–41. <https://doi.org/10.1016/j.apsusc.2016.03.063>
41. Yermolenko IY, Ved MV, Sakhnenko ND, Sachanova YI (2017) Composition, morphology, and topography of galvanic coatings Fe-Co-W and Fe-Co-Mo. *Nanoscale Res Lett* 12(1):352. <https://doi.org/10.1186/s11671-017-2128-3>
42. Karakurkchi AV, Ved' MV, Sakhnenko ND, Ermolenko IY (2015) Electrodeposition of iron–molybdenum–tungsten coatings from citrate electrolytes. *Russ J Appl Chem* 88:1860–1869. <https://doi.org/10.1134/S1070427215011018X>
43. Li J, Meng S, Han J, Zhang X (2008) Valence electron structure and properties of the ZrO<sub>2</sub>. *Sci China Ser E-Technol Sci* 51:1858–1866. <https://doi.org/10.1007/s11431-008-0119-4>

44. Hu J, Zhang C, Cui B et al (2011) In vitro degradation of AZ31 magnesium alloy coated with nano TiO<sub>2</sub> film by sol-gel method. *Appl Surf Sci* 257:8772–8777
45. Cesiulis H, Tsyntaru N, Budreika A, Skridaila N (2010) Electrodeposition of CoMo and CoMoP alloys from the weakly acidic solutions. *Surf Engineering Appl Electrochem* 46:406–415. <https://doi.org/10.3103/S1068375510050030>
46. Yar-Mukhamedova GS (2000) Influence of thermal treatment on corrosion resistance of chromium and nickel composite coatings. *Mater Sci* 36:922–924
47. Yar-Mukhamedova GS (2000) Investigation of corrosion resistance of metallic composite thin-film systems before and after thermal treatment by the “Corrodokote” method. *Mater Sci* 37:140–143
48. Gennero MR, Chialvo AC (1998) Kinetics of hydrogen evolution reaction with Frumkin adsorption: re-examination of the Volmer-Heyrovsky and Volmer-Tafel routes. *Electrochim Acta* 44:841–851

## Chapter 2

# Multifunctional Magnetic Nanocomposites on the Base of Magnetite and Hydroxyapatite for Oncology Applications



Ie. V. Pylypchuk, M. V. Abramov, A. L. Petranovska, S. P. Turanksa, T. M. Budnyak, N. V. Kusyak, and P. P. Gorbyk

In works [11–13, 16, 20, 36–38], the concept of a chemical design of magnetosensitive nanocomposites with a multilevel hierarchical nano-architecture was substantiated which are characterized by the functions of “nano-clinics” [12] and medico-biological nanorobots [10–13, 16, 36, 37]: recognition of microbiological objects in biological media; targeted drug delivery into target cells and organs and deposition; complex local chemo-, immuno-, neutron capture, hyperthermic, photodynamic therapy and real-time magnetic resonance imaging diagnostics, detoxification of the body by adsorption of residual cell debris, virus particles, heavy metal ions, etc. and their removal by the means of a magnetic field.

In terms of synthesis of the abovementioned magnetosensitive nanocomposites (NCs), the researchers have a significant interest in nanostructures of the core-shell type on the basis of single-domain magnetite ( $\text{Fe}_3\text{O}_4$ ) and hydroxyapatite (HA) that retain oncologic drugs of different functional purposes and different mechanisms of action. Such NCs are characterized by the unique combination of physical, chemical, and biological properties, by the possibility of production of ferrofluids (FFs) on their basis [2, 3, 6, 7, 9, 17, 18, 22, 24, 34, 41]. Widespread application as oncologic drugs has, in particular, the cytostatic drug cisplatin (CP), the anthracycline antibiotic doxorubicin (DR) that are used practically in all the schemes of modern chemotherapy as well as antibodies that allow realizing the principles of recognition of antigens and immunotherapy.

---

Ie. V. Pylypchuk · M. V. Abramov · A. L. Petranovska · S. P. Turanksa · T. M. Budnyak (✉)  
P. P. Gorbyk  
Chuiko Institute of Surface Chemistry of National Academy of Sciences of Ukraine, Kyiv,  
Ukraine

N. V. Kusyak  
Ivan Franko Zhytomyr State University, Zhytomyr, Ukraine

The choice of single-domain magnetite as an input material for NC synthesis is due to its unique magnetic properties, satisfactory biocompatibility and biodegradation, accumulated experience in the field of surface modification, possibilities to control the movement of nanoparticles by the means of the external magnetic field, use of the magnetic separation method at the stages of separation, and removal of adsorbents. The special features of single-domain state of magnetic particles include the homogeneity of magnetization at any values and directions of the  $H$  field, the possibility of an existence of domains not only in solid ferro- and ferrimagnetic alloys and compounds but also in liquid media (suspensions and colloids).

The usage of HA as a coating for magnetosensitive carriers is due to its high biocompatibility with a living organism, stability in biological media, adsorbent activity of the surface, possibility to ensure the necessary chemical functionalization of the carrier surface for further biofunctionalization.

This work gives a short overview of the research studies done at the Chuiko Institute of surface chemistry of the National Academy of Sciences of Ukraine aimed at the development of the concept of creation of magnetosensitive NCs of a multilevel hierarchical nano-architecture and a function of medico-biological nanorobots. The data are provided in relation to the synthesis of magnetosensitive NCs of the core-cell type on the basis of single-domain magnetite and hydroxyapatite, specificity of immobilization on the surface of oncologic drugs of different mechanisms of action, bioactivity checking, development of the methodology of creation of ferrofluids on the basis of synthesized NCs, and determination of perspective of their application in oncology.

**Synthesis of Magnetite/Hydroxyapatite Nanocomposites** Synthesis of the hydroxyapatite coating on the surface of a highly dispersed magnetite was carried out by solgel method, according to reaction:  $10\text{Ca}(\text{NO}_3)_2 + 6(\text{NH}_4)_2\text{HPO}_4 + 8\text{NH}_3 + 2\text{H}_2\text{O} \rightarrow \text{Ca}_{10}(\text{PO}_4)_6(\text{OH})_2 + 20\text{NH}_4\text{NO}_3$ .

XRD patterns confirmed the presence of a magnetite phase ( $\text{Fe}_3\text{O}_4$ , JCPDS №19-629) and hydroxyapatite ( $\text{Ca}_{10}(\text{PO}_4)_6(\text{OH})_2$ , JCPDS №74-0566).

**Synthesis of  $\text{Fe}_3\text{O}_4$ /HA/Ag Nanocomposites** The modification of  $\text{Fe}_3\text{O}_4$ /HA nanocomposite by silver nanoparticles was made from  $\text{AgNO}_3$  solution. The quantity of silver input in the reaction mixture made 1% of the mass of  $\text{Fe}_3\text{O}_4/\text{Ca}_{10}(\text{PO}_4)_6(\text{OH})_2$  sample. The reduction of silver ions was made by 0.005% hydrazine hydrate on heating and stirring according to the reactions:  $4\text{Ag}^+ + \text{N}_2\text{H}_4 + 4\text{OH}^- \rightarrow 4\text{Ag}^0 + \text{N}_2 + 4\text{H}_2\text{O}$ .

The presence of silver on the surface is confirmed by the XRD analysis. The mean size of Ag nanoparticles calculated as per the Scherrer formula was  $\sim 10$  nm.

**Cytotoxic Properties of Ferrofluids on the Basis of Cisplatin (CP)** The synthesized nanostructures as part of a ferrofluid (FF) were used for development of a new form of the oncology drug "Ferroplat" which was for the first time experimentally substantiated at the R.E. Kavetsky Institute for experimental pathology, oncology,

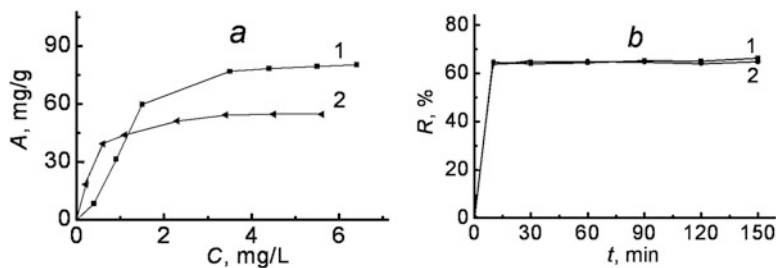


**Fig. 2.1** Isotherms (a) and kinetics (b) of the CP adsorption on magnetite (1) and Fe<sub>3</sub>O<sub>4</sub>/HA NC (2)

and radiobiology of the National Academy of Sciences of Ukraine, which is now at the stage of putting into production. The idea of the mentioned new form lies in the strategy of overcoming the resistance of malignant tumors to cisplatin via pharmacological correction of endogenous iron metabolism which is ensured by utilization of a ferriferous nanocomposite and cisplatin.

For the adsorption investigations of CP on the Fe<sub>3</sub>O<sub>4</sub> and Fe<sub>3</sub>O<sub>4</sub>/HA samples were used (Fig. 2.1a, b).

It was found that the highest cytotoxic activity of the nanocomposite for the MCF-7/CP resistant line is related to a more active accumulation of ferromagnetic nanoparticles in the cells, due a high level of transferrin receptors and a disturbance of the system of antioxidant protection of the resistant cells. It was shown that a ferrofluid is able to cause in cells of the resistant line more pronounced cytomorphological changes and genotoxic effects compared to cells of the sensitive line.

In the case of therapy of rats of the Wistar line with an FF containing inoculated Geren carcinoma resistant to cisplatin, a positive antitumor effect on tumors of the strain resistant to cisplatin was found: the mean volume of tumors decreased from  $20.2 \pm 1.0 \text{ cm}^3$  in the control group to  $12.1 \pm 2.4 \text{ cm}^3$  in animals that were injected with the nanocomposite; the percentage of slowdown of the tumor growth was 40%.

**Antibodies Binding to the Fe<sub>3</sub>O<sub>4</sub>/HA/Ag Nanocomposites** The formation on the surface of modified magnetosensitive carriers of the regions with spacers for binding monoclonal antibodies is one of the important stages of synthesis of biofunctionalized nanocomposites. The purpose of this research was to study the processes of antibody immobilization on the surface of Fe<sub>3</sub>O<sub>4</sub>/HA and Fe<sub>3</sub>O<sub>4</sub>/HA/Ag. It was found that the shape of the obtained isotherms of immunoglobulin adsorption varies between different buffer systems (Figs. 2.2 and 2.3; Table 2.1).

Taking into account a high adsorption ( $A = 34\text{--}38 \text{ mg/g}$ ) of immunoglobulin, the formation of a compact packing of adsorbed antibodies on the NC surface modified by HA and silver can be assumed. The given results of experimental research [10]

**Fig. 2.2** Isotherms of adsorption of human normal Ig on the surface of  $\text{Fe}_3\text{O}_4/\text{HA}$  and  $\text{Fe}_3\text{O}_4/\text{HA}/\text{Ag}$  nanocomposites from phosphate buffer

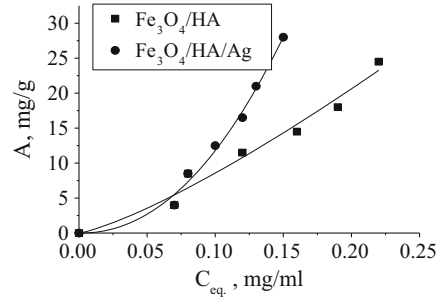


**Fig. 2.3** Isotherms of adsorption of human normal Ig on the surface of  $\text{Fe}_3\text{O}_4/\text{HA}$  and  $\text{Fe}_3\text{O}_4/\text{HA}/\text{Ag}$  nanocomposites from saline solution

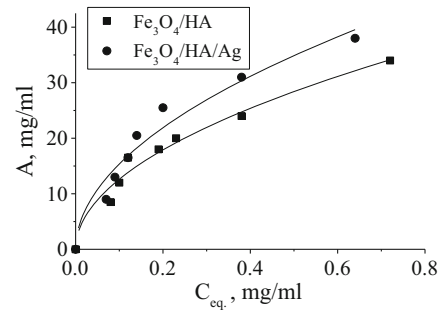


**Table 2.1** Effect of magnetosensitive NCs with adsorbed CP conjugated with monoclonal antibodies on the survivability of MCF-7 line cells

Comparison control	Dead cells, %			
	Action of control samples	$\text{Fe}_3\text{O}_4/\text{HA} + \text{CP}$	$\text{Fe}_3\text{O}_4/\text{HA} + \text{CD 95}$	$\text{Fe}_3\text{O}_4/\text{HA} + \text{CP} + \text{CD 95}$
Cisplatin (CP) $C = 2.5 \mu\text{g/ml}$	25	48		
Antibody CD 95 $C = 0.2 \mu\text{g/ml}$	10		27	

show that the use of nanocomposites with antibodies in principle allows to realize the recognition of specific cells.

### Adsorption of Doxorubicin by Magnetite/Hydroxyapatite Nanocomposites

The adsorption of doxorubicin by magnetite/hydroxyapatite nanocomposites is studied in [2].

Doxorubicin [26] is an antitumor antibiotic of anthracyclines range; the empirical formula is  $\text{C}_{27}\text{H}_{29}\text{NO}_{11}$ . It is characterized by antimitotic and antiproliferative effects. The mechanism of antineoplastic activity is in an interaction with DNA, a formation of free radicals and a direct impact on cell membranes along with an inhibition of the synthesis of nucleic acids.

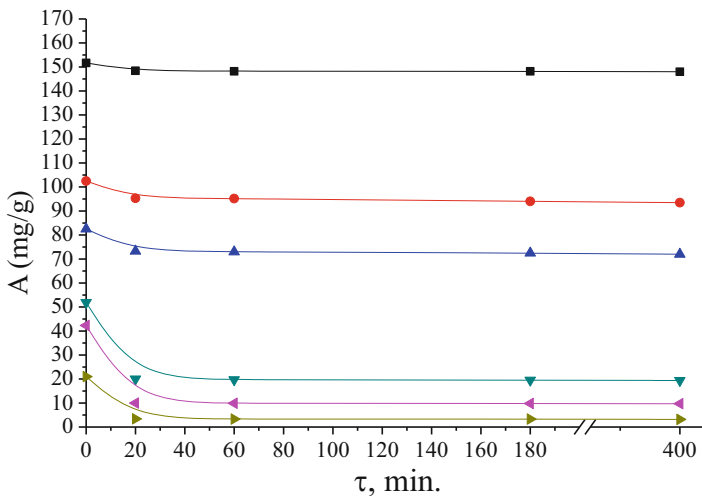


The study of DR adsorption isotherm on the surface of the  $\text{Fe}_3\text{O}_4/\text{HA}$  nanocomposite was carried out in a range of equilibrium concentrations  $C_0 = 0.1\text{--}1.04$  mg/ml. The experimental results prove that an increase in an equilibrium concentration of DR does not lead to a saturated adsorption of the surface of the  $\text{Fe}_3\text{O}_4/\text{HA}$  adsorbent.

The concavity (S-type) of the initial section of the isotherm relative to the axis of concentrations and the absence of saturation in the studied interval of equilibrium concentrations can be connected with a polymolecular type of adsorption and an insignificant porosity of the nanocomposite surface. Besides, the S-type of the isotherm may be caused, to a certain extent, by a joint adsorption of sodium chloride because a DR adsorption occurred from a physiological fluid. The coefficient of distribution ( $E$ , ml/g) of doxorubicin between the nanocomposite surface and the fluid was 366.8 ml/g at  $A = 91.7$  mg/g.

During the study of DR adsorption on the surface of  $\text{Fe}_3\text{O}_4/\text{HA}$  nanocomposite as a function of time (Fig. 2.4), it was found that during the first 2 hours, 60–70% of the substance is adsorbed and during 24 h the adsorption occurs almost completely (93–97%). The relationship of the degree of doxorubicin removal ( $R$ , %) vs. solutions concentration and an adsorption time is shown in Table 2.2.

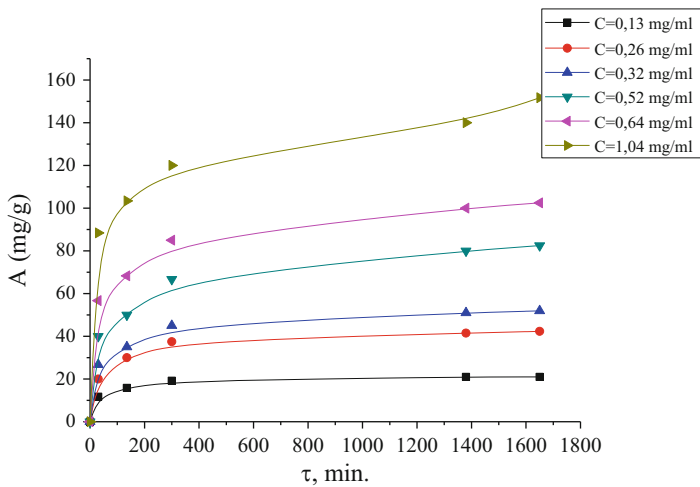
The results of desorption ( $A_D$ , mg/g) study are given in Fig. 2.5 and Table 2.3. The experimental relationships of desorption vs. time indicate that the DR release decreases as its quantity on the NC surface grows. At a quantity of adsorbed DR of 20–50 mg/g, 80–60% of DR is desorbed, respectively, while at large quantities of desorbed DR (100–150 mg/g), the release almost does not occur. Most of DR is desorbed during 20 min for all the studied concentrations.



**Fig. 2.4** Time-dependent  $\tau$  desorption of DR ( $A_D$ ) from the surface of  $\text{Fe}_3\text{O}_4/\text{HA}/\text{DR}$  NC into saline solution at different initial quantities of DR immobilized by adsorption

**Table 2.2** Degree of DR removal ( $R$ , %) by  $\text{Fe}_3\text{O}_4/\text{HA}$  NC as a function of a solution concentration and an adsorption time

$C_0$ , mg/ml	$R$ , %				
	30 min.	135 min.	300 min.	1380 min.	1620 min.
0.13	53.8	73.1	88.5	97.0	97.0
0.26	46.2	69.2	86.5	95.8	97.7
0.32	50.0	65.6	84.4	95.6	97.2
0.52	46.2	57.7	77.0	92.3	95.2
0.64	53.1	64.0	79.7	93.8	96.1
1.04	49.0	59.6	69.2	80.8	87.5

**Fig. 2.5** Relationship of DR adsorption by  $\text{Fe}_3\text{O}_4/\text{HA}$  NC in PF vs. time. The insertion shows the initial concentrations of DR solutions**Table 2.3** Relationship of DR desorption ( $A_{D\tau}$ , %) from the surface of  $\text{Fe}_3\text{O}_4/\text{HA}/\text{DR}$  NC into saline solution vs. time at different initial quantities ( $A$ ) of DR immobilized by adsorption

$A$ , mg/g	$D$ , %			
	20 min.	60 min.	180 min.	400 min.
21.0	83.8	84.3	84.3	84.8
42.3	76.4	76.6	76.8	77.0
51.9	61.5	62.1	62.4	62.6
82.5	11.6	11.5	12.1	12.7
102.5	7.0	6.1	8.3	8.7
151.7	2.2	2.3	2.3	2.4

It was found that an increase in an equilibrium concentration of DR does not lead to a saturated adsorption of the surface of the  $\text{Fe}_3\text{O}_4/\text{HA}$  adsorbent. It was discovered that the release of DR into saline solution has been decreasing as its quantity on the NC surface has been increasing.

### Investigation of Bioactivity of Nanocomposites on the Basis of Doxorubicin

The biocompatibility of  $\text{Fe}_3\text{O}_4/\text{HA}$  NC was studied in many works, for example, in [2, 6, 7, 9, 11, 12, 17, 18, 22, 24, 37]. In works [2, 24, 39], the biocompatibility and the bioactivity of the produced samples were controlled by their effect on the viability of baking yeast cells *Saccharomyces cerevisiae*.

In works [19, 23, 35], the interaction of DR with baking yeast cells *Saccharomyces cerevisiae* was studied. In particular, the presence of a cytotoxic effect of the antibiotic on the cells and a decrease in the rate of their proliferation were found. The mentioned effects are typical of DR and are caused, in particular, by its participation in cyclic redox reactions and a respective increase in the number of molecules of free radicals, an induction of oxidative stress and delays in the cell cycle in  $G_1$ - and S-phases. However, we did not manage to find in scientific sources the data related to the impact of magnetosensitive nanocomposites containing doxorubicin on baking yeast cells *Saccharomyces cerevisiae*.

Therefore, of interest was the research aimed at studying a cytotoxic effect of new magneto-controlled multifunctional NCs on the basis of single-domain  $\text{Fe}_3\text{O}_4$ , HA, and DR on *Saccharomyces cerevisiae* cells [39].

During the research of bioactivity of the input DR preparation, it was experimentally found that its solution in a physiological fluid of a concentration of 0.5 mg/ml leads to an almost total death of yeast cells (95%) within 3.5 days. In the methodology of cytotoxicity determination, usually use a  $\text{IC}_{50}$  dose at which the death of  $\sim 50\%$  of cells are observed [15]. That's why for bioactivity testing a quantity of nanocomposite material  $\text{Fe}_3\text{O}_4/\text{HA}/\text{DR}$  ( $\sim 20$  mg) with immobilized doxorubicin ( $\sim 50$  mg/g) which is used to make a suspension was selected as per the data of Fig. 18 and Table 2.2, to ensure that the concentration of released DR in the tested suspensions is equal to  $\sim 0.25$  mg/ml.

In total five samples of each of the following series were tested:

1. Suspension of yeast cells (initial concentration  $n_0 \approx 2.5 \cdot 10^7 \text{ ml}^{-1}$ ) in PF with MSM (Fig. 2.6a)
2. Suspension of yeast cells (initial concentration  $n_0 \approx 2.5 \cdot 10^7 \text{ ml}^{-1}$ ) in PF with MSM containing 20 mg of  $\text{Fe}_3\text{O}_4/\text{HA}$  NC
3. Suspension of yeast cells (initial concentration  $n_0 \approx 3.5 \cdot 10^7 \text{ ml}^{-1}$ ) in PF with MSM containing 20 mg of  $\text{Fe}_3\text{O}_4/\text{HA}/\text{DR}$  NC

All the samples contained 1.3 ml of saline solution (0.9% NaCl) and 1 ml of MSM. The samples of series 1 and 2 were used for control and comparison and of series 3 – for research of bioactivity of  $\text{Fe}_3\text{O}_4/\text{HA}/\text{DR}$  NC.

The data analysis shows that in the yeast suspensions ( $n_0 \approx 2.5 \cdot 10^7 \text{ ml}^{-1}$ ) in PF with MSM (type 1 control series) a cell proliferation typical of yeast is seen, which led to a twofold increase in their concentration within 16 h (to  $5 \cdot 10^7 \text{ ml}^{-1}$ ).

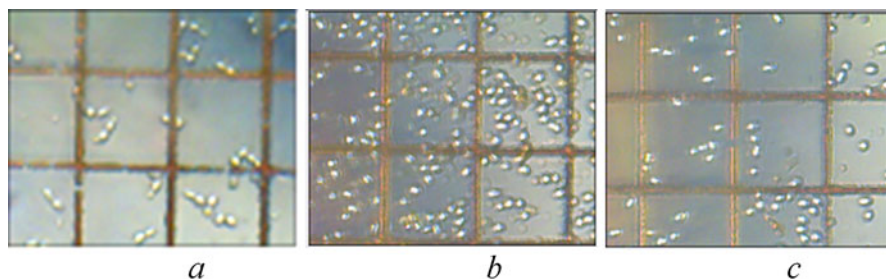


**Fig. 2.6** Type images of Goryaev's camera squares with yeast cells: at the beginning of research (a), after a reaction of yeast cells with  $\text{Fe}_3\text{O}_4/\text{HA}$  NC (b), after a reaction of yeast cells with  $\text{Fe}_3\text{O}_4/\text{HA}/\text{DR}$  NC (c)

Subsequently, the rate of their proliferation was slowing down (probably due to a smaller quantity of nutrient material). 3.5 days later their concentration was  $\sim 10^8 \text{ ml}^{-1}$ . The survivability of yeast cells in the series 1 tests changed insignificantly and reached  $\sim 98\text{--}99\%$ .

During testing the suspensions of type 2 control series, a rather active fission was recorded, as a result of which the yeast concentration was  $\sim 6.5 \cdot 10^7 \text{ ml}^{-1}$  after 18 h, while after 3.5 days, like in the previous case, it reached  $\sim 10^8 \text{ ml}^{-1}$  (Fig. 2.6b). The survivability of cells, like the in the previous case, at all the research stages of series 2 samples was  $\sim 98\text{--}99\%$ . The given data prove the biocompatibility of  $\text{Fe}_3\text{O}_4/\text{HA}$  NC in relation to yeast cells in experimental conditions.

By testing of the samples of series 3 suspensions, a considerable inhibition of cell proliferation was found (Fig. 2.6c). So, the concentration of yeast cells at the beginning of the experiment was  $\sim 3.5 \cdot 10^7 \text{ ml}^{-1}$  and practically did not change for 16 h; only after 3.5 days, their quantity grew up to  $\sim 4 \cdot 10^7 \text{ ml}^{-1}$ . Over the research time, the number of dead cells in series 3 samples (Fig. 2.6c) was  $\sim 10\%$ .

So, analyzing the results of series 1 and 2 experiments and comparing them with the series 3 data, it can be concluded that  $\text{Fe}_3\text{O}_4/\text{HA}/\text{DR}$  nanocomposites exert a cytotoxic effect on *Saccharomyces cerevisiae* cells and slow down the rate of their proliferation.

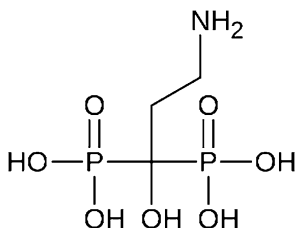
It should be noted that the observed peculiarities of the influence of magnetosensitive  $\text{Fe}_3\text{O}_4/\text{HA}/\text{DR}$  NCs on yeast cells are typical of an interaction of the mentioned cells with doxorubicin in a free form. The obtained results served as a basis for the elaboration of an efficient, reliable, safe, and relatively inexpensive methodology of control after the cytotoxic activity of nanocomposites which can be topical for the use in the development of new magneto-controlled targeted delivery drugs [39].

**Synthesis of Gadolinium-Comprising Magnetosensitive Nanocomposites for Neutron Capture Therapy** The development of scientific approaches to solving the problem of introduction of magneto-controlled polyfunctional nanocomposites into neutron capture therapy (NCT) is, certainly, an expedient and topical task

because they can serve as a basis for creation of new types of low-toxic selective drugs with added functions of magneto-controlled targeted delivery to target organs or cells and deposit, of hyperthermia and combined  $T_1$ - and  $T_2$ -MRI real-time diagnostics [4, 5, 8, 10, 14, 21, 27–30, 40].

With the aim of synthesizing magnetosensitive NCs of a high biocompatibility with bone tissues which are promising for the use in NCT, a new methodology [33] of immobilization of a DTPA-Gd complex on the surface of  $\text{Fe}_3\text{O}_4/\text{HA}$  NCs was developed.

It is known that amino bisphosphonates are used for prevention and treatment of osteoporosis because they inhibit resorption of bone tissue. Thanks for the presence of phosphonic groups, the drugs of this class bind to HA tightly and cause a therapeutic effect. For research one of the simplest and commercially available compounds of this class – pamidronic acid (PA) – has been chosen.



The adsorption of pamidronate on the HA surface occurs due to a formation of hydrogen bonds between protons of amino groups and of hydroxyl groups on the surface and to a coordination of a calcium atom with phosphate groups. Therefore, for pamidronate, a high affinity and a strong bond to the HA surface are observed, and the obtained  $\text{Fe}_3\text{O}_4/\text{HA}/\text{PA}$  nanocomposite can serve as a reliable basis for further fixation of necessary ligands.

Following a reaction between the  $-\text{NH}_2$  groups of pamidronic acid and DTPA anhydride, a  $\text{Fe}_3\text{O}_4/\text{HA}/\text{PA}/\text{DTPA}$  NC was obtained. Subsequently, free carboxyl groups on the surface of a  $\text{Fe}_3\text{O}_4/\text{HA}/\text{PA}/\text{DTPA}$  NC form strong complexes with gadolinium ions producing a  $\text{Fe}_3\text{O}_4/\text{HA}/\text{PA}/\text{DTPA}/\text{Gd}^{3+}$  NC.

A scheme of the nanocomposite formation is given in general in Fig. 2.7.

The structure of a  $\text{Fe}_3\text{O}_4/\text{HA}/\text{PA}/\text{DTPA}/\text{Gd}^{3+}$  NC was studied by using a complex of physicochemical methods at all the stages of its synthesis; the biocompatibility testing of a  $\text{Fe}_3\text{O}_4/\text{HA}/\text{PA}/\text{DTPA}/\text{Gd}^{3+}$  NC in vitro was performed on model cells [1, 33]. A conclusion on perspective of synthesized magnetosensitive NCs for further research with the aim of the creation of agents for therapy of oncological diseases by the neutron capture method was drawn.

It should be noted that biomimetic approach [25, 31, 32] to coating the magnetite surface with hydroxyapatite is promising and currently is under the development in our department.

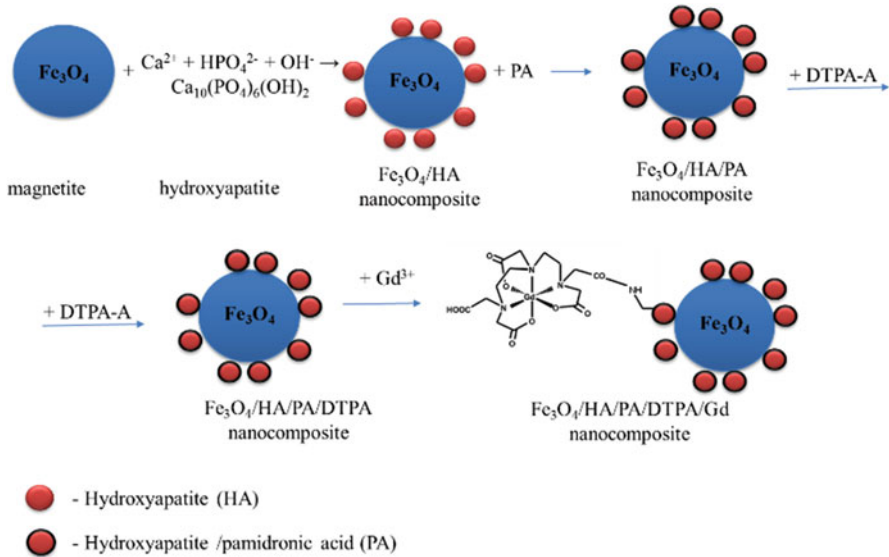


Fig. 2.7 Scheme of a  $\text{Fe}_3\text{O}_4/\text{HA}/\text{PA}/\text{DTPA}/\text{Gd}^{3+}$  NC formation

## 2.1 Conclusions

The processes of a DR adsorption of the surface of a  $\text{Fe}_3\text{O}_4/\text{HA}$  NC from the solution in a physiological fluid were studied. It was discovered that an increase in an equilibrium concentration of DR does not lead to a saturated adsorption on the surface of a  $\text{Fe}_3\text{O}_4/\text{HA}$  adsorbent. It was found that the release of DR into saline solution decreased as its quantity of the NC surface has been increased.

Magneto-sensitive  $\text{Fe}_3\text{O}_4/\text{HA}/\text{DR}$  NCs were synthesized. It was found that a cytotoxic effect and an antiproliferative activity of NCs in relation to *Saccharomyces cerevisiae* cells are typical of an interaction of the mentioned cells with doxorubicin in free form.

The ferrofluids containing  $\text{Fe}_3\text{O}_4/\text{HA}/\text{DR}$  NC stabilized by sodium oleate and polyethylene glycol were produced and studied. By using an assembly of  $\text{Fe}_3\text{O}_4$  carriers as a superparamagnetic probe, the Langevin theory of paramagnetism, and the density values of nanocomposite components, the parameters of their shells were assessed, which are confirmed by independent measurements of the specific surface area of nanostructures and the kinetic stability of respective ferrofluids. The obtained results can be used for development of new forms of magneto-controlled targeted delivery drugs and adsorbents on the basis of nanocomposites of a superparamagnetic core-shell type with a multilevel nano-architecture and for determination, control, and optimization of size parameters of its components.

It was found that an FF on the basis of a  $\text{Fe}_3\text{O}_4/\text{HA}$  NC and cisplatin is characterized by a cytotoxic activity in relation to cells with a drug resistance

phenotype and is not more toxic than the official antineoplastic drug cisplatin, which is indicative of perspective of its use for pathogenetically grounded targeted therapy of malignant neoplasms.

Fe<sub>3</sub>O<sub>4</sub>/HA NCs can be used for the creation of the newest magnetosensitive theranostic drugs for neutron capture oncology. Claimed use of a biomimetic approach for coating the surface of nano-sized magnetite with hydroxyapatite is given.

**Acknowledgments** The work was carried out with the support of the target comprehensive program of fundamental research of the National Academy of Sciences of Ukraine "Fundamental problems of the creation of new nanomaterials and nanotechnologies" for 2015–2019 (Project No. 38/17-n). The publication contains the results of research conducted with the grant support of the State Fund for Fundamental Research (project 31566).

## References

1. Abramov N (2014) Magnetic fluid on the basis of doxorubicin for the application in oncology. *Surface* 6(21):241–258
2. Abramov N, Turanska S, Kusyuk A, Petranovska A, Gorbyk P (2016) Synthesis and properties of magnetite/hydroxyapatite/doxorubicin nanocomposites and magnetic liquids based on them. *J Nanostruct Chem* 6:223–233
3. Anirudhan T, Sandeep S (2012) Synthesis, characterization, cellular uptake and cytotoxicity of a multi-functional magnetic nanocomposite for the targeted delivery and controlled release of doxorubicin to cancer cells. *J Mater Chem* 22:12888–12899
4. Bellin M-F (2006) MR contrast agents, the old and the new. *Eur J Radiol* 60:314–323
5. Caravan P (2006) Strategies for increasing the sensitivity of gadolinium based MRI contrast agents. *Chem Soc Rev* 35:512–523
6. Chen F, Li C, Zhu Y-J, Zhao X-Y, Lu B-Q, Wu J (2013) Magnetic nanocomposite of hydroxyapatite ultrathin nanosheets/Fe<sub>3</sub>O<sub>4</sub> nanoparticles: microwave-assisted rapid synthesis and application in pH-responsive drug release. *Biomater Sci* 1:1074–1081
7. Davaran S, Alimirzalu S, Nejati-Koshki K, Nasrabadi HT, Akbarzadeh A, Khandaghi AA, Abbasian M, Alimohammadi S (2014) Physicochemical characteristics of Fe. *Asian Pac J Cancer Prev* 15:49–54
8. Fukumori Y, Ichikawa H (2006) Nanoparticles for cancer therapy and diagnosis. *Adv Powder Technol* 17:1–28
9. Gopi D, Ansari MT, Shinyjoy E, Kavitha L (2012) Synthesis and spectroscopic characterization of magnetic hydroxyapatite nanocomposite using ultrasonic irradiation. *Spectrochim Acta A Mol Biomol Spectrosc* 87:245–250
10. Gorbyk P (2013) Nanocomposites with medico-biological properties: synthesis, properties and application. *Nanosyst Nanomater Nanotechnol* 11:323–436
11. Gorbyk P, Chekhun V, Vovk R, Nazyrov Z, Kruglyak V, Ogrin F, Edelman I, Malakhovskii A, Sokolov A, Sukhachev A (2012) Nanocomposites of medicobiologic destination: reality and perspectives for oncology. *Funct Mater* 19:145
12. Gorbyk P, Lerman L, Petranovska A & Turanska S (2014) Magnetosensitive nanocomposites with functions of medico-biological nanorobots: synthesis and properties. In book: *Advances in Semiconductor Research: Physics of Nanosystems, Spintronics and Technological Applications*. 161–198
13. Gorbyk, P., Petranovska, A., Usov, D. & Storozhuk, L. 2012. Nanocapsule with nanorobots function. *Patent of Ukraine*

14. Gorbyk P, Petranovskaya A, Pilipchuk E, Abramov N, Oranskaya E, Korduban A (2012) Synthesis of magnetosensitive Gd-containing nanostructures. *Chem Phys Technol Surface/Khimiya, Fizyka ta Tekhnologiya Poverhni* 2
15. Gorbyk P, Turov V (2011) Nanomaterials and nanocomposites in medicine, biology, ecology. Naukova Dumka, Kyiv
16. Grumezescu A (2016) Fabrication and self-assembly of Nanobiomaterials. *Appl Nanobiomater*, William Andrew
17. Huang C, Zhou Y, Tang Z, Guo X, Qian Z, Zhou S (2011) Synthesis of multifunctional Fe<sub>3</sub>O<sub>4</sub> core/hydroxyapatite shell nanocomposites by biom mineralization. *Dalton Trans* 40:5026–5031
18. Iwasaki T (2013) Mechanochemical synthesis of magnetite/hydroxyapatite nanocomposites for hyperthermia. In: Moshe H, Mastai Y (eds.) *Materials science-advanced topics*. InTech Open, UK
19. Kule C, Ondrejickova O, Verner K (1994) Doxorubicin, daunorubicin, and mitoxantrone cytotoxicity in yeast. *Mol Pharmacol* 46:1234–1240
20. Levy L, Sahoo Y, Kim K-S, Bergery EJ, Prasad PN (2002) Nanochemistry: synthesis and characterization of multifunctional nanoclinics for biological applications. *Chem Mater* 14:3715–3721
21. Lowe MP (2002) MRI contrast agents: the next generation. *Aust J Chem* 55:551–556
22. Mir A, Mallik D, Bhattacharyya S, Mahata D, Sinha A, Nayar S (2010) Aqueous ferrofluids as templates for magnetic hydroxyapatite nanocomposites. *J Mater Sci Mater Med* 21:2365–2369
23. Patel S, Sprung AU, Keller BA, Heaton VJ, Fisher LM (1997) Identification of yeast DNA topoisomerase II mutants resistant to the antitumor drug doxorubicin: implications for the mechanisms of doxorubicin action and cytotoxicity. *Mol Pharmacol* 52:658–666
24. Petranovska A, Abramov N, Turanska S, Gorbyk P, Kaminskiy A, Kussyak N (2015) Adsorption of cis-dichlorodiammineplatinum by nanostructures based on single-domain magnetite. *J Nanostruct Chem* 5:275–285
25. Petranovskaya A, Turelik M, Pilipchuk E, gorbik P, Korduban A, Ivashishin O (2013) Formation of biomimetic hydroxyapatite on the surface of titanium. *Metallophys Latest Technol* 35:1567–1584
26. Pharmacopoeia TE (2008) *The European Pharmacopoeia sixth edition, 2008*. In: ISBN
27. Pylypchuk E, Gorbyk P (2014) B- and Gd-containing nanomaterials and nanocomposites for neutron capture therapy. *Surface*:150–183
28. Pylypchuk E, Petranovska A, Gorbyk P (2012) Synthesis and properties of nanocomposites based on magnetite modified with DTPA. *Nanostrukturnoye Materialovedeniye (Nanostruct Mater Sci)* 3:47
29. Pylypchuk IV, Kolodyńska D, Gorbyk P (2017) Gd (III) adsorption on the DTPA-functionalized chitosan/magnetite nanocomposites. *Separat Sci Technol* 53(7):1006–1016
30. Pylypchuk IV, Kolodyńska D, Koziol M, Gorbyk P (2016) Gd-DTPA adsorption on chitosan/magnetite nanocomposites. *Nanoscale Res Lett* 11:168
31. Pylypchuk IV, Petranovska AL, Turelyk MP, Gorbyk PP (2014) Formation of biomimetic hydroxyapatite coating on titanium plates. *Mater Sci* 20:328–332
32. Pylypchuk IV, Petranovskaya A, Gorbyk P, Korduban A, Markovsky P, Ivasishin O (2015) Biomimetic hydroxyapatite growth on functionalized surfaces of Ti-6Al-4V and Ti-Zr-Nb alloys. *Nanoscale Res Lett* 10:338
33. Pylypchuk IV, Zubchuk YO, Petranovskaya A, Turanska S, Gorbyk P (2015) Synthesis and properties of Fe<sub>3</sub>O<sub>4</sub>/HA/pamidronic acid/DTPA-Gd nanocomposites. *Хімія, фізика та технологія поверхні* 6:326–335
34. Sadighian S, Hosseini-Monfared H, Rostamizadeh K, Hamidi M (2015) pH-Triggered magnetic-chitosan nanogels (MCNs) for doxorubicin delivery: physically vs. chemically cross linking approach. *Advan Pharmaceut Bull* 5:115
35. Saenko YV, Shutov A, Rastorgueva E (2010) Doxorubicin and menadione decrease cell proliferation of *Saccharomyces cerevisiae* by different mechanisms. *Cell Tissue Biol* 4:332–336



36. Shpak A, Gorbyk P (2007) Physical chemistry of Nanomaterials and Supramolecular structures. Naukova Dumka, Kyiv
37. Shpak AP, Gorbyk PP (2010) Nanomaterials and supramolecular structures. Physics chemistry and applications. Springer, Netherlands
38. Shylova OA, Shylov V (2003) Nanocomposite oxide and hybrid organo-inorganic materials produced by the sol-gel method. *Nanosyst Nanomater Nanotechnol* 1:9–83
39. Turanska S, Kusyak A, Petranovska A, Turov V, Gorbyk P (2016) Cytotoxic activity of magnet-guided doxorubicin-based nanocomposites with *Saccharomyces cerevisiae* cells as an example. *Chem Phys Technol Surface* 7:236–245
40. Turelik M, Gorobets S, Makedonska A, Gorbik P (2012) Biofunctionalization of nanocomposites on the basis of magnet-ite, modified by meso-2, 3-dimercaptosuccinic acid. *Research Bulletin of NTUU" Kyiv Polytechnic Institute*. 149–154
41. Wahajuddin SA (2012) Superparamagnetic iron oxide nanoparticles: magnetic nanoplatforms as drug carriers. *Int J Nanomedicine* 7:3445

# Chapter 3

## Structural Peculiarities and Properties of Silver-Containing Polymer Nanocomposites



V. Demchenko, S. Riabov, S. Kobylinskyi, L. Goncharenko,  
and N. Rybalchenko

### 3.1 Introduction

During the last decades, the interest in studying of nanosize particles of different metals and their oxides has constantly grown up [1–4]. Primarily, it is due to their unique characteristics, dramatically different from their analogues – micro-scale size objects. So, this fact opens new possibilities for diverse applications of nanomaterials, having advanced properties in industrial areas.

Hybrid materials, containing silver nanoparticles, show promising features for the design of catalytic systems, and they are currently used in optoelectronics and nanophotonics [5–10]. In turn, nanocomposite materials [10–12] with silver nanoparticles have found a wide application as effective antibacterial and antiviral preparations. Within the recent years (due to the emergence of microorganisms resistant to known antimicrobial agents), demand in new high-effective substances for saturation of dressing materials in medical facilities, as well as for the formation of antimicrobial coatings for providing of sterile conditions in biological and medical laboratories, for food packaging, for design of antimicrobial air filters for hospitals' and microbiological laboratories ventilation, etc., has appeared and is rapidly growing. Metal nanoparticles, such as copper, silver, and zinc, are in the focus of the researchers involved into development of effective antimicrobial agents due to their biocidal activity and high stability in extremal conditions.

---

V. Demchenko (✉) · S. Riabov · S. Kobylinskyi · L. Goncharenko  
Institute of Macromolecular Chemistry, The National Academy of Sciences of Ukraine, Kyiv,  
Ukraine

N. Rybalchenko  
Zabolotny Institute of Microbiology and Virology, The National Academy of Sciences of  
Ukraine, Kyiv, Ukraine

Developing of such materials is not possible without fundamental researches and studying their structure and physicochemical and mechanical properties.

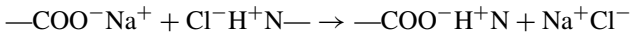
The current review of scientific sources revealed that data concerning investigations of structural organization and physical, mechanical, and antimicrobial properties of Ag-containing nanocomposites obtained by chemical or thermal reduction of  $\text{Ag}^+$  ions in the interpolyelectrolyte–metal complexes are not published yet.

So, the aim of this work is to study the structural organization and thermomechanical and antimicrobial properties of nanocomposites prepared involving natural and synthetic polymers – pectin, polyethyleneimine, poly(4-vinylpyridine), and Ag nanoparticles – obtained by the chemical and thermal reduction of silver ions in the interpolyelectrolyte–metal complexes.

### 3.2 Structural Formation and Thermomechanical Properties of Polymer Nanocomposites Based on Pectin–Poly(4-Vinylpyridine) Interpolyelectrolyte Complexes and Ag Nanoparticles

To obtain the interpolyelectrolyte complexes (IPEC), pectin–poly(4-vinylpyridine) (P4VP); the interpolyelectrolyte–metal complexes (IMC), pectin– $\text{Ag}^+$ –P4VP; and nanocomposites of IPEC–Ag, the following reagents were used: pectin sodium salt (Na-pectin), obtained by mixing citrus pectin production (“Cargill Deutschland GmbH” (Germany)),  $M = 3 \cdot 10^4$ , with NaOH; hydrochloride poly(4-vinylpyridine) (P4VP-Cl), obtained by protonation of pyridine ring poly(4-vinylpyridine) (Aldrich),  $M_w = 6 \cdot 10^4$ , with HCl; silver (I) nitrate ( $\text{AgNO}_3$ ) (Aldrich) with  $M = 169.9$ ; and sodium borohydride ( $\text{NaBH}_4$ ) (Aldrich) with  $M = 37.83$ .

IPEC samples were formed via mixing of 5% aqueous solutions of Na-pectin and P4VP-Cl taken at an equimolar ratio, at  $T = 20 \pm 2$  °C.



While mixing of anion and cation polyelectrolytes’ (PE) water solutions, one could observe immediate formation of clots as a result of a process of molecular “recognition” and self-assembly of oppositely charged PE macromolecules [13]. These clots, which are IPEC, were formed as thin films on polytetrafluorethylene plates, dried at  $T = 20 \pm 2$  °C to a constant mass, then washed in distilled water getting reached neutral pH, and then dried again till to a constant mass. The resulting films were 100–500  $\mu\text{m}$  thick.

IMC samples were prepared via immersion of IPEC films into an aqueous solution of  $\text{AgNO}_3$  with a concentration of 0.1 mol/L at  $T = 20 \pm 2$  °C for 24 h. The colorless IPEC films became dark red.

The absorption capacities of films,  $A$  (mmol/g), were calculated through the formula [14]:

$$A = (c_{\text{in}} - c_{\text{eq}}) V / m,$$

where  $m$  is the mass of the absorbent,  $V$  is the volume of the solution, and  $c_{\text{in}}$  and  $c_{\text{eq}}$  are the initial and the equilibrium concentrations of silver ions. For IMC films  $A = 2.2$  mmol/g.

The chemical reduction of  $\text{Ag}^+$  ions in the IMC was realized with  $\text{NaBH}_4$  (a molar ratio of  $[\text{BH}_4^-]:[\text{Ag}^+] \geq 1.0$ ) in an alkaline medium (pH 10.8) in a solvent mixture of water–isopropanol (4:1 vol %) at  $T = 20 \pm 2$  °C for 3 h (until the release of gaseous bubbles ceased). The concentration of  $\text{NaBH}_4$  in the aqueous alcohol solution was 0.1 mol/L. As a result of the reduction, IMC films changed color from red to a metallic silver one.

The features of the structuring of the IPEC (pectin–P4VP), the IMC (pectin– $\text{Ag}^+$ –P4VP), and nanocomposites of IPEC–Ag were studied by wide-angle X-ray scattering (WAXS) with a DRON-4-07 diffractometer (scientific-production company “Burevestnik,” Russia), whose X-ray optical scheme was used to “pass” primary-beam radiation through samples.

The heterogeneous structuring of these polymeric systems (at the nanometer level) was studied via small-angle X-ray scattering (SAXS) with a CRM-1 camera (Orel scientific equipment factory, Russia), having a slit collimator of the primary irradiation beam made via the Kratky method. The geometric parameters of the camera satisfied the condition of infinite height of the primary beam [15]. The intensity profiles were normalized to the volume of X-ray scattering and the attenuation factor of the primary beam of the test sample.

All X-ray diffraction studies were performed at  $T = 20 \pm 2$  °C in  $\text{CuK}\alpha$  radiation monochromated with a Ni filter.

Thermomechanical studies of polymer systems were conducted using the penetration method in the mode of a uniaxial constant load ( $\sigma = 0.5$  MPa) with a UIP-70 M device (central design engineering bureau of the special instrument making of the Russian Academy of Sciences). Linear heating of samples was performed at a rate of 2.5 °C/min in the temperature range 0 to +250 °C. Relative penetration (%) was calculated as:

$$\varepsilon = (\Delta l / l_0) \cdot 100,$$

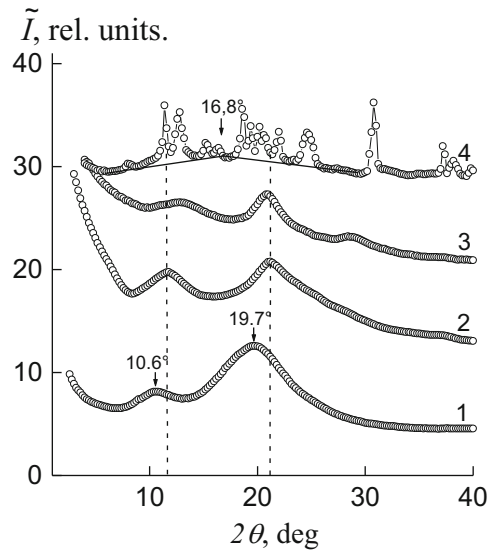
where  $\Delta l$  is penetration ( $\mu\text{m}$ ) at certain temperature and  $l_0$  is the initial thickness of the sample ( $\mu\text{m}$ ).

Comparing of the WAXS diffractograms of the cationic and anionic polyelectrolytes on whose basis the IPEC was formed (see Fig. 3.1), it was found that P4VP has only short-range ordering while translated in bulk fragments of the main macromolecular chains and their lateral branches – pyridine ring (curve 1) – and pectin has an amorphous–crystalline structure (curves 4).

The analysis of the atomic structure of macromolecules P4VP showed that low-intensity peak at  $2\theta_{\text{max}} \sim 10,6^\circ$  describes the near arrangement of basic macromolecular chains, while  $2\theta_{\text{max}} \sim 19,7^\circ$  characterizes pyridine ring (Fig. 3.1, curve 1).

Herewith, the average value of  $d$  period of the short-range ordering of fragments of basic macrochains at their positioning in a space (in a volume of P4VP) according

**Fig. 3.1** Wide-angle X-ray diffractograms of (1) the P4VP, (2) the IPEC pectin–P4VP, (3) a pectin film, and (4) a pectin powder



to the Bragg equation is:

$$d = \lambda(2 \sin \theta_m)^{-1},$$

where  $\lambda$  is the wavelength of the characteristic X-ray radiation, which is 8.3 Å, whereas Bragg in space at rotation cycles pyridine – 4.5 Å ( $\lambda = 1.54$  Å for  $\text{CuK}\alpha$  radiation).

On the X-ray profile of pectin, whose sample is a powder (Fig. 3.1, curve 4), there are many singlet and multiplet diffraction maxima having an imaginary amorphous halo with a vertex at  $2\theta_m \sim 16.8^\circ$  in the background, indicating to the amorphous–crystalline structure of this polysaccharide.

The relative crystallinity of pectin,  $X_{\text{cr}}$ , was determined via the Mathews method [16]:

$$X_{\text{cr}} = Q_{\text{cr}}(Q_{\text{cr}} + Q_{\text{am}})^{-1} \cdot 100,$$

where  $Q_{\text{cr}}$  is the area of the diffraction maxima, characterizing the crystalline structure of the polymer and  $Q_{\text{cr}} + Q_{\text{am}}$  is the total area of the X-ray pattern in the range of scattering angles  $2\theta_1 \div 2\theta_2$ , where the amorphous–crystalline structure of the polymer manifests itself. The calculations showed that  $X_{\text{cr}}$  approximates the value of 65%.

In turn, effective crystallite size  $L$  of pectin determined via the Scherrer method [17]:

$$L = K\lambda(\beta \cos \theta_m)^{-1},$$

where  $K$  is a constant related to a shape of the crystallites ( $K = 0.9$  if their shape is unknown) and  $\beta$  is the angular half-width (width at a half-height) of the singlet of a discrete diffraction maximum, showed that the average  $L$  value is 17.5 nm (for the calculation, singlet diffraction maxima at  $2\theta_m = 18.7^\circ$  and  $30.8^\circ$  were applied).

However, the X-ray pattern of the pectin sample in the form of a film prepared from a 5% aqueous solution displays only contours of the groups of diffraction maxima with basic intensities that are present on the X-ray pattern of the pectin powder (Fig. 3.1, curves 3, 4). This circumstance indicates a low rate of pectin crystallization, as well as the relaxation character of the structurization processes in the polymers.

IPEC formed from pectin and P4VP is characterized by short-range ordering during translation of fragments of oppositely charged polyelectrolyte macromolecular chains in a space. This fact is confirmed by the appearance of diffuse diffraction maximum at  $2\theta_m \sim 21.2^\circ$  on the X-ray profile of the IPEC sample (see Fig. 3.1, curve 2). The average value for the period of short-range ordering of macromolecular chains' fragments of oppositely charged polyelectrolytes in the IPEC (the average Bragg distance between chains of the polyanion and the polycation) is equal to 4.2 Å.

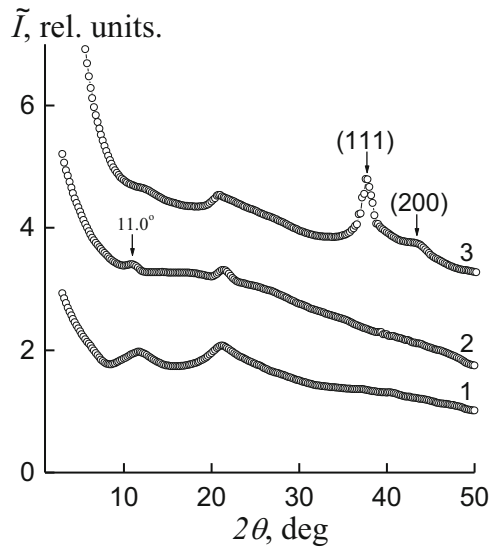
The following fact should be taken into consideration: in the IPEC profile obtained for equimolar quantity of pectin and P4VP, the angular location of the secondary (rated by intensity) diffraction maximum is shifted from  $10.6^\circ$  to  $11.8^\circ$  comparing with P4VP (Fig. 3.1, curves 1, 2), while the average Bragg distance ( $d$ ) between P4VP's main macrochains (as part of IPEC) is falling down from 8.3 Å to 7.5 Å.

Once the pectin–Ag<sup>+</sup>–P4VP IMC is formed, the diffraction pattern changes. This is confirmed by the appearance of a low-intense diffuse diffraction maximum at  $2\theta_m \sim 11.0^\circ$  (Fig. 3.2, curve 2) in the presence of a low-intensity amorphous halo, which, unlike that for the IPEC, has an angular position at  $2\theta_m \sim 21.4^\circ$ . According to [18], this diffraction maximum characterizes the existence of interpolyelectrolyte–metal complexes between the ions (Ag<sup>+</sup>) and ligands. Taking into account the angular position of this diffraction peak on the X-ray diffractogram of the IMC, average Bragg distance  $d$  between the macromolecular chains of polyelectrolytes coordinated with Ag<sup>+</sup> ions is found to be 8.0 Å.

Chemical reduction of the Ag<sup>+</sup> ions in the IMC by sodium borohydride results in formation of a nanocomposite based on the IPEC and Ag. In the nanocomposite's profile (Fig. 3.2, curve 3), one can see that the low-intense diffraction maximum at  $2\theta_m \sim 11.0^\circ$ , which is typical of the above interpolyelectrolyte–metal complexes, is absent, unlike two intensity diffraction peaks appeared at  $2\theta_m \sim 37.8^\circ$  and  $43.6^\circ$ , corresponding to the crystallographic plan of the face-centered cubic lattice of silver with (111) and (200) indexes, respectively, thus confirming presence of metallic silver in the polymeric system. Moreover, diffraction maximum intensity at  $2\theta_m \approx 20.8^\circ$ , characterizing structure of IPEC "pectin–P4VP," is enhanced.

Effective size  $L$  of Ag nanoparticle crystallites in the IPEC proved to be 4.0 nm (for the calculation, diffraction maxima at  $2\theta_m = 37.8^\circ$  and  $43.6^\circ$  were used, curve 3).

**Fig. 3.2** Wide-angle X-ray diffractograms of (1) the IPEC pectin–P4VP, (2) the IMC pectin–Ag<sup>+</sup>–P4VP, and (3) the IPEC–Ag nanocomposite



The revealed peculiarities and changes in structures while transiting from the IPEC to IMC and IPEC–Ag nanocomposites form the basis for the further study of their structural heterogeneity.

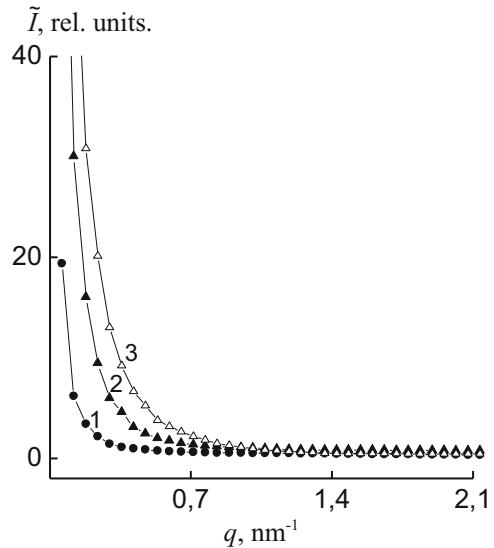
Analyzing the profiles of small-angle X-ray scattering of the polymer systems, presented in [19, 20], as dependences of  $\tilde{I}$  on  $q$  (Fig. 3.3) and  $s^3\tilde{I}$  on  $s^3$ , where  $\tilde{I}$  is the intensity of scattering without the collimation correction and  $q = (4\pi/\lambda)\sin\theta = 2\pi s$ , all these systems have heterogeneous structure, i.e., contrast electron densities  $\Delta\rho$  ( $\Delta\rho = \rho - \langle\rho\rangle$ , where  $\rho$  and  $\langle\rho\rangle$  are the local and average values of the electron density, respectively) are present in their volumes. This result means that in the IPEC, IMC, and the nanocomposites based on the IPEC and Ag, there are at least two types of regions of heterogeneity with different values of local electron density  $\rho$ .

As one can see, scattering intensity and thus  $\Delta\rho$  value are increasing for these systems in the following rank: IPEC pectin P4VP  $\rightarrow$  IMC pectin–Ag<sup>+</sup>–P4VP  $\rightarrow$  nanocomposite IPEC–Ag (Fig. 3.3, curves 1–3). However, the absence of the interference peak in the all profiles indicates the stochastic nature of the location of various types of heterogeneity areas in a space.

In order to assess semi-quantitatively the value of the relative level of structural heterogeneity of these polymer systems, their Porod invariants  $Q'$  were compared [21]:

$$Q' = \int_0^{\infty} q \tilde{I}(q) dq,$$

**Fig. 3.3** Profiles of the intensity of small-angle X-ray scattering of (1) the IPEC pectin-P4VP, (2) the IMC pectin-Ag<sup>+</sup>-P4VP, and the (3) IPEC-Ag nanocomposite



These values are invariant with respect to the shapes of the heterogeneity regions and are directly related to the rms values of electron density fluctuations ( $\langle \Delta\rho^2 \rangle$ ) in a two-phase system:

$$Q' \propto \langle \Delta\rho^2 \rangle,$$

Here,  $\langle \Delta\rho^2 \rangle = \varphi_1\varphi_2(\rho_1 - \rho_2)^2$ , where  $\varphi_1$  and  $\varphi_2$  are the volume ratios of heterogeneity domains in a two-phase system and  $\rho_1$  and  $\rho_2$  are the electron densities of heterogeneity domains ( $\varphi_1 + \varphi_2 = 1$ ) in a two-phase system. A comparison of the values of invariant  $Q'$  for the studied polymer systems (table) shows that the relative level of the structural heterogeneity increases significantly during the transition from the IPEC and the IMC into the nanocomposites based on the IPEC and Ag.

An evaluation of the effective sizes of the heterogeneity regions existing in these polymer systems was performed through the method from [19, 20] via calculation of structural parameters, such as the range of heterogeneity (range of inhomogeneity),  $l_p$ , which is directly related to the average diameters of heterogeneity regions,  $\langle l_1 \rangle$  and  $\langle l_2 \rangle$ , in the two-phase system:

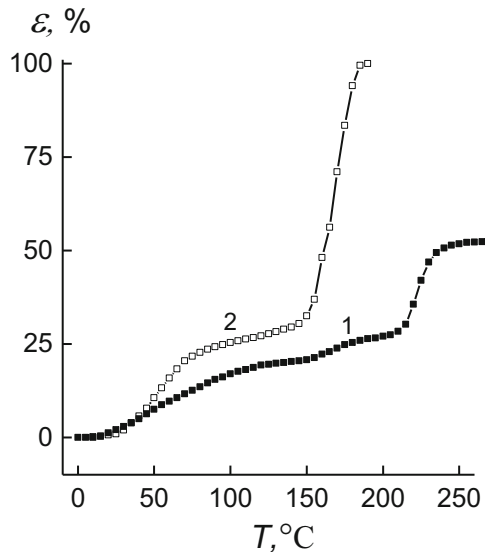
$$l_p = \varphi_2 \langle l_1 \rangle + \varphi_1 \langle l_2 \rangle.$$

After getting the result of the  $l_p$  calculation, the transition from the IPEC to the IMC was found to be accompanied with increasing of the effective size of region heterogeneity, while at transforming from the IMC into the IPEC-Ag nanocomposites, it decreased almost threefold (Table 3.1).



**Table 3.1** Structural parameters and temperature transitions for the investigated polymer systems

Polymer system	$l_p$ , nm	$Q'$ , rel. units	$T_g$ , °C	$T_f$ , °C	$\varepsilon$ , % ( $T = 140$ °C)
IPEC	35	10	63	207	23
IMC	43	24	57	199	18
IPEC–Ag	15	39	65	212	10

**Fig. 3.4** Thermomechanical curves of (1) pectin and (2) P4VP.  $\varepsilon$  is relative value of penetration

Alongside with the structural organization of the IPEC, the IMC, and the nanocomposites based on IPEC–Ag, their thermomechanical behavior was studied.

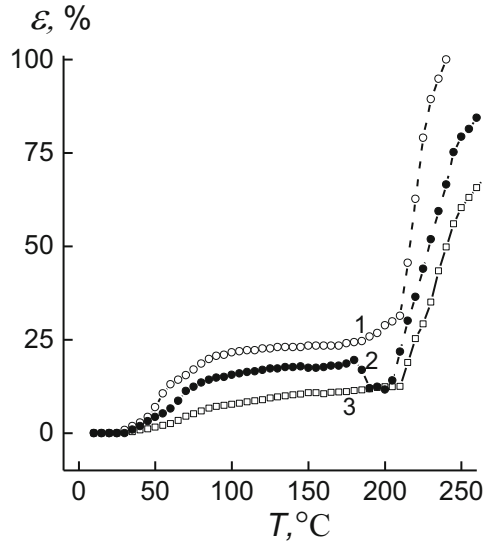
Analysis of the pectin thermomechanical curve (see Fig. 3.4, curve 1) demonstrated that temperature transitions which are associated with the glass transition and melting of the pectin crystallites occur in the temperature ranges 20–110 °C and 155–230 °C, respectively. Also, the strong deformational change has been observed in the melting process of pectin's crystalline phase [22]. As a contrast to anionic PE, the P4VP's thermomechanical curve has the usual (typical) shape with glass transition interval between 25 and 80 °C and flow temperature from 150 to 180 °C (curve 2).

So, the shape of thermomechanical curve for IPEC (pectin–P4VP formed of equimolar quantities of anionic and cationic PE) is similar to P4VP's one with glass transition temperature in the range between 30 and 85 °C and flow point from 180 to 240 °C (Fig. 3.5, curve 1).

Transferring from IPEC (pectin–P4VP) to the IMC (pectin–Ag<sup>+</sup>–P4VP), on the latter curve a temperature shift at  $T = 200$  °C appears, due to the AgNO<sub>3</sub> melting in the bulk of IPEC (curve 2).

It is possible to conclude that in the temperature range 160–200 °C, the following processes take place: destruction of interpolyelectrolyte–metal complexes, transfer

**Fig. 3.5** Thermomechanical curves of (1) the IPEC pectin–P4VP, (2) the IMC pectin–Ag<sup>+</sup>–P4VP, and (3) the IPEC–Ag nanocomposite



of AgNO<sub>3</sub> salt from ionic state to the crystalline one, and finally, its melting. So, changes occurred on the way from IPEC to IMC and to IPEC–Ag nanocomposite demonstrate that the level of relative penetration in these systems tends to be decreasing (Fig. 3.5).

Basing on the data of polymeric objects depicted in Fig. 3.5, the average-interval temperature values of glass transition, fluidity temperature, and relative penetration (in the high-elasticity state at  $T = 140$  °C) have been determined (Table 3.1).

### 3.3 Structure and Antimicrobial Properties of Nanocomposites Based on Pectin–PEI and Ag Nanoparticles, Prepared by the Chemical and Thermal Reduction of Silver Ions in the Interpolyelectrolyte–Metal Complexes

To obtain the IPEC, pectin–polyethyleneimine; the IMC, pectin–Ag<sup>+</sup>–polyethyleneimine; and nanocomposites of IPEC–Ag, the following reagents were used: anionic polyelectrolyte citrus pectin (Cargill Deutschland GmbH, Germany) with  $M = 3 \times 10^4$ , cationic polyelectrolyte anhydrous branched polyethyleneimine (PEI) (Aldrich) with  $M_n = 1 \times 10^4$  and  $M_w = 2.5 \times 10^4$ , silver (I) nitrate (AgNO<sub>3</sub>) (Aldrich) with  $M = 169.9$ , and sodium borohydride (NaBH<sub>4</sub>) (Aldrich) with  $M = 37.83$ .

IPEC samples were formed via mixing of 5% aqueous solutions of pectin and PEI taken at a molar ratio of 1:1, at  $T = 20 \pm 2$  °C. IPEC as films were prepared via

pouring onto PTFE plates and drying up to constant masses at the same temperature. Dry IPEC films were washed in distilled water up to neutrality and dried repeatedly at 20 °C up to constant masses. The resulting films were 100 μm thick.

IMC samples were prepared via immersion of IPEC films into an aqueous solution of AgNO<sub>3</sub> with a concentration of 0.1 mol/L at  $T = 20 \pm 2$  °C for 24 h. The colorless IPEC films became dark red. The absorption capacities of IMC films  $A = 5.0$  mmol/g.

The chemical reduction of Ag<sup>+</sup> ions in the IMCs was conducted with NaBH<sub>4</sub> (a molar ratio of [BH<sub>4</sub><sup>-</sup>]:[Ag<sup>+</sup>] ≥ 1.0) in an alkaline medium (pH 10.8) in a solvent mixture of water–isopropanol (4:1 vol %) at  $T = 20 \pm 2$  °C for 3 h (until the release of gaseous bubbles ceased). The concentration of NaBH<sub>4</sub> in the aqueous alcohol solution was 0.1 mol/L.

Thermal reduction of Ag<sup>+</sup> ions in the IMC's volume was performed by heating of films to 100–160 °C within 30 min. Specimens were heated in the oven using precise thermal regulator VRT-3. Temperature regulation precision was ±0.5 °C.

As a result of the reduction, IMC films changed color from red to metallic.

The features of the structuring of the IPEC (pectin–PEI), the IMC (pectin–Ag<sup>+</sup>–PEI), and nanocomposites of IPEC–Ag were studied by wide-angle X-ray diffraction on a DRON-4-07 diffractometer, whose X-ray optical scheme was used to “pass” primary-beam radiation through samples. X-ray diffraction studies were performed at  $T = 20 \pm 2$  °C in CuK<sub>α</sub> radiation monochromated with a Ni filter.

The antimicrobial activity of IPEC–Ag nanocomposites, prepared by chemical and thermal reduction of Ag<sup>+</sup> ions in IMC, was investigated using reference strains of opportunistic bacteria *Staphylococcus aureus* ATCC 6538 and *Escherichia coli* ATCC 35218 (as model gram-positive and gram-negative bacteria).

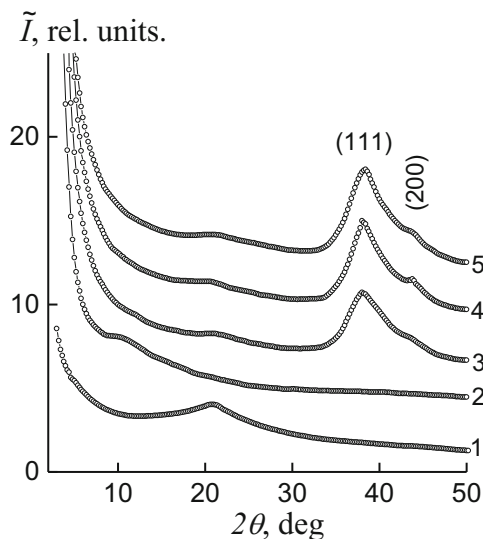
Investigations were carried out by agar diffusion method on a solid LB (Luria-Bertani) nutrient medium [23]. The nanocomposite films (size 10 × 10 mm) were placed on the surface of nutrient agar, which had been previously inoculated with 10 μL of bacterial suspension of *S. aureus* and *E. coli* at the rate of 2 × 10<sup>5</sup> CFU/ml. The plates were incubated at 37 °C for 24 h.

Clear zones, which has no bacteria around the film of composite, containing Ag were the indicator of antimicrobial activity. All experiments were repeated three times. The IPEC film was applied as a control sample.

The analysis of wide-angle X-ray diffractograms has shown that IPEC formed of pectin and PEI is characterized by short-range ordering during translation of fragments of oppositely charged polyelectrolyte macromolecular chains in space. This circumstance is indicated by the appearance of one diffuse diffraction maximum with  $2\theta_m \sim 20.8^\circ$  on the X-ray diffractogram of the IPEC sample (see Fig. 3.6, curve 1). The average value of the period of short-range ordering of fragments of complementary macromolecular chains of oppositely charged polyelectrolytes in the IPEC (the Bragg distance between the macromolecule chains of anionic and cationic polyelectrolytes in the IPEC) is 4.3 Å, i.e., slightly less than that in the cationic polyelectrolyte.

However, the sorption of AgNO<sub>3</sub> by the IPEC sample and formation of the IPEC–Ag<sup>+</sup> IMC is accompanied by a change in the diffractogram. This result is proved by

**Fig. 3.6** Wide-angle X-ray diffractograms of (1) the IPEC, (2) the IMC, and (3–5) the IPEC–Ag nanocomposites obtained via the chemical reduction of  $\text{Ag}^+$  ions in the IMC at molar ratios of  $\text{BH}_4^-:\text{Ag}^+ =$  (3) 1.0, (4) 2.0, and (5) 3.0



the appearance of an intense diffuse diffraction maximum at  $2\theta_m \sim 11.2^\circ$ , featuring the structure polyelectrolyte–metal complex pectin– $\text{Ag}^+$ –PEI [18] (curve 2). In its turn, the amorphous halo disappears at  $2\theta_m \sim 20.8^\circ$ , relating to the structural peculiarity of pectin–PEI IPEC. This indicates the full transfer of polyelectrolyte complexes into polyelectrolyte–metal complexes.

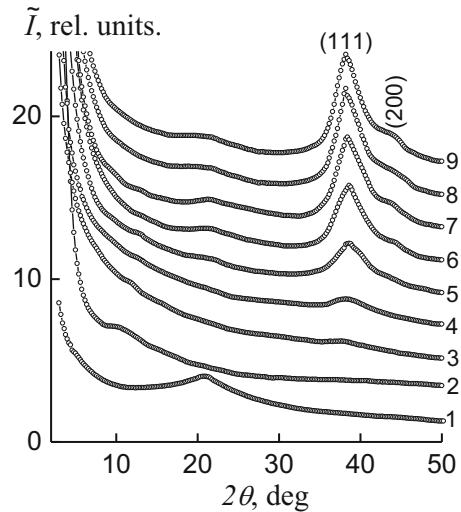
After the chemical reduction of the  $\text{Ag}^+$  ions in the IMC with the use of sodium borohydride (a molar ratio of  $[\text{BH}_4^-]:[\text{Ag}^+] = 1.0$ ) a nanocomposite based on the IPEC and Ag was formed. In the diffractogram of IPEC–Ag nanocomposite (curve 3), the diffraction maximum at  $2\theta_m \sim 11.2^\circ$ , which is typical of the abovementioned polyelectrolyte–metal complexes, is absent, unlike the two intense maxima at  $2\theta_m = 38.2^\circ$  and  $43.8^\circ$ , corresponding to the crystallographic plan of the face-centered cubic lattice of silver with (111) and (200) indexes, respectively, and confirming presence of metal silver in the polymeric system.

With an increase in the amount of the reducing agent (a molar ratio of  $[\text{BH}_4^-]:[\text{Ag}^+] = 2.0$ ), the X-ray diffractograms of nanocomposites based on the IPEC and Ag (curves 4) show a significant increase in the intensity of the diffraction peaks at  $2\theta_m = 38.2^\circ$  and  $43.8^\circ$ , characterizing the structure Ag nanoparticles. The increase in the amount of the reducing agent (a molar ratio of  $[\text{BH}_4^-]:[\text{Ag}^+] = 3.0$ ) does not change the structuring of the nanocomposites based on the IPEC and Ag nanoparticles (curves 4, 5).

Thus, according to wide-angle X-ray diffraction, it may be concluded that the molar ratio  $[\text{BH}_4^-]:[\text{Ag}^+] = 2.0$  is optimum for the formation of IPEC–Ag nanocomposites.

Analysis of diffractograms of silver-containing nanocomposites prepared by thermal reduction of  $\text{Ag}^+$  ions in IMC in the wide range of temperatures (100–160 °C) has shown, while the gradual increase of the temperature to  $T = 150^\circ\text{C}$  is

**Fig. 3.7** Wide-angle X-ray diffractograms of (1) the IPEC, (2) the IMC, and (3–9) the nanocomposites obtained by the thermal reduction method from IMC at the temperatures (3) 100, (4) 110, (5) 120, (6) 130, (7) 140, (8) 150, and (9) 160 °C for 30 min



taking place, that the content of silver nanoparticles is growing up. So, the enhancing of intensity of two diffraction maxima at  $2\theta_m \sim 38.2^\circ$  and  $43.8^\circ$  confirms the presence of metal silver in the system (Fig. 3.7, curves 3–8). The further increase in temperature (up to 160 °C) did not lead to the rise in the intensity of the diffraction maxima characterizing silver structure (Fig. 3.7, curves 8–9).

At the further increase in temperature in IMC (up to  $T = 160^\circ\text{C}$ ), the intensity of the diffraction maxima, characterizing the metal silver structure, did not change (Fig. 3.7, curves 8–9).

Therefore, according to the WAXS data, we can conclude that the optimal temperature for  $\text{Ag}^+$  ions' reduction in IMC with further formation of nanocomposite is to be 150 °C. In its turn, thermal reduction of silver ions is found out to take place owing to polyethyleneimine (namely, on account of electron transfer from the amino groups' nitrogen atoms of polyethyleneimine to  $\text{Ag}^+$  ions) [1].

IPEC–Ag nanocomposites created by thermal reduction of  $\text{Ag}^+$  ions in IMC at  $T = 150^\circ\text{C}$  within 30 min (Fig. 3.8) are found out to demonstrate higher antimicrobial activity against *S. aureus* and *E. coli* strains compared to IPEC–Ag, synthesized by chemical reduction (the chemical reduction of  $\text{Ag}^+$  ions in the IMC was conducted with  $\text{NaBH}_4$  (a molar ratio of  $[\text{BH}_4^-]:[\text{Ag}^+] = 2.0$ )). After incubation proceeds for 24 h at 37 °C, one can observe a clear zone around the films' contours, thus confirming inhibition of bacteria growth.

The growth inhibition's zone diameter for *S. aureus* was 27.6 mm for specimens prepared by thermal reduction and 18.2 mm for those obtained by chemical reduction. For *E. coli* these values are 26.6 mm and 17.6 mm, correspondingly (Table 3.2).

Active growth of the test bacteria and absence of growth inhibition have been observed in the test specimens (polymer film without nanoparticles).

**Fig. 3.8** Images of antimicrobial test results of agar plates containing IPEC–Ag nanocomposites, obtained via the thermoreduction and chemical reduction of  $\text{Ag}^+$  ions in the IMC against *E. coli* (a) and *S. aureus* (b)

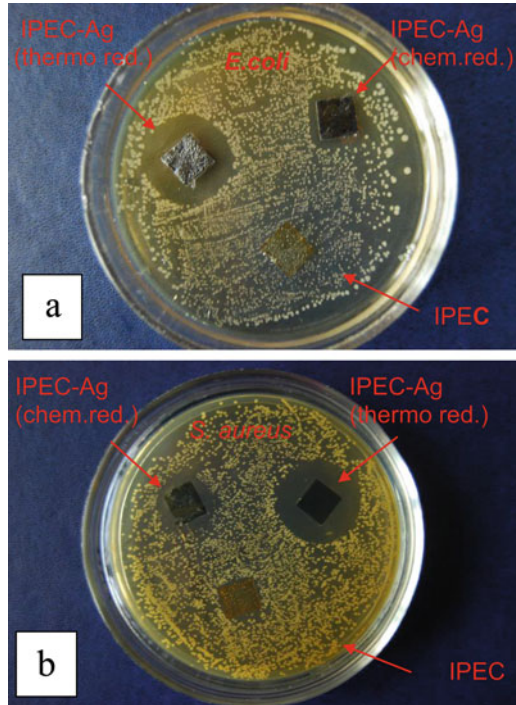


**Table 3.2** Antimicrobial activity of the IPEC–Ag nanocomposites, prepared via the thermoreduction and chemical reduction of  $\text{Ag}^+$  ions in the IMC

The method of obtaining nanocomposite films	Diameter of inhibition zone, mm	
	<i>Staphylococcus aureus</i>	<i>Escherichia coli</i>
Thermoreduction	IPEC–Ag	IPEC–Ag
	$27.6 \pm 1.2$	$26.6 \pm 1.2$
Chemical reduction	IPEC–Ag	IPEC–Ag
	$18.2 \pm 0.8$	$17.6 \pm 0.6$
Control sample	IPEC	IPEC
	0	0

## References

- Demchenko V, Riabov S, Rybalchenko N, Goncharenko L, Kobylinskiy S, Shtompel V (2017) X-ray study of structural formation, thermomechanical and antimicrobial properties of copper-containing polymer nanocomposites obtained by the thermal reduction method. *Eur Polym J* 96:326–336
- Demchenko V, Shtompel V, Riabov S (2016) Nanocomposites based on interpolyelectrolyte complex and Cu/Cu<sub>2</sub>O core–shell nanoparticles: structure, thermomechanical and electric properties. *Eur Polym J* 75:310–316
- Demchenko VL, Shtompel VI, Riabov SV (2015) DC field effect on the structuring and thermomechanical and electric properties of nanocomposites formed from pectin–Cu<sup>2+</sup>–polyethyleneimine ternary polyelectrolyte–metal complexes. *Polym Sci A* 57:635–643

4. Demchenko VL, Shtompel VI (2014) Structuring, morphology, and thermomechanical properties of nanocomposites formed from ternary polyelectrolyte–metal complexes based on pectin, polyethyleneimine, and  $\text{CuSO}_4$ . *Polym Sci B* 56:927–934
5. Pomogailo AD, Kestelman VN (2005) *Metallopolymer nanocomposites*. Springer, New York
6. Rosi NL, Mirkin CA (2005) Nanostructures in biodiagnostics. *Chem Rev* 105:1547–1562
7. Ballauff M, Lu Y (2007) “Smart” nanoparticles: preparation, characterization and applications. *Polymer* 48:1815–1823
8. Ruiz P, Macanas J, Munoz M, Muraviev DN (2011) Intermatrix synthesis: easy technique permitting preparation of polymer-stabilized nanoparticles with desired composition and structure. *Nanoscale Res Lett* 6:343–348
9. Bruening ML, Dotzauer DM, Jain P, Ouyang L, Baker GL (2008) Creation of functional membranes using polyelectrolyte multilayers and polymer brushes. *Langmuir* 24:7663–7673
10. Deng Z, Zhu H, Peng B, Chen H, Sun YF, Gang XD, Jin PJ, Wang JL (2012) Synthesis of PS/Ag nanocomposite spheres with catalytic and antibacterial activities. *ACS Appl Mater Interfaces* 4:5625–5632
11. Prozorova GF, Pozdnyakov AS, Kuznetsova NP, Korzhova SA, Emel’yanov AI, Ermakova TG, Fadeeva TV, Sosodova LM (2014) Green synthesis of water-soluble nontoxic polymeric nanocomposites containing silver nanoparticles. *Int J Nanomedicine* 9:1883–1889
12. Barud HS, Regiani T, Marques RFC, Lustrri WR, Messaddeq Y, Ribeiro SJL (2011) Antimicrobial bacterial cellulose–silver nanoparticles composite membranes. *J Nanomater* 2001:1–8
13. Shtompel VI, Sasa BS, Riabov SV, Kercha YY, Titov GV (2010) Polyelectrolyte complexes based on Na-carboxymethylcellulose and polyethyleneimine chloride: identification and structure. *Polym J* 32:204–209 (in Ukrainian)
14. Demchenko V, Shtompel V, Riabov S, Lysenkov E (2015) Constant electric and magnetic fields effect on the structuring and thermomechanical and thermophysical properties of nanocomposites formed from pectin– $\text{Cu}^{2+}$ –polyethyleneimine interpolyelectrolyte – metal complexes. *Nanoscale Res Lett* 10:479–485
15. Kratky O, Pilz I, Schmitz PJ (1966) Absolute intensity measurement of small-angle x-ray scattering by means of a standard sample. *J Colloid Interface Sci* 21:24–34
16. Shtompel VI, Kercha YY (2008) Structure of linear polyurethanes. *Naukova dumka, Kiev* [in Russian]
17. Guinier A (2000) *X-ray diffraction: in crystals, imperfect crystals, and amorphous bodies*. Dower Publications, New York
18. Demchenko V, Riabov S, Shtompel V (2017) X-ray study of structural formation and thermomechanical properties of silver-containing polymer nanocomposites. *Nanoscale Res Lett* 12:235–240
19. Ruland W (1971) Small-angle scattering of two-phase systems: determination and significance of systematic deviations from Porod’s law. *J Appl Crystallogr* 4:70–73
20. Perret R, Ruland W (1971) Eine verbesserte Auswertungsmethode für die Röntgenkleinwinkelstreuung von Hochpolymeren. *Kolloid Z Z Polym* 247:835–843
21. Porod G (1982) In: Glatter O, Kratky O (eds) *Small-angle X-ray scattering*. Academic Press, London
22. Teitelbaum BJ (1979) *Thermomechanical analysis of polymers*. Nauka, Moscow [in Russian]
23. Case CL, Johnson TR (1984) *Laboratory experiments in microbiology*. Benjamin Cummings Pub Inc., Menlo Park



# Chapter 4

## Effect of Incorporated Inorganic Nanoparticles on Porous Structure and Functional Properties of Strongly and Weakly Acidic Ion Exchangers

Ludmila Ponomarova, Yuliya Dzyazko, Yurii Volkovich, Valentin Sosenkin, and Sergey Scherbakov

### 4.1 Organic-Inorganic Ion Exchangers

Currently organic-inorganic sorbents are developed intensively. Combination of constituents of different natures allows us to obtain materials that are characterized by improved functional properties, such as high selectivity, considerable ion-exchange capacity, and facile regeneration [1–3]. Moreover, organic or inorganic matrices acquire new properties after modification with inorganic or organic constituents, respectively. For instance, modification of clay minerals with organics provides their ability to sorb synthetic dyes [3–6] or toxic anions containing U(VI) [7–9] or Cr(VI) [10–12]. Organic functional groups grafted to silica, which possess no cation exchange ability in acidic and neutral media, adsorb cations at  $\text{pH} < 7$  [13–15]. Coating of magnetic nanoparticles ( $\text{Fe}_3\text{O}_4$ ) with polymers gives a possibility to obtain finely dispersed core-shell sorbents, which can be easily removed from liquids [16–18].

From the practical point of view, the composites based on commercial ion-exchange resins are especially attractive since they can be applied to ion-exchange columns (ion exchange under dynamic conditions). The resins are modified with nanoparticles of inorganic ion-exchangers [19]. The materials are used for sorp-

---

L. Ponomarova · Y. Dzyazko (✉)

V. I. Vernadsky Institute of General and Inorganic Chemistry of the National Academy of Science of Ukraine, Kyiv, Ukraine

Y. Volkovich · V. Sosenkin

A. N. Frumkin Institute of Physical Chemistry and Electrochemistry of the Russian Academy of Science, Moscow, Russia

S. Scherbakov

M. G. Kholodny Institute of Botany of the National Academy of Science of Ukraine, Kyiv, Ukraine



tion of  $\text{Pb}^{2+}$  [20–22],  $\text{Cu}^{2+}$ ,  $\text{Zn}^{2+}$ ,  $\text{Ni}^{2+}$  [22], and  $\text{UO}_2^{2+}$  [23, 24] cations and  $\text{H}_2\text{PO}_4^-$  ( $\text{HPO}_4^{2-}$ ) [25],  $\text{ReO}_4^-$  [26], and  $\text{H}_2\text{AsO}_4^-$  ( $\text{HAsO}_4^{2-}$ ) [27–29] anions. As opposed to strongly acidic or strongly basic ion-exchange resins, which are traditionally applied to sorption processes, such inorganic materials as hydrophosphates [30–34] or hydrated oxides of multivalent metals [35–39] demonstrate high selectivity toward toxic ions. Regarding organic-inorganic ion exchangers based on the mentioned resins, small size of the embedded inorganic particles causes rather high sorption rate [23, 40]. The inorganic ion exchangers are also used for modification of macroporous ceramic membranes [41–43]. As a result, inert separators are transformed into ion-exchange materials, which can be used for electromembrane separation. Insertion of nanoparticles into polymer ion-exchange membranes improves their charge selectivity and accelerates ion transport particularly due to stability of the composites against fouling with organics [44, 45]. Moreover, the embedded particles prevent fouling of polymer materials during baromembrane processes [46–48].

Strongly acidic polymers were mainly applied to preparation of organic-inorganic ion-exchangers. In swollen state, ion-exchange polymers are characterized by complex porous structure. This structure involves hydrophilic pores (nanosized clusters and channels), where ions move [49–52]. These pores are formed from heterogeneities of air-dry polymers [49, 53, 54]. The heterogeneities are caused by fragments of polymer chains, which contain functional groups. During swelling, these fragments form so-called gel regions penetrated by a continuous system of hydrophilic clusters and channels (transport pores). Ion-exchange polymers contain also hydrophobic pores (voids between gel regions, structure defects). Depending on location, the embedded particles change size and volume of one or other pores [23, 40, 55]. This affects functional properties of the composites.

Weakly acidic ion-exchange resins show better selectivity toward toxic ionic components due to formation of complexes with functional groups [56, 57]. However, the composites based on these resins are practically unknown. The aim of the research involves obtaining nanocomposite using weakly acidic resin as a polymer matrix. Another purpose is to compare porous structure and functional properties of the composites based on strongly and weakly acidic resins.

## 4.2 Synthesis and Characterization of Nanocomposites

Following cation exchange resins that are produced by Dow Chemical Company were used for modification with nanoparticles of zirconium hydrophosphate (ZHP): Dowex MAC-3 (weakly acidic macroporous resin) and Dowex HCR-S (strongly acidic gel-like resin). The weakly acidic resin is polyacrylic polymer containing  $-\text{COOH}$  groups, and the strongly acidic ion-exchanger is styrene-divinylbenzene polymer with  $-\text{SO}_3\text{H}$  groups.

The modification procedure was similar to [40, 55]; it involved impregnation of a resin with 1 M  $\text{ZrOCl}_2$  solution followed by treatment with 1 M  $\text{H}_3\text{PO}_4$  solution,

drying at room temperature, and treatment with ultrasound to remove the precipitate from the outer surface of the grains. ZHP powder, which was obtained by this manner, was investigated further for comparison. Synthesis of ZHP inside polymers was carried out one (weakly acidic resin) or eight times (strongly acidic resin). In the last case, the nanocomposite containing large amount of ZHP shows much faster proton transport than the pristine resin [55].

TEM images were obtained with a *JEOL JEM 1230* transmission electron microscope (*Jeol*, Japan). Preliminarily the ion-exchangers were milled and treated with ultrasound.

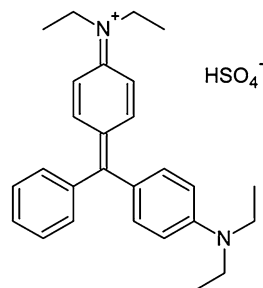
A method of standard contact porosimetry (MSCP) [58, 59], which had been accepted by the IUPAC [60], was applied to study porous structure of the polymers. Preliminarily the tested samples were dried at 80° C under vacuum. Water was used as a working liquid.

### 4.3 Sorption of Ni<sup>2+</sup> Ions and Cationic Dye

Ni<sup>2+</sup> cations and cationic dye (Brilliant Green, BG, Fig. 4.1) were used as model objects to research functional properties of the pristine resins, nanocomposites, and ZHP. Rate of sorption from one-component solutions containing BG (5 mg dm<sup>-3</sup>, i.e., 0.01 mmol dm<sup>-3</sup>) or Ni<sup>2+</sup> (0.2 mmol dm<sup>-3</sup>) was investigated under batch conditions. A series of weighted samples (0.2 g) were inserted to flasks, to which aliquots of the solution were added (20 cm<sup>3</sup>). The content of the flasks was stirred intensively using a water bath shaker type 357 (*Elpan*, Poland). After predetermined time, the liquid was removed from one flask; at the end of the next period, the solution was taken away from the second flask, etc. The solutions after BG adsorption were analyzed using a Shimadzu UV-mini 1240 spectrophotometer (*Shimadzu*, Japan) at 625 nm. Ni<sup>2+</sup> content was analyzed with an atomic absorption method using S9 Pye Unicam spectrophotometer (*Philips*).

In order to obtain sorption isotherms, the ratio of solid and liquid was 0.2 g:10 cm<sup>3</sup>. Removal of BG from one-component aqueous solution was also carried out under dynamic conditions. The initial concentration of the dye was 10 mg cm<sup>-3</sup>. A diameter of the column was 0.7 cm, a volume of the bed was 5 cm<sup>3</sup>, and the solution velocity was 5 cm<sup>3</sup> min<sup>-1</sup>.

**Fig. 4.1** Structure of Brilliant Green



$\text{Ni}^{2+}$  ions were removed from tap water under dynamic conditions. Initial concentration of the solution was ( $\text{mmol dm}^{-3}$ )  $\text{Ni}^{2+} - 0.1$ ,  $\text{Ca}^{2+} - 1.3$ , and  $\text{Mg}^{2+} - 0.4$ .

All experiments were carried out at  $25^\circ\text{C}$ .

#### 4.4 Visualization of Embedded Particles

As seen from the TEM images (Fig. 4.2), the resins contain globular non-aggregated nanoparticles with size of  $\approx 5\text{--}15\text{ nm}$  (Dowex MAC-3) and  $4\text{--}20\text{ nm}$  (Dowex HCR-S).

In the case of weakly acidic resin, additionally sorbed electrolyte ( $\text{ZrOCl}_2$ ) can penetrate into clusters and channels, since no dissociation of  $-\text{COOH}$  groups occurs in strongly acidic media. Diffusion part of the intraporous electric double layer (a barrier against additionally sorbed electrolyte) is absent under these conditions. On the contrary, the process of precipitation inside strongly acidic resin involves desorption of zirconium hydroxocomplexes sorbed according to ion-exchange mechanism. Since single nanoparticles are uniformly distributed through the gel phase, the modified resins can be related to nanocomposites. Larger particles, a size of which is from several tens to several hundred nanometers, and irregular formations of micron size are also seen. The particles of different sizes occupy one or other pores of the resin.

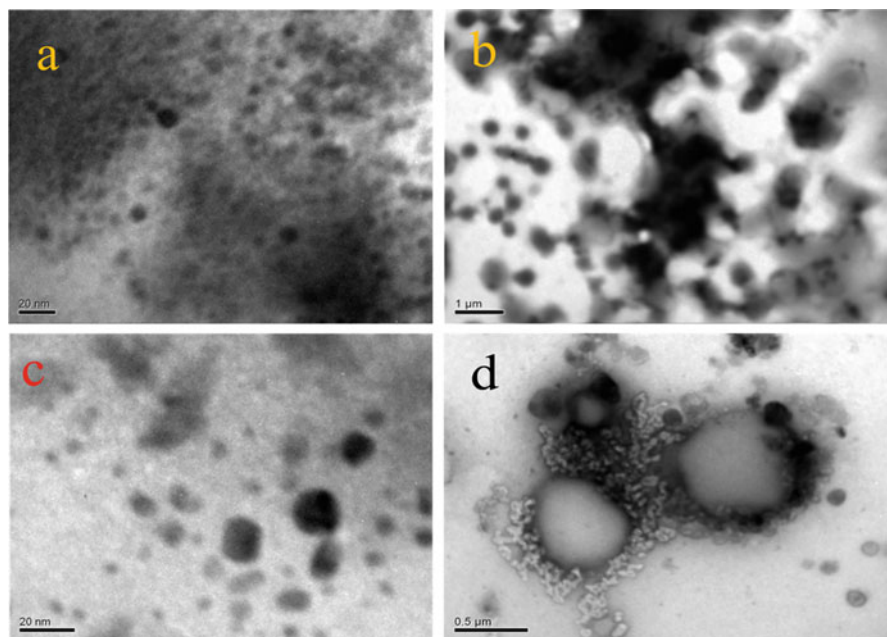


**Fig. 4.2** TEM images of ZHP particles embedded to weakly (a, b) and strongly (c, d) acidic resins

Mass fraction ( $m$ ) of ZHP was 0.08 (Dowex MAC-3) and  $\approx 0.39$  (Dowex HCR-S). It should be noted that this parameter for one-time modified Dowex HCR-S is 0.18 [40, 55]. The smaller  $m$  value for the weakly acidic resin is due to lower loading of the weakly acidic resin with acidic  $\text{ZrOCl}_2$  solution. This solution penetrates to the grains as an additionally sorbed electrolyte. In the case of strongly acidic resin, partial substitution of counterions by cations of soluble zirconium hydroxocomplexes is possible.

## 4.5 Porous Structure of Polymer Constituent

Since thermal pretreatment before the MSCP measurements provides no dehydration of ZHP, the results are related only to the polymer constituent. The data of porosimetric measurements for amorphous ZHP are given in [40]. Mesopores, a radius of which is 2.5 nm, are dominant.

Integral pore size distributions are plotted in Fig. 4.3a as dependencies of pore volume ( $V$ ) on logarithm of pore radius ( $r$ ). Figure 4.3a illustrates also distributions of energy of water bonding ( $E$ ). “Bonded” water is located in clusters and channels; this region corresponds to  $E \geq 1700 \text{ J mol}^{-1}$ . This  $E$  value is less by approximately two orders of magnitude than the hydration energy of ions that is comparable with the energy of hydrogen bonds [50]. Mobility of species is minimal in these pores. ZHP causes sufficient decrease of bonded water in transport pores due to their screening with nanoparticles.

Figure 4.3b illustrates differential pore size distributions. No shift of the stripes, which are related to clusters ( $\log r = 0.5$  (nm) for Dowex MAC-3 and 1 (nm) for Dowex HCR-S) and voids between gel regions ( $\log r = 1$  (nm) for Dowex MAC-3 and 1.3 (nm) for Dowex HCR-S), is observed for the nanocomposites comparing with the pristine resins. The peaks at  $\log r = 3.2\text{--}4.2$  (nm) are due to structure

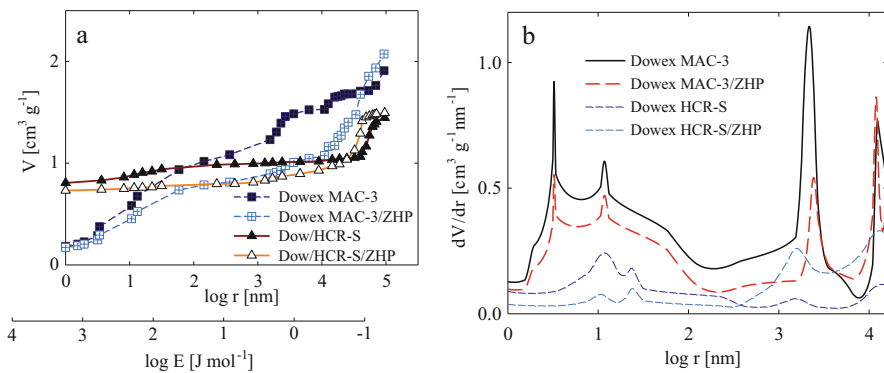


**Fig. 4.3** Integral distributions of pore volume and energy of water bonding (a), differential distributions of pore volume (b)

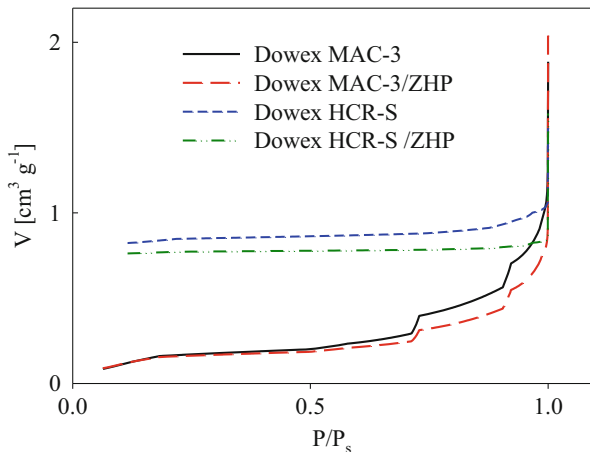


**Fig. 4.4** Isotherms of water adsorption

defects. Their volume decreases (weakly acidic resin) or increases (strongly acidic resin) after modification. The largest pores are attributed to voids between grains, and these pores are not considered.

Earlier the  $\alpha$  and  $\gamma$  parameters have been proposed for establishing the relationship between the structure of polymer and ion transport [55]. The  $\alpha$  parameter is a ratio of volumes of transport and non-transport pores, and the  $\gamma$  value is a ratio of volumes of pores containing only bonded water ( $r < 1.5$  nm) and pores filled with free water ( $r > 1.5$  nm). Modification increases the  $\gamma$  parameter indicating slower ion transport. The  $\alpha$  parameter remains practically constant (Dowex MAC-3) or decreases (Dowex HCR-S) due to blockage of clusters.

The isotherms of water adsorption for the composites are slightly shifted to the region of higher  $P/P_s$  values (Fig. 4.4; here  $P$  is the pressure of vapor, and  $P_s$  is related to saturated vapor). The shift indicates higher swelling pressure for the nanocomposites comparing with the pristine resins. The “swelling pressure” term corresponds to Gregor’s model [61]; it is different from the conventional characteristic for swollen polymers. According to the change of swelling pressure, the nanoparticles can be formally considered as a cross-linking agent, which reduces water content and increases Gregor’s swelling pressure.

An amount of water molecules ( $n$ ) in hydrate shells of fixed and counterions (hydration number) was calculated as  $n = \frac{A_{H_2O}}{A_p V_{H_2O}(1-m)}$  ( $V_{H_2O}$  is the molar volume ( $0.018 \text{ cm}^3 \text{ mmol}^{-1}$ ),  $A_p$  is the exchange capacity of pristine polymer,  $A_{H_2O}$  is water adsorption in clusters and channels, and  $V$  value is expressed as  $\text{cm}^3 \text{ cm}^{-3}$ ).

It is also possible to calculate a distance between functional groups ( $L$ ) as  $\sqrt{\frac{qS}{A_p F(1-m)}}$  [62]. Here  $q$  is the electron charge,  $F$  is the Faraday constant, and  $S$  is the specific surface area of clusters and channels.

**Table 4.1** Structure characteristics of polymer constituents

Sample	$L$ , nm	$n$	$\alpha$	$\gamma$
Dowex MAC-3	0.37	4.3	0.40	0.61
Dowex MAC-3/ZHP	0.38	3.9	0.39	0.91
Dowex HCR-S	0.78	10.4	1.71	1.01
Dowex HCR-S/ZHP	0.53	14.9	1.06	1.53

It is necessary to note that the  $A_p$  value is overstated for the nanocomposites. This distortion is stronger for the  $n$  parameter, which is inversely proportional to  $A_p$ , and smaller for the  $L$  parameter ( $L \sim \frac{1}{\sqrt{A_p}}$ ). Indeed, the  $L$  value is slightly higher for the nanocomposite based on weakly acidic resin comparing with the pristine polymer. At the same time, the hydration number is slightly smaller. The nanocomposite based on strongly acidic resin shows higher  $n$  value than the pristine resin (this indicates stretching of transport pores), but the  $L$  parameter is lower. It means that the hydration number is higher than 14.9 (Table 4.1).

## 4.6 Sorption Under Batch Conditions

$\text{Ni}^{2+} \rightarrow \text{H}^+$  exchange and BG adsorption were investigated. BG is a cationic triphenylmethane dye, and its topological polar surface area is  $2.3 \text{ nm}^2$  [63]. Thus, a radius of the molecule is  $\approx 0.85 \text{ nm}$ ; its diffusion through the cluster-channel system is possible. Dyes are adsorbed by hydrophobic [64] and hydrophilic [65] polymers as well as by inorganic ion-exchangers [66, 67]. For example, the mechanism of adsorption on metal oxides involves not only electrostatic attraction but also formation of hydrogen bonds between  $-\text{OH}$  groups and aromatic rings, as well as bonds between nitrogen atoms and oxygen atoms [67].

Isotherms demonstrate a growth of capacity followed by plateau (Fig. 4.5a, c).

Only the ascending parts of the curves are given for  $\text{Ni}^{2+}$  sorption on the samples based on weakly acidic resins (Fig. 4.5b). Modification of the resins results in decrease of capacity toward  $\text{Ni}^{2+}$  and improvement of BG adsorption. In the last case, it is possible to say about synergetic effect, when the polymers and inorganic ion-exchanger are combined into nanocomposite.

Among known approaches, the Langmuir (BG) and Freundlich ( $\text{Ni}^{2+}$ ) models [68] were found to be the most suitable to fit the ascending sections of the curves. The Freundlich isotherm of  $\text{Ni}^{2+}$  sorption is described as

$$A = K_F C^{1/p}. \quad (4.1)$$

Here  $K_F$  and  $p$  are the constants ( $p < 1$ ), which characterize a slope of the isotherm. The steepest buildup of the isotherms is for the nanocomposites despite the lowest  $K_F$  and  $p$  parameters for ZHP (Fig. 4.6a, Table 4.2).

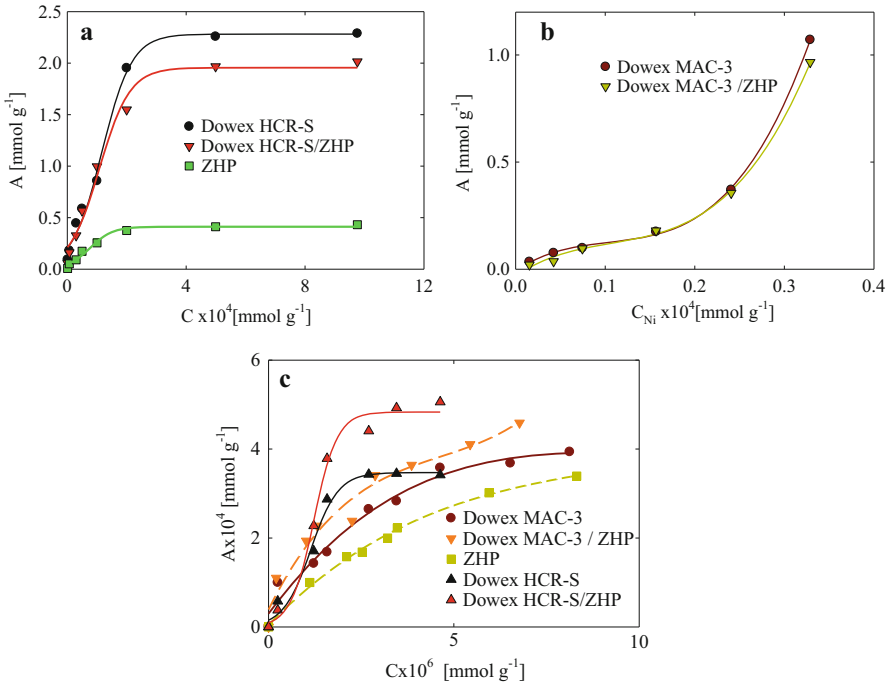


**Fig. 4.5** Isotherms of  $Ni^{2+} \rightarrow H^+$  exchange (a, b) and BG adsorption (c)

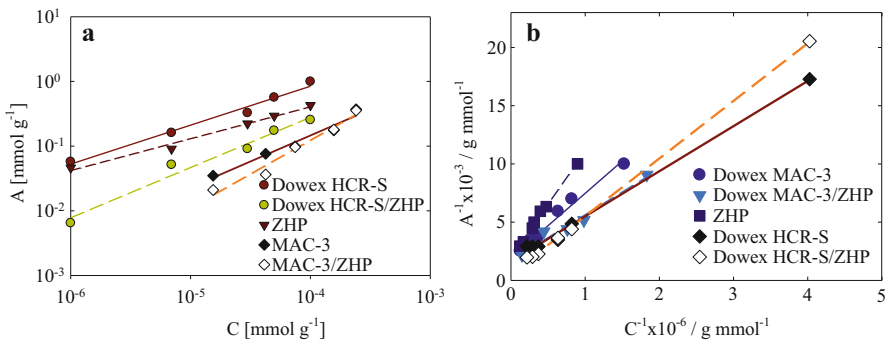


**Fig. 4.6** Isotherms of  $Ni^{2+} \rightarrow H^+$  exchange (a) and BG adsorption (b) plotted in Freundlich (a) and Langmuir (b) coordinates

The Langmuir equation is as follows:

$$\frac{1}{A} = \frac{1}{K_L A_L C} + \frac{1}{A_L} \quad (4.2)$$

**Table 4.2** Modeling of adsorption isotherms

Sample	BG (Langmuir model)				Ni <sup>2+</sup> (Freundlich model)		
	$A_L \times 10^4 \text{ mmol g}^{-1}$		$K_L \times 10^{-5} \text{ g mmol}^{-1}$	$R^2$	$A_F \text{ mmol g}^{-1}$	$1/n$	$R^2$
	Experimental	Calculated					
Dowex MAC-3	4.11	5.21	3.81	0.98	238	0.80	0.98
Dowex MAC-3/ZHP	4.89	5.83	4.36	0.97	1818	0.96	0.98
Dowex HCR-S	3.41	5.51	51.19	0.99	214	0.60	0.99
Dowex HCR-S/ZHP	5.55	7.57	27.26	0.99	338	0.77	0.98
ZHP	3.65	5.05	2.19	0.99	36	0,49	0.99

where  $C$  is the equilibrium concentration,  $A_L$  is the monolayer capacity, and the  $K_L$  constant characterizes energy of interaction of molecules with surface. The  $A_L$  values were determined also from the original data by extrapolation of the isotherms to infinity. The experimental and calculated  $A_L$  magnitudes are rather close to each other indicating validity of the Langmuir model for BG adsorption (Fig. 4.6b).

Modification of the weakly acidic resin causes increase of the  $A_L$  and  $K_L$  values. In comparison with the pristine strongly acidic resin, its nanocomposite shows higher monolayer capacity and weaker interaction with BG. ZHP demonstrates the lowest  $K_L$  magnitude.

Figure 4.7 illustrates BG and Ni<sup>2+</sup> sorption over time ( $\tau$ ). Among known approaches, the model of chemical reaction of pseudo-second order [69]

$$\frac{\tau}{A} = \frac{1}{K_2 A_\infty^2} + \frac{1}{A_\infty} \tau \quad (4.3)$$

is the most applicable to the data. Here  $A_\infty$  is the capacity at  $\tau \rightarrow \infty$ , and  $K_2$  is the rate constants. The  $A_\infty$  magnitudes are close to each other; moreover, the correlation coefficients are high indicating validity of the model (Table 4.3).

In all cases, the embedded particles slow down BG adsorption (decrease of the  $K_2$  parameter). The modifier inside the strongly acidic resin retards Ni<sup>2+</sup>  $\rightarrow$  H<sup>+</sup> exchange but accelerates this process on the weakly acidic resin. Chemical interaction of sorbed Ni<sup>2+</sup> ions with strongly and weakly acidic polymer matrices is probably redistribution of water molecules between hydrate shells of fixed and counterions.

The samples were tested in ion-exchange columns. Figure 4.8 illustrates Ni<sup>2+</sup> and BG concentration in the solution at the column outlet vs ratio of volumes of the solution ( $V_s$ ) and ion-exchanger ( $V_i$ ). The samples based on strongly acidic resins remove Ni<sup>2+</sup> practically completely. The residual concentration is lower than 0.1 mg dm<sup>-3</sup>. This is much lower than the maximal allowable concentration for wastewater, which can be dumped unto sewage (0.5 mg dm<sup>-3</sup>). Higher Ni<sup>2+</sup> content in the effluent is achieved in the case of the samples based on weakly acidic resin (about 1 mg dm<sup>-3</sup>). However, the breakthrough capacity of the nanocomposites is



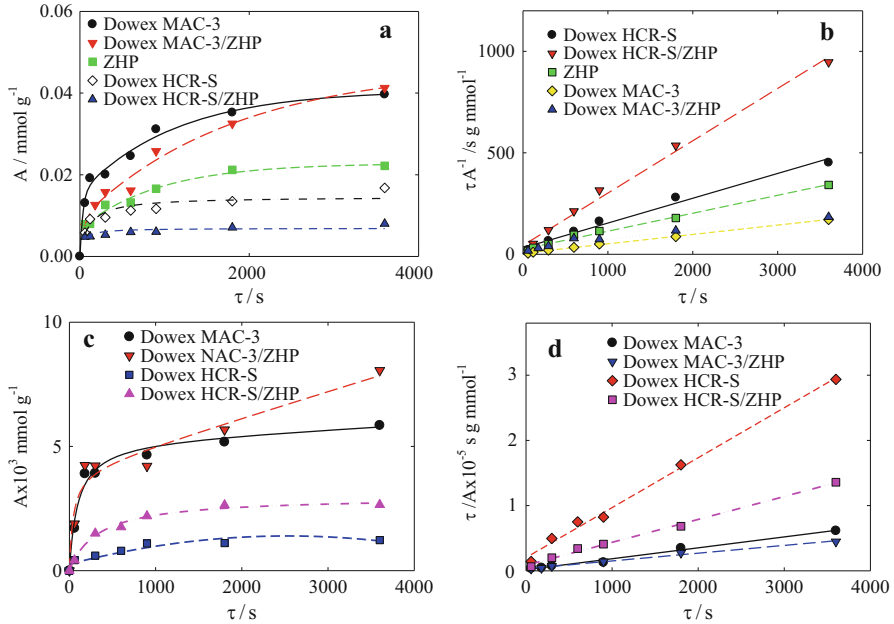


**Fig. 4.7** Capacity of ion-exchangers toward BG (a, b) and Ni<sup>2+</sup> (c, d) as a function of time. The model of chemical reaction of pseudo-second order was applied (b, d)

**Table 4.3** Modeling of sorption rate

Sample	$A_{\infty}, \times 10^2 \text{ mmol g}^{-1}$		$K_2 \times 10^2, \text{ g mmol}^{-1} \text{ s}^{-1}$	$R^2$
	Experimental	Calculated		
<i>BG</i>				
Dowex MAC-3	4.43	4.21	8.91	0.99
Dowex MAC-3/ZHP	4.60	4.23	3.24	0.96
Dowex HCR-S	1.68	1.75	10.04	0.99
Dowex HCR-S/ZHP	0.80	0.82	3.98	0.99
ZHP	2.23	2.37	1.61	0.99
<i>Ni<sup>2+</sup></i>				
Dowex MAC-3	0.69	0.84	44.95	0.99
Dowex MAC-3/ZHP	1.04	0.60	102.67	0.99
Dowex HCR-S	0.19	0.13	290.55	0.99
Dowex HCR-S/ZHP	0.28	0.28	153.00	0.99

higher compared with pristine resins and especially with ZHP. It should be stressed that this value is higher two times for the nanocomposite based on strongly acidic resin than that for the ion-exchanger based on weakly acidic resin.

Breakthrough capacity is determined by sorption rate, sorption capacity, and selectivity of the sorbent [61]. Comparing with the pristine strongly acidic resin, the nanocomposite shows reduced exchange capacity and lower constant of chemical

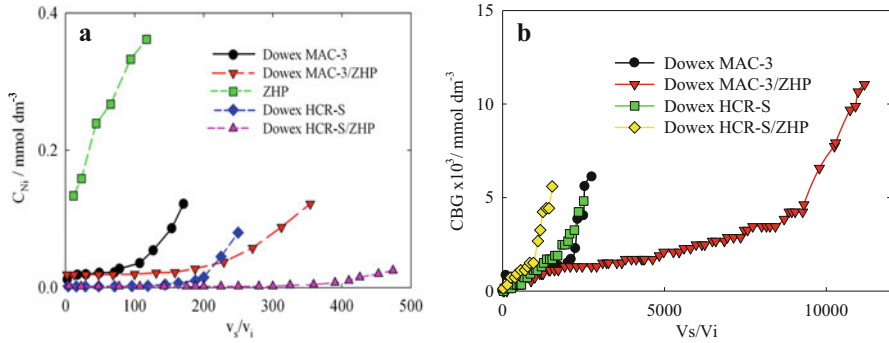


**Fig. 4.8**  $Ni^{2+}$  (a) and BG (b) concentration in the solution at the column outlet vs ratio of volumes of the solution ( $V_s$ ) and ion-exchanger

reaction (see Table 4.3 and Fig. 4.5). Thus, higher breakthrough capacity of the nanocomposite is due to its improved selectivity toward transition metal ions [23]. This material better removes  $Ni^{2+}$  ions from water containing also hardness ions. Regarding the modified weakly acidic resin, its advantage over the pristine resin is caused by faster sorption and evidently by better selectivity.

Modification decreases breakthrough capacity of the strongly acidic resin toward BG (due to slower adsorption on the nanocomposite comparing with the pristine resin) and increases this value for the weakly acidic ion exchanger (this is evidently caused by higher adsorption capacity and faster adsorption on the nanocomposite). In order to remove both organic dyes and inorganic anions from mixed solutions under dynamic conditions, a mixture of the nanocomposites based on strongly and weakly acidic resins is recommended.

## 4.7 Conclusions

The modified cation-exchanger contain ZHP particles with size from several nanometers to several microns. Single nanoparticles are located in pores containing functional groups; aggregates occupy inert pores. From the formal point of view, non-aggregated nanoparticles can be considered as a cross-linking agent, which increases swelling pressure. Swelling pressure provides stretching of transport pores. As a result, porous structure of the polymer constituent is transformed: some regions of the polymers, which are able to interact with species, become unavailable for them. However, embedded ZHP particles evidently expand the range of pores, where adsorption is possible. This is valid both for BG adsorptions on weakly and strongly acidic resins. It is the same for  $Ni^{2+}$  ion sorption on strongly acidic resins. The particles decrease sorption rate by this manner. At the same time, strong interaction with  $Ni^{2+}$  ions is attributed to the weakly acidic resin. Indeed,

this material shows higher Freundlich constants comparing with the strongly acidic resin. Partial screening of the polymer with particles causes acceleration of ion exchange.

## References

1. Naushad M (2009) Inorganic and composite ion exchange materials and their applications (review). *Ion Exchange Let* 2:1–14
2. Khan A, Asiri AM, Rub MA et al (2012) Review on composite cation exchanger as interdisciplinary materials in analytical chemistry. *Int J Electrochem Sci* 7:3854–3902
3. Kango S, Kalia S, Celli A et al (2013) Surface modification of inorganic nanoparticles for development of organic–inorganic nanocomposites – a review. *Progr Polym Sci* 38(8):1232–1261
4. Çakmak M, Taşar Ş, Selen V et al (2017) Removal of astrazon golden yellow 7GL from colored wastewater using chemically modified clay. *J Centr South Univer* 24(4):743–753
5. Öncü-Kaya EM, Şide N, Gök Ö et al (2017) Evaluation on dye removal capability of didodecyldimethylammonium-bentonite from aqueous solutions. *J Dispers Sci Technol* 38(8):1211–1220
6. Fernandes de Queiroga LN, Soares PK, Fonseca MG et al (2016) Experimental design investigation for vermiculite modification: intercalation reaction and application for dye removal. *Appl Clay Sci* 126:113–121
7. Houhoune F, Nibou D, Chegrouche S et al (2016) Behaviour of modified hexadecyltrimethylammonium bromide bentonite toward uranium species. *J Environ Chem Eng* 4(3):3459–3346
8. Sprynskyy M, Kowalkowski T, TutuIonic H et al (2015) Ionic liquid modified diatomite as a new effective adsorbent for uranium ions removal from aqueous solution. *Colloids Surfaces A: Physicochem Eng Aspects* 465:159–167
9. Yu H, Yang S, Ruan H et al (2013) Recovery of uranium ions from simulated seawater with palygorskite/amidoxime polyacrylonitrile composite. *Appl Clay Sci* 111:67–75
10. Zebedius K, Madhumita S, Segametsi B et al (2013) Exfoliated polypyrrole-organically modified montmorillonite clay nanocomposite as a potential adsorbent for Cr(VI) removal. *Chem Eng J* 222:186–197
11. Mohammadi E, Kaan K, Nihan Y et al (2013) Modeling of adsorption of toxic chromium on natural and surface modified lightweight expanded clay aggregate (LECA). *Appl Surf Sci* 287:428–442
12. Singha R, Donga H, Zengb Q et al (2017) Hexavalent chromium removal by chitosan modified-bioreduced nontronite. *Geochim Cosmochim Acta* 210:25–41
13. Snoussiab Y, Abderrabba M, Sayari A (2016) Removal of cadmium from aqueous solutions by adsorption onto polyethylenimine-functionalized mesocellular silica foam: equilibrium properties. *J Taiwan Institute Chem Eng* 66:372–378
14. Dasthaiah K, Selvan BR, Suneesh AS et al (2017) Ionic liquid modified silica gel for the sorption of americium(III) and europium(III) from dilute nitric acid medium. *J Radioanalytic Nucl Chem* 313(3):515–521
15. NiuY, QuR, Sun Cet al (2013) Adsorption of Pb(II) from aqueous solution by silica-gel supported hyperbranched polyamidoamine dendrimers. *J Hazard Mater* 244–245:276–286
16. Hu C, Deng J, Zhao Y et al (2014) A novel core-shell magnetic nano-sorbent with surface molecularly imprinted polymer coating for the selective solid phase extraction of dimetridazole. *Food Chem* 158:366–373
17. Liu Y, Zhang Z, Zhang M et al (2011) Preparation of core-shell magnetic ion-imprinted polymer for selective extraction of Pb(II) from environmental samples. *Chem Eng J* 178(15):443–450

18. Safari M, Yamini Y, Masoomi MY et al (2017) Magnetic metal-organic frameworks for the extraction of trace amounts of heavy metal ions prior to their determination by ICP-AES. *Microchim Acta* 184:1555–1565
19. Sarkar S, Guibal E, Quignard F et al (2012) Polymer-supported metals and metal oxide nanoparticles: synthesis, characterization, and applications. *J Nanopart Res* 14(2):715 <https://doi.org/10.1007/s11051-011-0715-2>
20. Zhang Q, Jiang P, Pan B et al (2009) Impregnating zirconium phosphate onto porous polymers for lead removal from waters: effect of nanosized particles and polymer chemistry. *Ind Eng Chem Res* 48:4495–4499
21. Pan B, Pan B, Chen X et al (2006) Preparation and preliminary assessment of polymer-supported zirconium phosphate for selective lead removal from contaminated water. *Water Res* 40:2938–2946
22. Sarkar S, Chatterjee P, Cumbal L et al (2011) Hybrid ion exchanger supported nanocomposites: sorption and sensing for environmental applications. *Chem Eng J* 166:923–931
23. Dzyazko YS, Perlova OV, Perlova NA et al (2017) Composite cation-exchange resins containing zirconium hydrophosphate for purification of water from U(VI) cations. *Desalin Water Treat* 69:142–152
24. Perlova N, Dzyazko Y, Perlova O et al (2017) Formation of zirconium hydrophosphate nanoparticles and their effect on sorption of uranyl cations. *Nanoscale Res Lett*:12–209 <https://doi.org/10.1186/s11671-017-1987-y>
25. Blaney LM, Cinar S, SenGupta AK (2007) Hybrid anion exchanger for trace phosphate removal from water and wastewater. *Water Res* 41:1603–1613
26. Lee B, Bao L, Im H et al (2003) Synthesis and characterization of organic–inorganic hybrid mesoporous anion-exchange resins for perrhenate ( $\text{ReO}_4^-$ ) anion adsorption. *Langmuir* 19(10):4246–4252
27. De Marco MJ, SenGupta AK, Greenleaf JE (2003) Arsenic removal using a polymeric/inorganic hybrid sorbent. *Water Res* 37(1):164–176
28. Mal'tseva TV, Kolomiets EA, Vasilyuk SL (2017) Hybrid adsorbents based on hydrated oxides of Zr(IV), Ti(IV), Sn(IV), and Fe(III) for arsenic removal. *J Water Chem Technol* 39(4):214–219
29. Cumbal L, SenGupta AK (2005) Arsenic removal using polymer-supported hydrated iron(III) oxide nanoparticles: role of Donnan membrane effect. *Environ Sci Technol* 39(17):6508–6515
30. Qingrui BP, Du ZW, Zhang W et al (2007) Selective heavy metals removal from waters by amorphous zirconium phosphate: behavior and mechanism. *Water Res* 41(14):3103–3111
31. Dzyazko YS, Trachevskii VV, Rozhdestvenskaya LM et al (2013) Interaction of sorbed Ni(II) ions with amorphous zirconium hydrogen phosphate. *Russ J Phys Chem A* 87(5):840–845
32. Borgo CA, Gushikem Y (2002) Zirconium phosphate dispersed on a cellulose fiber surface: preparation, characterization, and selective adsorption of  $\text{Li}^+$ ,  $\text{Na}^+$ , and  $\text{K}^+$  from aqueous solution. *J Colloid Interface Sci* 246(2):343–347
33. Zhang Q, Du Q, Jiao T et al (2013) Selective removal of phosphate in waters using a novel of cation adsorbent: zirconium phosphate (ZrP) behavior and mechanism. *Chem Eng J* 221:315–321
34. Bhaumik A, Inagaki S (2001) Mesoporous titanium phosphate molecular sieves with ion-exchange capacity. *J Am Chem Soc* 123(4):691–696
35. Chitrakar R, Tezuka S, Sonoda A et al (2006) Selective adsorption of phosphate from seawater and wastewater by amorphous zirconium hydroxide. *J Colloid Interface Sci* 297(2):426–433
36. Dixit S, Hering JG (2003) Comparison of arsenic(V) and arsenic(III) sorption onto Iron oxide minerals: implications for arsenic mobility. *Environ Sci Technol* 37(18):4182–4189
37. Guang PX, Dan MZ, Chong LH et al (2012) Use of iron oxide nanomaterials in wastewater treatment: a review. *Sci Total Environ* 424(1):1–10
38. Maltseva TV, Kudelko EO, Belyakov VN (2009) Adsorption of Cu(II), Cd(II), Pb(II), Cr(VI) by double hydroxides on the basis of Al oxide and Zr, Sn, and Ti oxides. *Russ J Phys Chem A* 83(13):2336–2339

39. Kudelko K, Maltseva T, Bieliakov V (2011) Adsorption and mobility of Cu (II), Cd (II), Pb (II) ions adsorbed on (hydr)oxide polymer sorbents  $M_xO_y \cdot nH_2O$ ,  $M = Zr$  (IV), Ti (IV), Sn (IV), Mn (IV). *Desalin Water Treat* 35(1–3):295–299
40. Dzyazko YS, Ponomareva LN, Volfkovich YM et al (2012) Effect of the porous structure of polymer on the kinetics of  $Ni^{2+}$  exchange on hybrid inorganic-organic ionites. *Russ J Phys Chem A* 86(6):913–919
41. Dzyazko YS, Belyakov VN, Vasilyuk SL et al (2006) Anion-exchange properties of composite ceramic membranes containing hydrated zirconium dioxide. *Russ J Appl Chem* 79(5):769–773
42. Dzyazko YS, Volfkovich YM, Sosenkin VE et al (2014) Composite inorganic membranes containing nanoparticles of hydrated zirconium dioxide for electro-dialytic separation. *Nanoscale Res Lett* 9(1):271 <https://doi.org/10.1186/1556-276X-9-271>
43. Martí-Calatayud MC, García-Gabaldon M, Pérez-Herranz V et al (2015) Ceramic anion-exchange membranes based on microporous supports infiltrated with hydrated zirconium dioxide. *RSC Adv* 5:46348–46358
44. Dzyazko YS, Rozhdstvenska LM, Vasilyuk SL et al (2017) Composite membranes containing nanoparticles of inorganic ion exchangers for electro-dialytic desalination of glycerol. *Nanoscale Res Lett* 12:438 <https://doi.org/10.1186/s11671-017-2208-4>
45. Hong JG, Chen Y (2015) Evaluation of electrochemical properties and reverse electro-dialysis performance for porous cation exchange membranes with sulfate-functionalized iron oxide. *J Membr Sci* 473:210–217
46. Pang R, Li X, Li J et al (2014) Preparation and characterization of  $ZrO_2$ /PES hybrid ultrafiltration membrane with uniform  $ZrO_2$  nanoparticles. *Desalination* 332:60–66
47. Myronchuk VG, Dzyazko YS, Zmievsii YG et al (2016) Organic-inorganic membranes for filtration of corn distillery. *Acta Periodica Technologica* 47:153–165
48. Dzyazko YS, Rozhdstvenskaya LM, Zmievsii YG et al (2015) Organic-inorganic materials containing nanoparticles of zirconium hydrophosphate for baromembrane separation. *Nanoscale Res Lett* 10:64. <https://doi.org/10.1186/s11671-015-0758-x>
49. Hsu WY, Gierke TD (1983) Ion transport and clustering in nafion perfluorinated membranes. *J Membr Sci* 13(3):307–326
50. Berezina NP, Kononenko NA, Dyomina OA et al (2008) Characterization of ion-exchange membrane materials: properties vs structure. *Adv Colloid Interf Sci* 139(1–2):3–28
51. Yaroslavtsev AB, Nikonenko VV, Zabolotsky VI (2003) Ion transfer in ion-exchange and membrane materials. *Russ Chem Rev* 72(5):393–421
52. Yaroslavtsev AB, Nikonenko VV (2009) Ion-exchange membrane materials: properties, modification, and practical application. *Nanotechnol Russia* 4(3–4):137–159
53. James PJ, Elliott JA, McMaster TJ et al (2000) Hydration of Nafion studied by AFM and X-ray scattering. *J Mater Sci* 35(20):5111–5119
54. Young SK, Trevino SF, Beck Tan NC (2002) Small-angle neutron scattering investigation of structural changes in Nafion membranes induced by swelling with various solvents. *J Polym Sci. Part B: Polym Phys* 40:387–400
55. Dzyazko YS, Ponomareva LN, Volfkovich YM et al (2013) Conducting properties of a gel ionite modified with zirconium hydrophosphate nanoparticles. *Russ J Electrochem* 49(3):209–215
56. Stöhr C, Horst J, Höll WF (2001) Application of the surface complex formation model to ion exchange equilibria: part V. Adsorption of heavy metal salts onto weakly basic anion exchangers. *React Funct Polym* 49(2):117–132
57. Saha B, Sreat M (2005) Adsorption of trace heavy metals: application of surface complexation theory to a macroporous polymer and a weakly acidic ion-exchange resin. *Ind Eng Chem Res* 44(23):8671–8681
58. Volfkovich YM, Sosenkin VE (2012) Porous structure and wetting of fuel cell components as the factors determining their electrochemical characteristics. *Russ Chem Rev* 86(6):936–959
59. Volfkovich YM, Bagotsky VS, Filippov AN (2014) Porous materials and powders used in different fields of science and technology. Springer, London/Heidelberg/New York/Dordrecht

60. Rouquerol J, Baron G, Denoyel R et al (2012) Liquid intrusion and alternative methods for the characterization of macroporous materials (IUPAC technical report). *Pure Appl Chem* 84(1):107–136
61. Helfferich F (1995) *Ion Exchange*. Dover, New York
62. Volkovich YM (1984) Influence of the electric double-layer on the internal interfaces in an ion-exchanger on its electrochemical and sorption properties. *Soviet Electrochem* 20(5):621–628
63. PubChem Open Chemistry Database. <https://pubchem.ncbi.nlm.nih.gov/compound/90474287#section=3D-Conformer>
64. Eckenrode HM, Jen SH, Han J et al (2005) Adsorption of a cationic dye molecule on polystyrene microspheres in colloids: effect of surface charge and composition probed by second harmonic generation. *J Phys Chem B* 109(10):4646–4653
65. Bayramoglu G, Altintas B, Arica MY (2009) Adsorption kinetics and thermodynamic parameters of cationic dyes from aqueous solutions by using a new strong cation-exchange resin. *Chem Eng J* 152:339–346
66. Maheria KC, Chudasama UV (2007) Sorptive removal of dyes using titanium phosphate. *ACS Publ Ind Eng Chem Res* 46(21):6852–6857
67. Abramian L, El-Rassy H (2009) Adsorption kinetics and thermodynamics of azo-dye Orange II onto highly porous titania aerogel. *Chem Eng J* 150:403–410
68. Rouquerol F, Rouquerol J, Sing H (1999) *Adsorption by powders and porous solids. Principles, methodology and application*. Academic Press, London/San Diego
69. Qiu H, Lv L, Pan B-C et al (2009) Critical review in adsorption kinetic models. *J Zhejiang Univ Sci A* 10(5):716–724



# Chapter 5

## Peculiarities of the Crystal-Chemical Structure of Spinel Ferrites $\text{Co}_x\text{Fe}_{3-x}\text{O}_4$ ( $0.25 \leq x \leq 1$ ) Obtained Under the Action of a Low-Temperature Contact Nonequilibrium Plasma

L. A. Frolova, O. A. Pivovarov, O. A. Kushnerov, and N. M. Tolstopalova

### 5.1 Introduction

The interest of researchers in the  $\text{Co}_x\text{Fe}_{3-x}\text{O}_4$  system has grown significantly in recent decades. This is due to the use of cobalt ferrites for the manufacturing of high-frequency devices in magnetic resonance imaging and biotechnology and due to high cubic magnetocrystalline anisotropy, high coercivity, moderate saturation of magnetization, and its ability to reduce magnetic losses at high frequencies [1–3]. It is on the basis of cobalt ferrite that the systems with special properties have been developed [4].

One way to improve the magnetic properties of ferrite powders is to improve the structure of the starting material. Hydrophase synthesis methods, including those initiated by various physical fields, are the basis for the creation of promising and high-tech ferrite materials [5], in connection with which the patterns of their formation are the object of in-depth study. A detailed study of the model reaction mechanism, which underlies the formation of ferrites, indicates the complex nature of this process, and the single-phase structure of ferrite is not a guarantee of its chemical homogeneity. The ability of ferrites to form continuous series of solid solutions, which also contain a different amount of oxygen and vacancies, leads to the fact that within the same phase, there can be significant gradients in the

---

L. A. Frolova (✉) · O. A. Pivovarov  
Ukrainian State Chemical Technology University, Dnipro, Ukraine

O. A. Kushnerov  
Oles Honchar Dnipropetrovsk National University, Dnipro, Ukraine

N. M. Tolstopalova  
National Technical University of Ukraine “Igor Sikorsky Kyiv Polytechnic Institute”, Kyiv, Ukraine

concentration of constituent components. This is unacceptable for ferrites, the properties of which are very sensitive to residual chemical inhomogeneities. All this encourages the search for methods of synthesis, different from classical ceramic technology, and, accordingly, the study of the crystal-chemical structure and the analysis of the physicochemical characteristics of cobalt ferrites.

A lot of research has been devoted to the formation of the spinel structure. The solid-phase technologies for the production of cobalt ferrites were considered in detail in works [6, 7], the concentration dependences of the crystal lattice parameter and the magnetic saturation moment in the region of spinel solid solutions of  $\text{Co}_3\text{O}_4$  with  $\text{Fe}_3\text{O}_4$  were described in [8, 9], and the results of studying the formation boundaries of single-phase solid solutions in the  $\text{CoO-Fe}_2\text{O}_3$  system were analyzed in [10]. The authors [11–13] studied the conditions for the formation of cobalt-doped magnetite with a spinel structure in the course of solid-phase synthesis. The structure and properties of the samples were also studied.

To achieve high homogeneity of nanodispersed-size particles of the synthesized product, chemical methods of production were used (sol-gel method [14], autoignition [15, 16], hydrothermal [17], and coprecipitation methods [18]). For example, in the work [19], ferrite was obtained with the hydrothermal method, which made possible to achieve/produce uniform sphere-shaped nanopowder sand to increase the magnetic properties as compared to systems synthesized by the traditional precipitation method.

The peculiarity of hydrophase synthesis lies in the fact that all the reagents are mixed at the atomic or molecular level, which ensures high stoichiometry and homogeneity of the distribution of the final product particles both in size and from a chemical point of view. No less important advantage of chemical methods of production is their high efficiency (much lower synthesis temperatures are used compared to the solid phase) and relatively simple and affordable equipment.

The properties of plasma treatment were used for the synthesis of complex inorganic compounds [20–22]. The synthesis of ferrites by CNP was considered in this work [23]. The authors [24] carried out a study of the crystal-chemical properties of cobalt ferrite compositions under plasma spraying. The paper described the mechanism of the action of low-pressure plasma with a liquid cathode on various salt solutions [25]. The authors introduced the technology of obtaining ferrite nanoparticles by an electrochemical method [26]. The work [15] studied the influence  $\text{Cr}^{3+}$  concentrations of the initial solution on the properties of cobalt ferrite obtained from the citrate solution. There are not enough works devoted to the investigation of the CNP influence on the formation of cobalt ferrites. The possibility of this synthesis was shown in the work [27].

In this paper, we presented the results of further studies in this direction. The aim of the study was to determine the crystal-chemical parameters of cobalt ferrites with a spinel structure in the  $\text{Co}_x\text{Fe}_{3-x}\text{O}_4$  system ( $0.25 \leq x \leq 1$ ) as well as to establish the dependence of the structure and magnetic characteristics of the resulting compounds.



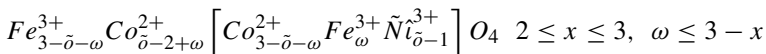
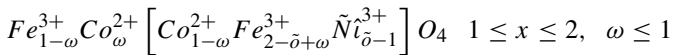
## 5.2 Methodology of the Experiment

Aqueous solutions of cobalt sulfate hexahydrate and ferrous sulfate hexahydrate have been used as starting precursors. The preparation of nanosized cobalt ferrite has been carried out on a laboratory plasma chemical plant, which consists of a single-stage plasma reactor of a discrete type, a step-up transformer, a transformer-igniter, and a vacuum pump. The pH of the solution was monitored at regular intervals, and the product obtained was washed and dried for further investigation. Infrared (IR) reflection spectra of cobalt ferrites  $\text{Co}_x\text{Fe}_{3-x}\text{O}_4$  ( $x = 0.25, 0.5, 0.75, 1.0$ ) were measured within a  $400\text{--}4000\text{ cm}^{-1}$  range by employing a Fourier-transform infrared (FTIR) spectrometer Nicolet iS10. The phase composition and structure of ferrite samples were studied using X-ray diffractometer DRON-2 with  $\text{Cu-K}_\alpha$  radiation. The magnetic properties of the final powder have been studied using a vibrating sample magnetometer.

## 5.3 Results and Discussion

It was established [27] that the formation of cobalt ferrites from coprecipitated hydroxides occurs during CNP treatment for 40 min. According to X-ray phase analysis, a spinel phase is formed at this time. It should be noted that a single-phase spinel of a similar composition is formed at  $1200\text{--}1400^\circ\text{C}$  in standard ceramic technology using oxides.

Cationic distributions in cobalt ferrites obtained with the help of different technologies were considered in [8, 9, 15]. Cobalt (II) ions are known [28] to tend to tetrahedral positions, which are related to the structure of their electron shell. With an increase in cobalt content in spinel, cobalt (II) cations are partially oxidized to trivalent cations.  $\text{Co}^{3+}$  cations replace  $\text{Fe}^{3+}$  cations in octahedral positions, and  $\text{Co}^{2+}$  cations migrate from tetrahedral to octahedral positions. For  $1 < x < 2$  and  $2 < x < 3$ , the authors [29] proposed structural formulas consistent with the general cationic distribution:



For the products being formed (in the investigated range of composition), studied in this paper, the use of structural formulas proposed by the authors [28–30] did not give a positive result. As a consequence, it is assumed that the tetrahedral  $\text{Co}^{2+}$  ions are not taken into account because of the strong octahedral preference of these ions. In addition, X-ray phase analysis data (Table 5.2) indicate the values of the lattice parameter to be significantly lower than those given in the literature for cobalt

**Table 5.1** Composition of the samples obtained

Code of the sample	1	2	3	4
$X$ in the formula $\text{Co}_x\text{Fe}_{3-x}\text{O}_4$	1.0	0.75	0.5	0.25
Gross formula	$\text{CoFe}_2\text{O}_4$	$\text{Co}_{0.75}\text{Fe}_{2.25}\text{O}_4$	$\text{Co}_{0.5}\text{Fe}_{2.5}\text{O}_4$	$\text{Co}_{0.25}\text{Fe}_{2.75}\text{O}_4$

**Table 5.2** Average cation-oxygen distances in tetrahedral ( $d_{\text{Td}}$ ) and octahedral ( $d_{\text{Oh}}$ ) sites

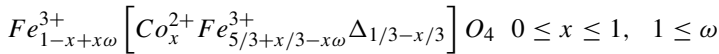
d(Me-O) bond lengths ( $\text{Å}^\circ$ )	$\text{Fe}^{3+}$	$\text{Co}^{2+}$	$\text{Co}^{3+}$	$\text{Fe}^{2+}$	$\Delta$
In tetrahedral site (Td) nm	0.1858	0.1974		0.2003	
In octahedral site(Oh) nm	0.2020	0.2123	0.1892	0.215	0.2240

$a$  is the lattice constant (nm)

**Table 5.3** Structural parameters at room temperature for the samples  $\text{Co}_x\text{Fe}_{3-x}\text{O}_4$ 

$x$	$a$ , nm	$L_1$ , Å	$M$ , %	$D$ , $\text{sm}^{-2}$
0.25	0.83373	418	$4.66 \cdot 10^{-4}$	$40.55 \cdot 10^{10}$
0.5	0.83154	481	$526 \cdot 10^{-4}$	$30.5 \cdot 10^{10}$
0.75	0.83382	460	$2.93 \cdot 10^{-4}$	$33.3 \cdot 10^{10}$
1.0	0.83401	350	$8.64 \cdot 10^{-4}$	$8.64 \cdot 10^{10}$

ferrites. This suggests that the spinels formed in the system have a defect structure similar to that of maghemite. Using this approach, a cationic distribution can be suggested, for  $x$  less than 1, in the form of the following structural formula:



$\omega$  is the degree of inversion (the fraction of divalent cations in the octahedral position or trivalent ones in tetrahedral)

$\Delta$  – vacancies in the crystal lattice

The dependences of the cation distribution and the crystal-chemical parameters of cobalt ferrites on the cobalt content in the samples calculated from the diffractograms are presented in Table 5.2. The lattice constant of the spinel phases was calculated by the equation:

$$a = 2.0995d_{\text{Td}} + \left[ 5, 8182(d_{\text{Oh}})^2 - 1, 4107d_{\text{Td}}^2 \right]^{1/2} \quad (5.1)$$

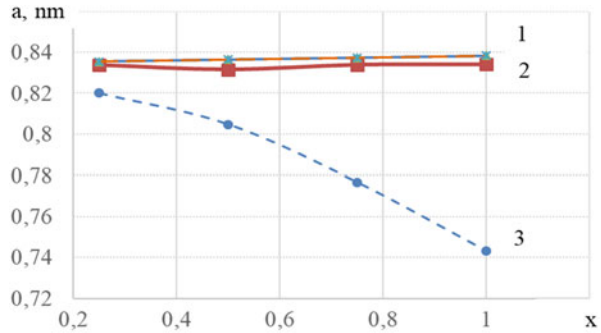
where  $d_{\text{Td}}$  and  $d_{\text{Oh}}$  are the average distances of the oxygen cation in tetrahedral and octahedral sites, respectively (Table 5.2) (nm).

Table 5.3 shows the results of X-ray phase analysis, where  $L_1$  is the crystallite size, Å;  $M$  is the degree of micro-stresses, %;  $D$  is the dislocation density,  $\text{sm}^{-2}$ .

Ion-atom tetrahedral and octahedral distances are more often attributed to a fictitious cation and are a weighted mean value of ion-atom distances of cations contained in certain positions. With this determining method of the cation distribution over the sublattice, we minimized the difference between the experimentally

**Table 5.4** Distribution of cations in ferrite determined by the Poix method

Distribution of cations in ferrite	$x$	$\omega$	$a$ , HM	$d_{Td}$ , HM	$d_{Oh}$ , HM
$Fe_{0.919}^{3+} [Co_{0.25}^{2+} Fe_{1.581}^{3+} \Delta_{0.25}] O_4$	0.25	0.675	0.833735	0.170704	0.214244
$Fe_{0.84}^{3+} [Co_{0.5}^{2+} Fe_{1.49}^{3+} \Delta_{0.16}] O_4$	0.5	0.68	0.83154	0.156183	0.222508
$Fe_{0.869}^{3+} [Co_{0.75}^{2+} Fe_{1.297}^{3+} \Delta_{0.083}] O_4$	0.75	0.826	0.833831	0.161553	0.21996
$Fe_{0.855}^{3+} [Co^{2+} Fe_{1.145}^{3+}] O_4$	1.0	0.855	0.83401	0.158339	0.222078

**Fig. 5.1** Dependence lattice parameters of the synthesized samples on the content of cobalt cations

(Table 5.3) and theoretically calculated parameters by the Poix (Eq. 5.1) lattice constants (calculated from the known chemical composition and the characteristic distances of the anion-cation [28]; Table 5.4).

Figure 5.1 shows theoretically calculated parameters of the synthesized sample lattice calculated according to the Poix equation (dashed lines) depending on the content of cobalt cations. Line 3 reflects the change in the lattice parameter in case of the normal spinel ( $\omega = 0$ ).

Line 1 corresponds to the inverse spinel, ( $\omega = 1$ ). As we can see, the lattice constant of the synthesized spinel occupies an intermediate position between normal and inverse one and changes nonlinearly, which is related to the features of ion distribution over the sublattices and the defectiveness of the ferrite structure. The dependence of the ferrite-cobalt lattice constant on the cobalt content can be conditionally divided into two regions: (I)  $x \leq 0.5$  and (II)  $0.5 \leq x \leq 1.0$ .

The change in the characteristics of ferrites in regions 1 and 2 is due to the change in the chemical composition, the distribution of cations in the sublattice being inverted. In region 2, while maintaining the general tendency to increase the lattice constant due to the change in composition, the increase in the degree of inversion leads to the increase in the lattice parameter comparable to the inverse spinel.

Analyzing Fig. 5.2, we can say that the interatomic distances change in the opposite direction: tetrahedral distances decrease, since the content of iron cations decreases, and the octahedral distances increase due to the increase in the number of vacancies. Thus, the cell parameter is largely determined by the octahedral distance. With the decrease in the number of ferric cations in octahedral positions,

**Fig. 5.2** Dependence of the degree of inversion of spinel (I), octahedral, and tetrahedral distances as a function of  $x$

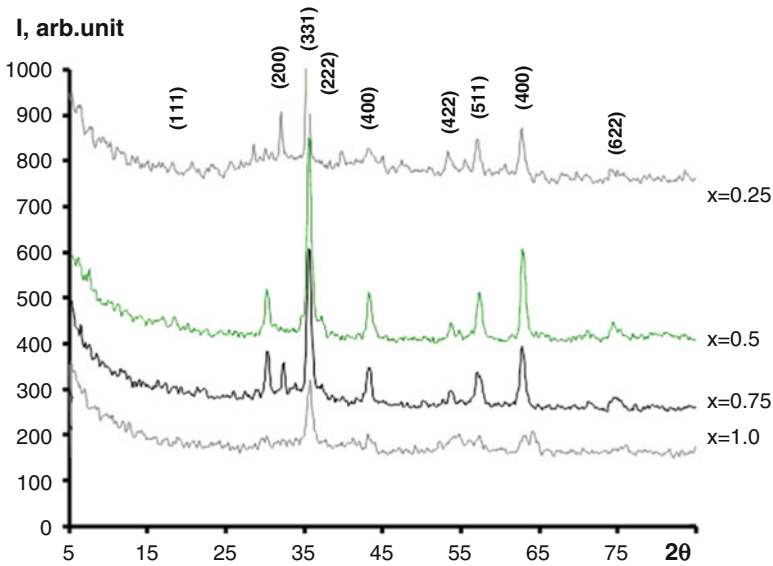
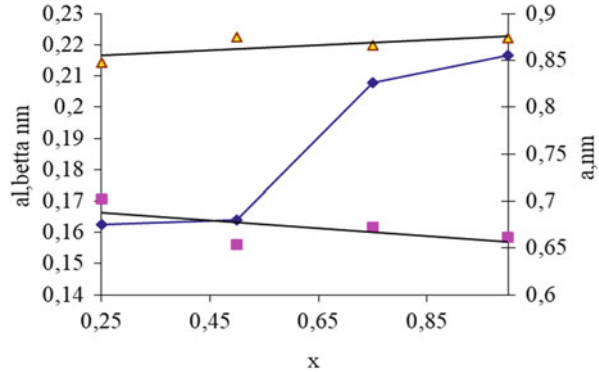


**Fig. 5.3** XRD patterns of ferrite obtained at different ratios of components (Table 5.1)

the octahedral distances increase, since the cobalt (II) radius is 0.82 Å and the iron (III) is 0.64 Å. The spinel degree of inversion is thus increasing.

XRD patterns corresponding to samples 1–4 with different molar ratios  $x$  have diffraction peaks corresponding to spinel oxide systems of cobalt ferrite (Fig. 5.3). All the main characteristic peaks of spinels are present on the diffractograms (220), (311), (222), (400), (422), and (511). Moreover, with the increase in cobalt content, the diffraction peaks are broadened, and their intensity decreases, which is due to the presence of crystallization water.

There are also peaks corresponding to  $\text{Fe}_3\text{O}_4$ , for the compositions enriched in iron. The calculations of the basic crystal-chemical parameters have shown that the formation of a structure with an iron content higher than stoichiometric takes place

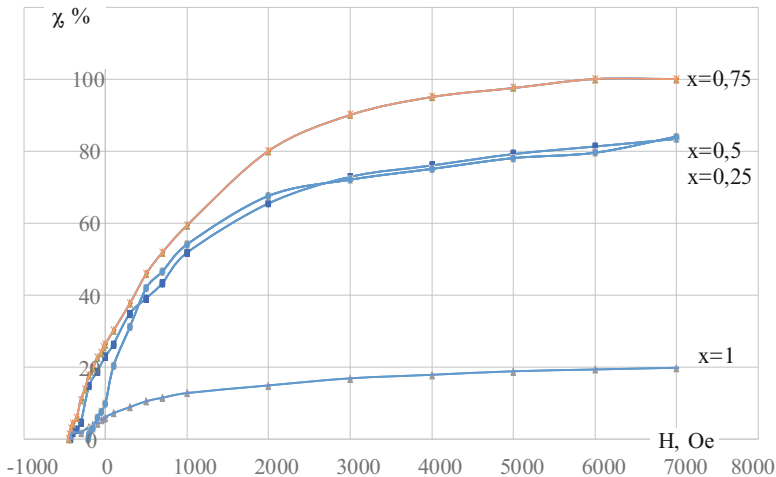


**Fig. 5.4** Magnetization curves for  $\text{Co}_x\text{Fe}_{3-x}\text{O}_4$  samples (Table 5.1)

according to the type of maghemite formation, as evidenced by the value of the lattice parameter. The structure of the inverse spinel is formed at the stoichiometric composition.

The magnetization curves of the samples are shown in Fig. 5.4. The synthesized samples have similar magnetic behavior. The magnetic curves show a high coercive field due to the high magnetic anisotropy of cobalt ferrite (for  $x = 1$ ). With the increase in the iron content, the saturation magnetization increases, and the value of the coercive force decreases.

Typical IR spectra for the samples under study are shown in Fig. 5.5. The spectra indicate the presence of absorption bands in the range from 400 to  $4000\text{ cm}^{-1}$ , which is a common feature of spinel ferrite.

The absorption band of the higher frequency ( $\nu_1$ ) lies in the range from 500 to  $600\text{ cm}^{-1}$  and is determined by the vibration of the complex of the tetrahedral metal cation, which consists of the bond between the oxygen ion and the tetrahedral cation ( $\text{O-M}_{\text{Tet}}$ ). The absorption band with a lower frequency ( $\nu_2$ ) in the range from 400 to  $490\text{ cm}^{-1}$  corresponds to the vibrations of the octahedral metal complex, which consists of the bond between the oxygen ion and the octahedral cation ( $\text{O-M}_{\text{Oct}}$ ).

## 5.4 Conclusion

A comparative study of cobalt ferrites  $\text{Co}_x\text{Fe}_{3-x}\text{O}_4$  with different compositions ( $x = 0.25, 0.5, 0.75, 1.0$ ) synthesized with the help of CNP has been carried out. Compositions other than stoichiometric have a defective structure, which is confirmed by crystal-chemical calculations. With the increase in cobalt content, the

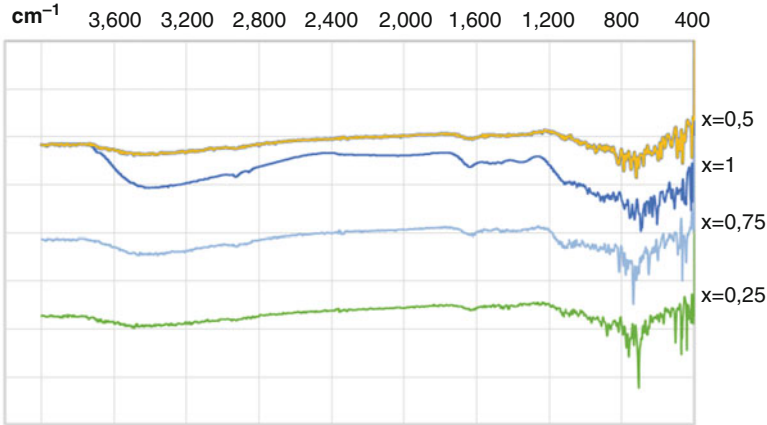


**Fig. 5.5** IR reflection spectra of samples synthesized at different cation ratios

inversion of spinel increases, and the number of vacancies decreases. Cobalt ferrite with a crystallite size of 350 nm and a coercive force of 480 Oe has been successfully synthesized by the coprecipitation method followed by CNP treatment at a molar ratio of  $\text{Co:Fe} = 1:2$ .

## References

1. Valenzuela R (2012) Novel applications of ferrites. *Phys Res Int*
2. Sharifi I, Shokrollahi H, Amiri S (2012) Ferrite-based magnetic nanofluids used in hyperthermia applications. *J Magn Magn Mater* 324(6):903–915
3. Bellido E, Domingo N, Ojea-Jiménez I, Ruiz-Molina D (2012) Structuration and integration of magnetic nanoparticles on surfaces and devices. *Small* 8(10):1465–1491
4. Liu C, Zou B, Rondinone AJ, Zhang ZJ (2000) Chemical control of superparamagnetic properties of magnesium and cobalt spinel ferrite nanoparticles through atomic level magnetic couplings. *J Am Chem Soc* 122(26):6263–6267
5. Mirgorod YA, Borshch NA, Fedosyuk VM, Yurkov GY (2012) The structure and magnetic properties of cobalt ferrite nanoparticles synthesized in a system of direct micelles of amphiphiles by means of ion floatoextraction. *Russian J Phys Chem A, Focus Chem* 86(3):418–423
6. Kim GY, Jeon JH, Kim MH, Suvorov D, Choi SY (2013) Microstructural development of cobalt ferrite ceramics and its influence on magnetic properties. *Met Mater Int* 19(6):1209
7. Cross WB, Affleck L, Kuznetsov MV, Parkin IP, Pankhurst QA (1999) Self-propagating high-temperature synthesis of ferrites  $\text{MFe}_2\text{O}_4$  ( $\text{M} = \text{Mg, Ba, Co, Ni, Cu, Zn}$ ); reactions in an external magnetic field. *J Mater Chem* 9(10):2545–2552
8. Liu SR, Ji DH, Xu J, Li ZZ, Tang GD, Bian RR et al (2013) Estimation of cation distribution in spinel ferrites  $\text{Co}_{1+x}\text{Fe}_{2-x}\text{O}_4$  ( $0.0 < x < 2.0$ ) using the magnetic moments measured at 10K. *J Alloys Compd* 581:616–624
9. Biswal D, Peeples BN, Peeples C, Pradhan AK (2013) Tuning of magnetic properties in cobalt ferrite by varying  $\text{Fe}^{+2}$  and  $\text{Co}^{+2}$  molar ratios. *J Magn Magn Mater* 345:1–6

10. Nlebedim IC, Snyder JE, Moses AJ, Jiles DC (2012) Effect of deviation from stoichiometric composition on structural and magnetic properties of cobalt ferrite,  $\text{Co}_x\text{Fe}_{3-x}\text{O}_4$  ( $x= 0.2$  to  $1.0$ ). *J Appl Phys* 111(7):07D704
11. Mozaffari M, Hadadian Y, Aftabi A, Moakhar MO (2014) The effect of cobalt substitution on magnetic hardening of magnetite. *J Magn Magn Mater* 354:119–124
12. Da Silva SW, Melo TFO, Soler MAG, Lima ECD, Da Silva MF, Morais PC (2003) Stability of citrate-coated magnetite and cobalt-ferrite nanoparticles under laser irradiation: a Raman spectroscopy investigation. *IEEE Transact Magnet* 39(5):2645–2647
13. Slonczewski JC (1958) Origin of magnetic anisotropy in cobalt-substituted magnetite. *Phys Rev* 110(6):1341
14. George M, Nair SS, Malini KA, Joy PA, Anantharaman MR (2007) Finite size effects on the electrical properties of sol–gel synthesized  $\text{CoFe}_2\text{O}_4$  powders: deviation from Maxwell–Wagner theory and evidence of surface polarization effects. *J Phys D Appl Phys* 40(6):1593
15. Raghasudha M, Ravinder D, Veerasomaiah P (2013) Magnetic properties of Cr-substituted Co-ferrite nanoparticles synthesized by citrate-gel autocombustion method. *J Nanostruct Chem* 3(1):63
16. Sutka A, Mezinskis G (2012) Sol-gel auto-combustion synthesis of spinel-type ferrite nano-materials. *Front Mater Sci*: 6(2):128–141
17. Allaadini G, Tasirin SM, Aminayi P (2015) Magnetic properties of cobalt ferrite synthesized by hydrothermal method. *Inter Nano Lett* 5(4):183–186
18. Frolova L, Derimova A, Khlopytskyi A, Galivets Y, Savchenko M (2016) Investigation of phase formation in the system  $\text{Fe}^{2+}/\text{Co}^{2+}/\text{O}_2/\text{H}_2\text{O}$ . *East Eur J Enterp Technol* 6(83):55–59
19. Khorrami SA, Manuchehri QS (2013) Magnetic properties of cobalt ferrite synthesized by hydrothermal and Co-precipitation methods: a comparative study. *J Appl Chem Res* 7(3):15–23
20. Obara G, Yamamoto H, Tani M, Tokita M (2002) Magnetic properties of spark plasma sintering magnets using fine powders prepared by mechanical compounding method. *J MagnMagnMater* 239:464–467
21. Frolova LA, Pivovarov AA, Baskevich AS (2014) Structure and properties of nickel ferrites produced by glow discharge in the  $\text{Fe}^{2+}\text{--Ni}^{2+}\text{--SO}_4^{2-}\text{--OH}^-$  system. *Russ J Appl Chem* 87(8):1054–1059
22. Major S, Kumar S, Bhatnagar M, Chopra KL (1986) Effect of hydrogen plasma treatment on transparent conducting oxides. *Appl Phys Lett* 49(7):394–396
23. Sangmanee M, Maensiri S (2009) Nanostructures and magnetic properties of cobalt ferrite ( $\text{CoFe}_2\text{O}_4$ ) fabricated by electrospinning. *Appl Phys A Mater Sci Process* 97(1):167–117
24. Lepeshev AA, Karpov IV, Ushakov AV, Nagibin GE, Dorozhkina EA, Karpova ON et al (2017) Structuring in fast-quenched ferrite compositions under plasma spraying. *Tech Phys* 62(6):911–914
25. Choukourov A, Manukyan AS, Shutov DA, Rybkin VV (2016) Physico-chemical properties of dc current discharge plasma with liquid cathode. *Izv Vyssh Uchebn Zaved Khim Khim Tekhnol* 59(12):4–16
26. Mazarío E, Herrasti P, Morales MP, Menéndez N (2012) Synthesis and characterization of  $\text{CoFe}_2\text{O}_4$  ferrite nanoparticles obtained by an electrochemical method. *Nanotechnology* 23(35):355708
27. Frolova LA, Kushnerov OI, Shpatakova RV Synthesis and magnetic properties of cobalt ferrite nanoparticles prepared by contact low-temperature non-equilibrium plasma method. 2017 IEEE International Young Scientists Forum on Applied Physics and Engineering YSF-2017 (in press)
28. Kumar L, Kumar P, Narayan A, Kar M (2013) Rietveld analysis of XRD patterns of different sizes of nanocrystalline cobalt ferrite. *Inter Nano Lett* 3(1):8
29. Le Trong H, Presmanes L, De Grave E, Barnabé A, Bonningue C, Tailhades P (2013) Mössbauer characterisations and magnetic properties of iron cobaltites  $\text{Co}_x\text{Fe}_{3-x}\text{O}_4$  ( $1 \leq x \leq 2.46$ ) before and after spinodal decomposition. *J Magn Magn Mater* 334:66–73
30. Murray PJ, Linnett JW (1976) Cation distribution in the spinels  $\text{Co}_x\text{Fe}_{3-x}\text{O}_4$ . *J Phys Chem Solids* 37(11):1041–1042

# Chapter 6

## The Dynamics of Water Molecules Confined in the Interior of DMPC Phospholipid Reverse Micelle



D. Makiela, Przemysław Raczyński, and Zygmunt Gburski

### 6.1 Introduction

Amphiphilic molecules like surfactants and lipids exhibit a variety of phases in aqueous environment. They undergo self-association under specific conditions to form aggregates such as vesicles, bilayers, micelles, etc. [1–5]. The geometrical form of these aggregates is a consequence of a delicate balance between two opposing forces. The attractive tail–tail hydrophobic interaction is the driving force for the aggregation of surfactant molecules, whereas the electrostatic repulsion between the head group sets a lower limit on the size that an aggregate can attain. A typical micelle is spherical with the hydrophilic “head” regions in contact with surrounding environment, sequestering the hydrophobic single-tail regions in the micelle center. Micelles have been the subject of intense interest for several decades, both from a fundamental physical chemistry point of view and because of their widespread applications in detergent, cosmetic, pharmaceutical, and food industries. In some nonpolar solvents can be formed the spherical aggregates of amphipathic molecules with the hydrophobic part of each molecule pointing outward. These aggregates are called reverse micelles because of the reverse of the situation in normal micelles. Reverse micelles have recently garnered significant attention as model systems to explore the effects of confinement [6–9]. Confined environments occur naturally in many biologically important systems as well as a range of physically interesting materials such as porous glasses. The beauty of the reverse micelle is that it is easily created, shows substantial stability, and provides a

---

D. Makiela · P. Raczyński · Z. Gburski (✉)  
Institute of Physics, University of Silesia, Katowice, Poland

Silesian Centre of Education & Interdisciplinary Research, Chorzów, Poland  
e-mail: [damian.makiela@smcebi.edu.pl](mailto:damian.makiela@smcebi.edu.pl); [zygmunt.gburski@us.edu.pl](mailto:zygmunt.gburski@us.edu.pl)

© Springer International Publishing AG, part of Springer Nature 2018  
O. Fesenko, L. Yatsenko (eds.), *Nanochemistry, Biotechnology, Nanomaterials,  
and Their Applications*, Springer Proceedings in Physics 214,  
[https://doi.org/10.1007/978-3-319-92567-7\\_6](https://doi.org/10.1007/978-3-319-92567-7_6)



well-characterized nanoscale pool for a range of chemistries. In recent years, the molecular dynamics (MD) computer simulation method has become a popular way to study micelles [5, 9–31], because of its ability to simulate phenomena at the atomic scale on very short time periods. In this work we have used MD technique to detailed study of the dynamics of water molecules confined in spherical reverse micelle composed of the important living cell biomembrane constituent, namely, 1,2-dimyristoyl-sn-glycero-3phosphocholine (DMPC) molecules.

### 6.1.1 Simulation Details

Molecular dynamics simulations were performed with NAMD 2.8 simulations code [32, 33], with the all-atom CHARMM27 force field [34] for modeling DMPC phospholipid. We used VMD 1.9.2 [35] to visualize the simulated system. The filled with water spherical reverse micelle, formed from 58 DMPC molecules, was constructed, and the sample composed of these micelles was simulated with the periodic boundary condition. The TIP3 [36] model of water was used. The equilibration process was performed over  $8 * 10^6$  time steps with step equal to 1 fs. After that initial simulation, the “production run” was conducted, up to 8 ns. We kept constant number of particles, constant volume, and constant temperature (NVT ensemble) for the system studied. During this stage of research, data were collected every 500 simulation steps for calculating physical observables and visualization of the systems. The simulations were performed for the temperature range  $280 \text{ K} \leq T \leq 320 \text{ K}$ . To better assess the impact of confinement on dynamics of water molecules, results were compared with the corresponding data for a bulk (unconfined) water.

### 6.1.2 Results

In order to visualize the system studied, we present the building block of micelle, i.e., DMPC molecule (see Fig. 6.1), and an example snapshot of the equilibrium configuration of the micelle formed from 58 DMPC molecules and filled with water (see Fig. 6.2).

Note that the interior of micelle happened to be approximately spherical.

First, we have calculated the radial distribution function  $g(r)$  of the center of mass of confined water molecules. The temperature dependence of  $g(r)$  is presented in Fig. 6.3.

Essentially, only one very sharp, pronounced peak connected with the nearest neighbors distance appears; it is the highest at the lowest temperature. With decreasing of temperature, the second wide peak is slowly appearing, reflecting the gradual development of the second coordination sphere of confined water at lower temperature, where the motion of water molecules slows down.

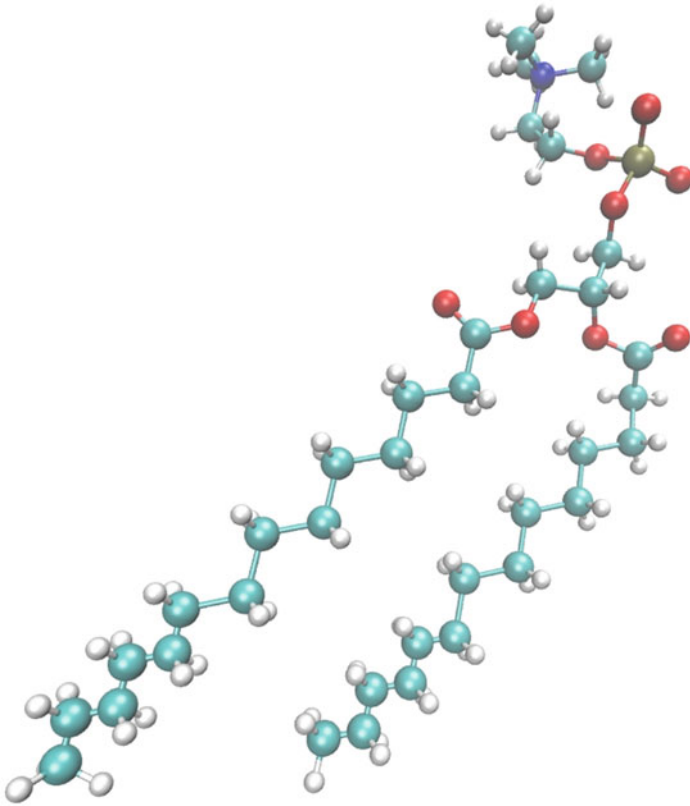


**Fig. 6.1** The structure of 1,2-dimyristoyl-sn-glycero-3-phosphocholine (DMPC) molecule (VMD software [35] picture)

Figure 6.4 shows for several temperatures the calculated mean square displacement  $\langle |\Delta \vec{r}(t)|^2 \rangle$  of the center of mass of confined water molecule, where  $\Delta \vec{r}(t) = \vec{r}(t) - \vec{r}(0)$  and  $\vec{r}$  is the position of a single molecule mass center.

Figure 6.4 indicates that the displacement  $\langle |\Delta \vec{r}(t)|^2 \rangle$  is quite sensitive to the change of temperature; it substantially increases with increasing temperature of the sample. Taking into account that the mean square displacement is connected with the translational diffusion coefficient  $D$ , via Einstein relation  $\langle |\Delta \vec{r}(t)|^2 \rangle \approx 6Dt$ , one can see that nonzero slope of  $\langle |\Delta \vec{r}(t)|^2 \rangle$  is an indicator of a mobility of molecules (translational diffusion) [37–39]. The values of  $D$ , related to the short-time translational dynamics of confined water, were estimated from the linear part of the slope of  $\langle |\Delta \vec{r}(t)|^2 \rangle$  and are shown in Table 6.1.

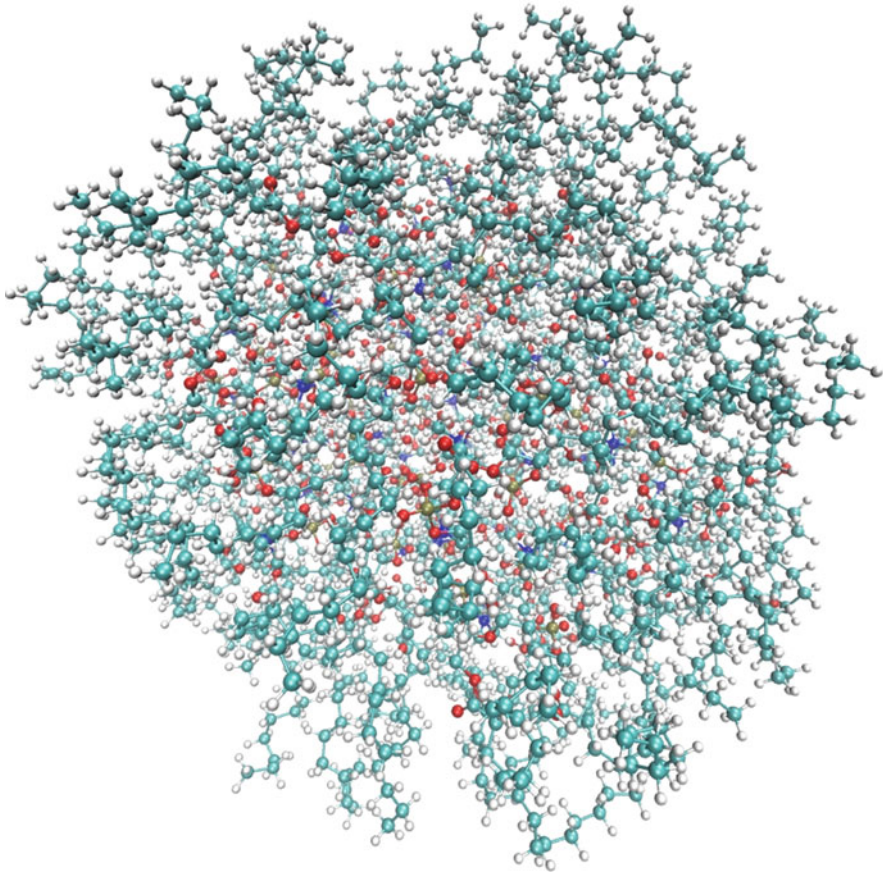


**Fig. 6.2** The instantaneous configuration of the reverse micelle formed from 58 DMPC and filled with water molecules,  $T = 300$  K (VMD software [35] snapshot)

We also calculated the corresponding  $\langle |\Delta \vec{r}(t)|^2 \rangle$  (see Fig. 6.5) and the diffusion coefficients  $D$  (Table 6.1) for bulk (unconfined) water.

In the comparison of  $\langle |\Delta \vec{r}(t)|^2 \rangle$  plots presented in Figs. 6.4 and 6.5, as well as the values of  $D$  coefficients from Table 6.1, one realizes the very substantial difference between dynamics of water molecules confined in reverse micelle and that in a bulk sample.

For all studied systems, the thermal activation of translational diffusion can be well described by Arrhenius law:

$$D = D_0 \exp\left(\frac{E_A}{K_B T}\right),$$

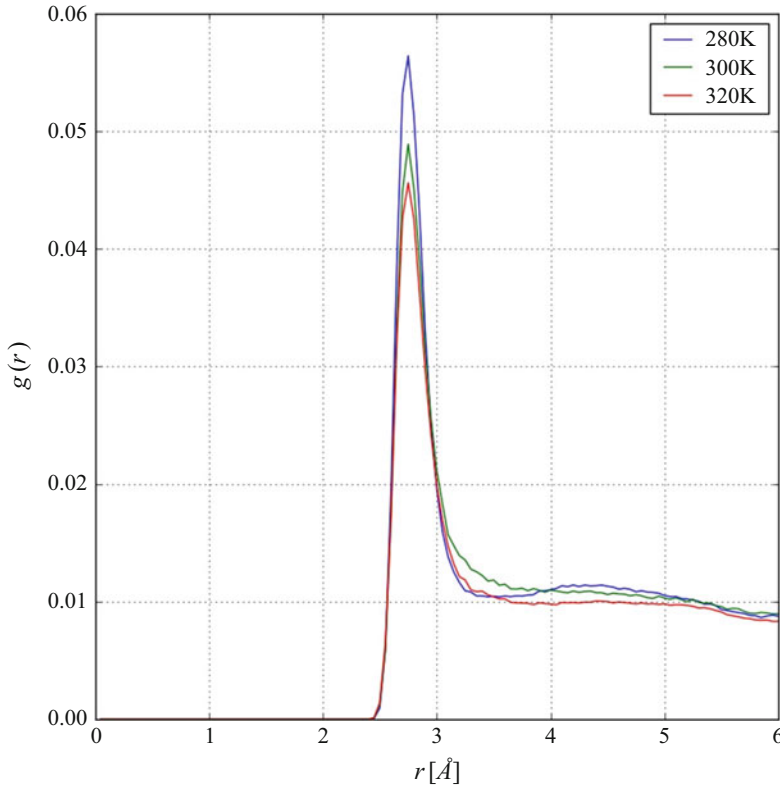


**Fig. 6.3** The radial distribution function  $g(r)$  of the center of mass of water molecules confined in reverse micelle formed from 58 DMPC molecules

where  $k_B$  is the Boltzmann constant and  $E_A$  is the activation energy. Fitting data using Arrhenius law (see Figs. 6.6 and 6.7) allowed us to estimate the diffusion activation energy  $E_A$  and  $D_0$  coefficient (Table 6.2), both for confined and bulk water.

The obtained values of the diffusion activation energy  $E_A$  for bulk water are at least two times lower than for corresponding values for confined water. This is consistent with the obtained values of diffusion coefficients (see Table 6.1).

In conclusion, the simulation results show that the dynamics of water molecules in reverse micelle 58 DMPC is significantly constrained in comparison to bulk water sample. Future studies taking into account the reverse micelles of various sizes and formed from other surfactant aggregates would be of interest.

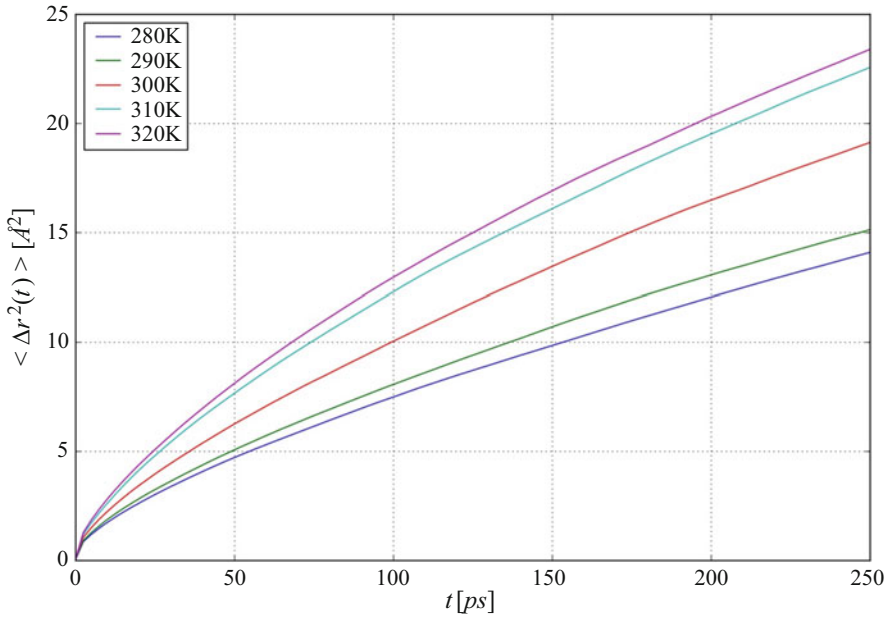


**Fig. 6.4** The mean square displacement  $\langle |\Delta \vec{r}(t)|^2 \rangle$  of the center of mass of water molecule confined in reverse micelle formed from 58 DMPC molecules

**Table 6.1** The calculated diffusion coefficients  $D$  of water confined in reverse micelle formed from 58 DMPC molecules and for the bulk water sample

Temperature [K]	Diffusion coefficient $D$ of water confined in reverse micelle [ $10^{-10} \text{ m}^2/\text{s}$ ]	Diffusion coefficient $D$ of bulk water [ $10^{-10} \text{ m}^2/\text{s}$ ]
280	1.19	61.2
290	1.27	66.4
300	1.6	71.4
310	2.01	76.7
320	2.12	80.4

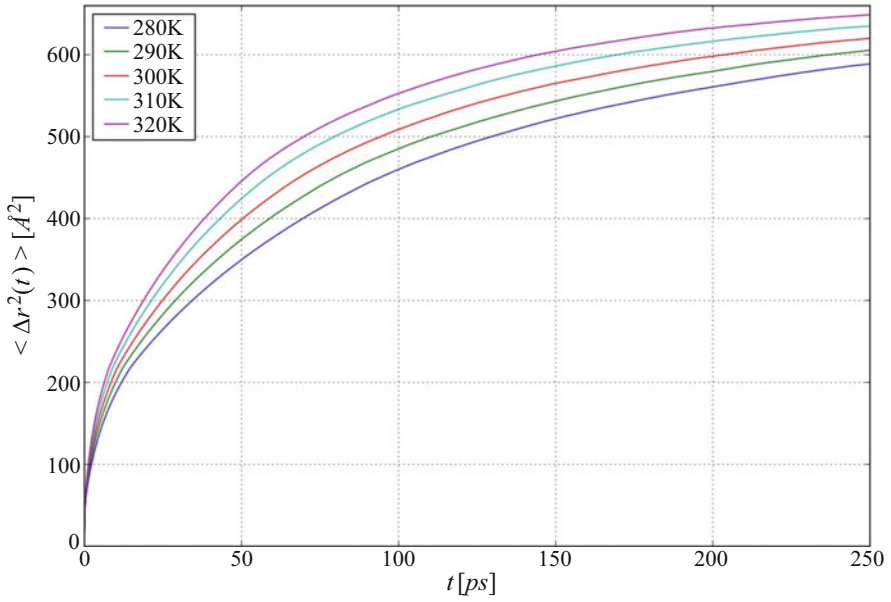


**Fig. 6.5** The mean square displacement ( $\langle |\Delta \vec{r}(t)|^2 \rangle$ ) of the center of mass of water molecule in bulk sample

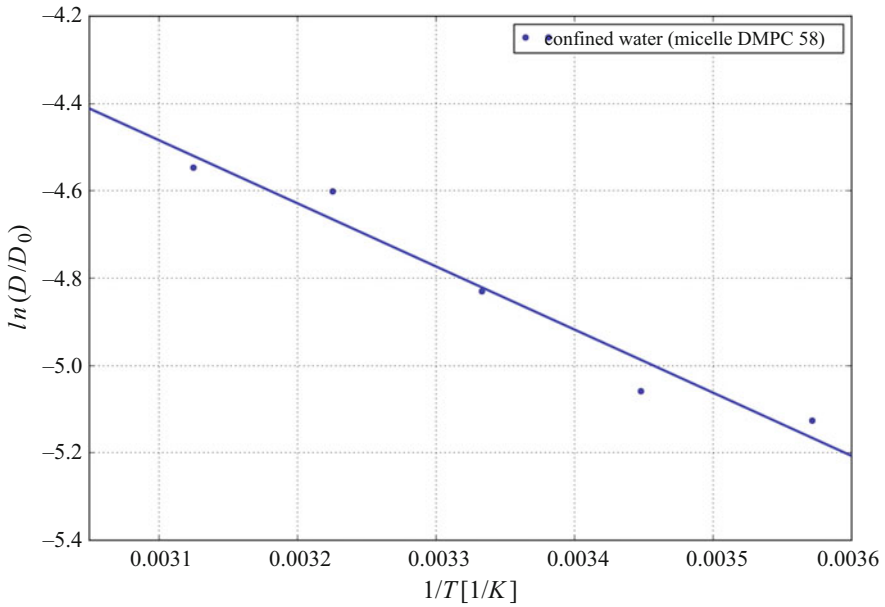


**Fig. 6.6** Thermal activation (Arrhenius plot) of the translational diffusion of water molecules confined in revers micelle formed from 58 DMPC molecules

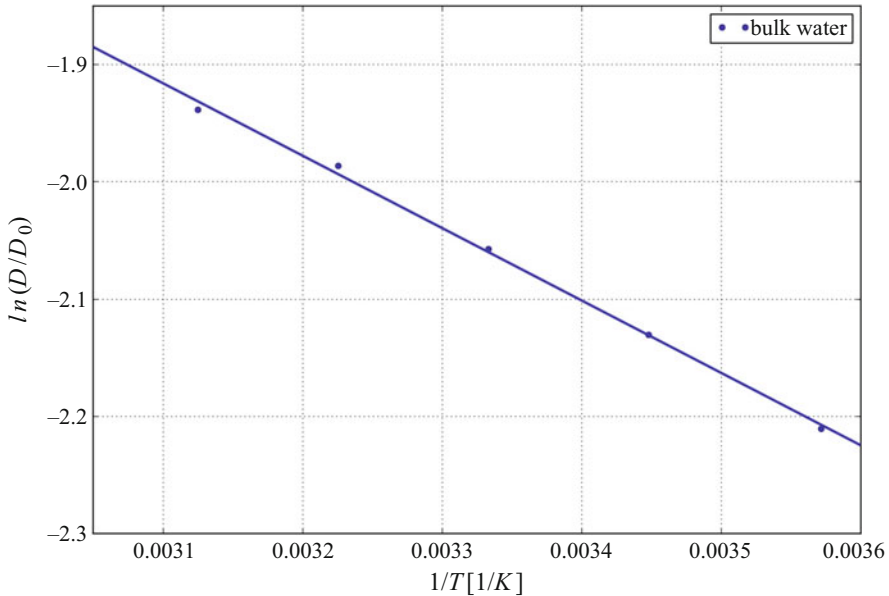


**Fig. 6.7** Thermal activation (Arrhenius plot) of the translational diffusion of water molecules in bulk system

**Table 6.2** The activation energy  $E_A$  and  $D_0$  coefficient of water confined in reverse micelle formed from 58 DMPC molecules and for the bulk water system

	Water confined in reverse micelle	Bulk water
$D_0 [10^{-8} \text{ m}^2/\text{s}]$	2.00	5.59
$E_A [\text{KJ/mol}]$	12.025	5.14

## References

1. Shah DO (1998) Micelles, microemulsions, and monolayers. Marcel Dekker, Inc, New York
2. Fathi H, Kelly JP, Vasquez VR, Graeve OA (2012) Ionic concentration effects on reverse micelle size and stability: implications for the synthesis of nanoparticles. *Langmuir* 28:9267–9274. <https://doi.org/10.1021/la300586f>
3. Kachel A, Gburski Z (1997) Chain formation in a model dipolar liquid: computer simulation study. *J Phys Condens Matter* 9:10095–10100. <https://doi.org/10.1088/0953-8984/9/46/007>
4. Pal S, Balasubramanian S, Bagchi B (2003) Identity, energy, and environment of interfacial water molecules in a micellar solution. *J Phys Chem B* 107:5194–5202. <https://doi.org/10.1021/jp022349+>
5. Piatek A, Dawid A, Gburski Z (2006) The existence of a plastic phase and a solid-liquid dynamical bistability region in small fullerene cluster (C-60)(7): molecular dynamics simulation. *J Phys Cond-Matter* 18:8471–8480. <https://doi.org/10.1088/0953-8984/18/37/006>
6. Raczynski P, Gorny K, Pabiszczak M, Gburski Z (2013) Nanoindentation of biomembrane by carbon nanotubes – MD simulation. *Comp Mat Science* 70:13–18. <https://doi.org/10.1016/j.commatsci.2012.12.031>

7. Senapati S, Berkowitz ML (2004) Computer simulation studies of water states in perfluoro polyether reverse micelles: effects of changing the counterion. *J Phys Chem A* 108:9768–9776. <https://doi.org/10.1021/jp048954p>
8. Gburski Z, Gorny K, Raczynski P (2010) The impact of a carbon nanotube on the cholesterol domain localized on a protein surface. *Solid State Commun* 150:415–418. <https://doi.org/10.1016/j.ssc.2009.12.005>
9. Kosmider M, Dendzik Z, Palucha S, Gburski Z Computer simulation of argon cluster inside a single-walled carbon nanotube. *J Mol Struct* 704:197–291. <https://doi.org/10.1016/j.molstruc.2004.02.050>
10. Feller SE, Yin D, Pastor RW, MacKerell AD (1977) Molecular dynamics simulation of unsaturated lipid bilayers at low hydration: parameterization and comparison with diffraction studies. *Biophys J* 73:2269–2279. [https://doi.org/10.1016/S0006-3495\(97\)78259-6](https://doi.org/10.1016/S0006-3495(97)78259-6)
11. Faramarzi S, Bonnett B, Scaggs CS, Ho A, Grodi D, Harvey E, Mertz B (2017) Molecular dynamics simulations as a tool for accurate determination of surfactant micelle properties. *Langmuir* 33:9934–9943. <https://doi.org/10.1021/acs.langmuir.7b02666>
12. Munusamy E, Luft C, Pemberton M, Schwartz SD Structural properties of nonionic Monorhamnolipid aggregates in water studied by classical molecular dynamics simulations. *J Phys Chem B* 121:5781–5793. <https://doi.org/10.1021/acs.jpcc.7b00997>
13. Dawid A, Gburski Z (2003) Interaction-induced light scattering in a fullerene surrounded by an ultrathin argon “atmosphere”: molecular dynamics simulation. *Phys Rev A* 68:065202. <https://doi.org/10.1103/PhysRevA.68.065202>
14. Abel S, Dupradeau FY, Raman EP, MacKerell AD, Marchi M (2011) Molecular simulations of dodecyl- $\beta$ -maltoside micelles in water: influence of the headgroup conformation and force field parameters. *J Phys Chem B* 115:487–499. <https://doi.org/10.1021/jp109545v>
15. Gburski Z (1985) Convergence of memory functions for the vibrational dephasing process in 123 liquids. *Chem Phys Lett* 115:236–240. [https://doi.org/10.1016/0009-2614\(85\)80687-4](https://doi.org/10.1016/0009-2614(85)80687-4)
16. Abel S, Dupradeau FY, Marchi M (2012) Molecular dynamics simulations of a characteristic DPC micelle in water. *J Chem Theory Comput* 8:4610–4623. <https://doi.org/10.1021/ct3003207>
17. Stassen H, Gburski Z (1994) Instantaneous normal-mode analysis of binary-liquid Ar-Kr mixtures. *Chem Phys Lett* 217:325–332. [https://doi.org/10.1016/0009-2614\(93\)E1390-3](https://doi.org/10.1016/0009-2614(93)E1390-3)
18. Bruce C, Senapati S, Berkowitz ML, Perera L, Forbes MDE (2002) Molecular dynamics simulations of sodium dodecyl sulfate micelle in water: the behavior of water. *J Phys Chem B* 106:10902–10907. <https://doi.org/10.1021/jp013616z>
19. Dawid A, Gburski Z (2003) Rayleigh light scattering in fullerene covered by a spherical argon film - a molecular dynamics study. *J Phys Cond-Matter* 15:2399–2405. <https://doi.org/10.1088/0953-8984/15/14/315>
20. Sanders SA, Sammalkorpi M, Panagiotopoulos AZ (2012) Atomistic simulations of micellization of sodium hexyl, heptyl, octyl, and nonyl sulfates. *J Phys Chem B* 116:2430–2437. <https://doi.org/10.1021/jp209207p>
21. Marrink SJ, deVries AH, Mark AE (2004) Coarse grained model for semiquantitative lipid simulations. *J Phys Chem B* 108:750–760. <https://doi.org/10.1021/jp036508g>
22. Gburski Z (1984) Line shape in collision-induced absorption – Mori theory. *Chem Phys Letters* 106:55–59. [https://doi.org/10.1016/0009-2614\(84\)87010-4](https://doi.org/10.1016/0009-2614(84)87010-4)
23. Santos AP, Panagiotopoulos AZ (2016) Determination of the critical micelle concentration in simulations of surfactant systems. *J Chem Phys* 144:044709. <https://doi.org/10.1063/1.4940687>
24. Marrink SJ, Tieleman DP, Mark AE (2000) Molecular dynamics simulation of the kinetics of spontaneous micelle formation. *J Phys Chem B* 104:12165–12173. <https://doi.org/10.1021/jp001898h>
25. Gwizdala W, Gorny K, Gburski Z (2008) Molecular dynamics and dielectric loss in 4-cyano-4-n-pentylbiphenyl (5CB) mesogene film surrounding carbon nanotube – computer simulation. *J Molec Struct* 887:148–151. <https://doi.org/10.1016/j.molstruc.2007.12.045>



26. Dawid A, Dendzik Z, Gburski Z (2004) Molecular dynamics study of ultrathin argon layer covering fullerene molecule. *J Molec Struct* 704:173–176. <https://doi.org/10.1016/j.molstruc.2004.01.065>
27. Schlenkrich M, Brickmann J, MacKerell AD, Karplus M (1996) An empirical potential energy function for phospholipids: criteria for parameter optimization and applications, In: K.M. Merz, B. Roux (eds), *Biol Membr Mol Perspect Comput Exp*, Birkhäuser Boston, Boston, pp 31–81. [https://doi.org/10.1007/978-1-4684-8580-6\\_2](https://doi.org/10.1007/978-1-4684-8580-6_2)
28. Piatek A, Dawid A, Gburski Z (2011) The properties of small fullerene cluster (C<sub>60</sub>(OH)<sub>24</sub>)<sub>7</sub>: computer simulation. *Spectrochim Acta A* 79:819–823. <https://doi.org/10.1016/j.saa.2010.08.059>
29. Gburski Z, Gray CD, Sullivan DE (1983) Information-theory of line-shape in collision-induced absorption. *Chem Phys Letters* 100:383–386. [https://doi.org/10.1016/0009-2614\(83\)80292-9](https://doi.org/10.1016/0009-2614(83)80292-9)
30. Mizuguchi T, Ishizuka R, Matubayasi N (2015) Effect of diffuseness of micelle boundary on the solute distribution upon solubilization. *Chem Phys Letters* 624:19–23. [doi.org/10.1016/j.cplett.2015.02.001](https://doi.org/10.1016/j.cplett.2015.02.001)
31. Dawid A, Gburski Z (1999) Interaction-induced light-scattering in xenon cluster: molecular dynamics study. *J Molec Struct* 482-483:271–276. [https://doi.org/10.1016/S0022-2860\(98\)00668-1](https://doi.org/10.1016/S0022-2860(98)00668-1)
32. Kale L, Skeel R, Bhandarkar M, Brunner R, Gursoy A, Krawetz N, Phillips J, Shinozaki A, Varadarajan K, Schulten K (1999) NAMD2: greater scalability for parallel molecular dynamics. *J Comput Phys* 151:283–312. <https://doi.org/10.1006/jcph.1999.6201>
33. Phillips JC, Braun R, Wang W, Gumbart J, Tajkhorshid E, Villa E, Chipot C, Skeel RD, Kalé L, Schulten K (2005) Scalable molecular dynamics with NAMD. *J Comput Chem* 26:1781–1802. <https://doi.org/10.1002/jcc.20289>
34. Lee S, Tran A, Allsopp M, Lim JB, Hémin J, Klauda JB (2014) CHARMM36 united atom chain model for lipids and surfactants. *J Phys Chem B* 118:547–556. <https://doi.org/10.1021/jp410344g>
35. Humphrey W, Dalke A, Schulten K (1996) VMD: visual molecular dynamics. *J Mol Graph Model* 14:33–38. [https://doi.org/10.1016/0263-7855\(96\)00018-5](https://doi.org/10.1016/0263-7855(96)00018-5)
36. Jorgensen WL, Chandrasekhar J, Madura JD, Impey RW, Klein ML (1983) Comparison of simple potential functions for simulating liquid water. *J Chem Phys* 79:926–935. <https://doi.org/10.1063/1.445869>
37. Dendzik Z, Gorny K, Gburski Z (2009) Cooperative dipolar relaxation of a glycerol molecular cluster in nanoscale confinement—a computer simulation study. *J Physics-Condensed Matter* 21:425101. <https://doi.org/10.1088/0953-8984/21/42/425101>
38. Dawid A, Gorny K, Gburski Z (2011) The structural studies of fullerene C-60(OH)<sub>24</sub> and nitric oxide mixture in water solvent - MD simulation. *Nitric Oxide Biol Chem* 25:373–380. <https://doi.org/10.1016/j.niox.2011.08.004>
39. Gorny K, Dendzik Z, Raczynski P, Gburski Z (2011) Dynamic properties of propylene glycol confined in ZSM-5 zeolite matrix—a computer simulation study. *Solid State Commun* 152:8–12. <https://doi.org/10.1016/j.ssc.2011.10.020>

# Chapter 7

## Applications Perspectives of Nanodispersed Chalcogenides of Transition Metals in Photocatalysis



Iryna Ivanenko, Tetiana Dontsova, and Yurii Fedenko

### 7.1 General

#### 7.1.1 Introduction

The scientific-technical progress of modern world requires more careful attention to environmental protection and rational appliance of mineral and energy resources. Modern chemical industry has need, first and foremost, for modern, economically justified and technologically simple methods for purification of industrial water and waste gases. One of the most promising ways of solving the afore-mentioned problems is the application of photocatalysis, based on highly effective photocatalysts.

Photocatalytic reactions can occur at room or lower temperature with visible light. It allows using the sun's energy for carrying out useful processes. Most processes occur using heterogeneous photocatalysts, which are semiconductors. Titanium (IV) oxide is frequently used due to its high catalytic activity, high chemical stability, low cost, and absence of toxicity. However, photocatalysis with application of titanium (IV) oxide has a number of significant disadvantages. The width of bandgap of titanium (IV) oxide is  $\sim 3.2$  eV, i.e., light absorption by titanium (IV) oxide is in the ultraviolet (UV) spectrum, because the efficiency of photocatalysts with visible light is less than 10%. Quantum yield of photoconversion that is not very high is also observed, due to the high level of recombination of charge carriers, low specific surface, and also low absorbability of  $\text{TiO}_2$ .

---

I. Ivanenko (✉) · T. Dontsova · Y. Fedenko  
Department of Inorganic Substances Technology, Water Treatment and General Chemical Engineering, National Technical University of Ukraine "Igor Sikorsky Kyiv Polytechnic Institute", Kyiv, Ukraine  
e-mail: [dontsova@xtf.kpi.ua](mailto:dontsova@xtf.kpi.ua)

In recent years, attention has been directed to graphene-like structures. This is due to the fact that in 2004 researchers from Manchester university (Novoselov and Gaym) [1] discovered a simple method of producing graphene and succeeded in revealing its new properties. Chalcogenides of transition metals fall under the category of graphene-like structures, the quantity of its investigations continuously increase.

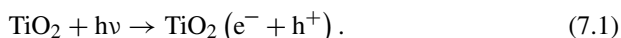
Chalcogenides of transition are widely investigated and considered for use in many branches, from producing of new oils to optoelectronics. Given that chalcogenides of transition metals are semiconductors and chemically inert, there is interest in them as photocatalysts.

Present-day literature contains conflicting data about the mechanism of photocatalytic reactions. Moreover, it is the titanium photocatalysts that are mainly investigated. The mechanisms of reactions on the surface of other photocatalysts are not investigated enough.

### ***7.1.2 The Mechanisms of Photocatalytic Reactions***

One of the well-known photocatalysts in present times is semiconductor titanium (IV) oxide  $\text{TiO}_2$  with crystal modification of anatase. It shows high photocatalytic activity, chemical stability, low toxicity, and comparatively low price. The photocatalytic properties of  $\text{TiO}_2$  are caused features of its electron structure, namely, existing of the valence band and the conduction band in it. Therefore, the most appropriate would be to consider the mechanism of reaction under light quanta on titanium (IV) oxide.

At absorption of light quanta, at titanium (IV) oxide irradiation by volume of particle, the electron vacation  $h^+$  is formed and free electron  $e^-$  by the route shown in reaction (7.1):



The vacation  $h^+$  and free electron recombine or transit in the body of semiconductor, partly localizing on defective structural centers of its lattice.

As is known, in semiconductor structures electrons can be in two states: free and bound [2]. In the first case, electrons move around the lattice of titanium (IV) oxide, formed by  $\text{Ti}^{4+}$  cations and  $\text{O}^{2-}$  anions. In the second case, electrons, mainly, bind with any ion of the lattice and take part in formation of chemical bonds. It is necessary to expend energy equal to the energy of bandgap (for  $\text{TiO}_2$  it is 3.2 eV) for transition of electron from bound state into free one [3].

Holes are formed on  $\text{TiO}_2$  surface reactive particles. The mechanism of hole formation is not yet clear. Hole reacts with water, or with some adsorbed organic, sometimes inorganic, compound according to reactions (7.2 and 7.3):



Radical  $\text{OH}^\bullet$  or  $\text{O}^-$  are also able to oxidize almost any organic compound. So, electron is able to interact with oxygen according to reactions (7.4 and 7.5):



In addition, the peroxide-ion  $\text{O}_2^{2-}$ , formed by reaction (7.5), reacts with proton  $\text{H}^+$  by reaction (7.6):



There are also possible options of electron interactions, reflected in reactions (7.7 and 7.8) [3]:



However, according to [3], such mechanism of photocatalytic reactions by the route of reactions (7.7 and 7.8) can be realized only in water solutions and at low oxygen concentration.

Several mechanisms of photocatalytic transformation have been described to date, but there are no definitive conclusions or a single model. The reason for this is the lack of scrutiny of these mechanisms, because is photogeneration of electric charges in system photocatalyst-adsorbate is in dynamic equilibrium with its migration and recombination. Analysis of literature concludes that the final mechanism depends on conditions of reactions (gas or liquid environment), and the chemical nature of precursors (organic or inorganic substances).

In view of the insufficient knowledge of the mechanism of photocatalytic reactions, there is a large number of possible and not studied photocatalytic structures. Data about potential photocatalysts for industrial application are practically absent. Therefore, there is an obvious need to investigate and analyze photocatalysts that can be used for solving specific problems of chemical technologies [4].

## 7.2 Classification of Photocatalysts

Photocatalysts for industrial application must have photo- and chemical stability, biological inertness, high photosensitivity, developed specific chemically active surface, ability to adsorb reagents under light quanta, and also to have available resource base and low price [5]. As is evident, the main property of a photocatalyst is its photocatalytic activity, which is determined by a combination of factors: type of material that forms a photocatalyst; type of crystal structure of particles; form of particles; porosity; concentration of surface hydroxide groups, etc. [6].

Photocatalytic structures can be classified taking into account the above features. From the technological point of view, the most appropriate is the classification by the type of solid-state material that forms the photocatalyst. This classification is presented in Table 7.1.

As apparent from the data (Table 7.1), the majority of materials used as photocatalysts are related to transitional d-elements. In its atoms the orbitals of pre-outer layer filled: cadmium, zinc, titanium, copper, iron, zirconium, wolfram, platinum, palladium, gold, silver, cobalt, vanadium, niobium, chromium, tantalum, nickel. P-elements also widely used as composite materials for producing photocatalysts; their valence electrons and orbitals of it are outer layers of the atom: selenium, indium, bismuth, bromine, tin, lead, and also carbon, nitrogen, chlorine, sulfur and oxygen. S-elements (strontium, potassium) and f-elements (cerium, samarium) are used the least frequently for producing photocatalysts. The solid-state photocatalysts with different crystal structure of particles can be used in the form of powders and films [6].

Powder photocatalysts are used commercially as suspensions in water and other solvents. Methods of obtain powder catalysts are relatively simple and consist of two stages: direct synthesis of powder and its continued layout.

Film photocatalysts have significant advantages compared with powder in terms of organization of technological process, especially at photocatalytic oxidation of volatile toxic compounds. However, such photo catalysts are not used in industrial conditions due to insufficient knowledge about them.

The substrate material plays a special role in its production, because it can affect the photocatalytic activity. Optic fiber, glass, quartz, different metals, oxides, etc., are used as substrates [4].

### 7.2.1 Branches of Photocatalysts Applications

Among the publications devoted to photocatalysis, it is possible to single out a number of articles of practical importance for the specialized application of synthesized photocatalytic structures [6, 7]. The main areas of application of photocatalysts in industry are: ecological purification of and industrial wastewaters

**Table 7.1** Classification of photocatalysts by the type of solid-state material [6]

The type of material		Examples
Chalcogenides of metals		CdS, ZnS, ZnSe, In <sub>2</sub> S <sub>3</sub> , ZnSe, Sb <sub>2</sub> S <sub>3</sub>
Metal oxides	Simple	TiO <sub>2</sub> , ZnO, CuO
	Complex	TiO <sub>2</sub> /ZnO, TiO <sub>2</sub> /SnO <sub>2</sub> , TiO <sub>2</sub> /Fe <sub>2</sub> O <sub>3</sub> , CeO <sub>2</sub> /TiO <sub>2</sub> , TiO <sub>2</sub> /Cu(OH) <sub>2</sub> , SnO <sub>2</sub> /ZnO, TiO <sub>2</sub> /ZrO <sub>2</sub>
	Binary-oxides	CdS/TiO <sub>2</sub> , CdS/ZrO <sub>2</sub> , PbS/TiO <sub>2</sub> , CdSe/TiO <sub>2</sub> , Bi <sub>2</sub> S <sub>3</sub> /TiO <sub>2</sub> , WS <sub>2</sub> /TiO <sub>2</sub>
	Chalcogenide-oxides	Pt/TiO <sub>2</sub> , Pd/TiO <sub>2</sub> , Au/ZnO, Ag/ZnO -Ce
	Metal-semiconductors	TiO <sub>2</sub> -Fe, -Co, -V, -Nb, -Zr, -Sm, -W, -Cr, -Cu, -Sn, -Ag, -Ta, -Ce
Doped	Metals cations	TiO <sub>2</sub> -N, -S, -C, -Cl
	Non-metal atoms	SrTiO <sub>3</sub> , ZrTiO <sub>4</sub> , K <sub>4</sub> Nb <sub>6</sub> O <sub>17</sub> , Bi <sub>3</sub> WO <sub>6</sub> , NiTiO <sub>3</sub>
Metal semiconductors		

and industrial gas waste; hydrogen production from different raw, CO production in methanol industry, in solar energy.

Photocatalytic water purification from organic pollutants, such as chlorine compounds, phenols, different dyes, acetic acid, 4-nitrophenol, isopropanol, etc., has the main advantage that during the oxidation process on the photocatalyst, organic impurities are subjected to complete destruction, forming mineral acids. Compounds are formed, which are safe for the environment. It should be noted, the majority of researches, despite them applied nature, had been conducted only in laboratory. Although, there are some data about industrial tests of purification devices and water disinfection with using of photocatalysts [8].

In scientific works, there is much description of photocatalytic air purification from different organic pollutants: toluene, trichloroethylene, acetone, formaldehyde, etc. [9, 10]. This method allows purifying air from pollutants, noted above, in industrial and residential areas. In present day there are known developments the prototypes of photocatalytic air purifiers, the part from them has already launched into production and realized successfully at modern market.

A single important question concerns photocatalytic air purification from wastes of diesel motors. Toward this objective, complex laboratory researches are being conducted to study the possibility of neutralization of CO, hydrocarbons, and nitrogen oxides in exhausts by different photocatalysts [11, 12]. At present, conventional catalytic converters are used [12]. However, they have significant disadvantages: low purification level, high investment, etc.

One of the major areas of industrial application of photocatalysts is in the producing of hydrogen from water by decomposition under radiation in the visible spectrum. A number of studies dedicated to the search for new, renewable energy, which is an alternative to coal, gasoline, natural gas, and other kinds of fuel, propose to use hydrogen, extracted by the method noted above [13, 14]. So far, this process has been successfully achieved in laboratories, with the potential of hydrogen production on a large scale [4].

There is in future the possibility of application of chalcogenides of molybdenum (IV) as photocatalyst. For example, in combination with  $\text{CdS}_2$ ,  $\text{MbS}_2$  increases the speed of hydrogen formation [13]. Few-layer or monolayer molybdenum (IV) chalcogenides have attracted the attention of researchers and are considered as potential alternatives to platinum catalysts in reaction of hydrogen evolution [15–17].

Chalcogenides of transition metals have a number of attractive properties. Their stable single layers can be used to create new nanoelectronic devices, which, as expected, have high thermal stability and provide lower energy consumption compared to similar existing devices. Di-chalcogenides of transition metals can be used together with graphene in optoelectronic devices, having exotic physical properties of monolayer materials, absent in their volume prototypes. The monolayer  $\text{MoS}_2$  has already been used to produce low-power field transistors, logic schemes, and phototransistors. Semiconductor two-dimensional (2D) chalcogenides of transition metals such as  $\text{MoS}_2$ ,  $\text{MoSe}_2$ ,  $\text{WS}_2$ , and  $\text{WSe}_2$  are considered as prospective materials for a number of applications. For example,  $\text{MoS}_2$  can find possible application

in transistor technology, sun batteries, photocatalysis, and optoelectronics. Other 2D TMDC are promising for tunnel field transistors, sun batteries with single transition, light diodes, optoelectronic devices, and photoelectric cells. Molybdenum (IV) sulfide had already been used in thin-layer transistors with ionic dielectric gel. They had shown excellent zone transport with low-threshold voltage, high mobility, and the ratio of the currents on and off.

Transistors on  $\text{MoS}_2$  had demonstrated excellent high mechanic flexibility and no deterioration of electrical characteristics in bending. Memory devices, based on  $\text{MoS}_2$ , have also been proposed. Ambipolar field transistors on thin layers of  $\text{WS}_2$  with ionic liquid as dielectric have been presented too [18].

## 7.3 The Structure of Chalcogenides of Transition Metals

### 7.3.1 $\text{MoS}_2$

Molybdenum in sulfides exists only in the form of ions Mo (II), Mo (III), Mo (IV), and Mo (V). Molybdenum sulfides are currently represented by  $\text{MoS}_2$ ,  $\text{Mo}_2\text{S}_3$ , and a variety of Shevrelia phases enriched with sulfur containing fragments of  $\text{Mo}_6\text{S}_8$ ,  $\text{Mo}_{15}\text{S}_{19}$ , and amorphous sulfides of  $\text{MoS}_x$  with  $x \geq 3$ .

$\text{MoS}_2$  as molybdenite was known to the ancient Romans, who confused it with graphite and  $\text{PbS}$  [20]. Differences between molybdenite and graphite had been found by Scheele in 1778. Later, molybdenite became the base of molybdenum ore and came to be used as lubricant. After the discovery of fullerene and carbon nanotubes, the focus was on so-called inorganic fullerenes, which also includes closed structures of  $\text{MoS}_2$ . After the discovery of graphene, the investigation of single layers of  $\text{MoS}_2$  began. This caused to the monolayer transistor producing on their based.

Molybdenum (IV) sulfide in nature is found in two phases: molybdenite and X-ray amorphous yordisite, both presented by soft minerals of lead-gray color [19]. Molybdenum (IV) sulfide has a structure consisting of trigonal prisms with molybdenum atoms in center, bonded with each other on the verge of creating a densely packed layer. Only relatively weak forces (van der Waals) are among layers, explaining the lubricating properties of  $\text{MoS}_2$ , as well as graphite, shown in Fig. 7.1a. The crystal structure and the lattice parameters of  $\text{MoS}_2$  are presented in Fig. 7.1b.

There are three crystal modification of  $\text{MoS}_2$ : hexagonal 2H, rhombic 3R, and tetragonal 1T (sulfur polyhedron around molybdenum is formed not as prism, but as a distorted octahedron [19, 24–26]). Noted modifications are presented in Fig. 7.2. Besides, there are numerous poly-types that differ from each other by different packing layers.

The presence of defects in the layers of  $\text{MoS}_2$  leads to the dependence of their chemical composition on temperature: at temperature of 750 °C the composition



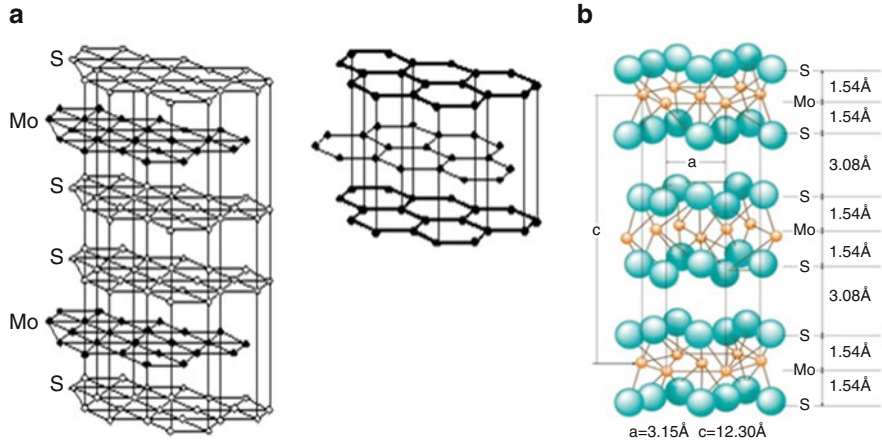


**Fig. 7.1** Placing of layers in structures MoS<sub>2</sub> and graphite (a) [22] and parameters of crystal lattice of MoS<sub>2</sub> (b) [23]

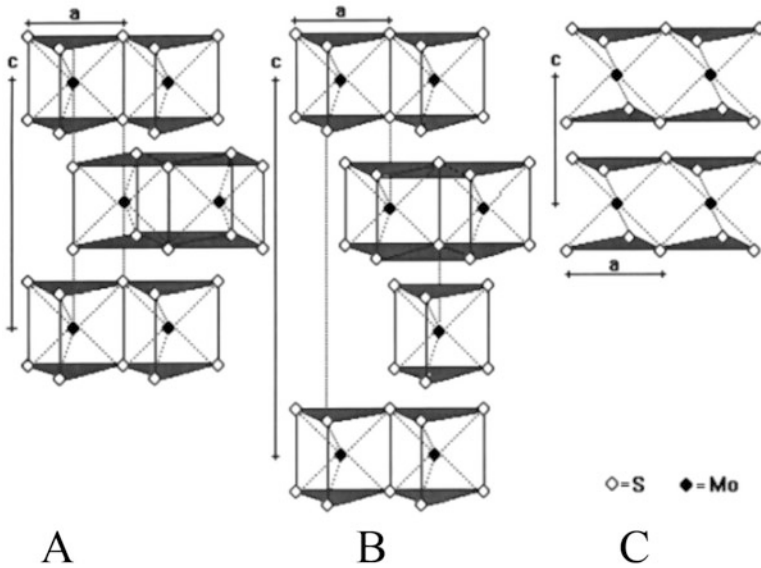


**Fig. 7.2** Crystal modifications of MoS<sub>2</sub>: (a) – hexagonal 2H; (b) – rhombic 3R; (c) – tetragonal 1T [30]

varies in MoS<sub>1.983</sub> ÷ MoS<sub>2.0</sub>, at 950 °C – from MoS<sub>1.978</sub> to MoS<sub>2.0</sub>. In terms of electron structure MoS<sub>2</sub> is a semiconductor. The bandgap for 2H modifications is from 0.77 to 1.2 eV for indirect transfer [28] and 1.9 eV for direct transfer [29]. The dispersion of obtained values for electron transfers is caused use of different measurement methods and calculation of electron structure.

### 7.3.2 *MoSe<sub>2</sub>*

The investigations review about phase structures of systems  $\text{MoSe}_{2-x} \div \text{Mo}_3\text{Se}_{4 \pm x}$  presented in [31]. Formation of two intermediate phases  $\text{Mo}_3\text{Se}_4$  and  $\text{MoSe}_2$  was determined by roentgen method [32]. According to the data, the compound  $\text{MoSe}_2$ , obtained at 1500 °C and pressure 4 GPa, is isostructural to  $\text{MoS}_2$  [33].

According to the chart, there are narrow fields of homogeneity in both compounds:  $\text{Mo}_3\text{Se}_4$  formed at interaction of solid Mo and gaseous  $\text{Se}_2$  at 0.1 MPa and the temperature  $(1400 \pm 100)$  °C;  $\text{MoSe}_2$  formed at interaction of solid  $\text{Mo}_3\text{Se}_4$  and gaseous  $\text{Se}_2$  at 0.1 MPa and the temperature  $(1150 \pm 50)$  °C. It is assumed that at temperatures lower than 527 °C, the solubility of Se in Mo is controlled by defects of lattice [34]. Molybdenum (IV) selenide, like  $\text{MoS}_2$ , is related to TMDC compounds. According to studies, these two compounds have similar structures, as shown in Fig. 7.3.

Molybdenum and selenium layers have hexagonal atomic net, and each molybdenum atom is in the center of a trigonal prism, formed by six selenium atoms [35].

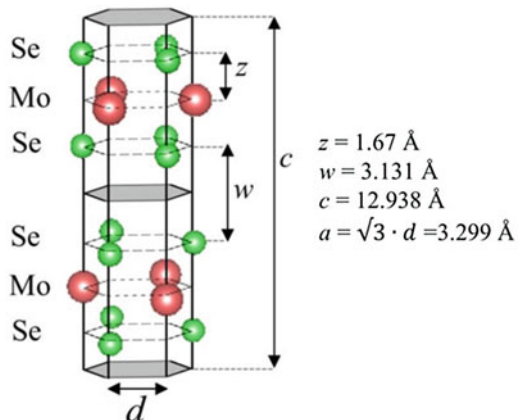
Layers like Se-Mo-Se with selenium atoms in two hexagonal planes divided by the plane of molybdenum atoms. The layer Se Mo Se in turn bonded with neighbor Se Se layers by weak van der Waals forces. Also found in a structure like octahedron prism [37].

## 7.4 Properties of Molybdenum (IV) Chalcogenides

### 7.4.1 Photocatalytic Properties

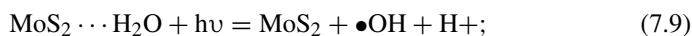
Photocatalytic properties of  $\text{MoS}_2$  were investigated by decomposition of methylene orange. The investigators considered the catalytic effect of microsized and nano-

Fig. 7.3 Parameters of crystal lattice  $\text{MoSe}_2$  [36]

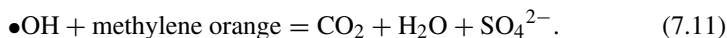


sized MoS<sub>2</sub> (nanolayers and nanoballs). Nanosized MoS<sub>2</sub> showed very good results of bleaching solution with methylene orange. The results are presented in Fig. 7.4.

The investigators clarified by IR-spectroscopy that high decolouration level of methylene orange did not result in its adsorption on surface. These are the same spectra before and after reaction. This indicates that methylene orange was adsorbed fully. It had been also decomposed on the surface of nanocatalyst MoS<sub>2</sub>. The photocatalytic effect of MoS<sub>2</sub> with visible light was related to formation of surface adsorbed hydroxide radicals •OH. They were formed from adsorbed water. Photoexcited electron reacts with oxygen in water and, finally, •OH radicals are formed. They decompose organic substances. The chemistry, in simple terms, is presented in Eqs. (7.9 and 7.10):

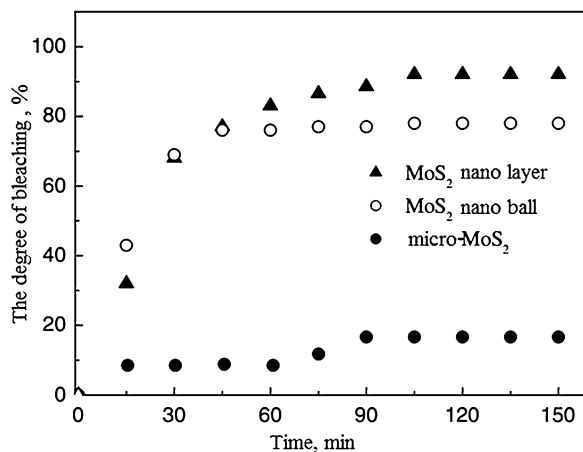


The methylene orange contains sulfur, so reaction causes formation of SO<sub>4</sub><sup>2-</sup>. These ions can be determined by precipitation during photocatalytic reaction by BaCl<sub>2</sub>. So, the reaction (7.10) becomes like (7.11) in the case with methylene orange:



The photocatalytic activity for MoSe<sub>2</sub> was evaluated by decomposition of tetraethylene rodamine (rodamine B, RhB) in solution at the radiation of visible light (over 420 nm) [39]. The initial concentration of RhB solution was 200 ppm. Before radiation, the mixture was kept in the dark during 3 h for achieving sorption

**Fig. 7.4** The Curves of discoloration of methylene orange on different kinds of MoS<sub>2</sub>



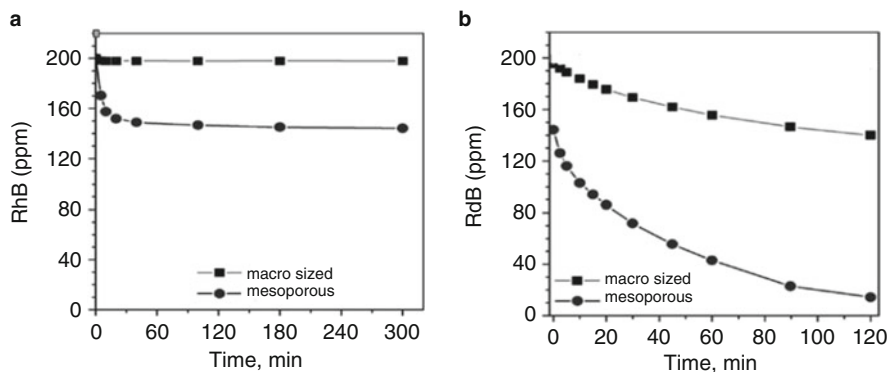


**Fig. 7.5** Kinetic of adsorption RhB on macrosized and mesoporous MoSe<sub>2</sub> (a) [39]; photodecomposition of RhB on macrosized and mesoporous MoSe<sub>2</sub> with visible light (b) [38]

equilibrium. The sample MoSe<sub>2</sub> did not show noticeable adsorption. This can be explained by low specific surface area. The adsorption on mesoporous MoSe<sub>2</sub> occurred rather fast and achieved equilibrium for 40 min. This can be seen in Fig. 7.5a. The concentration of RhB decreased in both cases after the transfer system in visible light. The dependence from the time is shown in Fig. 7.5b.

This result confirms that mesoporous and macrosized MoSe<sub>2</sub> have photocatalytic properties with visible light. Herewith, the mesoporous material 6,8 times more active, than macrosized. Increased activity of mesoporous MoSe<sub>2</sub> can be explained by larger surface area and volume of pores [38].

### 7.4.2 Sorption Properties

Latest investigations have shown that inorganic plate layered compounds have potential advantages at removing of dyes because of their high specific surface area and increased surface area between adsorbate and adsorbents, structural adaptability, chemical stability and structure, which is clearly determined [39–41]. Because MoS<sub>2</sub> has similar structure in connection with characteristics, noted above, it was considered in some works as potential adsorbent for purification of water. The sorption properties of MoS<sub>2</sub>, like nanoleaves, were investigated in relation to organic dyes [40]. Methylene blue, methylene orange, and rodamine B were used in experiments. The important moment is the separation of photocatalysis from adsorption, which is why experiments were carried out in the dark.

The results of adsorption of different dyes on MoS<sub>2</sub> are presented in Fig. 7.6a. It is shown in Fig. 7.6a that MoS<sub>2</sub> has better selectivity in relation to the methylene blue with removal degree 98.49% after 300 s. At the same time, the removing of rodamine B and methylene orange is 76.89% and 34.5%, respectively. This suggests

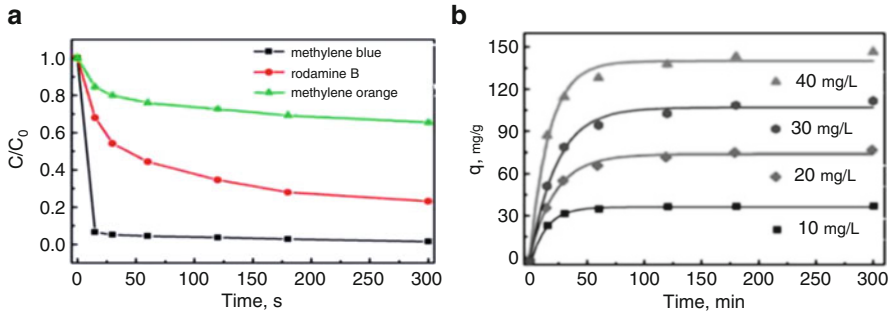


**Fig. 7.6** The adsorption of methylene blue, rodamine B, and methylene orange on  $\text{MoS}_2$  (a) [40]; adsorption isotherms of methylene blue on  $\text{MoS}_2$  (b) [28]

that  $\text{MoS}_2$  can be a highly effective sorbent for removing of methylene blue. Such selective adsorption can be due to electrostatic attraction between methylene blue and nanoleaves of  $\text{MoS}_2$  [41].

Adsorption isotherms of methylene blue on  $\text{MoS}_2$  are presented in Fig. 7.6b. It is shown in Fig. 7.6b that initial rates of adsorption are very fast from the beginning of the stage for all investigated doses. Such high effectiveness in adsorption can be related to the existence of large number of active centers on the surface of adsorbent and electrostatic attraction between  $\text{MoS}_2$  and methylene blue. The maximal adsorbability of  $\text{MoS}_2$  nanoleaves was  $\sim 146,43$  mg/g [40].

As well known, adsorbent should not only have high sorption effectivity, it should also have good stability and possibility of recycle use. It should allow decreasing of the cost of usage. Also it is important for water treatment application. Thus, the regeneration of  $\text{MoS}_2$  nanoleaves was investigated after adsorption of methylene blue [40]. Results had shown that nanoleaves of  $\text{MoS}_2$  have high stability. They also keep the removal efficiency more than 80% in four repeat cycles. More importantly, nanoleaves of  $\text{MoS}_2$ , adsorbed by methylene blue, can be regenerated by simple washing by deionized water. That is why nanoleaves of  $\text{MoS}_2$ , with excellent adsorption, stability, and ability to regenerate, can be seen as prospective adsorbents [40].

### 7.4.3 Electric Properties

In 1969, a review work was published. The attempt had been done in this work to explain the electron structure of different layered chalcogenides of transition metals. It had been done based on their optical absorption, dimensions of electric conduct, and magnetic susceptibility [28]. The authors had described the main properties of spectra of optical absorption, displaying features of electron structure. They summarized data that they had at that moment, giving the start for other

**Table 7.2** Values of the width of the bandgap, calculated theoretically for some chalcogenides of transition metals [45]

Material	Width of the Bandgap, eV
MoS <sub>2</sub>	1,84
MoSe <sub>2</sub>	1,60
WS <sub>2</sub>	1,97
WSe <sub>2</sub>	1,66

investigators. Unfortunately, the used them method of powerful bond couldn't be able to describe clearly the electron structure of molybdenum (IV) chalcogenides.

In 1973, another work was published. In this work, the authors used the method of plane waves. The investigation had shown that the bandgap for MoS<sub>2</sub> was is not less than 1 eV and it is not exactly 0,2 eV [29]. It was also shown that exciting maximums are 2 eV. They are observed in the spectra of optical absorption and related to d-orbitals of molybdenum. This allowed MoS<sub>2</sub> and similar compounds of the elements of the 4-th group to be classified as a separate class of semiconductors. These assumptions had been confirmed experimentally with the development of X-ray methods [42].

The work with the measurement of angle dependence of X-ray spectra of adsorption was published at the same time along with the work about data on electron structure of MoS<sub>2</sub>, MoSe<sub>2</sub>, and WS<sub>2</sub>. The data on electron structure had been obtained by the method of spherical waves [43, 44]. The authors also showed that MoS<sub>2</sub> is a semiconductor with indirect bandgap in deadline.

The values of width of the band gap of some chalcogenides of transition metals had been calculated theoretically in another work. The data are presented in Table 7.2.

## 7.5 Conclusions

Photocatalysis currently is a branch of science that is rapidly evolving and can contribute to solving many environmental and energy tasks in a world of growing scientific progress. For this it is necessary to actively explore the properties of those materials and compositions that can be used for obtaining effective photocatalysts. Contradictory data have been published concerning the mechanisms of photocatalytic reactions, and mainly titanium photocatalysts are researched. Mechanisms of reaction with other photocatalysts have not been studied sufficiently. Nanodispersed chalcogenides of transition metals in photocatalysis have a broad range and therefore deserve separate detailed consideration. Special attention in further studies should be given to obtaining film chalcogenides of transition metals as the most promising for industrial use.

**Acknowledgments** The authors thank the National Technical University of Ukraine "Igor Sikorsky Kyiv Polytechnic Institute" for the opportunity to carry out this research.

## References

1. Novoselov KS et al (2004) Electric field effect in atomically thin carbon films. *Science* 306:666
2. Fujishima A et al (2000) Titanium dioxide photocatalysis. *J Photochem Photobiol C: Photochem Rev* 1:1
3. Jović F et al (2011) Heterogena fotokataliza: osnove i primjena za obradu onečišćenog zraka. *Kem Ind* 60:387
4. Bykanova VV et al (2012) Technological aspects of the application of photocatalysts in the industry: an overview. *Integr Technol En Eff* 4(1):151
5. Colmenares JC (2004) Nanostructured photocatalysts and their applications in the photocatalytic transformation of lignocellulosic biomass: an overview. *Materials* 2:2228
6. Mauroa AD et al (2017) ZnO for application in photocatalysis: from thin films to nanostructures. *Mater Sci Semicond Proc* 69:44
7. Mills A et al (2002) A web-based overview of semiconductor photochemistry-based current commercial applications. *J Photochem Photobiol* 152:233
8. Dontsova T et al (2012) Synthesis and characterization of titanium (IV) oxide from various precursors. *Springer Proc Phys* 167:275
9. Mills A (2012) Photocatalytic oxidation of toluene in an NMR tube. *J Photochem Photobiol A* 233:34
10. Cjocararu B et al (2011) Influence of gold particle size on the photocatalytic activity for acetone oxidation of Au/TiO<sub>2</sub> catalysts prepared by dc-magnetron sputtering. *Appl Catal B* 107:140
11. Ivanenko IN et al (2016) Low-temperature synthesis, structure-sorption characteristics and photocatalytic activity of TiO<sub>2</sub> nanostructures. *Springer: Phys Chem Water Treat Proc/J Wat Chem Technol* 37(1):14
12. Ballari MM et al (2010) NO<sub>x</sub> photocatalytic degradation employing concrete pavement containing titanium dioxide. *Appl Catal B* 95:245
13. Ni M et al (2006) A review and recent developments in photocatalytic water-splitting using TiO<sub>2</sub> for hydrogen production. *Renew Sust Energ Rev* 11:401
14. Lu X-H et al (2011) Monodisperse CeO<sub>2</sub>/CdS heterostructured spheres: one-pot synthesis and enhanced photocatalytic hydrogen activity. *RSC Adv* 1:1207
15. Morales-Guio C et al (2014) Nanostructured hydrotreating catalysts for electrochemical hydrogen evolution. *Chem Soc Rev* 43:6555
16. Li X et al (2015) Engineering heterogeneous semiconductors for solar water splitting. *J Mater Chem A* 3:2485
17. Deng J et al (2014) High-performance hydrogen evolution electrocatalysis by layer-controlled MoS<sub>2</sub> nanosheets. *RSC Adv* 4:34733
18. Priscilla BP et al (2015) Two-dimensional dichalcogenides for light-harvesting applications. *Nano Today* 10(2):128
19. Afanasiev P et al (2008) Synthetic approaches to the molybdenum sulfide materials. *Compt Rend Chim* 11:159
20. Brenta JR et al (2017) Synthetic approaches to two-dimensional transition metal dichalcogenide nanosheets. *Prog Mater Sci* 89:411
21. Radisavljevic B et al (2011) Single-layer MoS<sub>2</sub> transistors. *Nature Nanotech* 6:147
22. <http://www.tribology-abc.com/abc/solidlub.htm>
23. <http://www.drilube.co.jp/english/product/molybdenum.html>
24. Petkov V et al (2002) Structure of nanocrystalline materials using atomic pair distribution function analysis: study of LiMoS<sub>2</sub>. *Phys Rev B* 65:92
25. Bell RE et al (1957) Preparation and characterization of a new crystalline form of molybdenum disulfide. *J Am Chem S* 79:3351
26. Py M et al (1983) Structural destabilization induced by lithium intercalation in MoS<sub>2</sub> and related compounds. *C J Phys* 61:76

27. Suzuki Y et al (1981) Phase relationship on Mo-S system at high temperatures. *Mater Res B* 16:1085
28. Wilson JA, Yoffe AD (1969) The transition metal dichalcogenides discussion and interpretation of the observed optical, electrical and structural properties. *Adv Phys* 18:193
29. Mattheiss LF et al (1973) Energy bands for 2H-NbSe<sub>2</sub> and 2H-MoS<sub>2</sub>. *Phys Rev Lett* 30:784
30. Wypych F (2002) Dissulfeto de molibdênio, um material multifuncional e surpreendente. *Quím Nova* 25:1
31. McMenamin JC, Spicer WE (1972) Photoemission studies of the layered dichalcogenides NbSe<sub>2</sub> and MoS<sub>2</sub> and a modification of the current band models. *Phys Rev Lett* 29:1501
32. Spiesser M et al (1969) Caractérisation et étude physico-chimique de séléniures et tellurures non stoechiométriques de molybdène. *Bull Soc Chim France* 5:1427
33. Bars O et al (1973) Étude structurale de combinaisons sulfurées et séléniées du molybdène: I. Structure cristalline de Mo<sub>3</sub>Se<sub>4</sub>. *Chemistry and Structure of Ternary Molybdenum Chalcogenides. J Solid State Chem* 6:48
34. Towie LC et al (1966) Dichalcogenides MeX<sub>2</sub>. *Science* 154:895
35. Greenwood NN, Earnshaw A (1997) *Chemistry of the elements*, 2nd edn. Butterworth-Heinemann, Amsterdam 1384 p
36. Brewer L, Lamoreaux RH (1980) Molybdenum: physico-chemical properties of its compounds and alloys. *Atom E R* 7:195
37. Parilla P et al (2004) Formation of nanooctahedra in molybdenum disulfide and molybdenum diselenide using pulsed vapor transport. *J Phys Chem* 108:6197
38. Hu KH et al (2010) The effect of morphology and size on the photocatalytic properties of MoS<sub>2</sub>. *Reac Kinet Mech Cat* 100:153
39. Shi Y et al (2013) Ordered mesoporous crystalline mose<sub>2</sub> material with efficient visible-light-driven photocatalytic activity and enhanced lithium storage performance. *Adv Func Mater* 23:1832
40. Qiao XQ et al (2016) Equilibrium and kinetic studies on MB adsorption by ultrathin 2D MoS<sub>2</sub> nanosheets. *RSC Adv* 6:11631
41. Yan AX et al (2014) Incorporating polyoxometalates into a porous MOF greatly improves its selective adsorption of cationic dyes. *Chem Eur J* 20:6927
42. Chevrel R, Sergent M (1982) Chemistry and structure of ternary molybdenum chalcogenides. In: Fischer O, Maple MB (eds) *Superconductivity in ternary compounds i*, Topics in current physics Vol. 32. Springer, Berlin
43. Coehoorn R, Haas C (1987) Electronic structure of MoSe<sub>2</sub>, MoS<sub>2</sub>, and WSe<sub>2</sub>. Band-structure calculations and photoelectron spectroscopy. *Phys Rev B* 35:6195
44. Williams AR et al (1979) Cohesive properties of metallic compounds: augmented-spherical-wave calculations. *Phys Rev B* 19:6094
45. Krivosheeva AV (2016) Prospective semiconducting compounds and nanostructures for optoelectronics, photovoltaics and spintronics. *Integr technol En Effic* 3(97):13



# Chapter 8

## Nanocomposites Based on Thermosetting Polyurethane Matrix and Chemically Modified Multiwalled Carbon Nanotubes



L. V. Karabanova, R. L. Whitby, V. A. Bershtein, P. N. Yakushev, A. W. Lloyd, and S. V. Mikhalovsky

### 8.1 Introduction

Carbon nanotubes (CNTs), which consist of cylindrical graphene layers, have attracted considerable attention because of their unique structure and excellent thermal, magnetic, electric and mechanical properties, in particular extremely high mechanical strength to density ratio and high chemical stability; this made them the outstanding candidates as nanofillers for polymers. It has been shown in numerous studies that incorporation of CNTs into polymer matrices may substantially modify their properties and lead to the nanocomposites with the enhanced performance [1, 2]. However, the final effect depends on the type of CNTs, whether as single-walled (SWCNTs), multiwalled (MWCNTs) and also spiral- and Y-shaped forms, as well as the physical and chemical state of their surface and the polymer mixing method utilised. In the direct mixing of pure CNTs into a host matrix, it is often difficult to separate agglomerated CNTs due to their intrinsic hydrophobic surface and to obtain a reasonable dispersion quality. Typically, the outer surface of CNTs contains a  $\pi$ -bond network that tends to promote CNT-CNT  $\pi$ - $\pi$  interactions to minimise the surface energy. The agglomeration of CNTs reduces the interfacial area in the nanocomposites and may lead even to zero or negative impact on the properties of polymer matrices. Therefore, achieving a homogeneous dispersion of

---

L. V. Karabanova (✉)

Institute of Macromolecular Chemistry of National Academy of Sciences of Ukraine, Kyiv, Ukraine

R. L. Whitby · A. W. Lloyd · S. V. Mikhalovsky  
University of Brighton, Brighton, UK

V. A. Bershtein · P. N. Yakushev  
Ioffe Institute, St. Petersburg, Russia

CNTs in a matrix (or at least decreasing the extent of CNT aggregation) is a key requirement for the realization of the desired enhancement in the final properties of nanocomposites. Additionally, enhancing interfacial interactions between the CNTs and the polymer matrix will promote efficient energy transfer within the system. To attain these aims, various methods have been used, in particular sonication at the mixing stage and also different approaches to chemical functionalization of CNT surface have been under investigation [1–5].

The most well-known approach to improving interfacial interactions in CNT-polymer nanocomposites is the chemical functionalization of the outer walls of CNTs that allows covalent attachment of a polymer directly to the nanotube framework [5]. The change in surface properties of CNTs also has an advantage by decreasing the hydrophobic character and improving interaction with different polar matrices. However, it is also possible that CNTs may become mechanically weaker after chemical treatment [6], where the reinforcement obtained through the concentric arrangement of the cylinders decreases through acid-oxidative sidewall digestion and, if acid oxidation continues over a long period of time, cylinders may allow slippage.

Polyurethane (PU) materials are extensively used in technical and biomedical applications, whether in blood contacting applications and organ reconstruction [7], in skin patches, coatings and catheter applications [8]. PU is seen as an attractive material with a complicated structure (randomised hard and soft nanodomains) [9]; therefore PU should highlight changes in its properties at the inclusion of CNTs that possess different surface functionalization. Previous investigations of MWCNT-PU composites have been focused on thermoplastic systems [10–21], and only a single piece of work was found in literature for thermosetting systems [22].

In general, the different extents of the improvement of mechanical properties, by tens of percent, including modulus and stress at break were observed for thermoplastic PU after its filling with functionalized MWCNTs [11, 14, 15, 17–19] although elongation at break occasionally decreased [19]. The higher thermal stability with the increased degradation temperature was observed for the thermoplastic PU-MWCNT nanocomposites [12]. The thermo-responsive shape recovery (shape memory) [13, 18] and electroactive shape-memory [19] effects were observed for the surface-modified MWCNT-linear PU nanocomposites. The PU crystallization was promoted at low contents of MWCNTs due to its action as a nucleation agent, although at high MWCNT contents, the crystallization was hindered because of restricting movement of PU chains [13, 18]. Targeting specific aerospace coating applications, CNTs were rigorously dispersed into PU matrices to produce nanocomposites for electrostatic dissipation and/or de-icing coatings [17]. The composites under consideration exhibited also good antistatic properties [15] as well as improved wear resistance, thermal conductivity and electrical conductivity [10]. The linear PU-MWCNT foams containing 0.1 wt% highly functionalized nanotubes, possessing carboxyl, hydroxyl or amide functional groups, manifested improved thermal stability, mechanical properties and acoustic damping; the nanotubes modified with carboxyl groups were found to have greater influence compared to the other two functional groups (i.e. lactone and phenol).

Functionalized graphene sheets (FGSs) were recently used as nanosized conductive fillers in thermoplastic PU [21]. Therein, the nanocomposite with 1 part of FGSs per 50 parts of PU had an electrical conductivity of  $10^7$  times increase over that of pristine PU, and DMA showed that the FGSs efficiently reinforced the PU matrix.

Information on molecular dynamics, as estimated from DMA, is rather limited for thermoplastic PU-MWCNT composites. According to Kwon et al. [15], the storage modulus and mechanical loss factor peak temperature (the glass transition temperature  $T_g$ ) of the nanocomposites increased with increasing functionalized MWCNT content, whereas Raja et al. [14] found only small changes in the glass transition or even slight decrease in  $T_g$  with increasing carbon nanotubes content for thermoplastic PU-MWCNT composites as compared with that for the neat matrix. For the thermosetting PU-non-functionalized MWCNT nanocomposites with CNT content of 0.1–1 wt%, McClory et al. [22] showed that CNTs were highly dispersed in the PU matrix, and the substantial enhancements in stiffness, strength and toughness were found for the nanocomposites compared with unfilled PU. Meantime, DMA showed only slight changes in glass transition dynamics in these nanocomposites.

The role of chemical processes at the interfaces and the character of the interfacial interactions are of a special significance in ascertaining the exact mechanism of nanocomposite performance including thermosetting PU-MWCNT nanocomposites that undoubtedly requires an in-depth study. Whilst this has been explored in a cursory sense [23–27], the direct comparison of CNT influence on dynamics of polymers, when nanotubes were functionalized through van der Waals interactions with an intermediate bridge to the polymer or those were directly covalently linked to the polymer, has not been made up to now. The significance of such studies is conditioned with a following problem. The acid oxidation procedure, as a traditional way for chemically functionalising CNTs, generates lattice oxidative fragments that behave similar to fulvic acids. Therein, these species are hydrophobic under acid conditions and therefore their creation prevents to immediate interaction of the matrix with the surface of CNTs. These lattice fragments, or fulvic acids, are connected with CNTs via van der Waals forces but simultaneously are extensively functionalised with acidic groups, which also participate in chemical reactions at interfaces and can account for up to 50% of the total number of acidic groups in oxidized CNT system [24, 25]. Their removal under base washing or reflux will leave purely covalent sites for target synthesis (direct covalent CNT-polymer bonding); however, the numerous works on CNT-polymer composites that involved acid-oxidized CNTs have neglected to include such a purification strategy and therefore raise questions about the mixture of covalent and van der Waals bonding at the interfaces and its relation to the final properties of the composite.

The goal of this study is the investigation of the structure and final mechanical performance of the thermosetting PU-based nanocomposites containing MWCNTs possessing acidic and other functional groups generated on the MWCNT surface and attached either through van der Waals forces or covalently bound to the CNT lattice at low filler content varying from 0.01 to 0.25 wt. %. The investigations of the thermodynamic parameters of polymer-filler interactions within formation of the

nanocomposites and also the impact of interfacial chemistry and interactions on the matrix glass transition dynamics, as estimated by DMA and laser-interferometric creep rate spectroscopy (CRS) techniques, were of essential interest and have been performed herein.

## **8.2 Materials and Testing Methods**

### **8.2.1 Materials**

#### **8.2.1.1 Carbon Nanotube Pretreatment**

MWCNTs with an outer diameter of 10–30 nm, inner diameter of 5–10 nm and length of 5–10  $\mu\text{m}$  were purchased from TMSpetsmash (Ukraine), which were grown using the CVD technique. Pristine MWCNTs (pMWCNTs) were prepared from raw samples through low-temperature oxidation to remove surface amorphous carbon and then refluxed in hydrochloric acid (HCl) to remove any residual metal catalytic particles. Samples were then washed extensively in water and dried at 100 °C.

#### **8.2.1.2 Hemin-Coated MWCNTs**

Hemin-coated MWCNTs (MWCNT-hemin) were prepared by sonicating pMWCNTs in a solution of excess hemin dissolved in tetrahydrofuran (THF). The mixture was adjusted to pH 1 with the addition of HCl (2 M) and left for 8 hrs. MWCNTs were separated from solution by centrifugation and washing with acidified methanol (MeOH)-THF mixture until no further colouration of the supernatant was observed (confirmed using UV-Vis analysis), then washed with MeOH and dried at 100 °C.

#### **8.2.1.3 Acid-Oxidized MWCNTs**

Acid-oxidized MWCNTs (MWCNT-ox) were prepared by refluxing MWCNTs in nitric acid ( $\text{HNO}_3$ , 70%, 6 h) and then washed with water until a neutral pH. Samples were then refluxed in sodium hydroxide (NaOH, 2 M, 1 h) to remove surface-immobilised fulvic acids and then washed in NaOH solution until no further colouration was obtained. The covalently attached surface groups were regenerated by refluxing in HCl (2 M, 10 min). Samples were finally washed in water till pH 7 and dried at 100 °C.

### 8.2.1.4 Reduction of MWCNT Surface Acidic Groups

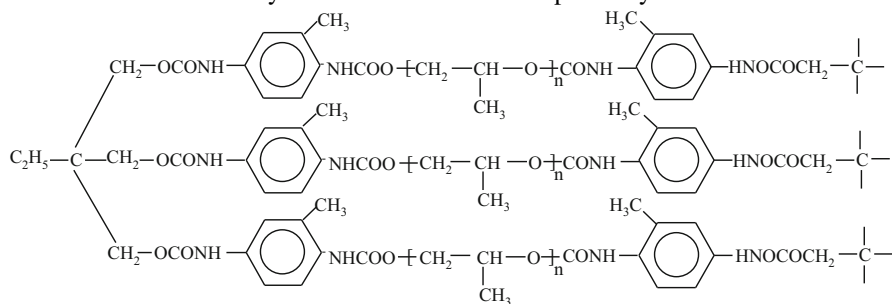
MWCNT-hemin and MWCNT-ox samples (100 mg) were sonicated in dry THF (50 ml) to obtain a dispersion. Lithium aluminium hydride ( $\text{LiAlH}_4$ ) in THF (1 M, 10 ml) was added under a nitrogen atmosphere, and the mixture was refluxed for 4 hrs. After cooling, excess  $\text{LiAlH}_4$  was decomposed with careful addition of MeOH. Reduced samples (MWCNT-hemin-red and MWCNT-red, respectively) were stirred in HCl in order to remove trace decomposition products and then washed thoroughly in water and dried at 100 °C. Samples were checked for the generation of additional fulvic acids through the reduction step, but none were detected.

### 8.2.1.5 Surface Group Analysis

All samples were titrated according to the Boehm method [11, 17]. MWCNT samples (50 mg) were sonicated in sodium bicarbonate, ( $\text{NaHCO}_3$ ), sodium carbonate ( $\text{Na}_2\text{CO}_3$ ) and NaOH solution (0.01 M, 20 ml, with 0.1 M NaCl) and stirred for 8 hrs. Samples were separated through centrifugation, and the supernatant was filtered through 0.2  $\mu\text{m}$  PTFE filters to ensure all MWCNTs were removed. Aliquots (5 ml) were titrated against HCl (0.01 M, with 0.1 M NaCl) using a pH meter to monitor the reaction. Titration analysis was repeated three times. Solutions were stored under nitrogen and were checked to ensure that atmospheric carbon dioxide had not affected the titration [18].

### 8.2.1.6 Polyurethane Nanocomposite Preparation

A PU network, to be used as the polymer matrix for nanocomposite preparation, was synthesised from poly(oxypropylene glycol) (PPG) with  $M_w = 2,000 \text{ g mol}^{-1}$  and adduct of trimethylolpropane (TMP) and toluene diisocyanate (TDI) using a two-step method, as described previously [28]. The adduct and PPG were used in a molar ratio of 2:3. The synthesized PU matrix is depicted by the formula:



Samples of the nanocomposites were prepared according to the procedures described in the previous work [26]. To prepare the nanocomposites, MWCNTs, as

MWCNT-hemin, MWCNT-ox, MWCNT-hemin-red or MWCNT-red (0.01, 0.1 or 0.25 wt. %), were mixed with the PPG and adduct prior to polyurethane synthesis. The prepared films with 1 mm thickness were post-cured for 2 h at 100 °C and then were held for 36 h at 80 °C in vacuum  $10^{-5}$  Pa to ensure the removal of any trace gas from the polymer composite.

## 8.2.2 Testing Methods

### 8.2.2.1 Vapour Sorption and Thermodynamic Calculations

The dichloromethane vapour sorption by PU samples and by nanocomposite's samples was studied using a vacuum installation and a McBain balance [9]. The changes in partial free energy of dichloromethane by sorption (dissolution)  $\Delta\mu_1$  were determined from the experimental data using Eq. 8.1:

$$\Delta\mu_1 = (1/M) RT \ln (P/P_0), \quad (8.1)$$

where  $M$  is the molecular mass of dichloromethane and  $P/P_0$  is the relative vapour pressure.

To calculate the free energy of mixing of the polymer components with the solvent, the changes in partial free energy of the polymers (native PU, nanocomposites) need to be determined. This requires the calculation of the difference between the polymer chemical potential in the solution of a given concentration and in pure polymer under the same conditions ( $\Delta\mu_2$ ).  $\Delta\mu_2$  for the polymer components were calculated using the Gibbs-Duhem equation:

$$\omega_1 d(\Delta\mu_1) / d\omega_1 + \omega_2 d(\Delta\mu_2) / d\omega_1 = 0, \quad (8.2)$$

where  $\omega_1$  and  $\omega_2$  are the weight fractions of a solvent and of a polymer. This can be rearranged to give Eq. 8.3:

$$\int d(\Delta\mu_2) = - \int (\omega_1/\omega_2) d(\Delta\mu_1) \quad (8.3)$$

Equation 8.3 allows the determination of  $\Delta\mu_2$  for each polymer from the experimental data by integration over definite limits. The average free energy of mixing of solvent with the individual PU and nanocomposites of various compositions for the solutions of different concentration was then estimated using Eq. 8.4 and using computational analysis.

$$\Delta g^m = \omega_1 \Delta\mu_1 + \omega_2 \Delta\mu_2 \quad (8.4)$$

### 8.2.2.2 Atomic Force Microscopy (AFM)

Surface topography and phase images of PU and nanocomposites were obtained using a multimode Nanoscope IIIa atomic force microscope. Tapping mode was employed in air using a 125  $\mu\text{m}$  silicon tip. Topographic and phase images were obtained simultaneously.

### 8.2.2.3 Transmission Electron Microscopy (TEM)

To enable TEM investigations, the nanocomposite samples were dehydrated in an ethanol series, passed through the transition solvent propylene oxide and embedded in TAAB Low Viscosity resin (TAAB Laboratories Ltd., Aldermaston, UK). Thin (100 nm) sections were cut on a Leica Ultracut ultramicrotome (Leica Microsystems [UK] Ltd., Milton Keynes UK), collected on nickel support grids and examined unstained in a Hitachi-7100 TEM at 100 kV. Images were acquired digitally with an axially mounted (2 K  $\times$  2 K pixel) Gatan Ultrascan 1000 CCD camera (Gatan UK, Oxford, UK).

### 8.2.2.4 Scanning Electron Microscopy (SEM)

Electron micrographs were obtained using Hitachi S-4800 CFE scanning electron microscope. Samples of nanocomposites were fractured in liquid nitrogen and chemically treated with aqueous iodine and potassium iodide. They were subsequently freeze-dried overnight before being examined by electron microscopy. Two sets of samples were examined: in the first set, samples were sputtered with gold to avoid electrostatic charging, and in the second set, samples were not coated.

### 8.2.2.5 Mechanical Testing

Mechanical properties of the nanocomposites were measured using a Series IX Automated Instron Materials Testing System. The samples were cut into micro dumb-bell shapes with gauge length of 20 mm, widths between 4–5 mm and sample thickness between 0.7–0.9 mm. Samples were processed at a continuous strain rate of 25 mm/min.

### 8.2.2.6 Dynamic Mechanical Analysis (DMA)

Dynamic mechanical behaviour of nanocomposites was analyzed in tension mode, basically at 1 Hz, using a Dynamic Mechanical Spectrometer DMS 6100 Seiko Instruments (Japan) at temperatures from  $-120$  to  $+190$   $^{\circ}\text{C}$ . Film samples with  $0.6 \times 10 \text{ mm}^2$  cross-section and 2-cm working length were used. A sample was

heated at a rate of  $3\text{ }^{\circ}\text{C min}^{-1}$ . Loss modulus  $E''$ , storage modulus (dynamic modulus)  $E'$  and mechanical loss factor  $\tan \delta = E''/E'$  as functions of temperature were measured.

In two cases, for neat PU and for one nanocomposite (PU-MWCNT-ox), the effective activation energy  $Q$  of segmental motion versus temperature dependence was estimated within the  $-70$  to  $+150\text{ }^{\circ}\text{C}$  range covering the extraordinarily broadened glass transition range. This was determined from the DMA measurements performed at frequencies of 0.1, 1 and 10 Hz. Typically,  $Q$  values are calculated by the displacement of temperature in the maximum of the relaxation peak with frequency; where partial overlap of neighbouring peaks occurs, their separation into Gaussian or Lorentz peaks is analyzed. However, very complicated DMA spectra in the broad temperature region of the glass transition were observed for the PU network and PU-based composites (see below) suggesting the substantial overlapping of a few constituent peaks, that is, the pronounced dynamic heterogeneity within the glass transition range. This prevented the possibility for calculating the strict  $Q$  values. Therefore, we chose the nontraditional way for estimating, semi-quantitatively, a tendency of changing  $Q$  with temperature over the temperature range of the glass transition. This was performed proceeding from the displacement of the experimental points in the complicated  $\tan \delta$  spectrum along temperature axis with frequency at a series of chosen  $\tan \delta$  levels, using the initial equation for a frequency of relaxation acts ( $\nu = \nu_0 \exp. (-Q/RT)$ ), and the resultant relation:

$$Q = 0.038T_1T_2/(T_2 - T_1) \text{ kJ mol}^{-1} \quad (8.5)$$

where  $T_1$  and  $T_2$  (in Kelvin) relate to the temperature points in the DMA spectra obtained at 0.1 and 10 Hz, respectively, for a chosen mechanical loss level.

### 8.2.2.7 Laser-Interferometric Creep Rate Spectroscopy (CRS)

CRS, an original high-resolution method of relaxation spectrometry and thermal analysis, allows the characterization in a discrete way of the dynamics, dynamic heterogeneity and creep resistance of materials over a broad temperature region; the CRS setups, experimental technique and numerous possibilities have been described in detail elsewhere [29]. This technique comprises precise measuring of creep rates at a constant low stress, much less than the yield stress, as a function of temperature (creep rate spectrum). To this end, the laser interferometer, based on the Doppler effect, is used. The time evolution of deformation is registered as a sequence of low-frequency beats in an interferogram whose beat frequency  $\nu$  yields a creep rate:

$$\dot{\epsilon} = \frac{\lambda \nu}{2l_0} \quad (8.6)$$

Here  $\lambda = 630\text{ nm}$  is a laser wavelength, and  $l_0$  is the initial length of the working part of a sample. The film samples with  $0.6 \times 10\text{ mm}^2$  cross-section and

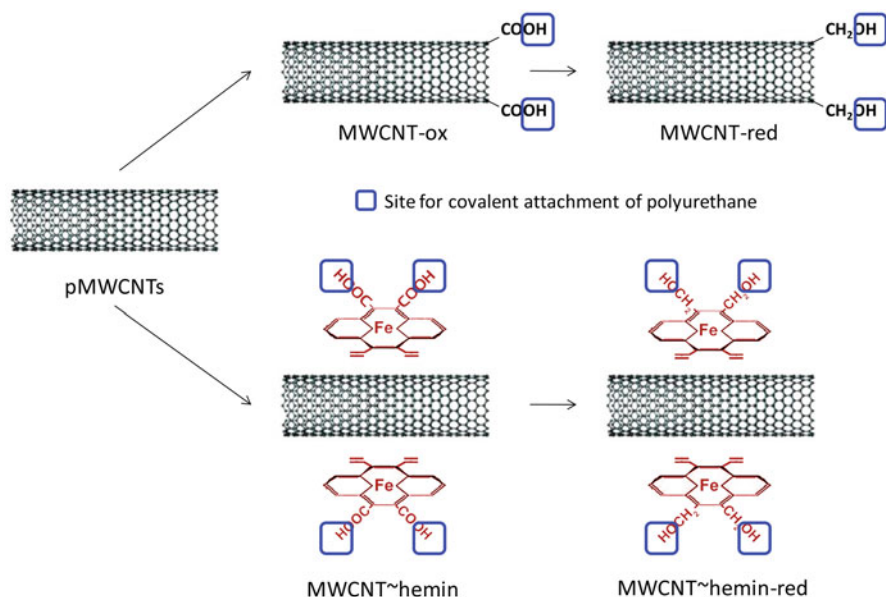


2-cm working length were used. The creep rate spectra were measured over the temperature range from  $-100$  to  $+140$  °C at the tensile stress of 0.3 MPa. A stress was chosen in the preliminary experiments as capable of inducing sufficient creep rates to be measured, whilst maintaining also a high spectral resolution, without smoothing out and distortion of a spectral contour. At heating with the rate  $V = 1$  °C  $\text{min}^{-1}$ , every 5 °C the sample was loaded, and an interferogram was recorded 10 s after loading. Then the sample was unloaded, heated to a temperature 5° higher and loaded again with the same stress; again the interferogram was registered, and the sample was unloaded and so on. The instrumental error in measuring creep rates does not exceed 1%, but scattering in the peak height and temperature location may change by up to 20% and 3–5 °C, respectively, when measuring identical samples [29]. The correlative frequency of the CRS experiments  $\nu_{\text{corr}} = 10^{-3}$ – $10^{-2}$  Hz.

### 8.3 Results and Discussion

#### 8.3.1 MWCNT Surface Chemistry for Interaction with PU

A single batch of MWCNTs was used from the supplier to ensure consistency across the experiments. MWCNTs were modified (Scheme 8.1), where appropriate, to



**Scheme 8.1** Chemical groups on MWCNT-ox, MWCNT-red, MWCNT-hemin and MWCNT-hemin-red are generated for bonding to polyurethane. The first two possess covalent bonding sites direct to the MWCNT lattice and the latter two involve surface adsorbed (non-covalent bonding) hemin

introduce functional groups for the attachment of PU, where the functional groups were either surface immobilised on or covalently bound directly to the surface of carbon nanotubes. MWCNT-ox and MWCNT-red both possess covalent sites directly on the lattice and were purified free of fulvic acids to ensure no competition with surface-immobilised functional groups resulted. Therein, connecting atomic units (fragments) of PU network are directly attached to the MWCNT lattice. MWCNT-hemin and MWCNT-hemin-red also have covalent sites for attachment, but only through the hemin molecules that decorate the surface of the nanotubes through non-covalent bonding. Ultimately this approach will facilitate a direct comparison across the type of MWCNTs to assess which type of interactions may reflect superior mechanical performance and also elucidate whether acid-oxidative lattice fragments (fulvic acids) can exert a detrimental effect to the final mechanical performance of the composite. Moreover, it is recognised that in chemically modifying the carbon lattice, the surface tension of the MWCNTs will also change and will alter the dispersibility of MWCNTs into a polymerising solution/matrix and in turn affect the size and distribution of the hard and soft domains of PU.

The oxidation of MWCNTs in nitric acid digests part of the outer walls, introducing acidic groups directly to the lattice, as well as generating fulvic acids, which are removed through the reflux in alkali solution. The types of groups identified on the MWCNT surface include carboxylic, lactone and phenolic groups as the chief moieties. Acid anhydride, carbonyl, alcohol and ether groups may also be present, though only the first would be accounted in the titrations using the standard three bases of  $\text{NaHCO}_3$ ,  $\text{Na}_2\text{CO}_3$  and  $\text{NaOH}$  [30]. The carboxylic, phenolic and alcohol groups are of particular interest as they can participate in the polymerisation reaction with the (di)isocyanate monomers to form an amide and two urethane bonds, respectively [31]. Therefore, this study may also make inference to the reactivity comparison of carboxylic and phenolic groups by using MWCNTs with the same degree of oxidation, where carboxylic acids are predominant in MWCNT-ox and phenolic and alcohol groups are the principal ones in MWCNT-red.

Titration of the surface acidic groups show (Table 8.1) the increase in the number of carboxylic, lactone and phenolic groups when acid-oxidising pMWCNTs. pMWCNTs exhibit a low number of functional groups, which are recognised as being generated through their CVD synthesis, representing terminal groups near lattice vacancies [32]. On reduction of MWCNT-ox to MWCNT-red, the number of carboxylic groups decreases by around 70%. The increase in the number of lactone groups may result from the reduction of acid anhydride groups. There was no increase in the number of phenolic groups; however, it was determined in a previous study by XPS analysis that aliphatic alcohol groups, undetectable via the titrations used, are present [33].

Hemin is a polycyclic aromatic hydrocarbon with an  $\text{Fe}^{3+}$  core and two carboxylic groups at the outer edges of the cyclic structure. Its enforced surface immobilisation (through non-covalent interaction) to the surface of unfunctionalised carbon nanotubes in the presence of an acid renders the molecule hydrophobic and

**Table 8.1** The number of carboxylic, lactone and phenol groups as determined for MWCNT samples through Boehm titration assessment

Type of MWCNT surface	Number of Groups (meq g <sup>-1</sup> )		
	carboxyl	lactone	phenol
pMWCNT	0.01	0.01	0.02
MWCNT-ox	0.14	0.03	0.18
MWCNT-red	0.04	0.08	0.16
MWCNT-hemin	0.29	0.00	0.01
MWCNT-hemin-red	0.00	0.00	0.00

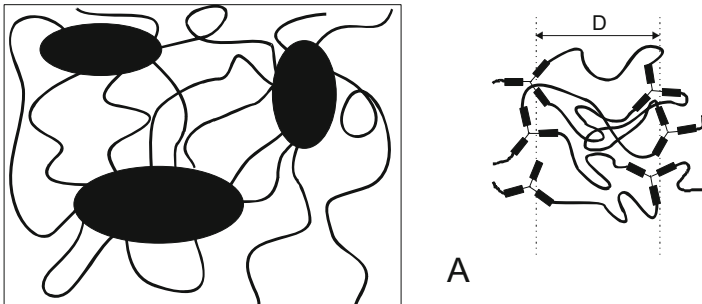
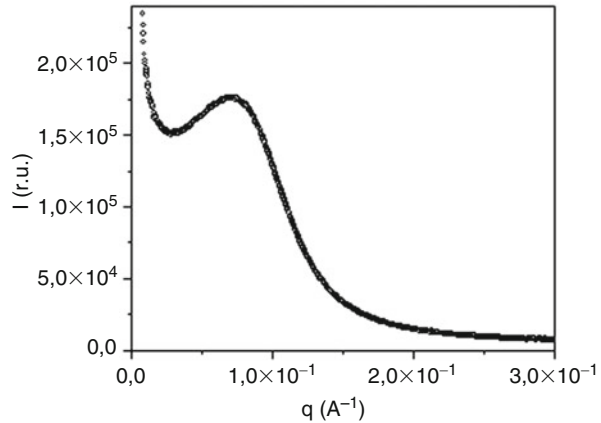
promotes van der Waals interactions with the  $\pi$  electron network of the MWCNT surface. The presence of hemin on the surface is detected by the increase in the number of carboxylic groups. It was possible to elute all hemin from the surface of MWCNT-hemin and MWCNT-hemin-red using a sodium hydroxide washing, which protonates the acidic groups on hemin rendering the molecule more hydrophilic. The number of carboxylic groups present on MWCNT-hemin sample is greater than that for MWCNT-ox (Table 8.1); however, MWCNTs-ox possess a higher total number of acidic groups and may also possess undetected additional alcohol generated by acid oxidation, which the MWCNT-hemin sample will not. Reduction of MWCNT-hemin to MWCNT-hemin-red decreases the number of carboxylic groups by 100% and demonstrates the complete chemical availability of surface immobilised species which is greater than that of the covalently bound acidic groups in MWCNT-ox. Given that conventional reduction chemistry of a carboxylic group leads to an aliphatic alcohol, it is reasoned that MWCNT-hemin-red has followed a similar route where aliphatic alcohol species are undetected using titration analysis. The presence of lactone and phenol groups on the underlying nanotube structure (pMWCNT) for MWCNT-hemin and MWCNT-hemin-red may have been masked by the hemin coating and, therefore, was not recorded in the titration analysis.

The reaction between the MWCNT samples and PU should occur where carboxylic, phenolic and alcohol groups are available to form amide or urethane bonds with the diisocyanate monomer.

### 8.3.2 Structure of the PU Matrix

The structure of the polyurethane matrix, which was used for nanocomposites formation, was investigated by small-angle X-ray scattering (SAXS) [34] and is shown in Fig. 8.1. In the case of native PU, there is a distinct interference maximum on the  $I(q)$  vs  $q$  plot at  $0.072 \text{ \AA}^{-1}$ , which corresponds to Bragg periodicity of  $87 \text{ \AA}$ . The existence of such a maximum is connected with a quasiperiodic type of spatial distribution of hard and soft segments of polyurethane [35], i.e., a microphase separation within the PU materials. Scheme 8.2 illustrates some ordering of the

**Fig. 8.1** Scattering intensity  $I(q)$  versus scattering vector  $q(\text{Å}^{-1})$  curves obtained for neat PU network. The intensity values are taken in relative scale



**Scheme 8.2** A sketch of the polyurethane structure exhibiting hard and soft domains discretely spaced at distance  $D$

hard and soft segments within the frame of the polyurethane materials. Thus, the polyurethane matrix consists of ordered parts (black areas) and cross-passing chains.

Embedding MWCNTs into such a polymer matrix could result in the following situations. The covalent bonding of the MWCNTs (MWCNT-ox) with PU or van der Waals interactions of the unfunctionalised areas of the MWCNT surface with polyurethane matrix should lead to improved disagglomeration of the nanotube bundles and the good dispersibility of MWCNTs in a polymer [23]. At the same time, however, such interactions that result in a good distribution (dispersion) of the nanotubes could partly or completely destroy the ordering of hard and soft segments of the PU matrix. As a result, not only enhancing but also the drop in mechanical properties of the PU matrix may occur.

### 8.3.3 AFM Investigation of the Nanocomposites

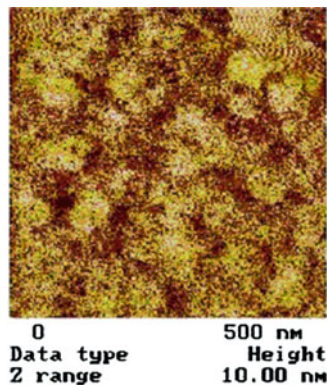
In Fig. 8.2 the topography of the PU matrix is presented. The ordering of hard (dark regions) and soft (light regions) segments of PU, i.e., microphase separation, is exhibited. This is in agreement with the SAXS investigation of this matrix (Fig. 8.1).

In Fig. 8.3 the phase images of PU nanocomposites with different loadings of MWCNT-ox are presented. The MWCNT filler was not observed in the matrix, but AFM images reveal changes in the structure of PU matrix induced by their inclusion. For nanocomposites, containing 0.01% MWCNT-ox, the nanodomain structure of polyurethane is preserved, and the hard and soft domain microphase separation is observed (Fig. 8.3a, b). Increasing the MWCNT-ox content up to 0.1% in the nanocomposites results in dramatic changes in the PU structure which exhibits nearly complete disappearance of the hard and soft domains in the matrix structure (Fig. 8.3c, d).

When increasing the amount of nanotubes up to 0.25 wt. %, the nanostructure of polyurethane matrix is partly retained (Fig. 8.3e, f). Therein, the higher loading of MWCNTs increases the possibility of re-agglomeration which, obviously, entails poorer dispersibility (which can be observed when comparing TEM images in Fig. 8.4). It is therefore surmised that some regions of PU are not penetrated by MWCNTs at high filler contents, thus allowing polymerization with the restricted influence of MWCNTs and the generation of hard and soft domains.

When small quantities of MWCNTs (0.01%) are used in the preparation of nanocomposites, the number of nanotubes is insufficient to noticeably influence the domain structure of PU. When increasing the amount of MWCNTs up to 0.1% and a good dispersion of nanotubes, the effective surface of MWCNT-ox becomes large enough to prevent the formation of hard and soft domains. At 0.25% MWCNT-ox (0.25%), part of nanofiller is present in agglomerates allowing the formation of the soft and hard domains. Introduction of MWCNT-hemin changed the structure of polyurethane less dramatically, but the change in the size of the hard and soft

**Fig. 8.2** Tapping mode AFM topography for pure PU matrix. The size of square is 500 nm



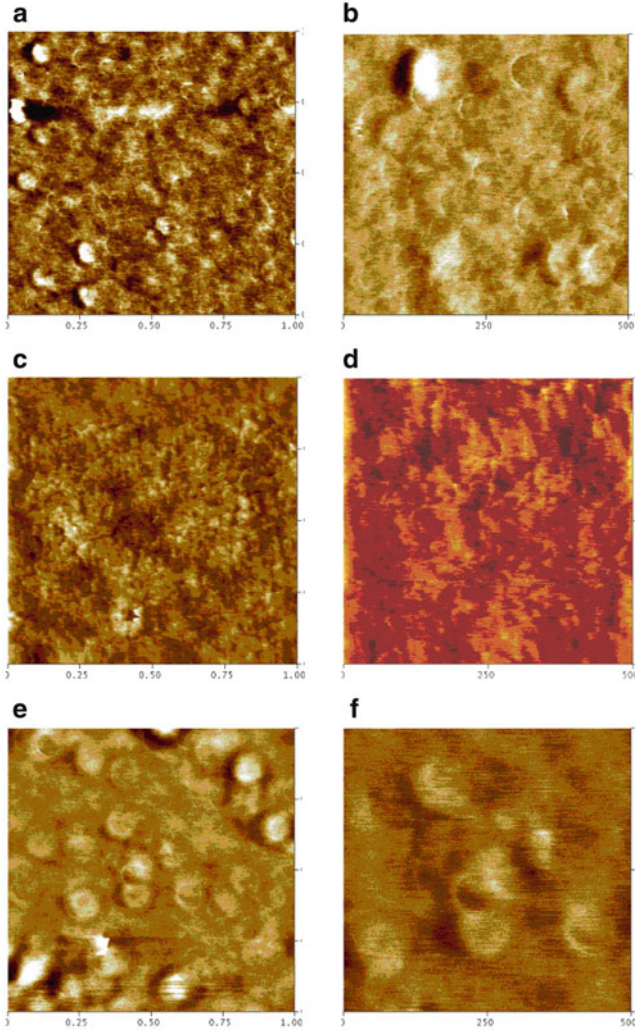


**Fig. 8.3** Tapping mode AFM phase images of nanocomposites based on PU containing (a, b) 0.01, (c, d) 0.1 and (e, f) 0.25% MWCNT-ox

domains of PU was also observed. Thus, it appears that the influence of MWCNT-ox on PU structure in the nanocomposites does not fully correlate with the amount of nanotubes in the matrix, though their presence influences noticeably on the matrix microstructure.

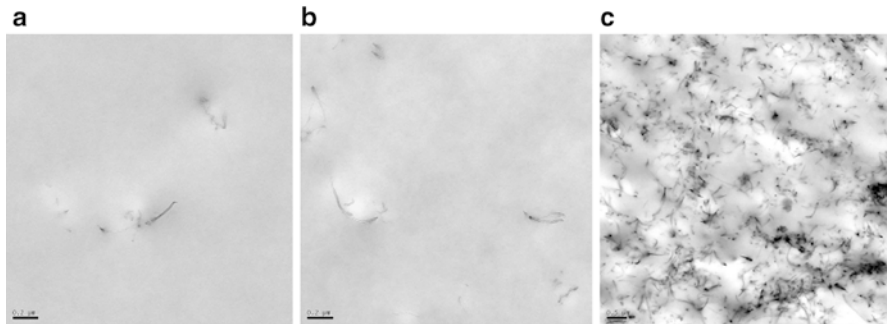


**Fig. 8.4** TEM images of PU nanocomposites containing (a) 0.01, (b) 0.1 and (c) 0.25% MWCNT-ox

### 8.3.4 TEM and SEM Analyses of MWCNTs Dispersion in the PU Matrix

It has been previously demonstrated that the degree of dispersibility of MWCNTs in polymers affects their final tensile strength [36], where well-dispersed MWCNTs with sufficient interface with the surrounding polymer can toughen and strengthen the whole system. Strong adhesion of MWCNTs to the polymer matrix limits their pull-out, such that crack propagation is hindered by the carbon nanotubes. The high aspect ratio and large interfacial area of MWCNTs denote greater load transfer across their length leading to improved strength. However, where agglomeration of MWCNTs occurs, the real interface area with the surrounding polymer is reduced, and MWCNTs may then serve as crack initiator sites.

As the carbon nanotubes become less hydrophobic under acid-oxidative functionalisation, the introduction of surface groups on the MWCNTs disrupts the  $\pi$ - $\pi$  bond network in the outer layers, which limits van der Waals interactions. Through the high-temperature action of the oxidative medium, it is possible to promote the “disentanglement” of the MWCNT bundles and improve their ability to interfacial interaction with solvent and polymers, which may also retard re-agglomeration. Figure 8.4 shows the TEM images of the nanocomposites containing MWCNT-ox. For the nanocomposites with 0.01 wt. % MWCNT-ox, separate nanotubes could be observed in the matrix (Fig. 8.4a). A good dispersion of MWCNT-ox is preserved also for the nanocomposites containing 0.1 wt. % MWCNT-ox (Fig. 8.4b). However, for the nanocomposites containing 0.25 wt. % MWCNT-ox (Fig. 8.4c), both separate nanotubes and their agglomerates are present; the latter prevents the complete interaction of the surface of MWCNTs with the matrix.

Similarly, the TEM images of MWCNT-red, MWCNT-hemin and MWCNT-hemin-red in PU showed that the carbon nanotubes were well dispersed at their low weight content (0.01 and 0.1 wt. %), but at higher filler percentage (0.25 wt. %), the extensive agglomeration occurred.

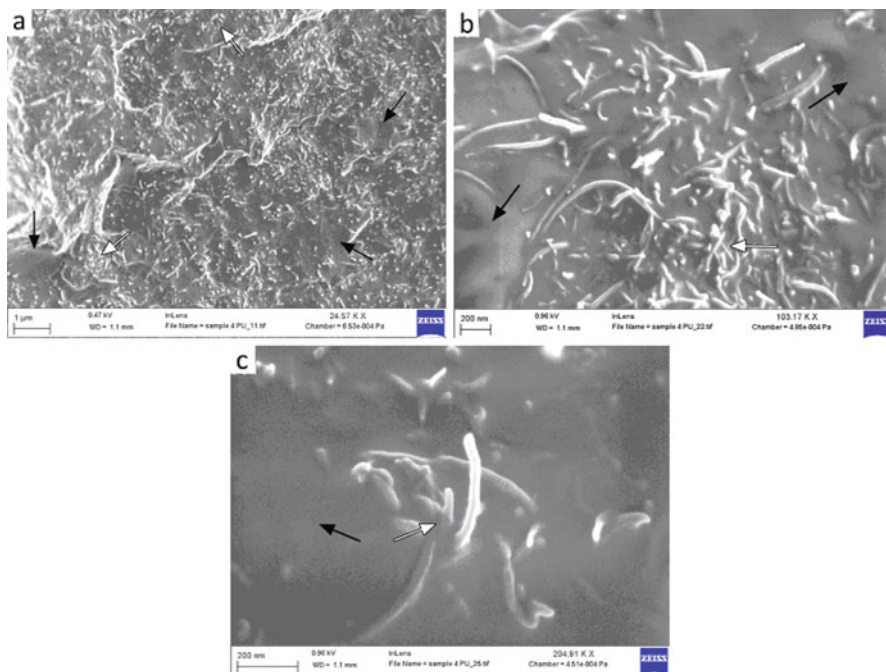


**Fig. 8.5** SEM images of PU with 0.25% MWCNT-ox where the agglomeration of MWCNTs is revealed (white nanotubes) resulting in areas of nearly pure PU (dark areas). Scale bars are 1  $\mu\text{m}$  (a), 200 nm (b) and 200 nm (c)

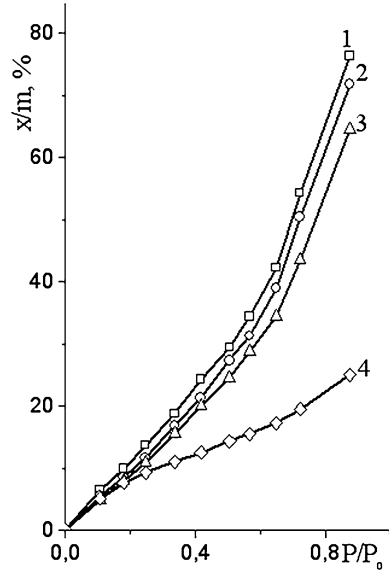
SEM images (Fig. 8.5) show the morphology of PU nanocomposites containing 0.25 wt. % MWCNT-ox, which confirms the results of TEM analysis. Both individually separated nanotubes (Fig. 8.5a) and their agglomerates (Fig. 8.5b) are observed. Additionally, nanotubes appear to be well coated by the polymer matrix (Fig. 8.5c). This means that the covalent bonding of MWCNTs to the polymer matrix creates a stable interfacial layer on the nanotube surface in order to generate nanocomposites with improved properties.

### 8.3.5 Thermodynamics of Polymer-Filler Interactions in the Nanocomposites

The calculation of the thermodynamic parameters of interaction between MWCNT with functionalized surfaces and polymer matrix in the created nanocomposites was carried out. The basis for the calculation of the thermodynamic parameters was the experimental isotherms of solvent vapour sorption by the samples. The vapour sorption of dichloromethane at 20 °C by samples of polyurethane, fillers



**Fig. 8.6** Isotherms of dichloromethane vapour sorption at 20 °C by samples: 1, polyurethane; 2, nanocomposite with 0.1% MWCNT-ox; 3, nanocomposite with 0.25% MWCNT-ox; 4, MWCNT-ox



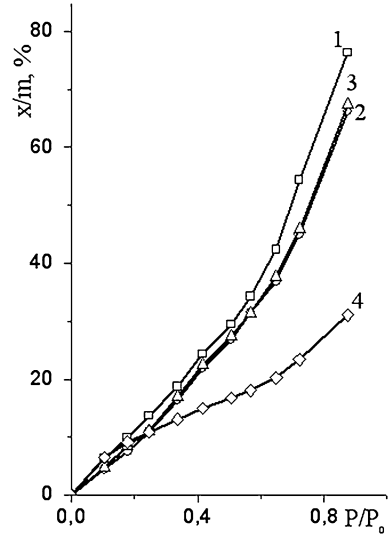
and nanocomposites was studied using a vacuum installation and a McBain balance with a sensitivity of 3–4 mg/mm.

Figure 8.6 shows the isotherms of dichloromethane vapour sorption at 20 °C by PU (curve 1), nanocomposites with 0.1% MWCNT-ox (curve 2), 0.25% MWCNT-ox (curve 3) and nanofiller MWCNT-ox (curve 4). As could be seen from Fig. 8.6, the isotherm of dichloromethane vapour sorption by PU looks like curve typical for vapour sorption by elastomer sample. PU absorbs a significant amount of dichloromethane (about 75% by weight). The introduction of MWCNT-ox into PU leads to decreasing of dichloromethane vapour sorption (Fig. 8.6, curves 2, 3). Moreover, with an increase of amount of nanofiller in the nanocomposite, the sorption of vapour by nanocomposites, naturally, falls (curves 2 and 3).

It should be noted that the nanofiller also adsorbs the essential amounts of dichloromethane vapour (Fig. 8.6, curve 4). The reduction of dichloromethane vapour sorption by nanocomposite samples compared to the native polymer matrix may indicate the formation of densely packed boundary layers of polyurethane in samples filled by MWCNT-ox.

Figure 8.7 shows the isotherms of dichloromethane vapour sorption at 20 °C by PU and by nanocomposites containing 0.1% MWCNT-red (curve 2) and 0.25% MWCNT-red (curve 3) and by nanofiller MWCNT-red (curve 4). As could be seen, the sorption by nanocomposite samples (Fig. 8.7, curves 2, 3) is smaller in comparison with the PU matrix. But in this case, the sorption isotherms of nanocomposites containing different amounts of MWCNT-red are almost identical. On the qualitative level, the reduction of sorption by nanocomposites compared to the native polymer matrix can testify in favour of the formation of densely packed boundary layers of polyurethane in the filled samples containing MWCNT-red. But

**Fig. 8.7** Isotherms of dichloromethane vapour sorption at 20 °C by samples: 1, polyurethane; 2, nanocomposite with 0.1% MWCNT-red; 3, nanocomposite with 0.25% MWCNT-red; and 4, MWCNT-red

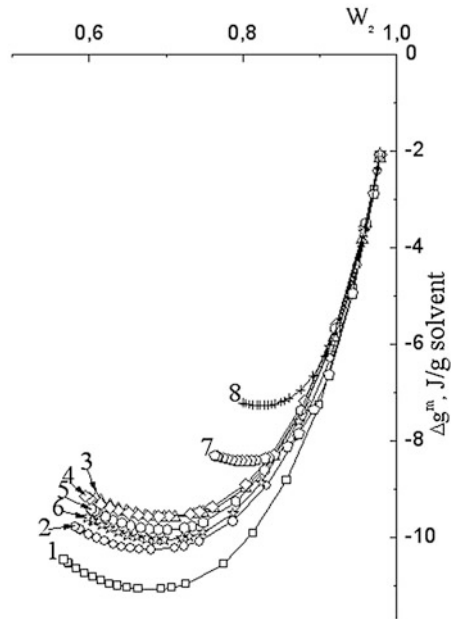


the coincidence of sorption isotherms for nanocomposites with different amounts of nanofiller could mean the worst distribution of MWCNT-red in the polymer matrix (relatively less of boundary layers in the nanocomposite with increasing amount of nanofiller).

The using of the thermodynamic methods and calculations based on experimental data of vapour sorption of dichloromethane by nanocomposites samples allowed us to estimate a number of characteristics of the systems, namely, the free energy of interaction of polymers with solid surfaces. In [37] the method calculation of thermodynamic parameters of the polymer-polymer interaction was proposed. For this, the approach based on the fundamental assumptions of independence of thermodynamics enthalpy and free energy of the system from the way of the process was used [37]. In [38, 39] this approach was applied for polymer-filler systems. Under this approach, we can calculate the parameters of interaction of polymer with a filler when parameters of the interaction of each of them and their mixtures with fluid are known. Based on isotherms of sorption, the change of the partial free energy of dichloromethane  $\Delta\mu_1$  was calculated using eq. (8.1). The change in the partial free energy of individual polymer and filled systems under sorption process  $\Delta\mu_2$  was determined in accordance with the Gibbs-Duhem Eq. (8.2). Free energy of mixing of individual polymer and nanocomposites with solvent  $\Delta g^m$  was determined in accordance with Eq. (8.4).

In Fig. 8.8 the calculated values  $\Delta g^m$  for neat polyurethane, for nanocomposites and for nanofillers MWCNT-ox and MWCNT-red are shown. It is evident that all the systems under investigation PU-dichloromethane, nanocomposites-dichloromethane and nanofillers-dichloromethane are thermodynamically stable ( $d^2\Delta g^m/dW_2^2 > 0$ ). Although the affinity of dichloromethane to PU (Fig. 8.8, curve 1) is the highest.

**Fig. 8.8** Free energies of mixing of polymer and nanocomposites with solvent dichloromethane  $\Delta g^m$ : 1, polyurethane; 2, nanocomposite with 0.1% MWCNT-ox; 3, nanocomposite with 0.25% MWCNT-ox; 4, nanocomposite with 0.25% MWCNT-hemin-red; 5, nanocomposite with 0.1% MWCNT-red; 6, nanocomposite with 0.25% MWCNT-red; 7, MWCNT-red; 8, MWCNT-ox



With the introduction of carbon nanotubes with functionalized surfaces into the polymer matrix, the affinity of dichloromethane to the nanocomposites decreases (Fig. 8.8, curves 2–7). Thus, comparing the nanocomposites with the same amount of nanofiller (0.25% by weight), we can conclude that affinity of dichloromethane to the nanocomposites decreases in a row: MWCNT-red > MWCNT-hemin-red > MWCNT-ox.

Based on the concentration dependence of the average free energy of mixing of the solvent with PU and with the nanocomposites, the values  $\Delta G_1$  and  $\Delta G_{111}$  were obtained.  $\Delta G_1$  and  $\Delta G_{111}$  are the free energies of interaction of polymer and nanocomposite with lots of solvent [37]. For  $\Delta G^*_{p-f}$  calculation (free energy of polymer-filler interaction), Eq. (8.7) was used [38]:

$$\Delta G^*_{p-f} = \Delta G_1 + n\Delta G_{11} - \Delta G_{111}, \quad (8.7)$$

where  $\Delta G_{11}$  is the free energy of interaction of the filler with lots of solvent.

The calculation  $\Delta\mu_{2(\text{fil})}$  of filler have been conducted according to the Gibbs-Duhem equation, as it was done above for polymers. Then Eq. (8.8) was used for calculation of free energy of interaction of dichloromethane with carbon nanotubes:

$$\Delta g^m = W_1 \Delta\mu_1 + W_2 \Delta\mu_{2(\text{fil})}, \quad (8.8)$$

**Table 8.2** The free energy  $\Delta G^*_{p-f}$  of interaction of polyurethane with MWCNTs with different surface chemistry in the nanocomposites

Nanocomposite sample	$\Delta G^*_{p-f}$ , J/g polymer
PU + 0.1% MWCNT-ox	-1.74
PU + 0.25% MWCNT-ox	-3.34
PU + 0.25% MWCNT-hemin-red	-3.10
PU + 0.1% MWCNT-red	-2.87
PU + 0.25% MWCNT-red	-2.43

The dependence  $\Delta g^m = f(W_2)$  for fillers (Fig. 8.8, curves 7, 8), as well as for three-dimensional polymers, has the form of curves with a minimum and cut off at the critical amount of solvent.

Using the obtained values of the free energy of interaction with solvent ( $\Delta G_{11}$ ), according to Eq. (8.7), the values of the free energy of interaction of PU with nanofillers were calculated. The results of such calculations are shown in Table 8.2.

It is evident that the free energy of interaction between carbon nanotubes with functionalized surfaces and with PU matrix is negative for all types of nanofillers (Table 8.2). This indicates that thermodynamic stability of filled PU samples and high adhesion of PU to carbon nanotubes with functionalized surfaces takes place. The free energy of interaction of MWCNT-ox with polyurethane varies with concentration: with increasing amount of MWCNT-ox in the nanocomposites, the value of free energy of mixing increases in magnitude. The latter could mean an increase in the fraction of surface layers of PU with the content of this nanofiller in the nanocomposite, which is the result of a uniform distribution of MWCNT-ox in the polymer matrix.

For the nanocomposites containing MWCNT-red, the value of the free energy of interaction of PU with the carbon nanotubes virtually remains unchanged with varying the amount of nanofiller. The latter could mean that with increasing of MWCNT-red content in the nanocomposites the part of the nanofiller forms agglomerates and hence the effective fraction of the surface layers decreases. The result is a reduction of the value of the free energy of interaction of polyurethane with MWCNT-red in magnitude. That is, it can be assumed that the MWCNT-red will be worse distributed in the matrix of polyurethane compared to MWCNT-ox.

### 8.3.6 Investigation of the Nanocomposites by DMA

Figure 8.9a–d presents the temperature dependencies of tangent of mechanical loss angle (mechanical loss factor,  $\tan \delta$ ) obtained under tension mode and a frequency of 1 Hz over the temperature range between  $-120$  and  $+180$  °C for neat PU and the nanocomposites studied. Generally, the glass transition peaks in all of these curves are extraordinarily broad and extend between about  $-70$  and  $+150$ – $170$  °C. Besides, their complicated spectral contours, with bends and shoulders, suggest the presence of a few strongly overlapping constituent relaxation peaks, that is, the pronounced dynamic heterogeneity within the glass transition range. Thus, three

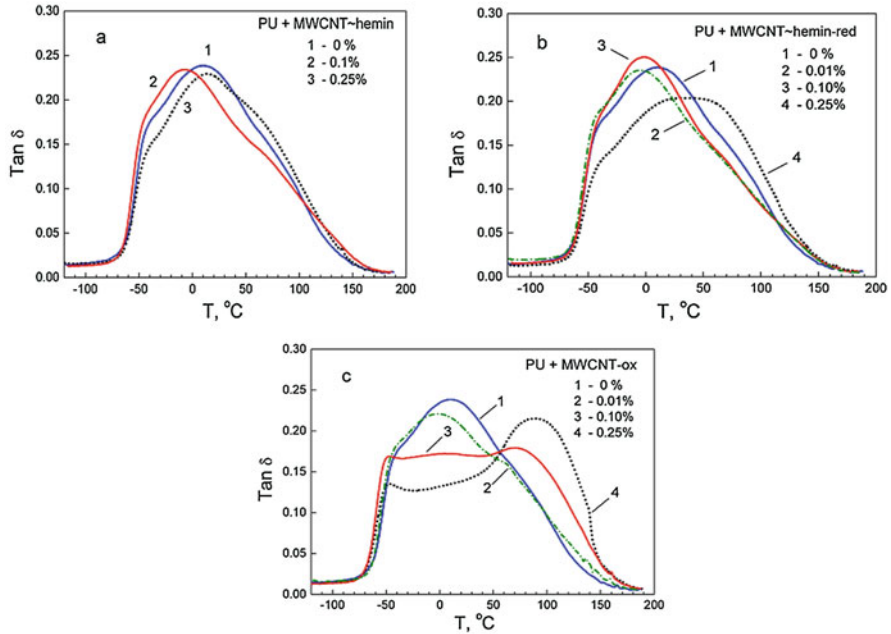


**Fig. 8.9** (a–d) DMA spectra measured at 1 Hz (tension) for a neat PU network and PU-MWCNT nanocomposites with different MWCNT filler levels and types of functionalisation

overlapping peaks may be deciphered in the mechanical loss spectrum of neat PU including peak I (curve bend) at  $-40$  to  $-50$  °C, the main peak II (maximum around  $0$  °C), and a slight tendency to manifestation of peak III at around  $+60$ – $70$  °C. Nevertheless, for neat PU DMA does not allow resolution of the side relaxation peaks with a certainty. In our previous dielectric relaxation study [40], it was possible to separate the extraordinarily broad peak of neat PU into two glass transitions. It was shown that this peak consisted of  $\alpha_1$  and  $\alpha_2$  relaxations connected presumably with motion of “soft” poly(propylene glycol) (PPG) segments and “hard” segments of PU (network junctions), respectively. However, it was possible to analyze the broad complicated spectral contour of PU glass transition in more detail in the discrete creep rate spectra only (see next section).

Figure 8.9a–d demonstrates the substantial and quite different impact of MWCNTs, at low filler levels, on the glass transition dynamics of PU matrix; these effects depend on both the filler content and the chemical type of MWCNT surface, whether MWCNT-ox, MWCNT-red, MWCNT-hemin or MWCNT-hemin-red. Additionally, the complicated shape of the nanocomposite spectra becomes more distinctive in some cases. The transformations of the PU spectral contour in the nanocomposites are due, obviously, to various contributions (intensities) of the constituent relaxations and changing the temperature location of peaks. Figure 8.9 shows that the main  $\tan \delta$  peak II may shift to higher temperatures, obviously, as

a consequence of interaction of the PU chains with the surface of nanotubes and restriction of glass transition dynamics, i.e., prevailing role of interfacial dynamics (“constrained dynamics” effect, see for example reviews [29, 41]). However, this peak may also retain the initial temperature position and even slightly shift to lower temperatures indicating acceleration of glass transition dynamics. As for the shoulder of  $\tan \delta$  peak located in the region of  $-40$  to  $-50$  °C, its contribution to the intensity decreases in the composites’ spectra, but its temperature position remains almost unchangeable. It means that the considerable part of the PU nanoregions is not disturbed by the addition of MWCNTs. As the segments contributing to low-temperature relaxations are definitely soft poly(propylene glycol) ones, we could expect that nanotubes are concentrated close to the hard nanodomains of PU matrix since chemical reaction of functionalised MWCNTs with isocyanate groups occurs.

The impact of nanotubes on the PU dynamics turned out to be minimal for the nanocomposite with MWCNT-hemin (Fig. 8.9a). After filling with 0.1% nanotubes, the main  $\tan \delta$  maximum displaces from  $+10$  to  $-10$  °C, and the temperature position of the other constituent relaxations remains almost unchangeable; this is due apparently to some loosening of the molecular packing in PU. Introducing of 0.25% MWCNT-hemin results in the restoration of the temperature position of the main  $\tan \delta$  maximum, a small decreasing mechanical losses over  $-40$  to  $+20$  °C range, but a slight increasing of mechanical losses in the temperature region of the higher-temperature shoulder. The hemin-modified nanotube surface is characterized with the highest content of functional COOH groups, which act as points for covalent PU attaching (Table 8.1); however, the hemin coating is immobilized on the nanotube surface only through non-covalent, van der Waals interactions with the  $\pi$  electron network of the MWCNTs; this led to decreased interfacial interactions.

After incorporating MWCNT-hemin-red into PU, similar effects of some relaxation peak displacement to lower temperatures (loosening molecular packing and acceleration of dynamics) are observed with nanofiller contents of 0.01 or 0.1% (Fig. 8.9b). At the same time, using 0.25% of nanotubes resulted in substantial constraining dynamics: a plateau at  $20$ – $60$  °C arises. The latter effect is registered despite the total disappearance of carboxyl and phenol functional groups as “covalent bonding points” at MWCNT-hemin-red surface (Table 8.1). This may be explained presumably by the above-mentioned fact that aliphatic alcohol groups, undetectable via the titrations used, are likely to be present in this case on the MWCNT surface serving as such anchoring sites.

The most dramatic changes are registered, however, in the mechanical loss spectrum after filling PU with MWCNT-ox (Fig. 8.9c) which possesses a high total number of covalently bound surface carboxylic and phenol groups (Table 8.1) and perhaps also undetectable at titration alcohol groups generated by acid oxidation. The  $\tan \delta$  ( $T$ ) contour slightly changes at 0.01% nanotubes, but it is strongly transformed at 0.1 and especially 0.25% nanotubes: the low-temperature shoulder and main peak II decrease, whereas the high-temperature shoulder increases by far with the displacement to higher temperatures. The plateau covering the temperature range from  $-60$  to  $+80$  °C rises at 0.1% nanofiller, which indicates that a good dispersion of MWCNT-ox in PU matrix [26] led to the formation of a large

interfacial area. When 0.25% MWCNT-ox is added, the main maximum at 10 °C in the spectrum of neat PU displaces to 90 °C in the spectrum of the nanocomposite and, additionally, the spectral contour shows a tendency to manifest relaxation (curve bend) at 120–140 °C.

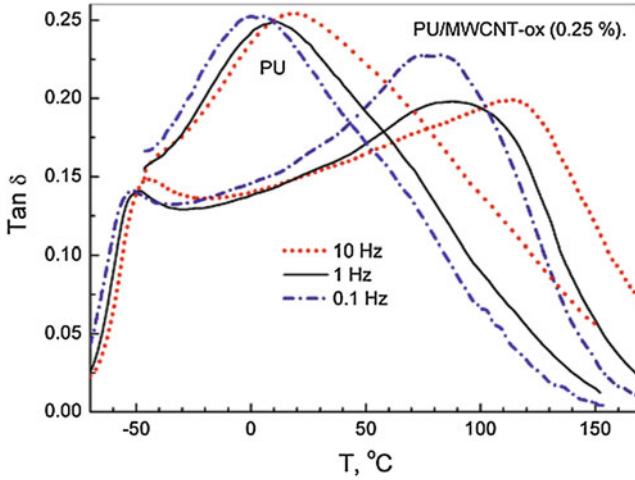
Thus, covalent bonding of some isocyanate groups (in fact the PU network junctions) with the functional groups covalently bound to MWCNT surface provides the strongest interfacial interactions in the nanocomposites with MWCNT-ox. As a result, the largest constrained dynamics effect is observed. This was attained even in spite of some MWCNT aggregation and disrupting of the initial (hard and soft domains) matrix structure [26].

Figure 8.9d shows that the incorporation of MWCNT-red particles, which have a strongly decreased number of surface carboxyl groups (Table 8.1), into the PU matrix results in the reduction of changes in the  $\tan \delta (T)$  curve, probably due to weakening of the interfacial covalent interactions. It may be also assumed that carboxylic groups attached to the MWCNT surface are more reactive than alcohol and phenol groups in the reaction with isocyanate groups. Of interest, in this case the maximal effect from filling is observed at 0.1% MWCNT-red, whereas at 0.25% nanofiller effect of constrained dynamics disappears. The latter could, obviously, be associated with the enhanced nanotube aggregation [26].

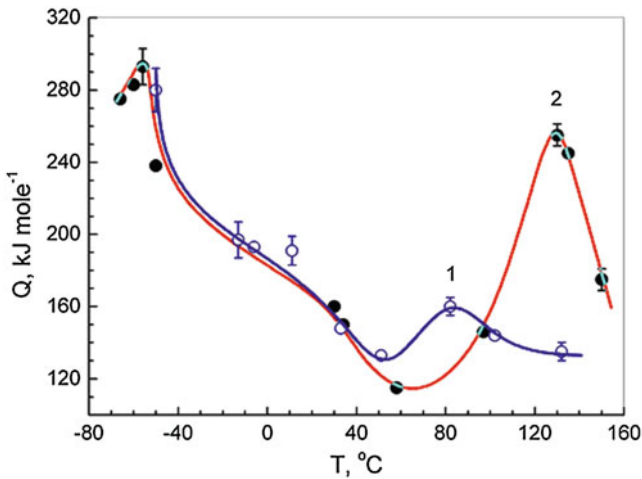
Thus, DMA data obtained for neat PU and the studied nanocomposites suggest the pronounced dynamic heterogeneity within their glass transitions. Such supposition was confirmed by the dependencies of the effective activation energy  $Q$  of segmental motion within the glass transition as a function of temperature, as obtained from the DMA experiments performed at different frequencies and also from the discrete creep rate spectra. These results allowed a comprehensive understanding of the origin of the complicated glass transition dynamics in these materials to be elucidated.

Figure 8.10 shows the DMA spectra obtained at 0.1, 1 and 10 Hz for neat PU and for the nanocomposite with 0.25% MWCNT-ox, and Fig. 8.11 presents the  $Q(T)$  dependencies obtained using these experimental data and the calculations by formula (8.5). In general, the peculiar  $Q(T)$  plots directly indicate a very broad dispersion of the effective activation barriers  $Q$  varying from 110 to 300 kJ mol<sup>-1</sup>, where a few  $Q$  levels characterize the glass transitions of neat PU and the nanocomposite based thereon. This means that the dynamics within their glass transitions is formed by several constituent relaxations (dynamic modes) over the temperature range from -60 to +150 °C. The substantial discrepancy between both dependencies obtained is observed only at temperatures between 50 and 150 °C.

PU network includes the flexible PPG cross-links with a molecular weight of 2.000 g mol<sup>-1</sup>, that is, each cross-link includes about five Kuhn segments, and the more rigid PU network junctions. Judging by the  $Q$  and temperature values, the  $Q(T)$  plots manifest the following dynamic modes with increasing temperature. First, the “normal” cooperative glass transition in PPG moieties between -60 and -50 °C is practically undisturbed by the network junctions or being located at some distance from them. This is confirmed by a high, cooperative value of  $Q = 280\text{--}300$  kJ mol<sup>-1</sup> and the temperature position of this relaxation which is



**Fig. 8.10** DMA spectra measured under tension and frequencies of 0.1, 1 and 10 Hz for neat PU network and PU-MWCNT-ox (0.25%) nanocomposite



**Fig. 8.11** Effective activation energy  $Q$  of segmental motion (relaxations that comprise the broad glass transition) as a function of temperature obtained for neat PU and PU-MWCNT-ox (0.25%) nanocomposite. The  $Q(T)$  dispersions were determined from the DMA spectra measured at 0.1, 1 and 10 Hz

close to the glass transition temperature of “free” PPG (around 200 K [42]).  $Q$  levels of 240, 200, 160 and 120 kJ mol<sup>-1</sup>, calculated for the temperatures of around -40, 0, 30 and 50 °C, respectively, characterize different PPG lower-cooperative and non-cooperative, Arrhenius segmental motions (last mode corresponds to  $Q = 120$  kJ mol<sup>-1</sup>). These motions are defined by reduction of intersegmental



motional cooperativity due to increasing free volume and loosening segmental packing with elevating temperature. Coincidence of  $Q(T)$  plots below 50 °C for neat PU and for the nanocomposite (Fig. 8.11) confirms the above-mentioned suggestion that nanotubes are concentrated mainly near the hard nanodomains of PU matrix, and therefore their presence does not change the activation barriers of motion in the PPG nanoregions undisturbed by MWCNTs.

However, at higher temperatures the  $Q(T)$  plots do not coincide (Fig. 8.11). In this region, the  $Q$  maxima observed are associated with unfreezing of the network-junction motion and the  $Q$  value increases to 160 kJ mol<sup>-1</sup> at about 80 °C for neat matrix but up to 260 kJ mol<sup>-1</sup> at 130 °C for the nanocomposite. Moreover, the latter peak covers the range from 100 to 150 °C, which suggests the occurrence of complicated dynamics in this region as well. Since the co-reaction of isocyanate groups in the formation of the PU network with functional groups of MWCNTs occurs, we assume that the high-temperature dynamics in the nanocomposite glass transition may be considered as network-junction motions that are hindered to different extents by their covalent attaching to MWCNTs. The notion about the complicated glass transition dynamics in the nanocomposites studied over the temperature range from -60 to 140 °C was directly confirmed also from the creep rate spectroscopy data (see next section).

It had been observed through another studies that varying the surface chemistry and in turn the interface, albeit in those cases high filler levels of MWCNTs were used and acid-oxidized-derived fulvic acids were not removed, could lead to substantial changes in the final composite properties. Therefore, it was anticipated that even at low filler levels, with a good degree of dispersion and after cleaning nanotubes from fulvic acids, such changes would reflect more correctly the actual interface state through the surface chemistry. Ultimately, the peculiar segmental dynamics in the nanocomposites studied manifested itself indeed in their enhanced mechanical properties.

Figure 8.12 shows the impact of MWCNTs introduced into PU on the polymer's dynamic modulus  $E'$  values when measured at 1 Hz over the broad temperature range. Figure 8.12a shows a considerable rise of  $E'$  with increasing MWCNT-ox content, up to three times at 20–100 °C at 0.25% nanofiller. Figure 8.12b compares the  $E'(T)$  plots for the nanocomposites with 0.25% nanofiller with different interfacial chemistry. Again, at van der Waals interfacial interactions (using MWCNT-hemin or MWCNT-hemin-red), effect is practically absent in comparison with unfilled matrix (Fig. 8.12b, curves 2 and 3). Whereas covalent interfacial bonding (using MWCNT-red and especially MWCNT-ox) provides the maximal enhancing of dynamic modulus of nanocomposites over the whole temperature range (Fig. 8.12b, curves 4 and 5).

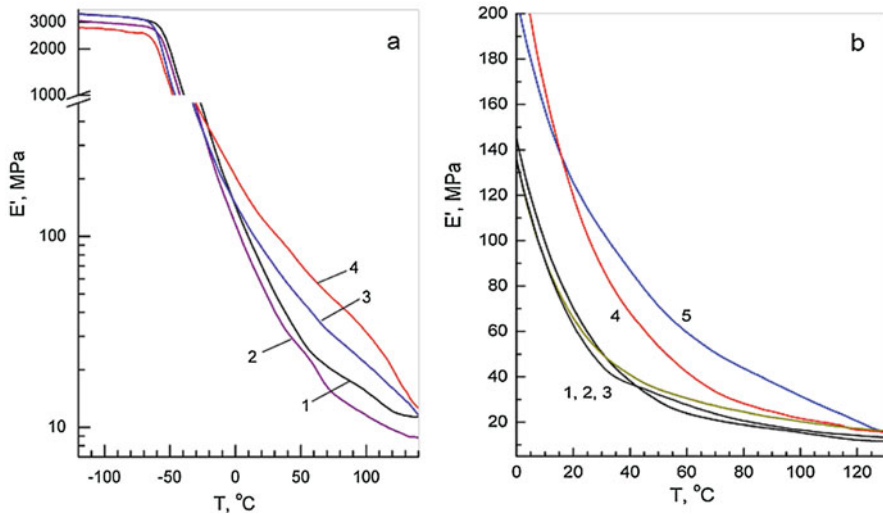


**Fig. 8.12** Dynamic (storage) modulus versus temperature plots obtained for neat PU (curve 1) and the PU-based nanocomposites. (a) PU-MWCNT-ox with 0.01 (curve 2), 0.1 (curve 3) and 0.25% nanotubes (curve 4); (b) PU-MWCNT nanocomposites at 0.25% loading with different functionalised nanotubes, MWCNT-hemin (curve 2), MWCNT-hemin-red (curve 3), MWCNT-red (curve 4) and MWCNT-ox (curve 5)

### 8.3.7 Creep Rate Spectra

Figure 8.13 shows the creep rate spectra obtained for neat PU and two PU-MWCNT-ox composites. As can be seen, this high-resolution technique allows the detailed study in a discrete way of the relaxation events where separate manifestations of a series of dynamic modes in the anomalously broadened glass transition occur.

It was previously shown for a neat PU network [43] that its creep rate spectrum located between  $-60$  and  $+50^{\circ}\text{C}$  consists of five partly overlapping peaks with the maxima at about  $-40$  (I),  $-30$  (II),  $-10$  (III),  $10$  (IV) and  $40^{\circ}\text{C}$  (V). Under testing at a chosen tensile stress of  $0.3$  MPa, the samples broke at  $50^{\circ}\text{C}$ . Peaks I–IV were assigned to the step-like “unfreezing” of a few segmental dynamic modes within the five-segmental PPG cross-links. Their manifestation could be explained by the different positions of segments regarding the network junctions and the operation of different hindering dynamics by those junctions. Peak V could be assigned to unfreezing of the network-junction motion.

Figure 8.13 shows that the introduction of  $0.1$  or  $0.25\%$  MWCNT-ox strongly enhances the mechanical/thermal performance of PU: at the same tensile stress of  $0.3$  MPa, sample breakage occurs at  $140^{\circ}\text{C}$  only. The main point herein is the cardinal changes within the creep rate spectrum. These changes consist first in a partial suppression of segmental dynamics (decreasing creep rates) at temperatures below  $30^{\circ}\text{C}$ ; the qualitatively similar effects were previously observed

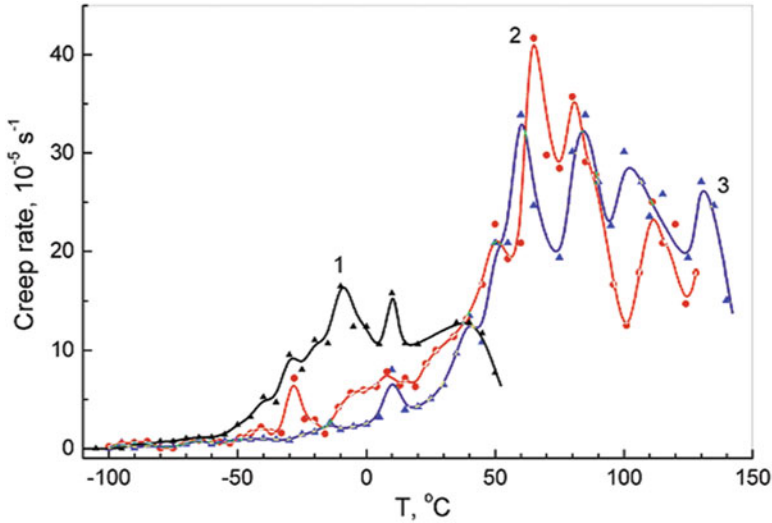


**Fig. 8.13** Creep rate spectra obtained under a tensile stress  $\sigma = 0.3$  MPa for neat PU (1), PU-MWCNT-ox (0.1%) (2) and PU-MWCNT-ox (0.25%) (3) nanocomposites

for PU-nanodiamond composites [44]. Secondly, Fig. 8.13 shows that four new intense peaks with their maxima at about 60–70, 80, 100–110 and 130 °C are recorded in the spectra of the PU-MWCNT-ox nanocomposites. This is surmised to occur in accordance with the above hypothesis about various constraining of network-junction dynamics caused by covalent attaching to nanotubes. At last, it could be seen that increasing nanotube content from 0.1 to 0.25% results in the larger suppression of dynamics below 30 °C and the redistribution of the higher-temperature peaks' intensities in favour of the peaks with the maxima at 100 and 130 °C characterizing network-junction motions hindered to the largest extent by their covalent attaching to MWCNTs.

### 8.3.8 Mechanical Properties of the Nanocomposites

The introduction of MWCNTs into PU alters the stress-strain curves, depending on the type and amount of MWCNTs used (Fig. 8.14a–d). On the whole, the tensile strength of nanocomposite films may be increased from 2 MPa to 4–5 MPa compared with that for neat matrix. With MWCNT-red only the 0.25 wt. % sample shows a significant increase in tensile strength, by around 100% over native PU (Fig. 8.15a). MWCNT-hemin-red-containing samples exhibit an improved tensile strength with increasing content of nanotubes (Fig. 8.15a), whereas introducing MWCNT-hemin results in the negligibly small changes in strength only. The most interesting results were obtained for nanocomposites containing MWCNT-ox. Even

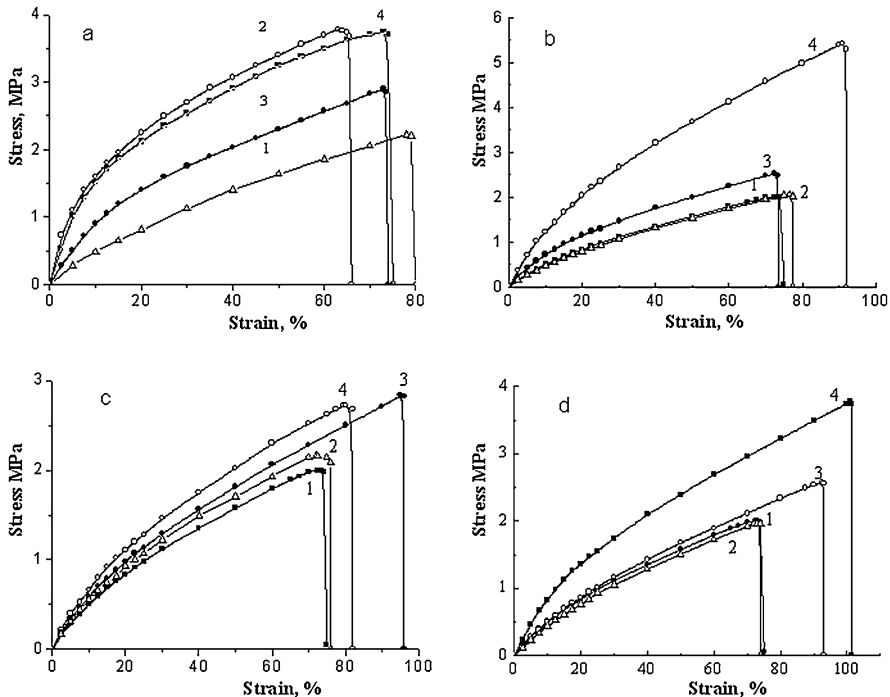


**Fig. 8.14** The effects of MWCNT type and content (wt. %) on the tensile stress-strain plots for neat PU (curve 1) and nanocomposites containing MWCNT-ox (a), MWCNT-red (b), MWCNT-hemin (c) and MWCNT-hemin-red (d) at their contents of 0.01 (curves 2), 0.10 (curves 3) and 0.25% (curves 4)

at low content of MWCNT-ox (0.01%), the mechanical performance of the PU host matrix can be enhanced twice (Fig. 8.14a).

The difference in Young's modulus values is also apparent, with samples exhibiting an increasing modulus with increasing filler concentration (Fig. 8.15b). The Young's modulus for the composites containing MWCNT-ox increased by up to 2–4 times depending on concentration of nanotubes. Such mechanical performance is probably the result of covalent bonding of MWCNT-ox with PU matrix. The nanocomposites containing MWCNT-ox, which are covalently bound with the matrix, exhibit interphase layers connecting the polymer to the surface of MWCNT-ox. These layers provide additional junctions with the surface of nanofiller and are stronger in comparison with the free polymer. These interphase layers retard stretching of the polymer chains when applying the force. As result, the Young's modulus values for the nanocomposites containing MWCNT-ox are higher in comparison with nanocomposites containing mechanically weaker interphase layers (Fig. 8.15b).

However, non-monotonic increase in Young's modulus with concentration of MWCNT-ox was also observed (Fig. 8.15b). For MWCNT-ox at 0.10 wt%, there is

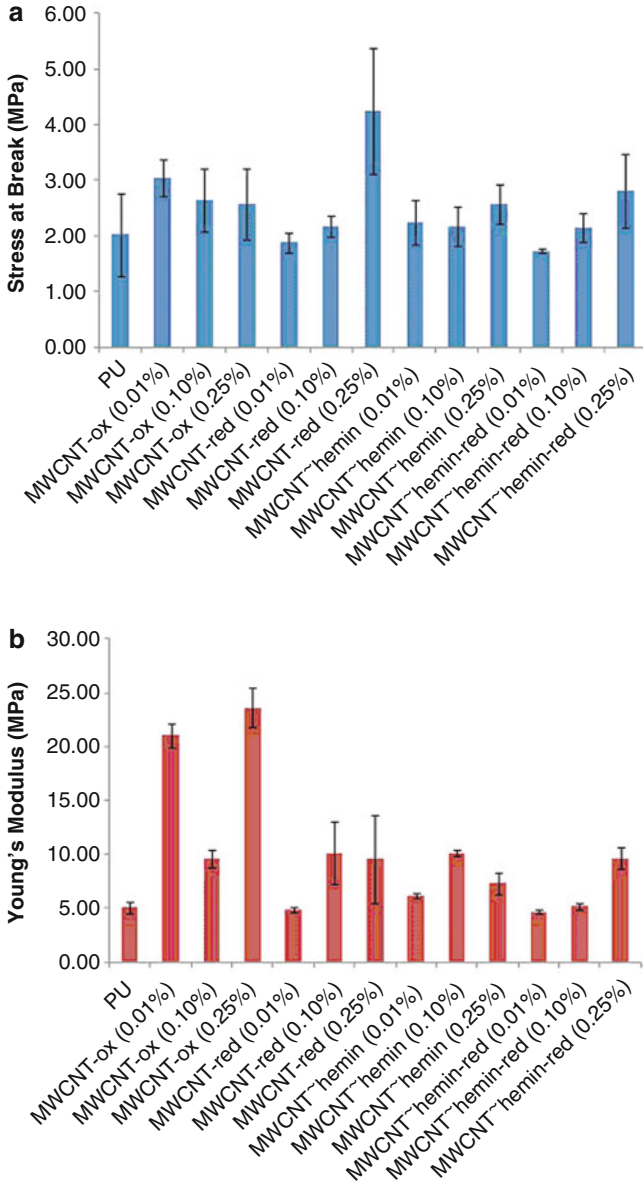


**Fig. 8.15** Comparative effects for (a) stress at break (MPa) and (b) Young's modulus (MPa) of PU nanocomposites containing MWCNT-ox, MWCNT-red, MWCNT-hemin and MWCNT-hemin-red (0.01, 0.10 and 0.25%)

a noticeable drop compared with 0.01 and 0.25 wt%, which could be connected with changes in structure of polyurethane matrix induced by the addition of MWCNT-ox (Fig. 8.3). The presence of 0.1% MWCNT-ox in the nanocomposites results in a dramatic change in the structure of polyurethane where the complete disappearance of the hard and soft domains could be observed (Fig. 8.3).

Although the highest additive of MWCNTs studied in our investigation was 0.25 wt. %, our results align well with studies carried out by Wei Chen et al. [45], where it was found that increasing the MWCNT fraction in a PU matrix also increased the tensile strength and modulus [45]. However, the authors [45] used the thermoplastic polyurethane elastomer as a matrix for the generation of nanocomposites and introduced the minimal amount of MWCNTs 5.6 wt.%. Significant improvement in Young's modulus and tensile strength in this work were achieved for MWCNT content of 9.3 wt.% only [45].

The comparison of covalent and ionic bonding between MWCNTs and PU has been previously explored by H-C Kuan et al. [46], but their MWCNT-ox did not include the procedure of removal of in situ generated and surface-immobilised fulvic acids. In this study, it was found that MWCNT-ox provide the higher Young moduli than MWCNT-red and also the non-covalent systems, but these results could be obtained because of the higher content of nanotubes (4%) [46].

McClory et al. [22] used thermosetting PU for synthesizing MWCNT nanocomposites with nanotube content up to 1 wt. % and also recorded significant enhancements in stiffness, strength and toughness. Wang et al. [11] created PU-MWCNT nanocomposites with good mechanical properties due to covalent cross-linking of MWCNTs to the PU matrix using poly(acryloyl chloride).

Given that hemin interacts with the MWCNT in the same manner as fulvic acids, generated by the lattice degradation through acid digestion under oxidation, it can be inferred that the presence of such fulvic acids on improperly treated and purified MWCNT-ox can lead to a retardation of the mechanical performance of the final nanocomposites.

In the case of MWCNT-red, the number of available alcohol sites increases over the number of carboxylic groups for MWCNT-ox, and yet the mechanical performance, by comparison, diminishes. The number of surface acidic groups on oxidised and reduced MWCNTs should be approximately the same given that the lithium aluminium hydride treatment does not exhibit any signs of surface group removal or lattice degradation and preferentially forms alcohol groups that should promote connectivity to PU during polymerisation. The increased performance of MWCNT-ox implies that either carboxylic groups on MWCNT-ox are more reactive than the alcohol (and phenol) groups on MWCNT-red or the formation of a urethane group through the now pendant aliphatic alcohol group (on MWCNT-red) is mechanically weaker than the linkage through the carboxylic group (on MWCNT-ox) in the reaction of the isocyanate monomer with surface acidic groups.

Given that the number of carboxylic groups on MWCNT-hemin is greater than MWCNT-hemin-red and MWCNT-ox and between the two hemin species there is little to separate their mechanical performance, it strongly suggests that mechanical strength does not solely come from a greater quantity of carboxylic groups, but

the nature in which those carboxylic groups are arranged and the strength of their interaction with the MWCNT surface is vitally important. Hemin being non-covalently bound to the surface of the carbon nanotube solely interacts with the nanotube surface through van der Waals forces. Whilst immobilised hemin improves the “functionalisation” equivalent of MWCNT-ox and also their dispersibility and greater bonding interaction with the PU without sacrificing the structural integrity of the carbon nanotube, it is apparent that the surface force interaction between the MWCNT and hemin molecule is weaker than the covalent system of MWCNT-ox. The underlying mechanical integrity of MWCNTs is therefore not reflected in the tensile performance of the non-covalent bonded systems.

## 8.4 Conclusions

Nanocomposites based on PU matrix and MWCNTs, containing carboxyl, lactone or phenol groups on the surface, were prepared and investigated. MWCNTs were incorporated into the PU matrix in the process of PU synthesis either through covalent or van der Waals forces. The structural peculiarities, the thermodynamic miscibility, dynamic and static mechanical properties and segmental dynamics of composites have been investigated. Overall, it was found that the functional groups for PU attachment that were covalently bonded to the MWCNT lattice possessed superior mechanical performance to those functional groups that were immobilised through van der Waals forces to the MWCNT surface. The necessity to remove acid-oxidative lattice fragments (fulvic acids) from MWCNT-ox samples to ensure only covalent bonding with PU matrix is shown.

The vapour sorption by nanocomposites and by nanofiller was studied, and thermodynamic affinity of polymer components to the MWCNT was estimated. It was shown that free energy of interaction between the carbon nanotubes with functionalized surfaces and with polyurethane matrix is negative for all types of nanofillers. This indicates the thermodynamic stability of filled polyurethane samples and suggests high adhesion of polyurethane to carbon nanotubes with functionalized surfaces.

The dynamics in PU-MWCNT nanocomposites with low filler contents was performed using a combined DMA-CRS approach. The strong dependence between matrix dynamics and variations in the nanotube surface chemistry was demonstrated. It was found that the interface between the nanotube and a van der Waals immobilized intermediate leads to unchanged dynamics and mechanically weaker composites. Only direct covalent bonding of matrix to carbon nanotube lattice, which is free from fulvic acids, results in the dramatic changes in the glass transition dynamics of PU matrix even at low filler content. As a result, the displacement of main PU relaxation maxima in the complicated DMA and creep rate spectra, manifesting a pronounced dynamic heterogeneity within the glass transition, from around 0 to 80–140 °C was shown.

Due to the change in fundamental interaction at the interface, two- or threefold enhancement in the dynamic and static mechanical properties is attained for low-filler content thermosetting PU-MWCNT nanocomposites compared with that of neat PU matrix.

## References

1. Spitalsky Z, Tasis D, Papagelis D, Galiotis S (2010) Carbon nanotube-polymer composites: chemistry, processing, mechanical and electrical properties. *Prog Polym Sci* 35:357–401. <https://doi.org/10.1016/j.progpolymsci.2009.09.003>
2. Sahoo NG, Rana S, Cho JW, Li L, Chan SH (2010) Polymer nanocomposites based on functionalized carbon nanotubes. *Prog Polym Sci* 35(7):837–867. <https://doi.org/10.1016/j.progpolymsci.2010.03.002>
3. Pagona G, Mountrichas G, Kotas G, Karousis N, Pispas S, Tarmatarchis N (2009) Properties, applications and functionalization of carbon nanotubes. *Int J Nanotechnol* 6:176–185
4. Wu H-C, Chang X, Liu L, Zhao F, Zhao Y (2010) Chemistry of carbon nanotubes in biomedical applications. *J Mater Chem* 20:1036–1052. <https://doi.org/10.1039/B911099M>
5. Gao C, Jin YZ, Kong H, Whitby RLD, Acquah SFA, Chen GY et al (2005) Polyurea-functionalized multi-walled carbon nanotubes: synthesis, morphology, and Raman spectroscopy. *J Phys Chem B* 109:11925–11932. <https://doi.org/10.1021/jp051642h>
6. Balasubramanian K, Burghard M (2005) Chemically functionalized carbon nanotubes. *Small* 1:180–192. <https://doi.org/10.1002/sml.200400118>
7. Leahy MD, Cooper SL (1986) *Polyurethane in medicine and surgery*. CRC Press, Boca Raton, pp 158–167
8. Lloyd AW, Faragher RG, Denyer SP (2001) Ocular biomaterials and implants. *Biomaterials* 22(8):769–785. [https://doi.org/10.1016/S0142-9612\(00\)00237-4](https://doi.org/10.1016/S0142-9612(00)00237-4)
9. Karabanova LV, Lloyd AW, Mikhalovsky SV, Helias M, Philips GJ, Rose SF, Mikhalovska L et al (2006) Polyurethane/Poly(hydroxyethyl methacrylate) semi-interpenetrating polymer networks for biomedical applications. *J Mater Sci Mater Med* 17:1283–1296. <https://doi.org/10.1007/s10856-006-0603-y>
10. Jiang F, Hu G, Zhang L (2008) Preparation and characterization of polyurethane/multi-walled carbon nanotubes composites with multifunctional performance. *Adv Mater Res* 47-50: 765–768
11. Wang X, Du Z, Zhang C, Li C, Yang X, Li H (2008) Multi-walled carbon nanotubes encapsulated with polyurethane and its nanocomposites. *J Polym Sci A Polym Chem* 46:4857–4865. <https://doi.org/10.1002/pola.22818>
12. Jana RN, Cho JW (2008) Thermal stability and molecular interaction of polyurethane nanocomposites prepared by in situ polymerization with functionalized multi-walled carbon nanotubes. *J Appl Polym Sci* 108(5):2857–2864. <https://doi.org/10.1002/app.27895>
13. Jana RN, Yoo HJ, Cho JW (2008) Synthesis and properties of shape memory polyurethane nanocomposites reinforced with poly( $\epsilon$ -caprolactone)-grafted carbon nanotubes. *Fibers Polym* 9:247–254
14. Raja M, Shanmugaraj AM, Ryu SH (2008) Influence of surface functionalized carbon nanotubes on the properties of polyurethane nanocomposites. *Soft Mater* 6:65–74
15. Kwon J-Y, Kim H-D (2005) Preparation and properties of acid-treated multi-walled carbon nanotube/waterborne polyurethane nanocomposites. *J Appl Polym Sci* 96:595–604. <https://doi.org/10.1002/app.21436>
16. Fernández M, Landa M, Muñoz ME, Santamaría A (2010) Thermal and viscoelastic features of new nanocomposites based on a hot-melt adhesive polyurethane and multi-walled carbon nanotubes. *Macromol Mater Eng* 295:1031–1041



17. Zhao W, Li M, Peng H-X (2010) Functionalized MWNT-doped thermoplastic polyurethane nanocomposites for aerospace coating applications. *Macromol Mater Eng* 295:838–845. <https://doi.org/10.1002/mame.201000080>
18. Meng Q, Hu J, Zhu Y (2007) Shape-memory polyurethane/multi-walled carbon nanotube fibers. *J Appl Polym Sci* 106:837–848. <https://doi.org/10.1002/app.26517>
19. Cho JW, Kim JW, Jung YC, Goo NS (2005) Electroactive shape-memory polyurethane composites incorporating carbon nanotubes. *Macromol Rapid Commun* 26:412–416. <https://doi.org/10.1002/marc.200400492>
20. Bandarian M, Shojaei A, Rashidi AM (2011) Thermal, mechanical and acoustic damping properties of flexible open-cell polyurethane/multi-walled carbon nanotube foams: effect of surface functionality of nanotubes. *Polym Int* 60:475–482. <https://doi.org/10.1002/pi.2971>
21. Nguyen DA, Lee YR, Raghu AV, Jeong HM, Shin CM, Kim BK (2009) Morphological and physical properties of a thermoplastic polyurethane reinforced with functionalized graphene sheets. *Polym Int* 58:412–417
22. McClory C, McNally T, Brennan GP, Erskine J (2007) Thermosetting polyurethane multiwalled carbon nanotube composites. *J Appl Polym Sci* 105:1003–1011. <https://doi.org/10.1002/app.26144>
23. Coleman JN, Khan U, Blau WJ, Gun'ko YK (2006) Small but strong: a review of the mechanical properties of carbon nanotube-polymer composites. *Carbon* 44:1624–1652. <https://doi.org/10.1016/j.carbon.2006.02.038>
24. Wang ZW, Shirley MD, Meikle ST, Whitby RLD, Mikhailovsky SV (2009) The surface acidity of acid oxidized multi-walled carbon nanotubes and the influence of in-situ generated fulvic acids on their stability in aqueous dispersions. *Carbon* 47:73–79. <https://doi.org/10.1016/j.carbon.2008.09.038>
25. Wang Z, Korobeinyk A, Whitby RLD, Meikle ST, Mikhailovsky SV, Acquah SFA, Kroto HW (2010) Direct confirmation that carbon nanotubes still react covalently after removal of acid-oxidative lattice fragments. *Carbon* 48:916–918. <https://doi.org/10.1016/j.carbon.2009.10.025>
26. Karabanova LV, Whitby RLD, Korobeinyk A, Bondaruk O, Salvage JP, Lloyd AW, Mikhailovsky SV (2012) Microstructure changes of polyurethane by inclusion of chemically modified carbon nanotubes at low filler contents. *Compos Sci Technol* 72:865–872. <https://doi.org/10.1016/j.compscitech.2012.02.008>
27. Karabanova LV, Whitby RLD, Bershtein VA, Korobeinyk AV, Yakushev PN, Bondaruk OM, Lloyd AW, Mikhailovsky SV (2013) The role of interfacial chemistry and interactions in the dynamics of thermosetting polyurethane-multi-walled carbon nanotube composites with low filler content. *Colloid Polym Sci* 291(3):573–583. <https://doi.org/10.1007/s00396-012-2745-4>
28. Karabanova LV, Boiteux G, Gain O et al (2004) Miscibility and thermal and dynamic mechanical behaviour of semi-interpenetrating polymer networks based on polyurethane and poly(hydroxyethyl methacrylate). *Polym Int* 53(12):2051–2058. <https://doi.org/10.1002/pi.1627>
29. Bershtein VA, Yakushev PN (2010) Laser-interferometric creep rate spectroscopy of polymers. *Adv Polym Sci* 230:73–219. [https://doi.org/10.1007/12\\_2009\\_36](https://doi.org/10.1007/12_2009_36)
30. Boehm HP (2002) Surface oxides on carbon and their analysis: a critical assessment. *Carbon* 40(2):145–149. [https://doi.org/10.1016/S0008-6223\(01\)00165-8](https://doi.org/10.1016/S0008-6223(01)00165-8)
31. Yang M, Gao Y, Li HM, Adronov A (2007) Functionalization of multiwalled carbon nanotubes with polyamide 6 by anionic ring-opening polymerization. *Carbon* 45(12):2327–2333. <https://doi.org/10.1016/j.carbon.2007.07.021>
32. Sun YP, Fu KF, Lin Y, Huang WJ (2002) Functionalized carbon nanotubes: properties and applications. *Acc Chem Res* 35(12):1096–1104 Indexed for MEDLINE
33. Liu LQ, Qin YJ, Guo ZX, Zhu DB (2003) Reduction of solubilised multi-walled carbon nanotubes. *Carbon* 41(2):331–335. [https://doi.org/10.1016/S0008-6223\(02\)00286-5](https://doi.org/10.1016/S0008-6223(02)00286-5)
34. Shilov VV, Karabanova LV, David L, Boiteux G, Seytre G, YuP G, Nesin SD, Sergeeva LM, Lutsyk ED, Svyatina AV (2005) The structure peculiarities of the polyurethane/poly(hydroxyethyl methacrylate) semi-interpenetrating polymer networks. *Polym J Ukr* 27(4):255–263

35. Bonart R, Muller EH (1974) Phase separation in urethane elastomers as judged by low-angle x-ray-scattering. 1. Fundamentals. *J Macromol Sci Phys* 10(B):177–189
36. Ryszkowska J, Jurczyk-Kowalska M, Szymborski T, Kurzydowski KJ (2007) Dispersion of carbon nanotubes in polyurethane matrix. *Phys E Low Dimens Syst Nanostruct* 39(1):124–127. <https://doi.org/10.1016/j.physe.2007.02.003>
37. Тагер АА (1972) Термодинамическая устойчивость систем полимер – растворитель и полимер – полимер. *Высокомолекулярсоед Сер А* 14(12):2690–2698
38. Бессонов ЮС, Тагер АА, Юшкова СМ et al (1978) Термодинамическое исследование взаимодействия в наполненных композициях поливинилхлорида. *Высокомолекулярсоед Сер А* 20(1):99–105
39. Kwei T (1965) Polymer-filler interaction thermodynamic calculations and a proposed model. *J Polym Sci A* 3(9):3229–3237. <https://doi.org/10.1002/pol.1965.100030917>
40. Karabanova LV, Boiteux G, Seytre G, Stevenson I, Gain O, Shady C, Lutsyk ED, Svyatyna A (2009) Semi-interpenetrating polymer networks based on polyurethane and poly(2-hydroxyethyl methacrylate): dielectric study of relaxation behavior. *J Non-Cryst Solids* 355:1453–1460. <https://doi.org/10.1016/j.jnoncrysol.2009.05.002>
41. Giannelis EP, Krishnamoorti R, Manias E (1999) Polymer-silicate nanocomposites: model systems for confined polymers and polymer brushes. *Adv Polym Sci* 138:107–147 Google Scholar
42. Sidebottom DL, Bergman R, Börjesson L, Torell LM (1993) Scaling behaviour in poly(propylene glycol) in the glass transition range. *Progr Colloid Polym Sci* 91:43–45
43. Karabanova LV, Sergeeva LM, Svyatyna AV, Yakushev PN, Egorova LM, Ryzhov VA, Bershtein VA (2007) Heterogeneity of glass transition dynamics in polyurethane-poly(2-hydroxyethyl methacrylate) semi-interpenetrating polymer networks. *J Polym Sci B Polym Phys* 45:963–975. <https://doi.org/10.1002/polb.21108>
44. Karabanova LV, Bershtein VA, Sukhanova TE, Yakushev PN, Egorova LM, Lutsyk ED, Svyatyna AV, Vylegzhanina ME (2008) 3D diamond-containing nanocomposites based on hybrid polyurethane-poly(2-hydroxyethyl methacrylate) semi-IPNs: composition-nanostructure-segmental dynamics-elastic properties relationships. *J Polym Sci B Polym Phys* 46:1696–1712. <https://doi.org/10.1002/polb.21506>
45. Chen W, Tao X, Liu Y (2006) Carbon nanotube-reinforced polyurethane composite fibers. *Compos Sci Technol* 66(15):3029–3034. <https://doi.org/10.1016/j.compscitech.2006.01.024>
46. Kuan H-C, Ma C-C, Chang W-P, Yuen S-M, Wu H-H, Lee T-M (2005) Synthesis, thermal, mechanical and rheological properties of multiwall carbon nanotube/waterbone polyurethane nanocomposite. *Compos Sci Technol* 65(11–12):1703–1710. <https://doi.org/10.1016/j.compscitech.2005.02.017>

# Chapter 9

## Polymeric Composite Films with Controlled Release of Natural Antioxidant Enoxil



Roman Kozakevych, Yulia Bolbukh, Lucian Lupascu, Tudor Lupascu,  
and Valentin Tertykh

### 9.1 Introduction

Among the biologically active plant compounds, one of the first places in the prevalence is polyphenols, which are an outstanding source of variety of compounds with extraordinary diverse composition [1, 2]. Several thousand molecules having a polyphenol structure have been identified in higher plants. These compounds may be classified into different groups as a function of the number of phenol rings that they contain and of the structural elements that bind these rings to one another. The polyphenols fall into the following types of chemical substances: phenolic acids, flavonoids, stilbenes, lignans, catechins, etc.

In addition, residual materials containing polyphenols are widely available, which is why it is a very attractive subject for study. Recent interest in food polyphenols has increased greatly, owing to their antioxidant capacity [3] (free radical scavenging and metal chelating activities) and possible beneficial implications in human health, such as in the treatment and prevention of cancer, cardiovascular disease, and antimicrobial activity [4–6].

As is well known, the disruption of normal levels of free radicals and reactive oxygen species causes damage to organs and tissues [7]. That will, in turn, contribute to the decreased immunity and a number of infectious diseases. The inflammatory process is a normal reaction of the mucosa to infection, which usually leads to the destruction of pathogens. However, the long-term presence of highly active cells and free radicals in the area of inflammation leads to an uncontrolled reaction and

---

R. Kozakevych (✉) · Y. Bolbukh · V. Tertykh  
Chuiiko Institute of Surface Chemistry, National Academy of Sciences of Ukraine, Kyiv, Ukraine

L. Lupascu · T. Lupascu  
Institute of Chemistry of the Academy of Sciences of Moldova, Chisinau, Republic of Moldova

serious and even irreversible tissue damage due to the destruction of collagen and the peroxidation of cell membranes. Antibiotics are increasingly used to prevent and treat bacterial infectious diseases. The stability of pathogenic bacteria is developed when their application is excessive and uncontrolled. In the future of increasing antibiotic resistance, the development of new strategies to fight bacteria will be welcome [8].

Antimicrobial and antiviral properties of plant polyphenols were found in extracts isolated from various plant objects. The decoction of *Cocos nucifera L.* husk fibers has been used in northeastern Brazil traditional medicine for treatment of diarrhea and arthritis. Water extract obtained from coconut husk fiber revealed antimicrobial activity against *Staphylococcus aureus*. One of the fractions rich in catechin also showed inhibitory activity against acyclovir-resistant herpes simplex virus [9]. The native tannin also can be used as biologically active materials with antioxidant and bacteriostatic properties. Oxidized tannins are utilized as effective biologically active matters in nutritional supplements [10]. The wide distribution of polyphenol compounds in plants, low toxicity, and high pharmacological activity may be promising for the development of a number of drugs based on them.

The article [11] presents data about the antimicrobial activity of the autochthonous compound of tannin source Enoxil. Enoxil preparation was obtained from wine waste following oxidation of enotannins with hydrogen peroxide. It was established that the Enoxil compounds suppress activity of *Pseudomonas* bacteria.

The search for carriers will be promising for this purpose. Further improvement of the preparations of Enoxil group may be performed by immobilizing such natural antioxidant on the surface of nonporous nanosilica, allowed for use as food additives and fillers [12, 13].

Among the polymeric carriers, gelatin stands out strongly due to several key advantages, namely, this natural polymer is highly biocompatible and biodegradable in a physiological environment. In addition, release kinetics from gelatin depends on carrier degradation, which can be tuned by varying gelatin molecular weight, the extent of material cross-linking, or synergistic use of gelatin with several other polymeric materials. Gelatin and chitosan form polyionic complexes, and therefore composite construction, drug release kinetics, and degradation can be modified. In work [14] gelatin/chitosan sponges have been investigated for use as release vehicles for wound treatment. In addition to sponges, gelatin/chitosan microparticles have been successfully designed, with sustained delivery of basic fibroblast growth factor for over 2 weeks in vitro. In study [15] it was reported on simultaneous copolymerization of 2-hydroxyethyl methacrylate with gelatin using blending and casting method, where simultaneous evaporation at room temperature was the driving force.

The aim of this work was to prepare the silica-Enoxil nanobiocomposites and Enoxil-polymer films to study the active substance release rate.

## 9.2 Materials and Methods

The Enoxil preparation, developed by the Institute of Chemistry of the Academy of Sciences of Moldova, is a set of biological polyphenols and served as an antimicrobial agent. It was obtained by extraction from grape seeds using ethanol p.a. as a solvent. For increasing the solubility in water, enotannins were chemically treated with  $\text{H}_2\text{O}_2$ , which has led to depolymerization of catechin and epicatechin oligomers, and, as a result, novel hydrophilic product (Enoxil) has been obtained.

The composite system of nanosized nonporous hydrophilic fumed silica A-300 (specific surface area of  $300 \text{ m}^2/\text{g}$ , Kalush, Ukraine) with Enoxil was performed by mixing 3 g of silica with 75 mL of Enoxil aqua solution (8.0 mg/mL). After impregnation, the composite was dried at  $80^\circ\text{C}$ .

The Enoxil-silica gel composites were prepared by in situ polycondensation (gelation) of the precursors tetraethoxysilane (TEOS) or mixture of TEOS and phenyltrimethoxysilane (PhTMS). In a typical process, initially 0.6 g of Enoxil was dissolved in 15 ml of a mixture (10 ml  $\text{H}_2\text{O}$  + 5 ml  $\text{C}_2\text{H}_5\text{OH}$ ) at  $40^\circ\text{C}$  under acidic conditions produced by the addition of 1 mL HCl (0.1 M). A dissolution was achieved after 1 h of continuous mechanical stirring of the solution. Then, 11 mL TEOS or 5 ml of mixture (2 ml TEOS and 3 ml PhTMS) was added to the abovementioned solution followed by continuous stirring for another 2 h at  $40^\circ\text{C}$ . And the solution was remained constant over 12 h to aging of a gel. Thereafter, the solution was treated at  $80^\circ\text{C}$  for 4 h. After cooling down to room temperature, the solid products were washed and dried at  $70^\circ\text{C}$ .

Gelatin commercially available and chitosan of low viscosity and deacetylation degree of 70% (Fluka) were used without addition treatment. The monomers used 2-hydroxyethyl methacrylate (HEMA), (3-aminopropyl)triethoxysilane, and triethoxyvinylsilane were purchased from Aldrich with purity  $\geq 99\%$ .

### 9.2.1 Preparation of Polymeric Composite Films

Various polymers were used to form composite films.

For preparation of gelatin/HEMA (Gel/HEMA) films into the gelatin water solution were added HEMA and HEMA pretreated with a mixture amino- and vinylsilane (3-aminopropyl)triethoxysilane and triethoxyvinylsilane) in the 1:1 molar ratio (silica precursor content was 10 wt%) for preparing Gel/HEMA/VA films.

Gelatin/chitosan films were prepared by a casting solvent evaporation technique. 3 wt % chitosan solution in 1 wt% acetic acid was mixed with 3 wt% gelatin aqueous solution under stirring at the room temperature. Initial mixture was divided into two parts, to forming pure (Gel/Chit) and filled with carbon nanotubes (Gel/Chit/NT) materials. The filling degree was 0.1 wt% MWCN obtained from the Chuiko Institute of Surface Chemistry of National Academy of Sciences of Ukraine.

Multicomponent systems, namely, gelatin/chitosan/HEMA (Gel/Chit/HEMA) and gelatin/chitosan/HEMA composite, cross-linked with mixture of functional amino- and vinylsilane (Gel/Chit/HEMA/VA) were composed in weight ratio of polymers 1:1:1.

Then all solutions are left to stand until trapped air bubbles were removed. The mixtures were poured into a 75 mm petri dish; the dishes were placed in an oven at 70 °C for 4 h.

Loading of Enoxil into the composite films was performed by mixing 0.5 g of dried films with 3 mL of Enoxil solution (33.0 mg/mL). After impregnation for 24 h, the polymer films were dried at 80 °C for 2 h.

Infrared (FTIR) spectra were collected using a Thermo Nicolet Nexus 450 from 4000 to 500  $\text{cm}^{-1}$  and resolution of 4  $\text{cm}^{-1}$ , using KBr pellets in weight ratio sample: KBr as 1:20.

The ATR spectra were recorded using spectrometer Bruker (Germany) in the spectral range of 600–4000  $\text{cm}^{-1}$  with 16 scans per spectrum at a resolution of 4  $\text{cm}^{-1}$ .

Differential scanning calorimetry (DSC) was performed under nitrogen atmosphere in the temperature range from 20 to 450 °C using a NETZSCH DSC 204F1 Phoenix instrument.

The swelling capacity of the composition films was measured at the room temperature in the distillate water using gravimetric techniques on three replicas. For this, the hydrogel samples were dried at 70 °C in oven overnight. The drying procedure was completed upon reaching constant mass loss values.

Then after the samples were immersed in deionized water for 3 days and the wet weight of each sample was recorded, the percentage of swelling was calculated from the formula

$\alpha = (m - m_0/m_0) \times 100\%$ , where  $m_0$  and  $m$  are the masses of film before and after sample swelling.

In vitro Enoxil release test (dissolution test) has been performed according to the requirements of the State Pharmacopoeia of Ukraine using the rotating basket method. The distilled water has been used as a dissolution medium; for each formulation, dissolution test has been conducted on 200 mg of active component (Enoxil) using 500 mL of dissolution medium. The distance between inside bottom of dissolution vessel and basket is maintained at  $25 \pm 2$  mm. The release experiment was performed at 37 °C under stirring rate of 100 r/min. Samples for measurement of drug release were taken in time intervals (shown in experimental). Samples of 2 mL were taken, and each sampling was followed by addition of 2 mL of fresh medium into dissolution vessels. Enoxil concentration in aqueous solution was determined spectrophotometrically. Prior to determination of Enoxil concentration, samples were filtered.

Different dissolution models (such as Higuchi and Korsmeyer-Peppas) were applied to active compound release data in order to evaluate release mechanisms and kinetics. A very frequently used and easy-to-apply model to describe drug release is the so-called Korsmeyer-Peppas equation or power law:

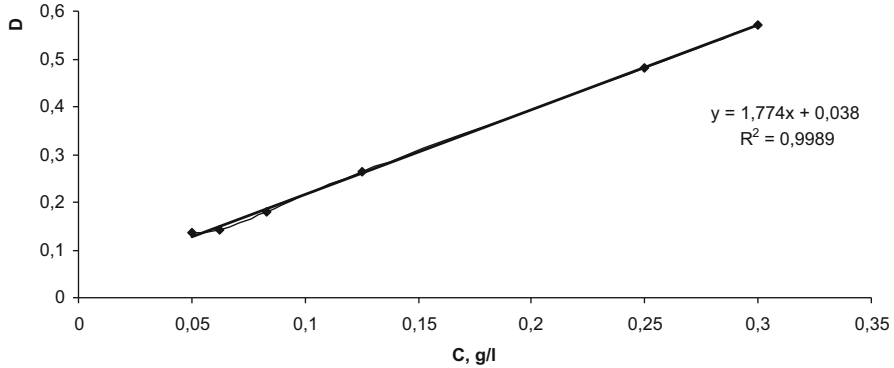


**Fig. 9.1** The calibration curve of spectrophotometrical determination of Enoxil in water at  $\lambda = 310$  nm

$F = m_t/m_\infty = kt^n$ , where  $F$  is the fractional release of drug;  $m_t$  and  $m_\infty$  are the absolute cumulative amount of drug released at time  $t$  and infinite time, respectively;  $k$  is the kinetic release constant incorporating structural and geometrical characteristics of the dosage form ( $\text{h}^{-n}$ );  $t$  is the elapsed time; and  $n$  is the release exponent describing the drug release mechanism. The release exponent  $n = 0.5$  corresponds to a fully Fickian diffusion based on transport of drug to the dissolution medium. In such case, the Korsmeyer-Peppas model would be reduced to the Higuchi equation:  $F = kt^{1/2}$ , where  $k$  is the Higuchi dissolution constant.

Criteria for selecting the most appropriate model were based on linearity (coefficient of correlation).

Determination of Enoxil concentration has been carried out using UV spectrophotometer Specord M-40 (absorption wavelength 310 nm). The calibration curve constructed according to experimentally obtained data using the linearization method is depicted in Fig. 9.1.

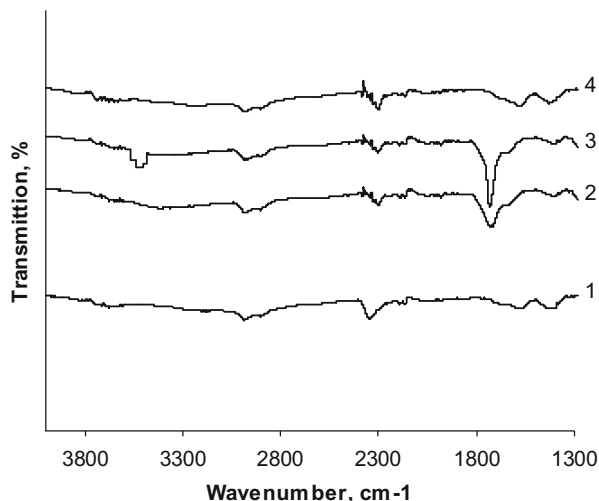
As microbial cultures, served several pathogens with severe complications in many contagious diseases-bacteria, namely, *Pseudomonas aeruginosa*.

## 9.3 Results and Discussion

### 9.3.1 IR Spectral Study

Interaction of Enoxil with silica matrix was performed using IR spectroscopy. IR spectra of Enoxil, Enoxil-A-300 composite, Enoxil-sol-gel silica composite, and Enoxil-sol-gel silica with phenyl groups are given in Fig. 9.2. The Enoxil spectrum (curve 3) shows the broad band with a absorption maximum at  $3420 \text{ cm}^{-1}$  due

**Fig. 9.2** FTIR spectra of Enoxil (3), Enoxil-A-300 composite (2), Enoxil-sol-gel silica composite (1), and Enoxil-sol-gel silica with phenyl groups (4)



to O–H vibrations and strong hydrogen bindings, the band at  $2928\text{ cm}^{-1}$  related to the symmetric C–H stretching vibrations of  $\text{CH}_2$  and  $\text{CH}_3$  groups, the band at  $1730\text{ cm}^{-1}$  that corresponds to C=O stretching vibrations and is associated with the presence of carboxylic acids (dimers), the band at  $1630\text{ cm}^{-1}$  assigned to the symmetric C–O– stretching vibrations in the aromatic rings, and the band at  $1400\text{ cm}^{-1}$  attributed to the deformation vibrations of the C–C bonds in phenolic groups.

The obtained result testified that Enoxil on the surface A-300 was not significantly affected by the functional groups of the silica surface. In contrast, a capsulation of Enoxil inside silica gel network coursed the stronger silica-Enoxil interaction. It is confirmed by FTIR spectra (curves 1 and 4). The profile of IR spectra is changed in the region of carbonyl-carboxyl vibrations.

### 9.3.2 Enoxil Release from Composite with Silicas

The analysis of the profile release of Enoxil from pristine fumed silica carrier and silica composites prepared by sol-gel method with different surface functionalities has shown different regularities. The Enoxil release profiles for silica composite carriers are presented in Fig. 9.3. The Enoxil contents for all samples under study were similar.

The Enoxil release from pristine fumed silica is characterized by high initial rate: 95% of the loaded Enoxil was removed for 15 min. In the case of composite prepared by sol-gel method with hydrolyzed TEOS leads to slower elimination of Enoxil. After 15 min of the process, the Enoxil desorption amounted to 17%, and after 10 h, the release amount reached about 50%. A release rate of Enoxil from the



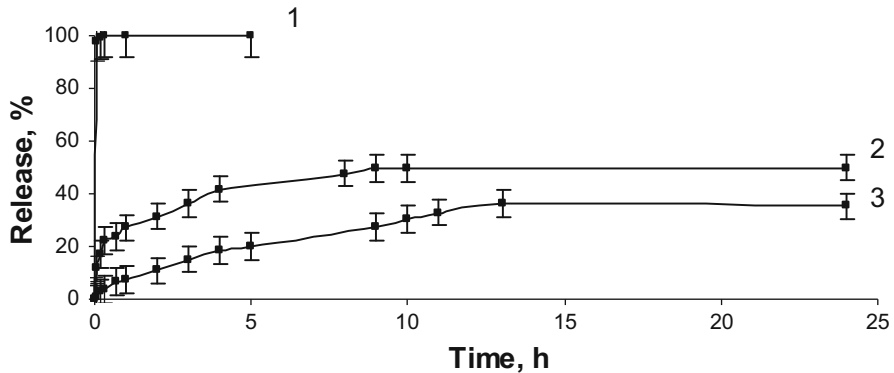


**Fig. 9.3** Enoxil release from composites with pristine fumed silica (1), sol-gel silica (2), and sol-gel silica with phenyl groups (3)

**Table 9.1** Release kinetics constants for Enoxil immobilized on silica composites

Sample	Higuchi model		Korsmeyer-Peppas model		
	$k, h^{-0.5}$	$R^2$	$n$	$k, h^{-n}$	$R^2$
Pristine fumed silica	2.574	0.911	0.014	1.016	0.999
Sol-gel silica	1.382	0.931	0.283	0.268	0.982
Sol-gel silica with phenyl groups	0.102	0.984	0.643	0.072	0.987

composite after hydrolyzed mixture TEOS-PhTMS during the first 15 min was even lower, and the quantity of dissolved drug was 5%. After 10 h the release amount reached about 30%.

### 9.3.3 Modeling of Drug Release Kinetics

The Korsmeyer-Peppas and Higuchi models fitted to the Enoxil release from the fumed silica and silica compositions with different functional groups obtained sol-gel method are presented in Table 9.1.

Higher rate coefficient corresponds to higher release rate of Enoxil from the pristine fumed silica A-300 and demonstrates the unrestricted diffusion of the active substance to the dissolution medium due to the high accessibility on the surface of nonporous silica.

Analyses of the cumulative Enoxil release profiles using the kinetic models reveal that the lowest rate coefficient is associated with the materials with phenyl groups, compared to unmodified silica. Phenolic surface moieties of silica materials appear to reduce the rates of Enoxil release by a combination of electrostatic, hydrophobic, steric effects and less wettability of the carrier by the release medium that is worsening washout of the loaded compound.

The Korsmeyer-Peppas kinetic model for drug release provides complementary insight about the diffusion of Enoxil molecules within porous silica materials, in particular whether diffusion occurs by Fickian or non-Fickian processes. Cumulative Enoxil release profiles associated with silica materials are fitted well by the Korsmeyer-Peppas model, according to the  $R^2$  values listed in Table 9.1.

The all-silica samples fitted better with the Korsmeyer-Peppas model that is based on the power law, which establish an exponential correlation between drug release and time. For the Korsmeyer-Peppas model, the value of release exponent ( $n$ ) correlated with mechanism that drives the drug release process and  $n$  release exponent values of studied samples presented in Table 9.1 that characterize an anomalous transport for this compositions.

### 9.3.4 Polymeric Composite Films

ATR spectra of polymer composite films depicted the characteristic absorption bands of chitosan and gelatin ( $3200\text{--}3450\text{ cm}^{-1}$  (O–H and N–H stretching),  $1030\text{--}1100\text{ cm}^{-1}$  (C–O–C stretching),  $1640\text{ cm}^{-1}$  (C=O stretching), and  $1530\text{--}1580\text{ cm}^{-1}$  (amide II). The absorptions at  $2920\text{--}2950$  ( $\text{CH}_2$ ) and  $2850\text{--}2870\text{ cm}^{-1}$  ( $\text{CH}_3$ ) are attributed to C–H stretching vibrations of methylene in chitosan and alkyl pendant groups in gelatin. The absorption bands observed at  $1700\text{--}1600$  and  $1560\text{--}1500\text{ cm}^{-1}$  are attributed to C=O stretching of amide I and amide II of type B in gelatin. The absorptions around  $1200$  and  $3450\text{ cm}^{-1}$  (N–H) are typical for the amide III and amide A vibrational modes, respectively. C=O, N–H, and C–N bond stretching and H–N–C bending usually appear in the amide I, A, II, and III regions, respectively. The absorption in the range  $1550\text{--}1500\text{ cm}^{-1}$  is due to N–H bending motions (Fig. 9.4).

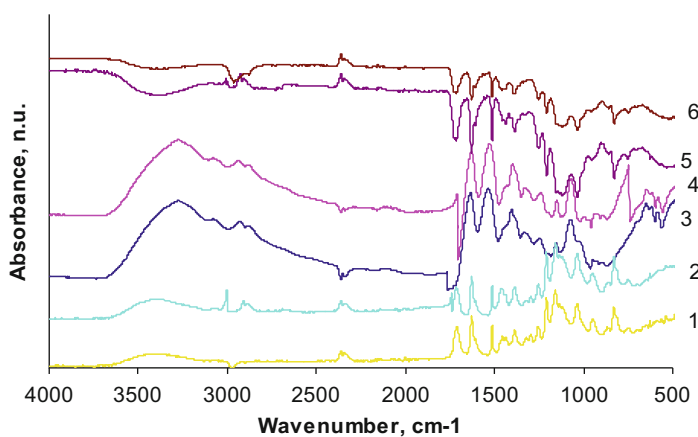


**Fig. 9.4** ATR spectra of composite films Gel/Chit/HEMA (1), Gel/HEMA (2), Gel/Chit (3), Gel/Chit/NT (4), Gel/HEMA/VA (5), and Gel/Chit/HEMA/VA (6)

In spectrum of polymeric films with HEMA, the characteristic vibrations of ester groups  $1100\text{--}1300\text{ cm}^{-1}$  and deformation vibrations of (CH) bonds at  $1300\text{--}1500\text{ cm}^{-1}$  have been detected [16]. The absorption bands at  $1079$  and  $1022\text{ cm}^{-1}$  corresponded to d(CO) in  $\text{--O--CH}_2\text{--}$  (gosh) and d(OH), respectively. The characteristic bands of HEMA are ( $\text{--O--C=O}$ ) group vibration mode near  $1740\text{ cm}^{-1}$ , valence vibration of CH= in  $(\text{C}(\text{CH}_3)=\text{CH}_2)$  group at  $1640\text{ cm}^{-1}$ , as well as double band of d(C-H) in  $\text{--CH}_2\text{--C}$  vibration at  $1457\text{ cm}^{-1}$  (bending) and  $1488\text{ cm}^{-1}$  (scissoring) [17].

Samples of 8–16 mg in mass, cut from the produced plate, were closed in standard Tzero aluminum pans. Cooling and heating rates were  $10\text{ }^\circ\text{C}/\text{min}$ . During the 1st heating scan, the samples stayed at  $100\text{ }^\circ\text{C}$  for 5 min (isothermally) and during the 2nd heating scan at  $20\text{ }^\circ\text{C}$  for 3 min in order to stabilize the materials. The DSC curve of first heating (Fig. 9.5) shows smooth heat consumption during the volatile matter and moisture eliminating with an extremum near  $101.5\text{ }^\circ\text{C}$  (Table 9.2, Fig. 9.5). During the first heating, the copolymer Gel/HEMA was post-cured, and on the next heating run, the exothermic band at  $161\text{ }^\circ\text{C}$  was marked that can point on high crystallinity degree of obtained structure. The crystallization and melting peaks are only observed for polymers that can form crystals. Most likely the main contribution to the material structure ordering is made by gelatin, since HEMA is a glass-like but amorphous polymer. While purely amorphous polymers will only undergo a glass transition, crystalline polymers typically possess amorphous domains and will also exhibit a glass transition as seen in Fig. 9.5a, b (samples Gel/Chit/HEMA and Gel/Chit/HEMA/VA, 2nd heat run curves). For these materials the exothermic band near  $299\text{ }^\circ\text{C}$  caused by chitosan presence. The amorphous portion only undergoes the glass transition, while the crystalline regions only undergo melting. The melting point for the Gel/HEMA sample was  $264\text{ }^\circ\text{C}$  followed by an endotherm, which refers to the thermal destruction of the material. In contrast, a sample of a similar polymer part composition with the addition of organosilanes (Gel/HEMA/VA) does not have an ordered structure (Fig. 9.5b). At the same time, it is possible to select on the curve a section related to the glass transition at  $T_g\ 83\text{ }^\circ\text{C}$ . The subsequent endotherm probably refers to the thermal destruction of the material. The exact temperatures at which the polymer chains undergo these transitions depend on the structure of the polymer. Namely, another effect has the presence of organosilanes on the ternary composite containing chitosan Gel/Chit/HEMA/VA. The resulting material has an amorphous ( $T_g$ ) and a crystalline part ( $T_c$ ). The high ordering of the structure is indicated by a narrow intense crystallization peak due to the presence of chitosan. Subtle changes in polymer structure can result in huge changes in  $T_g$ . For the Gel/Chit copolymer, during first heat run, the glass transition was found at  $56\text{ }^\circ\text{C}$ . After removal of moisture and post-curing during isothermal stage, the glass transition temperature shifts to  $92\text{ }^\circ\text{C}$ , and a narrow exotherm is retained at  $290\text{ }^\circ\text{C}$ . The introduction of carbon nanotubes into the material reduces the crystallinity of the polymer, but the internal architecture of the copolymer in general is not violated, and only change in the thermal resistance of the material was noted.

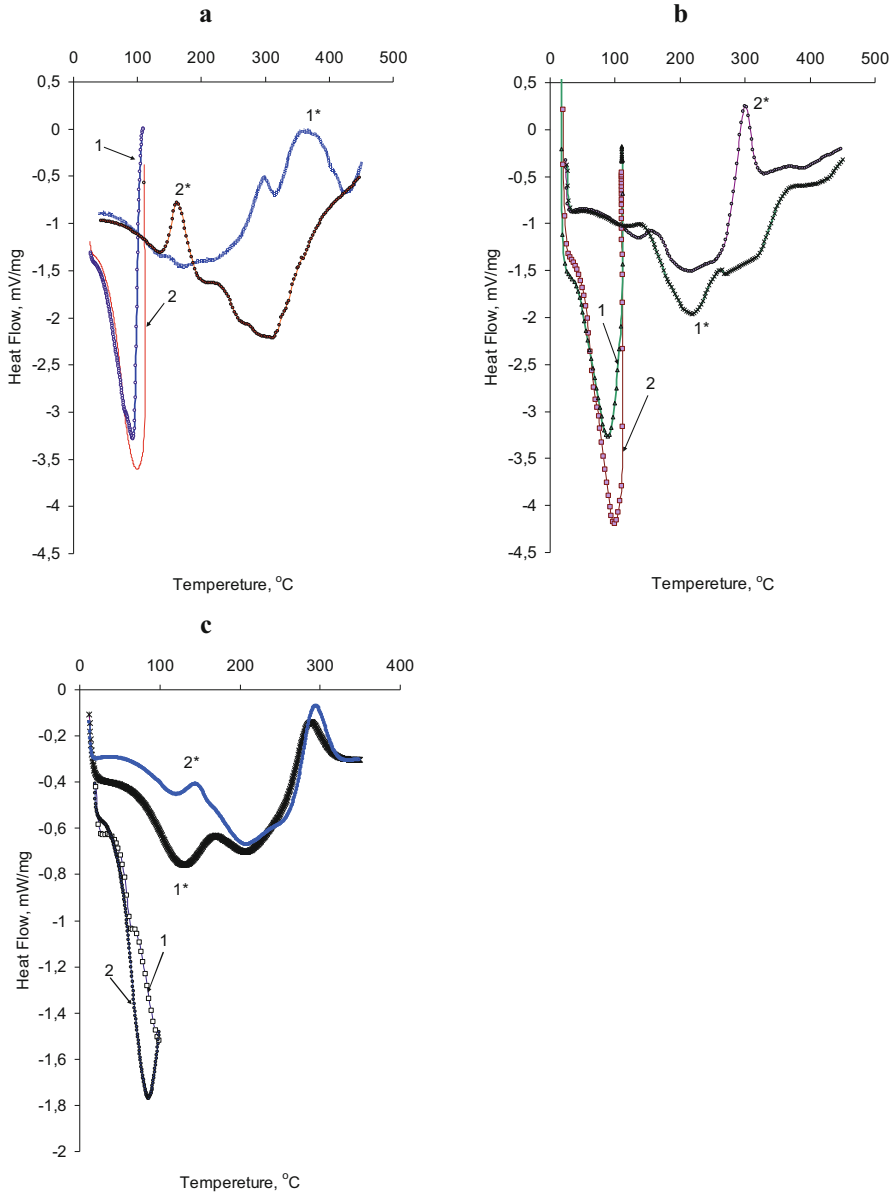


**Fig. 9.5** DSC thermograms 1st and 2nd heat(\*) of polymeric composite films: Gel/Chit/HEMA (1a), Gel/HEMA (2a), Gel/HEMA/VA (1b), Gel/Chit/HEMA/VA (2b), Gel/Chit (1c), Gel/Chit/NT (2c)

**Table 9.2** Thermal behavior parameters and characteristics of polymeric composites from DSC measurements

Samples Parameters	Gel/HEMA	Gel/Chit/HEMA	Gel/HEMA/VA	Gel/Chit/HEMA/VA	Gel/Chit	Gel/Chit/NT
First heating scan from 20 to 100 °C						
$T_{\text{endo}}$ , °C	101	94	88	72/99	99	85
$\Delta H$ , J/g	99.8	62.7	77.4	125.8	33.1	52.8
Second heating scan from 20 to 450 °C						
$T_{\text{endo}}$ , °C	292	169/422	219/317	217	208	210
$\Delta H$ , J/g	–	4.9/9.4	20.2/–	34.4	25.1	48.2
$T_{\text{exo}}$ , °C		364		374		
$\Delta H$ , J/g		144.3		–		
$T_c$ , °C	162	299		299	290	297
$\Delta H_c$ , J/g	18.5	22.8		43.2	27.0	6.2
$T_m$ , °C	264					
$\Delta H_m$ , J/g	12.6					
$T_g$ , °C		98	83	98	92	81
$\Delta C_p$ , J/g °C		0.40	0.20	0.30	0.35	0.2
$E_{\text{coh}}$ , kJ/mol		31.3	37.6	33.7	29.5	29.7
$R$ , $\Delta C_p/\Delta T_g$		182.5	280.0	233.3	214.3	350.0

Crystallization temperature  $T_c$ , heat of crystallization  $\Delta H_c$ , glass transition temperature  $T_g$ , heat capacity step at glass transition  $\Delta C_p$ , cohesion energy  $E_{\text{coh}}$ , thermal resistance  $R$

Water uptake ability of polymeric composites is represented in Table 9.3. Introducing HEMA into polymeric composition was found to provide a decrease in water uptake. In comparison to gelatin-based composition, the films based on chitosan had higher swelling degree. Additional cross-linking of HEMA with organosilanes mixture does not significantly reduce swelling behavior of materials. The higher volume of water uptake was found for composition Gel/Chit, as well as lowest swelling degree had composition Gel/HEMA.

The Enoxil release from swellable hydrophilic matrices can be controlled by physical and chemical processes, involving the liquid penetration within the polymer network, the swelling of hydrated polymer, and Enoxil diffusion throughout swollen matrix and, sometimes, its erosion. In vitro Enoxil dissolution profiles from composite films are shown in Fig. 9.6.

The analysis of the profiles indicated that the initial Enoxil release rate was higher for composite film Gel/HEMA/VA, Gel/HEMA, and Gel/Chit/HEMA/VA. But after 1 h, the release rate for film Gel/HEMA/VA is increased, and the release degree

**Table 9.3** Swelling degree of polymeric films

Sample	Swelling degree, %
Gel/HEMA	208
Gel/HEMA/VA	263
Gel/Chit	2235
Gel/Chit/NT	2044
Gel/Chit/HEMA	1453
Gel/Chit/HEMA/VA	1324

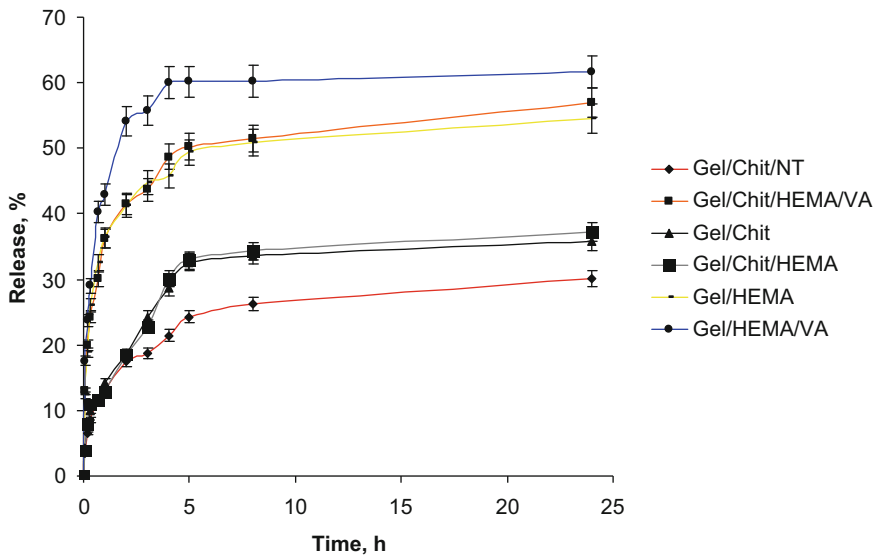


**Fig. 9.6** Enoxil release from polymeric films: Gel/HEMA, Gel/HEMA/VA, Gel/Chit, Gel/Chit/NT, Gel/Chit/HEMA, and Gel/Chit/HEMA/VA

for this material amount of polymeric samples under study becomes the largest. Desorption of the active compound from the films Gel/Chit/HEMA, Gel/Chit, and Gel/Chit/NT was found to be complicated due to polymer matrix swelling during contacting with the release medium, which, undoubtedly, complicates diffusion both the solvent and the adsorbate. In vitro drug desorption patterns from Gel/Chit/HEMA and Gel/Chit films are shown in Fig. 9.2 and Table 9.4. It was found that 30 wt% of Enoxil are released during 5 h of test, while for the Gel/Chit/NT film for this time, the release quantity was of 20 wt%.

### 9.3.5 Modeling of Drug Release Kinetics

The mechanism of drug release from hydrophilic matrix tablets after consumption is complex and based on diffusion of the drug through the outer hydrated polymer on the surface of the matrix. In the case of a highly soluble drug, this phenomenon may lead to an initial burst release due to the presence of the drug on the surface of the polymer film. The gel layer grows with time as more water permeates to the depth of the composition, thereby increasing the thickness of the gel layer and providing a diffusion barrier to Enoxil release. The gel layer thickness behavior is crucial in describing the release kinetics of swellable matrices.

The release profiles of Enoxil from polymeric hydrophilic matrices were fitted to various models such as Higuchi and Korsmeyer-Peppas to ascertain the transport-kinetic model of drug release. These results are presented in Table 9.4.

Analysis of  $n$  values in Table 9.3 indicated that the mechanism of Enoxil release from polymer films was anomalous. Both models have better fitting coefficient ( $R^2$ ) for composite with higher degree of swelling. The Korsmeyer-Peppas model better describes the complicate diffusion in condition of polymeric structure relaxation. The increase in coefficient  $n$  (Table 9.4) confirms a change in diffusion mechanism with adsorbate release limitation due to polymeric material swelling. As known, the Higuchi model better describes the process where the limitation stage of the release process is simple diffusion. Taking into account the values of both models, we can conclude that for composites Gel/HEMA, Gel/HEMA/VA, and Gel/Chit/HEMA,

**Table 9.4** Release kinetics constants for Enoxil immobilized into polymeric composite films

Sample	Higuchi model		Korsmeyer-Peppas model		
	$k, h^{-0.5}$	$R^2$	$n$	$k, h^{-n}$	$R^2$
Gel/HEMA	0.169	0.853	0.292	0.320	0.937
Gel/HEMA/VA	0.207	0.838	0.280	0.399	0.956
Gel/Chit	0.126	0.976	0.392	0.144	0.949
Gel/Chit/NT	0.094	0.968	0.414	0.124	0.975
Gel/Chit/HEMA	0.174	0.877	0.259	0.315	0.930
Gel/Chit/HEMA	0.128	0.970	0.450	0.146	0.961

active compound release is complicated less by swelling of matrices. However, for polymeric composites, understanding for desorption process better described by the Korsmeyer-Peppas model pointed on decisive role of gel fraction of polymer in active substrate desorption.

### 9.3.6 Bactericidal Activity of Polymeric Films

The main parameter for polymeric carriers of biological active matter is stability toward bacteria pollution. In order to prevent bacteria action, usually medical composite includes appropriate organic or inorganic compounds. As supposed the polymeric carriers based on chitosan will have resistance against bacteria growth. The study was performed using *Pseudomonas aeruginosa*. It was found that the more effective bactericide is Gel/HEMA composite material. The composites Gel/Chit and Gel/Chit/HEMA had worse results but also show a good bactericidal activity (Fig. 9.7). All other polymeric materials are inactive toward *Pseudomonas aeruginosa*. It should be noted that carbon nanotube presence reduces the bactericidal properties of the material.

## 9.4 Conclusions

Systems based on silica and polymer matrices that can be used as carriers for biological antioxidant, namely, natural tannin, were synthesized. The release rate of Enoxil from the fumed silica A-300 that was much higher compared with the release rate from the composites prepared by sol-gel method was found. The control of the Enoxil release was achieved using a silica matrix containing phenyl groups in the surface layer, which makes it possible to consider the developed material as a promising carrier for biologically active substances.

Among the studied polymeric compositions synthesized polymeric materials the films containing HEMA has the most rigid structure. Polymeric films based on gelatin and chitosan were found to show the highest swelling degree and reduced release. A composite based on gelatin and chitosan is promising, but the best carriers in this line of samples were Gel/HEMA/VA. According to the results of testing the synthesized polymer films, the bactericidal activity was found for Gel/HEMA, Gel/Chit/HEMA, and Gel/Chit composites. The obtained result of biological test demonstrated that introducing nanotubes into polymeric materials reduced their bacteriostatic stability. The composites elaborated can be utilized as Enoxil carriers for oral and transdermal applications.



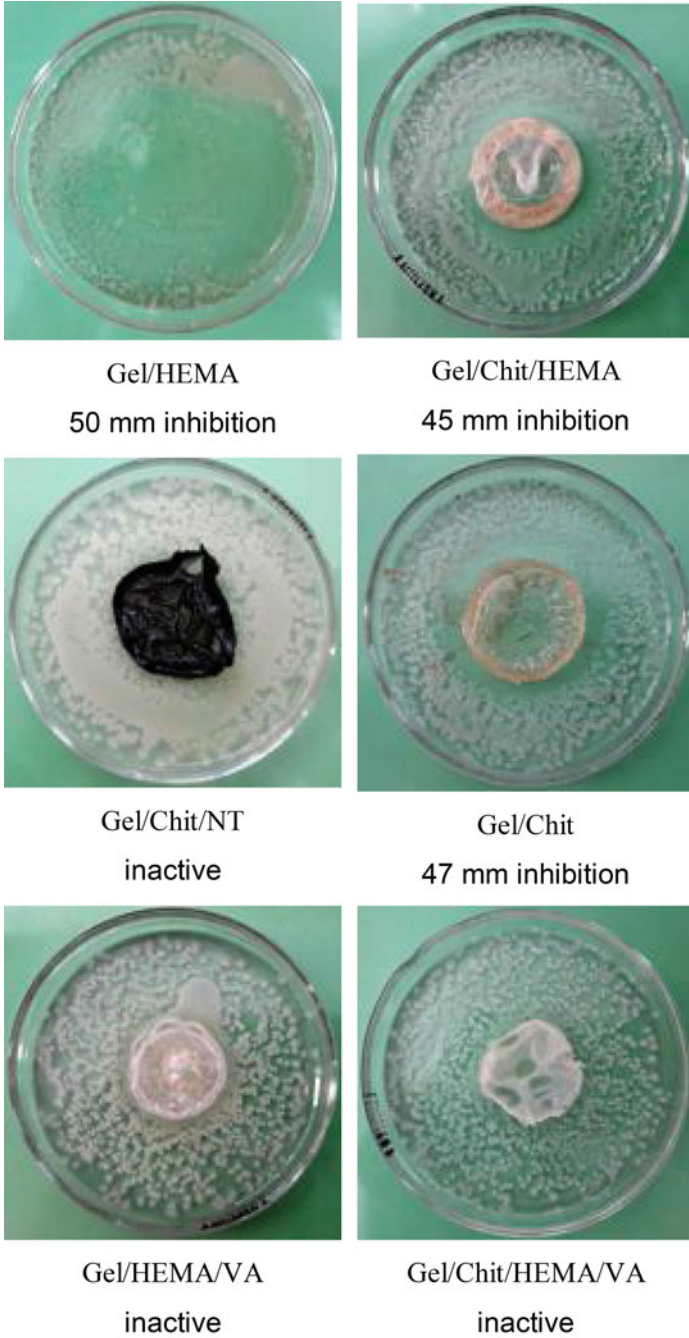


Fig. 9.7 Diffusion disc results of polymeric composite films against *Pseudomonas aeruginosa*

**Acknowledgments** The research leading to these results has received funding from the People Programme (Marie Curie Actions) of the European Union's Seventh Framework Programme FP7/2007–2013/ under REA grant agreement no PIRSES-GA-2013-612484, "NANOBIOMAT."

**Competing Interest** The authors declare that they have no competing interest.

## References

1. Sytar O, Hemmerich I, Zivcak M, Rauh C, Brestic M (2016) Comparative analysis of bioactive phenolic compounds composition from 26 medicinal plants. *Saudi J Biol Sci.* <https://doi.org/10.1016/j.sjbs.2016.01.036>
2. Tringali C (2001) Bioactive compounds from natural sources: isolation, characterization and biological properties. *Phytother Res* 16(6):503–602
3. Lupascu TGA (2011) Studies on the antioxidant activity of the compound Enoxil and its related forms. *Chem J Moldova* 6(2):58–64
4. Ivanova D, Gerova D, Chervenkov T, Yankova T (2005) Polyphenols and antioxidant capacity of Bulgarian medicinal plants. *J Ethnopharmacol* 96(1):145–150 <https://doi.org/10.1016/j.jep.2004.08.033>
5. Liu H, Qiu N, Ding H, Yao R (2008) Polyphenols contents and antioxidant capacity of 68 Chinese herbals suitable for medical or food uses. *Food Res Int* 41(4):363–370 <https://doi.org/10.1016/j.foodres.2007.12.012>
6. Manach C, Mazur A, Scalbert A (2005) Polyphenols and prevention of cardiovascular diseases. *Curr Opin Lipidol* 16(1):77–84
7. Aprioku JS (2013) Pharmacology of free radicals and the impact of reactive oxygen species on the testis. *J Reprod Infertility* 14(4):158–172
8. Hellinger WC (2000) Confronting the problem of increasing antibiotic resistance. *South Med J* 93(9):842–848
9. Esquenazi DWM, Miranda MM, Rodrigues HM, Tostes JB, Rozental S, Silva AJ, Alviano CS (2002) Antimicrobial and antiviral activities of polyphenolics from *Cocos nucifera* Linn. (Palmae) husk fiber extract. *Res Microbiol* 10(153):647–652
10. Daglia M (2012) Polyphenols as antimicrobial agents. *Curr Opin Biotechnol* 23(2):174–181 <https://doi.org/10.1016/j.copbio.2011.08.007>
11. Lucian Lupaşcu VR, Cotos V, Lupaşcu T (2010) Antimicrobial activity of the autochthonous compound Enoxil. *J Biomed Sci Eng* 3:758–762
12. Turov VV, Lupascu T, Krupska TV, Povar I (2015) Nanosilica A-300 influence on water structures formed on the bioactive agent Enoxil. *Can J Chem* 94(1):88–94. <https://doi.org/10.1139/cjc-2015-0360>
13. Kuzema PO, Laguta IV, Stavinskaya ON, Kazakova OA, Borysenko MV, Lupaşcu T (2016) Preparation and characterization of silica-Enoxil Nanobiocomposites. *Nanoscale Res Lett* 11(1):68. <https://doi.org/10.1186/s11671-016-1287-y>
14. Yao KD, Yin YJ, Xu MX, Wang YF (1995) Investigation of pH-sensitive drug delivery system of chitosan/gelatin hybrid polymer network. *Polym Int* 38(1):77–82. <https://doi.org/10.1002/pi.1995.210380110>
15. Zaman HU, MAK RAK (2012) Studies on the thermo-mechanical properties of gelatin based films using 2-Hydroxyethyl methacrylate by gamma radiation. *OJCM* 2(1):15–21
16. Bolbukh Y, Klonos P, Roumpos K et al (2016) Glass transition and hydration properties of polyhydroxyethylmethacrylate filled with modified silica nanoparticles. *J Therm Anal Calorim* 125(3):1387–1398
17. Bolbukh Y, Tertykh V, Klonos P, Pissis P (2012) DSC study of polyhydroxyethylmethacrylate filled with modified silicas. *J Therm Anal Calorim* 108(3):1111–1119. <https://doi.org/10.1007/s10973-011-2030-7>

# Chapter 10

## High-Temperature Electrochemical Synthesis of Nanostructured Coatings of Molybdenum (Tungsten)–Nickel (Cobalt) Alloys and Intermetallic Compounds



Viktor Malyshev, Nataliia Uskova, Dmytro Shakhnin, Tetiana Lukashenko, Viktor Antsibor, and Zafer Ustundag

### Abbreviations

$C$	Electroactive particle concentration
$E$	Potential value
$E_p$	Peak potential
$E_{p/2}$	Half-peak potential
$F$	Faraday constant
$H$	Microhardness
$I$	Current
$i$	Current value
$i_d$	Diffusion current
$i_p$	Peak current
$M$	Metal atom
$n$	Electron number
$R$	Universal gas constant
$T$	Thermodynamic temperature
$v$	Polarization rate
$V$	Voltage

---

V. Malyshev (✉) · N. Uskova · D. Shakhnin · T. Lukashenko · V. Antsibor · Z. Ustundag  
University “Ukraine”, Kyiv, Ukraine

Dumlupinar University, Kutahya, Turkey

## 10.1 Introduction

For the cathodic codeposition of metals, the correspondence of their crystalline lattices and the difference in their standard electrode potentials are of great importance. An analysis of the results of studying the electrochemical production of alloys [1] shows that the “thermodynamic” regime of their formation is observed at similar deposition potentials of components ( $\leq 0.2$  V) and that the alloy composition is independent of the current density over a wide concentration range. For a high potential difference ( $> 0.2$  V), the “kinetic” regime is observed, and the alloy composition depends weakly on the potential difference. The cathodic codeposition of molybdenum and rhenium was studied in a chloride melt [2, 3]; they have crystalline lattices of different types and a high difference in the standard electrode potentials (0.45 V in a NaCl–KCl melt at 1073 K). In this case, the violation of the growth of continuous alloy layers was ascribed to considerable diffusion difficulties in the transport of more electropositive rhenium ions to a cathode.

The cathodic codeposition of molybdenum and tungsten in a chloride melt was studied in [2]. They have crystalline lattices of the same type and an insignificant difference in the standard electrode potentials (0.09 V in a NaCl–KCl melt at 1073 K). In this case, no violation was observed for the growth of continuous layers of molybdenum–tungsten alloys. The cathodic codeposition of molybdenum and silver, which have different types of crystalline lattices and a considerable difference in the standard electrode potentials (0.5–0.6 V in a  $\text{Na}_2\text{WO}_4$  melt at 1173 K), in a tungstate melt was studied in [4]. Since molybdenum is virtually insoluble in silver, the latter exerts an insignificant effect on the electrodeposition of molybdenum coatings and their properties.

It seems significant from a practical point of view to study the electrodeposition of alloys whose components have crystalline lattices of different types but similar electrode potentials. Molybdenum (tungsten) and nickel in a NaCl–KCl melt satisfy these requirements. They have bcc and fcc lattices, respectively [5], and their standard electrode potentials differ by 0.14 V in a pure halide–chloride melt based on NaCl–KCl at 1073 K [2] and by 0.15–0.35 V (depending on the melt basicity) in a halide–oxide melt NaCl–KCl– $\text{Na}_2\text{MoO}_4$ – $\text{NiCl}_2$  at 1023 K [5]. As compared to nickel, the potential of molybdenum (tungsten) in both melts is more positive, and the compositions of the resulting continuous molybdenum (tungsten), molybdenum (tungsten)–nickel, and nickel deposits depend on the electrolyte composition and electrolysis conditions. A protective medium over a bath is necessary in this case. Connected deposits are formed only on graphite, copper, nickel, and precious metal substrates.

Oxide tungstate–molybdate melts  $\text{Na}_2\text{WO}_4$ – $\text{MO}_3$ , where M is Mo or W, were used for the electrodeposition of molybdenum (tungsten) coatings [6, 7]. In the present work, we study the electrochemical behavior of nickel and cobalt in a  $\text{Na}_2\text{WO}_4$  melt and the possibility of electrodeposition of molybdenum (tungsten)–nickel (cobalt) alloys from this melt. From a practical viewpoint, we are interested in these alloys due to the use of nickel- and cobalt-based structural materials for

the electrosynthesis of powders of molybdenum and tungsten carbides and to the considerable enhancement in the plasticity of molybdenum and tungsten having nickel and cobalt additions.

Therefore, it is important to study the electroreduction of nickel and cobalt against the background of tungstate–molybdate melts in both the theoretical and practical aspects, the more so as, in oxide melts (unlike halide–oxide melts), these metals are more precious (inert) than molybdenum (tungsten), and, hence, the range of substrates for deposition becomes larger and includes different steels. Moreover, these melts need no protective medium over a bath.

## 10.2 Materials and Methods

The main procedure of the study was chronovoltammetry with potential sweep rates ranging from  $5 \times 10^{-3}$  to 5.0 V/s. The experiments were carried out in air in a reactor of quartz or a heat- and corrosion-resistant steel. A platinum crucible served as an anode and a container for a melt in chronovoltammetric measurements. An alundum crucible was used in the experiments on alloy deposition. Platinum, nickel, and cobalt electrodes served as indicator electrodes. A platinum/oxygen electrode  $0.8\text{Na}_2\text{WO}_4\text{--}0.2\text{WO}_3|\text{Pt}$ , air, was a reference electrode. A thin-walled alundum tube [8] was used as a membrane separating the melt of the reference electrode from the melt under study. Sodium tungstate was of special purity grade. Molybdenum, nickel, and cobalt oxides were of reagent grade. Reagents were dried before use for 10–12 h in vacuo at 200–250 °C and then calcined at 400–450 °C.

The kinetic parameters of the electrode process were diagnosed and estimated using the theory of stationary and nonstationary electrode processes [8].

Plates of MPG-7 graphite, nickel, copper, St. 3 steel, and grade 45 steel with a surface area of 2.0–3.5 cm<sup>2</sup> served as substrates for the electrodeposition of metals and alloys. The deposits prepared were studied by X-ray diffraction, electron microprobe analysis, and metallography using DRON-4.0, Cameca, and Neophot-21 instruments, respectively. The microhardness was measured on a PMT-3 device. The initial electrolyte was purified via electrolysis at 850–900 °C using an anode made of a metal that is like to ions in the melt.

## 10.3 Results and Discussion

### 10.3.1 *Electrochemical Behavior of Nickel(II) and Cobalt(II) Against the Background of a Tungstate Melt*

The I–V characteristics in the tungstate melt containing nickel(II) or cobalt(II) oxide exhibit a reduction wave at the potentials ranging from –0.7 to –0.8 V and from –0.8 to –0.9 V, respectively (Fig. 10.1). An increase in the oxide

**Fig. 10.1**  $I$ - $V$  characteristics of (1) the  $\text{Na}_2\text{WO}_4$  melt upon the addition of oxides ( $\text{mol}/\text{cm}^3$ ): (2)  $3 \times 10^{-4}$  NiO, (3)  $2.5 \times 10^{-3}$  CoO, (4)  $7 \times 10^{-4}$   $\text{MoO}_3$ , and (5)  $6 \times 10^{-4}$   $\text{WO}_3$ , Platinum cathode,  $T = 1173$  K, the polarization rate is 10 V/s

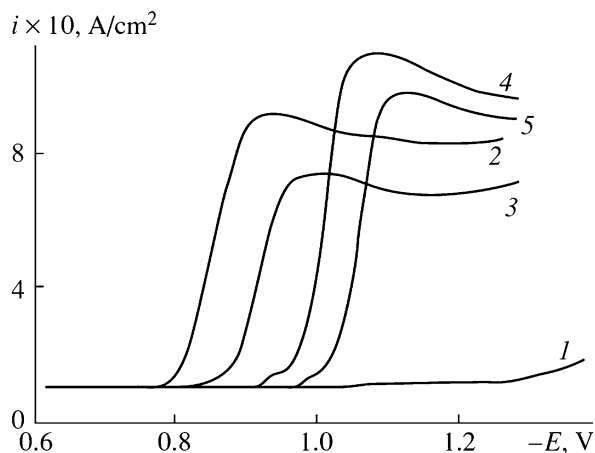
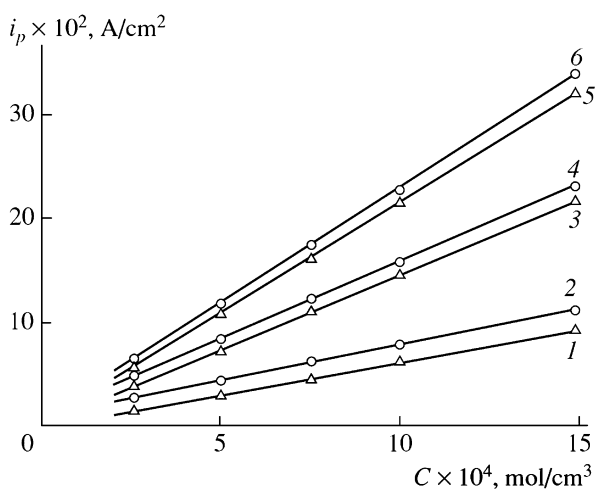


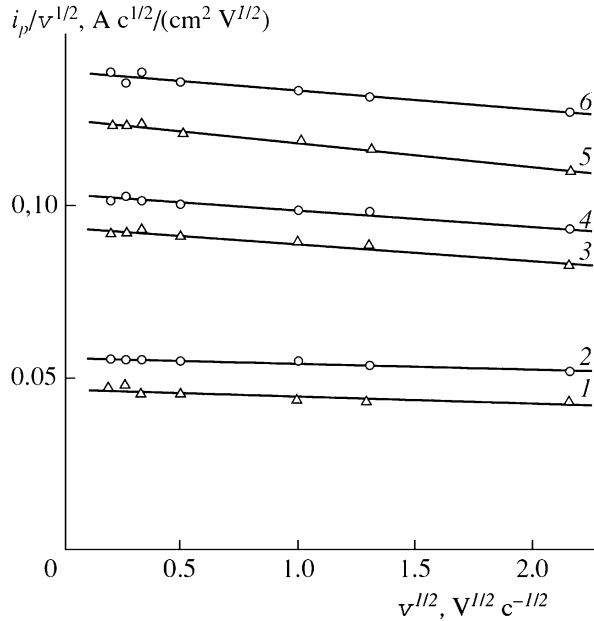
**Fig. 10.2** Current peak  $i_p$  as a function of the concentrations of (1, 3, 5) CoO and (2, 4, 6) NiO in a tungstate melt at  $T = 1173$  K and different polarization rates: (1, 2) 0.2, (3, 4) 1.0, and (5, 6) 5.0 V/s



concentration results in an increase in the corresponding wave and its shift toward a positive direction. The reduction process proceeds in one step. An increase in the polarization rate to 5.0 V/s does not reveal steps in this process. Potentiostatic electrolysis at the wave potentials detects the only product, namely, nickel or cobalt, respectively.

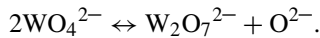
The peak current remains directly proportional to the concentration of nickel and cobalt oxides at different polarization rates at  $T = 1173$  K (Fig. 10.2). The ratio  $i_p/\nu^{1/2}$  is virtually constant in the interval of polarization rates from 0.05 to 2.0 V/s at  $T = 1173$  K (Fig. 10.3). The mass transfer constant  $i_p/nFC$  (cm/s), which characterizes the method of transporting the reactants to the electrode surface, equals  $(2.3\text{--}2.9) \times 10^{-4}$  (for NiO used as a depolarizer) and  $(2.1\text{--}2.7) \times 10^{-4}$  (for CoO as a depolarizer), which agrees with diffusion-controlled transport. The

**Fig. 10.3** Plot of  $i_p/v^{1/2}$  versus  $v^{1/2}$  for the electroreduction of (1, 3, 5) cobalt- and (2, 4, 6) nickel-containing melts at  $T = 1173$  K and different  $C_{MO} \times 10^{-4}$  values: (1, 2) 10, (3, 4) 12.5, and (5, 6)  $15.0 \text{ mol/cm}^3$



directly proportional dependence of the ultimate current on the oxide concentration, the  $i_p/nFC$  ratio constant over a wide interval of polarization rates, and the  $i_p/nFC$  value indicate that the electrode process is limited by the diffusion of electroactive particles to the electrode surface. Therefore, under these polarization conditions, the rate of formation of electrochemically active particles imposes no restrictions on the electrode process.

The mechanism of formation of electroactive particles becomes clear when using the concept of acid–base equilibria in tungstate melts. The following equilibrium exists in a purely tungstate melt:



The stability constant is

$$K = \frac{[\text{WO}_4^{2-}]^2}{[\text{O}^{2-}][\text{W}_2\text{O}_7^{2-}]} = 10^{10-12},$$

and the equilibrium constant of oxygen ions is  $[\text{O}^{2-}] = 10^{-5}$  [6, 7]. The addition of nickel and cobalt(II) oxides increases the activity of oxygen ions and decreases the potential of the oxygen electrode (Fig. 10.4). A similar dependence is explained by the occurrence of the reaction

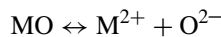


**Fig. 10.4** Equilibrium potentials of the indicator platinum/oxygen electrode in a sodium tungstate melt versus the concentration of (1) nickel oxide, (2) cobalt(II) oxide, (3) cobalt tungstate, and (4) cobalt molybdate.  $T = 1173$  K

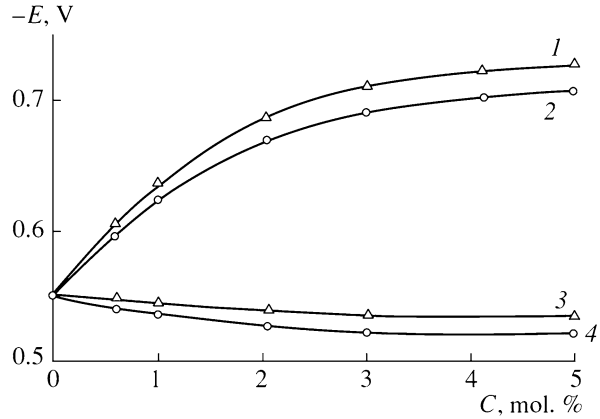
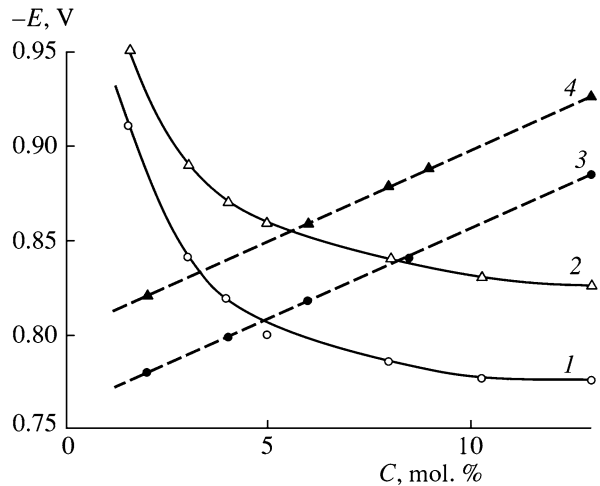


**Fig. 10.5** Equilibrium potentials of (1, 3) nickel and (2, 4) cobalt electrodes in a sodium tungstate melt in the (1, 2) standard and (3, 4) logarithmic coordinates versus the concentration of (1, 3) nickel(II) oxide and (2, 4) cobalt(II) oxide.  $T = 1173$  K



with the electrode process



According to the dependences of the equilibrium potentials of the nickel and cobalt electrodes on the oxide concentration in the sodium tungstate melt (Fig. 10.5), the number of electrons per electroactive particle is 1.91–2.23 and 1.83–2.28, respectively. Electrode reaction (10.1) corresponds to these values.

To reveal the character of charge-transfer step (1) and to determine the number of electrons transferred in the electrode process, we analyzed the stationary  $I$ – $V$  characteristics in the semilogarithmic coordinates  $E - \log(i/i_d - i)$ . The slopes of these curves for different NiO concentrations are 107–127 mV and  $n = 1.8$ –2.1 V. For different CoO concentrations, the slopes of the curves are 103–122 mV and  $n = 1.7$ –2.1 V. The theoretical value of the slope of the curve for a two-electron reversible reaction is 112 mV. The experimentally determined slope coincides with



the theoretical value, which indicates that the charge-transfer step is reversible. The latter is also confirmed by the following experimental facts: the deposition and half-wave potentials are independent of the polarization shift rate up to 0.2 V/s, and the concentration dependence of the equilibrium potential of (1) is described well by the Nernst equation.

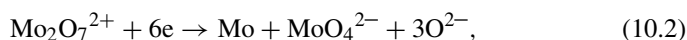
The number of electrons participating in the electrode process was also determined from the difference in the peak and half-peak potentials of the stationary  $I$ - $V$  characteristics  $E_{p/2} - E_p = 2.2RT/nF$ . For different oxide concentrations and polarization rates from 0.05 to 0.2 V/s, we have  $n = 1.9$ – $2.1$  (for NiO) and  $1.7$ – $2.0$  (for CoO).

A transition from a reversible to a quasireversible electrode process is observed at a polarization rate higher than 0.5 V/s. This is confirmed by a deviation of the  $i_p - \nu^{1/2}$  dependence from the directly proportional dependence and by the appearance of the dependence of the peak and half-peak potentials on the polarization rate.

Thus, the analysis of the experimental data suggests that reversible equilibria and processes involving nickel and cobalt(II) can occur in the sodium tungstate melt.

### ***10.3.2 Combined Electroreduction of Nickel (Cobalt) and the Oxide Forms of Molybdenum(VI) (Tungsten(VI)) from a Tungstate Melt and the Synthesis of Nickel (Cobalt)–Molybdate (Tungstate) Alloys***

The addition of molybdenum(VI) oxide to the nickel-containing tungstate melt induces the dimolybdate-ion reduction wave



which was studied in detail in [6, 7]. The difference in the potentials of nickel and molybdenum deposition is 0.09–0.115 V at 1173 K. Unlike halide and halide–oxide melts, nickel exhibits a more precious behavior than molybdenum in an oxide melt.

A  $\text{Na}_2\text{WO}_4$ –2.5 mol %  $\text{MoO}_3$  melt was used as a stock electrolyte to deposit alloys of various compositions. After the electrolyte had been cleaned by electrolysis, we electrodeposited molybdenum coatings using a molybdenum anode in the temperature range 1123–1173 K at a cathodic current density ranging from 0.02 to 0.15 A/cm<sup>2</sup> to determine the structure of the molybdenum deposits. It was found that, at the current density from 0.02 to 0.1 A/cm<sup>2</sup>, the molybdenum coatings have a columnar structure, a thickness of 100–150  $\mu\text{m}$ , and a microhardness of 1.8–1.9 kN/mm<sup>2</sup>. Further electrolysis does not increase the coating thickness: dendrites or isolated powdered deposits grow. The depth profiles of the molybdenum and nickel concentrations in the coating and nickel substrate indicate interdiffusion of the elements of the coating and substrate, which provides their good adhesion (Fig. 10.6).

For the cathodic codeposition of metals to form an alloy, the molybdenum anode was replaced by a more inert nickel electrode, and electrolysis was carried out at

**Fig. 10.6** (a) Trace of an electron probe on the polished section of a sample and (b) the depth profiles of the molybdenum and nickel concentrations in the coating and nickel substrate.  $[\text{NiO}] = 0.1 \text{ mol } \%$ ,  $[\text{MoO}_3]/[\text{NiO}] = 22$ ,  $T = 1173 \text{ K}$ ,  $i_c = 0.1 \text{ A/cm}^2$ , and  $t = 1 \text{ h}$

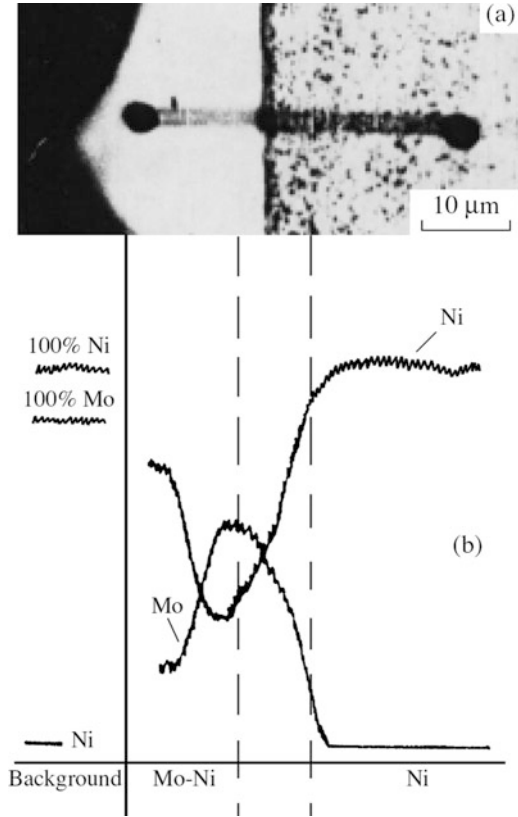


**Table 10.1** Effect of the electrolysis conditions on the composition and structure of the molybdenum–nickel alloys deposited from a  $\text{Na}_2\text{WO}_4$ –(1.0–2.5) mol %  $\text{MoO}_3$ –(0.01–1.0) mol %  $\text{NiO}$  melt

$[\text{NiO}]$ , mol %	$\frac{[\text{MoO}_3]}{[\text{NiO}]}$	$T$ , K	$i_c$ , $\text{A/cm}^2$	Phase composition	$H$ , $\text{kN/mm}^2$	Structure
0.01	250	1123	0.100	Mo	1.70	Columnar
0.02	120	1173	0.100	Mo, MoNi	1.80	Columnar
0.1	22	1173	0.075	MoNi	7.15	Layered
0.1	22	1173	0.100	MoNi, MoNi <sub>3</sub>	—	Layered
0.5	4	1173	0.065	MoNi <sub>3</sub>	5.60	Layered
0.6	8	1173	0.065	MoNi <sub>3</sub> , MoNi <sub>4</sub>	4.17	Layered
0.7	2	1173	0.060	MoNi <sub>4</sub>	3.45	Fine-grained
1.0	1	1173	0.050	Ni	1.15	Columnar

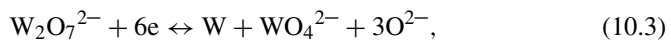
cathodic current densities of 0.05 and 0.1  $\text{A/cm}^2$  in the same temperature range (1123–1173 K). The concentration of  $\text{MoO}_3$  was maintained at 1.0–2.5 mol%, and the  $\text{NiO}$  concentration was varied from 0.1 to 1.0 mol %. The molar ratio of the molybdenum and nickel ions changed from 250 to 1. The experimental results are given in Table 10.1. An increase in the  $\text{NiO}$  concentration or the temperature

**Table 10.2** Effect of the electrolysis conditions on the composition and structure of the tungsten-nickel alloys deposited from a  $\text{Na}_2\text{WO}_4$ –(1.0–5.0) mol %  $\text{WO}_3$ –(0.01–1.0) mol % NiO melt

[NiO], mol %	$\frac{[\text{WO}_3]}{[\text{NiO}]}$	$T$ , K	$i_c$ , A/cm <sup>2</sup>	Phase composition	$H$ , kN/mm <sup>2</sup>	Structure
0.01	500	1123	0.100	W	3.80	Columnar
0.1	50	1173	0.075	W, WNi	9.25	Layered
0.5	10	1173	0.065	WNi <sub>3</sub>	7.20	Layered
0.7	6	1173	0.065	WNi <sub>3</sub> , WNi <sub>4</sub>	5.10	Layered
0.8	6	1173	0.060	WNi <sub>4</sub>	4.20	Layered
1.0	2	1173	0.050	Ni	1.20	Columnar

and a decrease in the cathodic current density increase the nickel content in the deposit. Continuous layers of the intermetallics MoNi, MoNi<sub>3</sub>, and MoNi<sub>4</sub> are sequentially deposited on the cathode at 1123–1173 K from the melts containing 0.1–1.0 mol % NiO. The possibility of formation of these intermetallic compounds is confirmed by the Mo–Ni phase diagram [9]. All of them have a fine-grained or a layered structure, and their microhardness  $H$  decreases in this series from 7.15 to 3.45 kN/mm<sup>2</sup>. At current densities up to 0.05 A/cm<sup>2</sup>, the melts containing no MoO<sub>3</sub> form complex nickel layers with a block or columnar–block structure 40–50 μm thick having a microhardness of 1.15–1.20 kN/mm<sup>2</sup>. They transform into dendrites upon the further growth of nickel coatings or an increase in the current density above 0.05 A/cm<sup>2</sup>.

The introduction of tungsten(VI) oxide into a nickel-containing tungstate melt produces the ditungstate-ion reduction wave



which was considered in detail in [7]. The difference in the potentials of nickel and tungsten deposition is 0.13–0.16 V at 1173 K, and this potential is higher for nickel. The procedure of alloy deposition is similar to the procedure described above, but the starting melt was the  $\text{Na}_2\text{WO}_4$ –5.0 mol %  $\text{WO}_3$  melt. The experimental results are presented in Table 10.2. In this case, the deposition dependences are similar to those obtained for the Mo–Ni alloys.

The addition of tungsten(VI) oxide to a cobalt-containing tungstate melt results in the appearance of the ditungstate-ion reduction wave corresponding to reaction (10.3). The difference in the potentials of cobalt and tungsten deposition is 0.08–0.14 V at 1173 K, and, unlike halide and halide–oxide melts, cobalt in the oxide melt is more inert than tungsten (molybdenum). Cobalt and tungsten (molybdenum) have crystalline lattices of different types (hexagonal and cubic, respectively) and have similar electrode potentials ( $\Delta E^0 < 0.2$  V). Two intermediate phases can exist in the Co–W(Mo) systems: CoW (CoMo) and Co<sub>3</sub>W (Co<sub>3</sub>Mo) [9].

The  $\text{Na}_2\text{WO}_4$ –1.5 mol %  $\text{WO}_3$  melt was used as a stock electrolyte for alloy deposition. In this electrolyte, tungsten coatings with a columnar structure form at current densities of 0.04–0.12 A/cm<sup>2</sup>: they are 0.2 mm thick and have a microhardness of 3.40–4.20 kN/mm<sup>2</sup>. For the cathodic codeposition of metals, the

**Table 10.3** Effect of the electrolysis conditions on the composition and structure of the tungsten–cobalt alloys deposited from a  $\text{Na}_2\text{WO}_4$ –(0.01–1.0) mol %  $\text{CoO}$ –(0.1–1.5) mol %  $\text{WO}_3$  melt

[CoO], mol %	[WO <sub>3</sub> ], mol %	T, K	$i_c$ , A/cm <sup>2</sup>	Phase composition	H, kN/mm <sup>2</sup>	Structure
0.01	1.5	1123	0.12	W	3.72	Columnar
0.1	1.0	1123	0.10	W, CoW	4.11	Columnar
0.1	0.3	1173	0.12	CoW	8.23	Layered
0.5	0.3	1173	0.08	CoW, Co <sub>3</sub> W	6.56	Layered
0.7	0.2	1173	0.07	Co <sub>3</sub> W	5.09	Layered
1.0	0.1	1173	0.05	Co	1.56	Columnar

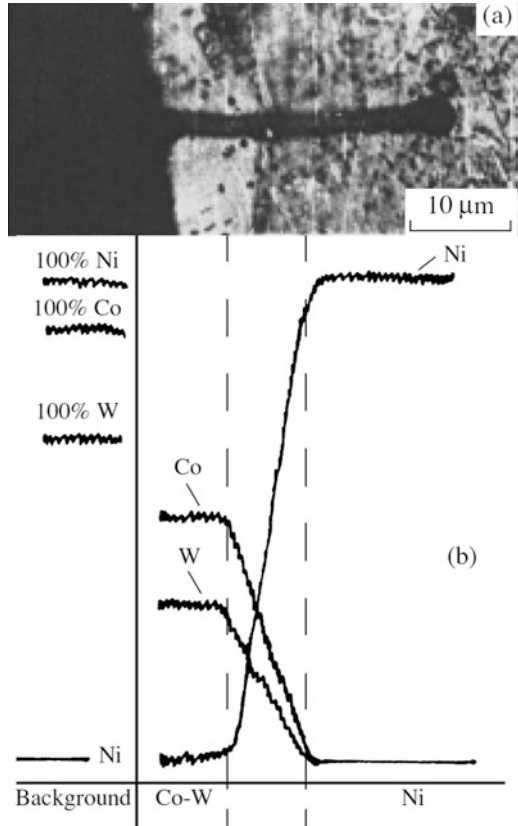
tungsten anode was replaced by a more inert cobalt anode. The experiments were carried out at cathodic current densities of 0.075–0.12 A/cm<sup>2</sup> in the temperature range from 1123 to 1173 K. The  $\text{WO}_3$  concentration was maintained at 0.1–1.5 mol %, and that of  $\text{CoO}$  was changed from 0.01 to 1.0 mol %. The molar ratio of the tungsten to cobalt ions was varied from 250 to 1. The experimental results are given in Table 10.3.

An increase in the  $\text{CoO}$  concentration, a rise in temperature, and a decrease in the cathodic current density increase the cobalt content in the deposit. Continuous layers of the CoW and Co<sub>3</sub>W intermetallics are sequentially deposited on the cathode at 1123–1173 K from the melts containing 0.1–1.0 mol %  $\text{CoO}$ . The structures of the intermetallics are fine-grained or layered. Their microhardnesses exceed those of the individual components of the alloys, being 8.40 and 5.00 kN/mm<sup>2</sup>, respectively. Continuous cobalt deposits 50  $\mu\text{m}$  thick with a microhardness of 1.5–1.8 kN/mm<sup>2</sup> form at current densities as high as 75 mA/cm<sup>2</sup> from the melts without  $\text{WO}_3$ . They transform into dendrites with the further growth of the cobalt coatings at current densities higher than 0.05 A/cm<sup>2</sup>. The depth profiles of the tungsten and cobalt concentrations in the coating and nickel substrate indicate interdiffusion of the elements of the coating and substrate (Fig. 10.7).

The addition of molybdenum(VI) oxide to the cobalt-containing tungstate melt of  $\text{MoO}_3$  induces the dimolybdate-ion reduction wave corresponding to reaction (10.2). The difference in the potentials of cobalt and molybdenum deposition is 0.06–0.110 V at 1173 K (cobalt is more inert than molybdenum). These dependences of electrodeposition of tungsten–cobalt alloys are also characteristic of the deposition of molybdenum–cobalt alloys. Depending on the ratio of the  $\text{MoO}_3$  and  $\text{CoO}$  concentrations and the cathodic current density, continuous deposits of Mo, CoMo, Co<sub>3</sub>Mo, and Co can be prepared from a  $\text{Na}_2\text{WO}_4$ – $\text{MoO}_3$ –NiO melt.

The dependences of electrodeposition of the cobalt–tungsten (molybdenum) alloys and intermetallic compounds are retained when cobalt tungstate or molybdate is used as a cobalt source during synthesis.

**Fig. 10.7** (a) Trace of an electron probe on the polished section of a sample and (b) the depth profiles of the tungsten, cobalt, and nickel concentrations in the coating and nickel substrate. [CoO] = 0.7 mol %, [WO<sub>3</sub>] = 0.2 mol %,  $T = 1173$  K,  $i = 0.07$  A/cm<sup>2</sup>, and  $t = 1.5$  h



## 10.4 Conclusions

Molybdenum (tungsten)–nickel (cobalt) alloys and intermetallics can be deposited as continuous layers on a cathode from oxide melts. The composition and structure of the deposits can be controlled by varying the concentration of the corresponding components in the melt, the temperature, and the cathodic current density. An increase in the nickel (cobalt) content in an alloy with an increase in its concentration in the melt, a decrease in the cathodic current density, or an increase in the electrolysis temperature are most likely due to an increase in the fraction of the total current consumed to deposit nickel (cobalt) and to a decrease in the diffusion retardation for the ions of the more electrochemically negative component of the alloy.

**Acknowledgments** Authors of the present paper acknowledge support of all the Dum lupinar University and the University “Ukraine” staff in conducting scientific researches and writing this paper.

**Competing Interests** Authors of the present paper have no competing interests.

**Authors’ Contributions** Authors of the present paper have made equal contributions in conducting scientific researches and writing this paper.

**Funding** Authors of the present paper have not used any external sources of funding in addition to regular financing for scientific investigations provided by the Dum lupinar University and by the University “Ukraine.”

## References

1. Malyshev VV, Novosyolova IA, Shapoval VI (1997) High-temperature electrochemical synthesis of refractory metal-nonmetal compounds in ionic melts. *Molten Salts Bull* 63:2–8
2. Anderson CD, Taylor PR, Anderson CG (2013) Extractive metallurgy of rhenium: a review. *Miner Metall Process* 30:59–73
3. Kolobov GA, Pecheritsa KA, Karpenko AV, Moseyko YV, Ochinskyi VN (2015) *Rafinirovaniie volframa i molibdena* (Tungsten and molybdenum refining). *Meta* 33:45–51
4. Malyshev VV, Pisanenko AD, Shapoval VI (1996) *Elektrokhimicheskoe povedenie serebra v volframatno-molibdatnyih rasplavah i ego vliyanie na elektroosazhdenie pokryitiiy karbida molibdena* (electrochemical behavior of silver in tungsten–molybdate melts and its effect on the electrodeposition of molybdenum carbide coatings). *Ukr Khim Zh* 62:35–38
5. Novoselova IA, Malyshev VV, Shapoval VI, Supatashvili DT, Kushkhov KB (1997) High-temperature electrochemical synthesis of binary and ternary intermetallic high-melting molybdenum and tungsten compounds with cobalt, nickel, and carbon. *Russ J Appl Chem* 70:1218–1224
6. Malyshev VV, Gab AI, Uskova NN, Soloviev VV (2003) Structure and electrochemistry of tungsten-containing ionic melts. In: *Proceedings of the international symposium of ionic liquids in honour of Marcelle Gaune-Escard, Carry le Rouet, 26–28 June 2003*
7. Malyshev V, Gab A, Gaune-Escard M (2008) Molybdenum electrometallurgical processes in ionic melts. *Mater Manuf Process* 23:748–751
8. Zoski CG (2007) *Handbook of electrochemistry*, 1st edn. Elsevier, Amsterdam
9. Okamoto H (2010) *Desk handbook: phase diagrams for binary alloys*, 2nd edn. ASM International, New York

# Chapter 11

## Structure and Electrical/Dielectric Properties of Ion-Conductive Polymer Composites Based on Aliphatic Epoxy Resin and Lithium Perchlorate Salt



Liubov K. Matkovska, Maksym V. Iurzhenko, Yevgen P. Mamunya, Valeriy Demchenko, and Gisele Boiteux

### 11.1 Background

Liquid electrolytes are commonly used in lithium or lithium-ion batteries at room temperature with the ionic conductivity from  $10^{-3}$  to  $10^{-2}$  S/cm [1, 2].

It would be useful if the batteries could work at higher temperatures, since it will be no need to use a separate cooling circuit at the system level, or such need will be significantly reduced. However, high temperatures create difficulties because of quick degradation of liquid electrolytes [3]. In addition, there are two main problems that hinder the development of liquid electrolytes. First, formation of the lithium dendrites on electrodes leads to serious danger due to the potential possibility of internal short circuits. Second, the electrochemical instability of the lithium electrodes causes an insignificant life cycle of batteries during repeated processes of charging/discharging [4].

In addition, the first generation of batteries prototypes, which used liquid electrolytes, has a high risk of leaks affecting on the reliability of a device [1]. Safety is one of the most pressing issues related to the further progress in development of the next-generation batteries. That makes solid electrolytes one of the most

---

L. K. Matkovska

Institute of Macromolecular Chemistry of National Academy Sciences of Ukraine, Kyiv, Ukraine

Université de Lyon, Université Lyon 1, Ingénierie des Matériaux Polymères, UMR CNRS 5223, Villeurbanne, France

M. V. Iurzhenko (✉) · Y. P. Mamunya · V. Demchenko

Institute of Macromolecular Chemistry of National Academy Sciences of Ukraine, Kyiv, Ukraine

G. Boiteux

Université de Lyon, Université Lyon 1, Ingénierie des Matériaux Polymères, UMR CNRS 5223, Villeurbanne, France

© Springer International Publishing AG, part of Springer Nature 2018

O. Fesenko, L. Yatsenko (eds.), *Nanochemistry, Biotechnology, Nanomaterials, and Their Applications*, Springer Proceedings in Physics 214,

[https://doi.org/10.1007/978-3-319-92567-7\\_11](https://doi.org/10.1007/978-3-319-92567-7_11)

promising candidates for replacement of flammable and potentially dangerous liquid electrolytes [5].

Solid polymer electrolytes (SPE) have been used in different applications as the ion conductors in various electrochemical devices such as lithium batteries, ultracapacitors, fuel cells, solar cells, etc. [6]. Rechargeable lithium and lithium-ion batteries play an important role on the market of electrochemical energy storage devices, since they are widely used for charging of portable electronic devices and for autonomous controlling devices [2]. Therefore, recently the development of new solid polymer electrolytes was an important objective, since optimal balance between high ionic conductivity and technological conditions of material has not been still achieved [7, 8]. SPE have such properties as good compatibility with electrodes, low self-discharging rate, easy processing for various shapes and sizes, lack of leakage, flexibility, and self-sufficiency for form changes during charge-discharge cycles [7–10].

Polyethylene oxide (PEO) [11, 12] is one of the mostly studied oligomers, which are used for SPE creation due to the effective coordinating of metal ions in it because of the optimum distance and orientation of ether oxygen atoms in its molecular chains [12]. The disadvantage of PEO is amorphous-crystalline structure [4, 13, 14] that leads to the conductivity through the amorphous area of a polymer only [11, 15] above the glass transition temperature  $T_g$  [6, 12, 16] and, as a result, PEO has low ionic conductivity at room temperature because of the presence of high crystalline phase [4, 14, 17].

Nowadays, as a rule, solid polymer electrolytes include inorganic salts dissolving in oligomers which, in their turn, form a solid matrix with the ionic conductivity [10, 12, 18, 19]. Added salt serves as a source of ions and contributes their movement along the polymer chains, so that plays the crucial role in ions transport in polymer electrolytes [16]. Hereby, concentration and mobility of ions are significant parameters affecting the conductivity in polymer electrolytes [14, 17]. Understanding of mechanism of the ion transport in a polymer requires the study of ion-ion and ion-polymer interactions that is of great interest [10, 14]. Many studies of ion transport in polymer electrolytes have been conducted using various types of cations such as  $\text{Na}^+$ ,  $\text{Li}^+$ ,  $\text{Ag}^+$ , and  $\text{Mg}^+$  [20]. However, the composites based on lithium salts are preferably studied, because the  $\text{Li}^+$  cations are the smallest and can easily move in a polymer matrix [17, 20, 21]. Another important characteristic is thermal stability of ions and their inertness to the cell components [22].

In [23] a model of the mechanism of charge transfer that takes into account the accuracy of ion association in the PEO-salt (PEO- $\text{Li}^+$ ) system was proposed. According to this model, the charge transport through the polymer matrix can occur in four ways:

- The lithium cation motion along the single polymer chain of PEO
- The lithium cation motion from one to another polymer chain
- The lithium cation motion along the polymer chain of PEO between ion clusters (cation-anion)
- Cation motion between ion clusters and the polymer chain



High ionic conductivity can be achieved by increasing the salt concentration in polymer [6]; however the authors [9] have shown that conductivity of the composites based on PEO is limited by certain value of a salt concentration. At higher salt concentration conductivity decreases because of formation of the ion complexes, which, in turn, cause reduction of the ionic mobility and the number of charge carriers [10].

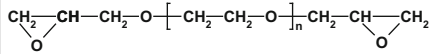
For application as electrolytes, polymers should have certain properties, such as amorphousness, the presence of ether oxygen in their structure, low glass transition temperature, high dimensional stability, mechanical strength, and the ability to form thin films [9, 18].

Thermosetting polymers such as epoxy resins are materials for extensive use in the aerospace industry, in automobile and marine applications, and in micro-electronics and food-packaging industries [24–26]. Properties of epoxy resins depend on specific combination of the used type of epoxy resins and curing agents [27]. Epoxy resins are important thermoset materials due to their excellent thermomechanical, barrier, chemical, and electrical properties, low shrinkage upon cure, and outstanding adhesion to various substrates [25, 26, 28–30]. They are highly used as matrix in conducting polymer composites [29]. Versatility is one of the strong features of epoxy polymers [25]. Molecular structure of epoxy resin can be easily modified for various applications considering its versatile properties [31]. Polymer blending technique is a quick and economic alternative, which has been widely used for obtaining materials with optimized properties and potentially can offer easy control of physical properties by compositional change for a wide variety of application prospects [32, 33]. Adding a more flexible aliphatic epoxy oligomer while mixing allows changing of thermal and mechanical properties [34].

One of the suitable materials that satisfies these requirements is aliphatic epoxy oligomer, namely, the diglycide aliphatic ester of polyethylene glycol (DEG-1). It has similar to polyethylene oxide chain structure (Table 11.1); however it is amorphous and is able to dissolve the high concentration of lithium perchlorate salt similarly to PEO.

Therefore, the aim of the present research is synthesis of solid amorphous polymer composites based on aliphatic epoxy oligomer and the study of influence of lithium perchlorate salts on their structure and properties.

**Table 11.1** Chemical structures of PEO and DEG-1

Code	Oligomer name	Chemical formula
PEO	Polyethylene oxide	$\text{HO} - \left[ \text{CH}_2 - \text{CH}_2 - \text{O} \right]_n - \text{H}$
DEG-1	Diglycide aliphatic ester of polyethylene glycol	$\text{CH}_2 - \text{CH} - \text{CH}_2 - \text{O} - \left[ \text{CH}_2 - \text{CH}_2 - \text{O} \right]_n - \text{CH}_2 - \text{CH} - \text{CH}_2$ 

Comparison of the chemical structures of PEO and epoxy oligomer of diglycide aliphatic ester of DEG-1

## 11.2 Experimental

**Materials and Synthesis** The epoxy oligomer (diglycide aliphatic ester of polyethylene glycol, DEG-1), Macromer, Vladimir, Russia, and salt of lithium perchlorate ( $\text{LiClO}_4$ , Sigma-Aldrich, USA) were used for synthesis of ion-conductive epoxy polymer composites. These components were previously pre-dried in vacuum at  $80^\circ\text{C}$  during 24 hours. After drying, the salt was dissolved in the DEG-1 oligomer. Solutions of DEG-1- $\text{LiClO}_4$  were prepared with  $\text{LiClO}_4$  content from 0 to 50 phr (parts per hundred) on 100% of polymer matrix. Ten percent of polyethylene polyamine hardener (PEPA, Chimia, Kharkov, Ukraine) was used as a curing agent for synthesis of the composites.

**Methods** The thermal characteristics were studied by differential scanning calorimetry (DSC) using TA Instruments DSC Q2000 (TA Instruments, New Castle, DE, USA) in the temperature range from  $-70^\circ\text{C}$  to  $+150^\circ\text{C}$  with the heating rate of  $10^\circ\text{C}/\text{min}$ . Glass transition temperature ( $T_g$ ) was determined from the DSC curves at the second heating. The experimental error of determination of the glass transition temperatures was  $\pm 1^\circ\text{C}$ .

The electrical and dielectric characteristics of the synthesized composites were investigated by broadband dielectric analyzer Novocontrol Alpha coupled with Novocontrol Quatro Cryosystem (Novocontrol Technologies, Montabaur, Germany) that was equipped with a two-electrode circuit, in the frequency range  $10^{-1}$  to  $10^7$  Hz and the temperature range from  $-60^\circ\text{C}$  to  $+200^\circ\text{C}$ . The voltage applied to a sample was equal to 0.5 V. The test samples had diameter of 20 mm and a thickness of 0.5 mm and were previously coated by aluminum under vacuum. The obtained data was analyzed using Novocontrol WinDeta 3.8 software.

Structural organization and features of macromolecular ordering of the synthesized polymer systems were investigated by wide-angle X-ray spectra (WAXS) using X-ray diffractometer DRON-4.07 (Burevestnik, Saint Petersburg, Russia). X-ray optical scheme was performed by Debye-Scherrer method on passing the primary beam through the polymer sample using  $\text{Cu K}_\alpha$  emission ( $\lambda = 1.54 \text{ \AA}$ ) that was made monochromatic using Ni filter. The X-ray tube BSV27Cu ( $U = 30 \text{ kV}$ ,  $I = 30 \text{ mA}$ ) was used as a source of characteristic X-ray irradiation. The investigations were carried out by automatic step scanning in the range of scattering angles ( $2\theta$ ) from  $2.6^\circ$  to  $40^\circ$ ; the exposure time was 5 s.

Infrared (IR) spectroscopic studies have been performed using spectrometer with Fourier transformation “Tensor 37” from Bruker Corp. in the range of wave numbers  $(600\text{--}3800)^\circ \text{cm}^{-1}$ . According to the passport of the device, the relative measurement error is  $<2\%$ .

Morphological features of the synthesized composites were studied using transmission optical microscopy (TOM) with the microscope Carl Zeiss Primo Star and reflective optical microscopy (ROM) with Unicorn NJF 120A polarization microscope at polarization angles  $0\text{--}90^\circ$ . Microphotographs analysis was performed using Carl Zeiss Imaging Solutions AxioVision V4.7.1 software.

Structural features of the synthesized composites have been studied using electron microscopy (SEM) by JEOL 100CX II transmission electron microscope, equipped with scanning system. Elemental analysis of inclusions was performed using analytical complex consisting of the scanning electron microscope JEOL JSM-35CF and X-ray spectrometer with dispersive in energy X-ray quanta (Model INCA Energy-350 from "Oxford Instruments"). An important feature of such electron microprobe analysis is its locality: maximum size of the excitation area is 2  $\mu\text{m}$ . According to the morphological characteristics and the chemical composition basing on the energy dispersive spectral analysis, the automatic separation of inclusions on types (elemental composition) and measuring of their sizes has been carried out. The results have been analyzed using a special program for quantitative phase distribution and inclusions investigation. All results are presented in weight percent. The experimental error was 0.1%.

WAXS, IR, ROM, and SEM studies and elemental analysis were carried out at the temperature  $T = 20 \pm 2$  °C.

All investigations were repeated three times for statistical data manipulation.

### 11.3 Results and Discussion

*The Thermal Characteristics* DSC thermogram of the salt of lithium perchlorate (Fig. 11.1a) has endothermic peaks at 79, 95, 133, and 150 °C, which correspond to different melting of its crystalline structure. In the plot of epoxy system with different content of  $\text{LiClO}_4$ , a glass transition temperature ( $T_g$ ) is only present; thus the composites are amorphous (Fig. 11.1b). The values of the glass transition temperature derived from the curves of the obtained composites depending on the content of  $\text{LiClO}_4$  in the reaction mixture are shown in Fig. 11.2. It is obvious that the increase of  $\text{LiClO}_4$  amount in reactive mixture from 0 to 50 phr leads

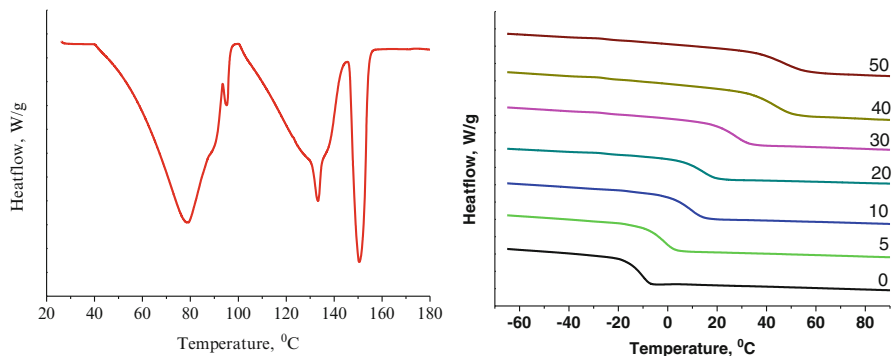


**Fig. 11.1** DSC thermograms of lithium perchlorate salt (a) [42] and of the composites with different content (in phr) of  $\text{LiClO}_4$  (b)

**Fig. 11.2** Dependence of the glass transition temperature  $T_g$  on  $\text{LiClO}_4$  salt content [43]

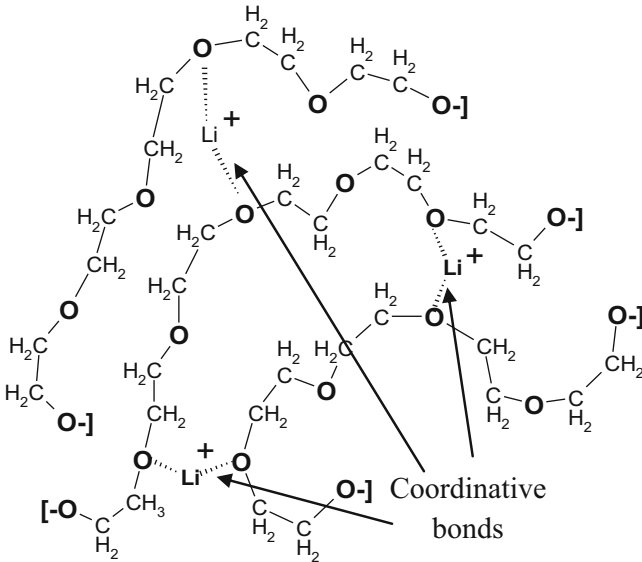
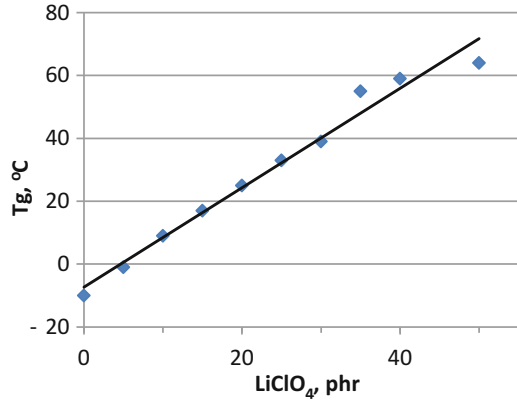


**Fig. 11.3** DEG/ $\text{LiClO}_4$  composite consists of DEG polymer chains with coordinative bonds between lithium cations and ether oxygen [44]

to a linear increase of the glass transition temperature from  $-10\text{ }^\circ\text{C}$  to  $64\text{ }^\circ\text{C}$ . This can be a result of the electrostatic interactions between lithium cations  $\text{Li}^+$  and the macromolecular chain of DEG-1 with immediate forming of coordinative complexes, such as {ether oxygen-lithium cations-ether oxygen} (Fig. 11.3), which are accompanied by displacement of electron density of the oxygen atoms and their partial polarization [35]. The result is a substantial reduction of segmental mobility of DEG-1 chains within the complexes formed that shows up in a glass transition temperature rise of polymer matrix. The linear dependence of  $T_g$  on the salt content testifies that all the lithium ions participate in the formation of coordination bonds.

The similar dependences were found in various sources [36–38]. In [39] the growth of  $T_g$  from  $-46\text{ }^\circ\text{C}$  to  $-30\text{ }^\circ\text{C}$  at low salt content of  $\text{LiClO}_4$  in PEO (1 mol/kg) and the subsequent slow decrease to  $-35\text{ }^\circ\text{C}$  for the concentration of 7.5 mol/kg was reported. At the same time, according to [9], the addition of lithium salt  $\text{LiPF}_6$  in a PEO with high molecular weight reduces both glass transition temperature and melting point. The injection of another lithium salt  $\text{LiCF}_3\text{SO}_3$  in PEO results in lowering of  $T_g$  from  $-65\text{ }^\circ\text{C}$  to  $-71\text{ }^\circ\text{C}$  [40]. In these cases, the coordination bonds were absent, and, contrary to DEG-1, the molecular mobility of the polymer chains increases. According to [41], in the poly(acrylonitrile-co-butyl acrylate)-LiTFSI systems, the  $T_g$  is lowered with the increased salt content: from  $+48\text{ }^\circ\text{C}$  for pure copolymer to  $-44\text{ }^\circ\text{C}$  for the electrolyte containing 95 wt.% of the salt. That can be a result of different strength of interactions between polymer matrices and salts with no stiffening of chains due to physical cross-linking that occurs because the solution of salt acts as a plasticizer.

*Electrical and Dielectric Properties* Figure 11.4 shows the isothermal spectra of the real part of the conductivity ( $\sigma'$ ) and the complex permittivity ( $\epsilon'$ ) for different concentrations of  $\text{LiClO}_4$  in DEG-1 obtained in the temperature range from  $-60\text{ }^\circ\text{C}$  to  $200\text{ }^\circ\text{C}$ . One can see that values and character of the  $\sigma'$  and  $\epsilon'$  curves depend on two factors: the content of  $\text{LiClO}_4$  and the temperature of measurements. At temperatures below the glass transition, the permittivity has low values and hardly varies with frequency indicating the “blocking effect” of free charge carriers due to the low mobility of macromolecular chains of the polymer matrix. In the same temperature range, the values of the real part of the complex conductivity vary linearly with frequency, i.e., such systems are insulators. At temperatures higher than  $T_g$ , “defrosting” of the polymer chains occurs that leads to the release of lithium cations and growth of  $\epsilon'$  values. Free lithium cations pass into the conducting band and begin to move along the polymer chain through the interactions with oxygen ether atoms, which exist in macromolecular chains (Fig. 11.5). This charge transfer leads to an increase in the electrical conductivity of the systems and the appearance of a plateau at low frequencies (the so-called DC conductivity plateau, an isotherms area, where conductivity values are independent on frequency) on the spectra of the real part of the complex conductivity. The  $\sigma'$  dependence on angular frequency  $\omega = 2\pi f$  is described by the following equation [45, 46]:

$$\sigma'(\omega) = \sigma_0 + A\omega^s \quad (11.1)$$

where  $\sigma_0$  is the conductivity that is independent on frequency, the exponent factor  $s$  equals  $0 < s \leq 1$ , and  $A$  is a numeric factor. The contribution of the second part is insignificant at low frequencies, and the conductivity, which is independent on frequency (plateau on the graph), is associated with the DC conductivity. At high frequencies above the critical frequency  $f_c$ , the main role is played by the second frequency-dependent parameter  $\sigma_{ac}(\omega) \sim \omega^s$  that characterizes the jumping conductivity in a disordered solid state (AC conductivity). The critical frequency  $f_c$  and the parameters  $A$  and  $s$  in the Eq. 11.1 depend on the temperature and the conductivity of the systems [46].

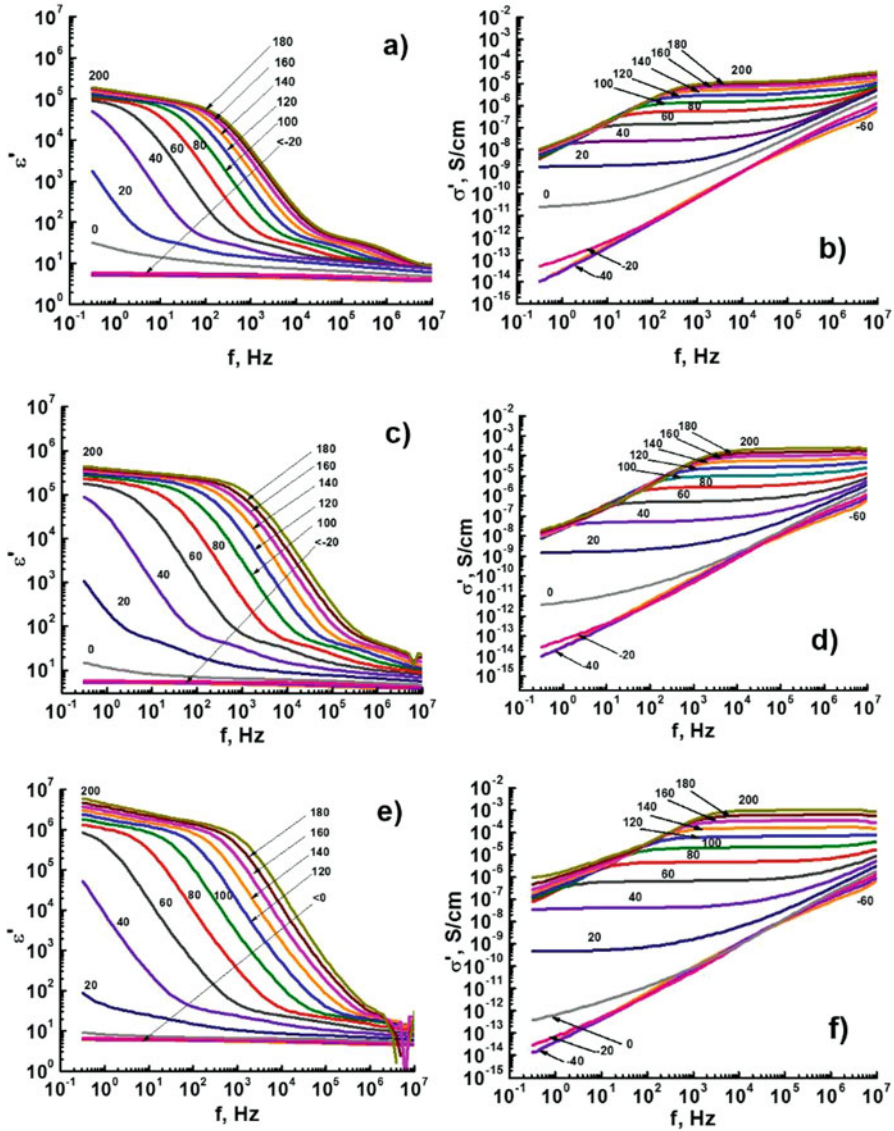


**Fig. 11.4** Permittivity (a, c, e, g) and real part of complex conductivity (b, d, f, h) spectra at different temperatures (from  $-60$  to  $+200$  °C) of the obtained composites with LiClO<sub>4</sub> contents: (a, b) 0; (c, d) 5; (e, f) 10; (g, h) 30 phr

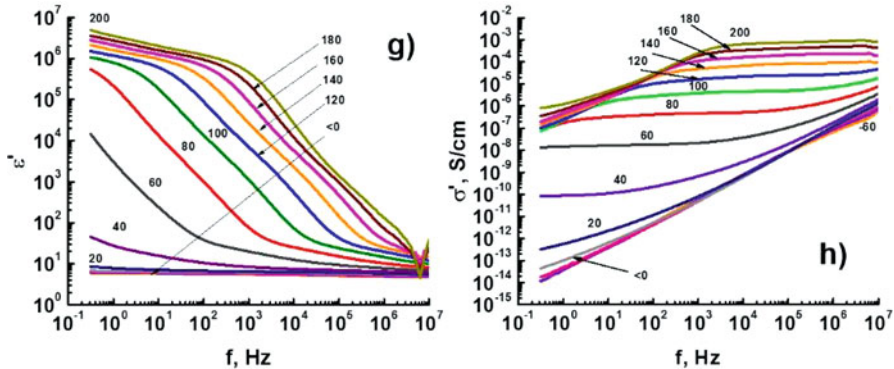


Fig. 11.4 (continued)

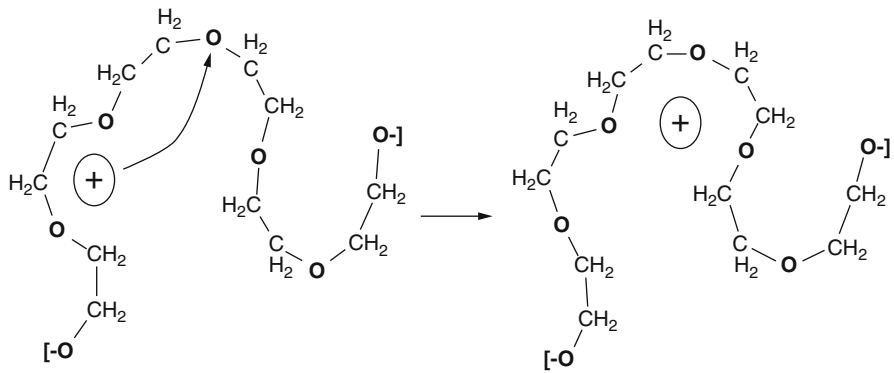


Fig. 11.5 Transfer of lithium cation along the DEG-I polymer chain [44]

The values of the permittivity  $\epsilon'$  at frequency  $10^3$  Hz are represented in Table 11.2. The values of the real part of the complex conductivity  $\sigma'$  for different temperatures throughout the range of the lithium salt content in the epoxy resin are also presented.

A number of free charge carriers, namely, the lithium ions  $\text{Li}^+$ , which overcome the energy barrier and move into conductive state, grow with further increase of the temperature (above  $40^\circ\text{C}$  to  $60^\circ\text{C}$ ). This leads to the blocking effect of electrodes that is caused by the space charge polarization. The blocking effect is manifested in appearance of a plateau on the  $\epsilon'$  isotherms at low frequencies and falling values of the real part of the complex conductivity left from plateau of the DC conductivity. The dominance of the conductivity relaxation is observed at high frequencies.

The frequency dependences of the impedance of the systems studied on temperature were also analyzed. Figure 11.6a shows the isothermal spectra of  $\tilde{W} = f(Z')$ , where  $Z' = M''/(\omega \cdot C_0)$  is the real part of the complex impedance,  $Z'' = M'/(\omega \cdot C_0)$  is the imaginary part of the complex impedance,  $M'$  and  $M''$  are the real and the

**Table 11.2** Characteristics of the composites with different content of LiClO<sub>4</sub> [44]

Content LiClO <sub>4</sub> , phr	$\varepsilon'$ ( $10^3$ Hz) <sup>a</sup>					
	$\sigma'$ (S/cm)/ $\sigma_{dc}$ (S/cm) <sup>b</sup>		100°C	160°C	200°C	
0	36		254	3,220	6,040	
5	1.7 × 10 <sup>-7</sup> /1.52 × 10 <sup>-7</sup>		1.4 × 10 <sup>-6</sup> /1.47 × 10 <sup>-6</sup>	8.1 × 10 <sup>-6</sup> /7.9 × 10 <sup>-6</sup>	1.3 × 10 <sup>-5</sup> /1.21 × 10 <sup>-5</sup>	
10	4.7 × 10 <sup>-7</sup> /5.1 × 10 <sup>-7</sup>		3,140	60,800	128,000	
20	6.96 × 10 <sup>-7</sup> /6.5 × 10 <sup>-7</sup>		1.0 × 10 <sup>-5</sup> /1.01 × 10 <sup>-5</sup>	9.6 × 10 <sup>-5</sup> /9.85 × 10 <sup>-5</sup>	2.3 × 10 <sup>-4</sup> /2.3 × 10 <sup>-4</sup>	
30	1.5 × 10 <sup>-7</sup> /1.48 × 10 <sup>-7</sup>		2,720	208,000	680,000	
			1,650	3.2 × 10 <sup>-4</sup> /3.16 × 10 <sup>-4</sup>	9.97 × 10 <sup>-4</sup> /1.01 × 10 <sup>-3</sup>	
			1,124	212,000	626,000	
			4.59 × 10 <sup>-6</sup> /4.6 × 10 <sup>-6</sup>	3.2 × 10 <sup>-4</sup> /3.26 × 10 <sup>-4</sup>	1.1 × 10 <sup>-3</sup> /1.17 × 10 <sup>-3</sup>	
			1,124	88,741	457,320	
			1.65 × 10 <sup>-8</sup> /1.67 × 10 <sup>-8</sup>	2.2 × 10 <sup>-4</sup> /2.17 × 10 <sup>-4</sup>	9.14 × 10 <sup>-4</sup> /9.18 × 10 <sup>-4</sup>	

Electrical and dielectric characteristics of the epoxy systems with different contents of LiClO<sub>4</sub> at different temperatures

<sup>a</sup>Experimental error on  $\varepsilon'$  was ±1

<sup>b</sup>Experimental error on  $\sigma'$  was ±1 × 10<sup>-10</sup> S/cm



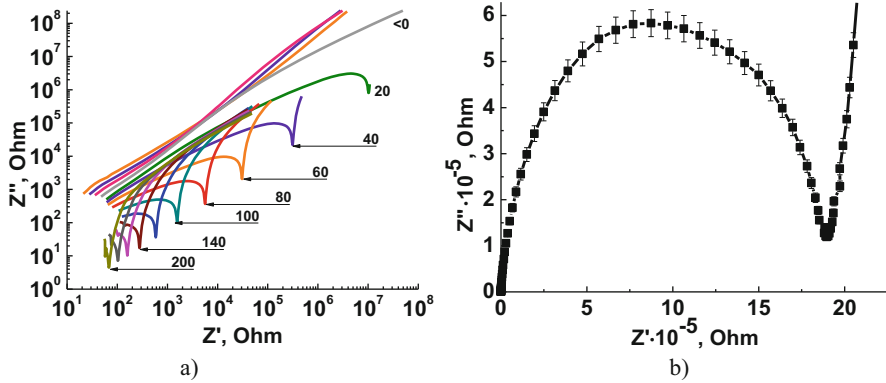


**Fig. 11.6**  $Z''/Z'$  plots for epoxy system with 5 phr of  $\text{LiClO}_4$  in the temperature range from  $-60$  to  $+200$  °C in double logarithmic coordinates (a) and in Cole-Cole coordinates at  $30$  °C (b) [44]

imaginary parts of electrical modulus, and  $C_0$  is the cell capacitance without the sample in vacuum, in double logarithmic coordinates for the DEG system containing 5 phr  $\text{LiClO}_4$  in the temperature range from  $-60$  °C to  $+200$  °C. It is evident that the Cole-Cole plots ( $Z'' = f(Z')$ ) were built for calculating the DC conductivity  $\sigma_{\text{dc}}$ . Figure 11.6 shows the classical Cole-Cole plots built for the composite of DEG-1 with 5 phr  $\text{LiClO}_4$  at temperature  $30$  °C. The dependence  $Z'' \sim Z'$  forms a clear minimum at a certain value of  $Z'$  in Cole-Cole coordinates. Conductivity values were calculated from the Eq. 11.2:

$$\sigma_{\text{dc}} = \frac{1}{R_{\text{dc}}} \frac{l}{S} \quad (11.2)$$

where  $R_{\text{dc}}$  is a bulk resistance of the system (Ohm) that equals the value of  $Z'$  on the minimum of the Cole-Cole plot;  $l$  is a thickness of the sample (cm), and  $S$  is an area of the sample ( $\text{cm}^2$ ). The right part of the curve corresponds to surface polarization effects, which are observed in the low-frequency region. The left part of the curve corresponds to volume polarization effects in the high-frequency region. The calculated values of the conductivity  $\sigma_{\text{dc}}$  are presented in Table 11.2. The identity of the values of the conductivity  $\sigma_{\text{dc}}$  calculated with impedance analysis and the conductivity  $\sigma'$  values defined by plateau on the primary experimental spectra of the real part of the complex conductivity prove the eligibility of such analysis approaches for studying the behavior of the ion-conductive systems in wide temperature and frequency ranges and validity of the obtained values of the conductivity [47].

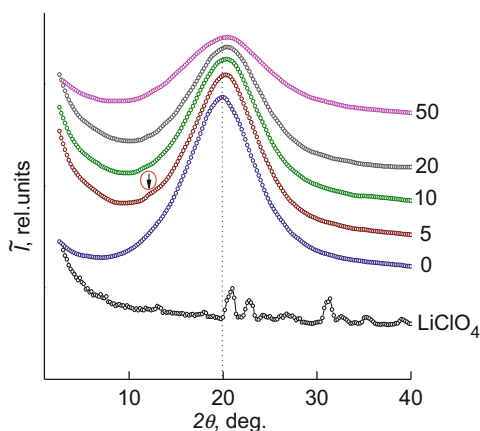
On the other hand, a high level of the conductivity (approximately  $1 \times 10^{-3}$  S/cm) obtained at  $200$  °C decreases rapidly with cooling so the conductivity at  $100$  °C is two orders of magnitude lower than at  $200$  °C. Apparently,

the reason for that is the presence of coordinative bonds between lithium ions and DEG macromolecules, which are more stable at low temperatures and reduce the molecular mobility of the polymer chains. This can lead to a drop of “decoupling index” (index of lithium ion mobility by jumping from one to another oxygen atom). Also, the formation of ion pairs in the systems with increased contents of  $\text{LiClO}_4$  in the epoxy resin (higher than 20 phr) reduces the number of free charge carriers in the systems and, consequently, decreases the electrical conductivity and the permittivity. So, the conductivity of the system DEG-1 with 20 phr  $\text{LiClO}_4$  at 60 °C is on the same level as for pure DEG-1. However, this effect is significant only at temperatures up to 100 °C. A rapid growth of the electrical conductivity and the permittivity due to the destruction of aggregates that is accompanied by release of charge carriers, namely, lithium cations  $\text{Li}^+$ , occurs when the temperature rises. The maximum values of the conductivity  $\sigma' = 1.1 \times 10^{-3} \text{ S/cm}$  and the permittivity  $\epsilon' = 6.3 \times 10^5$  are attained for the system DEG-1 with 20 phr of  $\text{LiClO}_4$  at 200 °C (Table 11.2).

Another possible way to improve the electrical characteristics of the synthesized composites is the incorporation of charge carriers by the phase of ionic liquids (IL), which is regarded as a promising approach to enhance the ionic conductivity and electrochemical properties of the SPEs [36]. The  $\text{Li}^+$  transport is significantly better in consequence of the plasticizing effect of the IL that decreases the glass transition temperature and makes easier the polymer chain mobility [48]. The IL-rich phase accompanies the easiest movement of ions and an increase of the conductivity is expected [36]. In addition, the injection of ionic liquid leads to a significant enhancement in a contribution of  $\text{Li}^+$  ions to the overall conductivity of the composites with lithium salt [49].

*Wide-Angle X-Ray Spectra* Analysis of the wide-angle X-ray diffraction patterns of the systems has shown that all of them are amorphous (Fig. 11.7). In particular, epoxy oligomer DEG-1 that was cured with polyethylene polyamine is characterized by short-range ordering in the space translation of molecular fragments of its cross-

**Fig. 11.7** Wide-angle X-ray diffraction patterns of the lithium perchlorate salt  $\text{LiClO}_4$  and composites with different salt content (shown near curves) [43]



site links. That is confirmed by presence of one diffraction peak (calculated from the angular half-width) of the diffusion type (amorphous halo), in which the angular position ( $2\lambda$ ) is about  $20.0^\circ$ .

The average value of the period ( $d$ ) of a short-range molecular ordering of DEG-1 internodal molecular segments in a polymer volume can be calculated using Bragg equation:

$$d = \lambda(2 \sin \theta_m)^{-1} \quad (11.3)$$

where  $\lambda$  is the wavelength of the characteristic X-ray emission ( $\lambda = 1.54 \text{ \AA}$  for Cu  $K_\alpha$  emission) and it equals to  $4.44 \text{ \AA}$ .

However, the introduction of  $\text{LiClO}_4$  salt that has a crystalline structure into the epoxy resin is accompanied by changes in the diffraction pattern. This is evidenced by the presence of subtle diffraction peak of the diffuse type at  $2\theta_m \approx 12.2^\circ$  on the background of the amorphous halo, which is similar to the angular position of the DEG-1 at  $2\theta_m \approx 20.0^\circ$  ( $d \approx 4.39 \text{ \AA}$ ). According to [50], this diffraction peak characterizes the existence of metal-polymer complexes of the donor-acceptor type, in our case, between central ions ( $\text{Li}^+$ ) and ether oxygen of the epoxy chains in the intermolecular volume of the epoxy resin.

The gradually increasing  $\text{LiClO}_4$  content from 0 to 50 phr in the volume of epoxy resin leads to the displacement of the amorphous halo at  $2\theta_m \approx 20.0^\circ$ , which characterizes the short-range order of fragments of the DEG-1 internodal molecular segments, in the region of large scattering angles. That indicates a tendency to decrease the Bragg distance between the molecular segments (Table 11.3).

*Infrared Spectroscopic Studies* Structure of the polymer composites has been investigated by means of infrared spectroscopy. The main absorption bands of  $\text{LiClO}_4$  (Fig. 11.8a), DEG-1 (Fig. 11.8b), and PEPA (Fig. 11.8c) with relevant groups are presented in Table 11.4. These absorption bands were interpreted in accordance with [51, 52] and [53], respectively.

As one can see, the characteristic absorption bands of epoxies' ring are absent in the spectra (Fig. 11.9, 0 phr  $\text{LiClO}_4$  content) that indicates the complete curing of epoxy component. These absorption bands are also absent in the IR spectra (Fig. 11.9, 5–50 phr) of the cured composites. The absorption bands in the range

**Table 11.3** Bragg distances between molecular segments of the composites with different content of  $\text{LiClO}_4$  [43]

Content of $\text{LiClO}_4$ , phr	$2\theta_m$ , degrees <sup>a</sup>	$d$ , $\text{\AA}$
Pure $\text{LiClO}_4$ (for comparison)	20.0	4.44
0	20.0	4.44
5	20.2	4.39
10	20.4	4.35
20	20.4	4.35
50	20.6	4.30

<sup>a</sup>Experimental error on  $2\theta_m$  was  $\pm 0.05^\circ$

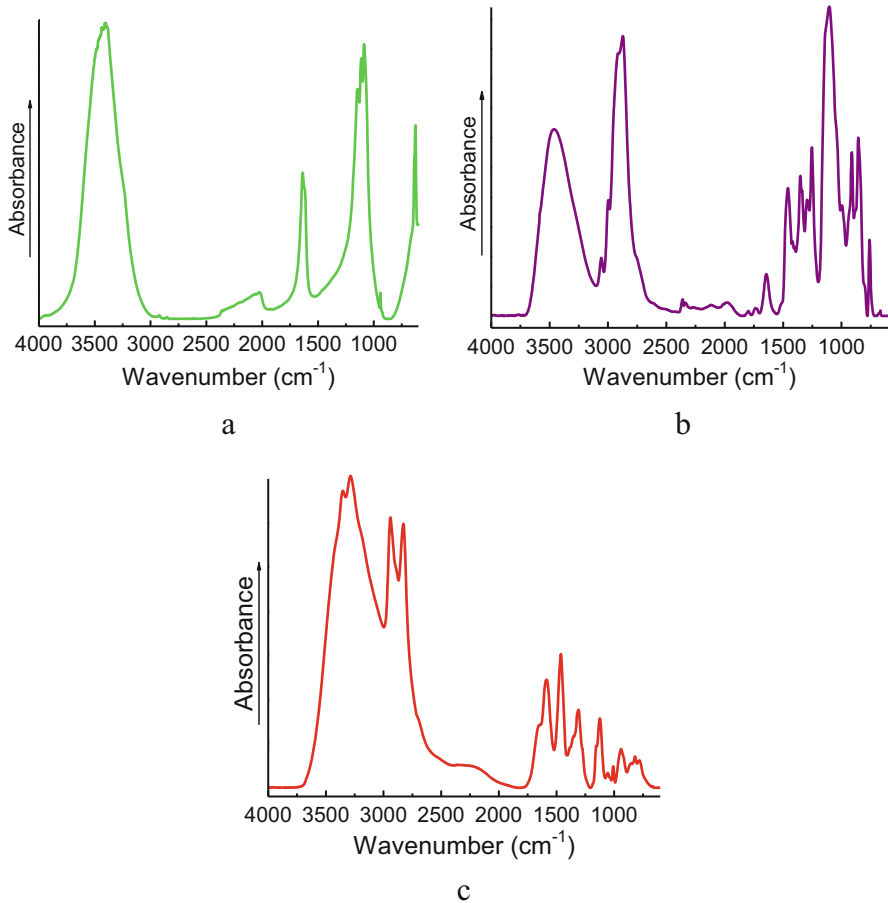


**Fig. 11.8** Infrared spectra of  $\text{LiClO}_4$  (a), DEG-1 (b), and PEPA (c) [60]

of wave numbers  $1300\text{--}1520\text{ cm}^{-1}$  and  $1000\text{--}1190\text{ cm}^{-1}$ , which, respectively, correspond to fluctuations of  $\text{-CH}_2\text{-}$  and (C-O-C and C-NC) groups, expand and shift to the low-frequency region with  $\text{LiClO}_4$  content increase. It is known that this can be associated with the formation of coordination bonds between  $\text{Li}^+$  cations and  $\text{ClO}_4^-$  anions and polymer chains [54, 55]. It is generally accepted that  $\text{Li}^+$  cations can easily form complexes with polyethylene ether bonds [51, 52, 55–58] as well as with polyamines [59]. The absorption band at  $1637\text{ cm}^{-1}$  in the IR spectrum of  $\text{LiClO}_4$  indicates its undissociated state (Table 11.4) [51, 52]. It should be noted that this band in the IR spectra of 5–50 samples is absent. This indicates that the pure (undissociated) form of  $\text{LiClO}_4$  in the composites is not contained. In accordance to this, in Fig. 11.10 the possible ion-dipole interactions of  $\text{Li}^+$  ion with the ether bond of polyethylene oxide fragment and OH-group of the disclosed epoxy ring of DEG-1 (Fig. 11.10a–d) and with secondary amine group of PEPA (Fig. 11.10e), with

**Table 11.4** Interpretation of the absorption bands in IR spectra of LiClO<sub>4</sub>, DEG-1, and PEPA [43, 60]

LiClO <sub>4</sub>		DEG-1		PEPA	
Wave number, cm <sup>-1</sup>	Group, type fluctuations	Wave number, cm <sup>-1</sup>	Group, type fluctuations	Wave number, cm <sup>-1</sup>	Group, type fluctuations
3100-3600	-OH, ν (a water)	3100-3600	-OH, ν	3352	NH <sub>2</sub> + NH, ν <sub>asym</sub>
1637	LiClO <sub>4</sub>	2914	-CH <sub>2</sub> -, ν <sub>asym</sub>	3287	NH <sub>2</sub> + NH, ν <sub>sym</sub>
1086, 1113, 1146	ClO <sub>4</sub> <sup>-</sup> , ν <sub>asym</sub>	2872	-CH <sub>2</sub> -, ν <sub>sym</sub>	2941	-CH <sub>2</sub> -, ν <sub>asym</sub>
941	ClO <sub>4</sub> <sup>-</sup> , ν <sub>sym</sub>	1458	-CH <sub>2</sub> -, δ	2827	-CH <sub>2</sub> -, ν <sub>sym</sub>
627	ClO <sub>4</sub> <sup>-</sup> (not associated with Li <sup>+</sup> )	1352	CH <sub>2</sub> -, δ	1641, 1585	NH <sub>2</sub> + NH, δ
-	-	1253	Epoxy group, ν <sub>sym</sub>	1462	CH <sub>2</sub> -, δ
-	-	1105	C-O-C, ν	1310	CH <sub>2</sub> -, δ
-	-	910, 856	Epoxy group, ν <sub>asym</sub>	1124	C-N-C, ν

ν, valence vibration; ν<sub>sym</sub> and ν<sub>asym</sub>, valence symmetric and asymmetric vibrations; δ bending vibration

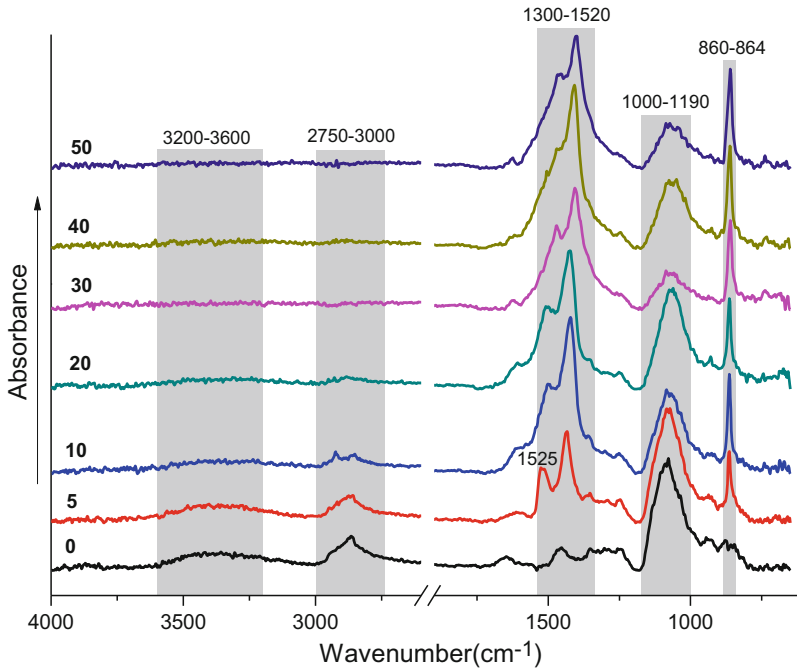
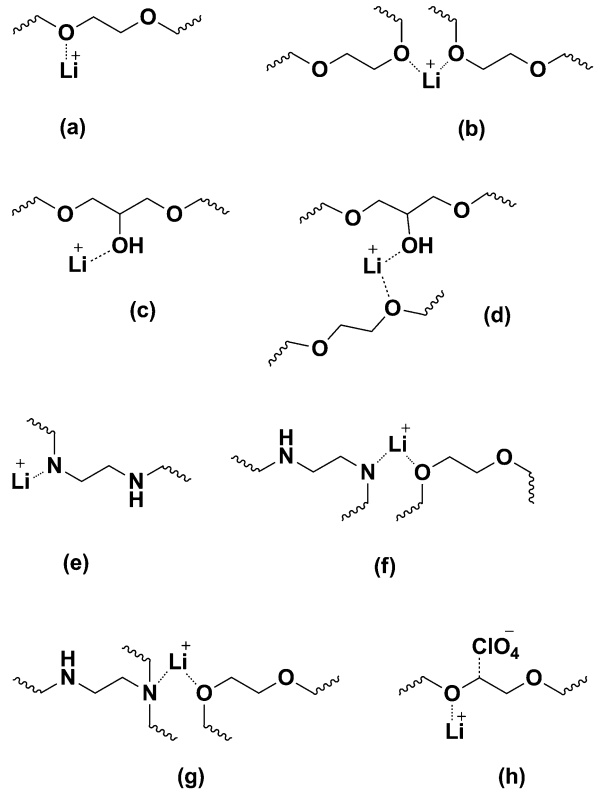


**Fig. 11.9** Infrared spectra of the composites with different lithium perchlorate salt content (marked by numbers near curves) [43]

secondary or tertiary amine group and ether bond simultaneously (Fig. 11.10e–g), are shown. As an example of coordinated  $\text{ClO}_4^-$  ion, Fig. 11.10h represents the scheme of this anion interaction with positively charged carbon atom that is located near the electronegative oxygen atom.

It should be noted that in the sample with adding of 5 phr lithium perchlorate and after solidification a new absorption band at  $864\text{ cm}^{-1}$  appears in its IR spectrum, which maintains in the samples with 10–50 phr salt content. Considering that the most of the absorption bands of metal complexes are located in the low-frequency region [61], it is obvious that this absorption band is associated to complexes involving  $\text{LiClO}_4$ . The interaction of PEO and  $\text{LiClO}_4$  is widely studied in literature, and in presented materials the absorption band around  $860\text{ cm}^{-1}$  is absent [51, 52, 55–58]. Probably this band refers to formation of lithium amino-complex, whose presence influences the fluctuations of methylene groups located nearby. That is confirmed by appearance of a new absorption band in the IR spectrum of composite with 5 phr of  $\text{LiClO}_4$  at  $1525\text{ cm}^{-1}$  (Fig. 11.9), which is shifted to the low-frequency region with increasing of the salt content up to 50 phr. In accordance to [54], this is due to the increasing number of coordination bonds. It is important to note that when film samples with 5–50 phr of  $\text{LiClO}_4$  were crushed into a powder and molded in the KBr tablets, the described absorption bands at  $\leq 1525\text{ cm}^{-1}$  and  $860\text{--}864\text{ cm}^{-1}$

**Fig. 11.10** Complexes, which possibly exist in the composites  $\text{LiClO}_4/\text{DEG-1}/\text{PEPA}$  [43] due to ion-dipole interactions of  $\text{Li}^+$  ion with the ether bond of polyethylene oxide fragment and OH-group of the disclosed epoxy ring of DEG-1 (a-d), with secondary amine group of PEPA (e), with secondary or tertiary amine group and ether bond simultaneously (e-g), or coordinated  $\text{ClO}_4^-$  ion with  $\text{C}^+$ , located near  $\text{O}^-$  (h).



disappeared, since crushing leads to destruction of the weak coordination bonds. That also confirms the coordination nature of these bands. As an example, Fig. 11.11 shows the IR spectra of the samples with 5 and 30 phr of  $\text{LiClO}_4$  contents.

Generally, the increasing quantity of  $\text{LiClO}_4$  leads to the increase of the coordination bonds, which reduce mobility of macromolecular chains [56]. Figure 11.9 shows a gradual decrease in intensity of the absorption bands associated with valence fluctuations of OH-, NH-, and  $-\text{CH}_2-$  groups. At the destruction of coordination bonds in the samples molded in the KBr tablets, these valence bonds are clearly manifested (Fig. 11.11).

In addition to the coordination bonds, other important factors which influence on the structure of the obtained composites should be indicated. Thus, the reaction between DEG-1 and PEPA in the presence of  $\text{LiClO}_4$  occurs more completely, apparently (to a certain limit of salt), since it is known that  $\text{LiClO}_4$  is an effective aminolysis catalyst of oxiranes ring [62]. Another structure-forming factor can be realized as a net of hydrogen bonds, including ones with the participation of  $\text{ClO}_4^-$  ions [58].

In our case the complexes of  $\text{Li}^+$  ions with maximum coordination number 2 are presented in Fig. 11.10, but the coordination number of ions can reach 8 [59].

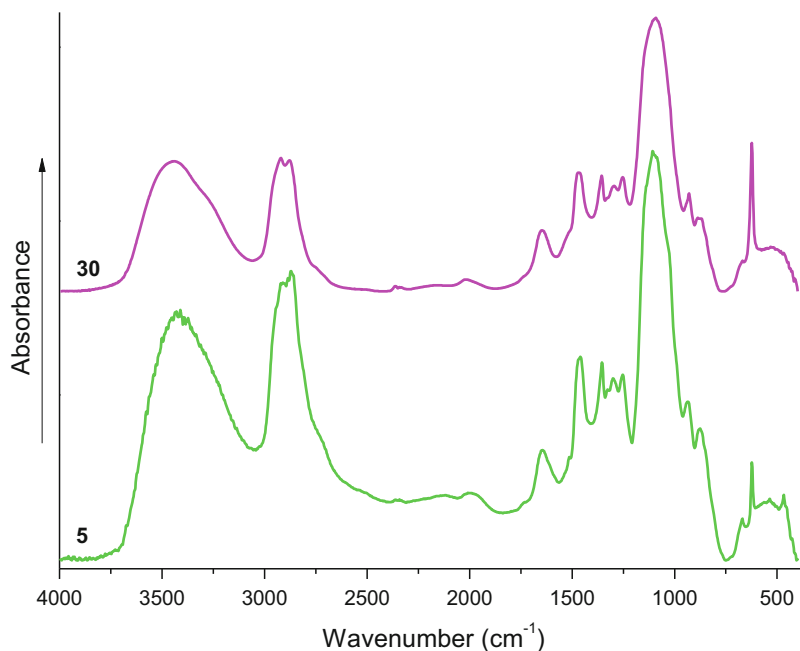


**Fig. 11.11** IR spectra of the composites with different  $\text{LiClO}_4$  content (marked by numbers near curves) [43]

Due to small radius (0.6 Å), the  $\text{Li}^+$  ions are highly mobile, so they can create as well as destroy the complexes easily [57, 59], and because of that it is difficult to define complex structure involving lithium perchlorate salt that was formed during the curing reaction.

*The Morphological Features* Figures 11.12 and 11.13 present the micrographs of transmission and reflective optical microscopes of the synthesized composites, respectively, with different content of lithium perchlorate salt. The formation of ordered structures in the composites with addition of the salt into the system was observed. In this case the reflective optical microscopy that used polarized mode revealed the presence of the distributed inclusions, probably, of inorganic nature with sizes ranging from 2 to 20  $\mu\text{m}$ . In order to confirm the presence of inclusions in the composites, the structural investigation that used scanning electron microscopy was conducted. The results are presented in Fig. 11.14. One can see the presence of the inclusions observed by ROM (for the samples with some  $\text{LiClO}_4$  content) and the increase of their number and size with the increase of  $\text{LiClO}_4$  content in the composites.

In order to determine the nature of found inclusions, the elemental analysis of nine different areas of surface of the composite with 50 phr  $\text{LiClO}_4$  has been fulfilled (Fig. 11.15). Normalized mass distribution of elements in the microareas shown



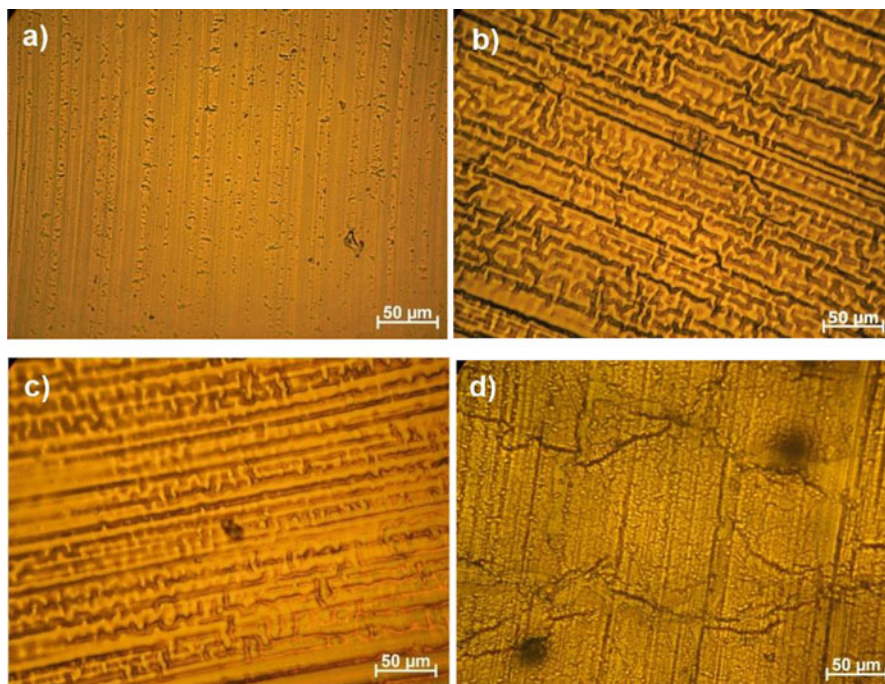


**Fig. 11.12** Transmission optical microscopy results of the composites with 0 (a), 10 (b), 20 (c), and 50 (d) phr of  $\text{LiClO}_4$  salt

in Fig. 11.15 are presented in Table 11.5. It is evident that content of elements in spectra is different. It is important that the inclusions identified by ROM (Fig. 11.13) and SEM (Fig. 11.14) are characterized with the decreased content of carbon and the increased content of oxygen and chlorine, which enter into the composition of  $\text{LiClO}_4$  (Spectra 3–5), comparing to the spectra of the polymer matrix (Spectra 7–9). That can be explained by the oxygen and chlorine atoms aggregation and, perhaps, also with aggregation of lithium atoms (however it was impossible to determine such aggregation with the conducted investigations) from the lithium perchlorate salts dissolved in DEG-1 during its synthesis. The presence of a number of carbon atoms (even in the Spectra 3–5 of the inclusions) can be explained by the overlapping of their high content in macromolecular chains of polymer matrix that may partially cover the inclusions.

The elemental composition of the initial lithium perchlorate salt was also determined (Fig. 11.16). It was found that the chlorine in salt is 41.61%<sub>wt</sub> and oxygen is 58.39%<sub>wt</sub>. Lithium content could not be determined.

Summary elemental map (Fig. 11.17d) of the composite with 20 phr of  $\text{LiClO}_4$  was constructed from elemental maps of individual elements (carbon, Fig. 11.17a; oxygen, Fig. 11.17b; chlorine, Fig. 11.17c) for determination of distribution of elements on its surface. The calculations have shown that the content of the elements

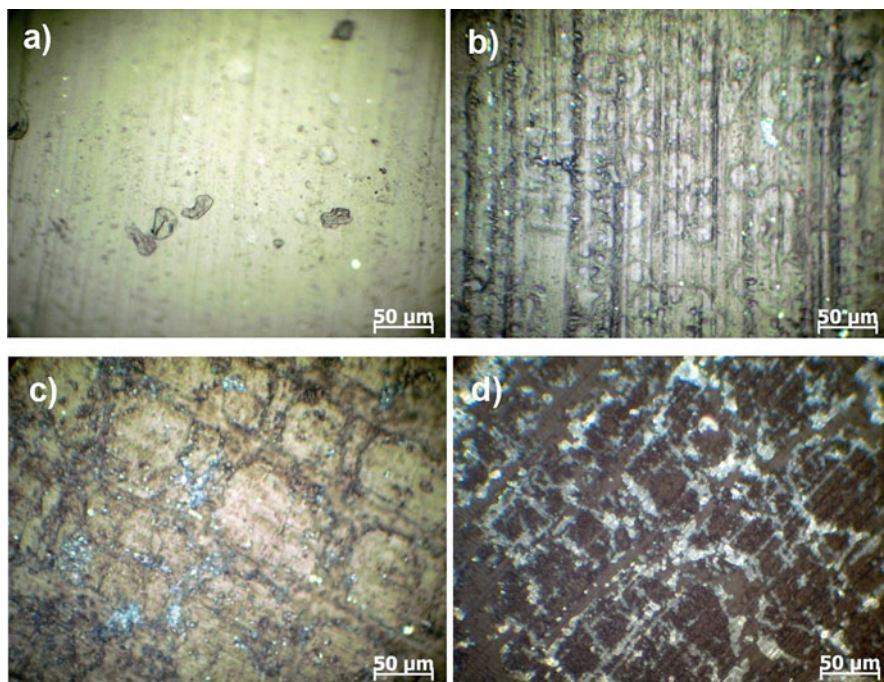


**Fig. 11.13** Reflective optical microscopy results of the composites with 0 (a), 10 (b), 20 (c), and 50 (d) phr of  $\text{LiClO}_4$  salt [43]

on the surface of the composite is the following: carbon is 51.57 wt.%, oxygen is 43.79 wt.%, and chlorine is 4.64 wt.%, while their distribution coincides with the ordering of inclusions identified by the means of optical and electron microscopy. This allows concluding that the nature of these inclusions with oxygen and chlorine saturation is inorganic.

## 11.4 Conclusions

The comprehensive study of composites based on aliphatic epoxy oligomer (diglycide aliphatic ester of polyethylene glycol, DEG-1) containing different amounts of  $\text{LiClO}_4$  salt (0–50 phr.) revealed creation of interactions between lithium cations  $\text{Li}^+$  and the macromolecular chain of DEG-1 with forming of coordinative complexes. It is reflected in a substantial reduction of segmental mobility of DEG-1 chains within the formed complexes that linearly increase glass transition temperature  $T_g$  of polymer matrix with salt content.

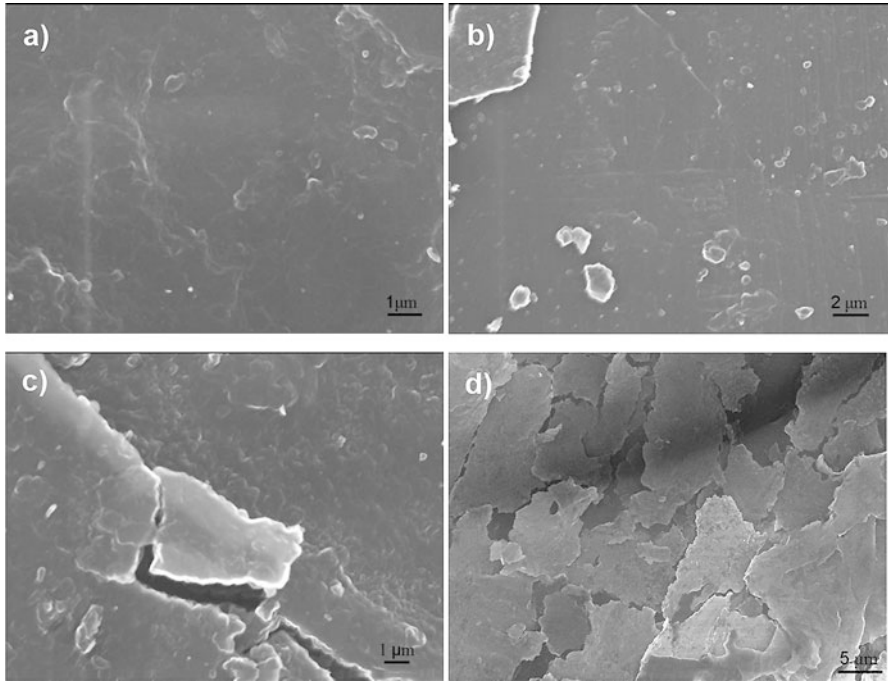


**Fig. 11.14** Scanning electron microscopy results of the composites with 0 (a), 10 (b), 20 (c), and 50 (d) phr of LiClO<sub>4</sub> salt [43]

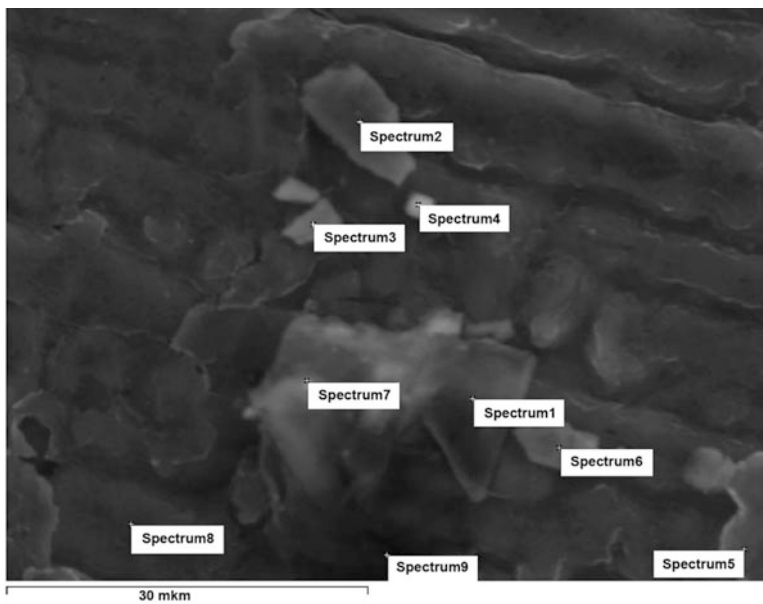


**Fig. 11.15** SEM of the composite with 50 phr of LiClO<sub>4</sub> surface with the appointment of elemental analysis spectra [43]

**Table 11.5** The mass distribution (%wt) of elements in different areas of the composite surface with 50 phr of LiClO<sub>4</sub> [43]

Spectrum	C	O	Cl	Total
Spectrum1	68.8	25.2	6.0	100.0
Spectrum2	34.9	62.9	2.2	100.0
Spectrum3	52.8	36.9	10.3	100.0
Spectrum4	61.6	29.8	8.6	100.0
Spectrum5	55.2	39.8	5.0	100.0
Spectrum6	40.9	56.2	2.9	100.0
Spectrum7	55.1	42.9	2.0	100.0
Spectrum8	54.7	41.2	4.1	100.0
Spectrum9	58.8	37.3	3.9	100.0

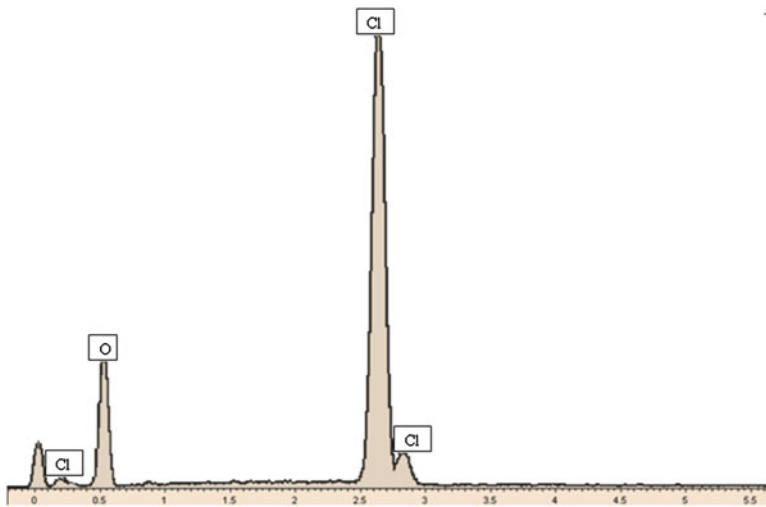


**Fig. 11.16** Elemental spectra of the original lithium perchlorate salts

The synthesis of epoxy polymers in the presence of lithium perchlorate made it possible to obtain an ion-conductive polymeric material with a high level of ionic conductivity ( $\sim 10^{-3}$  S/cm) and the permittivity ( $6 \cdot 10^5$ ) at elevated temperatures (200 °C).

It was found that at higher temperature (200 °C versus 60 °C) the values of conductivity  $\sigma$  are three orders of magnitude higher with maximum at 20 phr of LiClO<sub>4</sub>. Such conductivity behavior is explained by existence of two opposite competitive processes, namely, the growth of salt content in composite gives the increase of carrier number and the raise of conductivity. On the other hand, the restriction of molecular movements of DEG-1 because of forming of the coordinative complexes reduces the carrier mobility. At higher temperatures the raising of molecular movements compensates this mechanism, and conductivity becomes essentially higher.

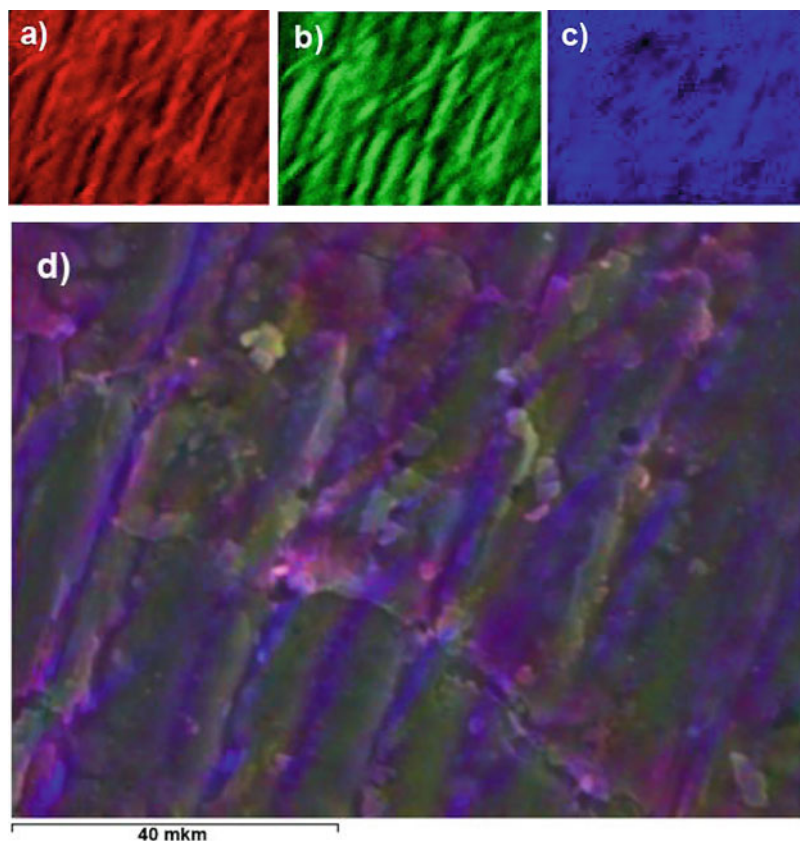


**Fig. 11.17** The elemental map of surface of the composite with 20 phr of  $\text{LiClO}_4$ : C (a), O (b), Cl (c), and the combined map (d) [43]

The detailed IR spectroscopy study allowed suggesting the scheme of  $\text{LiClO}_4$  interaction with polymer chains, namely, the possible ion-dipole interactions of  $\text{Li}^+$  ion with the ether bond of polyethylene oxide fragment and OH-group of the disclosed epoxy ring of DEG-1, with secondary amine group or tertiary amine group of PEPA and ether bond simultaneously.

The results of morphological and structural studies by means of optical and electron microscopes as well as by elemental analysis have revealed the presence of inclusions with sizes from nanometers up to  $\sim 20$  micrometers, probably, of inorganic nature distributed in the polymer matrix.

## References

1. Sudhakar YN, Selvakumar M, Krishna BD (2013) LiClO<sub>4</sub>-doped plasticized chitosan and poly(ethylene glycol) blend as biodegradable polymer electrolyte for supercapacitors. *Ionics* 19:277–285
2. Zygadlo-Monikowska E, Florjańczyk Z, Ostrowska J, Boltromiuk P, Frydrych J, Sadurski W, Langwald N (2011) Synthesis and characterization of new trifluoroalkoxyborates lithium salts of ionic liquid properties. *Electrochim Acta* 57:66–73
3. Bergman M, Bergfelt A, Sun B, Bowden T, Brandell D, Johansson P (2015) Graft copolymer electrolytes for high temperature Li-battery applications, using poly(methyl methacrylate) grafted poly(ethylene glycol)methyl ether methacrylate and lithium bis (trifluoromethanesulfonimide). *Electrochim Acta* 175:96–103
4. Bo C, Qiang X, Zhen H, Yanran Z, Shaojie C, Xiaoxiong X (2016) One-pot preparation of new copolymer electrolytes with tunable network structure for all-solid-state lithium battery. *J Power Sources* 331:322–331
5. Wei L, Nian L, Jie S, Po-Chun H, Yuzhang L, Hyun-Wook L, Yi C (2015) Ionic conductivity enhancement of polymer electrolytes with ceramic nanowire fillers. *Nano Lett* 15:2740–2745
6. Mohamed TA, Padmanathan N, Selladurai S (2014) Effect of nanofiller CeO<sub>2</sub> on structural, conductivity, and dielectric behaviors of plasticized blend nanocomposite polymer electrolyte. *Ionics* 21:825–840
7. Guilherme LA, Borges RS, Moraes EMS, Silva GG, Pimentac MA, Marletta A, Silva RA (2007) Ionic conductivity in polyethylene-b-poly(ethylene oxide)/lithium perchlorate solid polymer electrolytes. *Electrochim Acta* 53:1503–1511
8. Chai MN, Isa MIN (2012) Investigation on the conduction mechanism of carboxyl methylcellulose-oleic acid natural solid polymer electrolyte. *Int J Adv Technol Eng Res* 2:36–39
9. Ibrahim S, Johan MR (2012) Thermolysis and conductivity studies of poly(ethylene oxide) (PEO) based polymer electrolytes doped with carbon nanotube. *Int J Electrochem Sci* 7: 2596–2615
10. Ahmad. Z, Isa MIN (2012) Ionics conduction via correlated barrier hoping mechanism in cmc.sa solid biopolymer electrolytes. *Int J Latest Res Sci Technol* 1:70–75
11. Sharma P, Kanchan DK (2013) A comparison of effect of PEG and EC plasticizers on relaxation dynamics of PEO–PMMA–AgNO<sub>3</sub> polymer blends. *Ionics* 19:1285–1290
12. Karan NK, Pradhan DK, Thomas R, Natesan B, Katiyar RS (2008) Solid polymer electrolytes based on polyethylene oxide and lithium trifluoro- methane sulfonate (PEO–LiCF<sub>3</sub>SO<sub>3</sub>): ionic conductivity and dielectric relaxation. *Solid State Ionics* 179:689–696
13. Kesavan K, Mathew CM, Rajendran S, Subbu C, Ulaganathan M (2015) Solid polymer blend electrolyte based on poly(ethylene oxide) and poly(vinyl pyrrolidone) for lithium secondary batteries. *Brazilian J Physics* 45:19–27
14. Das S, Ghosh A (2015) Ionic conductivity and dielectric permittivity of PEO–LiClO<sub>4</sub> solid polymer electrolyte plasticized with propylene carbonate. *AIP Adv* 5. <https://doi.org/10.1063/1.4913320>
15. Pradhan DK, Tripathy SN (2013) Effect of plasticizer concentration on microstructural and dielectric properties of polymer composite electrolyte. *Adv Chem Sci* 2:114–121
16. Dey A, Karan S, De SK (2009) Effect of nanofillers on thermal and transport properties of potassium iodide polyethylene oxide solid polymer electrolyte. *Solid State Commun* 149:1282–1287
17. Yao Z, Jingqing L, Hong H, Shichun J (2012) Effects of lithium perchlorate on poly(ethylene oxide) spherulite morphology and spherulite growth kinetics. *J Appl Polym Sci* 123: 1935–1943
18. Machado GO, Prud'homme RE, Pawlicka A (2007) Conductivity and thermal analysis studies of solid polymeric electrolytes based on plasticized hydroxyethyl cellulose. *e-Polymers* 7(1):1335–1343

19. Kyung JL, Yong WK, Joo HK, Jong HK (2007) Supramolecular polymer/metal salt complexes containing quadruple hydrogen bonding units. *J Polym Sci B Polym Phys* 45:3181–3188
20. Anji RP, Hee-Woo R (2016) The effects of LiTDI salt and POSS-PEG ( $n = 4$ ) hybrid nanoparticles on crystallinity and ionic conductivity of PEO based solid polymer electrolytes. *Sci Adv Mater* 8(10):931–940
21. Marcinek M, Syzdek J, Marczewski M, Piszcz M, Niedzicki KM, Plewa-Marczewska A, Bitner A, Wieczorek P, Trzeciak T, Kasprzyk M, Łęzak P, Zukowska Z, Zalewska A, Wieczorek W (2015) Electrolytes for Li-ion transport – review. *Solid State Ionics* 276:107–126
22. Mindemark J, Sun B, Törmä E, Brandell D (2015) High-performance solid polymer electrolytes for lithium batteries operational at ambient temperature. *J Power Sources* 298:166–170
23. Gray FM (1997) *Polymer electrolytes*. Published Royal Society of Chemistry, London
24. Feng Q, Yang J, Yu Y, Tian F, Zhang B, Feng M, Wang S (2017) The ionic conductivity, mechanical performance and morphology of twophase structural electrolytes based on polyethylene glycol, epoxy resin and nano-silica. *Mater Sci Eng B* 219:37–44
25. Kim JG, Son B, Mukherjee S, Schuppert N, Bates A, Kwon O, Choi MJ, Chung HY, Park S (2015) A review of lithium and non-lithium based solid state batteries. *J Power Sources* 282:299–322
26. Amereller M, Schedlbauer T, Moosbauer D, Schreiner C, Stock C, Wudy F, Zugmann S, Hammer H, Maurer A, Gschwind RM, Wiemhöfer H-D, Winter M, Gores HJ (2014) Electrolytes for lithium and lithium ion batteries: from synthesis of novel lithium borates and ionic liquids to development of novel measurement methods. *Prog Solid State Chem* 42:39–56
27. Yu Y, Zhang B, Wang Y, Qi G, Tian F, Yang J, Wang S (2016) Co-continuous structural electrolytes based on ionic liquid, epoxy resin and organoclay: effects of organoclay content. *Mater Des* 104:126–133
28. Wu F, Chen N, Chen R, Wang L, Li L (2017) Organically modified silica-supported ionogels electrolyte for high temperature lithium-ion batteries. *Nano Energy* 31:9–18
29. Jinisha B, Anilkumar KM, Manoj M, Pradeep VS, Jayalekshmi S (2017) Development of a novel type of solid polymer electrolyte for solid state lithium battery applications based on lithium enriched poly (ethylene oxide) (PEO)/poly (vinyl pyrrolidone) (PVP) blend polymer. *Electrochim Acta* 235:210–222
30. Lv P, Yang J, Liu G, Liu H, Li S, Tang C, Mei J, Li Y, Hui D (2017) Flexible solid electrolyte based on UV cured polyurethane acrylate/succinonitrile-lithium salt composite compatibilized by tetrahydrofuran. *Compos Part B* 120:35–41
31. Thayumanasundaram S, Rangasamy VS, Seo JW, Locquet J-P (2017) Electrochemical performance of polymer electrolytes based on poly(vinyl alcohol)/poly(acrylic acid) blend and Pyrrolidinium ionic liquid for lithium rechargeable batteries. *Electrochim Acta* 240:371–378
32. Polu AR, Rhee H-W (2017) Ionic liquid doped PEO-based solid polymer electrolytes for lithium-ion polymer batteries. *Int J Hydrog Energy* 42(10):7212–7219
33. Rocco AM, Fonseca CP, Loureiro FAM, Pereira RP (2004) A polymeric solid electrolyte based on a poly(ethylene oxide)/poly(bisphenol A-co-epichlorohydrin) blend with  $\text{LiClO}_4$ . *Solid State Ionics* 166:115–126
34. Łasińska AK, Marzantowicz M, Dygas JR, Krok F, Florjańczyk Z, Tomaszewska A, Zygadło-Monikowska E, Żukowska Z, Lafont U (2015) Study of ageing effects in polymer-in-salt electrolytes based on poly(acrylonitrile-co-butyl acrylate) and lithium salts. *Electrochim Acta* 169:61–72
35. Kiselev YM (2008) *Coordination chemistry*. Integral, Moscow
36. Johnston K, Pavuluri SK, Leonard MT, Desmulliez MPY, Arrighi V (2015) Microwave and thermal curing of an epoxy resin for microelectronic applications. *ThermochimActa* 616: 100–109
37. Boumedienne N, Faska Y, Maaroufi A, Pinto G, Vicente L, Benavente R (2017) Thermostructural analysis and electrical conductivity behavior of epoxy/metals composites. *J Phys Chem Solids* 104:185–191
38. Fache M, Monteréal C, Boutevin B, Caillol S (2015) Amine hardeners and epoxy cross-linker from aromatic renewable resources. *Eur Polym J* 73:344–362

39. Wieczorek W, Raducha D, Zalewska A, Stevens JR (1998) Effect of salt concentration on the conductivity of PEO-based composite polymeric electrolytes. *J Phys Chem B* 102:8725–8731
40. Johan MR, Ting LM (2011) Structural, thermal and electrical properties of nano manganese-composite polymer electrolytes. *Int J Electrochem Sci* 6:4737–4748
41. Daigle J-C, Asakawa Y, Vjih A, Hovington P, Armand M, Zaghib K (2016) Exceptionally stable polymer electrolyte for a lithium battery based on cross-linking by a residue-free process. *J Power Sources* 332:213–221
42. Matkovska LK, Iurzhenko MV, Mamunya YP, Matkovska OK, Boiteux G, Lebedev EV (2017) The ion-conducting composites based on the aliphatic and aromatic epoxy oligomers and the lithium perchlorate salt. *Polym J* 39(3):147–153
43. Matkovska L, Iurzhenko M, Mamunya Y et al (2017) Structural peculiarities of ion-conductive organic-inorganic polymer composites based on aliphatic epoxy resin and salt of lithium perchlorate. *Nanoscale Res Lett* 12:423 [doi.org/10.1186/s11671-017-2195-5](https://doi.org/10.1186/s11671-017-2195-5)
44. Matkovska L, Iurzhenko M, Mamunya Y, Matkovska O, Demchenko V, Lebedev E, Boiteux G, Sergeï A (2014) Electrophysical behavior of ion-conductive organic-inorganic polymer system based on aliphatic epoxy resin and salt of lithium perchlorate. *Nanoscale Res Lett* 9:674. <https://doi.org/10.1186/1556-276X-9-674>
45. Kremer F, Schonhals A (2003) *Broadband dielectric spectroscopy*. Springer, Berlin-Heidelberg
46. Psarras GC, Manolaki E, Tsangaris GM (2003) Dielectric dispersion and ac conductivity in iron particles loaded polymer composites. *Compos Part A* 34:1187–1198
47. Pershina KD, Kazdobin KO (2012) *The impedance spectroscopy of the electrolytic materials*. Ukrainian Education, Kyiv
48. Li L, Wang F, Li J, Yang X, You J (2017) Electrochemical performance of gel polymer electrolyte with ionic liquid and PUA/PMMA prepared by ultraviolet curing technology for lithium-ion battery. *Int J Hydrog Energy* 42(17):12087–12093
49. Poornima Vijayan P, Puglia D, Al-Maadeed MASA, Kenny JM, Thomas S (2017) Elastomer/thermoplastic modified epoxy nanocomposites: the hybrid effect of ‘micro’ and ‘nano’ scale. *Mater Sci Eng* 116. <https://doi.org/10.1016/j.mser.2017.03.001>
50. Shtompel VI, Kercha YY (2008) *Structure of linear polyurethanes*. Scientific Mind, Kiev
51. Sim LH, Gan SN, Chan CH, Yahya R (2010) ATR-FTIR studies on ion interaction of lithium perchlorate in polyacrylate/poly (ethylene oxide) blends. *Spectrochim Acta A Mol Biomol Spectrosc* 76:287–292
52. Abarna S, Hirankumar G (2014) Study on new lithium ion conducting electrolyte based on polyethylene glycol-p-tertoctyl phenyl ether and lithium perchlorate. *Int J ChemTech Res* 6:5161–5167
53. Bellamy L (1963) *Infrared spectra of complex molecules*. Foreign Lit. Pub. House, Moscow
54. Selvasekarapandian S, Baskaran R, Kamishima O, Kawamura J, Hattori T (2006) Laser Raman and FTIR studies on Li<sup>+</sup> interaction in PVAc–LiClO<sub>4</sub> polymer electrolytes. *Spectrochim Acta A Mol Biomol Spectrosc* 65:1234–1240
55. Mamunya Y, Iurzhenko M, Lebedev E, Levchenko V, Chervakov O, Matkovska O, Sverdlukovska O (2013) *Electroactive polymer materials*. Alpha-Reklama, Kyiv
56. Chiu CY, Chen HW, Kuo SW, Huang CF, Chang FC (2004) Investigating the effect of miscibility on the ionic conductivity of LiClO<sub>4</sub>/PEO/PCL ternary blends. *Macromolecules* 37:8424–8430
57. Fullerton-Shirey SK, Maranas JK (2009) Effect of LiClO<sub>4</sub> on the structure and mobility of PEO-based solid polymer electrolytes. *Macromolecules* 42:2142–2156
58. Kuo PL, Liang WJ, Chen TY (2003) Solid polymer electrolytes V: microstructure and ionic conductivity of epoxide-crosslinked polyether networks doped with LiClO<sub>4</sub>. *Polymer* 44:2957–2964



59. Olsher U, Izatt RM, Bradshaw JS, Dalley NK (1991) Coordination chemistry of lithium ion: a crystal and molecular structure review. *Chem Rev* 91:137–164
60. Matkovska L, Tkachenko I, Demchenko V, Iurzhenko M, Mamunya Y (2017) Influence of lithium perchlorate on structure of epoxy polymeric composites. *Nanosistemi Nanomateriali Nanotehnologii* 15:175–184 Ukraine
61. Nakamoto K (1986) *Infrared and Raman spectra of inorganic and coordination compounds*. Wiley, Ltd, New York
62. Chini M, Crotti P, Macchia F (1990) Metal salts as new catalysts for mild and efficient aminolysis of oxiranes. *Tetrahedron Lett* 31:4661–4664

# Chapter 12

## Mechanical and Thermal Characteristics of Irradiation Cross-linked Hydrogels



O. Nadtoka, N. Kutsevol, A. Onanko, and V. Neimash

### 12.1 Introduction

The research and development trend of hydrogels as polymeric transitory dressing membranes are becoming the main commercial target. Hydrogels meet all the requirements for wound healing and are necessary for burn patients in the shortest time possible because of the following justifications: (1) hydrogels control the lost fluids and liquid from the body, (2) they maintain the wettability and moisture in the wound zone, and (3) they possess tissue-like structure and compatibility. Hydrogels are reported to be the best choice compared to other dressing forms because they have the needed requirements for the ideal wound dressings.

Dressings from hydrogels present as transparent elastic films with thickness  $h = 2 \div 4 \times 10^{-3}$  m and consist of 85  $\div$  90% distilled water [1]. They can contain antiseptic, anesthetic, and hemostatic substances also.

Hydrogels are usually stabilized by means of chemical or physical interactions among the polymer chains which are known as cross-linking methods. After cross-linking hydrogels have the ability to retain greatly the absorbed water in their mesh structure.

The radiation technology employed in the present work has advantage for obtaining wound dressing hydrogel membranes because the cross-linked hydrogel network is generated and sterilized in a single technological process. This way the product obtained does not require additional operation process. Examples of polymers cross-

---

O. Nadtoka (✉) · N. Kutsevol · A. Onanko  
National Taras Shevchenko University of Kyiv, Kyiv, Ukraine

V. Neimash  
Institute of Physics of the National Academy of Sciences of Ukraine, Kyiv, Ukraine

linked by the radiation method are poly(vinyl alcohol), poly(ethylene glycol), and poly(acrylic acid) [2–4].

It is shown that the radiation cross-linking of polymers upon irradiation in aqueous solutions is achieved at lower doses than when the polymer is irradiated in a solid or molten state, due to the participation in the cross-linking of free OH radicals formed as a result of radiolysis of water [5].

Hydrogels, particularly highly swollen ones, usually possess poor mechanical properties. So, the aim of our research focuses on cross-linked PVA to obtain hydrogels with improved mechanical properties that will be further used as wound dressing materials. We investigate mechanical and thermal properties of cross-linked hydrogels depending on the PVA's concentration.

## 12.2 Experimental

### 12.2.1 Hydrogel Synthesis

Polyvinyl alcohol from Fluka with  $M_w = 4 \times 10^5$  g/mol was used for hydrogel synthesis. Polymer was dissolved in distilled water ( $T = 70$  °C); solution was cooled and kept at room temperature. PVA solutions with concentrations 0.04, 0.06, and 0.08 g/ml were used for gel preparation. All these concentrations were above the critical crossover concentration ( $C^*$ ) for PVA sample chosen for this study. Value of  $C^*$  was determined by viscometry method [6] and was equal to 0.03 g/ml. Homogeneous solutions were hermetically placed in PE ziplock packages, and the thickness of solution in each pack was about 3 mm. Then, samples were irradiated under electron beam by pulsed electron accelerators of “ARGUS” (the electron energy  $E_e = 1$  MeV) and “Electronic” ( $E_e = 4$  MeV) models with dose 50 kGy to become cross-linked [7]. The electron flux intensity was varied within an interval from 0.1 to 2.5  $\mu\text{A}/\text{cm}^2$ . The control of the current density in the electron beam and the integral dose of the irradiation were carried out by the Faraday cylinder method. Measurement of sample temperature during electron irradiation was carried out using a differential thermocouple “alumel-chromel.” The required temperature (25 °C) was supported by the balance of heating by the electron beam of the incandescent lamp and cooling by the air fan. The hydrogels in the final form were transparent sheets of few millimeters.

### 12.2.2 Experimental Methods

#### 12.2.2.1 Morphological Analysis

The sample morphology was examined by using a scanning electron microscope mod, Stereoscan 440 (LEO), Cambridge, UK instrument. This analysis aimed to

visualize the internal structure morphology. The cryogenically fractured film in liquid nitrogen was mounted vertically on the SEM stub by silver adhesive paste. The specimens were sputter coated with gold to avoid electrostatic charges and to improve image resolution before being examined by the electron microscopy.

#### 12.2.2.2 Mechanical Analysis

The tensile strength of the swollen polymer samples were tested using a modernized IMASH-20-75 ALA-TOO test machine (Russia) [8]. Measurements of the static elastic module  $E$ , elastic limit  $\sigma_E$ , and yield point  $\sigma_T$  which were carried out by stress-strain ( $\sigma$ - $\varepsilon$ ) diagram at the brief monaxonic extension were plotted.

#### 12.2.2.3 Thermogravimetric Analysis (TGA)

Thermogravimetric analysis (TGA) was done to study thermal decomposition behavior of dried in vacuum samples using a Q50 TA Instrument (US) in nitrogen atmosphere at a heating rate of  $10\text{ }^\circ\text{C} \times \text{min}^{-1}$  from 20 to 600  $^\circ\text{C}$ . Processing of the results was performed using specialized TA Universal Analysis program.

#### 12.2.2.4 Differential Scanning Calorimetry (DSC)

A differential scanning calorimeter Q2000, TA Instruments (Inc., DE, USA), was used for study of thermophysical characteristics (glass transition temperature,  $T_g$ ) of hydrogels. All the samples were previously dried up to fixed weight in vacuum. The DSC curves were obtained by sample heating (at  $5\text{ }^\circ\text{C}/\text{min}$ ) from room temperature to 200  $^\circ\text{C}$ , followed by a recooling until reaching 25  $^\circ\text{C}$ . Rescans were performed immediately after each scan, in order to erase the thermal history of the samples and to confirm the location of the  $T_g$ , based on the reversibility of this second-order transition. The melting temperature ( $T_m$ ) of the samples was also measured. The results were processed using the TA Universal Analysis program.

### 12.3 Results and Discussion

#### 12.3.1 Radiation Cross-linked Hydrogels

In the present study, the irradiated hydrogel dressing membranes, prepared by means of electron beam, were obtained as 2.5–2.7-mm-thick sheets. The irradiation of aqueous polymer solution initiates the generation of macro-radicals on polymer chains. Radiolysis of water molecules leads to the appearance of hydroxyl radicals,

**Fig. 12.1** Sample of cross-linked hydrogel



which also can attack polymer chains, resulting in the formation of macro-radicals too. Recombination of the macro-radicals on different chains causes the formation of covalent bonds (crosslinks). Thus a cross-linked structure appears. Additionally, radiolysis of water leads to the formation of gas substances (molecular oxygen and molecular hydrogen) that are observed as bubbles in the hydrogel samples (Fig. 12.1) [9].

Obtained hydrogel dressing was flexible and did not dissolve in hot water but had high sorption capacity. They were easy to handle and pleasant in touch.

It is known that physical and mechanical characteristics of hydrogels are dependent on its morphology. The morphology of hydrogel samples obtained by irradiation process is determined by a number of factors: molecular weight and polymer concentration, the additives used, and radiation-absorbed dose [10].

Increasing the irradiation dose leads to an increase in the gel fraction due to growth of cross-link density. The dose range of radiation should be the optimal and limited by sterilizing dose from below and the maximum allowable dose from above. For medical devices, this range of doses is usually from 15 to 50 kGy. It is established [11] that a radiation dose of at least 20 kGy is required to form a polymer base with the necessary structural and mechanical properties. When the dose exceeds 50 kGy, the mechanical strength and elasticity decreased, and a large number of gas bubbles are formed inside. So, a radiation dose of 50 kGy was used in a present study to form cross-linked hydrogels.

### **12.3.2 Mechanical Properties**

The microstructure of radiation cross-linked hydrogels, prepared from water solution of PVA at different concentration, was examined by SEM. The drastic difference in internal hydrogels structure was not observed for studied samples. Images for all tested samples demonstrated internal structure corresponding to elastomers. Figure 12.2 represents SEM image for hydrogel prepared by irradiation of PVA solution with  $C = 0.8$  g/ml. The mesh size does not exceed 1000 nm, which allows liquids or gases to pass through it.

**Fig. 12.2** SEM image of radiation cross-linked PVA hydrogel

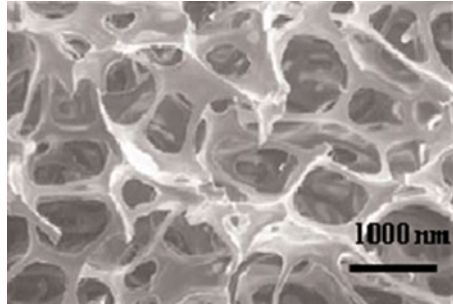
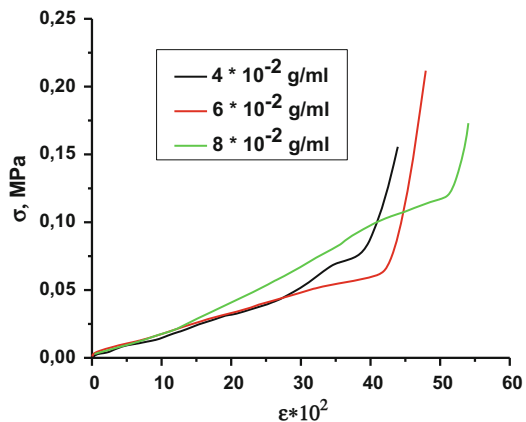


**Fig. 12.3** Diagram of strain – deformation  $\sigma-\varepsilon$  of cross-linked hydrogels at different PVA concentrations



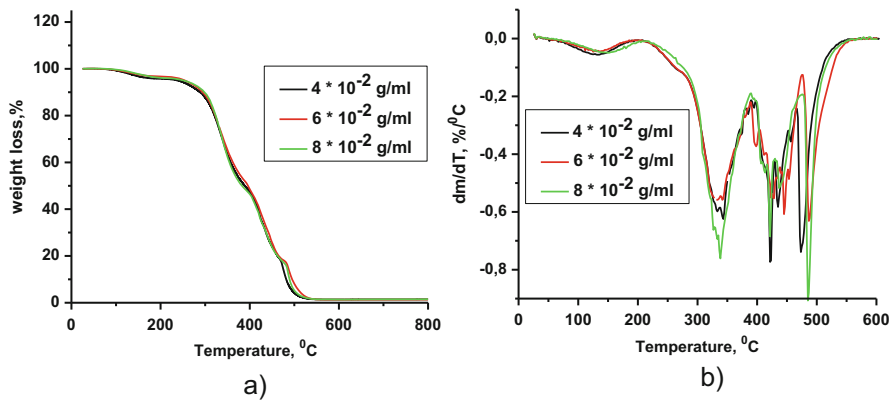
It is known that PVA is a polymer with flexible chains able to form intramolecular hydrogen bonds. High flexibility of PVA chains between cross-links and hydrogen bonds between OH groups of PVA moiety can determine the mechanical properties of prepared hydrogels. Thus, the chemical structure of hydrogel on the one side and the size of mesh on the other side should affect the amount of hydrogen bonds in the sample and determine the flexibility of polymer chains. Therefore increasing of the number  $t$  of intra- and intermolecular hydrogen bonds leads to enhance the rigidity of hydrogel structure. This suggestion is confirmed by data represented in Fig. 12.3 which demonstrated the dependence the stress verse strain for hydrogels prepared at different PVA concentrations.

Therefore, to break the hydrogen bonds in hydrogel structure, the additional stress is needed. Thus, mechanical properties are determined by both factors: amount of cross-links and hydrogen bonds in the samples of hydrogel.

As can be seen in Table 12.1, the elastic modulus  $E$ , elastic limit  $\sigma_E$ , and yield point  $\sigma_T$  increase with increasing of PVA concentration that indicates on improving of mechanical properties of samples.

**Table 12.1** Elastic module  $E$  extension, elastic limit  $\sigma_E$ , and yield point  $\sigma_T$ , of cross-linked polymers

$C_{PVA} 10^2, \text{g/ml}$	Static elastic module $E$ at extension, KPa	Elastic limit $\sigma_E$ , KPa	Yield point $\sigma_T$ , KPa
4	69,0	38	48
6	105,3	43	82
8	272,3	73	108

**Fig. 12.4** TGA (a) and DTG (b) thermograms of PVA hydrogels at different polymer concentrations

### 12.3.3 Thermogravimetric Analysis (TGA)

The morphology of hydrogel is influenced on its thermal characteristic [12]. TG curves for analyzed samples revealed four stages of thermal behavior (Fig. 12.4, Table 12.2). The thermal degradation values such as the initial-final degradation temperatures ( $T_i - T_f$ ), temperature interval value ( $\Delta T$ ), the temperature of maximum speed ( $T_{max}$ ), and weight loss ( $W$ ) were analyzed for hydrogels obtained at various polymer concentrations (Fig. 12.4a, b; Table 12.2) and were given in Table 12.2.

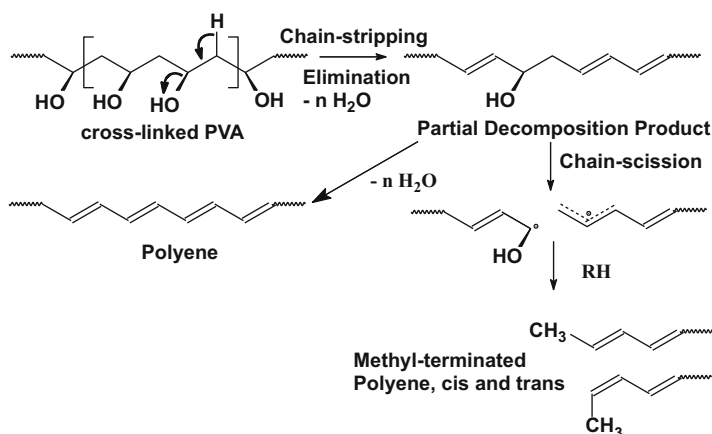
Stage I corresponds to weight loss of samples at the temperature range of 50–200 °C caused by water evaporation. The next three stages of weight loss located at about 200, 390, and 470 °C and related to chemical transformation leading to thermal degradation of polymer.

The concentration of the polymer before irradiation affects the cross-link density and mesh size in final hydrogel. It is observed that the concentration of PVA is inversely proportional to the amount of moisture retained from the sample (Table 12.1, Stage I).

It is known that the thermal chemical degradation of PVA starts between 170 and 200 °C [13], and complete pyrolysis of the polymer chain occurs at 500 °C. The analysis of prepared PVA hydrogels demonstrated two regions of weight

**Table 12.2** Thermogravimetric parameters of prepared hydrogels

$C_{\text{PVA}}, \times 10^2 \text{ g/ml}$	Stage	$(T_i - T_f), ^\circ\text{C}$	$\Delta T, ^\circ\text{C}$	$T_{\text{max}}, ^\circ\text{C}$	$W, \%$	Residue
4	I	50–204	154		4.31	1.43
	II	204–390	186	342	50.25	
	III	390–466	76	422	30.82	
	IV	466–552	86	473	17.5	
6	I	50–210	160		4	1.4
	II	210–388	178	338	51.16	
	III	388–475	87	422	31.45	
	IV	475–560	85	488	15.98	
8	I	50–207	157		3.3	1.32
	II	207–388	181	342	47.87	
	III	388–475	87	426	33.87	
	IV	475–561	86	486	16.94	

**Fig. 12.5** Proposed cross-linked PVA hydrogel pyrolysis reactions

loss about  $200^\circ\text{C}$  (Stage II) and  $390^\circ\text{C}$  (Stage III) (Fig. 12.4b). Weight loss at  $200^\circ\text{C}$  (Stage II) was attributed to the degradation of polymer chain via rapid chain-stripping elimination of  $\text{H}_2\text{O}$ . This process is represented in Fig. 12.5 [14, 15]. This transformation coupled with sample melting caused the material to foam or intumesces as it decomposes. At  $390^\circ\text{C}$  the elimination reaction appears complete, and the formed polyenes are converted into aliphatic groups. The Diels-Alder intramolecular cyclization and radical reactions, shown in Fig. 12.5, may be responsible for this conversion (Stage III).

Stage IV ( $T > 470^\circ\text{C}$ ) was attributed to the decomposition of remaining materials, which were more thermally stable structures due to cross-linking reaction. At the last stage of thermal degradation of sample, the following decomposition of polyenes chains occurs to carbon and hydrocarbons.



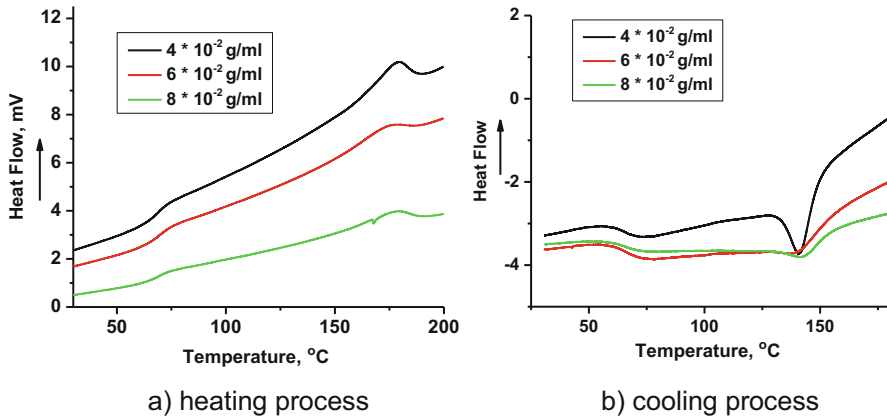


**Fig. 12.6** DSC curves of PVA hydrogels. (a) heating process. (b) cooling process

Analysis of data represented in Fig. 12.4b demonstrated that temperature maxima for all stages are slowly increased with the increasing of polymer concentration. Enhancement of the thermal resistance with increasing of PVA concentration may be caused by the formation of more rigid chemical structure during thermal degradation.

### 12.3.4 Differential Scanning Calorimetry (DSC)

The thermal behavior of hydrogels prepared at various initial PVA concentrations was studied by means of DSC measurements (Fig. 12.6). At heating the endothermic peak in DSC curves at about 67 °C marked the transition from the glassy to the rubbery state ( $T_g$ ) [16]. The following peaks at 160 °C correspond to the melting points ( $T_m$ ) of the samples and indicate the existence of crystalline domains [17]. Cooling process reveals a prominent exothermic peak at about 140°, attributed to the  $\beta$ -sheet crystallization ( $T_c$ ) of cross-linked PVA sample.

The DSC data series of hydrogels characterize the typical thermal behavior of cross-linked polymers (Table 12.3). It should be noted that downward shift of the glass transition at increasing of PVA concentration was registered. This effect can be explained by reduction of segmental motion in polymer chains of mesh. Actually the significant influence of initial polymer concentration and cross-linking density on the thermal behavior of the PVA hydrogels in these parameter ranges is not observed. However evident difference in the region of melting and crystallization of crystalline domains was observed for various samples. The most crystallization ability was registered for the sample with lowest cross-link density (Fig. 12.6a, b).

**Table 12.3** DSC data of thermal behavior of cross-linked polymers

$C_{PVA} 10^2, \text{g/ml}$	$T_g, ^\circ\text{C}$	$T_m, ^\circ\text{C}$	$T_c, ^\circ\text{C}$
4	68.8	179	140
6	68.6	179	142
8	67.3	179	143

## 12.4 Conclusions

Hydrogels based on polyvinyl alcohol were prepared by electron beam radiation method (irradiation dose was 50 kGy). During synthesis process only, the concentration of polymer was varied. It was found that in order to obtain hydrogels with applicable characteristics for wound dressings the concentrations of PVA should equal to  $8 \times 10^{-2}$  g/ml. It was shown that the microstructure of hydrogels corresponds to elastomers.

Analysis of mechanical characteristics of hydrogels proved the effect of two factors on its elasticity: a number of cross-links and hydrogen bonds of 3D sample structure.

TGA data demonstrated four stages of thermal behavior of hydrogels. Temperature maxima for all stages were increased with the increasing of polymer concentration in sample. It was supposed that enhancement of the thermal resistance with increasing of PVA concentration may be caused by the formation of more rigid chemical structure during thermal degradation.

Downward shift of the glass transition at increasing of PVA concentration was registered. The difference in the region of melting and crystallization of crystalline domains was observed for various samples. The most crystallization ability was registered for the sample with lowest cross-link density.

This study allows to predict the mechanical properties of hydrogels obtained by irradiation method.

## References

1. Choate CS (1994) Wound dressings. A comparison of classes and their principles of use. *J Am Podiatr Med Assoc* 84(9):463–469
2. Park KR, Chang NY (2003) Synthesis of PVA/PVP hydrogels having two-layer by radiation and their physical properties. *Radiat Phys Chem* 67:361–365
3. Wu M, Bao B, Yoshii F, Makuuchi K (2001) Irradiation of cross-linked, poly (vinyl alcohol) blended hydrogel for wound dressing. *J Radioanal Nucl Chem* 250(2):391–295
4. Saraydın D, Karadag E, Ya I et al (2004) The influence of preparation methods on the swelling and network properties of acrylamide hydrogels with crosslinkers. *J Macromol Sci A* 41(4):419–431
5. Yoshii F (2002) Hydrogel wound dressing by radiation (2002) Proc 2002 Symp Nucl Dat, JAERI, Tokai, Japan 3:11–15
6. Khorolskyi OV, Rudenko OP (2015) Viscometric research of concentration regimes for polyvinyl alcohol solutions. *Ukr J Phys* 60(9):880–884

7. Neimash VB, Kupianskyi HD, Olkhovyk IV et al (2017) Physical properties of radiation-crosslinked polyvinyl alcohol–polyethylene glycol hydrogels from the viewpoint of their application as medical dressings. *Ukr J Phys* 62(5):402–412
8. Onanko YA, Prodayvoda GT, Vyzhva SA et al (2011) Automated system of treatment of ultrasound longitudinal and transversal velocities measuring. *Metallofiz Noveishie Tekhnol* 33(13):529–533
9. Hamill W (1969) Model for the radiolysis of water. *J Phys Chem* 73(5):1341–1347
10. Alfayyadha AAM, Lotfyc S, Basfara AA et al (2017) Influences of poly (vinyl alcohol) molecular weight and carbon nanotubes on radiation crosslinking shape memory polymers. *Prog Nat Sci Mat Int* 27:316–325
11. Mondino AV, González ME, Romero GR et al (1999) Physical properties of gamma irradiated poly(vinyl alcohol) hydrogel preparations. *Radiat Phys Chem* 55(5–6):723–726
12. Kutsevol NV, Zheltonozhskaya TB, Demchenko OV et al (2004) Effect of the structure of poly(vinyl alcohol)-graft-polyacrylamide copolymers on their thermooxidative stability. *Polym Sci Ser A* 46(5):518–525
13. Gilmanl JW, VanderHart DL, Kashiwagi T (1994) Thermal decomposition chemistry of poly(vinyl alcohol). *Proc ACS Symposium Fire and Polymers American Chemical Society*. Washington, DC, USA 599(2):161–185
14. Cullis CF, Hirschler MM (1981) *The combustion of organic polymers*. Clarendon Press, Oxford, pp 117–119
15. Anders H, Zimmerman H (1987) A comparison of the thermal degradation behaviors of poly(vinyl acetate), poly(vinyl alcohol) and poly(vinyl chloride). *Polym Degr Stab* 18:111–122
16. Wilkers CE (ed.) (2005) *PVC Handbook*. Hanser, Munich
17. Guirguis OW, Manal Moselhey TH (2012) Thermal and structural studies of poly (vinyl alcohol) and hydroxypropyl cellulose blends. *Nat Sci* 4(1):57–67

# Chapter 13

## Nanostructural and Nanochemical Processes in Peloid Sediments Aided with Biogeocenosis



A. V. Panko, I. G. Kovzun, O. M. Nikipelova, V. A. Prokopenko, O. A. Tsyganovich, and V. O. Oliinyk

### 13.1 Introduction

Polymineral iron-oxide-hydroxide-silicate systems (IOHSS) and pelagic sediments (PS) have important place among natural dispersed mineral formations. Some of these possess therapeutic properties and they are attributed to so-called peloids. Such IOHSS, PS, and peloids have always had great importance in biomedical and colloid–chemical investigations. In the last decades, peloids in IOHSS have been studied increasingly more widely by physicochemists for the purpose of uncovering their influence on biocolloid interactions. Such interactions can be explained as interfacial colloid–chemical transformations in peloid and same disperse systems under influence of microorganism metabolic processes. However, in various specific cases observing of such influence on complex polymineral IOHSS and PS is still not completed due to insufficient definiteness of multipronged physicochemical, colloid-chemical, and biocolloid methods of their investigation [1–9]. Today it is known in general that physicochemical, colloid–chemical, nanochemical transformations, and contact interfacial interactions in IOHSS and PS aided with microbiological processes result in the forming of new and in many cases at least of

---

A. V. Panko (✉) · I. G. Kovzun · O. A. Tsyganovich · V. O. Oliinyk

F. D. Ovcharenko Institute of Biocolloid Chemistry of National Academy of Sciences of Ukraine, Kyiv, Ukraine

V. A. Prokopenko

F. D. Ovcharenko Institute of Biocolloid Chemistry of National Academy of Sciences of Ukraine, Kyiv, Ukraine

National Technical University of Ukraine “KPI”, Kyiv, Ukraine

O. M. Nikipelova

State Agency “Ukrainian Research Institute of Medical Rehabilitation and Balneology, Ministry of Health of Ukraine”, Odessa, Ukraine

© Springer International Publishing AG, part of Springer Nature 2018

O. Fesenko, L. Yatsenko (eds.), *Nanochemistry, Biotechnology, Nanomaterials, and Their Applications*, Springer Proceedings in Physics 214,

[https://doi.org/10.1007/978-3-319-92567-7\\_13](https://doi.org/10.1007/978-3-319-92567-7_13)

same complexity polymineral nanostructured materials with new properties [4, 5]. These materials as PS consist of iron, aluminum, and silicon oxides in general, often in the form of montmorillonite and glauconite clay minerals and also many, but in fewer quantities, other inorganic and organic components [2–5, 10, 11].

Such materials and disperse systems of IOHSS type, except for PS, which are being widely used in practice, include iron-oxide-silicate sedimentary ores, iron-contained bentonitic and other clays, pelitic marine and lake sediments, coastal and shelf sands, and other sedimentary and solid ore deposits, the total capacity of which in the Earth's crust reaches 98%. During their geological history, many of them were transformed under the influence of microbiological and secondary tectonic processes. For example, it was recently established that solid iron quartzites (jaspellites), which are the basis of general iron ore deposits, started to form within 2 billion years till the present as a result of microorganism activity with further tectonic cementing of formed dispersed formations [12]. Thus, microorganisms play a significant role in structural formation of different iron-oxide-silicate materials and including PS.

As the practical importance of PS and other similar nanostructured materials is increasing constantly, the attention of scientists investigating fundamental microbiological and biocolloid processes is also increasing.

## 13.2 Methods and Materials

The following study is related to the investigation of deep-water clay-carbonate pelitic sediments of gigantic peloid deposit, taken in the west region of the Black Sea from a 2 km depth. Black Sea peloid properties, and peloid specimen taken from Kuyalnik estuary (Odessa) for comparison, are described in [4, 5]. Bentonitic (montmorillonite) clay and glauconite were used as model specimens, and hydromica as a comparative specimen.

Chemical composition of studied bentonite is (wt%): 49.52 SiO<sub>2</sub>; 21.06 Al<sub>2</sub>O<sub>3</sub>; 2.72 Fe<sub>2</sub>O<sub>3</sub>; 5.70 CaO; 1.61 MgO; 0.37 Na<sub>2</sub>O; 0.28 K<sub>2</sub>O; 0.02 C<sub>org</sub>. Aqueous bentonite suspension with 57% water had the following physicochemical indices: pH 7.3; Eh + 370 mV; shear stress 821 Pa; stickiness 1840 Pa. Clay fraction of 1–10 μm particle size content was 19.10%, and of sizes less than 1–10 μm 2.90%.

Chemical composition of studied bentonite is (wt%): 57.46 SiO<sub>2</sub>; 7.49 Al<sub>2</sub>O<sub>3</sub>; 17.50 Fe<sub>2</sub>O<sub>3</sub>; 0.36 FeO; 0.35 TiO<sub>2</sub>; 3.06 CaO; 2.41 MgO; 0.07 Na<sub>2</sub>O; 5.35 K<sub>2</sub>O. Aqueous glauconite suspension with 39.5% water had the following physicochemical indices: pH 7.7; Eh + 210 mV; shear stress 405 Pa; stickiness 1250 Pa. Clay fraction of 1–10 μm particle size content was 22.5%, and of sizes less than 1–10 μm – 6.8%.

Investigation of the selected materials, partially shown in Figs. 13.1 and 13.2, was conducted using XRD, sorption, rheological, SEM, chemical and biomedical methods [3–6, 8]. XRD images were taken on X-Ray diffractometer DRON-UM-1 with a pair of Soller slits with CuKα filter. SEM images of samples were taken on SELMI electron microscope in light field mode and sample morphology

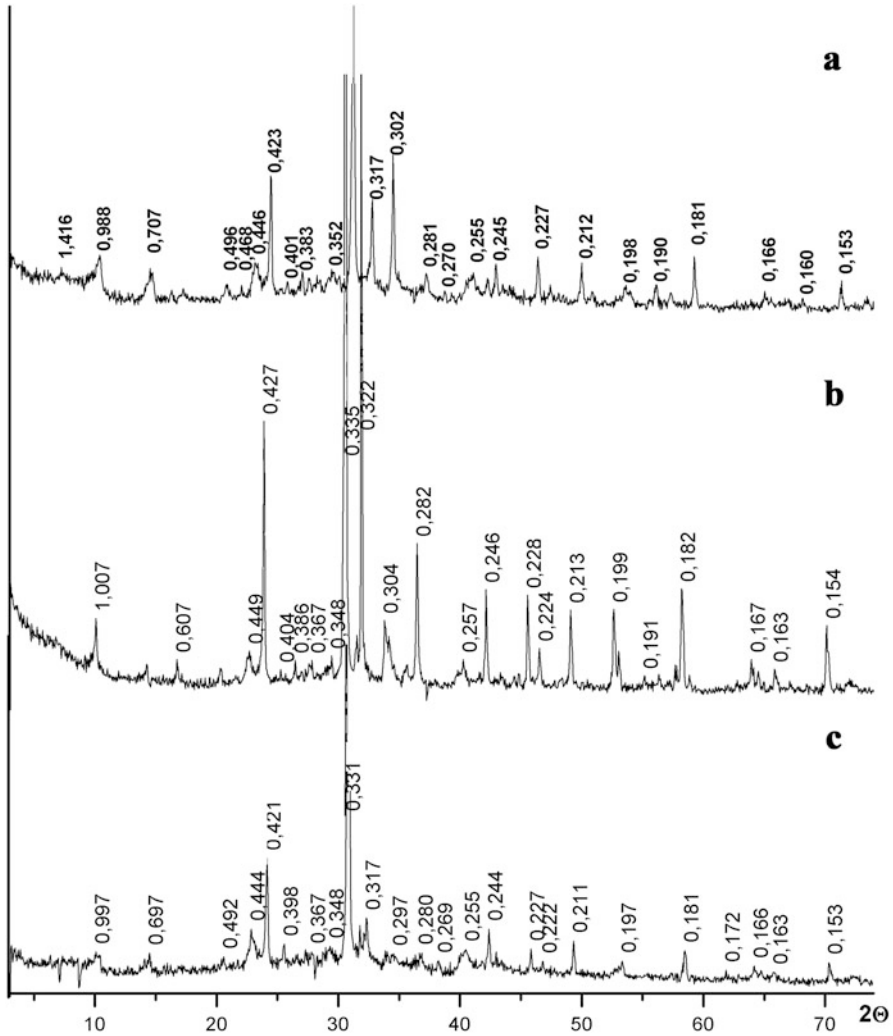


**Fig. 13.1** XRD images of the Black Sea (a), Kuyalnik estuary (b), and Azov Sea (c) pelagic sediments

was studied on JEOL electron microscope JSM6490LV (Japan). Nitrogen sorption (77 K) isotherms were studied on high-speed gas sorption analyzer NOVA 2200 E. Rheological investigations were conducted on Rheotest-2 unit connected to PC for data recording. Physicochemical and microbiological testing was done according to methods described in [13, 14].

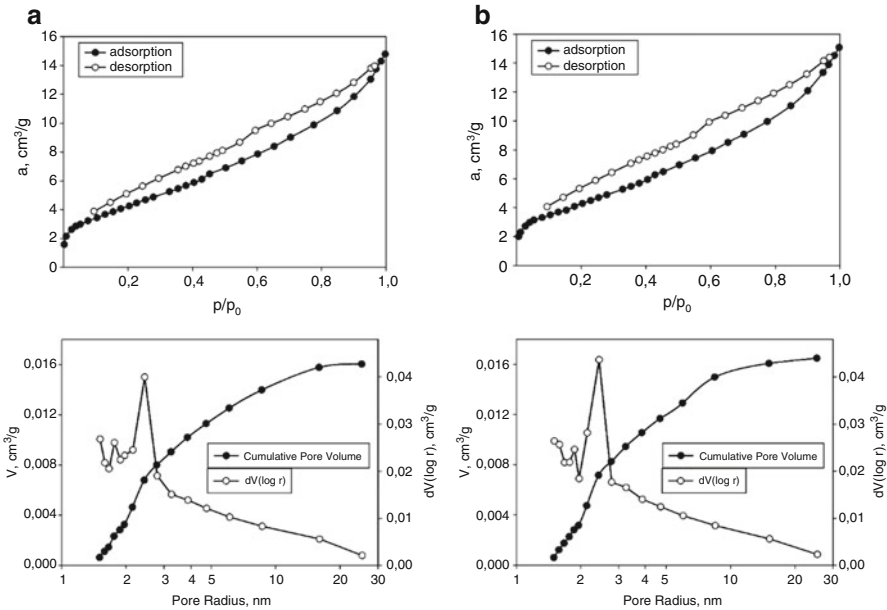


**Fig. 13.2** Nitrogen sorption isotherms (a –  $p/p_0$ ) and dependence of pore size ( $V-r$ ,  $dV(\log r) - r$ ) for two Black Sea pelagic sediment samples (a and b), collected from different distant points

### 13.3 Experiment and Discussion

According to the data shown in Fig. 13.3, the process of peloid sediment biocolloid reduction proceeds with symbate changing of process indices: lgCFU, peloid suspension viscosity, and reduced iron content. The data in Table 13.1 also proves this conclusion. The indicated correlation of biocolloid reduction indices points out that the investigated process goes according general complex biocolloid mechanism under the influence of organisms' metabolism. Its products have an influence on the structural and nanochemical transformations of peloid inorganic mineral components [15]. And the latter respectively influences rheological properties of tested suspensions, which is proved by preliminary investigations of biocolloid recovery of pelagic sediments [16].

First of all, a matter concerning microbiological processes – the received data (Fig. 13.3, Table 13.1) clearly indicate their significant role in formation of conditions for biocolloid reducing iron contained in peloids. This is also proved by literature data, showing that bacterial reactions in nature lead to formation of unstable nanostructures of layered double hydroxides  $\text{Fe}^{2+} - \text{Fe}^{3+}$  (LDX) type or green rust (GR), which are easily transformed while oxidation in lepidocrocite, hematite, and magnetite [17–21]. Thus, in [17] the process of chemical transformation GR of  $\text{GR}(\text{CO}_3^{2-})$  and  $\text{GR}(\text{SO}_4^{2-})$  types into  $\gamma\text{-FeOOH}$  (lepidocrocite) is considered, and in [18–21] – the processes of phase formation aided with microorganisms. In [20], a microorganism interaction with minerals and organic matter in natural ecosystems was studied. It was also established that nonfermentative bacterium are adopted to

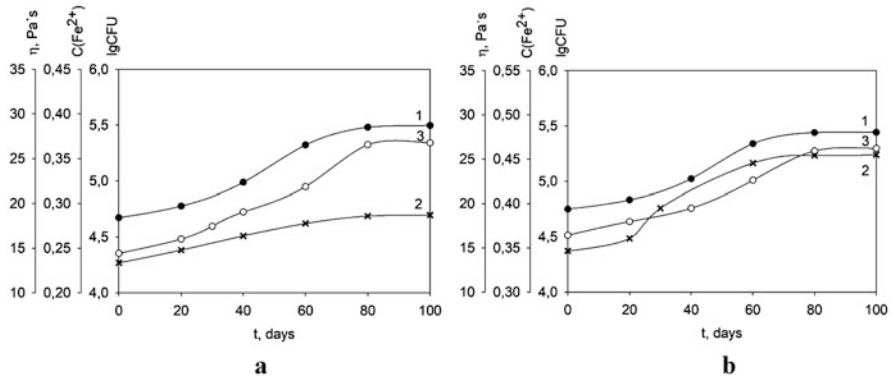


**Fig. 13.3** Dependence of properties for the Black Sea (a) and Kuyalnik (b) pelagic sediments on time of their biocolloid treatment: 1 – colony forming unit ( $\lg CFU$ ); 2 – concentration of reduced iron  $C(Fe^{2+})$ ; 3 – viscosity ( $\eta$ , Pa·s)

**Table 13.1** Average indices changing dynamics for biocolloid recovery of Kyalnik sediments depending on exposure duration

Exposure duration, days	Mass fraction of moisture, %	Shear stress, Pa	Concentration of reduced iron, $C_{Fe^{2+}}$	pH	Eh, mV
0	53	1211	0.35	6.9	-179
30	53	1164	0.39	6.7	-189
60	53	1149	0.44	6.8	-192
90	53	1128	0.51	6.9	-195
120	53	1187	0.50	6.9	-183
150	53	1196	0.49	6.8	-177

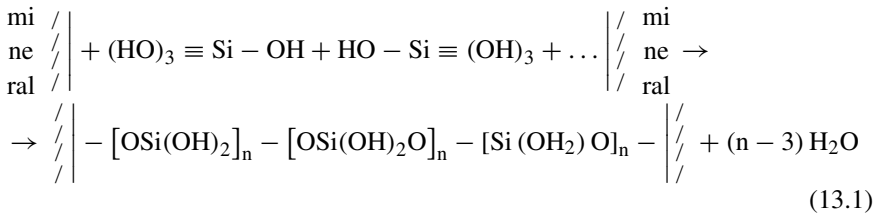
bacterial iron-reducing mechanism suit, which breathe with the help of iron, as well as fermentative bacterium of IRB, DIRB (dissimilation iron-reducing bacteria). A complex investigation of processes of reduction, solution, and iron extraction from mentioned nanodispersed minerals were completed. And the general role of IRB in GR formation in natural conditions was confirmed [22–25]. Such mechanism comes to reducing of  $Fe^{3+}$  and interaction of  $Fe^{2+}$  ions with mineral structure. The processes in seawater have their own features. Bacterial reactions in such conditions occur both with the aid of iron-reducing bacteria *Clostridium* sp. uncultured, and with sulfate-reducing bacteria *Desulfovibrio caledoniensis* (SRB). Vital activity of SRB is activated due to pyrite  $FeS_2$  particles, with formation of  $GR(SO_4^{2-})$  [21–24], DIRB decreases this process [25]. In [16, 26], interaction mechanism between SRB and DIRB is considered. Results from [16] have proved that in the presence of *Shewanella putrefaciens* (DIRB),  $GR(CO_3^{2-})$  and  $GR(SO_4^{2-})$  are formed, and their ratio depends on carbonate and sulfate concentration (C) ratio in solution. At  $C \geq 0.17$ , only  $GR(CO_3^{2-})$  is formed, and at  $C < 0.17$  there is a mixture of  $GR(SO_4^{2-})$  and  $GR(CO_3^{2-})$  [16]. And it follows that if there is a contact of



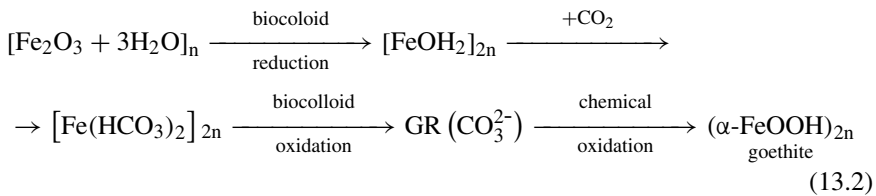
solutions with air, then obtaining of pure  $\text{GR}(\text{SO}_4^{2-})$  structures is a hard task. The latter can accordingly influence results of kinetic investigations of  $\text{GR}(\text{SO}_4^{2-})$  formation in sulfate solutions due to uncontrollable  $\text{CO}_2$  from air migration into solution. It also complicates unmistakable modeling of GR formation processes of some types of microorganisms whose vital activity product is  $\text{CO}_2$ .

Thus, analysis of literature data indicates that GR formation in natural conditions at oxygen deficit (deep-water processes in seawater, in groundwater) is conditioned by the microorganism vital activity, iron-reducing ones being foremost. In most cases there are low concentrations of  $\text{SO}_4^{2-}$  ions then  $\text{Fe}^{2+}$ - $\text{Fe}^{3+}$  LDX of  $\text{GR}(\text{CO}_3^{2-})$  type forms mostly. The latter are unstable substances and so they are active reductants. Their chemical activity increases also because GR particle sizes lie within the range of typical nanosized ones (10–100 nm). It is quite possible that all aforesaid in specific conditions provokes some not yet studied nanochemical reactions both in IOHSS and in PS along with ferrioxide minerals with other ferrioxide minerals where metabolism is the prime mover. Thus the drawback of the investigations made so far could be the lack of proper attention paid to colloid–chemical mechanisms of transformation processes and their role in formation of more complex mineral and polymineral iron-oxide-silicate systems and pelagic sediments.

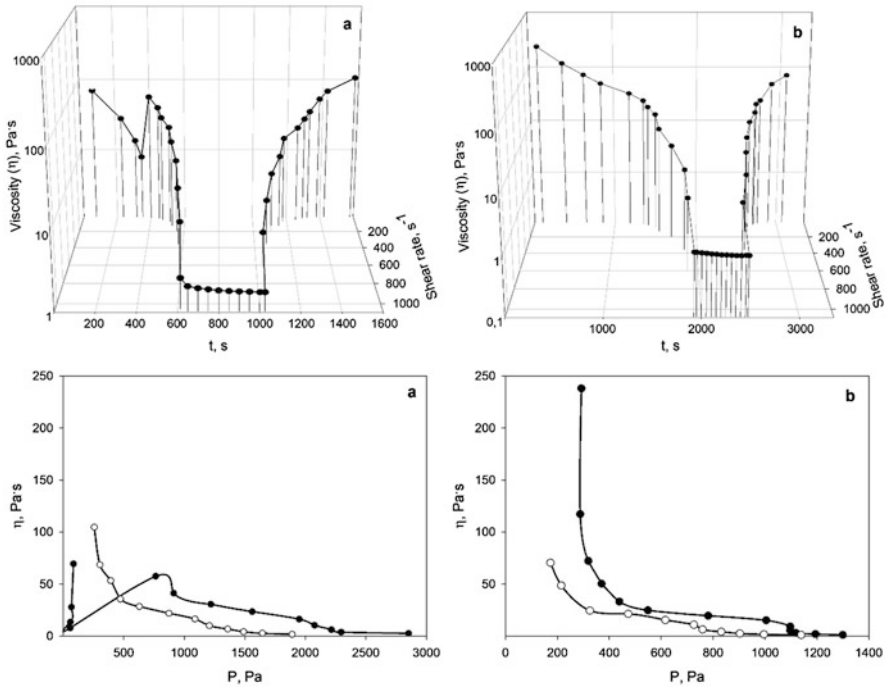
There are some conclusions could be made relating to experimental data (Figs. 13.1, 13.2, 13.3, 13.4, 13.5, 13.6, 13.7, 13.8, 13.9, and 13.10), which add and specify known or substantiate new conceptions concerning biocolloid processes in pelagic sediments. They are being followed by nanochemical, nanostructural and physical–mechanical interfacial contact interactions, which are being conditioned by chemical and bacterial processes and reactions [27, 28]:



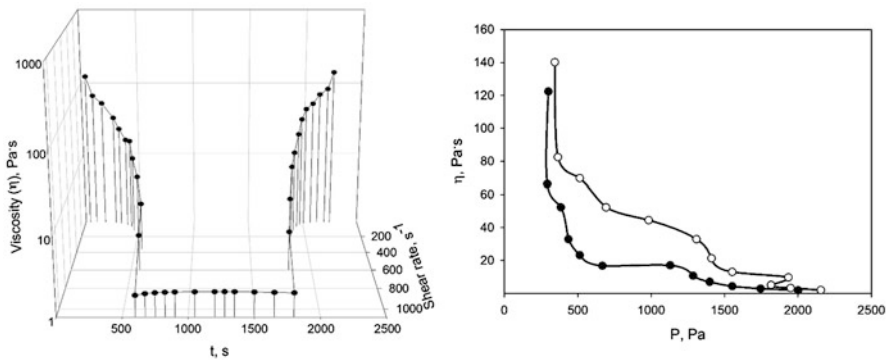
(interfacial nanochemical structure polycondensation of silicate nanoclusters and nanoparticles);



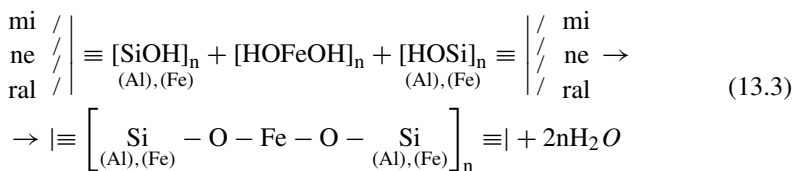
(iron biocolloid reduction-oxidation aided with biogeocenos);



**Fig. 13.4** Rheograms of the Black Sea pelagic sediments with 65% moisture mass fraction (a) and 77% (b); • – straight direction and ○ – reverse direction of curve



**Fig. 13.5** Rheograms of Kuyalnik pelagic sediment sample with 55% moisture mass fraction; • – straight direction and ○ – reverse direction of curve



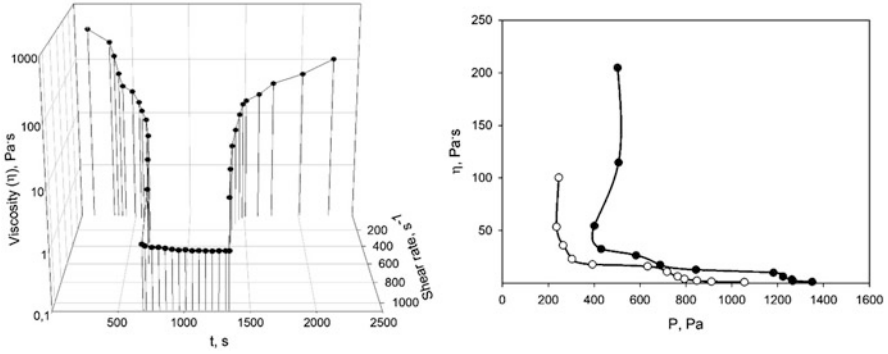


**Fig. 13.6** Rheograms of the Azov Sea pelagic sediment sample with 77% moisture mass fraction; ● – straight direction and ○ – reverse direction of curve

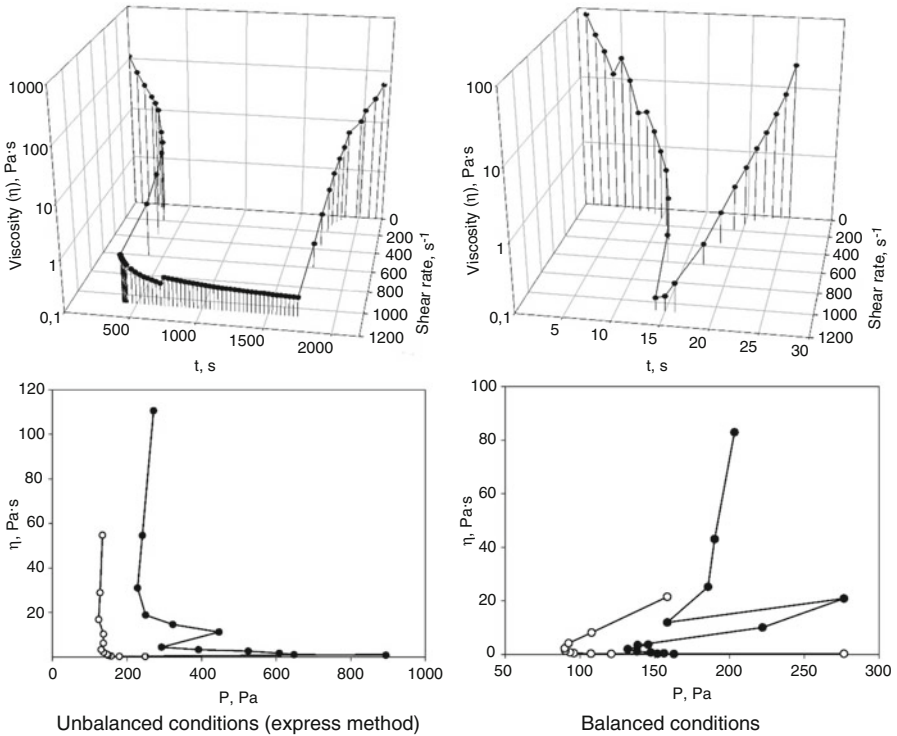


**Fig. 13.7** Rheograms of bentonite (montmorillonite) clay suspension with 55% moisture mass fraction; ● – straight direction and ○ – reverse direction of curve

(interfacial nanochemical interaction and structuration in IOHSS aided with nanoclusters and nanoparticles of silicon hydroxide, bivalent iron, aluminosilicates or GR);

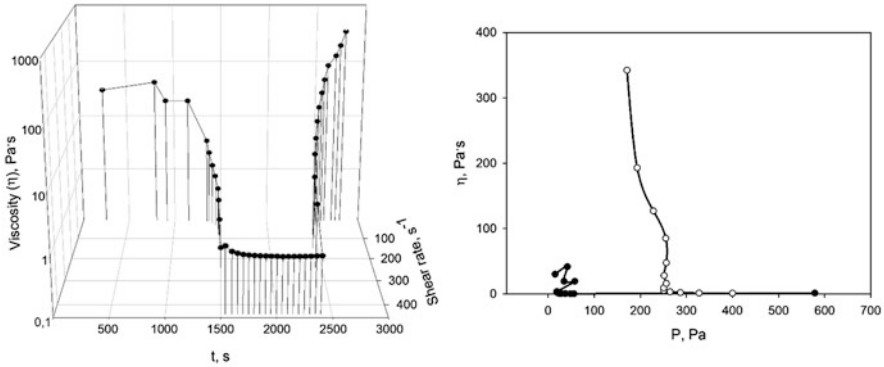


**Fig. 13.8** Rheograms of glauconite suspension with 50% moisture mass fraction; • – straight direction and o – reverse direction of curve

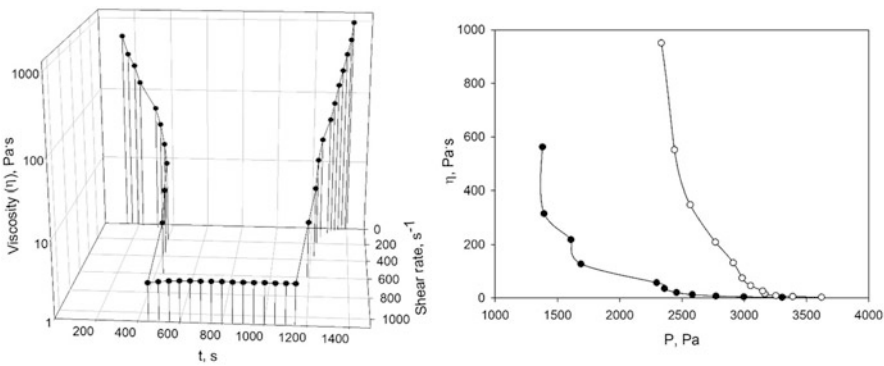
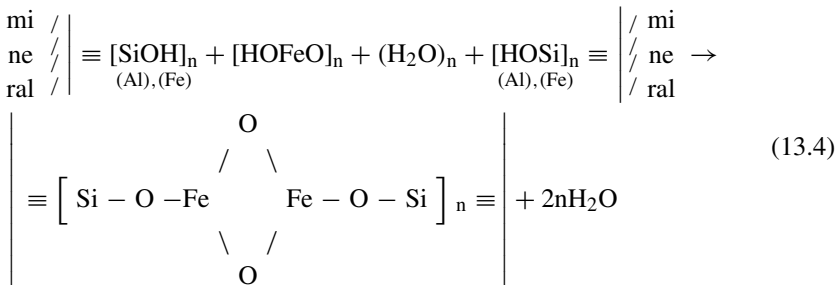


**Fig. 13.9** Rheograms of hydromica suspension with 50% moisture mass fraction; • – straight direction and o – reverse direction of curve



(interfacial nanochemical contact interaction in IOHSS aided with nanoclusters and nanoparticles of goethite, which was formed as a result of partial microbiological oxidation of preliminary reduced bivalent iron hydroxide into GR, and its further chemical oxidation).

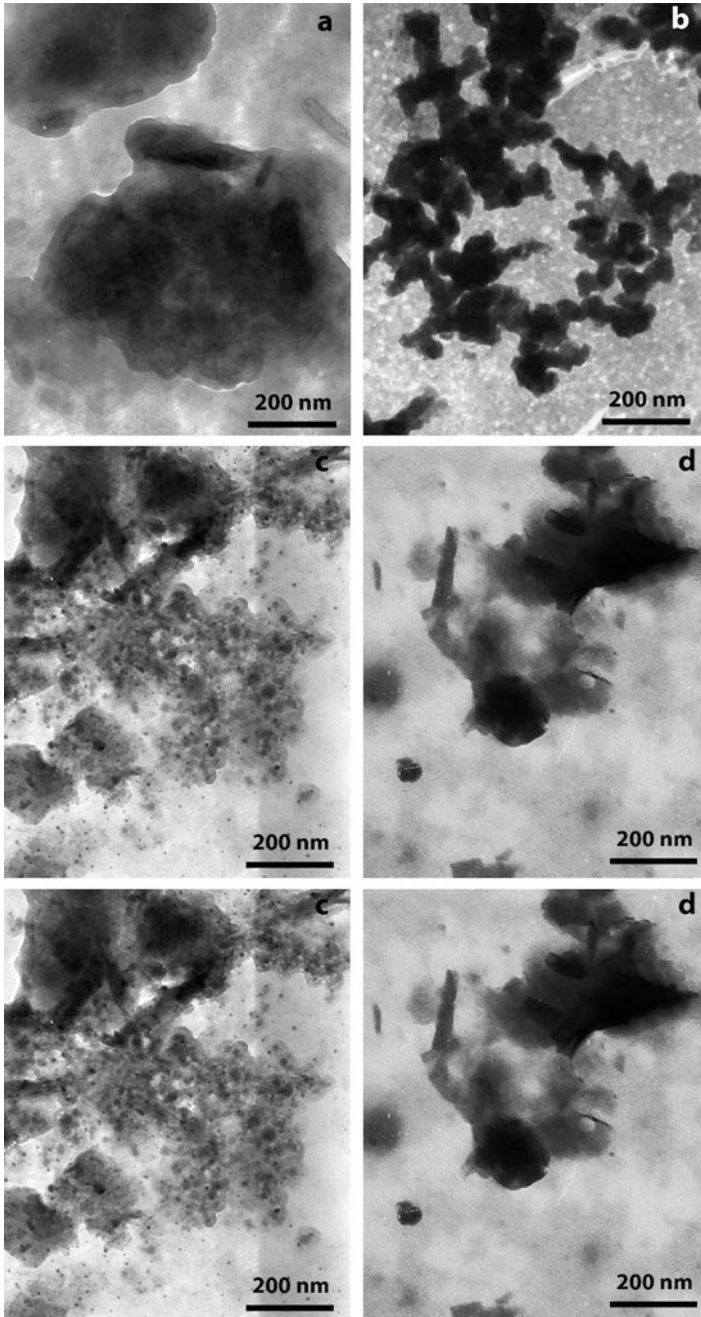


**Fig. 13.10** SEM images of peloid sediments and clays: (a) Black Sea sediment, (b) Kuyalnik sediment, (c) Azov Sea sediment, (d) bentonitic clay, (e) glauconite, (f) hydromica

As we can see from some shown process and reaction schemes, there are chemically and microbiologically formed nanoclusters and nanoparticles of silicon and iron hydroxides, and aluminum silicates involved in interfacial nanochemical contact interactions [27, 28]. Iron compounds have the general role in those processes, and it is confirmed by data in Fig. 13.3 and Table 13.1. Besides, nanocluster structural interactions between separate microparticles according to Scheme (13.3) are conditioned by -O-Fe-O-Fe-O- bonds, which do not fully correspond to the character of shear stress curve for peloid dispersion [28], shown also in Fig. 13.3. Thus, according to the data received, if exposure of dispersion with biogeocenosis presence increases, then the quantity of reduced iron would increase, and shear stress of dispersion would increase too. It indicates on presence of formal dispersion nanostructurization by Scheme (13.3). But more detailed investigation [28] has shown that concurrent to reduction processes of unstable  $\text{Fe}(\text{OH})_2$  and GR nanostructure formation, are the simultaneous processes of their microbiological and chemical oxidation occur into goethite at the cost of air oxygen with following contact interactions by Scheme (13.4). According to this scheme, the quantity of iron–oxygen bonds increases 1.5 times if compared to the Scheme (13.3), pointing to the higher strength and stability of interfacial contact nanostructured bonds in systems of IOHSS type, which include  $\text{Fe}^{3+}$  compounds. At the same time, bonds formed by Scheme (13.3) are intermediate and less strong. They are less stable, because such structures are liable to transformation due to oxidation processes, and it weakens contact interactions, i.e., decreases shear stress. That is why the nanogoethite only participates in contact nanostructured interfacial processes between separate mineral colloid and microparticles of PS on final stage of biocolloid interactions. Except for biogeocenosis influence on complex biocolloid processes in IOHSS and peloid sediments, physicomechanical nanostructuration processes play important role in those processes. The latter ones associate with chemicomineralogical composition of PS clay components (Fig. 13.1), their sorption (Fig. 13.2) and rheological properties (Figs. 13.4, 13.5, 13.6, 13.7, 13.8, and 13.9), which are substantially dependent on moisture mass fraction in composition of the dispersion. Peloid sediment composition includes clay minerals like kaolinite, hydromica, and montmorillonite as a part of bentonite and glauconite (Figs. 13.1 and 13.10). Montmorillonite is most capable of nanoparticle formation, where nanoparticles are being placed in contact zones between colloid particles (Fig. 13.10d). Hydromica demonstrates same character but with bigger nanoparticle sizes (Fig. 13.10f). Small colloid particles of glauconite compose aggregates of nanoparticles and surface of bigger ones are usually partly covered with small nanoparticles (Fig. 13.10e). Similar structuration character with clay particles are being observed in the Black (Fig. 13.10a) and Azov (Fig. 13.10c) Sea peloid sediments.

Kuyalnik estuary peloid sediment in its composition has aggregates of clay mineral nanoparticles of 30–100 nm sizes, which are firmly connected by phase [27] contacts (Fig. 13.10b). The above results are also proved by adsorption data (Fig. 13.2), where distant samples of the Black Sea peloids have relative structural-sorption properties. Thus, for example, they have effective pore radius

close to 2.5 nm. According stoichiometric conceptions this witnesses that minimal nanoparticle sizes approach 4 nm. It is quite possible that they are connected with phase contacts too, as already indicated for Kuyalnik peloid (Fig. 13.10b). Physicomechanical properties of IOHSS and PS are most influenced by moisture mass fraction in their composition. Thus, comparatively low-concentrated Black Sea peloid suspensions (35% and 23% of solid phase) are characterized by thixotropic flow mode of those suspensions (Fig. 13.4). Abnormal rheopectic flow mode for Kuyalnik peloid is observed at solid phase mass fraction of 45% (Fig. 13.5), and, as already mentioned, it is explained by strong phase nanocontacts in aggregates of colloid particles (Fig. 13.10b). The Azov Sea pelagic sediment suspensions at 23% moisture mass fraction have thixotropic flow mode, similar to low-concentrated Black Sea peloid (Fig. 13.4b). At the same time, flow curves for concentrated suspensions of bentonite clay (Fig. 13.7), glauconite (Fig. 13.8), and hydromica (Fig. 13.9) have abnormal character. The same character was also detected for concentrated suspension of IOHSS from marine PS, where its composition had 16% of clay components and 84% of goethite [28]. All four specimens had concentrations close to Atterberg plasticity limit, which separates plastic state from conditionally solid (semisolid) state. Such results need additional description using conceptions of classic mechanics.

Figure 13.11 shows material theoretical load and unload curves typical for elastoviscous state of tested material. At loading of a specimen (OCA curve segment) solid material elastic state turns into viscous (OA curve segment). At unloading (on AD segment), plastic sample properties are disappearing and elasticity usual for solid (semisolid) material is being back at condition of irreversible process (point B). At further specimen loading (dashed-line curve BA') its plastic properties appear at AA' segment and disappear at A'D' segment. Estimated view of viscosity curve for plastic flow at CAD segment (Fig. 13.11, curves 1 and 2) shows that specimen viscosity change at loading is described by curve 1 at lower shear stress values than for unloading (curve 2). Those curves (1 and 2) compared with respective abnormal rheological curves on Figs. 13.7, 13.8, and 13.9, and in [28], shows first of all that curves have similar curve trend as a result of identical structures' plastic flow mechanism. The latter is based upon effect of system transition from solid-like to plastic state in conditions of phase contacts formation [27]. Interaction of micro- and colloid particles in phase contacts according to Rebinder is conditioned by short-range forces of cohesion or adhesion. The latter ones are realized on surface much bigger than the surface of elemental lattice. Adhesion of solid-like structures in such conditions is formed from not less than  $10^2$ – $10^3$  of atomic bonds, i.e., on nanolevel or on colloid level with formation of structural–mechanical barrier according to Rebinder. Such bonds can be seen in Fig. 13.10, formed with nanoparticle participation. As distinct from coagulation ones such bonds are dissociated irreversibly, and it can be seen on experimental curves in Figs. 13.7, 13.8, and 13.9 and theoretical curves in Fig. 13.11. Thus, it can be considered as proven that abnormal rheological curve trend for concentrated suspensions of clay minerals, IOHSS, PS, and peloids is conditioned by irreversible dissociation of phase solid-like contacts built from nanoparticle blocks of silicates,

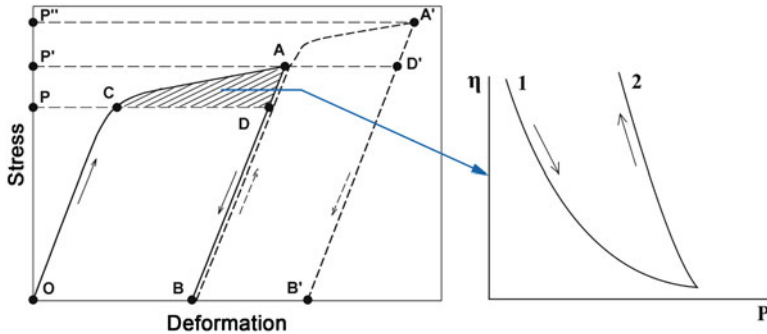


**Fig. 13.11** Curves of loading (OCA) and unloading (ADB) for elastoviscous material. CAD – plastic flow area, OC and DB – elastic deformation; BAA'B' – repeated loading and unloading;  $\eta$  – viscosity; CA, AD, 1 and 2 – curves for loading and unloading in condition of plastic flow

aluminosilicates, and iron-oxide-silicates. The latter ones, as mentioned above, play a general role in those processes [reactions (13.1), (13.3), (13.4)] and they are intensified by metabolism of microorganisms as a part of biogeocenosis – Scheme (13.2).

Obtained results have not only fundamental, but also practical importance for scientific usability basis of peloid sediments and their compounds as application materials for treatment of burnt surfaces, injuries and articulations, in cosmetology, in ecotechnologies for environmental protection, and for other purposes. It seems interesting to use general mineral compounds of peloid sediments in pure form – clay minerals after their processing with biogeocenosis. Most perspective among such minerals are montmorillonite as the compound of bentonites, and glauconite. Tested bentonite for applications had total bacterial count (CFU/g)  $1.1 \cdot 10^5$ ; pathogenic staphylococcus, intestinal enterococcus, and blue pus bacillus were absent – it proves that bentonite is compliant to sanitary needs. Specimen had no bactericide effect, but they can be used as protection of ecological bacteria from UV-radiation or from toxic substances due to inorganic nutrients (microelements) and ability for ion exchange, and also they can be used as minimal vivifying substrate for bacteria breeding. It was determined, that bentonite gives medioprophylactic effect at gastric ulcer and hepatitis treatment; those effects originate due to adsorption and ion exchanging organism detoxification with simultaneous anti-inflammatory and positive immunodeficiency action, and due to iron-oxide-silicate nanoparticle action.

Glauconite has displayed moderate bactericide action. The following was determined in specimen:

1. Saprophytic bacteria presence, which produces catalase
2. Microorganisms, which assimilate nitrogen
3. Microorganisms, which assimilate carbon
4. Heterotrophic bacterium, which produce surface-active amino acids
5. Manganese and iron red-ox bacteria



There were no micro- and spore-forming bacteria, yeasts, actinomycetes, and streptomycetes. Glaucinite was the most effective for treatment of dexamethasone arthrosis and endogenic intoxication.

In addition to stated advantages, it was proven that tested clays and peloids with their content are effective for state correction of hemophilic genic-broken blood coagulation due to their chemical composition (presence of iron and microelements) and extremely high adsorption ability [29].

Conducted investigations of bentonite and glauconite in modeling conditions of their biogeocenosis impacted influence on properties of more complex materials – peloids and pelagic sediments, allowed to conclude that their physicochemical properties' changing correlates with nanostructure-and-nanochemical clay mineral transformations with oxide and silicate compounds of iron – Schemes (13.1, 13.2, 13.3 and 13.4). The latter ones are connected respectively with changing of therapeutic properties of peloids and clays in peloid composition.

## 13.4 Conclusions

Investigation was made of the processes of nanochemical structuration in iron-oxide-hydroxide-silicate systems aided with biogeocenosis by using peloid sediments, peloids and clays in peloid composition – bentonitic and glauconitic, using physicochemical, colloid–chemical, and biological methods, and theoretical concepts of physicochemical and classic geomechanics. It was shown that nanochemical structuration of such systems and sediments is limited by metabolic processes of microorganisms, first of all iron-reducing ones and autotrophic bacterium producing surface-active substances. These bacterial reactions induce transformation of  $\text{Fe}^{3+}$  micro- and macroparticles of iron-contained minerals into nanoparticles and nanoclusters of  $\text{Fe}^{2+}$  hydroxides. The latter are chemically or microbiologically transformed under the influence of  $\text{CO}_2$  and  $\text{O}_2$  from air into unstable nanostructured layered double hydroxides (LDX) of  $\text{Fe}^{2+}$ .  $\text{Fe}^{3+}$  (green rust) of  $\text{GR}(\text{CO}_3^{2-})$  type. Chemical LDX transformation at further interaction with  $\text{O}_2$  from air results in forming of nanogoethite ( $\alpha$ -  $\text{FeOOH}$ ), which structures disperse minerals by general Scheme (13.4) in contact zones of micro- and colloid particles of silicate or alumino-iron-silicate minerals by interactions (13.1, 13.2, and 13.3). In so doing, there are new iron-oxide-hydroxide systems with new properties being formed. It is shown that along with the general process there are also clay minerals contained in iron-oxide-silicate systems, peloid sediments, and peloids taking part in structure transformations. For bentonite and glauconite the processes of their structuration in peloid sediment composition were modeled according to concepts of physicochemical and classical mechanics and geomechanics. It is shown that rheological processes in concentrated clay and clay–peloid suspensions are characterized by abnormal flow character and viscoplastic properties close to Atterberg plasticity limit. The mechanism of such process was determined. It is shown that clay minerals not only have influence on properties for practical use of

peloids, but they can be the basis for creation of antibactericide clay compositions with special properties, and for creation of antifiltration membranes for designing different ecotechnologies. The latter needs further investigations.

## References

1. Prokopenko VA, Kovzun IG, Ulberg ZR (2014) The creative potential of scientific discovery. *Her Natl Acad Sci Ukr* 10:52–61
2. Oleinik VA, Panko AV, Kovzun IG et al (2013) Nanochemical processes in solid-phase reduction of Ferrioxide-silicate materials. *Proc NAP* 2(3):03AET10
3. Kovzun IG, Ulberg ZR, Panko AV et al Colloid-chemical and Nanochemical processes in Peloids on basis of ferrous clay minerals. In: Fesenko O, Yatsenko L (eds) *Nanoplasmionics, Nanooptics surface studies and applications*, springer proceedings in physics, vol 167. Springer Proceedings in Physics, Heidelberg, pp 233–243
4. Panko AV, Kovzun IG, Ulberg ZR, Oleinik VA, Nikipelova EM, Babov KD (2016) Colloid-chemical modification of peloids with nano- and microparticles of natural minerals and their practical use. In: Fesenko O, Yatsenko L (eds) *Nanophysics, nanophotonics, surface studies, and applications*, vol 183. Springer Proceedings in Physics, Heidelberg, pp 163–177
5. Oleinik VA, Panko AV, Kovzun IG et al (2016) Processes of metamorphism in iron-oxide-silicate rocks, their microbiological, nanochemical and nanostructural transformations. *Proc NAP* 5(3):02NABM01
6. Loboda MV, Babov KD, Zolotarjova TA, Nikipelova EM (2006) *Lechebnye grjazi (peloidy) Ukrainy. Chast 1 (Therapeutical muds (peloids) of Ukraine. Part 1)*. Kuprijanova, Kyiv
7. Emel'janov VA (2003) *Osnovy morskoy geojekologii (Basics of marine geoecology)*. Naukova dumka, Kyiv
8. Nikipelova OM (2014) Results of physicochemical studies of Dashukov deposit's bentonite (*Rezul'taty fizyko-khimichnykh doslidzhen bentonitu Dashukivs'koho rodovyshcha*). *Odesa Natl Univ Herald Chem* 3:70–75
9. Nikipelova OM, Nikolenko SI, Nedoluzhenko DI (2014) Physico-chemical properties and mechanism of bactericidal action of different clays (*Fizyko-khimichni vlastyvoli ta mekhanizm bakterytsydnoyi diyi hlyn riznoho pokhodzhennya*). *Med Rehabil Spa Ther Physiother* 1:39–43
10. Frye K (ed) (1981) *The encyclopedia of mineralogy, encyclopedia of earth sciences*, vol IV B. Hutchinson Ross Publishing Company, Stroudsbu
11. Shherbak NP (ed) (1990) *Mineraly Ukrainy: kratkij spravochnik (Minerals of Ukraine: quick-reference book)*. Naukova dumka, Kyiv
12. Rozanov AJ, Zavarzin GA (1997) Bakterial'naja paleontologija (Bacterial paleontology). *Vestnik RAN* 67(3):241–245
13. Nikipelova OM, Solodova LB (2008) *Manual on control methods of peloids and preparations on their basis. Physico-chemical research (Posibnyk z metodiv kontrolyu peloyidiv ta preparativ na yikh osnovi. Fizyko-khimichni doslidzhennya)*. Ukrainian Publishing Union named after Yuri Lipy, Odesa
14. Nikipelova OM, Hluchovs'ka SM, Koval'ova IP (2010) *Manual on control methods of medical muds (peloids), spices and preparations on their basis, microbiological research (Posibnyk z metodiv kontrolyu likuval'nykh hryazey (peloyidiv), ropy ta preparativ na yikh osnovi, Mikrobiolohichni doslidzhennya)*. Even, Odesa
15. Oleynik VA, Panko AV, Kovzun IG et al (2016) Influence of nanodispersed and microdispersed structures on metamorphism of iron oxide silicate ore materials (*Vliyaniye nanodispersnykh i mikrodipersnykh struktur na protsessy metamorfizma zhelezooksidnosilikatnykh rudnykh materiaov*). *Nanosistemi Nanomateriali, Nanotehnologii* 14(2):245–258

16. Refait P, Abdelmoula M, Genin J-MR (1998) Mechanisms of formation and structure of green rust one in aqueous corrosion of iron in the presence of chloride ions. *Corros Sci* 40:1547–1560
17. Cornell RM, Schwertmann U (2003) *The iron oxides: structure, properties, reactions, occurrence and uses*, 2th edn. Wiley-VCH, Weinheim
18. Jambor JL, Dutrizac JE (1998) The occurrence and constitution of natural and synthetic ferrihydrite, a widespread iron oxyhydroxide. *Chem Rev* 98(7):2549–2585
19. Huang PM, Bollag J-M, Senesi N (2002) Interactions between soil particles and microorganisms: impact on the terrestrial ecosystem. Wiley, New York
20. Grassian VH (2005) *Environmental catalysis*. Taylor & Francis Group, New York
21. Deng Y, Stumm W (1994) Reactivity of aquatic iron(III) oxyhydroxides simplications for redox cycling of iron in natural water. *Appl Geochem* 9:3–36
22. Geosci CR, Ona-Nguema G, Stemmler S et al (2006) Bioreduction of ferric species and biogenesis of green rusts in soils. *Comptes Rendus Geosci* 338:447–455
23. Ona-Nguema G, Carteret C, Benali O et al (2004) Competitive formation of hydroxycarbonate green rust I vs hydroxysulphate green rust II in *Shewanella putrefaciens* cultures. *Geomicrobiol J* 21:79–90
24. Zachara JM, Kukkadapu RK, Fredrickson JK et al (2002) Biomineralization of poorly crystalline Fe(III) oxides by dissimilatory metal reducing bacteria (DMRB). *Geomicrobiol J* 19:179–207
25. Glasauer S, Weidler PG, Langley S, Beveridge TJ (2003) Controls on Fe reduction and mineral formation by a subsurface bacterium. *Geochim Cosmochim Acta* 67:1277–1288
26. Ona-Nguema G, Carteret C, Benali O et al (2004) Competitive formation of Hydroxycarbonate Green Rust 1 versus Hydroxysulphate Green Rust 2 in *Shewanella putrefaciens* Cultures. *Geomicrobiol J* 21(2):79–90
27. Shchukin YD, Pertsov AV, Amelina YA (2006) *Colloid chemistry (Kolloidnaya khimiya) “High School”*, Moscow
28. Panko AV, Tsyganovich YA, Kozun IG, Prokopenko VA, Oleynik VA, Nikipelova EM (2016) Modeling of nanostructural processes in ore materials and peloids (Modelirovaniye nanostrukturnykh protsessov v rudnykh materialakh i peloidakh). *Nanosistemi Nanomateriali Nanotehnologii* 14(4):609–626
29. Kozun IG, Pan'ko AV, Yats'kiv EV, Nikipelova OM et al (2008) Application of Nanosize Clay-Minerals' Systems in the Complex Therapy for Haemophilia 'A' patients. *Nanosistemi Nanomateriali Nanotehnologii* 6(2):613–623

## **Part II**

# **Nanocomposites and Nanomaterials**

# Chapter 14

## Directional Synthesis of SnO<sub>2</sub>-Based Nanostructures for Use in Gas Sensors



Svitlana Nahirniak, Tetiana Dontsova, and Ihor Astrelin

### 14.1 General

#### 14.1.1 Introduction

Among the wide range of semiconductor metal oxides, a nanocrystalline tin (IV) oxide is considered as an effective sensor material due to a combination of its electrophysical parameters. Firstly, SnO<sub>2</sub> is a wide-band n-type semiconductor ( $\Delta E = 3.6$  eV) [1], and therefore its electrical conductivity is extremely sensitive to the state of the surface just in the temperature range (300 ÷ 800 K), in which molecules adsorbed on the surface actively engage in chemical reactions. Secondly, the surface of the tin (IV) oxide has high adsorption properties and reactivity, which is caused by the presence of free electrons in the conduction band, by surface and volume oxygen vacancies, and also by active chemisorbed oxygen [2].

Nevertheless, sensors manufactured on the SnO<sub>2</sub> basis do not possess sufficient sensitivity and selectivity [3, 4], which limit their use. To improve these characteristics, different approaches are used: reducing the particles size of sensitive layers [5]; modifying [6, 7], doping [8, 9], and creating SnO<sub>2</sub> composite structures [10,

---

S. Nahirniak (✉)

National Technical University of Ukraine “Igor Sikorsky Kyiv Polytechnic Institute”, Faculty of Chemical Technology, Kyiv, Ukraine

T. Dontsova

Department of Inorganic Substances Technology, Water Treatment and General Chemical Engineering, National Technical University of Ukraine “Igor Sikorsky Kyiv Polytechnic Institute”, Kyiv, Ukraine

I. Astrelin

Department of Chemistry, National Technical University of Ukraine “KPI”, Kyiv, Ukraine  
e-mail: [i.m.astrelin@xtf.kpi.ua](mailto:i.m.astrelin@xtf.kpi.ua)

11]; controlling the operating temperature [12]; and using particles of different morphology [13].

### ***14.1.2 Nanostructured SnO<sub>2</sub> Layers for Their Use in Gas Sensors***

Parameters of SnO<sub>2</sub>-based gas sensors (stability, sensitivity, selectivity, and response time) can be greatly improved by reducing the size of SnO<sub>2</sub> particles to nanometer dimensions and by using the single-crystalline SnO<sub>2</sub> nanoparticles of different morphology (0D and 1D). The latter will significantly improve the sensor response due to less defects in crystals, large specific surface area, and bigger surface to volume ratio of particles.

Nanocrystalline materials are characterized by the highest values of the sensor signal through the high specific surface area and, thus, higher adsorption capacity [5]. SnO<sub>2</sub> particles with a diameter of 10 ÷ 30 nm are capable to adsorb much larger number of molecules of different gases than massive materials by reason of more branched structure of their surface [14].

In addition to the crystallites' size and the relationship between them, the ratio of surface area to volume also has a great influence. The increase of it causes significant changes in sensitivity of the sensor [15]. From this point of view, one-dimensional (1D) nanostructures deserve special attention [16]. Semiconductor 1D nanostructures represent an important and broad class of nanosized wirelike structures that can be rationally and predictably synthesized in the same crystalline form with controlled chemical composition, diameters, length, and high-precision doping levels [17, 18].

Nanoscale materials, with their large specific surface area and possible quantum retention effects, show excellent mechanical, thermal, chemical, electrical, and optical properties in contrast to their bulk analogues. Control of the determined size, crystallinity, and composition of 1D nanostructures leads to the discovery of their unique properties, thus enabling different applications that would not be possible in the case of materials of massive dimension [19]. Among the various 1D nanostructures, semiconductor tin (IV) oxide nanostructures are particularly interesting through their promising application in optoelectronic and electrical devices due to good conductivity and transparency in the visible region.

With the use of 1D SnO<sub>2</sub> nanostructures as sensitive elements of gas sensors, the following advantage is predicted: the morphology of one-dimensional materials provides a high value of the specific surface area while maintaining their sufficient chemical and thermal stability with minimal energy consumption and low mass. High values of the specific surface area indicate that a significant part of atoms (or molecules) will be concentrated on the surface. Thereby, the reaction between the target gas and the chemisorbed molecules (O<sup>-</sup>, O<sup>2-</sup>, H<sup>+</sup>, and OH<sup>-</sup>) becomes possible at low temperatures.

## 14.2 Experimental

### 14.2.1 *The Influence of the Synthesis Method on Structural Characteristics of Tin (IV) Oxide Samples*

As it is known, the properties of the material (in particular, the morphology, the crystals size, the pore distribution, and microstructure development) extremely depend on the obtaining method. In this work, the synthesis of tin (IV) oxide was carried out by three different methods: thermal [20], sol-gel in an alcoholic medium [21], and the CVD method [22, 23] (Table. 14.1).

#### 14.2.1.1 Electron Microscopy

Particle sizes and morphology of the obtained tin (IV) oxide powders were determined with a transmission electron microscope TEM 100-01. As one can see from TEM microphotographs, all three methods allow to obtain nanosized SnO<sub>2</sub> particles (Fig. 14.1). SnO<sub>2</sub> samples, synthesized by thermal and sol-gel methods, have almost round shape of the particles. The more crystalline structure is typical for TSnO<sub>2</sub> and 0D SnO<sub>2</sub> samples. An average diameter of particles obtained by these methods is 50–100 nm. In the case of CVD, particles have more elongated shape. The selected area electron diffraction (SAED) image of the 0D SnO<sub>2</sub> particles (Figs. 14.1, 14.2, 14.3, 14.4, and 14.5, insert) indicated that those are single-crystalline particles.

#### 14.2.1.2 IR Spectroscopy

The infrared spectra of SnO<sub>2</sub> nanostructured samples collected using FTIR spectrometer are shown in Fig. 14.2.

According to the presented data, in the spectrum of the TSnO<sub>2</sub> sample, there are only one strong vibration band at 650 cm<sup>-1</sup> and a weakly expressed shoulder at 590 cm<sup>-1</sup>, which correspond to stretching vibration Sn-O of Sn-OH and Sn-O-Sn bonds, respectively.

Spectra of samples synthesized by sol-gel method in an alcoholic medium (SESnO<sub>2</sub>, SPSnO<sub>2</sub>, and SBSnO<sub>2</sub>), in addition to vibrations of SnO<sub>2</sub> atomic

**Table 14.1** Obtained SnO<sub>2</sub> samples

Synthesis method	Sample	
Thermal	TSnO <sub>2</sub>	
Sol-gel in ethyl alcohol medium	SESnO <sub>2</sub>	
Sol-gel in isopropyl alcohol medium	SPSnO <sub>2</sub>	
Sol-gel in butyl alcohol medium	SBSnO <sub>2</sub>	
CVD	0D SnO <sub>2</sub>	1D SnO <sub>2</sub>

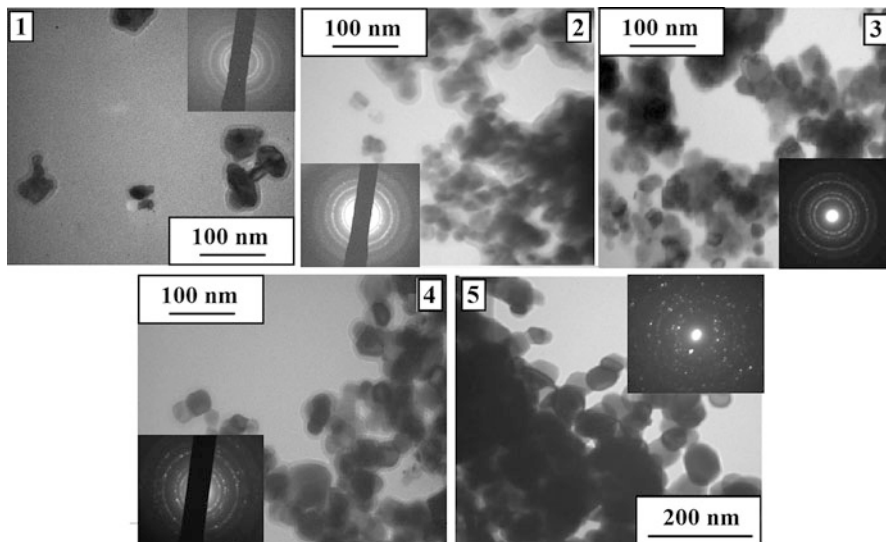


**Fig. 14.1** TEM images of SnO<sub>2</sub> samples: 1, TSnO<sub>2</sub>; 2, SESnO<sub>2</sub>; 3, SPSnO<sub>2</sub>; 4, SBSnO<sub>2</sub>; 5, 0D SnO<sub>2</sub>

structure, contain weak vibration bands in the range of 1630–1640 cm<sup>-1</sup> and more distinct oscillation bands at 3390–3420 cm<sup>-1</sup>. The first corresponds to deformation vibrations of the Sn-OH bond, indicating the presence of bound H<sub>2</sub>O molecules. The latter relates to the valence oscillations of the Sn-OH bond, which corresponds to the adsorbed water molecules. Vibrations at 1065, 1387, 1561, 2857, and 2926 cm<sup>-1</sup> belong to adsorbed molecules of gases (O<sub>2</sub> and CO<sub>2</sub>) of various forms and are observed only in the spectrum of the 0D SnO<sub>2</sub> sample. This indicates that this sample is more sensitive to gas molecules and, therefore, is most suitable for use in sensitive layers of gas sensors.

#### 14.2.1.3 The Specific Surface Area

The specific surface area of the samples was studied by adsorption methods of benzene vapor and adsorption of toluene from its solutions in isooctane. Determined values for all synthesized powders show that TSnO<sub>2</sub> and SBSnO<sub>2</sub> samples are characterized by the smallest values of the specific surface area. For samples synthesized by sol-gel method in an alcoholic medium, a significant dependence of the specific surface area and particle size on the alcohol solubility is observed. SnO<sub>2</sub> sample, obtained by CVD method, has the highest specific surface area (Table 14.2).

Consequently, studies of tin (IV) oxide samples, synthesized by various methods, have shown that all methods allow to synthesize SnO<sub>2</sub> particles of nanometer



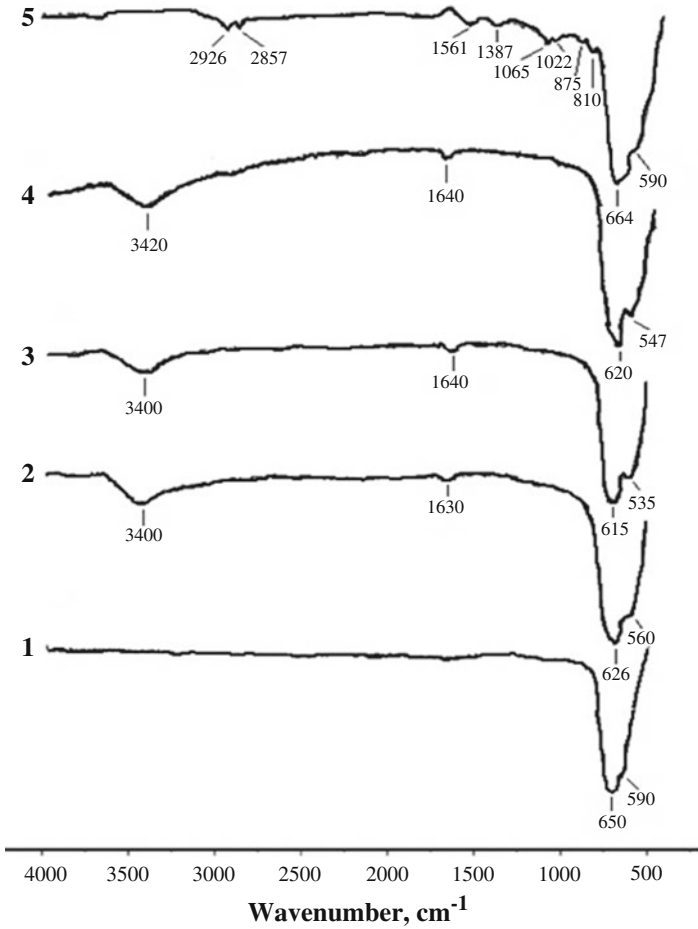


**Fig. 14.2** IR spectra of tin (IV) oxide samples: 1, TSnO<sub>2</sub>; 2, SESnO<sub>2</sub>; 3, SPSnO<sub>2</sub>; 4, SBSnO<sub>2</sub>; 5, 0D SnO<sub>2</sub>

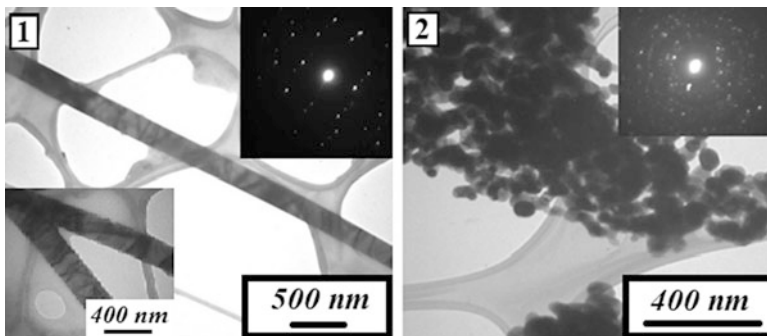


**Fig. 14.3** TEM images of SnO<sub>2</sub> samples: 1, 1D SnO<sub>2</sub>; 2, 0D SnO<sub>2</sub>

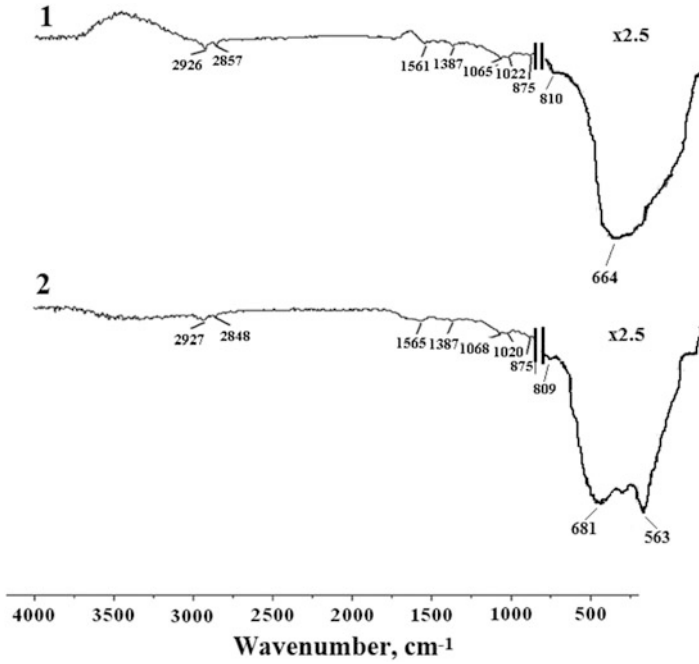


Fig. 14.4 IR spectra of tin (IV) oxide samples: 1, 0D  $\text{SnO}_2$ ; 2, 1D  $\text{SnO}_2$

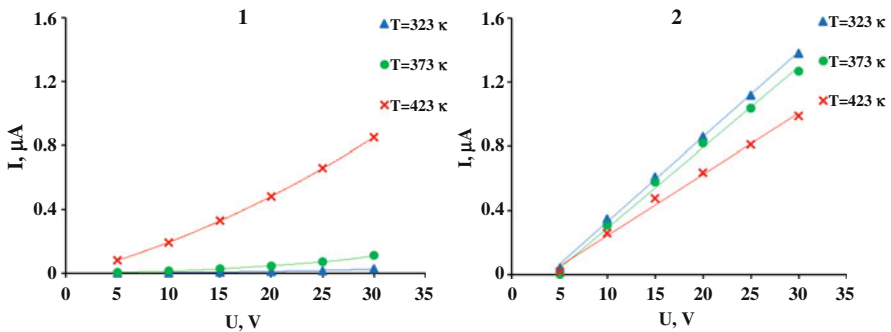


Fig. 14.5 I–V curves of  $\text{SnO}_2$  samples.: 1, 0D  $\text{SnO}_2$ ; 2, 1D  $\text{SnO}_2$

dimensions. However, the most promising is the CVD method, which results in the obtaining of  $\text{SnO}_2$  single crystals of high crystallinity degree; the synthesized powders have higher values of the specific surface area and are characterized by better adsorption properties.

**Table 14.2** Calculated specific surface area of SnO<sub>2</sub> samples

Sample	Crystallites' size, nm	Specific surface area, m <sup>2</sup> /g		Particles size, calculated by $d = \frac{6}{S \cdot \rho_{\text{SnO}_2}}$ , nm	
		By benzene	By toluene	By benzene	By toluene
TSnO <sub>2</sub>	121,7	8,4	8,9	101,9	89,2
SESnO <sub>2</sub>	23,5	13,5	16,1	63,4	53,2
SPSnO <sub>2</sub>	34,1	13,9	14,6	61,6	58,6
SBSnO <sub>2</sub>	39,4	3,9	4,5	219,7	190,2
ODSnO <sub>2</sub>	57,8	17,2	–	49,8	–

### 14.2.2 Characterization and Comparison of 0D and 1D SnO<sub>2</sub> Nanostructures, Obtained by CVD

In order to establish the scientific basis for obtaining of SnO<sub>2</sub> nanostructures of different morphologies, the influence of temperature, gas composition, and heating rate in the CVD process was investigated. It was found that the pure SnO<sub>2</sub> phase is formed at 1123 K [22]; dosage of 5% vol. oxygen to a carrier gas leads to a change in morphology of tin (IV) oxide particles from rounded to elongated form [24]; and the change in the morphology of SnO<sub>2</sub> from 0D to 1D nanostructures can be achieved by reducing the heating rate [13].

#### 14.2.2.1 Electron Microscopy

As seen on electronic microphotograph of 1D SnO<sub>2</sub> sample, it has a ribbonlike one-dimensional structure. The diameters of these ribbons are 100–300 nm and a length up to 7 μm. A sample of zero-dimensional SnO<sub>2</sub> has round and hexagonal shape of particles with an average diameter of 50–150 nm. The SAEDs of 0D and 1D structures show the single-crystalline nature of samples (Fig. 14.3).

#### 14.2.2.2 IR Spectroscopy

A further comparison of zero-dimensional and one-dimensional tin (IV) oxide structures, synthesized by CVD method at a different heating rate, showed that 0D SnO<sub>2</sub> and 1D SnO<sub>2</sub> have not only visual differences. The infrared spectra of both samples are similar and indicate the presence of Sn-O vibrations in Sn-O-Sn and Sn-OH bonds. However, the IR spectrum of 1D SnO<sub>2</sub>, in contrast to 0D SnO<sub>2</sub>, contains a characteristic feature of 1D SnO<sub>2</sub> structures at 563 cm<sup>-1</sup> [13] (Fig. 14.4).

### 14.2.2.3 I-U Measurements

The study of current-voltage characteristics was carried out by the method described in [13, 25]. In accordance with obtained results, 0D and 1D tin (IV) oxide indicate different nature of the curves due to differences in the morphology of their structures. For zero-dimensional SnO<sub>2</sub>, I-U dependences are nonlinear at all temperatures, whereas 1D SnO<sub>2</sub> is characterized by ohmic current-voltage curves (Fig. 14.5).

It is known that ohmic behavior of current-voltage dependencies is very important for sensing properties of material because the sensitivity is maximal for ohmic semiconductors [26]. Therefore, one-dimensional SnO<sub>2</sub> is more promising for usage in gas sensors.

Calculated resistance values at different voltages are shown in Fig. 14.6. As can be observed, zero-dimensional and one-dimensional tin (IV) oxide samples differ not only in the resistance value but also in the nature of its temperature dependence. For 0D SnO<sub>2</sub>, the value of the electric resistance decreases with temperature increasing, which is typical for semiconductor materials. While the temperature dependences of the electric resistance of 1D SnO<sub>2</sub> pass through the maximum, the highest values of the electric resistance are observed at 373–423 K.

Considering that for conductor materials electric resistance increases with increasing temperature and the presence of an extremum on the temperature dependences may indicate a change in the conductivity type of the material, it can be argued that the presence of a maximum on the temperature dependences of resistance for 1D SnO<sub>2</sub> sample may be connected with the transition of conductor properties of this material to semiconductors.

### 14.2.3 Investigation of Modifier Effect on the Properties of Tin (IV) Oxide Powders

Doping or modifying of SnO<sub>2</sub> powders with platinum metals improves their thermal stability, sensitivity, and selectivity [27]. These parameters are very important for the use of SnO<sub>2</sub> as a sensitive layer in gas sensors. In this paper, an argentine was chosen as a modifier, due to its approachability and lesser studying. Samples of zero-dimensional (0D SnO<sub>2</sub>) and one-dimensional (1D SnO<sub>2</sub>) tin (IV) oxides were synthesized by CVD method at 1123 K and afterward modified by argentine with different mass contents of the modifier [28].

Optical properties of tin (IV) oxide samples were studied using a two-beam spectrophotometer Specord 210. The optical band gap of synthesized samples was determined by graphic method using optical density dependencies of the suspensions of tin (IV) oxide powders in the range of wavelength  $\lambda = 200\text{--}400$  nm. Obtained absorption spectra of pure and modified samples of 0D and 1D SnO<sub>2</sub> nanostructures testify that one-dimensional tin (IV) oxide powders absorb

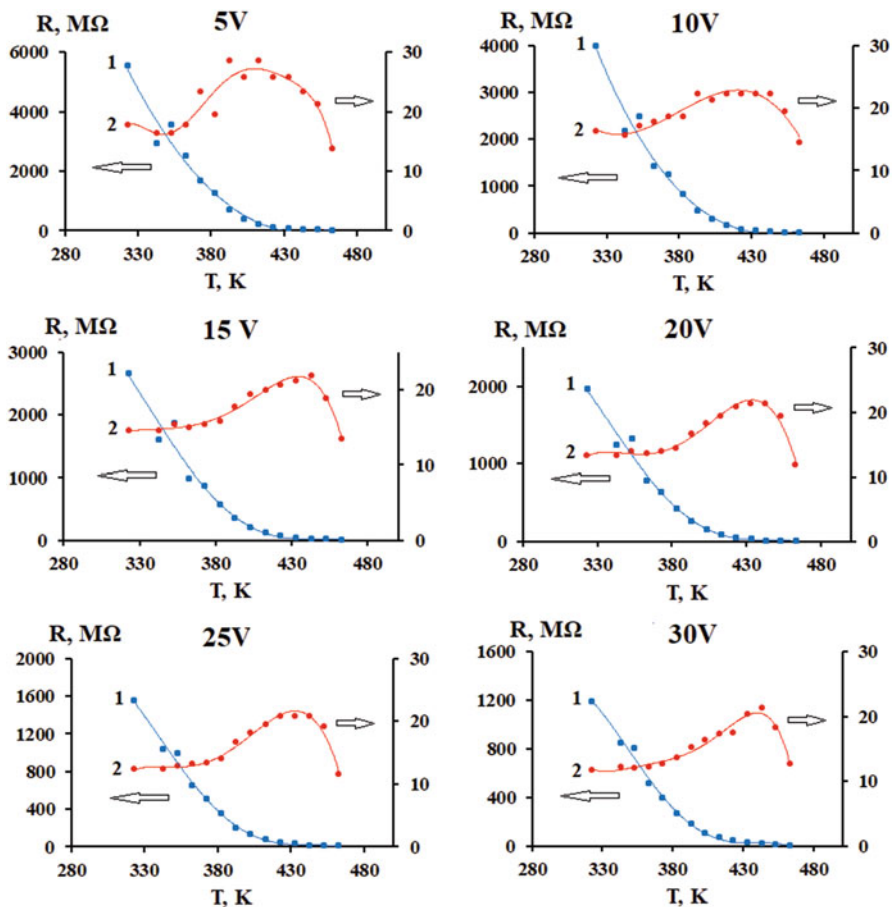
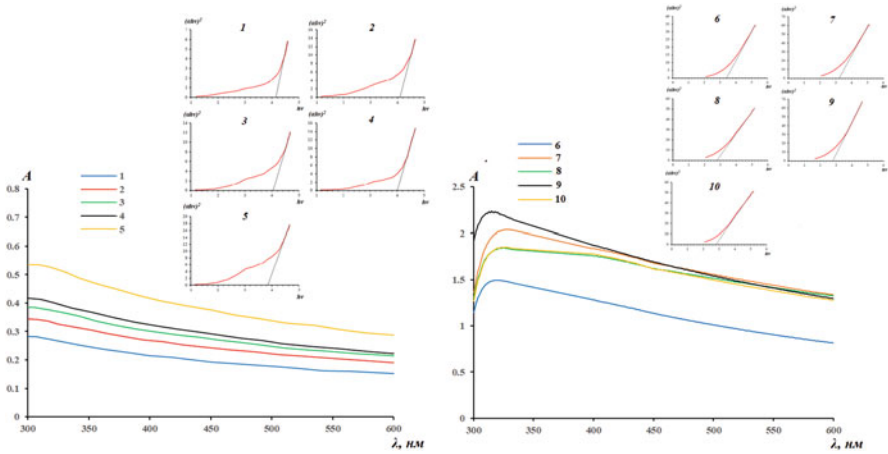


Fig. 14.6 Temperature dependencies of resistance of SnO<sub>2</sub> samples.: 1, 0D SnO<sub>2</sub>; 2, 1D SnO<sub>2</sub>

UV radiation more intensively than zero-dimensional SnO<sub>2</sub> samples (Fig. 14.7). The determined values of the band gap width for 0D and 1D SnO<sub>2</sub> nanostructures are in the range 3.85–4.2 eV and from 2.8 to 3.4 eV, respectively. That is, unlike zero-dimensional tin (IV) oxide samples, 0D SnO<sub>2</sub> is characterized by slightly lower values of the band gap width in comparison with the theoretical value. Thus, the morphology of the tin (IV) oxide particles has a direct effect on the optical properties.

For both zero-dimensional and one-dimensional SnO<sub>2</sub>, the lack of linear regularity between the value of the electrical resistance and the modifier percentage was detected. With the increase of argementum, content values of resistance for modified 0D tin (IV) oxide powders pass through the maximum. Adding more than 5% of Ag causes change in the nature of current-voltage curves from non-ohmic to ohmic. In the case of 1D SnO<sub>2</sub> structures, the value of the electrical resistance increases with



**Fig. 14.7** Optical spectra of SnO<sub>2</sub> samples.: 1, 0D SnO<sub>2</sub>; 2, 0D 2AgSnO<sub>2</sub>; 3, 0D 5AgSnO<sub>2</sub>; 4, 0D 7AgSnO<sub>2</sub>; 5, 0D 10AgSnO<sub>2</sub>; 6, 1D SnO<sub>2</sub>; 7, 1D 2AgSnO<sub>2</sub>; 8, 1D 5AgSnO<sub>2</sub>; 9, 1D 7AgSnO<sub>2</sub>; 10, 1D 10AgSnO<sub>2</sub>

adding of argementum but does not depend on the percentage of the modifier. Obtained results indicate that the modification by argementum will lead to improvement of sensory properties for 0D SnO<sub>2</sub> and deterioration of sensing characteristics in the case of 1D SnO<sub>2</sub>.

As mentioned above, in order to characterize sensor performance, a set of parameters is used. The most important of them are sensitivity, selectivity, response time, detection limit, stability, and recovery time. In this paper the sensitivity of obtained zero-dimensional and one-dimensional tin (IV) oxide powders toward acetone was studied. The gas sensitivity (sensor response) was determined by

$$S = \frac{R_g}{R_a}$$

where  $R_g$  is resistance values of gas sensor in gas environment and  $R_a$  is resistance values in air.

As seen from the calculated values of the sensitivity of SnO<sub>2</sub> samples (Tables 14.3 and 14.4), one-dimensional tin (IV) oxide shows the best sensitivity to acetone among unmodified tin (IV) oxide powders.

Among the modified SnO<sub>2</sub> powders, the highest sensory response is observed for zero-dimensional tin (IV) oxide modified by 10% argementum. Modification of 1D SnO<sub>2</sub> samples leads to decreasing of sensor response toward acetone. Obtained data concerning modifier effect on the gas sensitivity toward acetone for pure and modified tin (IV) oxide samples are completely consistent with electrical properties of 0D and 1D SnO<sub>2</sub> structures.

Since the modification takes into account not only the type of modifier and the nature of the detected gas but also the optimal percentage of the added modifier, the

**Table 14.3** Sensitivity values of pure and modified zero-dimensional SnO<sub>2</sub> samples

Sample	U, B		
	5	15	30
<i>T</i> = 323 K			
0D SnO <sub>2</sub>	4, 5	4, 3	4, 2
0D 2AgSnO <sub>2</sub>	4, 4	4, 6	4, 8
0D 5AgSnO <sub>2</sub>	1, 5	2, 9	3, 2
0D 7AgSnO <sub>2</sub>	1, 8	1, 8	1, 7
0D 10AgSnO <sub>2</sub>	10, 9	10, 4	8, 6
<i>T</i> = 373 K			
0D SnO <sub>2</sub>	2, 4	2, 1	2, 2
0D 2AgSnO <sub>2</sub>	3, 0	3, 5	3, 2
0D 5AgSnO <sub>2</sub>	1, 5	2, 0	1, 9
0D 7AgSnO <sub>2</sub>	1, 3	1, 4	1, 3
0D 10AgSnO <sub>2</sub>	10, 7	7, 6	6, 1
<i>T</i> = 423 K			
0D SnO <sub>2</sub>	1, 4	1, 6	1, 6
0D 2AgSnO <sub>2</sub>	2, 3	2, 4	2, 3
0D 5AgSnO <sub>2</sub>	2, 6	2, 5	2, 2
0D 7AgSnO <sub>2</sub>	0, 8	1, 2	1, 2
0D 10AgSnO <sub>2</sub>	9, 8	7, 2	5, 8

**Table 14.4** Sensitivity values of pure and modified one-dimensional SnO<sub>2</sub> samples

Sample	U, B		
	5	15	30
<i>T</i> = 323 K			
1D SnO <sub>2</sub>	4, 1	1, 1	1, 3
1D 2AgSnO <sub>2</sub>	1, 1	1, 1	1, 0
1D 5AgSnO <sub>2</sub>	1, 1	1, 0	1, 0
1D 7AgSnO <sub>2</sub>	1, 1	1, 1	1, 1
1D 10AgSnO <sub>2</sub>	1, 0	1, 0	1, 0
<i>T</i> = 373 K			
1D SnO <sub>2</sub>	67, 3	1, 3	1, 3
1D 2AgSnO <sub>2</sub>	1, 1	1, 0	1, 0
1D 5AgSnO <sub>2</sub>	1, 0	1, 0	1, 0
1D 7AgSnO <sub>2</sub>	1, 1	1, 1	1, 0
1D 10AgSnO <sub>2</sub>	1, 0	1, 0	1, 0
<i>T</i> = 423 K			
1D SnO <sub>2</sub>	8, 5	1, 2	0, 8
1D 2AgSnO <sub>2</sub>	1, 1	1, 0	1, 0
1D 5AgSnO <sub>2</sub>	1, 0	1, 0	1, 0
1D 7AgSnO <sub>2</sub>	1, 0	1, 0	1, 0
1D 10AgSnO <sub>2</sub>	1, 0	1, 0	1, 0

decrease in the sensitivity of the modified 1D SnO<sub>2</sub> samples may be connected with the fact that either the Ag acts as a trap for electrons or its optimal percentage lies in a different range than investigated.

Thus, the best response to acetone among the investigated one-dimensional SnO<sub>2</sub> samples is observed for unmodified 1D SnO<sub>2</sub>.

### 14.3 Conclusions

The methods of synthesis of tin (IV) oxide powders and the comparison of physical and chemical properties of the obtained powders were investigated. CVD as the most rational and promising method for obtaining of SnO<sub>2</sub> powders of nanometer dimensions was chosen. The conditions of directional synthesis of tin (IV) oxide nanostructures of different morphologies were invented. The comparison of different properties of 0D and 1D SnO<sub>2</sub> nanostructures is presented. It was shown that morphology and modification have a significant influence on the nature of current-voltage curves. For zero-dimensional SnO<sub>2</sub> samples, I-U curves are non-ohmic at all temperatures, while one-dimensional SnO<sub>2</sub> structures are characterized by linear current-voltage dependencies. The highest sensor response to acetone showed unmodified one-dimensional tin (IV) oxide powder.

**Acknowledgments** The authors thank the National Technical University of Ukraine “Igor Sikorsky Kyiv Polytechnic Institute” for support in conducting this research.

### References

1. Munnix S, Schmeits M (1982) Surface electronic structure of tin (IV) oxide. *Solid State Commun* 43:867–873
2. Krivetskiy VV, Rumyantseva MN, Gaskov AM (2013) Chemical modification of nanocrystalline tin dioxide for selective gas sensors. *Russ Chem Rev* 82(10):917–941 [In Russian]
3. Bochenlov VE, Sergeev GB (2010) Sensitivity, selectivity and stability of gas-sensitive metal-oxide nanostructures. In: *Metal oxide nanostructures and their applications*, vol 3. American Scientific Publishers, USA, pp 31–52
4. Nagirnyak SV, Dontsova TA (2015) Ways for improvement selectivity of semiconductor gas sensors. *Young Sci* 10(25):15–17
5. Miller TA, Bakrania SD, Perez V, Wooldridge MS (2006) Nanostructured tin dioxide materials for gas sensor applications. *Funct Nanomater* 30:1–24
6. Tournier G, Pijolat C, Lalauze R, Patissier B (1995) Selective detection of CO and CH<sub>4</sub> with gas sensors using SnO<sub>2</sub> doped with palladium. *Sensors Actuators* 27:24–28
7. Wang S, Zhao Y, Huang J, Wang Y, Wu S et al (2006) Low-temperature carbon monoxide gas sensors based gold/tin dioxide. *Solid State Electron* 50:1728–1731
8. Choi JK, Hwang IS, Kim SJ, Park JS, Park SS (2010) Design of selective gas sensors using electrospun Pd-doped SnO<sub>2</sub> hollow nanofibers. *Sensors Actuators* 150:191–199
9. Schwarz JA (1995) Methods for preparation of catalytic materials. *Chem Rev* 95:477–510



10. Leghrib R, Felten A, Pireaux JJ, Llobet E (2011) Gas sensors based on doped-CNT/SnO<sub>2</sub> composites for NO<sub>2</sub> detection at room temperature. *Thin Solid Films* 520:966–970
11. Dontsova TA, Ivanenko IM, Astrelin IM, Nagirnyak SV (2014) Stabilization of nanoscale tin (IV) oxide on the surface of carbon nanotubes. *J Electr Eng* 2:34–38
12. Ahlers S, Müller G, Doll T (2005) A rate equation approach to the gas sensitivity of thin film metal oxide materials. *Sensors Actuators B* 107:587–599
13. Dontsova TA, Nagirnyak SV, Zhorov VV, Yasiievych YV (2017) SnO<sub>2</sub> nanostructures: effect of processing parameters on their structural and functional properties. *Nanoscale Res Lett* 12(332):1–7
14. Petruk VH, Kravec AH (2007) Sensors based on SnO<sub>2</sub> nanoparticles for carbon monoxide CO detection. *J Tech Phys* 77(2):86–90
15. Pan J-M, Maschhoff BL, Diebold U, Madey TE (1993) Structural study of ultrathin metal films on TiO<sub>2</sub> using LEED, ARXPS and MEED. *Surf Sci* 291(3):381–394
16. Nagirnyak SV, Dontsova TA, Astrelin IM (2015) One-dimensional tin (IV) oxide nanostructures as gas-sensing materials. *Res Bull Natl Tech Univ Ukr «Kyiv Polytech Institute»* 5:119–128
17. Alivasators AP (1996) Semiconductor clusters, nanocrystals and quantum dots. *Science* 271(5251):933–937
18. Cui Y, Lieber CM (2001) Functional nanoscale electronic devices assembled using silicon nanowire building blocks. *Science* 291(5505):851–853
19. Pan J, Shen H, Mathur S (2012) One dimensional SnO<sub>2</sub> nanostructures: synthesis and application. *J Nanotechnol* 2012:1–12
20. Nagirnyak SV, Dontsova TA, Astrelin IM, Alekseev OF, Romanenko YM (2012) Synthesis and characterization of nanosized tin (IV) oxide powders from tin (II) oxalate. *Res Bull Natl Tech Univ Ukr «Kyiv Polytechnic Institute»* 2:151–155 [In Ukrainian]
21. Nagirnyak SV, Dontsova TA (2012) The method of synthesis of superdispersed tin (IV) oxide by sol-gel method. Thesis, Kyiv (Ukraine) [In Ukrainian]
22. Nagirnyak SV, Lutz VA, Dontsova TA, Astrelin IM (2016) The effect of the synthesis conditions on morphology of tin (IV) oxide obtained by vapor transport method. In: *Nanophysics, nanophotonics, surface studies, and applications*, vol 183. Springer, Springer Proceedings in Physics, Europe, pp 331–342
23. Nagirnyak SV, Lutz VA, Dontsova TA, Astrelin IM (2016) Synthesis and properties of tin (IV) oxide obtained by chemical vapor deposition method. *Nanoscale Res Lett* 11(343):1–7
24. Lutz VA, Nagirnyak SV, Dontsova TA (2015) Optical properties of tin (IV) oxide nanoparticles obtained by CVD method. *Young Sci* –12(27), P1:61–64 [In Ukrainian]
25. Nagirnyak S, Zhorov V, Dontsova T, Astrelin I (2016) Electrical properties of pure and Ag-doped SnO<sub>2</sub> nanostructures obtained by chemical vapor deposition technique. *Nano Stud* 13:233–240
26. Zhai T, Fang X, Liao M, Xu X, Zeng H, Yoshio B, Golberg D (2009) A comprehensive review of one-dimensional metal-oxide nanostructure photodetectors. *Sensors* 9:6504–6529
27. Nagirnyak S, Dontsova TA (2017) Effect of modification/doping on gas sensing properties of SnO<sub>2</sub>. *Nano Res Appl* 2(8):1–5
28. Lutz VA, Nagirnyak SV, Dontsova TA (2016) Synthesis and properties of doped and undoped tin (IV) oxide. *Eur J Sci Res* 1(13), V.II:881–889 [In Ukrainian]

# Chapter 15

## “Polymer–Oxide”

### Micro-/Nanocomposites: Background and Promises



S. G. Nedilko

## 15.1 Introduction

The small review of published data, the results that have been published recently by the author’s research team, and our new findings are presented in this chapter. We deal here mainly with data that are related with optical, especially luminescent, properties noted in the chapter title materials.

New nanosized materials emerged from the last decade both in traditional and advanced technologies, e.g., industry of consumer goods, high-tech aircraft industry, electronics, biomedicine, etc. It is obvious there is now a demand for environmental- and human-friendly materials. Advanced materials based on polymer matrix and incorporated with some nanosized particles provide many advantages. Complex inorganic oxides are considered as important components of polymer composites which are perspective for many practical applications. Opportunities to use such composites are related with peculiarities of micro-/nanoparticle confinement in polymers. As for scientific impact, current and future interest is in touch with effect of oxide particles on mechanical, thermomechanical properties, as well as their impact on dielectric and conductivity characteristics. Spectroscopic studies are one of the most important techniques that allow providing scientifically based prediction of mentioned material properties. Particularly, when we speak about oxides that reveal luminescent behavior, luminescent studies are of principal priority.

As the volume of this chapter is limited, we’d like to direct the readers to well-known reviews where the main features, current status, and recent developments in the field of polymer matrix micro-/nanocomposites are available [1–5]. In this introduction, we provide only some definitions and short descriptions related with

---

S. G. Nedilko (✉)

Taras Shevchenko National University of Kyiv, Kyiv, Ukraine

e-mail: [SNedilko@univ.kiev.ua](mailto:SNedilko@univ.kiev.ua)

the object under study. First, it should be emphasized that in this work we deal only with micro- or nanocomposites. These notations mean that one or more of their components are of sizes in nano- (up to 200 nm) and/or microscale ranges up to 200  $\mu\text{m}$  [6]. It is known that properties of the super small particles change when their size is lesser than the so-called critical size. It is of 50 nm when refractive index changes arise or 100 nm when electromagnetic phenomena changes, strengthening and toughening occur, or hardness and plasticity are modified [7]. So, if we believe to find manifestation of processes actual in optics, we have to operate with materials that contain components of size smaller than 100 nm.

It is important to note when the particle sizes are of nanosized scale, the role of interface interactions becomes significant that allows enhancement of the composite properties. In the most experimental cases, we dealt with mixture of micro- and nanosized components of the composites. So, it could be better to denote them as micro-/nanocomposites, we suppose.

The micro-/nanocomposite materials can be classified, according to their matrix materials, in three different types: ceramic matrix micro-/nanocomposites (CMM/NCs), metal matrix micro-/nanocomposites (MMM/NCs), and polymer matrix micro-/nanocomposites (PMM/NCs) [1]. We will be in touch here only with the last ones. The PMM/NCs are of wide applications due to their higher developed level and specific or sometimes unique properties and characteristics if compared to metal and ceramic composites. Thus, various types of polymer-based micro-/nanocomposites containing dielectric or semiconductor nanoparticles have already been developed for specific applications. As for polymers themselves, they are widely used in industry and technology due to their easy production and lightweight and ductile nature as well. However, they possess some disadvantages such as low modulus and strength compared to metals and ceramics. When the fibers, whiskers, or particles are added into polymer matrix, then it is an approach to effectively enhance mechanical and other polymers' properties. To do it, various polymers have been filled with some inorganic compounds in order to increase heat and impact resistance and mechanical strength or to modify their electrical conductivity or permeability to oxygen and water molecules [8]. Some metal or ceramic reinforcements opened the way to add new magnetic, electronic, optical, or catalytic properties possessed to inorganic, e.g., metal and oxide nanoparticles. Incorporation of these additives allowed improvement of the polymer characteristics simultaneously keeping their lightweight and ductile nature [2, 9, 10].

Thus, one of the aims of this work was to provide brief summary about morphology, structure, and optical properties of the PMM/NC incorporated with inorganic, particularly oxide, compounds which makes them attractive for modern devices, primarily optical ones. We will compare some of these data with ones obtained about PMM/NC made by us. Then, we will give a closer look on the original data concerning, made by us, composites, namely, composites made on the basis of well-known, but promising in the future, polymer, which is cellulose.

## 15.2 Embedded with Inorganic Oxide Polymer Matrix Micro-/Nanocomposites as Optical Materials

The wide set of polymers are suitable to be used as matrix components of the PMM/NC, e.g., vinyl polymers, condensation polymers, polyolefin, and so on. As for the fillers, various inorganic crystalline compounds have been used. Those were  $\text{SiO}_2$ ,  $\text{TiO}_2$ , and other simple metal oxides, but layered silicates were of the most attractive some time ago [10, 11]. No doubt they are the most suitable just due to low particle sizes, peculiarities of surface structure, morphology, and well-known chemistry of their intercalation [11, 12]. Details of the procedures of the polymer matrix composites fabrication are the same either for micro- or nanocomposites, and description of these techniques can be found in [13–18] or elsewhere. The most important ones are the following: intercalation of the polymer or prepolymer from solution, in situ intercalative polymerization, in situ polymerization, template synthesis, melt intercalation, direct mixture of polymer and fillers, and sol–gel process. It seems the last four of them are more suitable for preparation of the PMM/NC incorporated with oxide particles, e.g., with  $\text{TiO}_2$ ,  $\text{SiO}_2$ ,  $\text{Fe}_2\text{O}_3$ ,  $\text{AgNO}_3$ ,  $\text{NiSO}_4$ , and  $\text{CuSO}_4$ . Despite of well elaborated different procedures of the PMM/NC preparation there are many factors influence of which on the made products is unforeseen, especially if new "matrix – oxide" combinations are under studies. Those can be size, morphology of the particles, their optimal concentration, and distribution over the sample volume and surface. Therefore, composites made by new methods have to be comprehensively investigated using both experimental and theoretical approaches, and their mechanical, thermal, electrical, and optical characteristics have to be evaluated as well.

Micro-/nanosized components of the PMM/NC usually are in the form of particles, whiskers, fibers, nanotubes, etc. They are classified according to their dimensions [19]. When all three dimensions are of the same micro- or nanoscale range, they are called as iso-dimensional particles [19]. The second kind is constructed from the units that possess two dimensions of the same scale, and the third dimension is larger. (The carbon nanotubes and cellulose whiskers are the patterns of this type.) The third type is characterized by only one dimension in the micro-/nanometer range. In this case, the filler has a view of sheet of one to a few micro-/nanometers thick and hundreds to thousands micro-/nanometers long. The PMM/NCs made on the base of such type fillers are called polymer-layered micro-/nanocomposites [19, 20].

Really, it is difficult to perform composites of perfect structure, e.g., to polyester/ $\text{TiO}_2$  [14]. The authors noted that up to the  $\text{TiO}_2$  concentration 3 vol. %, the samples showed excellent dispersion of the particles. If concentration was 4 vol. %, a considerable agglomeration took place (see Fig. 15.1a). The similar is also true for the PMM/NC- $\text{K}_2\text{Eu}(\text{PO}_4)(\text{MoO}_4)$  made and studied by author of this work. A lot of  $\text{K}_2\text{Eu}(\text{PO}_4)(\text{MoO}_4)$  rodlike particles of sizes near 20–30 nm cover the surface of the polymer matrix. At the same time, their large agglomerates of lateral sizes near 1–2  $\mu\text{m}$  and up to 400 nm pierce through composite surface

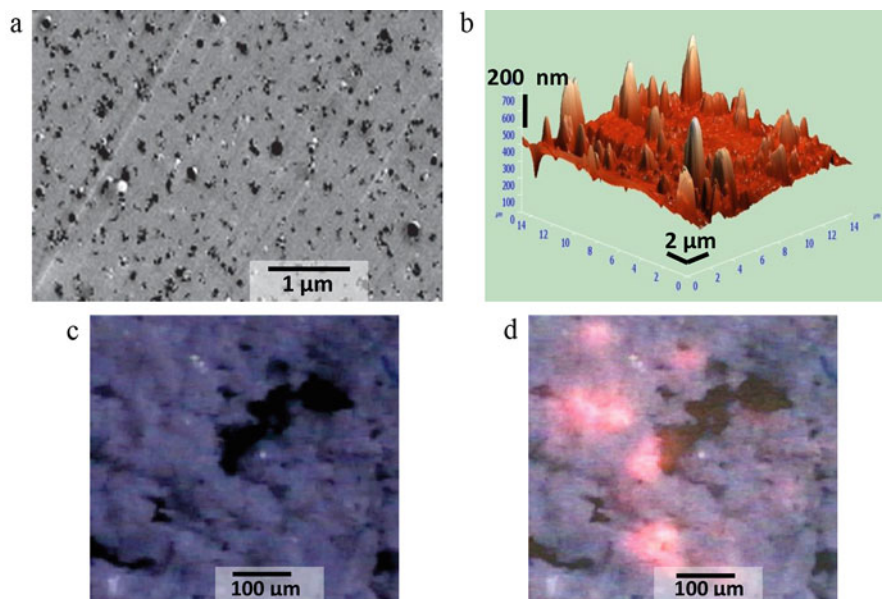


**Fig. 15.1** SEM (a), AFM (b), and optical microscopy images of the polymer-based composites containing  $\text{TiO}_2$  (a) and  $\text{K}_2\text{Eu}(\text{PO}_4)(\text{MoO}_4)$  (b–d) oxides. The image (c) was taken under incident white scattered light. The image (d) was taken under incident violet ( $\lambda_{\text{ex}} = 405 \text{ nm}$ ) laser radiation. (Image (a) is reproduced from [1])

(Fig. 15.1b). Thus, these samples, in fact, were micro-/nanocomposites. Owing to luminescence properties of such composites, it was possible to illustrate their heterogeneous distribution in significant limits of the sample (Fig. 15.1c, d).

Many properties of PMM/NC systems are directly related to their structure. We see manifestation of those relation, e.g., in the luminescence properties of the *poly(styrene-alt-maleic anhydride)* (PSM) embedded with CdSe nanocrystals. The composite emits luminescence light in emission band peaked at 540 nm. As this type of near-band-edge luminescence is typical for surface-passivated nanoparticles, the authors concluded that the structure of the nanoparticles surface is modified by PSM molecules that results in enhancement of luminescence properties [21, 22].

The PMM/NCs of layered structure have attracted great interest as they were able to reveal new or improved properties, if compared with starting polymers [23].

Despite of the fact that a number of the PMM/NC embedded with inorganic was made, studied and have been used in practice applications, a few work were performed in the field of optics of PMM/NC containing inorganic oxides (see e.g. [24]). It seems undeserved, since firstly oxide compounds have become highly sought after in modern optical devices and, secondly, due to the mutual influence of the micro-/nanosized components of the matrix and filler, the optical properties of PMM/NC can be substantially modified, comparatively with properties of starting materials.

As for the first statement, one can point out the very well-known example of the polymer–oxide composite use. It is related with possible luminescent properties of some polymer–oxide composites. Luminescent materials are attractive materials as they show many areas of application. Luminescent modifiers can be introduced to the various polymer materials and processed by different methods to produce films, fibers, molded pieces, etc. Despite stated above, there is some information about polymer matrices incorporated with inorganic compounds containing active luminescence trivalent rare-earth ions or ions of transition elements (see, e.g., [25–28]). The various polymers were used for preparation of the polymer–oxide composites. Those were nonpolar monofunctional monomer (isooctyl acrylate, IOA) in combination with a multifunctional low polar monomer (bisphenol A ethoxylate diacrylate SR349), and they were used in a weight ratio of 20 wt% SR349:80 wt% IOA [25]. This polymer was incorporated with ZrO<sub>2</sub> doped with Eu<sup>3+</sup>. The same oxide was taken for preparation of polymer composite with polyurethane matrix [26]. Methyl methacrylate (MMA) and lauryl acrylate (LA) polymer matrixes were used for doping by YVO<sub>4</sub>:Eu vanadate. The obtained materials were highly transparent (transmission ~90% at 600 nm) and showed red photoluminescence upon UV excitation caused by Eu<sup>3+</sup> ion emission in the composite materials [27]. The optical properties of lanthanide oxide nanoparticles (Gd<sub>2</sub>O<sub>3</sub>:Tb) dispersed in the poly(ethylene oxide) (PEO) network as thermally stable polymeric films were studied in [28]. Obtained films were still transparent and keep their original mechanical properties.

One more example is a photoluminescence coating (PLC) of UV or blue LEDs for white LED creation on their base. Indeed, it is a common knowledge that most commercially attractive WLEDs contain the PLC made on the base of yttrium aluminum garnet (YAG) doped with cerium, Y<sub>3</sub>Al<sub>5</sub>O<sub>12</sub>:Ce<sup>3+</sup> (YAG:Ce) and dispersed in polymer (silicone) matrix [29]. Similarly, polymer matrix (polymethyl methacrylate or polyvinyl acetate, etc.) incorporated with YAG co-doped with Pr and Yb (YAG:Pr-Yb) or with Er and Yb (YAG:Yb-Er) is elaborated as PLC for solar cells [30, 31].

Some examples of the successful creation of the polymer–oxide composites just as optical materials are discussed below. So, let's take a look at the chromium-doped forsterite (Cr-Mg<sub>2</sub>SiO<sub>4</sub>) in the tribromostyrene/naphthyl methacrylate matrix. This system was directed to the solid-state laser material elaboration, so, polymer matrix was taken with the average refractive index of forsterite (1.652 at 589.3 nm). Performed optical measurements on the composite films to examine amplification behavior showed good results [24]. The Cr diopside (Cr-CaMgSi<sub>2</sub>O<sub>6</sub>) is a material that manifests luminescence in the near-IR range (700–1200 nm). However, a single crystal of this material cannot be prepared due to incongruent melting. Composite system similar to described above, but containing Cr-CaMgSi<sub>2</sub>O<sub>6</sub>, is an example of how the PMM/NC can be used to improve the process ability and functionality of starting material (Cr-CaMgSi<sub>2</sub>O<sub>6</sub>), which could not be obtained by another way [24]. The set of composites based on polymethyl methacrylate (PMMA) and doped with luminescent particles of the Pr<sup>3+</sup>:LaAlO<sub>3</sub>, Pr<sup>3+</sup>:Y<sub>2</sub>O<sub>3</sub>, and Er<sup>3+</sup>:Y<sub>2</sub>O<sub>3</sub> were manufactured and characterized [32, 33]. These materials

keep the luminescent properties of the original oxide nanopowders. In addition, optimization of the erbium dopant concentration was possible; thus it was found that PMMA  $\text{Er}^{3+}:\text{Y}_2\text{O}_3$  composites are available to a limited extent for solid laser development [32].

We have examined above the cases where a polymer was used only as a matrix for fixing an active optic component. Thus, interactions between matrix and filler and their ability to determine the difference between optical properties of the composite and optical properties of matrix and filler were practically ignored.

Below, we give positive examples of such type issues [34]. So, from the physics of scintillation point of view, polymer scintillators possess some advantages such as high operation speed, high light yield, and low cost of their production. However, if compared with inorganic scintillators, the polymer scintillators due to low absorption efficiency have to be of large sizes to register high-energy radiation. Substantial increase of light output can be achieved by the way of embedding into polymer matrix inorganic nanoparticles which are characterized by high atomic numbers  $Z$  that promote higher efficiency of hard radiation absorption. Then, excitation energy transfer from nanoparticles to polymer matrix determines larger light yield of composite scintillator (up to 30 times). Thus, such type of PMM/NC scintillators combine advantages of both polymer scintillators and scintillators based on inorganic crystals: high light yield and short times scintillation decay, respectively. Described possibility goes from overlapping luminescence spectra with doped  $\text{Pr}^{3+}$  ions  $\text{LaPO}_4$  nanoparticles to absorption spectrum of polystyrene matrix.

### 15.3 Cellulose-Based Micro-/Nanoscaled Polymer Composites Incorporated with Oxide Compounds

There is a great request now to replace materials that are widely used both in technology and production with newer environmentally friendly, are harmless to humans, and have simultaneously cheap materials. The PMM/NCs, where polymer host is micro-/nanocrystalline cellulose and fillers are some inorganic compounds of micro-/nanoscale, are among them. These PMM/NCs are sustainable and renewable materials and paid great attention in biomedical technologies (membranes and filters, scaffolds, antimicrobial films, pharmaceuticals, drug delivery, etc. [35–38]) or as adsorbents for toxic chemical removal [39–41]. Due to their mechanical flexibility, they can be useful in the manufacturing of electronic and optoelectronic devices (solar cells, supercapacitors, lithium-ion batteries, “paper” electronics [42–44], luminescence sensors [45–47]). Incorporated with luminescent oxides, cellulose-based composites have showed their importance as advanced optical materials [48–51]. That is why, the next part of this chapter is devoted to description of the main properties of some cellulose-based materials.

### 15.3.1 *Optical Properties of the “Pure” Cellulose Materials*

Cellulose is a biopolymer built on D-glucose units linked to unbranched chains by  $\beta$ -1,4-glycosidic bonds. The microcrystalline cellulose (MCC) is a pure partially depolymerized cellulose. The linear cellulose chains are connected as microfibrils spiraled together in the walls of plant cell. Each microfibril shows a high level of three-dimensional internal bonding resulting in the crystalline phase of cellulose. Some part of the microfibrils form amorphous phase of the last one [35–38], APP.

Cellulose fibers—both those obtained from vegetable raw materials and the man-made—are widespread materials available in many areas of life. The ongoing development of the methods of modifications of cellulose fiber properties and giving specific functionalities allow finding new uses in many, however not so obvious, applications such as substrate for electronic component, military industry (e.g., paper patching jacketed bullets, filters), aircraft, and cosmic space industry [49, 52].

Manifestations of the various cellulose materials’ photoluminescence (PL) are known and described long ago [45–47, 53–55]. It is intensive observable luminescence. Up to now, there are no reliable conclusions about origins of the cellulose-based materials’ luminescence, but undoubtedly, there are several of them. Regarding electronic structure of the basic elements of cellulose composition,  $\beta$ -(1,4)-glycosidic-linked glucose unit, it is hard to think that it was capable to emit luminescence light. At the same time, these constituents can be involved in absorption of incident light which exits photoluminescence.

The PL emission of various types of cellulose materials revealed quite similar luminescence characteristic. So, three different PL bands with peak positions lying near 370, 430–470, and 505–510 nm were found and then ascribed to three different luminescence centers in the work [56]. The PL bands with maxima near 420–460 nm and 495 nm were also described [57, 58]. Above-noted statement concerns the luminescence of the various cellulose materials, and those are made from different sources such as bleached craft and sulfite pulps, Whatman filter paper, biomedical cellulose [58, 59], etc.

We have seen that the physical properties as well as the degree of crystallinity and chain order of cellulose-based materials depend highly on conditions of the manufacturing and treatment procedure. Thus, we have performed experiments on luminescence spectroscopy for our cellulose samples. There were four types of cellulose samples used for the study. Sample labeled SC or CT was the starting tablet of chemically pure microcrystalline cellulose (MCC) manufactured at ANCYR-B, Ukraine. The next samples, CD, were prepared from the CT samples by their dispersion using mechanical milling of the cellulose tablet followed by ultrasonic treatment ( $f = 4:2$  kHz). Then, the powder was pressed into a disc using light pressure.

All, made by us, cellulose samples are characterized with intensive PL. The widely composed emission band located in the 325–750 nm range is observed in the PL spectra of cellulose samples SC and CD under excitation in a wide range of excitation wavelengths,  $\lambda_{\text{ex}} = 300\text{--}532$  nm.



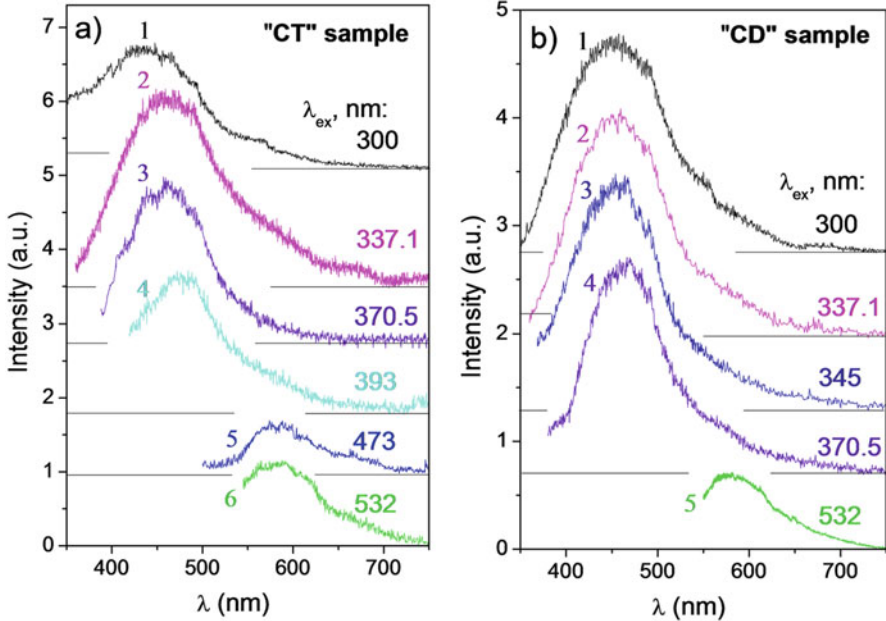


**Fig. 15.2** The PL spectra of the starting cellulose samples: CS (CT) (a) and dried powder CD (b);  $\lambda_{\text{ex}} = 300$  (a, 1; b, 1), 337.1 (a, 2; b, 2), 345 (b, 3), 370.5 (a, 3; b, 4), 393 (a, 4), 473 (a, 5), and 532 nm (a, 6; b, 5);  $T = 300$  K [41]

The shape, peak position, and intensity of the PL band depend on the  $\lambda_{\text{ex}}$ . The dependences of the spectra on  $\lambda_{\text{ex}}$  have a similar character for the mentioned cellulose samples:  $\lambda_{\text{ex}}$  increases as the peak position,  $\lambda_{\text{max}}$ , reveals a tendency to the long wavelength side shifting of the spectra (see Fig. 15.2). Mainly, the component with the peak position,  $\lambda_{\text{max}}$ , near 430–470 nm dominates in the spectra at UV excitation. It is clearly seen for the dispersed cellulose sample CD (Fig. 15.2b). An additional band is also observed if visible radiation ( $\lambda_{\text{ex}} = 450\text{--}530$  nm) is used for PL excitation. The band is situated at longer wavelengths than UV excitation. This has a range of 500–700 nm, and the  $\lambda_{\text{max}}$  of the band is near 680–590 nm (Fig. 15.2, curves 5) [41].

So, it is reasonable to note it as characteristic luminescence. Therefore, we suppose that it can be classified as the so-called own photoluminescence (PL). Own luminescence of some solid-state material is one that occurs without special incorporation of any additive luminescence agents, but it can be related with constituents of the lattice or some intrinsic defects of the solid material.

In fact, an absorption band with maximum near 265 nm measured for “pure” cellulose was assigned to the glycosidic  $\text{—C=O}$  bonding in groups produced after isolation and purification of cellulose [57]. In some cases cellulose absorption was assigned to the energy state aroused as a result of molecular group interaction [60]. The absorbance in the 190–500 nm range of oxidized lignin-free xylan isolated from

unbleached and ozone-bleached hardwood kraft pulps as well as monocarboxyl cellulose in NaOH solution was studied in the work [61]. The spectra were obtained in alkaline media, so the dissociation of carboxyl groups as well as the ionization followed by the isomerization of keto- and aldo-groups took place. The carried out study had shown that cellulose demonstrates six intensive absorption bands and the last ones were proposed to assign as related with absorption transitions in chromophore composition of oxypolysaccharides as follows: carboxyl and carbonyl groups absorbing at 200–220 and 270–290 nm, respectively, heteroaromatics of furan and pyron type absorbing additionally at 230–250 and 290–320 nm, as well as conjugated heteroaromatics absorbing above 300 nm with maximums at 350–370 and 430–450 nm due to the charge-transfer complexes.

In some cases dependence of the luminescent characteristics (the PL intensity and peak positions) on the cellulose source was found. Thus, the bleached hardwood papers chemically modified to increase the carboxylic content in the anhydroglucose, Avicel, cotton linters, sisal holocellulose, and sisal cellulose were made. The cellulose samples were acetylated in homogeneous solution (DMAc/LiCl) to obtain soluble polymers in dichloromethane. These soluble samples allowed comparison of the fluorescence behavior in the solid and liquid states. It was found that the presence of carboxylic groups in the anhydroglucose units shifts the emission maxima by 10 nm to shorter wavelength and increases their intensity. Oxidizing decreased the cellulose PL intensity by creating carbonyl groups. This effect is common for various cellulose samples regardless of their source [62]. At the same time, it was observed that position of the PL band ( $\lambda_{\max}$ ) is not correlated with either the average molecular weight ( $M_{\text{vis}}$ ) or with the crystallinity index. In this regard the following order was observed:  $\lambda_{\max}$  cotton linters >  $\lambda_{\max}$  mercerized sisal cellulose >  $\lambda_{\max}$  microcrystalline cellulose whereas  $M_{\text{vis}}$  mercerized sisal cellulose >  $M_{\text{vis}}$  cotton linters >  $M_{\text{vis}}$  microcrystalline cellulose and the PL intensity ( $I$ ) for the microcrystalline cellulose  $I_{\text{MCC}} > I_{\text{CL}}$  cotton linters >  $I_{\text{SC}}$  sisal cellulose. This indicates that anhydroglucose units emit as single chromophores without strong interactions between them.

Some reasons were also discussed as those influenced the PL intensity via emission quenching. For example, cotton linter pulps, wood pulps, and several filter papers have been evaluated as substrates for room temperature phosphorescence in the work [45]. The authors concluded that the difference in performance between the poorest paper and the best paper is considerably less than an order of magnitude.

In contrast, some other researchers stated that aldehyde and ketone carbonyl groups have a quenching effect on fluorescence, and the formation of carbonyl groups after oxygen and ozone lignification decreases pulp fluorescence (see also above noted), while sodium borohydride is able to recover the PL by reducing carbonyl groups in the cellulose [62, 63].

The sources of the cellulose PL can be related with external factors. We emphasize here those related with the pulp processing and treatment. Really, the residual traces of the proteins or lignin, dityrosine, and coumarin acids were regarded as possible sources of the cellulose PL [62, 64].

Possible contribution of transition-metal ions such as Cr, Cu, Fe, Mn, Mo, Ni, and Ti remaining after normal preparation procedures to the cellulose PL was studied under excitation of emission by power laser radiation of the cotton-derived samples of cellulose [53]. We think that mentioned impurity impact on the cellulose luminescence is negligible in the most cases, as the PL of mentioned ions is quite specific. It concerns both the PL and excitation spectra-specific features and luminescence decay, as well. That is why manifestations of their PL could be easily found on the background of own cellulose luminescence. (See, for comparison our earlier published data, [65–67].)

More information about properties of the cellulose fibers materials doped with some luminescent inorganic can be found below.

### ***15.3.2 Luminescence of the Cellulose Fibers Embedded with Oxide Inorganic Compounds***

The cellulose fibers contained in their structure-specific chemical luminescent compounds can be effective modifiers of both textile products and paper documents and those made of plastic [68]. They can also be helpful in management and control of production and transport and storage of products (not only the textile ones) [52]. The process of cellulose fiber manufacturing makes it possible to modify them by introducing materials of various chemical and physical properties and structure that allow obtaining functional fibers with specific properties [52]. In this way cellulose fibers with luminescent properties were obtained [68].

The new interest aroused last time in luminescent modifications of cellulose fibers with three plus rare-earth ions ( $\text{RE}^{3+}$ ) [49, 51, 52, 68]. Such materials have been studied widely last decade owing to their interesting and important possible application properties.

Complex inorganic oxides containing europium three plus ions,  $\text{Eu}^{3+}$ , and doped with polymers had been intensively studied before [69] (see also References noted above in the Sect. 15.1). The nanosized zirconium oxide  $\text{ZrO}_2$  (zirconia) that has been used as a filler is also a very interesting compound due to its very important own characteristic, and luminescent ones are among them [51, 70]. The tetragonal structure of modifier was stabilized by 7 mol% of  $\text{Y}_2\text{O}_3$ . The concentration of  $\text{Eu}^{3+}$  ions in this system was 0.5 mol% per  $\text{ZrO}_2$ .

The luminescent properties of the modified man-made cellulose fibers were monitored and then compared with the PL properties of pure cellulose fibers, as well as with the PL properties of the modifier (see Figs. 15.3 and 15.4).

The PL data concerning pure components are consistent with the well-known literature data, but if characteristics of complex system were observed, then noticeable differences had been found. So, the excitation spectra of the doped fibers monitored at the same wavelength are strongly different. The lines are much broader and a wide maximum near around 240 nm was monitored. The spectral

**Fig. 15.3** Excitation and emission spectra of pure regenerated cellulose fibers [51]

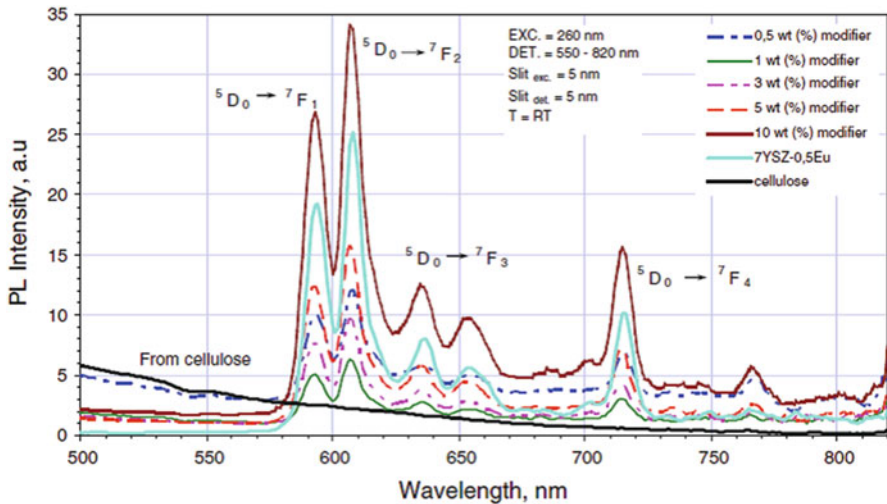
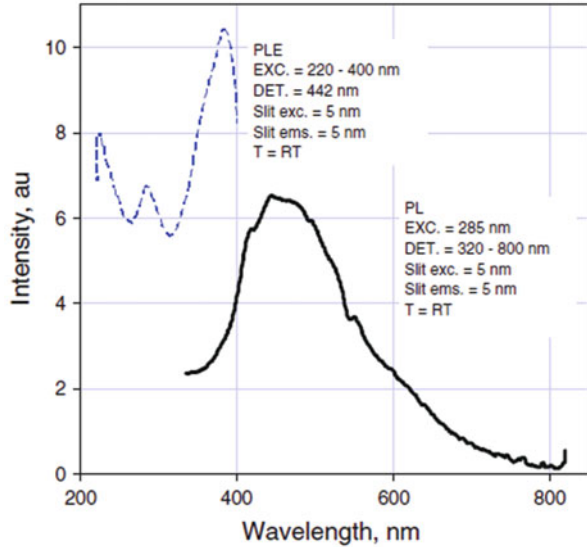


**Fig. 15.4** Photoluminescence spectra of pure cellulose fibers, cellulose fibers with 7YSZ-0.5Eu, and reference powder; the samples were excited by 260 nm wavelength [51]

position of this maximum that differs from the maximum position observed for pure additive may suggest the presence of energy transfer processes between the cellulose fiber and the incorporated fillers. The luminescence spectra of the modified cellulose exhibit several PL peaks associated with the electronic transitions  ${}^5D_0 \rightarrow {}^7F_j$  within  $\text{Eu}^{3+}$  ion. Regarding data shown in the Fig. 15.4, it can be concluded that manifestation of the own cellulose luminescence is minimal [51].

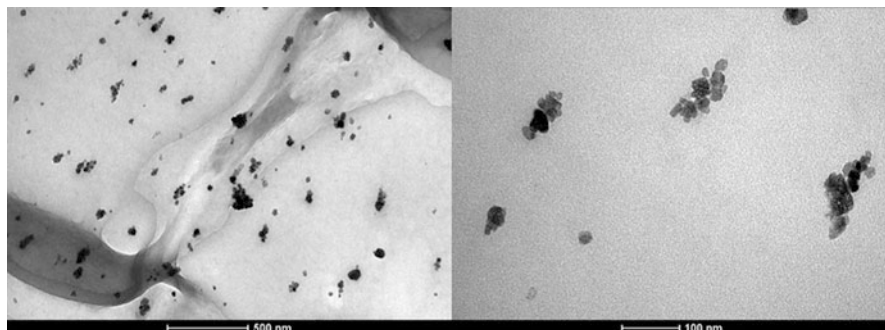


**Fig. 15.5** The TEM images of the cellulose fibers with  $\text{Ce}_{0.85}\text{Tb}_{0.15}\text{F}_3$  nanocrystals in cellulose fiber matrix [50]

The analysis of the spectral PL characteristics of the modified cellulose fibers showed that the emission intensity depends on the luminescence active particle concentration in the cellulose matrix, as well as on the exciting photon energy. Moreover, obtained data confirmed that the particles of the modifier are statistically distributed within the cellulose matrix. Increase of the modifier concentration as well as mentioned peculiarity of distribution increases the amount of relatively big size particles that indicate a tendency of the modifier to agglomeration [51].

The oxyfluoride-based luminophors, like  $\text{Gd}_4\text{O}_3\text{F}_6:\text{Eu}^{3+}$  and  $\text{CeF}_3:\text{Tb}^{3+}$ , were chosen for a study as they are promising for industrial applications due to their effective luminescence as well as high chemical and thermal stability [49, 50]. The luminescence emission spectra of  $\text{Gd}_4\text{O}_3\text{F}_6:\text{Eu}^{3+}$  nanopowder incorporated into a cellulose matrix showed good PL caused by  $f-f$  transitions in the europium ions [49].

The  $\text{CeF}_3$  doped with 15% of  $\text{Tb}^{3+}$  ions was found to be the most promising system as modifier for cellulose fibers due to suitable morphology of this material. The structure and morphology of the modified fibers are similar to those of the fibers made by the same dry-wet spinning method but without modifier. The thickness of modified cellulose fibers does not exceed several micrometers.

Small sizes of nanocrystals as well as their decreased agglomeration facilitate the introduction of particles inside the fibers during their synthesis (see Fig. 15.5).

Furthermore, mechanical properties of such fibers are similar to unmodified ones [50]. This material reveals allowed  $f-d$  radiation transitions in the  $\text{Ce}^{3+}$  ions which realize effectively in the range of 200–300 nm of the UV light (Fig. 15.6). The energy could be transferred to the  $\text{Tb}^{3+}$  ions, and as a result the green emission arises.

The authors of described papers stated that this kind of the innovative materials seems to be one of the most interesting, and due to their unique properties, it has many potential applications, for example, paper and clothing protection (the so-called fingerprint effect), etc. [49–52].

Some suitable amount of the modifier with luminescent properties ensures the usage of these systems for application as an optical marker, for the protection of textiles, documents, and various products. One of the most important advantages in

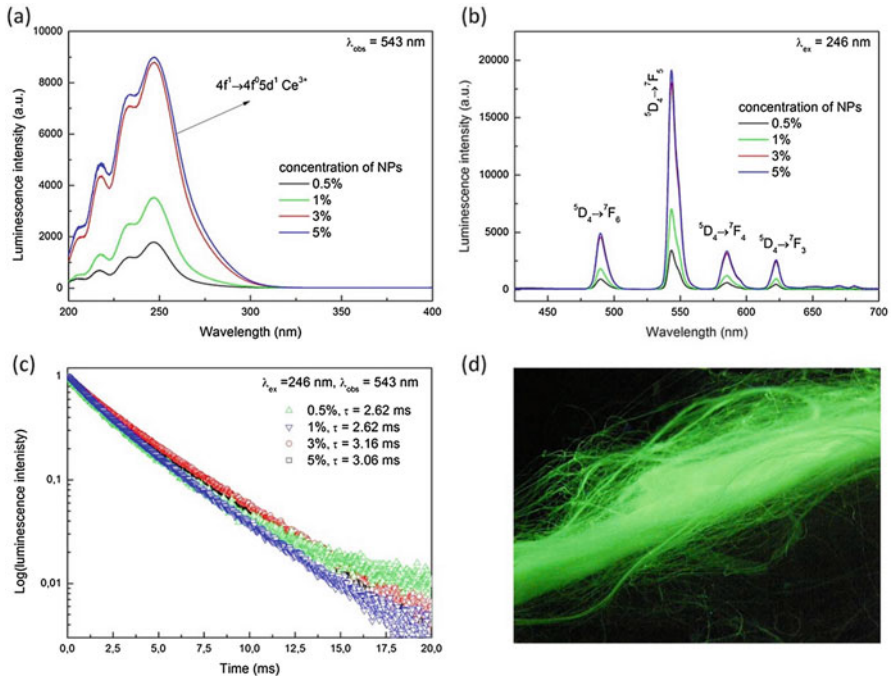


**Fig. 15.6** Luminescent properties of cellulose fibers doped with  $\text{Ce}_{0.85}\text{Tb}_{0.15}\text{F}_3$  nanocrystals: (a) excitation spectra, (b) emission spectra, (c) luminescence decays, and (d) luminescence of fibers under UV irradiation ( $\lambda_{\text{exc}} = 254 \text{ nm}$ ) [50]

the case of textiles is that incorporated inorganic modifiers are stable and cannot be easily removed from the fibers under some treatments [49–52].

We have noted above that cellulose combines crystalline and amorphous parts. It is easy to imagine that the luminescent properties of a cellulose material can depend on the degree of its crystallinity. So, it was important for us to examine the properties of cellulose with a high degree of crystallinity. Such is the so-called microcrystalline cellulose (MCC). The next part of the chapter is devoted to studying the MCC luminescence and properties of the composites based on the MCC.

## 15.4 Structure, Morphology, and Some Physical Properties of the Composites Based on the Microcrystalline Cellulose Matrix (MCC) Containing Luminescent Inorganic Oxide Micro-/Nanoparticles

The set of oxide compounds were used by us as modifiers (fillers). They were doped with active luminescence samarium or europium three plus ions ( $\text{Sm}^{3+}$  or  $\text{Eu}^{3+}$ ) lanthanum orthovanadate,  $\text{LaVO}_4$ , and potassium lanthanum phosphate–molybdate,  $\text{K}_2\text{Eu}(\text{PO}_4)(\text{MoO}_4)$ , compounds.

Described below the MCC composites were prepared by “dry” cool-pressed methods. Chemically pure microcrystalline cellulose tablets manufactured at ANCYR-B (Ukraine) were used as starting material for preparation of the composite samples under study. (Starting cellulose materials are marked below as SC.) First, cellulose tablets were grinded and dispersed using high-speed rotation mill. Then, some part of the resulting powder was mixed with a certain amount of the previously made nanosized oxide powder. (The sample of un-doped micro-/nanocellulose is marked as C0.) The mix of  $\sim 0.5$  g mass was dissolved in 50 ml of high purity ethanol and undergone ultrasonic treatment (frequency,  $f = 4.2$  kHz; time of the treatment,  $t = 20$  min.). After that, obtained suspense stood for 30 min, and obtained precipitate was filtered via paper filter. Prepared powder was dried at ambient air conditions and room temperature (RT) followed by compression at high pressure of  $1.8 \cdot 10^4$  kPa/m<sup>2</sup>. The samples under experiments were of the discs form of  $\sim 10$  mm average diameter. The thickness of the discs was  $\sim 1$  mm. The amount of oxide was in the range 1–200 mg for different “dry” samples, while the mass of MCC was 450 mg for each of those samples. Thus, below we denote the sample only as mass and formulae of corresponding oxide, e.g., 10-K<sub>2</sub>Eu(PO<sub>4</sub>)(MoO<sub>4</sub>) denotation means that the sample contains 10 mg of K<sub>2</sub>Eu(PO<sub>4</sub>)(MoO<sub>4</sub>) oxide incorporated into 450 mg of MCC. Used oxides could be made by three various procedures: solid-state reaction, coprecipitation, and sol–gel. We have found recently that luminescence intensity for each oxide depends on the RE ion concentration and on the way of their synthesis [71, 72]. In fact, we have found that for LaVO<sub>4</sub> doped with RE, the average size was 1–2  $\mu$ m for solid-state way of the synthesis, 0.2–0.5  $\mu$ m for the coprecipitation, and 0.1–0.2  $\mu$ m for the sol–gel way. Moreover, luminescence of these oxides made by sol–gel method was near three times higher than for the oxides made by coprecipitation and about ten times higher than for the samples made by solid-state synthesis [71]. So, the samples made by the sol–gel way were selected for experiments with composites. In this way, that oxide procedure and that RE concentration which showed higher PL intensity were selected for composite preparation and further experiments.

As we have noted in the Sects. 15.1 and 15.1.1, the morphology, structure, and other properties of the PMM/NC samples depend on their composition and on the way of the sample preparation. Thus, various characteristics had to be studied, as the samples were made for the first time. This required us to use a variety of experimental methods. Those were scanning electron microscopy (SEM), chemical element analysis, X-ray diffractometry (XRD), luminescence spectroscopy, and dielectric characteristic measurements.

Characterization of the sample topology was performed by means of the scanning electron microscopy (SEM). Scanning electron microscope JAMP-9500F Field Emission Auger Microprobe (JEOL, USA) equipped with X-ray microanalyzer INCA PentaFetx3 (Oxford instruments) was used for SEM measurements. Besides the SEM imaging, microelement analysis of various areas of the samples was also performed using the same microscope.

The X-ray diffraction patterns (XRD) were collected using a conventional powder diffractometer DRON-3 M equipped with BSV-28 tube ( $\lambda_{\text{rad}} = 1.54178$  Å)

and operating in Bragg–Brentano ( $\theta/2\theta$ ) geometry. The XRD patterns were obtained in the ( $2\theta$ ) diffraction angle range  $10\text{--}70^\circ$  at  $0.1^\circ$  step.

The Netzsch 402C dilatometer (NETZSCH, Selb, Germany) with 3% accuracy was used to study thermoexpansion characteristics, and a coefficient of thermal expansion was measured in the temperature range of  $25\text{--}110^\circ\text{C}$ . The dilatometric measurements were carried out along to normal the disc base. The heating rate used during measurements was  $10^\circ\text{C}/\text{min}$ .

Differential scanning calorimetry (DSC) and thermogravimetric analysis (TGA) testing were made using Jupiter STA 449 F3 calorimeter by Netzsch (NETZSCH, Selb, Germany). The same heating rate was used as in the dilatometric measurements.

The sample for dielectric studies was placed into thermostatic four-electrode cell that enabled monitoring the sample thickness by means of additional air capacitor. Measurements of the capacity and dielectric losses index of mentioned cell were carried out at four fixed frequencies,  $f = 5, 10, 20,$  and  $50$  kHz in the temperature range  $-180 \div 130^\circ\text{C}$ . The automatic homemade equipment on the base of the P5083 alternate current bridge was used for noted above measurements.

The PL (photoluminescence) and the PL excitation spectra were measured using the spectrometric equipment SDL-2 M. The PL emission spectra were analyzed using a single-grating (1200 grooves/mm) monochromator MDR-23 (linear dispersion  $0.5$  mm/nm) and DFS-12 (linear dispersion  $1$  mm/nm) equipped with FEU-100 and FEU-79 photomultipliers, respectively. The  $\text{N}_2$  laser ( $\lambda_{\text{ex}} = 337.1$  nm), two diode-pumped lasers ( $\lambda_{\text{ex}} = 473$  and  $532$  nm, respectively), and a xenon lamp (DKsSh-150) were used as sources of PL excitation. The PL spectra were studied as a function of the exciting radiation wavelength ( $\lambda_{\text{ex}}$ ) and were analyzed over a wide range of excitation and emission wavelengths ( $200\text{--}800$  nm) and sample temperatures ( $77\text{--}300$  K).

The samples surfaces were scanned using electron microscopy instruments. Figure 15.7 shows the typical SEM image (the sample  $100\text{-K}_2\text{Eu}(\text{PO}_4)(\text{MoO}_4)$  was taken as example). A lot of tightly packed grains of  $5\text{--}10$   $\mu\text{m}$  of size can be seen over there. Usually, they packed into large plates of  $\sim 20\text{--}50$   $\mu\text{m}$  of size. Some crannies are also seen between the plates (see, e.g., in the left part and in the center of Fig. 15.7). Other shape pieces also are on this image. They look like different inclusions on the sample surface (e.g., see rectangles #3 and #4 on Fig. 15.2). Their sizes are in  $10\text{--}200$  nm range. Conglomerates of such particles form larger pieces of  $2\text{--}10$   $\mu\text{m}$  in size. The largest of them is near rectangle #5 on the Fig. 15.7.

The chemical element analysis was made for some zones of the samples when SEM studies were carried out. For example, such zones are marked by rectangles on Fig. 15.7. The average content of carbon (C) atoms (the range of its value is  $74\text{--}76$  at.% for all of the samples under study) and oxygen (O) atoms ( $25\text{--}23$  at.%) was predominant in zones of the plates (e.g., see zones 1 and 2) that allowed us to conclude that the plates are blocks of the MCC matrix. The results of analysis also pointed that mentioned above inclusions (e.g., see zones 3, 4, and 5) are the areas where the oxide particles located, as their composition is close to the chemical formulas of corresponding oxides. Average content of the chemical elements for the



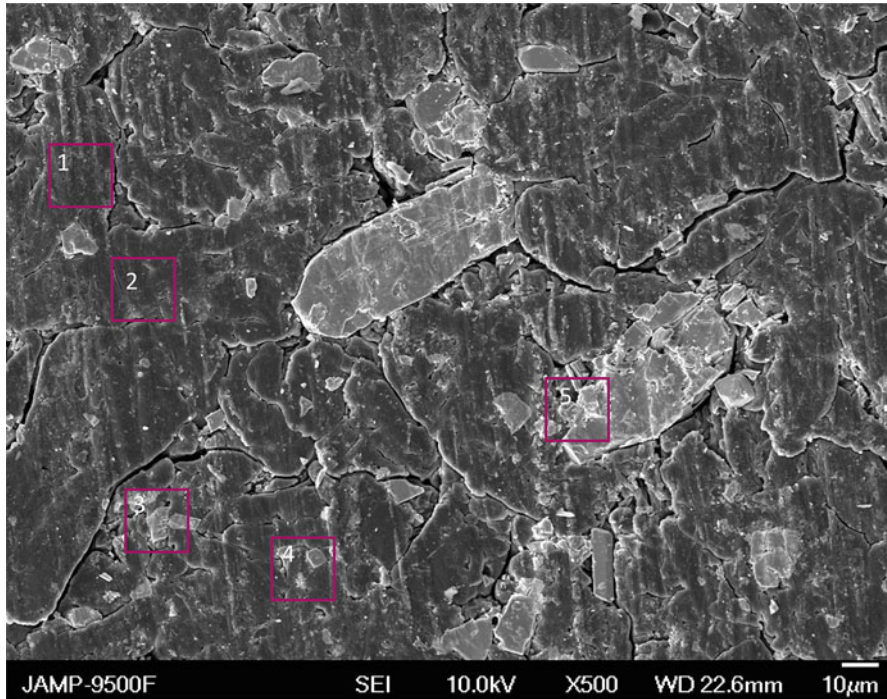


**Fig. 15.7** The typical SEM image of the cellulose-based composite (the sample 100-K<sub>2</sub>Eu(PO<sub>4</sub>)(MoO<sub>4</sub>)). The rectangles show areas where chemical analysis was performed

**Table 15.1** The average values of the chemical elements content in 10-La<sub>0.7</sub>Sm<sub>0.3</sub>VO<sub>4</sub>, 10-La<sub>0.7</sub>Eu<sub>0.3</sub>VO<sub>4</sub>, and 100-K<sub>2</sub>Eu(PO<sub>4</sub>)(MoO<sub>4</sub>) composites (in at. %); cellulose crystallinity index (*k*); and the value of the reorientation energy barrier (*U*) (in kJ/mol)

Sample	C	K	La	Sm	Eu	V	P	Mo	O	<i>k</i>	<i>U</i>
MCC	65.3	–	–	–	–	–	–	–	34.5	66	75
10-La <sub>0.7</sub> Sm <sub>0.3</sub> VO <sub>4</sub>	0.3	–	11.2	5.8	–	16.9	–	–	65.8	57	62
10-La <sub>0.7</sub> Eu <sub>0.3</sub> VO <sub>4</sub>	5.2	–	10.9	–	6.1	16.4	–	–	61.4	57	55
100-K <sub>2</sub> Eu(PO <sub>4</sub> )(MoO <sub>4</sub> )	6.5	9.41	–	–	6.87	–	6.96	8.31	62.51	58	54

MCC and some composites in the zones of particles inclusions is accumulated in Table 15.1.

The XRD patterns of the samples under study showed the set of diffraction peaks related with X-ray scattering on the MCC lattice in the range 10–45° of 2θ (Fig. 15.8) [73–75]. The relatively wide intensive peaks are located at 16, 22.5 and 34.5° of 2θ. Several features of low intensity also were found as shoulders for all the samples, and the similar XRD results were obtained for SC and C0 micro-/nanocellulose samples. Other observed XRD peaks are not related with MCC XRD scattering. The intensity of those peaks increases when oxide content increases. So, we concluded that additive peaks are caused by oxide components of composites.

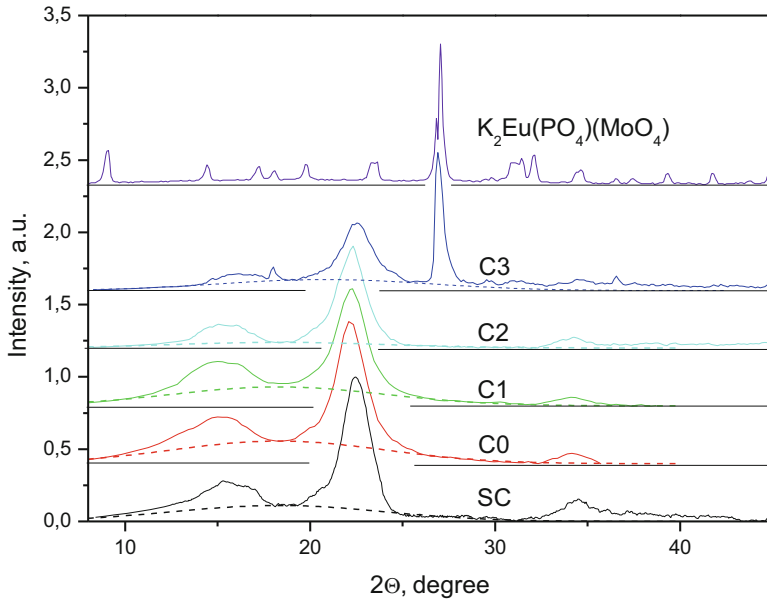


**Fig. 15.8** The XRD pattern of the starting MCC (SC), micro-/nanocellulose (C0), cellulose–oxide micro-/nanocomposites (MCC-oxide) with oxide concentrations 0.2% (C1), 2.2% (C2), and 18.2% (C3) samples. The XRD pattern of the  $\text{K}_2\text{Eu}(\text{PO}_4)(\text{MoO}_4)$  oxide is shown at the top of the figure. The dotted lines are Gauss curves that approximate contribution of the cellulose amorphous phase XRD scattering [48]

It was confirmed by those peak positions in comparison with XRD pattern of the  $\text{La}_{1-x}\text{Sm}_x\text{VO}_4$ ,  $\text{La}_{1-x}\text{Eu}_x\text{VO}_4$ , and  $\text{K}_2\text{Eu}(\text{PO}_4)(\text{MoO}_4)$  compounds [71, 72, 76].

On the base of the XRD results, index of the cellulose crystallinity ( $k$ ) was calculated for all studied samples. For this aim the contribution of the amorphous phase ( $I_{\text{am}}$ ) to the overall XRD spectrum ( $I_{\text{cryst}} + I_{\text{am}}$ ), where  $I_{\text{cr}}$  is an area under XRD peaks caused by crystal phase of cellulose, was extracted. (This procedure had been already previously described in details [48].) Thus, the crystallinity level was evaluated as a ratio:

$$k = \frac{I_{\text{cr}}}{I_{\text{cr}} + I_{\text{am}}} \quad (15.1)$$

Calculated  $k$  values were found to be near 57–58% for the composites, while for the un-doped micro-/nanocellulose (C0), this value was higher—66% (Table 15.2). Thus, we can note that oxide particles affect the structure and morphology of the MCC host and somewhat destroy its crystal lattice. Undoubtedly, future experiments are needed to clarify a mechanism of this effect. Moreover, as described below the results of the study of MCC and MCC-oxide composite dielectric properties also revealed that oxide component influences cellulose characteristics.

**Table 15.2** Lattice periods ( $d_{hkl}$ , nm) and crystallinity ( $k$ , %) for cellulose samples: starting microcellulose (SC), un-doped micro-/nanocellulose (C0), MCC-oxide micro-/nanocomposites with  $K_2Eu(PO_4)(MoO_4)$  oxide concentration 0.2% (C1), 2.2% (C2), and 18.2% (C3) [48]

Sample	$d_{1\bar{1}0}$	$d_{200}$	$d_{004}$	$k$
SC	5.56	3.95	2.60	66
C0	5.85	4.02	2.62	56
C1	5.79	3.95	2.62	57
C2	5.72	3.98	2.61	58
C3	5.55	3.95	2.60	58

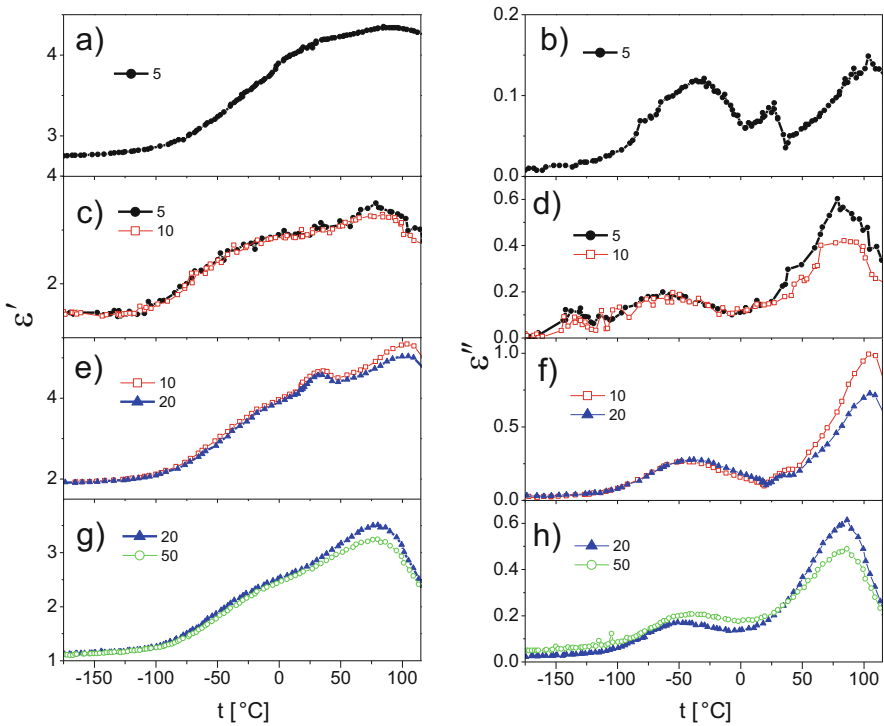


**Fig. 15.9** Dependencies on temperature of the real (a, c, e, g) and imaginary (b, d, f, h) parts of dielectric permittivity for un-doped cellulose (a, b) and composites (c–h); 10- $La_{0.7}Sm_{0.3}VO_4$  (c, d), 10- $La_{0.7}Eu_{0.3}VO_4$  (e, f), and 10- $K_2Eu(PO_4)(MoO_4)$  (g, h). Frequencies used at experiments (in kHz) are marked on the figure

Dielectric properties, in other words, dependences of the real ( $\epsilon'$ ) and imaginary ( $\epsilon''$ ) parts of the complex dielectric permittivity ( $\epsilon^*$ ) on temperature measured for studied MCC and MCC-oxide at different frequencies of probing electromagnetic field (EMF), can be seen on the Fig. 15.9. If we compare the dependences taken for composites with ones obtained for un-doped MCC (Fig. 15.9a, b), it is easy to find that general view of these curves is similar. At the same time, some differences

should be noted. First, we see that if an oxide is added, the shape of the  $\epsilon'$  and  $\epsilon''$  curves changes. In fact, relative intensity of the  $\epsilon'$  curves increases in the range  $-125$ – $25$  °C, and the  $\epsilon''$  values increase in the whole temperature range. Especially, it concerns the temperature range  $25$ – $125$  °C, where the  $\epsilon''$  values in the maximum of the curves increase four to six times. We can note that only ( $\epsilon'$ ,  $\epsilon''$ ) value changes occur in the range  $25$ – $125$  °C, if EMF frequency or oxide content increases and there is no ( $\epsilon'$ ,  $\epsilon''$ ) curve shifts in this temperature range. In contrast, it is easy to see that  $\epsilon''$  curves in the range  $-125$ – $25$  °C shift to the higher temperature side when EMF frequency increases. So, we assume that two kinds of impact of oxide particles on the surface MCC molecular groups take place, and their responses on this influence are different. Obviously, some amount of water molecules, hydroxyl groups, and ambient gases had been incorporated into MCC host as associated with the surface of oxide particles. There they bind to molecular groups on the surface of MCC microfibrils that promote increasing of the dipole moment (polarizability) of the samples. As a result,  $\epsilon''$  values increase when oxide is added (please compare Fig. 15.9b and Fig. 15.9d, f, h). These changes manifested in the dielectric permittivity behavior during first heating of the sample in the EMF of lower frequency. The next heating made under action of the higher EMF frequency removes more water and some ambient gas molecules and leads to the decrease of the ( $\epsilon'$ ,  $\epsilon''$ ) values. These changes noticeably revealed in the temperature range  $25$ – $125$  °C.

Described data correspond to, measured by us, the thermogravimetric analysis (TGA) data. The TGA curves for the un-doped, C0 sample and C1 intersect at  $25$  and  $125$  °C, while in the whole temperature range between these points,  $25$ – $125$  °C, C0 sample curve is higher than C1 curve (Fig. 15.10a). The behavior of these curves is different: first of them is convex and second is concave. So, the difference between them is largest in the temperature range near  $60$ – $80$  °C. The TGA curves for C2 and C3 samples show similar temperature behavior, but difference between them increases when temperature increases. In fact, the difference is near  $0.3\%$  at  $25$  °C, and it is near  $0.6\%$  when temperature rises up to  $125$  °C. Thus, we can note that difference between dependence for the C0 sample, which doesn't contain oxide component, and C1 sample, where oxide amount is minimal, is appreciable. The dependences for C2 and C1 samples are close, while characteristics of the C3 sample differ considerably from the C2 sample, in spite of the similar difference in the oxide contents: about ten times in both cases.

The differential scanning calorimetry (DSC) curves (Fig. 15.10b) have demonstrated similar behavior for the C0, C2, and C3 samples up to temperature near  $70$  °C, when difference has aroused between them. As a result, calorimetric singularity is near  $103$ ,  $92$ , and  $98$  °C for the C0, C2, and C3 samples. A big difference is observed between the DSC curve for C1 sample and other DSC curves. Mentioned fact concerns both of the curve shape and singularity positions. The last one is near  $67$  °C for the C1 sample.

Thus, we can note that considerable difference between characteristics of the C0 sample, which doesn't contain oxide component, and C1 sample is obvious. This difference can be regarded as predictable, as it reflects radical difference in

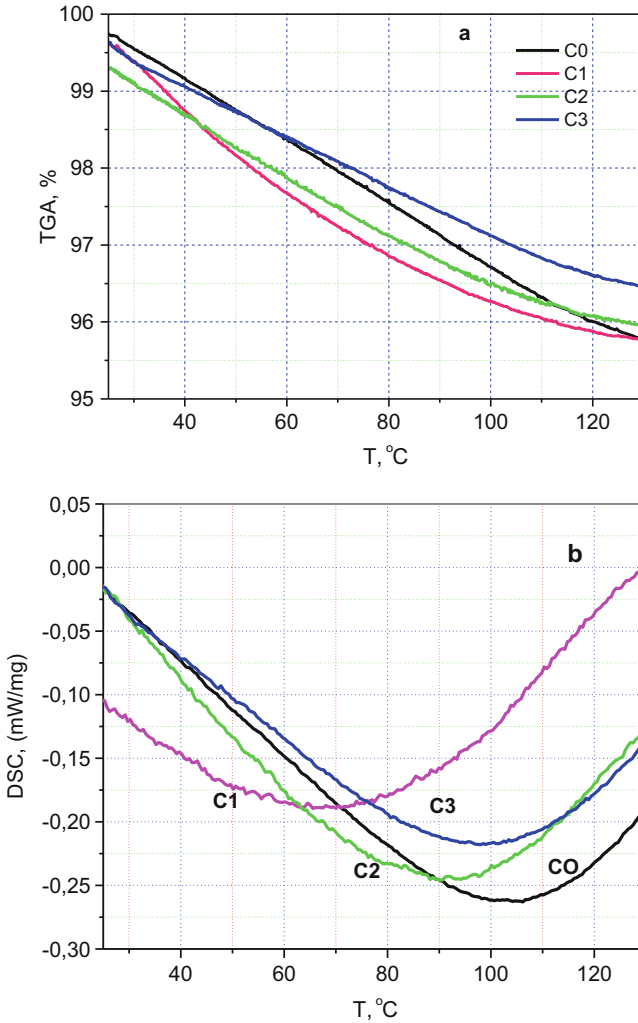


**Fig. 15.10** Thermogravimetry (a) and differential scanning calorimetry curves (b) for the cellulose–oxide micro-/nanocomposite: un-doped sample (C0), samples with oxide content 0.22 (C1), 2.2 (C2), and 18.2% (C3) [48]

their composition. At the same time, noticeable similarity of the C0 and C3 sample properties is unexpected and has to be an object of the future studies [48].

Temperature and frequency behavior of the ( $\epsilon'$ ,  $\epsilon''$ ) values in low temperature range,  $-125$ – $25$  °C, are typical for over-barrier reorientations of molecules between their two equilibrium positions in solid state. We assume that, found by us, reorientations occur as thermal transitions (from *tg* to *tt* conformation) of methyl groups located on the surface of the MCC microfibrils.

It is of interest to note that behavior of the ( $\epsilon'$ ,  $\epsilon''$ ) in the whole temperature range is similar to temperature behavior of the viscoelastic characteristics (storage modulus and  $\tan \delta$ ) of hydroxypropyl cellulose composites reinforced with cellulose nanofibers [77–79]. The authors had related, measured by them, dependences with two types of relaxations both involving large-scale molecular motions [77] and changes of the amount of crystalline, amorphous, and intermediate-order phases [77–79]. We suppose similar processes occur in the case of the MCC-oxide which are under our study. Moreover, we think that relaxations which are realized in the low temperature range,  $-125$  to  $25$  °C, promote to phase transformations of mentioned above type, which take place in the higher temperature range  $25$ – $125$  °C.

Fitting of experimental  $\epsilon'(T, f)$  curves with corresponding theoretical dependencies in Debye approximation was performed for the temperature range  $-125$  to  $25$  °C (Fig. 15.9), and the energy barrier between two equilibrium positions,  $U$ , have been evaluated. Corresponding values are accumulated in the Table 15.1. It is easy to see that  $U$ -values show significant influence of the oxide component on the relaxation conditions in cellulose matrix that confirm the role of the microfibril surface molecular groups.

It is clear that these issues are far from their total understanding; that is why further study in this direction has to be performed. Nevertheless, placed below data concerning effect of oxide particles on luminescence properties of studied composites confirm the role of the cellulose–oxide interactions.

Photoluminescence (PL) of the MCC and MCC-oxide composites is excited in the wide spectral range from UV to yellow light ( $250$ – $570$  nm) (Figs. 15.11 and 15.12). The PL spectra consist of wideband that extends from  $350$  up to  $750$  nm (Fig. 15.11, curves 1, 2). Besides, the sets of relatively narrow lines are in the spectra of the composites embedded with oxides doped with RE ions  $\text{Sm}^{3+}$  (Fig. 15.4, curve 4) and  $\text{Eu}^{3+}$  (Fig. 15.11, curves 5 and 6). Relative intensities of the wideband and narrow lines depend on the sample composition. So, some traces of the fine structure can be found in the spectral ranges  $560$ – $580$ ,  $580$ – $615$ , and  $645$ – $665$  nm of the PL spectra of the  $10\text{-La}_{0.7}\text{Sm}_{0.3}\text{VO}_4$  composites (Fig. 15.11, curve 3). If oxide amount is higher ( $100\text{-La}_{0.7}\text{Sm}_{0.3}\text{VO}_4$  composite), the lines are significantly enhanced (Fig. 15.11, curve 4).

The shape and peak position ( $\lambda_{\text{max}}$ ) of the wide PL band also depend on the sample preheating and on the sample composition. Taking into account previously found results [36, 37, 44], we can conclude that the wideband at least consists of four strongly superposed components with  $\lambda_{\text{max}}$  near  $420$ – $430$ ,  $505$ ,  $565$ , and  $600$  nm. Contributions of these components to the total spectra change in different way after MCC heating (Fig. 15.11, curve 2) or if oxide is embedded into MCC. The former leads to the short wavelength side domination in the spectra (Fig. 15.4, curve 2). As for the last, as a rule, short wavelength luminescence components dominate in the spectra of composites; however, middle components become predominant when amount of oxide increases (Fig. 15.11, curve 4).

The spectra of the wideband PL excitation similarly to emission spectra showed complex structure (Fig. 15.12). As for starting MCC sample, excitation spectra

**Fig. 15.11** The PL spectra of starting cellulose MCC (1), MCC heated to  $T = 130\text{ }^\circ\text{C}$  (2), and composites: 10-La<sub>0.7</sub>Sm<sub>0.3</sub>VO<sub>4</sub> (3), 100-La<sub>0.7</sub>Sm<sub>0.3</sub>VO<sub>4</sub> (4), 10-La<sub>0.7</sub>Eu<sub>0.3</sub>VO<sub>4</sub> (5), and 10-K<sub>2</sub>Eu(PO<sub>4</sub>)(MoO<sub>4</sub>) (6);  $\lambda_{\text{ex}} = 405\text{ nm}$ ;  $T = 300\text{ K}$

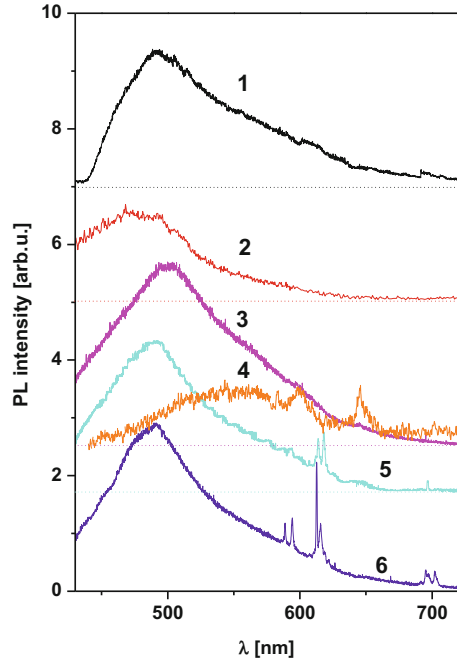
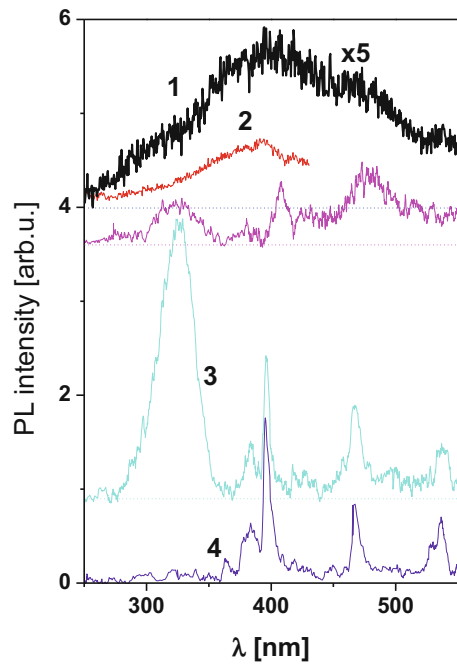


**Fig. 15.12** The PL excitation spectra of the MCC (1, 2) and composites: 10-La<sub>0.7</sub>Sm<sub>0.3</sub>VO<sub>4</sub> (3), 1-La<sub>0.7</sub>Eu<sub>0.3</sub>VO<sub>4</sub> (4), and 10-K<sub>2</sub>Eu(PO<sub>4</sub>)(MoO<sub>4</sub>) (5);  $\lambda_{\text{reg}} = 460$  (2, 3), 475 (4), 580 (1), 612.5 (7), 613.3 (6), and 644.6 nm (5);  $T = 300\text{ K}$



consist of several overlapping bands lying in the ranges  $\sim 250$ – $350$ ,  $300$ – $425$ ,  $350$ – $475$ , and  $425$ – $525$  nm. Excitation spectra change if wavelength of the PL registration ( $\lambda_{\text{reg}}$ ) changes. Thus, short wavelength band in excitation ( $250$ – $350$  nm) vanishes if  $\lambda_{\text{reg}}$  changes from  $580$  to  $460$  nm (Fig. 15.12, curves 1, 2). The same was observed for excitation of luminescence of the  $100\text{-La}_{0.7}\text{Sm}_{0.3}\text{VO}_4$  composite. We see that only  $300$ – $450$  nm range of excitation is actual, while other ones diminished (Fig. 15.12, curve 3).

Our results revealed also correspondence between components in luminescence and excitation spectra and confirmed that several origins contribute to the luminescence of cellulose matrix. Namely, we can state that the shortwave side of the MCC luminescence is excited in the bands ranging from  $300$  to  $450$  nm. We state also that both heating and oxide particle action on these sources are selective and different, which may be due to the features of molecular relaxations and due to features of the molecular anions of oxides (vanadate,  $\text{VO}_4^{3-}$ ; phosphate,  $\text{PO}_4^{3-}$ ; or molybdate,  $\text{MoO}_4^-$ ) binding with molecular groups on the surface of cellulose microfibrils.

When the PL is registered near the narrow PL lines, new details of the excitation spectra have been measured (Fig. 15.12, curves 3–5). No doubt, these additives, as well as narrow lines in the PL spectra, are related with absorption and radiation transitions in the  $f^n$ -shells of  $\text{Sm}^{3+}$  or  $\text{Eu}^{3+}$  ions and  $\text{O}^{2-} \rightarrow \text{RE}^{3+}$  charge-transfer transitions in oxide component of the composites. Really, the positions of these groups of lines, their shapes, and their intensity coincide with excitation and luminescence data for corresponding “free” powder oxides taken by us recently [70–71].

As for composites containing  $\text{Sm}^{3+}$  ions, it is easy to conclude that additive narrow PL lines and lines in excitation spectra are related with  $f$ – $f$  transitions in the electronic shell of the  $\text{Sm}^{3+}$  ions. In fact, the positions of these groups of lines, their shapes, and distribution of their intensity coincide with absorption and emission lines of the  $\text{Sm}^{3+}$  ions in various crystalline [71, 80–82], glasslike hosts [83, 84], and liquids [85]. So, we can state that observed PL groups of lines are due to radiation transitions  ${}^4\text{G}_{5/2} \rightarrow {}^6\text{H}_{9/2}$ ,  ${}^6\text{H}_{7/2}$ ,  ${}^6\text{H}_{5/2}$ , from excited  ${}^4\text{G}_{5/2}$  level to the lowest levels of the ground  ${}^6\text{H}$  state.

As for composites containing  $\text{Eu}^{3+}$  ions, a comparison of described emission and excitation spectra with the corresponding spectra of the free  $\text{K}_2\text{Eu}(\text{MoO}_4)(\text{PO}_4)$  or  $\text{La}_{1-x}\text{Eu}_x\text{VO}_4$  powder compounds show that the observed PL lines have to be ascribed to the  ${}^5\text{D}_0 \rightarrow {}^7\text{F}_J$  ( $J = 1 \div 4$ ) radiation transitions in the inner  $f$ – $f$  electronic shells of the  $\text{Eu}^{3+}$  ions which are in the composition of oxide compounds [70, 71].

Changes of the shape and decrease of MCC host PL intensity, when content of the oxide increases, can be related with influence of the oxide particles on the morphology and dynamics of various cellulose molecular groups located on the microfibril surface. It is worth to note that distributions of intensity of the  $\text{Sm}^{3+}$  and  $\text{Eu}^{3+}$  ion PL lines differ from one corresponding to “free” oxide powders [70, 71]. We have known that these  $\text{RE}^{3+}$  ions locate in the volume and on the surface of used oxide particles [70, 71]. Positions of the lines in the PL and excitation spectra of the  $\text{Sm}^{3+}$  and  $\text{Eu}^{3+}$  ions noted “at surface” and “in volume” types of ions are different. Obviously, “at surface” ions, in the first place, have been sensitive to the influence of



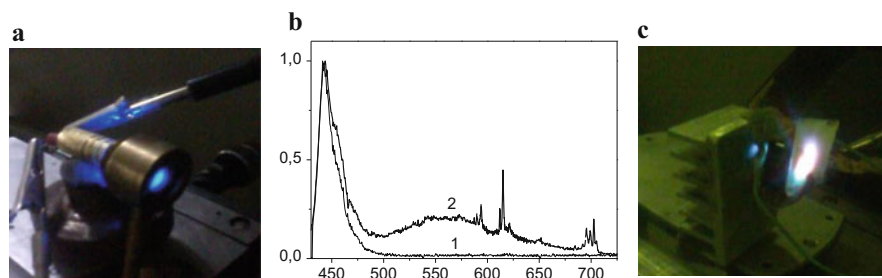


**Fig. 15.13** (a) The view, on the eye, of the blue LED emission; (b) normalized emission spectrum of the blue LED (1) and the emission spectrum of the system (2); (c) view, on the eye, of the “blue LED+100-K<sub>2</sub>Eu(PO<sub>4</sub>)(MoO<sub>4</sub>)” composite system emission

the cellulose surface molecular groups. Thus, interaction between surface molecular groups of cellulose and surface molecular groups of oxide determines peculiarities of luminescence and dielectric behavior of the studied composites also.

Described luminescence characteristics make studied composites suitable for transformation of the UV and violet or blue light to the emission of wide spectral range at longer wavelengths. To combine emission of the LED as excitation light (Fig. 15.13a) and the luminescence of studied composite, e.g., we will take emission of complex system “blue LED + oxide composite” (Fig. 15.13b). Spectrum of this system emission extends from 450 up to 750 nm, and it is a combination of wideband LED blue emission, wideband green-yellow emission of the cellulose host, and red emission of the oxide. As a result, we obtained white on the eye emission of such modeling device (Fig. 15.13c).

## 15.5 Conclusions

Short review about properties of the polymer incorporated with inorganic, particularly oxide particles, micro-/nanocomposites showed their perceptiveness to be used as materials for modern optics and optoelectronic devices.

The sets of the new polymer micro-/nanocomposites based on the microcrystalline cellulose host and embedded with micro-/nanoparticle of various luminescent complex oxides La<sub>1-x</sub>Sm<sub>x</sub>VO<sub>4</sub>, La<sub>1-x</sub>Eu<sub>x</sub>VO<sub>4</sub>, and K<sub>2</sub>Eu(PO<sub>4</sub>)(MoO<sub>4</sub>) were made by “dry” cool pressing procedure. Their morphology can be described as ensemble of cellulose plates, and located between them or inside them are oxide particles.

Dielectric and luminescence properties of composites were studied, and their characteristics were evaluated. It was found that studied micro-/nanocomposites are not ordinary mechanical mixture of the microcrystalline cellulose and oxide compound. The luminescence characteristics display effect of cellulose on the electron-vibration system of the Sm<sup>3+</sup> and Eu<sup>3+</sup> ions, and, on the other hand, effect of the oxide particles on the microfibril components of cellulose was showed, too.

Dependences of the dielectric permittivity of the composites cellulose host also revealed influence of oxide particles on the characteristics of the microcrystalline cellulose.

Both wideband and narrow lines of visible luminescence (350–750 nm range) of the composites are excited in the range 250–550 nm. Spectral characteristics and high intensity of luminescence determine these composites as perspective for creation on their base of luminescent covers for ultraviolet and violet LED with the aim to transform their radiation into white light.

**Acknowledgments** The author is grateful to the leaders of the chemistry groups, Prof. M. Slobodyanyk and Prof. S.A. Nedilko; researchers from these groups, Ass. Prof. K. Terebilenko and Senior researcher T. Voitenko; and PG student A. Slepets for their work on the synthesis of phosphate–molybdate and vanadate compounds, respectively.

Many thanks to senior researcher O. Alekseyev and Ass. Prof. M. Lazarenko for the study of dielectric properties and analysis of the results.

Thanks to leading engineer M. Nediello for her work on SEM and optical microscopy.

My thanks to senior researcher O. Chukova, junior researcher V. Chornii, and leading engineer V. Scherbatskii for the study of oxides and composite luminescence.

## References

1. Camargo PHC, Satyanarayana KG, Wypych F (2009) Nanocomposites: synthesis, structure, properties and new application opportunities. *Mater Res* 12:1. <https://doi.org/10.1590/S1516-14392009000100002>
2. Jordan J, Jacob KI, Tannenbaum R, Sharaf MA, Jasiuk I (2005) Experimental trends in polymer nanocomposites: a review. *Mater Sci Eng A* 393:1. <https://doi.org/10.1016/j.msea.2004.09.044>
3. Vaia RA, Wagner HD (2004) Framework for nanocomposites. *Mater Today* 7:32. [https://doi.org/10.1016/S1369-7021\(04\)00506-1](https://doi.org/10.1016/S1369-7021(04)00506-1)
4. Nalwa HS (2000) Hand book of nanostructured materials and technology. Academic Press, New York eBook ISBN: 9780080533643
5. Ajayan PM, Schadler L, Braun PV (2003) Nanocomposites science and technology. Wiley-VCH, Verlag GmbH & Co. KGaA, Weinheim
6. Roy R, Roy RA, Roy DM (1986) Alternative perspectives on “quasi-crystallinity”: non-uniformity and nanocomposites. *Mater Lett* 4:323. [https://doi.org/10.1016/0167-577X\(86\)90063-7](https://doi.org/10.1016/0167-577X(86)90063-7)
7. Kamigaito O (1991) What can be improved by nanometer composites? *J Jpn Soc Powder Metall* 38:321. <https://doi.org/10.2497/jjspm.38.315>
8. Fischer H (2003) Polymer nanocomposites: from fundamental research to specific applications. *Mater Sci Eng C* 23:763. <https://doi.org/10.1016/j.msec.2003.09.148>
9. Zavyalov SA, Pivkina AN, Schoonman J (2002) Formation and characterization of metal-polymer nanostructured composites. *Solid State Ionics* 147:415. [https://doi.org/10.1016/S0167-2738\(02\)00038-3](https://doi.org/10.1016/S0167-2738(02)00038-3)
10. Thompson CM, Herring HM, Gates TS, Connel JW (2003) Preparation and characterization of metal oxide/polyamide nanocomposites. *Compos Sci Technol* 63(11):1591–1598. [https://doi.org/10.1016/S0266-3538\(03\)00062-9](https://doi.org/10.1016/S0266-3538(03)00062-9)
11. Alexandre M, Dubois P (2000) Polymer-layered silicate nanocomposites: preparation, properties and uses of a new class of materials. *Mater Sci Eng* 28:1. [https://doi.org/10.1016/S0927-796X\(00\)00012-7](https://doi.org/10.1016/S0927-796X(00)00012-7)

12. Ogawa M, Kuroda K (1997) Preparation of inorganic composites through intercalation of organo-ammonium ions into layered silicates. *Bull Chem Soc Jpn* 70:2593. <https://doi.org/10.1246/bcsj.70.2593>
13. Jeon HG, Jung HT, Lee SW, Hudson SD (1998) Morphology of polymer silicate nanocomposites. High density polyethylene and a nitrile copolymer. *Polym Bull* 41:107. <https://doi.org/10.1007/s002890050339>
14. Evora VMF, Shukla A (2003) Fabrication, characterization, and dynamic behavior of polyester/TiO<sub>2</sub> nanocomposites. *Mater Sci Eng* 361:358
15. Di Lorenzo ML, Errico ME, Avella M, Di Lorenzo ML, Errico ME, Avella M (2002) Thermal and morphological characterization of poly(ethylene terephthalate)/calcium carbonate nanocomposites. *J Mater Sci* 37:2351. <https://doi.org/10.1023/A:1015358425449>
16. Park SS, Bernet N, de La Roche S, Hanh HT (2003) Thermal and morphological characterization of poly (ethylene terephthalate)/calcium carbonate nanocomposites. *J Compos Mater* 37:465. <https://doi.org/10.1177/0021998303037005036>
17. Dutta A, Das D, Grilli ML, Di Bartolomeo E, Traversa E, Chakravorty D (2003) Preparation of sol-gel nano-composites containing copper oxide and their gas sensing properties. *J Sol-Gel Sci Technol* 26:1085. <https://doi.org/10.1023/A:1020706707243>
18. Herron N, Thorn DL (1998) Nanoparticles: uses and relationships to molecular cluster compounds. *Adv Mater* 10:1173. [https://doi.org/10.1002/\(SICI\)1521-4095\(199810\)10:15](https://doi.org/10.1002/(SICI)1521-4095(199810)10:15)
19. Schmidt D, Shah D, Giannelis EP (2002) New advances in polymer/layered silicate nanocomposites. *Curr Opin Solid State Mater Sci* 6:205. [https://doi.org/10.1016/S1359-0286\(02\)00049-9](https://doi.org/10.1016/S1359-0286(02)00049-9)
20. Ray SS, Okamoto M (2003) Polymer - layered silicate nanocomposites: a review from preparation to processing. *Prog Polym Sci* 28:1539. <https://doi.org/10.1016/j.progpolymsci.2003.08.002>
21. Liu SH, Qian XF, Yuan JY, Yin J, He R, Zhu ZK (2003) Synthesis of monodispersed CdSe nanocrystals in poly(styrene-alt-maleic anhydride) at room temperature. *Mater Res Bull* 38:1359. [https://doi.org/10.1016/S0025-5408\(03\)00148-X](https://doi.org/10.1016/S0025-5408(03)00148-X)
22. Trindade T, Neves MC, Barros AMV (2000) Preparation and optical properties of CdSe/polymer nanocomposites. *Scr Mater* 43:567. [https://doi.org/10.1016/s1359-6462\(00\)00437-1](https://doi.org/10.1016/s1359-6462(00)00437-1)
23. Krishnamoorti R, Vaia RA, Giannelis EP (1996) Structure and dynamics of polymer-layered silicate nanocomposites. *Chem Mater* 8:1728. <https://doi.org/10.1021/cm960127g>
24. Beecroft LL, Ober CK (1997) Nanocomposite materials for optical applications. *Chem Mater* 9:1302. <https://doi.org/10.1021/cm960441a>
25. Ninjbadgar T, Garnweitner G, Börger A, Goldenberg ML, Sakhno VO, Stumpe J (2009) Synthesis of luminescent ZrO<sub>2</sub>:Eu<sup>3+</sup> nanoparticles and their holographic submicrometer patterning in polymer composites. *Adv Funct Mater* 19:1819. <https://doi.org/10.1002/adfm.200801835>
26. Ryszkowska J, Zawadzka EA, Hreniak D, Lojkowski W, Opalinska A, Kurzydowski KJ (2007) Structure and properties of polyurethane nanocomposites with zirconium oxide including Eu. *J Mater Sci Eng C* 27:994. <https://doi.org/10.1016/j.msec.2006.09.046>
27. Althues H, Simon P, Kaskel S (2007) Transparent and luminescent YVO<sub>4</sub>:Eu/polymer nanocomposites prepared by in situ polymerization. *J Mater Chem* 17:758. <https://doi.org/10.1039/B611917D>
28. Goubard F, Vidal F, Bazzi R, Tillement O, Chevrot C, Teyssie D (2007) Synthesis and luminescent properties of PEO/lanthanide oxide nanoparticle hybrid films. *J Lumin* 126:289. <https://doi.org/10.1016/j.jlumin.2006.07.009>
29. Tucureanu V, Matei A, Avram AM (2015) Synthesis and characterization of YAG:Ce phosphors for white LEDs. *Opto-Electron Rev* 23:239. <https://doi.org/10.1515/oere-2015-0038>
30. Klampaftis E, Rossa D, McIntoshb KR, Richards BS (2009) Enhancing the performance of solar cells via luminescent down-shifting of the incident spectrum: a review. *Sol Energy Mater Sol Cells* 93:1182. <https://doi.org/10.1016/j.solmat.2009.02.020>
31. Ramasamy P, Manivasakan P, Kim J (2014) Upconversion nanophosphors for solar cell applications. *RSC Adv* 4:34873. <https://doi.org/10.1039/C4RA03919J>

32. Dudek M, Jusza A, Lipińska L (2011) Luminescent properties of praseodymium doped  $Y_2O_3$  and  $LaAlO_3$  nanocrystallites and polymer composites. *J Rare Earths* 29:1123. [https://doi.org/10.1016/S1002-0721\(10\)60610-2](https://doi.org/10.1016/S1002-0721(10)60610-2)
33. Anders K, Jusza A, Baran M, Lipińska L, Piramidowicz R (2012) Emission properties of polymer composites doped with  $Er^{3+}:Y_2O_3$  nanopowders. *Opt Mater* 34:1964. <https://doi.org/10.1016/j.optmat.2011.11.011>
34. Vistovsky V, Mitina N, Shapoval A, Malyy T, Gektin A, Konstantinova T, Voloshinovskii A, Zaichenko A (2012) Luminescence properties of  $LaPO_4$ –Eu nanoparticles synthesized in the presence of surface active oligoperoxide as template. *Opt Mater* 34:2066. <https://doi.org/10.1016/j.optmat.2012.04.010>
35. Kumar A, Negi YS, Choudhary V, Bhardwaj NK (2014) Characterization of cellulose nanocrystals produced by acid-hydrolysis from sugarcane bagasses agro-waste. *J Mater Phys Chem* 2:1. <https://doi.org/10.12691/jmpc-2-1-1>
36. Moon RJ, Martini A, Nairn A, Simonsen J, Youngblood J (2011) Cellulose nanomaterials review: structure, properties and nanocomposites. *Chem Soc Rev* 40:3941. <https://doi.org/10.1039/C0CS00108B>
37. Siro I, Plackett D (2010) Microfibrillated cellulose and new nanocomposite materials: a review. *Cellulose* 17:459. <https://doi.org/10.1007/s10570-010-9405-y>
38. Ummartyotin S, Pechyen C (2016) Microcrystalline-cellulose and polypropylene based composite: a simple, selective and effective material for microwavable packaging. *Carbohydr Polym* 142:133. <https://doi.org/10.1016/j.carbpol.2016.01.020>
39. Zhou Z, Wang Q (2012) Two emissive cellulose hydrogels for detection of nitrite using terbium luminescence. *Sensors Actuators B* 173(833). <https://doi.org/10.1016/j.snb.2012.07.117>
40. Nedilko S, Revo S, Nediello M, Avramenko T, Ivanenko K, Scherbatskii V (2015) Luminescence of the alkali-metals nitrites incorporated into cellulose matrix. *Solid State Phenom* 230:147. <https://doi.org/10.4028/www.scientific.net/SSP.230.147>
41. Nedilko SG, Revo SL, Chornii VP, Scherbatskyi VP, Nediello MS (2015) Luminescent determination of nitrite traces in water solutions using cellulose as sorbent. *J Sens Sens Syst* 4:31. <https://doi.org/10.5194/jsss-4-31-2015>
42. Karakawa M, Chikamatsu M, Nakamoto C, Maeda Y, Kubota S, Yase K (2007) Organic light-emitting diode application of fluorescent cellulose as a natural polymer. *Macromol Chem Phys* 208:2000. <https://doi.org/10.1002/macp.200700154>
43. Yun S, Jang SD, Yun GY, Kim JH, Kim J (2009) Paper transistor made with covalently bonded multiwalled carbon nanotube and cellulose. *Appl Phys Lett* 95:104102. <https://doi.org/10.1063/1.3224200>
44. Wang N, Ding E, Cheng R (2008) Preparation and liquid crystalline properties of spherical cellulose. *Langmuir* 24:5. <https://doi.org/10.1021/la702923w>
45. Bateh RP, Winefordner JD (1982) An evaluation of cellulose as a substrate for room-temperature phosphorescence. *Talanta* 29:713. [https://doi.org/10.1016/0039-9140\(82\)80083-0](https://doi.org/10.1016/0039-9140(82)80083-0)
46. Pikulev V, Loginova S, Gurtov V (2012) Luminescence properties of silicon-cellulose nanocomposite. *Nanoscale Res Lett* 7:426. <https://doi.org/10.1186/1556-276X-7-426>
47. Tylli H, Forsskahl I, Olkkonen C (2000) The effect of heat and IR radiation on the fluorescence of cellulose. *Cellulose* 7:133. <https://doi.org/10.1023/A:1009225624732>
48. Nediello M, Hamamda S, Alekseev O, Chornii V, Dashevskii M, Lazarenko M, Kovalov K, Nedilko SG, Tkachov S, Revo S, Scherbatskyi V (2017) Mechanical, dielectric, and spectroscopic characteristics of "micro/Nanocellulose + oxide" composites. *Nanoscale Res Lett* 12:98. <https://doi.org/10.1186/s11671-017-1862-x>
49. Kulpinski P, Erdman A, Grzyb T, Lis S (2016) Luminescent cellulose fibers modified with cerium fluoride doped with terbium particles. *Polym Compos* 37:153. <https://doi.org/10.1002/pc.23166>
50. Smiechowicz E, Kulpinski P, Niekraszewicz B, Bacciarelli A (2011) Cellulose fibers modified with silver nanoparticles. *Cellulose* 18:975. <https://doi.org/10.1007/s10570-011-9544-9>
51. Kulpinski P, Erdman A, Namyślak M, Fidelus JD (2012) Cellulose fibers modified by  $Eu^{3+}$ -doped yttria-stabilized zirconia nanoparticles. *Cellulose* 19:1259. <https://doi.org/10.1007/s10570-012-9704-6>

52. Erdman A, Kulpinski P, Olejnik K (2016) Application of nanocomposite cellulose fibers with luminescent properties to paper functionalization. *Cellulose* 23:2087. <https://doi.org/10.1007/s10570-016-0943-9>
53. Atalla R, Nagel S (1972) Laser-induced fluorescence in cellulose. *J Chem Soc Chem Commun* 19:1049. <https://doi.org/10.1039/C39720001049>
54. Castellan A, Choudhury H, Davidson RS, Grelier S (1994) Comparative study of stone-ground wood pulp and native wood. 2. Comparison of the fluorescence of stone-ground wood pulp and native wood. *J Photochem Photobiol A: Chem* 81:117. [https://doi.org/10.1016/1010-6030\(94\)03783-3](https://doi.org/10.1016/1010-6030(94)03783-3)
55. Korntner P, Hosoya T, Dietz T, Eibinger K, Reiter H, Spitzbart M, Röder T, Borgards A, Kreiner W, Mahler AK, Winter H, Groiss Y, French AD, Henniges U, Potthast A, Rosenau T (2015) Chromophores in lignin-free cellulosic materials belong to three compound classes. *Chromophores Cellulosics XII Cellulose* 22:1053. <https://doi.org/10.1007/s10570-015-0566-6>
56. Gavrilov MZ, Ermolenko IN (1966) A study of cellulose luminescence. *J Appl Spectr* 5:542. <https://doi.org/10.1007/BF00606982>
57. Olmstead JA, Gray DG (1993) Fluorescence emission from mechanical pulp sheets. *J Photochem Photobiol A Chem* 73:59. [https://doi.org/10.1016/1010-6030\(93\)80034-7](https://doi.org/10.1016/1010-6030(93)80034-7)
58. Macalese DL, Dunlap RB (1984) Reduction of background emission in room-temperature phosphorescence. *Anal Chem* 56:600
59. Schmidt J (2010) Electronic spectroscopy of lignins. In: Heitner C, Dimmel D, Schmidt J (eds) *Lignins and lignans*. CRC Press, Boca Raton, p 683 ISBN 9781574444865 - CAT# DK3286
60. Nevell TP, Zeronian SH (1987) Cellulose chemistry and its applications. *J Polym Sci Part C: Polym Lett* 25:87. <https://doi.org/10.1002/pol.1987.140250212>
61. Bikova T, Treimanis A (2004) UV-absorbance of oxidized xylan and monocarboxyl cellulose in alkaline solutions. *Carbohydr Polym* 55:315. <https://doi.org/10.1016/j.carbpol.2003.10.005>
62. Castellan A, Ruggiero R, Frollini E, Ramos L, Chirat C (2007) Studies on fluorescence of cellulosics. *Holzforschung* 61:504. <https://doi.org/10.1515/HF.2007.090>
63. Liukko S, Tasapuro V, Liitiä T (2007) Fluorescence spectroscopy for chromophore studies on bleached Kraft pulps. *Holzforschung* 61:509. <https://doi.org/10.1515/HF.2007.107>
64. Davidson RS, Dunn LA, Castellan A, Nourmamode A (1991) A study of the photobleaching and photoyellowing of paper containing lignin using fluorescence spectroscopy. *J Photochem Photobiol A: Chem* 58:359 ISSN: 1010-6030 CODEN: JPPCEJ
65. Nedilko S, Mogilevsky R, Sharafutdinova L, Burlay S, Sherbatskii V, Boyko V, Mittl S (2009) Luminescence study of grown sapphire: from starting material to single crystal. *Phys Status Solidi* 6:S179. <https://doi.org/10.1002/pssc.200881323>
66. Mogilevsky R, Nedilko S, Sharafutdinova L, Burlay S, Sherbatskii V, Boyko V, Mittl S (2009) Sapphire: relation between luminescence of starting materials and luminescence of single crystals. *Opt Mater* 31:1880. <https://doi.org/10.1016/j.optmat.2008.11.023>
67. Mogilevsky R, Nedilko S, Sharafutdinova L, Gavrilov V, Verbilo D, Mittl S (2009) Hydrogen effect on the properties of sapphire. *Proc SPIE* 7302:11. <https://doi.org/10.1117/12.818148>
68. Kulpinski P, Namyslak M, Grzyb T, Lis S (2012) Luminescent cellulose fibers activated by Eu<sup>3+</sup>-doped nanoparticles. *Cellulose* 19:1271. <https://doi.org/10.1007/s10570-012-9709-1>
69. Ribeiro SJL, Dahmouche K, Ribeiro CA, Santilli CV, Pulcinelli SH (1998) Study of hybrid silica-polyethylene glycol xerogels by Eu<sup>3+</sup> luminescence spectroscopy. *J Sol-Gel Sci Technol* 13:427. <https://doi.org/10.1023/A:1008673211834>
70. Chornii V, Nedilko SG, Miroshnichenko M, Terebilenko K, Slobodyanik M (2017) Influence of fluorination on structure and luminescence of ZrO<sub>2</sub>:Eu nanocrystals. *Mater Res Bull* 90:237. <https://doi.org/10.1016/j.materresbull.2017.02.033>
71. Chornii V, Chukova O, Nedilko SG, Nedilko SA, Voitenko T (2016) Enhancement of emission intensity of LaVO<sub>4</sub>:RE<sup>3+</sup> luminescent solar light absorbers. *Phys Status Solidi C* 13:40. <https://doi.org/10.1002/pssc.201510116>
72. Hizhnyi Y, Chornii V, Nedilko S, Slobodyanik M, Terebilenko K, Boyko V, Gomenyuk O, Sheludko V (2016) Luminescence spectroscopy of In-doped bi-containing phosphates and molybdates. *Radiat Meas* 90:314. <https://doi.org/10.1016/j.radmeas.2016.01.014>

73. Driemeier C, Calligaris GA (2011) Structure of cellulose and microcrystalline cellulose from various wood species, cotton and flax studied by X-ray scattering. *J Appl Crystallogr* 44:184. <https://doi.org/10.1107/S0021889810043955>
74. Leppänen K, Andersson S, Torkkeli M, Knaapila M, Kotelnikova N, Serimaa R (2009) Structure of cellulose and microcrystalline cellulose from various wood species, cotton and flax studied by X-ray scattering. *Cellulose* 16:999. <https://doi.org/10.1007/s10570-009-9298-9>
75. Laue W, Thiemann M, Scheibler E, Wiegand KW (2002) Nitrates and nitrites, Ullmann's encyclopedia of industrial chemistry. Wiley-VCH, Weinheim. [https://doi.org/10.1002/14356007.a17\\_265](https://doi.org/10.1002/14356007.a17_265)
76. Hizhnyi YA, Nedilko SG, Chornii VP, Slobodyanik MS, Zatovsky IV, Terebilenko KV (2014) Electronic structures and origin of intrinsic luminescence in bi- containing oxide crystals  $\text{BiPO}_4$ ,  $\text{K}_3\text{Bi}_5(\text{PO}_4)_6$ ,  $\text{K}_2\text{Bi}(\text{PO}_4)(\text{MoO}_4)$ ,  $\text{K}_2\text{Bi}(\text{PO}_4)(\text{WO}_4)$  and  $\text{K}_5\text{Bi}(\text{MoO}_4)_4$ . *J Alloys Compd* 614:20. <https://doi.org/10.1016/j.jallcom.2014.06.111>
77. Pizzoli M, Scandola M, Ceccorulli G (1991) Dielectric and mechanical loss processes in hydroxypropyl cellulose. *Plast Rubber Compos Process Appl* 16:239 ISSN: 0959-8111
78. Rials TG, Glasser WG (1988) Thermal and dynamic mechanical-properties of Hydroxypropyl cellulose films. *J Appl Polym Sci* 36:749
79. Wojciechowski P (2000) Thermotropic mesomorphism of selected (2-hydroxypropyl) cellulose derivatives. *J Appl Polym Sci* 76:837. [https://doi.org/10.1002/\(SICI\)1097-4628\(20000509\)76:6<837::AID-APP9>3.0.CO;2-P](https://doi.org/10.1002/(SICI)1097-4628(20000509)76:6<837::AID-APP9>3.0.CO;2-P)
80. Liu X, Zhang Y, Wang Z, Sh L (1988) Luminescence and energy transfer bands of the  $\text{Sm}^{3+}$  and  $\text{Eu}^{3+}$  in  $\text{Mg}_3\text{BO}_3\text{F}_3$ . *J Lumin* 40:885. <https://doi.org/10.1016/j.jlumin.2016.07.043>
81. Malinowski M, Jacquier B, Boulon G (1988) Fluorescence quenching in  $\text{Sm}^{3+}$  doped  $\text{KY}(\text{PO}_4)_{12}$  crystals. *J Lumin* 39:301. [https://doi.org/10.1016/0022-2313\(88\)90011-7](https://doi.org/10.1016/0022-2313(88)90011-7)
82. Treadaway M, Powell R (1975) Energy transfer in samarium – doped calcium tungstate crystals. *Phys Rev B* 11:862
83. Maas J, Wollenhaupt M, Arbens H, Frobel P, Barner K (1994) The fluorescence of  $\text{Sm}^{3+}$  in lithium molybdate borate glasses. *J Lumin* 62:95. [https://doi.org/10.1016/0022-2313\(94\)90335-2](https://doi.org/10.1016/0022-2313(94)90335-2)
84. Venkatramu V, Babu P, Jayasankar CK, Troster T, Sievers W, Wortmann G (2007) Optical spectroscopy of  $\text{Sm}^{3+}$  ions in phosphate and fluorophosphate glasses. *Opt Mater* 29:1429–1439. <https://doi.org/10.1016/j.optmat.2006.06.011>
85. Elbanowski M, Lis S, Makowska B, Konarski J (1985) Fluorescence of Lanthanide (III) complexes in aqueous solutions. *Monatshefte Chem* 116:901. <https://doi.org/10.1007/BF00815318>

# Chapter 16

## Interactions Between Carbon-Based Nanostructures and Biomembranes: Computer Simulations Study



Przemysław Raczyński, Mateusz Pabiszczak, and Zygmunt Gburski

### 16.1 Introduction

The cell membranes were created by nature as efficient protective barriers. An important functional part of membrane is the phospholipid bilayer, the structure that protects an interior of the cell from the external factors like uncontrolled molecules transport from and into the cell [1–3]. Taking into account expansion of novel fields like nano-medicine, employing nanostructures to deliver cargo to cells via phospholipid bilayer is of considerable interests. Carbon nanotubes are recognized as a potential noninvasive vehicle because experimental and theoretical studies suggest that they are able to quite efficiently penetrate the membrane [4–9]. CNTs can be functionalized with different molecules such as proteins, nucleic acids, and drugs [10, 11]. The delivered substances can be attached to the outer surface of nanotube [12] as well as inner surface can be used [12–14]. Optical absorption in the near-infrared [15], photoluminescence [16], Raman scattering [17], photoacoustic [18], or echogenic properties [19] can be used to visualize the track of CNT in the biological milieu [20–23].

In this work, we analyze the interaction mechanism between phospholipid bilayer and carbon-based nanostructures during its movement via membrane. Besides of our earlier works [24–27], there are relatively few computer simulation studies that address the entry mechanism [28–30].

In this work, we present the results obtained for two armchair carbon nanotubes: (10, 10) and (12, 12). The force required to pierce the membrane and membrane

---

P. Raczyński (✉) · M. Pabiszczak · Z. Gburski  
Institute of Physics, University of Silesia, Katowice, Poland

Silesian Centre of Education & Interdisciplinary Research, Chorzów, Poland  
e-mail: [przemyslaw.raczynski@us.edu.pl](mailto:przemyslaw.raczynski@us.edu.pl)

deflection is discussed. We compare the results with capped (10, 10) CNT. We also present results for heterogeneous nanotube, namely, silicon-carbide nanotube (SiCNT). Recent studies show that SiCNT might have some advantages when compared to CNTs, because they exhibit larger reactivity and they can be applied in hydrogen storage components [31, 32]. Also graphene sheet was taken into consideration as it is a novel material and its interaction with biological samples is still relatively not well known.

The damage of phospholipid bilayer is equivalent with the death of the cell, and the nanostructure used during indentation process should not destroy the membrane if it is to be considered as possible drug carrier. To assess the impact of nanostructure on the membrane, we performed a set of simulations of removing the (10, 10) CNT from the membrane. During extraction process, we examined self-sealing abilities of phospholipid bilayer.

## 16.2 Materials and Methods

Molecular dynamics simulations were performed with NAMD 2.8 simulations code [33], with the all-atom CHARMM force field. VMD 1.9.2 was used to visualize the simulated systems [34]. The studied systems consisted of nanostructure, phospholipid (DMPC), and cholesterol molecules, which play in membrane an important role in the context of its fluidity [1, 2, 35–37]. Moreover, all simulations were performed in a water environment (TIP3P adapted CHARMM model of water [38, 39]).

All systems were initially equilibrated in NPT ensemble. The pressure was set to 1 atm and controlled using Langevin barostat implemented in NAMD. Next the systems were equilibrated in NVT ensemble, and after these initial runs, where the nanostructures were kept at constant positions, the indentation simulations were started. All indentation simulations were performed in NVT ensemble.

Nanoindentation of a phospholipid bilayer was modeled by means of SMD simulations. In case of nanotubes, the springs were added between the most distant from bilayer ring of nanotube and imaginary points moving with constant velocity perpendicularly to bilayer surface. For graphene sheet springs were added at the closest to bilayer carbon atoms due to the fact that it was difficult to keep the sheet perpendicularly to bilayer surface when the springs were added to the atoms most distant from the bilayer.

The simulated systems consist of approximately 130,000 atoms. All simulations were performed at physiological temperature equal to 310 K. The integration time step was set to 0.5 fs. During equilibration process, the distance between the closest to the bilayer nanostructure atoms and average positions of phospholipid heads was approximately equal to 0.8 nm. All interactions were described with CHARMM potential. The CHARMM-adapted parameters and topologies for CNTs and graphene sheet were taken from [40–42] and for silicon-carbide nanotube from [43]. The atomic charges and model for cholesterol molecule were taken from



[44]. DMPC molecules were modeled using CHARMM27 force field [45, 46]. To improve the sampling of state space, all simulations were repeated several times, and the results presented in this work are the averages over all independent simulation runs.

The simulations were performed as follows:

1. Firstly indentation using two armchair CNTs (10, 10) and (12, 12) was executed with the speed equal to 1.5 m/s.
2. Next part of simulations was to use capped (10, 10) CNT as a nanoindenter. The CNT was moving through bilayer with the speed  $v = 2$  m/s.
3. Thirdly we used heterogeneous (10, 10) SiCNT nanotube, which pierced the membrane with speed equal to 1.5 m/s.
4. We also used  $56 \times 32$  Å graphene sheet. The graphene sheet was moved with the speed equal to 2 m/s.
5. Last part of our simulations was extraction process for the open-ended (10, 10) CNT with the pullout speed equal to 1.5 m/s.

The results of these simulations are presented and discussed in the above order.

## 16.3 Results

### 16.3.1 Indentation of the Membrane by (10, 10) and (12, 12) CNTs

Figure 16.1 shows the initial configuration (Fig. 16.1a) for the (12, 12) CNT and the final configuration of this system (Fig. 16.1b).

In the Fig. 16.1b, one can observe that some lipids were pulled out of the membrane, but its consistency is saved. Moreover, the deflection of the membrane is observed after indentation process. Figure 16.2 presents the average dislocation of C2 carbon atoms from the phospholipid glycerol backbones with respect to the distance from nanotube main axis. The bending was calculated with respect to the positions of glycerol backbone C2 atoms at the edges of simulation cell. In case of nanotube with larger diameter, the deflection is larger because it is more difficult to accommodate the change imposed by moving (12, 12) CNT. In case of (12, 12) CNT, the C2 atoms located close to the nanotube surface were displaced about 2–3 Å deeper into the bilayer comparing to (10, 10) CNT. The C2 atoms located close to the CNT surface experience larger dislocation comparing to these located at the edges of simulation cell.

The average force required to insert the nanotube into bilayer, as a function of the indentation depth, is shown in Fig. 16.3. It can be seen that force required to indent phospholipid bilayer is larger in case of CNT with larger diameter. The higher amount of the force required is clearly observed mainly in the last part of indentation process where the bilayer is almost pierced by CNT. The maximums of

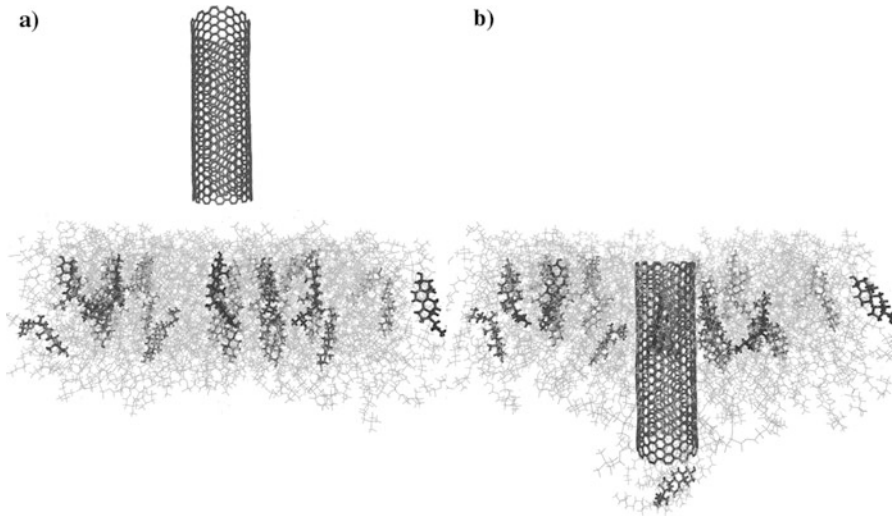


**Fig. 16.1** The initial (a) and final (b) configuration of the system consisted of (12, 12) CNT and bilayer

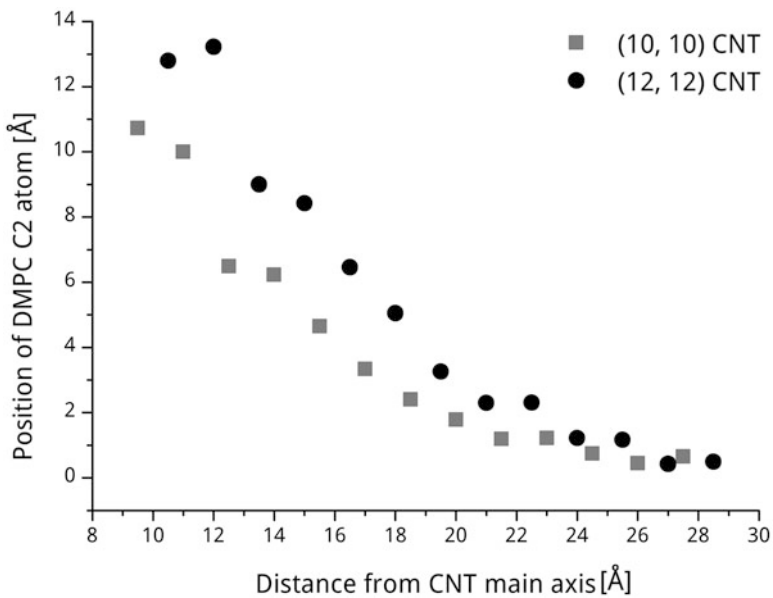


**Fig. 16.2** The comparison of average dislocation of the C2 DMPC atoms

the curves are located between 18 and 20 Å. This indentation depth can be associated with CNTs pressing apart the strongly interacting and meshed hydrocarbon tails of phospholipids. After crossing this part of bilayer, the force begins to diminish.

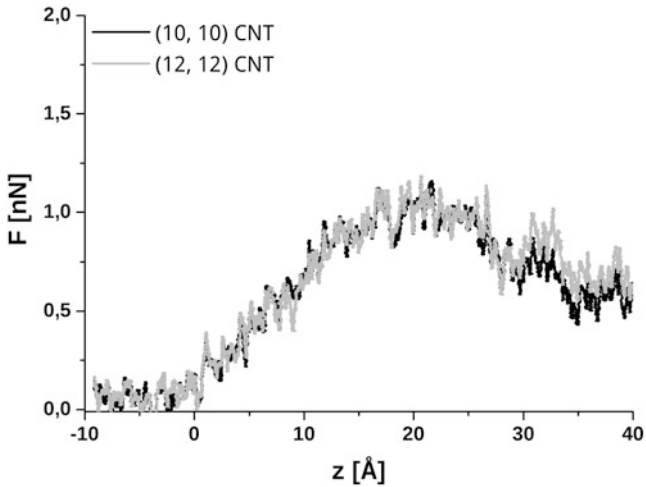


**Fig. 16.3** The comparison of average force required to insert CNT into bilayer

### ***16.3.2 Comparison Between Capped and Uncapped (10, 10) CNT***

In this part of simulations, the indentation speed was equal to 2 m/s. Direct comparison between force profile for open-ended and capped CNT is shown in Fig. 16.4. The average force acting on open-ended CNT is higher comparing to the capped nanotube. Although the maximal force required to penetrate membrane is similar for both CNTs, the average force decays faster in case of capped nanotube. This leads to the conclusion that the capped CNT penetrates the phospholipid bilayer less invasively than their open-ended counterpart. Moreover, analysis of Figs. 16.3 and 16.4 allows to conclude that higher indentation speed means higher force required to pierce the membrane and, consequently, larger membrane damage.

### ***16.3.3 Nanoindentation of the Membrane by Heterogeneous Nanotube***

In this part of simulation, we have used silicon-carbide nanotube which pierced phospholipid bilayer with speed equal to 1.5 m/s. Figure 16.5 shows the comparison between forces required for indentation process in case of (10, 10) SiCNT and (10, 10) CNT. The required force is smaller for the heterogeneous nanotube. The bonds between silicon and carbon atoms are longer than between carbon-carbon. This causes that SiCNT deforms easier and more readily adapts to bilayer. It diminishes mutual interactions between nanotube and bilayer, and the average force is smaller

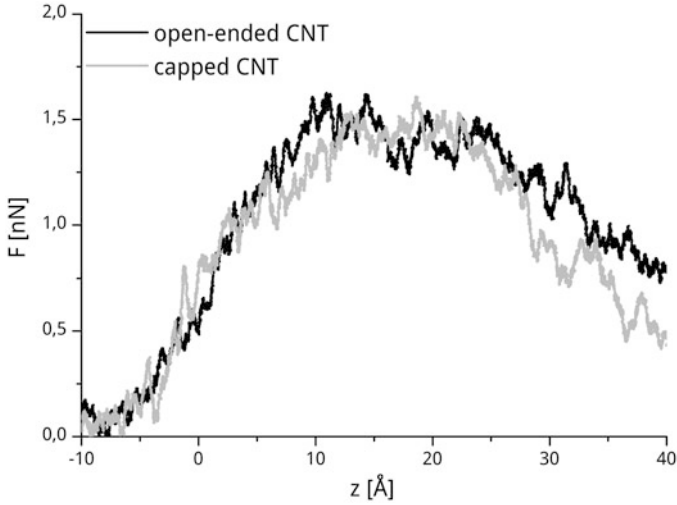


**Fig. 16.4** The comparison of average force required to insert open-ended and capped nanotube into bilayer

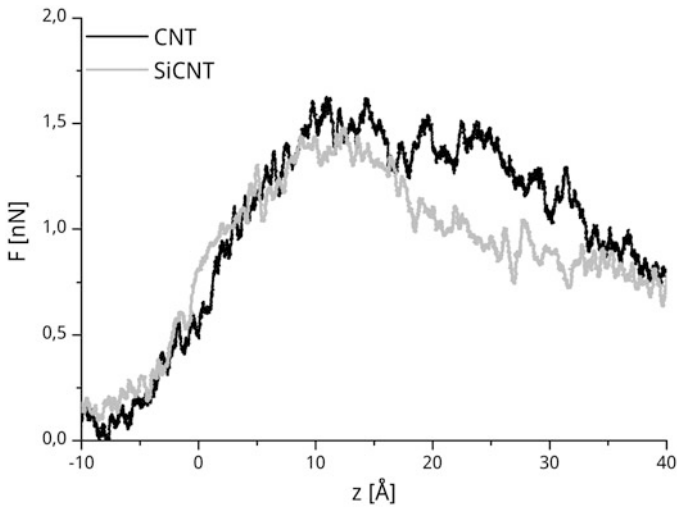


**Fig. 16.5** The comparison of average force required to insert CNT and SiCNT into bilayer

than in case of pure CNT. Note that average force for SiCNT is smaller despite the fact that it has larger diameter, and as one can see from Fig. 16.3, for homogeneous nanotubes, the required force increases with the diameter.

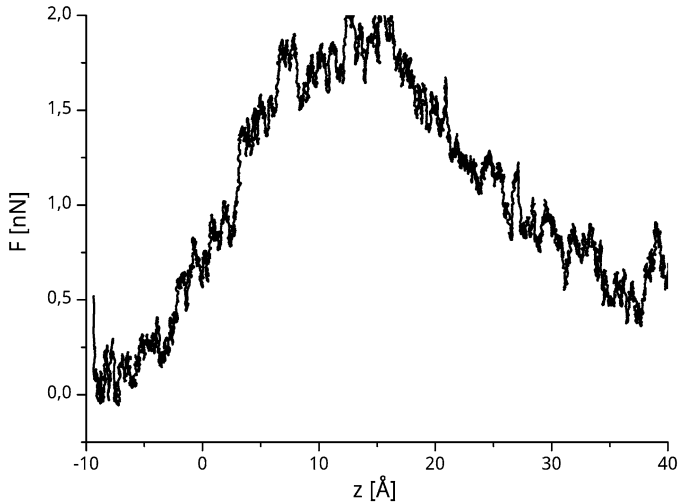


**Fig. 16.6** The average force required to insert graphene sheet into bilayer

### 16.3.4 Indentation with Graphene Sheet

The results shown in Fig. 16.6 were obtained for 56 Å width and 32 Å height graphene sheet which pierced the bilayer with speed equal to 2 m/s. Note that in case of this part of our studies, the springs were added to the carbon atoms closest to the membrane. The shape of force plot is similar to the curves obtained for other discussed systems. At the first part of diagram, the force required for the indentation process grows. The maximum force is about 2.5 nN, and it is connected with the region where graphene sheet presses apart the glycerol backbones or hydrocarbon tails of phospholipids (between 12 and 16 Å). Next, the force starts to diminish.

### 16.3.5 Extraction and Self-Sealing Processes

The last part of our studies was performed for open-ended (10, 10) CNT. The pulling speed was equal to 1.5 m/s. Figure 16.7 shows the average force required for extraction process. This chart should be analyzed from right to left.

The average force required to pull CNT out of the membrane is significantly lower comparing to the nanoindentation process (see Fig. 16.3). After the initial part of extraction, where the force grows to, approximately, 0.5 nN, the maximum width can be observed. It is wider compared to the indentation example, because the opposite to deflection process occurs and, firstly, CNT overcomes the deflection and, next, it “raises” whole membrane up. At the last part of extraction process, where the membrane is not able to accommodate changes caused by nanotube, CNT starts to leave the membrane definitely, and the force starts to diminish.

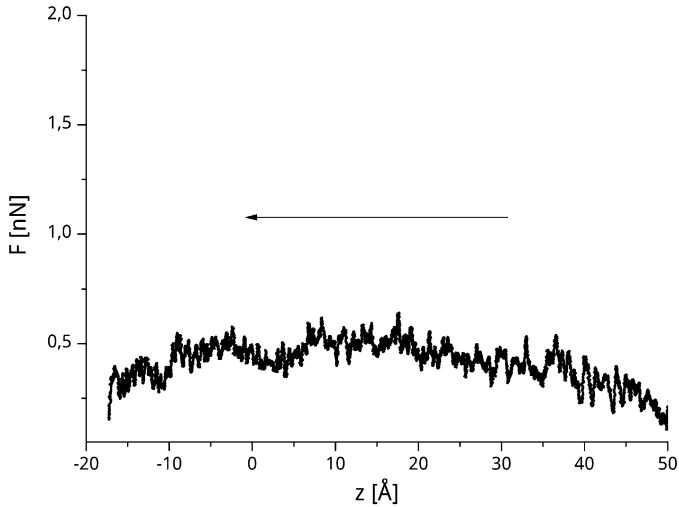
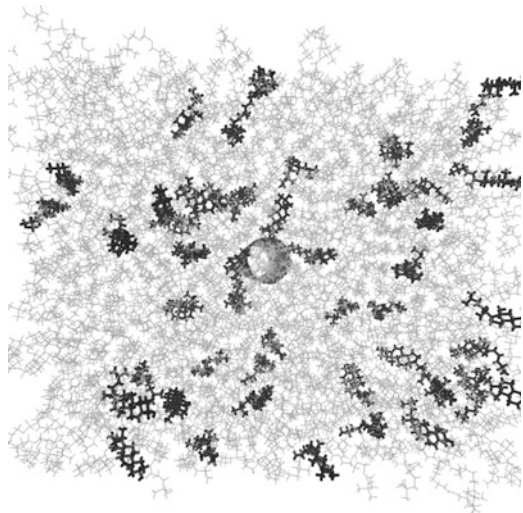


**Fig. 16.7** The average force required to pull CNT out of the membrane

**Fig. 16.8** The snapshot of membrane self-sealing process



During extraction process, the self-sealing process occurs. Figure 16.8 presents the snapshot of final configuration (after extraction process) when the nanotube left the membrane permanently (bottom view). There are no water molecules remaining in the membrane after nanotube extraction process and no defects through which water could easily penetrate the membrane. For the studied extraction speed, the self-sealing process occurs almost instantaneously.

## 16.4 Conclusions

We have performed a series of computer experiments on nanoindentation process. The pure CNTs, heterogeneous silicon-carbide nanotube, and graphene sheet were used to deeply examine the indentation process. Our simulations show that the larger diameter of CNT means higher force required to pierce the membrane. The membrane also experienced larger deflection when (12, 12) CNT was used. The capped CNT is less invasive comparing to open-ended. Heterogeneous SiCNT requires smaller force to pierce the membrane comparing to its homogeneous carbon counterpart. The nature of nanoindentation with graphene sheet is somehow similar to indentation with nanotubes because the shapes of force are congruous. The average force required to pull CNT out of the membrane is smaller than in case of indentation, and effective self-sealing process of the bilayer occurs.

Our findings might contribute to the quest for effective drug delivery into the interior of the mammals cells and can be helpful in future real-life experiments.

**Acknowledgment** Calculations were performed at ICM University of Warsaw, Grant No. G53-6.

## References

1. Alberts B (2008) *Molecular biology of the cell*. Garland Science, New York [etc.]
2. Nelson DL, Cox MM, Lehninger AL (2013) *Lehninger principles of biochemistry*. W.H. Freeman, New York
3. Sperelakis N (2012) *Cell physiology sourcebook essentials of membrane biophysics*. Elsevier/AP, Amsterdam; Boston
4. Obataya I, Nakamura C, Han S, Nakamura N, Miyake J (2005) Nanoscale operation of a living cell using an atomic force microscope with a nanoneedle. *Nano Lett* 5:27–30. <https://doi.org/10.1021/nl0485399>
5. Gagner J, Johnson H, Watkins E, Li Q, Terrones M, Majewski J (2006) Carbon nanotube supported single phospholipid bilayer. *Langmuir* 22:10909–10911. <https://doi.org/10.1021/la062038g>
6. Porter AE, Gass M, Bendall JS, Muller K, Goode A, Skepper JN, Midgley PA, Welland M (2009) Uptake of noncytotoxic acid-treated single-walled carbon nanotubes into the cytoplasm of human macrophage cells. *ACS Nano* 3:1485–1492. <https://doi.org/10.1021/nn900416z>
7. Raffa V, Ciofani G, Nitodas S, Karachalios T, D'Alessandro D, Masini M, Cuschieri A (2008) Can the properties of carbon nanotubes influence their internalization by living cells? *Carbon* 46:1600–1610. <https://doi.org/10.1016/j.carbon.2008.06.053>
8. Ali-Boucetta H, Kostarelos K (2013) Carbon nanotubes in medicine & biology — therapy and diagnostics. *Adv Drug Deliv Rev* 65:1897–1898. <https://doi.org/10.1016/j.addr.2013.11.002>
9. Debouzy JC, Crouzier D, Flahaut E (2010) Hydrophobic double walled carbon nanotubes interaction with phospholipidic model membranes: <sup>1</sup>H-, <sup>2</sup>H-, <sup>31</sup>P NMR and ESR study. *Environ Toxicol Pharmacol* 30:147–152. <https://doi.org/10.1016/j.etap.2010.05.002>
10. Wong BS, Yoong SL, Jagusiak A, Panczyk T, Ho HK, Ang WH, Pastorin G (2013) Carbon nanotubes for delivery of small molecule drugs. *Adv Drug Deliv Rev* 65:1964–2015. <https://doi.org/10.1016/j.addr.2013.08.005>
11. Luo X, Matranga C, Tan S, Alba N, Cui XT (2011) Carbon nanotube nanoreservoir for controlled release of anti-inflammatory dexamethasone. *Biomaterials* 32:6316–6323. <https://doi.org/10.1016/j.biomaterials.2011.05.020>

12. Kotchey GP, Zhao Y, Kagan VE, Star A (2013) Peroxidase-mediated biodegradation of carbon nanotubes in vitro and in vivo. *Adv Drug Deliv Rev* 65:1921–1932. <https://doi.org/10.1016/j.addr.2013.07.007>
13. Bianco A, Kostarelos K, Prato M (2011) Making carbon nanotubes biocompatible and biodegradable. *Chem Commun (Camb)* 47:10182–10188. <https://doi.org/10.1039/c1cc13011k>
14. Dendzik Z, Kosmider M, Sokół M (2008) Dielectric relaxation of water clusters encapsulated in carbon nanotubes – computer simulation study. *J Non-Cryst Solids* 354:4300–4303. <https://doi.org/10.1016/j.jnoncrsol.2008.06.042>
15. Tong L, Liu Y, Dolash BD, Jung Y, Slipchenko MN, Bergstrom DE, Cheng J-X (2012) Label-free imaging of semiconducting and metallic carbon nanotubes in cells and mice using transient absorption microscopy. *Nat Nanotechnol* 7:56–61. <https://doi.org/10.1038/nnano.2011.210>
16. Welsher K, Sherlock SP, Dai H (2011) Deep-tissue anatomical imaging of mice using carbon nanotube fluorophores in the second near-infrared window. *Proc Natl Acad Sci* 108:8943–8948. <https://doi.org/10.1073/pnas.1014501108>
17. Keren S, Zavaleta C, Cheng Z, de la Zerda A, Gheysens O, Gambhir SS (2008) Noninvasive molecular imaging of small living subjects using Raman spectroscopy. *Proc Natl Acad Sci* 105:5844–5849. <https://doi.org/10.1073/pnas.0710575105>
18. De La Zerda A, Zavaleta C, Keren S, Vaithilingam S, Bodapati S, Liu Z, Levi J, Smith BR, Ma T-J, Oralkan O, Cheng Z, Chen X, Dai H, Khuri-Yakub BT, Gambhir SS (2008) Carbon nanotubes as photoacoustic molecular imaging agents in living mice. *Nat Nanotechnol* 3:557–562. <https://doi.org/10.1038/nnano.2008.231>
19. Delogu LG, Vidili G, Venturelli E, Ménard-Moyon C, Zoroddu MA, Pilo G, Nicolussi P, Ligios C, Bedognetti D, Sgarrella F, Manetti R, Bianco A (2012) Functionalized multiwalled carbon nanotubes as ultrasound contrast agents. *Proc Natl Acad Sci* 109:16612–16617. <https://doi.org/10.1073/pnas.1208312109>
20. Lu F, Gu L, Meziani MJ, Wang X, Luo PG, Veca LM, Cao L, Sun Y-P (2009) Advances in bioapplications of carbon nanotubes. *Adv Mater* 21:139–152. <https://doi.org/10.1002/adma.200801491>
21. Saito N, Usui Y, Aoki K, Narita N, Shimizu M, Hara K, Ogiwara N, Nakamura K, Ishigaki N, Kato H, Taruta S, Endo M (2009) Carbon nanotubes: biomaterial applications. *Chem Soc Rev* 38:1897–1903. <https://doi.org/10.1039/B804822N>
22. Zhang Y, Bai Y, Yan B (2010) Functionalized carbon nanotubes for potential medicinal applications. *Drug Discov Today* 15:428–435. <https://doi.org/10.1016/j.drudis.2010.04.005>
23. Battigelli A, Ménard-Moyon C, Da Ros T, Prato M, Bianco A (2013) Endowing carbon nanotubes with biological and biomedical properties by chemical modifications. *Adv Drug Deliv Rev* 65:1899–1920. <https://doi.org/10.1016/j.addr.2013.07.006>
24. Raczyński P, Gorny K, Pabiszczak M, Gburski Z (2013) Nanoindentation of biomembrane by carbon nanotubes - MD simulation. *Comput Mater Sci* 70:13–18. <https://doi.org/10.1016/j.commatsci.2012.12.031>
25. Raczyński P, Górný K, Dawid A, Gburski Z (2014) Delivery of nitric oxide to the interior of mammalian cell by carbon nanotube: MD simulation. *Arch Biochem Biophys* 554:6–10. <https://doi.org/10.1016/j.abb.2014.04.014>
26. Raczynska V, Raczyński P, Gorny K, Gburski Z (2016) Nanoindentation of DMPC layer by nanotubes of various diameters. In: Fesenko O, Yatsenko L (eds) *Nanophysics, Nanophotonics, surface studies, and applications*. Springer, Berlin, pp 23–31
27. Raczyński P, Gorny K, Raczynska V, Pabiszczak M, Dendzik Z, Gburski Z (2017) On the impact of nanotube diameter on biomembrane indentation - computer simulations study. *Biochim Biophys Acta*. <https://doi.org/10.1016/j.bbame.2017.10.030>
28. Wallace EJ, Sansom MSP (2008) Blocking of carbon nanotube based nanoinjectors by lipids: a simulation study. *Nano Lett* 8:2751–2756. <https://doi.org/10.1021/nl801217f>
29. Pogodin S, Baulin VA (2010) Can a carbon nanotube pierce through a phospholipid bilayer? *ACS Nano* 4:5293–5300. <https://doi.org/10.1021/nn1016549>
30. Gangupomu VK, Capaldi FM (2011) Interactions of carbon nanotube with lipid bilayer membranes. *J Nanomater* 2011:e830436. <https://doi.org/10.1155/2011/830436>



31. Mpourmpakis G, Froudakis GE, Lithoxoos GP, Samios J (2006) SiC nanotubes: a novel material for hydrogen storage. *Nano Lett* 6:1581–1583. <https://doi.org/10.1021/nl0603911>
32. Lithoxoos GP, Samios J, Carissan Y (2008) Investigation of silicon model nanotubes as potential candidate nanomaterials for efficient hydrogen storage: a combined ab initio/grand canonical Monte Carlo simulation study. *J Phys Chem C* 112:16725–16728. <https://doi.org/10.1021/jp805559a>
33. Phillips JC, Braun R, Wang W, Gumbart J, Tajkhorshid E, Villa E, Chipot C, Skeel RD, Kalé L, Schulten K (2005) Scalable molecular dynamics with NAMD. *J Comput Chem* 26:1781–1802. <https://doi.org/10.1002/jcc.20289>
34. Humphrey W, Dalke A, Schulten K (1996) VMD: visual molecular dynamics. *J Mol Graph Model* 14:33–38. [https://doi.org/10.1016/0263-7855\(96\)00018-5](https://doi.org/10.1016/0263-7855(96)00018-5)
35. Casciola M, Bonhenry D, Liberti M, Apollonio F, Tarek M (2014) A molecular dynamic study of cholesterol rich lipid membranes: comparison of electroporation protocols. *Bioelectrochemistry* 100:11–17. <https://doi.org/10.1016/j.bioelechem.2014.03.009>
36. Dufourc EJ, Parish EJ, Chitrakorn S, Smith ICP (1984) Structural and dynamical details of cholesterol-lipid interaction as revealed by deuterium NMR. *Biochemistry (Mosc)* 23:6062–6071. <https://doi.org/10.1021/bi00320a025>
37. Raczynski P, Dawid A, Dendzik Z, Gburski Z (2005) Dielectric relaxation in water-cholesterol mixture cluster: molecular dynamics simulation. *J Mol Struct* 750:18–21. <https://doi.org/10.1016/j.molstruc.2005.03.036>
38. Jorgensen WL, Chandrasekhar J, Madura JD, Impey RW, Klein ML (1983) Comparison of simple potential functions for simulating liquid water. *J Chem Phys* 79:926. <https://doi.org/10.1063/1.445869>
39. MacKerell ADJ, Banavali N, Foloppe N (2000) Development and current status of the CHARMM force field for nucleic acids. *Biopolymers* 56. [https://doi.org/10.1002/1097-0282\(2000\)56:4<257::AID-BIP10029>3.0.CO;2-W](https://doi.org/10.1002/1097-0282(2000)56:4<257::AID-BIP10029>3.0.CO;2-W)
40. Guo CY, Montgomery Pettitt B, Wheeler LT (2006) Force field comparisons of the heat capacity of carbon nanotubes. *Mol Simul* 32:839–848. <https://doi.org/10.1080/08927020600962956>
41. Alexiadis A, Kassinos S (2008) Molecular simulation of water in carbon nanotubes. *Chem Rev* 108:5014–5034. <https://doi.org/10.1021/cr078140f>
42. Shi B, Zuo G, Xiu P, Zhou R (2013) Binding preference of carbon nanotube over pro line-rich motif ligand on SH3-domain: a comparison with different force fields. *J Phys Chem B* 117:3541–3547. <https://doi.org/10.1021/jp312423y>
43. Moradi Garakani F, Kalantarnejad R (2012) A molecular dynamics simulation of water transport through C and SiC nanotubes: application for desalination. *Int J Nano Dimens* 2:151–157
44. Henin J, Chipot C (2006) Hydrogen-bonding patterns of cholesterol in lipid membranes. *Chem Phys Lett* 425:329–335. <https://doi.org/10.1016/j.cplett.2006.04.115>
45. Schlenkrich M, Brickmann J, MacKerell AD, Karplus M (1996) An empirical potential energy function for phospholipids: criteria for parameter optimization and applications. In: Merz KM, Roux B (eds) *Biological membranes: a molecular perspective from computation and experiment*. Birkhäuser Boston, Boston, pp 31–81
46. Feller SE, Yin D, Pastor RW, MacKerell AD (1997) Molecular dynamics simulation of unsaturated lipid bilayers at low hydration: parameterization and comparison with diffraction studies. *Biophys J* 73:2269–2279. [https://doi.org/10.1016/S0006-3495\(97\)78259-6](https://doi.org/10.1016/S0006-3495(97)78259-6)



# Chapter 17

## Percolation Threshold of 5-Cyanobiphenyl Mesogene Phases Between Graphene Planes: Computer Simulation Study

Violetta Raczyńska, Krzysztof Górny, Przemysław Raczyński,  
and Zbigniew Dendzik

### 17.1 Introduction

Liquid crystals (LCs) combine the mobility of an isotropic liquid with the long-range orientational order normally associated with crystalline solids and have been used for applications that rely on their anisotropic electrooptical properties. The series of n-cyanobiphenyls (nCB; 4-n-alkyl- 4'-cyanobiphenyl) exhibit liquid crystalline phases at the temperatures near room temperature and have been intensively studied through experiment and with the use of computer simulation methods. 5-Cyanobiphenyl (5CB) was synthesized in 1972 as an outcome of research aiming at finding a mesogen for use in liquid crystal displays.

Ordering of the mesogene layers anchored at different substrates strongly depends on substrate morphology and homogeneity [1]. Because of this, anchoring of mesogenes at their interfaces with such substrates as graphene [2], carbon nanotubes [3], or polymer nanofibers [4] proved to significantly affect their electrooptic and dielectric properties and has been studied for fundamental scientific reasons as well as because of potential applications, such as designing and optimizing a variety of devices ranging from displays to organic field-effect transistors [5]. Graphene is one of the most promising substrates due to its unique 2D structure and mechanical, electrical, and optical properties. Aromatic nature of graphene and presence of

---

V. Raczyńska  
Institute of Physics, University of Silesia, Chorzow, Poland

K. Górny · P. Raczyński (✉) · Z. Dendzik  
Institute of Physics, University of Silesia, Chorzow, Poland

Silesian Center for Education and Interdisciplinary Research, University of Silesia, Chorzow,  
Poland

e-mail: [przemyslaw.raczynski@us.edu.pl](mailto:przemyslaw.raczynski@us.edu.pl)

two benzene rings in 5CB structure lead to the formation of planar alignment of anchored mesogene molecules.

## 17.2 Simulation Details

The model of 5CB mesogene, which has been proved to well describe the isotropic–nematic phase transition temperatures and the appropriate values of the order parameter assigned to these phases, has been adopted from the CHARMM-type united atom potential developed by Tiberio and co-workers [6].

Interactions between the mesogens have been described taking into account electrostatics and van der Waals forces modeled with Lennard-Jones 12–6 potential with Lorentz–Berthelot mixing rules and cutoff of 12 Å. Interactions between graphene sheets and 5CB molecules have been described with a model that accounts for van der Waals interactions modeled with Lennard-Jones 12–6 potential. Periodic boundary conditions (PBC) were applied and long-range interactions were calculated using particle mesh Ewald (PME) summation technique with grid spacing of 1.5 Å. Equations of motion were integrated for 20 ns, using the Brunger-Brooks-Karplus (BBK) scheme implemented in NAMD 2.9 [7] with the time step of integration of 1 fs. The simulation was performed in NVT ensemble, for temperature  $T = 270$  K, controlled with Langevin thermostat (damping coefficient  $\gamma = 5.0$  ps $^{-1}$ ). Visualizations were prepared with the use of VMD software [8].

The simulated system was composed of 63 5CB molecules located between two parallel graphene sheets (approx.  $70 \times 70$  Å). The distance between the sheets varied from 9 Å to 18 Å. The simulation cell was set to  $70.7 \times 72.4 \times 90.0$  Å. The value of z-component of simulation cell was large enough to minimize the self-interaction component of long-range electrostatic interaction between the primary layer and its PBC image. The remaining x- and y-components were selected to accommodate for the periodicity of the graphene sheets. Figure 17.1 shows the snapshot of the instantaneous configuration of 5CB mesogene phase between the graphene sheets at the lowest studied distance – 9 Å, forming single homogeneous layer.

## 17.3 Results and Discussion

We have studied the properties of the phases of 5CB embedded between two parallel graphene sheets. Geometrical constraints and anchoring effects moderate strongly structure and inner dynamics of the mesogenes. The accessible volume per 5CB molecule varies from 0.7 to 1.4 nm<sup>3</sup> for different distances between graphene planes (9–18 Å). Taking into account only the geometrical constraints, one would expect that dynamics of the system should significantly accelerate. Figure 17.2 shows calculated values of the Lindemann index  $\delta_L$  defined as [9].

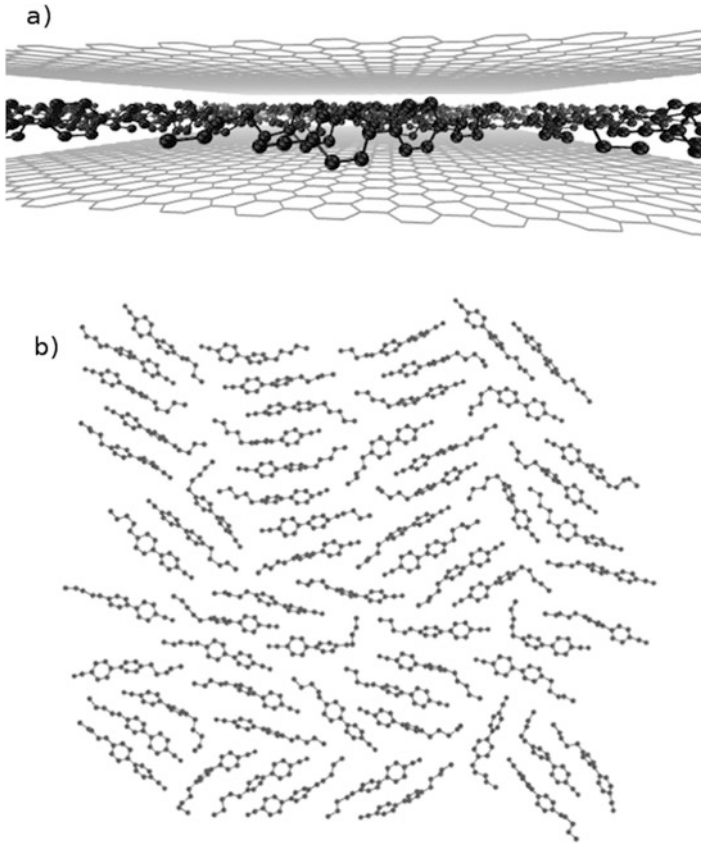


**Fig. 17.1** The instantaneous configurations of 5CB mesogene phase between the graphene sheets at the distance 9 Å: (a) side view; (b) top view

$$\delta_L = \frac{2}{N(N-1)} \sum_{i < j}^N \frac{\left( \langle r_{ij}^2 \rangle - \langle r_{ij} \rangle^2 \right)^{\frac{1}{2}}}{\langle r_{ij} \rangle},$$

where  $r_{ij}$  is the distance between the center of mass of  $i$ th and  $j$ th molecules.

Lindemann index can be related to the mobility of the molecules, and it seems too reasonable to expect that it will raise with the increasing value of the distance between the graphene planes. We can observe that the values of  $\delta_L$  are increasing up to the distance of 14 Å, but it decreases in the case of larger distances. This phenomenon can be explained in terms of physisorption (or anchoring) of the mesogenes at the graphene [10].

**Fig. 17.2** Lindemann index of the 5CB mesogenes located between graphene sheets, for different values of the distance between sheets

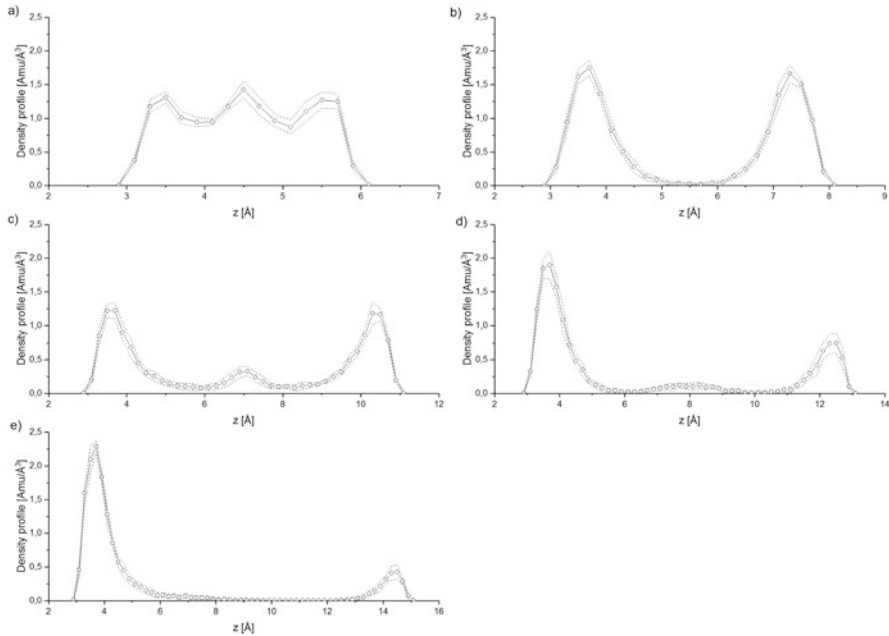
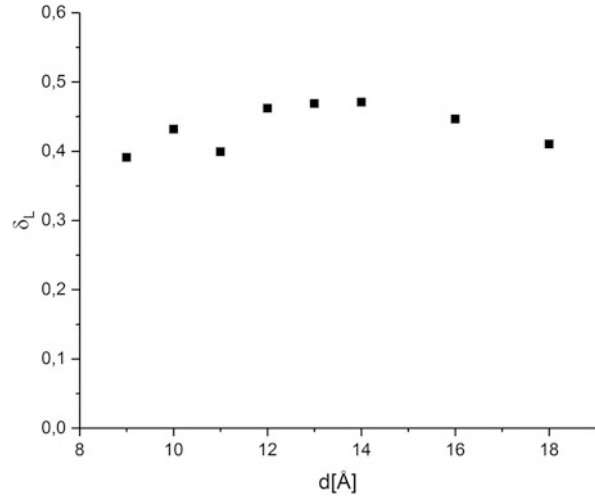
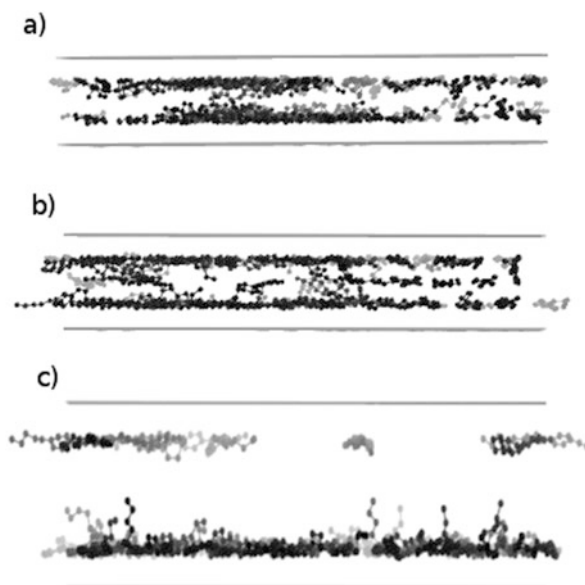


**Fig. 17.3** 5CB density profiles along  $z$ -axis calculated for different values of the distance between the graphene sheets: (a) 9 Å, (b) 11 Å, (c) 14 Å, (d) 16 Å, and (e) 18 Å

In order to confirm this, we calculated density profiles along  $z$ -axis using the VMD density profile plug-in [11]. Figure 17.3 shows the density profiles determined for different values of the distance between the graphene planes.

**Fig. 17.4** The visualizations of 5CB structure for different values of the distance between the graphene planes: (a) 13 Å, (b) 14 Å, and (c) 18 Å



The density profiles suggest that the increase of Lindemann index at interplanar distances  $d < 14$  Å can be attributed to the splitting of the single 5CB layer into two incomplete layers anchored on opposite graphene planes and frustration of 5CB molecules (Fig. 17.3b) – the molecules jump between two equivalent energy minima located in the vicinity of each graphene plane. For the distance  $d = 14$  Å, we can observe formation of additional residual intermediate layer (Fig. 17.3c). This configuration leads to the relaxation of this frustration. The molecules “choose” one out of two local minimas located near each graphene surface. This, in turn, leads to formation of single layer at randomly selected graphene plane (Fig. 17.3d, e).

These findings are supported by the visual inspection of 5CB configurations. Figure 17.4 presents the instantaneous configurations of the mesogenes located between graphene sheets. In Fig. 17.4a we can observe two incomplete layers formed at the interplanar distance of  $d = 13$  Å. In the next snapshot (Fig. 17.4b), these mesogen layers start to break apart and form the residual, highly unstable layer. Finally, the configuration shown in Fig. 17.4c represents relaxed 5CB structure, formed at interplanar distance  $d > 16$  Å.

The relaxation of the frustration process leading to the formation of single mesogen layer results with reduced molecular mobility reflected in the observed decrease of the Lindemann index (Fig. 17.2). Some residual remnants of the second layer (approx. 10% of the total number of mesogenes) still exists near the opposite graphene layer that can still be observed (Fig. 17.4c). The obtained density profiles and their evolution with the distance between restraining substrate surfaces suggest that the effect of anchoring is predominant in the formation of 5CB mesogen phases.

## 17.4 Conclusions

The process of forming 5CB mesogene phases anchored between graphene sheets is an outcome of a counterbalance between the interaction of the graphene surfaces with mesogene molecules and the volume accessible for the mesogenes. The increase of the distance between the planes while keeping the constant number of the mesogenes leads to the frustration of the system, relaxed eventually by further reduction of the mesogene density induced by further increase of the distance between the substrate surfaces. The reduction of mobility reported for the systems with higher distance between graphene planes can be attributed to the breaking of balance between the layers located near the opposite graphene sheets and rebuilding its structure as a single layer.

**Acknowledgment** This research was supported in part by PAAD Infrastructure co-financed by Operational Programme Innovative Economy, Objective 2.3.

## References

1. Roscioni OM, Muccioli L, Zannoni C (2017) Predicting the conditions for homeotropic anchoring of liquid crystals at a soft surface. 4-n-Pentyl-4'-cyanobiphenyl on Alkylsilane self-assembled monolayers. *ACS Appl Mater Interfaces* 9:11993–12002. <https://doi.org/10.1021/acsami.6b16438>
2. Alam TM, Pearce CJ (2014) Impact of graphene incorporation on the orientational order of graphene/liquid crystal composites. *Chem Phys Lett* 592:7–13. <https://doi.org/10.1016/j.cplett.2013.11.044>
3. Manjuladevi V, Gupta RK, Kumar S (2012) Effect of functionalized carbon nanotube on electro-optic and dielectric properties of a liquid crystal. *J Mol Liq* 171:60–63. <https://doi.org/10.1016/j.molliq.2012.03.026>
4. Rasna MV, Zuhail KP, Manda R, Paik P, Haase W, Dhara S (2014) Discontinuous anchoring transition and photothermal switching in composites of liquid crystals and conducting polymer nanofibers. *Phys Rev E* 89:052503. <https://doi.org/10.1103/PhysRevE.89.052503>
5. Rahman M, Lee W (2009) Scientific duo of carbon nanotubes and nematic liquid crystals. *J Phys D Appl Phys* 42:063001–063013. <https://doi.org/10.1088/0022-3727/42/6/063001>
6. Tiberio G, Muccioli L, Berardi R, Zannoni C (2009) Towards in silico liquid crystals. Realistic transition temperatures and physical properties for n-cyanobiphenyls via molecular dynamics simulations. *ChemPhysChem* 10:125–136. <https://doi.org/10.1002/cphc.200800231>
7. Phillips JC, Braun R, Wang W, Gumbart J, Tajkhorshid E, Villa E, Chipot C, Skeel RD, Kalé L, Schulten K (2005) Scalable molecular dynamics with NAMD. *J Comput Chem* 26:1781–1802. <https://doi.org/10.1002/jcc.20289>
8. Humphrey W, Dalke A, Schulten K (1996) VMD – visual molecular dynamics. *J Molec Graphics* 14:33–38. [https://doi.org/10.1016/0263-7855\(96\)00018-5](https://doi.org/10.1016/0263-7855(96)00018-5)
9. Allen MP, Tildesley DJ (1989) *Computer simulation of liquids*. Clarendon Press/Oxford University Press, Oxford [England]/New York

10. Górny K, Raczyński P, Dendzik Z, Gburski Z (2015) Odd–even effects in the dynamics of liquid crystalline thin films on the surface of single walled carbon and silicon carbide nanotubes: computer simulation study. *J Phys Chem C* 119:19266–19271. <https://doi.org/10.1021/acs.jpcc.5b05961>
11. Giorgino T (2014) Computing 1-D atomic densities in macromolecular simulations: the density profile tool for VMD. *Comput Phys Commun* 185:317–322. <https://doi.org/10.1016/j.cpc.2013.08.022>



# Chapter 18

## The Ultrasonic Treatment as a Promising Method of Nanosized Oxide CeO<sub>2</sub>-MoO<sub>3</sub> Composites Preparation



V. A. Zazhigalov, O. V. Sachuk, O. A. Diyuk, V. L. Starchevskyy,  
S. V. Kolotilov, Z. Sawlowicz, S. M. Shcherbakov, and O. I. Zakutevskyy

### 18.1 Introduction

The mixed systems based on cerium and molybdenum oxides were applied as photocatalysts for organic dyes degradation [1–3], catalysts supports, and also effective catalysts for environment protection, namely, oxidation CO [4], selective reduce of nitrogen oxides to ammonia [5, 6], etc. The number of publications connected with the use of Ce-/Mo-containing catalysts for acetaldehyde production from ethanol as an intermediate product for the synthesis of other chemicals such as acetic acid, acetic anhydride, ethyl acetate, butyl aldehyde, crotonaldehyde, pyridine, peracetic acid, and vinyl acetate exists, also [7–11].

The synthesis of Ce(x)/MoO<sub>3</sub> microparticles by impregnation method was presented in [1], and their agglomeration was shown. The mesoporous materials in highly dispersed state for this system were prepared by coprecipitation method

---

V. A. Zazhigalov (✉) · O. V. Sachuk · O. A. Diyuk · O. I. Zakutevskyy  
Institute for Sorption and Problems of Endoecology, National Academy of Sciences of Ukraine,  
Kyiv, Ukraine  
e-mail: [zazhigal@ispe.kiev.ua](mailto:zazhigal@ispe.kiev.ua)

V. L. Starchevskyy  
National University «Lviv Polytechnic», Lviv, Ukraine

S. V. Kolotilov  
L. V. Pisarzhevskii Institute of Physical Chemistry, National Academy of Sciences of Ukraine,  
Kyiv, Ukraine

Z. Sawlowicz  
Institute of Geology, Jagiellonian University, Krakow, Poland

S. M. Shcherbakov  
M. G. Kholodny Institute of Botany of the National Academy of Science of Ukraine, Kyiv,  
Ukraine

with high-temperature treatment [4]. The  $\text{MoO}_3\text{:CeO}_2$  nanofibers were obtained by a combination of sol-gel method and electrospinning technique [2] in water-ethanol solution with citric acid and polyvinyl alcohol addition. It is necessary to note that all known traditional methods of preparation of  $\text{CeO}_2\text{-MoO}_3$  compositions used the salts  $(\text{NH}_4)_6\text{Mo}_7\text{O}_{24} \times 4\text{H}_2\text{O}$  and  $\text{Ce}(\text{NO}_3)_3 \times 6\text{H}_2\text{O}$  as raw materials.

In this study the ultrasonic treatment as alternative method for nanocomposites preparation in Ce/Mo-O system was used. The commercial oxides of Ce and Mo were utilized as raw materials which permit characterizing this method as “environmentally clean” technology by the absence of harmful substances in production and the possibility to simplify of synthesis realization. It is possible to note that this technique was utilized for  $\text{Ce}(\text{MoO}_4)_2$  nanoparticles preparation [3], but the cerium and molybdenum salts and glucose as surfactant were used.

In this work the effect of sonochemical treatment on the properties of  $\text{CeO}_2\text{-MoO}_3$  mixtures with different composition ( $\text{CeO}_2/\text{MoO}_3 = 15:85, 25:75, 50:50, 75:25$ , molar ratio) was studied, and the structural, morphological, catalytic, and sorption properties of the prepared samples were determined.

## 18.2 Experimental

### 18.2.1 Sample Preparation and Synthesis

The preparation of the initial cerium-molybdenum oxide compositions with a molar ratio of  $\text{CeO}_2/\text{MoO}_3 = 15:85, 25:75, 50:50, \text{ and } 75:25$  was realized by mixing of  $\text{CeO}_2$  and  $\text{MoO}_3$  powders in agate mortar. All reagents employed were commercially available and directly used without further purification. For the sonochemical modification of composites, a dispersant UZDN-2 was used. The powder mixture (10 g) was placed in glass reactor and irradiated in aqueous medium during 1 h in effect of acoustic cavitation at a frequency of 22–40 kHz and a load of  $3 \text{ W/cm}^2$ . The temperature of the reaction medium was maintained at  $80 \text{ }^\circ\text{C}$  by circulating cold water around the reactor. Obtained suspensions were filtrated and dried in the air at  $120 \text{ }^\circ\text{C}$ .

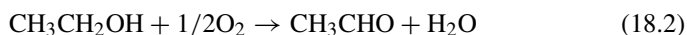
### 18.2.2 Characterization Methods and Techniques

Powder X-ray diffraction measurements were carried out on a diffractometer PW 1830 (Philips) with monochromatic  $\text{Cu K}\alpha$ -radiation ( $\lambda \approx 0.154 \text{ nm}$ ) in the range from  $10^\circ$  to  $90^\circ$  ( $2\Theta$ ). The average crystallite sizes ( $L$ ) were estimated by using Eq. (18.1), which is known as the Scherrer formula:

$$L = \frac{K\lambda}{\beta \cos \Theta} \quad (18.1)$$

where  $\beta$  represents the constant of FWHM,  $\lambda$  is the wavelength of the Cu  $K\alpha$  radiation,  $K$  is the constant parameter connector with crystal form and is 0.9, and  $\Theta$  is the diffraction angle.

FT-IR spectra ( $4500\text{--}400\text{ cm}^{-1}$ ) of the prepared samples were recorded on a "Spectrum-One" (Perkin-Elmer Instruments) spectrometer to use powder KBr (mass ratio sample/KBr = 1:20). EPR spectra were obtained on a Bruker Elexsys E580 FT/C at room temperature at a frequency of 9.2–9.9 GHz. Nitrogen physisorption experiments were carried out in a NOVA-2200 Gas Sorption Analyzer by Quantachrome. The measurement was performed at the boiling point of liquid  $N_2$  (77 K). The surface area was calculated according to the BET equation. Scanning electron microscopy was performed to use of Jeol JSM-6490 instrument in conjunction with an energy-dispersive spectrometer after deposition on a gold monolayer. TEM images were obtained with JEM-1230 (JEOL) high-resolution transmission electron microscope with an 80 kV accelerating voltage. Catalytic activity of the samples in the ethanol oxidation was tested in a flow fixed-bed stainless microreactor at atmospheric pressure in the temperature range of 25–300 °C. The catalyst ( $V = 0.5\text{ cm}^3$  with fraction 0.25–0.50 mm) was loaded into a reactor. Gas mixture containing 1 vol %  $C_2H_5OH$  in air was passed through the reactor at a total flow rate of 20  $\text{cm}^3/\text{min}$ . Initial components and reaction products have been analyzed by online gas chromatography, with flame ionization (FID) and thermal conductivity detectors (TCD). The reaction of ethanol partial oxidation to acetaldehyde occurs to the equation:



The ethanol conversion, acetaldehyde selectivity, and its yield were according to the following formulas:

$$X_{EtOH} (\%) = \frac{(C_{EtOH} (\text{in}) - C_{EtOH} (\text{out}))}{C_{EtOH} (\text{in})} \times 100\%, \quad (18.3)$$

$$S_{Ac} (\%) = \frac{C_{Ac}}{(C_{EtOH} (\text{in}) - C_{EtOH} (\text{out}))} \times 100\%, \quad (18.4)$$

$$Y_{Ac} (\%) = \frac{X_{EtOH} S_{Ac}}{100} \quad (18.5)$$

where  $X_{EtOH}$ , ethanol conversion %;  $S_{Ac}$ , selectivity of acetaldehyde;  $Y_{Ac}$ , acetaldehyde yield %;  $C_{EtOH} (\text{in})$ , initial ethanol molar concentration;  $C_{EtOH} (\text{out})$ , ethanol molar concentration after reactor; and  $C_{Ac}$ , acetaldehyde molar concentration after reactor.

The adsorption properties of obtained samples were studied in sorption organic dye safranin-T by the method [12]. The equilibrium concentration of safranin-T was determined by spectrophotometric method on the UV-2450 Shimadzu instrument. The initial ratio of the solid sample mass to volume solution was 1:4 (12.5 mg:

50 ml). The sorption degree ( $S$ ) and adsorption capacity ( $a$ ) were calculated by the Eqs. 18.6 and 18.7:

$$S = \frac{(C_0 - C_p)}{C_0} \times 100\%, \quad (18.6)$$

$$a = \frac{(C_0 - C_p) \times V}{m_c}, \quad (18.7)$$

where  $a$ , adsorption capacity, g/l;  $C_0$ , initial concentration of dye solution, g/l;  $C_p$ , equilibrium concentration, g/l;  $V$ , solution volume, ml; and  $m_c$ , sorbent mass, g.

### 18.3 Results and Discussion

Figure 18.1 shows the XRD patterns of  $\text{CeO}_2\text{-MoO}_3$  samples with different  $\text{CeO}_2$  and  $\text{MoO}_3$  content after sonochemical modification and initial composition  $\text{CeO}_2\text{-MoO}_3 = 50:50$  for comparison. Any new reflexes were observed in diffractograms. The XRD patterns exhibit sharp peaks of crystalline  $\alpha\text{-MoO}_3$ . It was established that treatment leads to an increase of  $\text{MoO}_3$  reflex intensity and changes the ratio of intensity of the main peaks of  $\text{MoO}_3$  for the planes (020) and (040). The last reflex is dominant for the samples after treatment in comparison with initial mixtures. The intensity of all reflexes connected with  $\text{CeO}_2$  decreases after UST. As result after treatment, the ratio between intensity of the crystallographic planes of  $\text{MoO}_3$  (040)/ $\text{CeO}_2$  (111) increases and in major degree for the sample  $\text{Ce/Mo} = 50:50$  where the change from 3.44 up to 13.2 was observed. The calculation of the particle dimensions shows that after UST, the crystallite size of  $\text{CeO}_2$  decreases for all compositions from 53–56 nm up to 35–45 nm. The most complex situation was observed for  $\text{MoO}_3$  (Table 18.1). The treatment leads to a decrease of particle dimensions according (020) to the plane and their sizes according (040) to the plane rest practically without change (or little increase of the size was observed). The obtained results permit to conclude that the chaotic destruction of  $\text{CeO}_2$  and anisotropic deformation of  $\text{MoO}_3$  proceed at sonochemical treatment of the oxides mixtures. The chemical reaction between components reported in [3] was not observed which can be connected with different raw materials used.

On the other hand, the destruction of initial oxides can be accompanied by formation of defects in their structure. This fact confirms by EPR data which demonstrate an appearance of  $\text{Ce}^{+3}$  signal with  $g = 1.96$  on the background of the singlet signal with  $g = 1.98$  which can assigned to  $\text{Mo}^{5+}$  in  $\text{MoO}_3$  for the samples after treatment.

The dimension of the oxides particles size leads to an increase of the samples specific surface area in 2–4 times (Table 18.1). Analogous changes in value of SSA were observed after sonochemical treatment of  $\text{ZnO-MoO}_3$  system [13, 14].

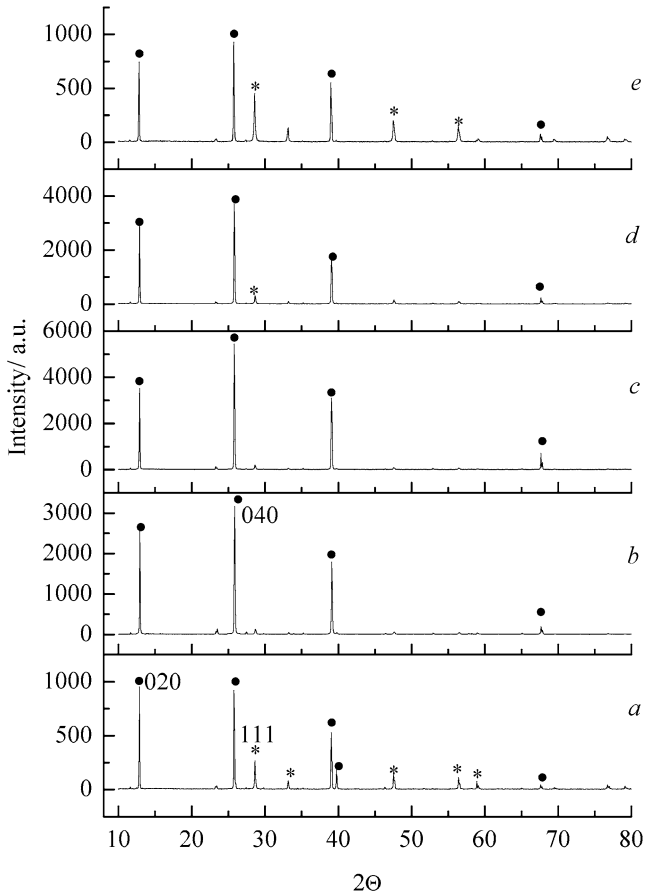


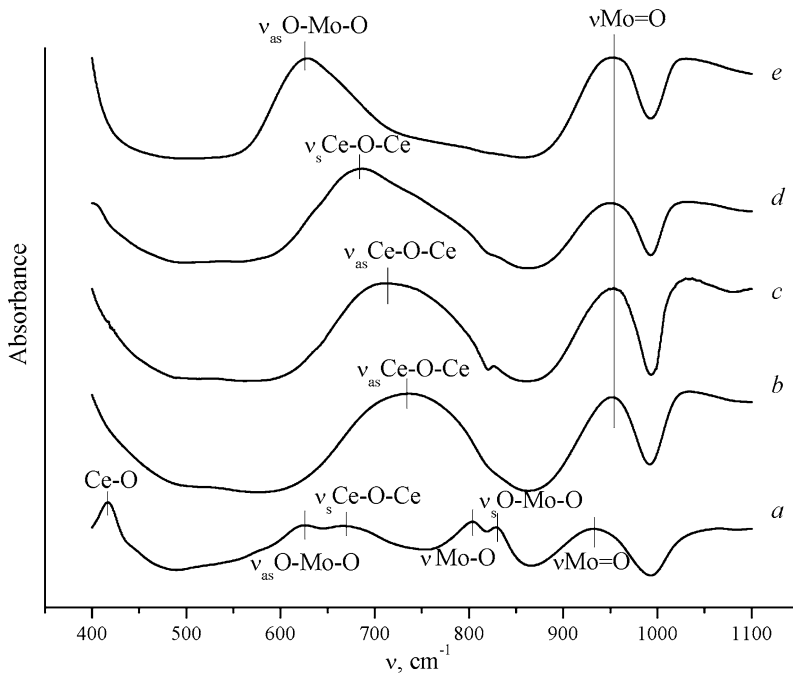
**Fig. 18.1** Diffractograms of the composition  $\text{CeO}_2\text{-MoO}_3$ : initial composition ( $\text{Ce}/\text{Mo} = 50:50$ ) (a), after UST for the compositions with ratio of  $\text{Ce}/\text{Mo} = 15:85$  (b),  $25:75$  (c),  $50:50$  (d),  $75:25$  (e) •  $\text{MoO}_3$ , \*  $\text{CeO}_2$

The data of  $\text{CeO}_2\text{-MoO}_3$  samples study by FT-IR method was presented in Fig. 18.2. It is necessary to note that presented spectrum of initial  $\text{Ce}/\text{Mo} = 50:50$  composition (Fig. 18.2a) is a characteristic for all other initial samples. This spectrum contains the wavenumbers at  $933$ ,  $830$ ,  $804$ ,  $670$ ,  $626$ , and  $416\text{ cm}^{-1}$  which can be attributed to the  $\text{Mo} = \text{O}$  vibrations [15],  $\nu_s$  O-Mo-O symmetric stretching of the distorted octahedral  $[\text{MoO}_6]$  units [16],  $\nu$  Mo-O vibrations [17], symmetric stretching vibrations in bridging  $\nu_s$  Ce-O-Ce linkages, distorted octahedral  $[\text{MoO}_6]$  units assigned as an asymmetric stretching  $\nu_{as}$  O-Mo-O, and  $\nu_{as}$  Ce-O terminal bonds of stretching modes, respectively.

It was found that UST leads to a change of samples spectra (Fig. 18.2b–e). The shift of the terminal  $\nu_{\text{Mo} = \text{O}}$  band from  $933\text{ cm}^{-1}$  up to  $954\text{ cm}^{-1}$  which is

**Table 18.1** Particles size of MoO<sub>3</sub> (XRD) and specific surface area (SSA) of CeO<sub>2</sub>-MoO<sub>3</sub> samples

Parameters	State of the sample	Molecular ratio CeO <sub>2</sub> /MoO <sub>3</sub>			
		15:85	25:75	50:50	75:25
L α-MoO <sub>3</sub> , 020/040, nm	Initial	95/62	90/61	93/61	96/60
	a.t. <sup>a</sup>	78/60	69/65	70/66	77/58
S <sub>BET</sub> , m <sup>2</sup> /g	Initial	1.5	1.5	1.7	2.0
	a.t.	3.2	3.6	5.5	6.6

<sup>a</sup>a.t. after treatment**Fig. 18.2** FT-IR spectra of the composition CeO<sub>2</sub>-MoO<sub>3</sub>: initial composition (Ce/Mo = 50:50) (a), after UST for the compositions with ratio of Ce/Mo = 15:85 (b), 25:75(c), 50:50 (d), 75:25 (e)

characteristic for layered, orthorhombic MoO<sub>3</sub> phase was observed. The peaks at 830, 804, and 626 cm<sup>-1</sup> connected with O-Mo-O and Mo-O-Mo bonds have very little intensity (exclusion is sample Ce/Mo = 75:25). These changes well correspond with proposed from XRD data anisotropic deformation of MoO<sub>3</sub> and formation of defects which will be confirmed by SEM and TEM study (see below). The shift in different direction of the bands for Ce-O-Ce and Ce-O bonds can testify the chaotic destruction of this oxide as result of treatment corresponding to XRD data.

The surface morphology of the compositions according to SEM data on example of the most typical sample with Ce/Mo = 50:50 is presented in Fig. 18.3. The initial

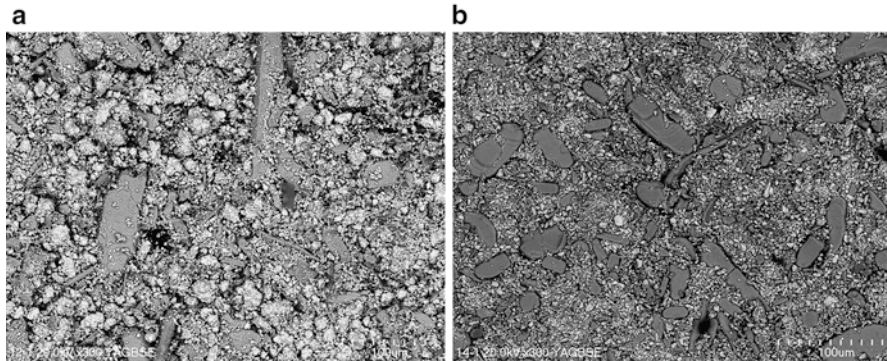


**Fig. 18.3** SEM images of  $\text{CeO}_2\text{-MoO}_3$  composition: initial (a) and after UST during 1 h (b)

**Table 18.2** Analysis of the Ce/Mo = 50:50 composition by EDS method

Sample Ce/Mo = 50:50	Analysis site	Element content, at. %	
		Ce	Mo
Initial	A	3.47	96.53
	B	100	–
UST 1 h	A	–	100
	B	95.97	4.03
	All surface	48.94	51.06

sample (Fig. 18.3a) is heterogeneous and contains two types of particles: big oblong particles (A) which according to EDS data (Table 18.2) can be destined to  $\text{MoO}_3$  and most finely dispersed particles (B) which correspond to  $\text{CeO}_2$ . The sonochemical treatment of the sample leads to a decrease of the dimensions of two types of particles (Fig. 18.3b). For  $\text{CeO}_2$  particles after UST, the same irregular shape (B) is observed. In contrary,  $\text{MoO}_3$  particles (A) change their habitus; more regular oblong platelet structures form. It is necessary to note that analogous change of  $\text{MoO}_3$  was observed at UST of  $\text{ZnO-MoO}_3$  system [13]. These results well correspond to data obtained by XRD method (see above) and confirm the chaotic destruction of  $\text{CeO}_2$  particles and anisotropic deformation of  $\text{MoO}_3$ .

The results of the samples study by TEM method were presented in Fig. 18.4. It can see for initial sample (Fig. 18.4a) presence of two types of particles: big oblong particles and more little particles with not defined shape, which can be determined in accordance with XRD and SEM data as  $\text{MoO}_3$  and  $\text{CeO}_2$ , respectively. The UST all samples (Fig. 18.4b–d) lead to a decrease of the dimensions of two types of particles and their habitus. The more determined oblong-like particles and rounded nanoparticles formed as result of treatment. The observed particles size practically corresponds to the data obtained from XRD (Table 18.1).

So, the different methods used for the UST sample properties study have shown the common results. The treatment was accompanied by a decrease of the initial oxides particles size and changed their habitus, but chemical reaction between

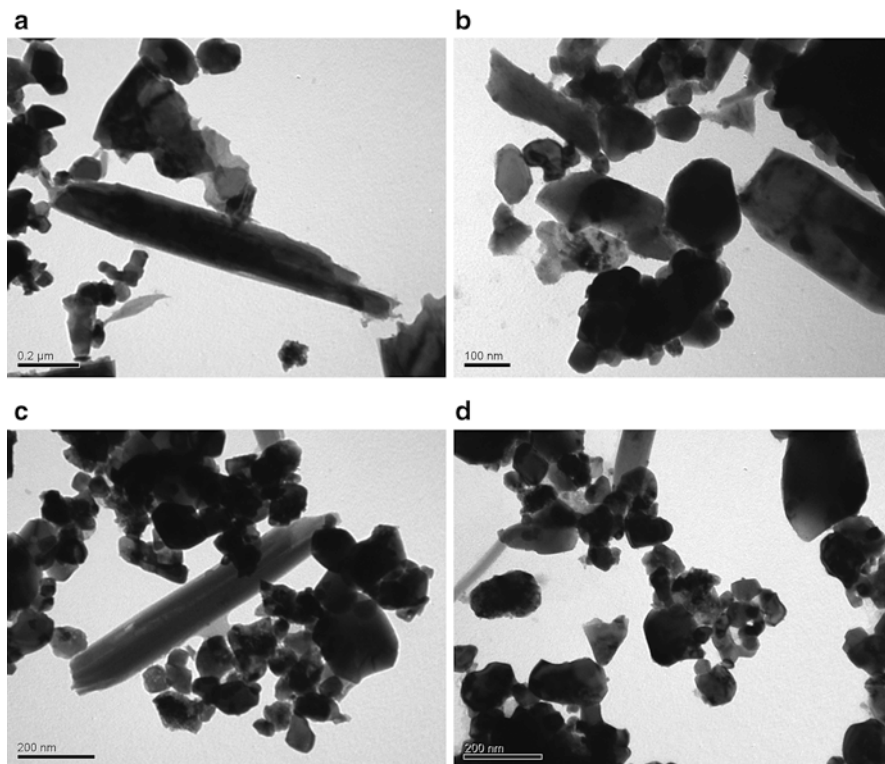


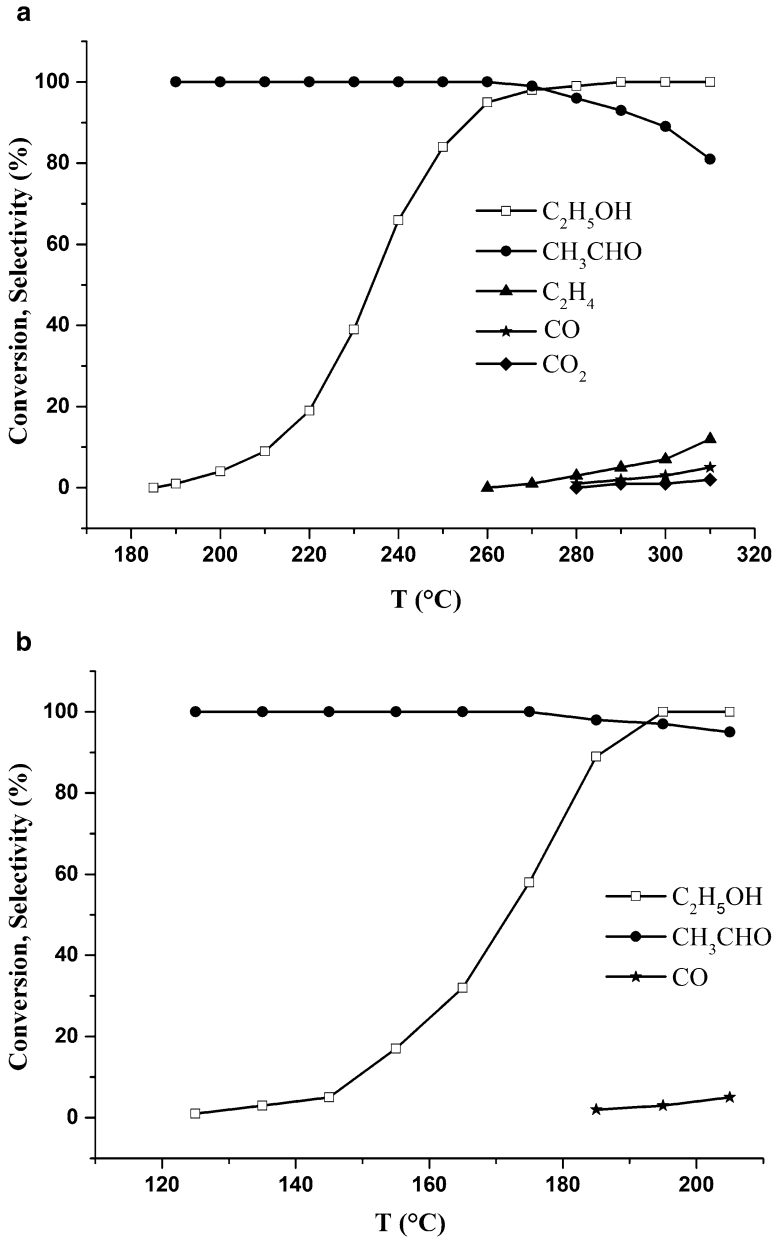
**Fig. 18.4** TEM images of  $\text{CeO}_2\text{-MoO}_3$  compositions: initial ( $\text{Ce}/\text{Mo} = 50:50$ ) (a), after UST ( $\text{Ce}/\text{Mo} = 15:85$ ) (b), ( $\text{Ce}/\text{Mo} = 50:50$ ) (c), and ( $\text{Ce}/\text{Mo} = 75:25$ ) (d)

oxides was not placed. On the other hand, the formation of structure defects was observed and not possible to exclude the presence of the more dense surface contact between oxides. These facts can influence on catalytic and adsorption properties of synthesized composites.

It is well known that the acetaldehyde production from ethanol has carried out Wacker's process with Pd and Cu chlorides as catalysts. The most promising method of acetaldehyde preparation is catalytic oxidative dehydrogenation of ethanol [18] or bioethanol as a renewable raw material. Some best-known results and catalysts for this reaction are presented in Table 18.3.

The study of the catalytic properties of  $\text{CeO}_2/\text{MoO}_3$  samples prepared by UST in this process shows that the better is composition with  $\text{CeO}_2/\text{MoO}_3 = 50:50$ . So, the temperature dependences of ethanol conversion and selectivity toward acetaldehyde and by-products ( $\text{CO}$ ,  $\text{CO}_2$ ,  $\text{C}_2\text{H}_4$ ) for initial  $\text{CeO}_2/\text{MoO}_3 = 50:50$  composition and after its UST are presented in Fig. 18.5. It is necessary to note that any other oxygen-containing products such as acetic acid, acetic anhydride, and ethyl acetate were observed in reactor outlet.

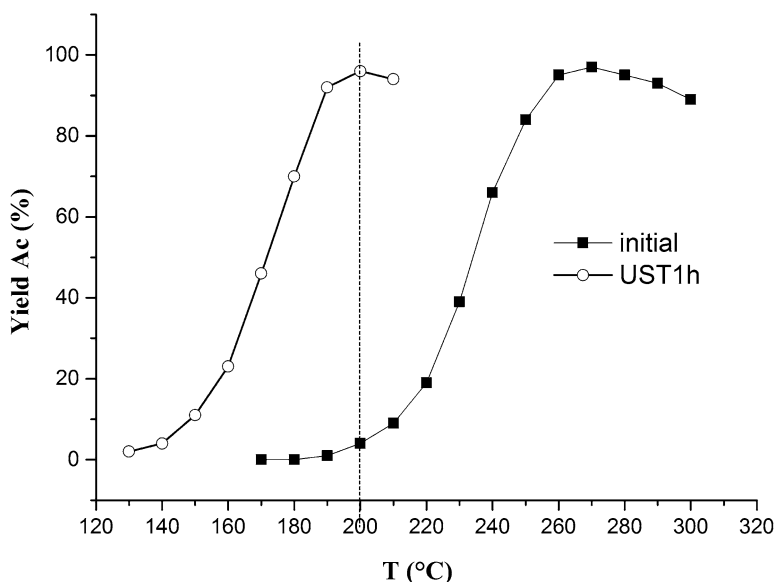




**Fig. 18.5** Temperature dependences of ethanol conversion (open symbols) and selectivity toward acetaldehyde and by-products (full symbols) for initial  $\text{CeO}_2/\text{MoO}_3 = 50:50$  composition (a) and after its UST (b)

**Table 18.3** Comparison of the catalysts properties in the gas-phase oxidation of ethanol to acetaldehyde

№	Catalysts	$T$ , °C	$X_{\text{EtOH}}$ , %	$S_{\text{Ac}}$ , %	$Y_{\text{Ac}}$ , %	References
1	Silver grid (industrial catalyst)	500	70	97	68	[10]
2	Mo-oxide/TiO <sub>2</sub>	200	85	90	77	[7]
3	CeO <sub>2</sub>	350	44	82	36	[11]
4	Ce/Mo–Sn–O	180	95	70	66	[9]
5	CeO <sub>2</sub> /MoO <sub>3</sub> = 50:50, initial	300	100	92	92	This paper
6	CeO <sub>2</sub> /MoO <sub>3</sub> = 50:50, UST	200	100	96	96	This paper

**Fig. 18.6** Temperature dependences of acetaldehyde yield for CeO<sub>2</sub>-MoO<sub>3</sub> = 50:50 samples before and after UST

The presented results (Fig. 18.5) show that the sample after UST demonstrates the better catalytic properties than initial composition: the full ethanol conversion is observed at lower reaction temperature ( $\Delta T = 100$  °C), and the selectivity to acetaldehyde is higher in this case (see Table 18.3, also). The dependence of acetaldehyde yield from temperature reaction presents in Fig. 18.6. It is shown that sample after UST at 200 °C permits to obtain the yield about 96%, while the initial composition demonstrates 4% only.

The increase of catalytic activity in accordance with literature data (e.g., [19, 20]) can be connected with an increase of specific surface area and decrease of particles size of the CeO<sub>2</sub>/MoO<sub>3</sub> composition (Table 18.1 and Fig. 18.4) as result of UST. On the other hand, the appearance of structural defects and more precise contacts between oxides can play role in an increase of catalytic effectiveness. The obtained results show (Fig. 18.7) that the yield of acetaldehyde remains without change after 15 h of operation.

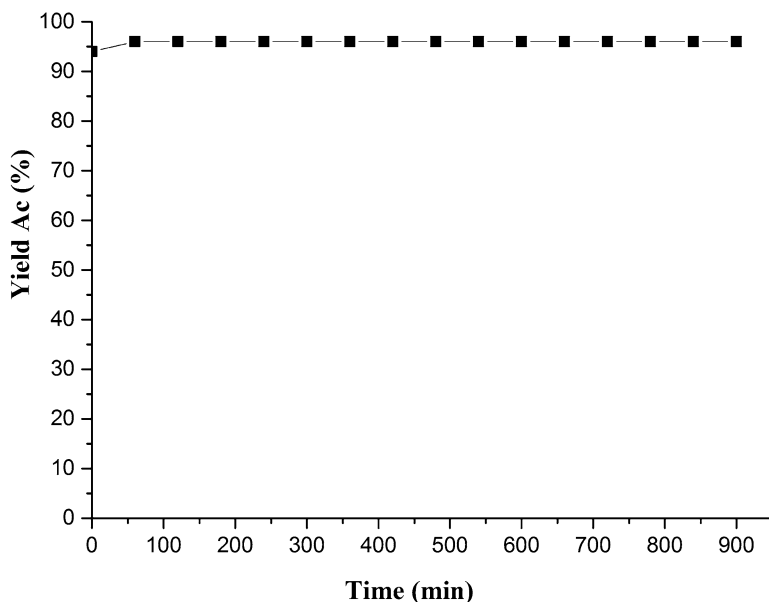


**Fig. 18.7** Influence of time operation on acetaldehyde yield. Reaction temperature is 200 °C. Catalyst –  $\text{CeO}_2/\text{MoO}_3 = 50:50$  after UST

The comparison of the obtained results with known literature data connected with oxidative dehydrogenation of ethanol to acetaldehyde (Table 18.3) shows that the  $\text{CeO}_2/\text{MoO}_3$  composition after sonochemical treatment demonstrates the better catalytic properties. This catalyst permits to obtain the high yield of acetaldehyde at low temperature reaction and demonstrate catalytic stability.

The adsorption of dye safranin-T from water solution on  $\text{CeO}_2/\text{MoO}_3$  samples is presented in Fig. 18.8. The obtained results show that linear dependence observes between adsorption capacity and specific surface area of the samples. All samples after UST demonstrate the higher adsorption compare with initial mixtures that is connected with an increase of specific surface area after treatment. The practically constant value of adsorption capacity determined to specific surface area (0.04–0.05  $\text{mg}/\text{m}^2$ ) of the samples confirms this assumption. The maximal quantity of dye adsorbed was observed for the sample with  $\text{CeO}_2/\text{MoO}_3 = 75:25$ . The removal efficiency of the dye in a series compositions  $\text{Ce}/\text{Mo} = 25:75$ , 50:50, and 75:25 is equal to 90, 94, and 97%, respectively.

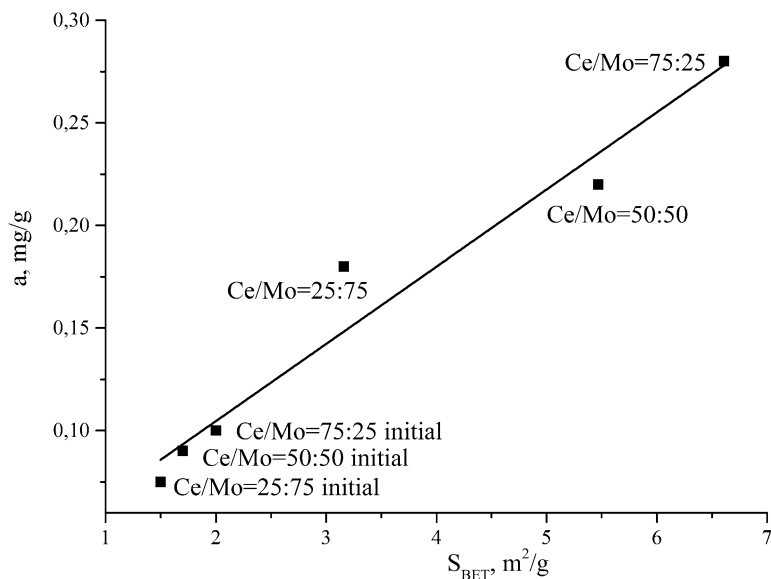


**Fig. 18.8** Dependence of safranin-T adsorption from specific surface area of the  $CeO_2$ - $MoO_3$  samples

## 18.4 Conclusion

The presented results show that ultrasonic treatment of oxide  $CeO_2$ - $MoO_3$  compositions leads to a decrease of molybdenum and cerium oxides particles size, without chemical reaction between them, as result of chaotic destruction of  $CeO_2$  and anisotropic deformation of  $MoO_3$ . An increase of specific surface area, the formation of structural defects (appearance of  $Ce^{3+}$  and  $Mo^{5+}$  ions), and possible strong surface interaction between oxides as result of treatment led to an essential activity of the treated samples in oxidative dehydrogenation of ethanol to acetaldehyde and high adsorption capacity for dye removal from water solutions.

**Acknowledgments** This work was financially supported by NASU Programs: Fundamental Research “New Functional Substances and Materials for Chemical Engineering” (project 7-17) and Program for Young Scientists (project 41- “Synthesis of new nanodispersed photocatalysts of environmental protection processes”).

## References

1. Jin Y, Li N, Liu H, Hua X, Zhang Q, Chen M, Teng F (2014) Highly efficient degradation of dye pollutants by Ce-doped  $MoO_3$  catalyst at room temperature. *Dalton Trans* 43(34):12860–12870

2. Zhao S, Li J, Wang L, Wang X (2010) Degradation of Rhodamine B and Safranin-T by  $\text{MoO}_3/\text{CeO}_2$  nanofibers and air using a continuous mode. *Clean (Weinh)* 38(3):268–274
3. Sobhani-Nasab A, Maddahfar M, Hosseinpour-Mashkani SM (2016)  $\text{Ce}(\text{MoO}_4)_2$  nanostructures: synthesis, characterization, and its photocatalyst application through the ultrasonic method. *J Mol Liq* 216:1–5
4. Mohamed MM, Katib SMA (2005) Structural and catalytic characteristics of  $\text{MoO}_3/\text{CeO}_2$  catalysts: CO oxidation activity. *Appl Catal A Gen* 287(2):236–243
5. Chang H, Jong MT, Wang C, Qu R, Du Y, Li J, Hao J (2013) Design strategies for P-containing fuels adaptable  $\text{CeO}_2\text{--MoO}_3$  catalysts for  $\text{DeNO}_x$ : significance of phosphorus resistance and  $\text{N}_2$  selectivity. *Environ Sci Technol* 47(20):11692–11699
6. Zhu J, Gao F, Dong L, Yu W, Qi L, Wang Z, Dong L, Chen Y (2010) Studies on surface structure of  $\text{M}_x\text{O}_y/\text{MoO}_3/\text{CeO}_2$  system ( $\text{M} = \text{Ni}, \text{Cu}, \text{Fe}$ ) and its influence on SCR of NO by  $\text{NH}_3$ . *Appl Catal B Environ* 95(1–2):144–152
7. Yoshitake H, Aoki Y, Hemmi S (2006) Mesoporous titania supported-molybdenum catalyst: the formation of a new mesophase and use in ethanol-oxygen catalytic reactions. *Microporous Mesoporous Mater* 93(1–3):294–303
8. Yang J-I, Lee D-W, Lee J-H, Hyun JC, Lee K-Y (2000) Selective and high catalytic activity of  $\text{Cs}_n\text{H}_{4-n}\text{PMo}_{11}\text{VO}_{40}$  ( $n \geq 3$ ) for oxidation of ethanol. *Appl Catal A Gen* 194–195:123–127
9. Gonçalves FM, Medeiros PRS, Appel LG (2001) The role of cerium in the oxidation of ethanol over  $\text{SnO}_2$ -supported molybdenum oxides. *Appl Catal A Gen* 208(1–2):265–270
10. Eckert M, Fleischmann G, Jira R, Bolt HM, Golka K (2006) Acetaldehyde, in: Ullmann's encyclopedia of industrial chemistry. Wiley-VCH, Weinheim. [https://doi.org/10.1002/14356007.a01\\_031.pub2](https://doi.org/10.1002/14356007.a01_031.pub2)
11. Li M, Wu Z, Overbury SH (2013) Surface structure dependence of selective oxidation of ethanol on faceted  $\text{CeO}_2$  nanocrystals. *J Catal* 306:164–176
12. Parfitt GD, Rochester CH (1983) Adsorption from solutions at the solid/liquid interface. Academic Press, London, p 416
13. Zazhigalov VA, Sachuk OV, Kopachevska NS, Starchevskyy VL, Sawlowicz Z (2017) Effect of ultrasonic treatment on formation of nanodimensional structures in  $\text{ZnO--MoO}_3$  system. *Theor Exp Chem* 53(1):51–57
14. Sachuk O, Kopachevska N, Kuznetsova L, Zazhigalov V, Starchevskyy V (2017) Influence of ultrasonic treatment on the properties of  $\text{ZnO--MoO}_3$  oxide system. *Chem Chem Technol* 11(2):152–157
15. Seguin L, Figlarz M, Cavagnat R, Lassegues J-C (1995) Infrared and Raman spectra of  $\text{MoO}_3$  molybdenum trioxides and  $\text{MoO}_3 \times x\text{H}_2\text{O}$  molybdenum trioxide hydrates. *Spectrochim Acta A* 51(8):1323–1344
16. Mancheva M, Iordanova R, Kamenova AA, Stoyanova A, Dimitriev Y, Kunev B (2007) Influence of mechanical treatment on morphology of the  $\text{MoO}_3$  nanocrystals. *Nanosci Nanotechnol* 7:74–76
17. Chiang TH, Yeh HC (2013) The synthesis of  $\alpha\text{-MoO}_3$  by ethylene glycol. *Materials* 6(10):4609–4625
18. Angelici C, Weckhuysen BM, Brijninx PCA (2013) Chemocatalytic conversion of ethanol into butadiene and other bulk chemicals. *ChemSusChem* 6(9):1595–1614
19. Solsona B, Zazhigalov VA, Lopez Nieto JM, Bacherikova IV, Diyuk EA (2003) Oxidative dehydrogenation of ethane on promoted VPO catalysts. *Appl Catal A Gen* 249(1):81–92
20. Zazhigalov VA, Diyuk EA, Sidorchuk VV (2014) Development of VPO catalysts supported on mesoporous modified materials based on an aerosil gel. *Kinet Catal* 55(3):380–389

# Chapter 19

## High-Temperature Electrochemical Synthesis of Nanopowders of Tungsten Carbide in Ionic Melts



Viktor Malyshev, Angelina Gab, Dmytro Shakhnin, Tetiana Lukashenko, Oleksandr Ishtvanik, and Marcelle Gaune-Escard

### Abbreviations

CNRS The National Center for Scientific Research of the French Ministry of Education and Research

### 19.1 Introduction

In [1, 2], it is shown that it is theoretically possible to achieve high-temperature electrochemical synthesis of highly dispersed powders of tungsten monocarbide. Lengthy experiments with high-temperature electrochemical synthesis of tungsten carbides have demonstrated significant variation in both the composition of the electrolyte and in the phase composition of the cathode deposit due to loss of some of the electrolyte with formation of a carbide-salt “bulb” (> 90% salt phase) and thermal decomposition and evaporation of the components of the melt. Adjustment of the melt and washing of the tungsten carbide free from electrolyte are, therefore, critical problems.

---

V. Malyshev · A. Gab · D. Shakhnin (✉) · T. Lukashenko · O. Ishtvanik  
University “Ukraine”, Kyiv, Ukraine  
e-mail: [ishtvanik@meta.ua](mailto:ishtvanik@meta.ua)

M. Gaune-Escard  
Ecole Polytechnique, CNRS UMR 6595, Technopôle de Chateau Gombert,  
Marseille Cedex 13, France

© Springer International Publishing AG, part of Springer Nature 2018  
O. Fesenko, L. Yatsenko (eds.), *Nanochemistry, Biotechnology, Nanomaterials, and Their Applications*, Springer Proceedings in Physics 214,  
[https://doi.org/10.1007/978-3-319-92567-7\\_19](https://doi.org/10.1007/978-3-319-92567-7_19)

## 19.2 Materials and Methods

To investigate the conditions under which tungsten carbide is synthesized, electrolyte having the following composition was selected, expressed in terms of mole percent,  $\text{Na}_2\text{WO}_4$ , 36.8;  $\text{Li}_2\text{WO}_4$ , 43.2; and  $\text{Li}_2\text{CO}_3$ , 20.0, or scaled on the basis of elements and oxides and expressed in terms of weight percent, Na, 7.18; Li, 3.72;  $\text{WO}_3$ , 78.21; and  $\text{CO}_2$ , 3.73. Sodium tungstate and lithium tungstate and lithium carbonate are carefully dried at  $T = 200\text{--}250\text{ }^\circ\text{C}$  for 3–4 h and mixed in an agate mortar. The prepared electrolyte is held in a platinum beaker at temperatures of 500, 800, and  $900\text{ }^\circ\text{C}$  until it attains a constant mass. At specified intervals of time, the beaker is removed from the furnace, cooled in a desiccator, and weighed. Once a constant mass is achieved, the melt is cooled and weighed and a sample selected for analysis in order to establish the content of Li, Na,  $\text{WO}_3$ , and  $\text{CO}_2$ .

Determination of the thermal stability of lithium carbonate and the dynamic course of variation of the concentration of lithium carbonate in the course of electrolysis is performed by means of chemical and thermogravimetric methods on the basis of the content of carbon dioxide in the electrolyte [3, 4]. The chemical method presupposes gasometric determination of the volume of  $\text{CO}_2$  released in the decomposition of a suspension of electrolyte by means of hydrochloric acid; the concentration of carbon dioxide is calculated in light of the dependence of the volume of the gas on temperature and atmospheric pressure.

The content of tungsten in the electrolyte is determined by the chemical method of acidic hydrolysis [5]; tungsten oxide formed as a result of decomposition by means of a mixture of  $\text{HNO}_3\text{-HF}$  (4:1) is subjected to calcination prior to analysis at a temperature of  $750\text{ }^\circ\text{C}$ .

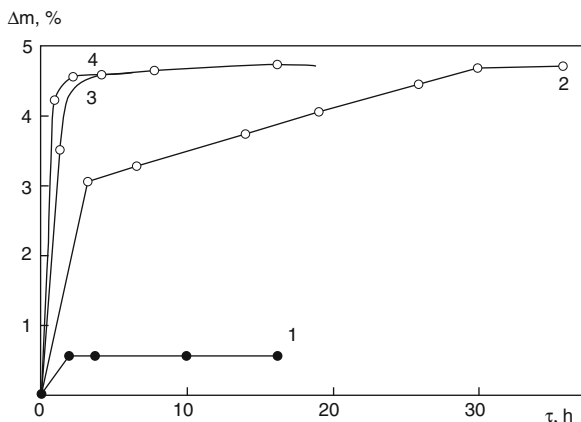
The content of Li and Na in the melt is estimated by means of atomic absorption spectroscopy [6] on a Pye-Unicam instrument; the percentage content of the elements was estimated from the intensity of waves of specific length from the given element upon combustion of the investigated solution in the flame of an air-acetylene or ethylene-oxide burner.

## 19.3 Results and Discussion

### 19.3.1 *Variation of Composition of Electrolyte in Isothermal Heating*

At a temperature of  $800\text{ }^\circ\text{C}$  and higher, lithium carbonate simultaneously evaporates (in the form of  $\text{Li}_2\text{CO}_3$ ) and decomposes with the release of  $\text{CO}_2$  until some steady state is attained. The latter steady state is established after 2–3 h under heating conditions at  $T = 800\text{--}900\text{ }^\circ\text{C}$  and after 30–35 h at  $T = 500\text{ }^\circ\text{C}$  (see Fig. 19.1). The maximum loss of the mass of electrolyte in the course of calcination is at most 4.5% (by weight). It is evident from the data of chemical and atomic

**Fig. 19.1** Loss of mass of electrolyte in calcination as a function of length of process. 1,  $\text{Na}_2\text{WO}_4\text{-Li}_2\text{WO}_4$  (53.6 M-%),  $T = 900\text{ }^\circ\text{C}$ ; 2, 3, 4,  $\text{Na}_2\text{WO}_4\text{-Li}_2\text{WO}_4$  (eutectic)- $\text{Li}_2\text{CO}_3$  (20 M-%),  $T = 500\text{ }^\circ\text{C}$  (2),  $T = 800\text{ }^\circ\text{C}$  (3),  $T = 900\text{ }^\circ\text{C}$  (4)



absorption analyses (Table 19.1) that loss of mass of a lithium tungstate or sodium tungstate eutectic is at most 0.5%. At the same time, lithium carbonate in  $\text{Na}_2\text{WO}_4\text{-Li}_2\text{WO}_4$  decomposes into 80–90% of the initial mass, with the concentration of  $\text{Li}_2\text{O}$  remaining practically constant. It may be supposed that in isothermal heating, free alkali ( $\text{Li}_2\text{O}$ ), a product of thermal decomposition of lithium carbonate, builds up in the melt.

Prior to melting down, the electrolyte contains 6.26% lithium carbonate, the source of carbon, or, scaled on the basis of  $\text{CO}_2$ , 3.73%, for use in synthesis of tungsten monocarbide. Once a steady state is attained at the electrolysis temperature, no more than 0.4%  $\text{CO}_2$  remains in the melt, 0.16% of which is consumed in the course of synthesis with optimal current conditions. In lengthy electrolysis, it is necessary to maintain a constant concentration of lithium carbonate to obtain a carbide with the stoichiometry of tungsten carbide. This requires analysis of the above data to determine the composition of the adjusting addition agent.

### 19.3.2 Influence of Length of Electrolysis on Composition of Bath and Cathode Deposit

Through the study of the dynamic nature of the development of the composition of the electrolyte in the course of electrolysis, it becomes possible to assess the overall process occurring in the electrolyte. Such a study also provides information necessary for determining the composition of the adjusting addition agent. Investigations were performed with an electrolyte having the composition given above with cathode current density  $1.5\text{ A/cm}^2$  and temperature  $850\text{ }^\circ\text{C}$  [2, 7].

A graphite crucible served as the anode and container for the melt. The composition of the salt component of the cathode deposit and of the electrolyte sample before and after electrolysis was studied by means of methods of chemical



**Table 19.1** Variation of composition of  $\text{Na}_2\text{WO}_4\text{-Li}_2\text{WO}_4\text{-Li}_2\text{CO}_3$  in the course of isothermal heating

Test no.	Composition of electrolyte	$T, ^\circ\text{C}$	$\Delta m, \%$	Composition of electrolyte, %									
				Before heating					After heating				
				Na	Li	$\text{WO}_3$	$\text{CO}_2$		Na	Li	$\text{WO}_3$	$\text{CO}_2$	
1	$\text{Na}_2\text{WO}_4\text{-Li}_2\text{WO}_4\text{-Li}_2\text{CO}_3$	500	4.48	7.17	3.72	76.62	4.18		7.78	4.25	75.7	1.08	
2	$\text{Na}_2\text{WO}_4\text{-Li}_2\text{CO}_3\text{-Li}_2\text{WO}_4$	800	4.45	7.14	3.7	78.2	3.71		7.77	3.59	76.15	0.19	
3	$\text{Na}_2\text{WO}_4\text{-Li}_2\text{WO}_4\text{-Li}_2\text{CO}_3$	900	4.46	6.82	3.85	78.2	4.65		6.75	3.99	77.74		
4	$\text{Na}_2\text{WO}_4\text{-Li}_2\text{WO}_4$	900	0.5	8.28	2.49	83.47	–		7.78	2.48	82.31	0.37	

**Table 19.2** Variation of electrolyte composition in the course of electrolysis without adjustment of electrolysis

$i_a \times 10^2, \text{ A/cm}^2$	Electric charge transmitted, $A \times h/l$	Composition of electrolyte, %			
		Na	Li	WO <sub>3</sub>	CO <sub>2</sub>
2.51	0	3.55	6.47	62.50	2.76
	15.0	3.41	6.64	63.50	1.80
	28.9	2.90	7.30	60.45	1.38
	0	3.47	6.20	59.74	1.60
4.80	28.0	3.32	7.79	60.75	2.30
	52.0	2.97	7.60	61.22	2.00
	72.0	2.63	–	62.63	1.60
	92.0	2.07	7.78	61.10	1.45
	0	4.05	6.81	61.12	2.06
10.0	60.0	2.78	7.12	60.59	2.05
	105.0	2.14	8.31	60.84	0.65

and atomic absorption analysis. In this study, as the electric charge transmitted through the melt is increased, it is found that the lithium and CO<sub>2</sub> concentration in the electrolyte decreases and the relative fraction of sodium decreases, while the content of tungsten remains practically constant (Table 19.2). This trend in the variation of the ratios between the concentrations of the components is characteristic of the entire range of anode current densities that were studied. The variation in the composition of the melt leads also to a qualitative variation in the phase composition of tungsten carbide (Table 19.3). It should be noted that the CO<sub>2</sub> concentration in the melt in the graphite crucible is significantly higher than in the platinum beaker (see Table 19.1) due to thermal oxidation of the graphite to CO<sub>2</sub>. From the data of Table 19.2, it also follows that at an anode current density  $1 \cdot 10^{-2} \text{ A/cm}^2$ , it is possible to achieve stabilization of the CO<sub>2</sub> content in the melt and, consequently, that of the Li<sub>2</sub>CO<sub>3</sub> content as well. Thus, through the use of the selected electrolysis parameters, it is possible to maintain a constant flux of electrolytic reducing components of the synthesis, a necessary condition for sustaining the lengthy process of producing tungsten carbide.

The variation in the phase composition of the cathode deposit points to the significant role played by the lithium content in the melt; as the lithium concentration in the melt falls down to 2.5%, a W<sub>2</sub>C phase appears in the cathode deposit, and it becomes necessary to adjust the melt with respect to lithium content. The data of Table 19.4 show that the lithium concentration in the salt component of the cathode deposit is roughly twice as high as in the melt; this supports the hypothesis of an electrochemical mechanism of synthesis described in [2, 7]. Moreover, the fact that the sodium content is insignificant may be ascribed to “mechanical” loss of Na<sub>2</sub>WO<sub>4</sub> from the melt.

On the basis of the data that have been obtained here, the composition of the adjusting addition agent needed to achieve an optimum electrolysis regime may be calculated; thus  $T = 850 \text{ }^\circ\text{C}$ ,  $i_c = 1.5 \text{ A/cm}^2$ ,  $i_a = 0.1 \text{ A/cm}^2$ , and electrolysis

**Table 19.3** Dependence of composition of cathode deposit on anode current density

Test no.	$i_a \times 10^2, A/cm^2$	Electric charge transmitted, $A \times h/l$	Phase composition
1	2.51	15.0	WC
2		13.9	WC
3		12.8	WC, $W_2C$
4		12.0	WC, $W_2C$
1	4.8	28.0	WC
2		24.0	WC
3		20.0	WC
4		20.0	$W_2C$
5		18.8	WC, $W_2C$
1	10.0	60.0	WC
2		45.0	WC

**Table 19.4** Composition of salt component of cathode deposits

Test no.	$i_a \times 10^2, A/cm^2$	Electric charge transmitted, $A \times h/l$	Composition of salt phase			
			Li	Na	W	CO <sub>2</sub>
1	4.8	28.0	4.75	1.06	56.7	0.6
2		24.0	8.12	0.94	53.5	0.65
3		20.0	7.63	0.95	62.6	0.50
4		20.0	7.69	1.62	64.8	0.45
1	10.0	60.0	7.74	0.63	53.64	0.4
2		45.0	7.10	0.97	64.76	0.6

time  $\tau = 1$  h. The adjusting addition agent constitutes a mixture of the following composition:  $Li_2WO_4$ , 86.45%;  $Li_2CO_3$ , 13.55%, and the initial electrolyte. The quantity of the mixture of lithium tungstate and lithium carbonate introduced into the electrolyte in the indicated ratio corresponds to the mass of the carbide-salt “bulb” removed from the melt. The mass of the initial electrolyte is determined from an analysis of the reduction of the level of the melt down to the break initial level.

The reliability of the calculated composition of the adjusting addition agent was repeatedly verified under laboratory conditions using the optimal electrolysis parameters presented above. The results of the analysis of the electrolyte in the course of electrolysis and the phase composition of the synthesis products show that it is possible to conduct long-term electrolysis in which a single-phase synthesis product is obtained, i.e., tungsten carbide (Table 19.5).

**Table 19.5** Phase composition of electrolysis products in melt  $\text{Na}_2\text{WO}_4\text{-Li}_2\text{WO}_4\text{-Li}_2\text{CO}_3$  with adjustment of electrolyte

Test no.	Electric charge transmitted, $A \times h/l$	Tungsten concentration in product, %	Lithium concentration in melt, %
1	20.0	82.3	3.66
2	18.4	84.6	–
3	17.0	86.7	3.37
4	20.0	85.9	–
5	18.4	89.9	–
6	16.6	89.8	2.73
7	20.0	88.9	–
8	18.0	89.8	3.42

Note.  $T = 850\text{ }^\circ\text{C}$ ,  $i_c = 1.5\text{ A/cm}^2$ ,  $i_a = 0.1\text{ A/cm}^2$ , product: tungsten carbide

### 19.3.3 *Technology of Washing Highly Dispersed Tungsten Monocarbide Cathode Powders from Electrolyte*

In high-temperature electrochemical synthesis of tungsten carbides, the cathode deposit constitutes a mixture of the target product with a salt phase. A technology for washing monocarbide from saline inclusions was developed. The conditions for washing were tried out with samples that had been synthesized under laboratory conditions. In this technology, the cathode deposits are added together with the electrodes and pulverized in order to accelerate their dissolution into heated water ( $T = 70\text{--}80\text{ }^\circ\text{C}$ ) with constant stirring. Following dissolution of the “bulb,” the sediment is filtered and washed in dilute hydrochloric acid to remove insoluble carbonates. Tungsten oxide and lithium carbonate are reclaimed from the filter (see next section). The deposit obtained following HCl treatment contains lowest tungstates and tungsten (VI) oxide that are poorly dissolved in water. These components are washed in alkaline solutions of sodium or ammonium hydroxide. When NaOH is used, the sediment is washed in a 10% solution heated to  $T = 60\text{--}70\text{ }^\circ\text{C}$  and then in heated water ( $60\text{--}70\text{ }^\circ\text{C}$ ) until  $\text{Na}^+$  is absent from the wash water. In the second variant, the deposit is washed in ammonium hydroxide, first in a concentrated (1:1) solution and then in a dilute 2.5% solution. Note that  $\text{NH}_4\text{OH}$  proves to be more preferable, since in the course of washing the target product free of  $\text{Na}^+$ , a portion of the deposit is lost as a result of peptization. The degree of washing of the deposit from  $\text{Na}^+$  and  $\text{Li}^+$  is adjusted on the basis of the content of these elements in the wash water. After having been washed free of salts, the tungsten monocarbide deposit is dried at  $T = 100\text{--}130\text{ }^\circ\text{C}$  to a constant mass. At higher temperatures, the sediment is rapidly oxidized from the oxygen in the air and may ignite. The conditions under which tungsten monocarbide is washed are presented in Table 19.6.

**Table 19.6** Conditions for washing tungsten monocarbide from electrolyte

Test no.	Mass of bulb, g	Volume of water in leaching, ml	V <sub>HCl</sub> (1:1), ml	V, ml	Yield of product, g	Tungsten content, %
Synthesis I						
1	564	2500	66	200	22.7	79.3
2	430	2000	100	700	27.8	89.0
Synthesis II						
1	500	4000	120	650	21.0	78.5
2	440	3520	110	800	21.2	82.0
3	425	3400	216	695	31.0	86.7
4	417	3400	100	880	26.9	84.0
5	400	3400	100	800	26.0	88.5
6	440	3500	100	950	29.5	89.1

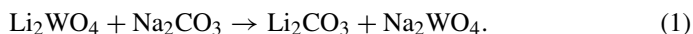
Note: Phase composition in all cases WC + C

The dried tungsten monocarbide is analyzed to determine the content of tungsten, bound carbon, and impurities, such as sodium, lithium, iron, nickel, copper, molybdenum, etc.; the content of impurities and of tungsten carbide is found at the level of several hundredths of a percent while that of free carbon 2–7% of the target product. The recommended regime of washing tungsten monocarbide free of the salt phase is as follows: leaching of the bulb of heated water ( $T = 70\text{--}80\text{ }^{\circ}\text{C}$ ) at a ratio  $W/S = 1:8$  and total yield of hydrochloric acid (1:1) 0.3 l and of ammonium hydroxide (1:1) 1.5 l per kilogram of cathode deposit. The yield of the target product amounts to 8–9% of the mass of the bulb.

Purification of tungsten monocarbide from free carbon is an important step. Free carbon may be removed from the carbides by annealing in a hydrogen medium [8, 9] at a temperature in the range 800–1000 °C. However, application of this annealing regime to powders measuring 0.1–0.5  $\mu\text{m}$  in dimension obtained by means of high-temperature electrochemical synthesis leads to removal of the carbon bound to the carbide even at temperatures of 700–800 °C. Positive results on purification of tungsten monocarbide were obtained by the present authors in [10, 11] in the course of annealing tungsten carbide in an activated hydrogen medium. The use of this strategy made it possible to remove free carbon and to reduce the content of sorbed oxygen down to 0.2–0.3%.

### ***19.3.4 Recovery of Tungsten and Lithium from Spent Electrolyte and Carbide-Salt Deposits***

In a carbide-salt bulb, the total mass of  $\text{Na}_2\text{WO}_4$ , lithium tungstate, and lithium carbonate significantly exceeds the mass of the target product. It is thus useful to recover these components of the synthesis for subsequent reuse. Electrolyte remaining in the electrolysis bath following conclusion of the synthesis process may also be subjected to reprocessing. Lithium is recycled into lithium carbonate. For this purpose the filtrate obtained following leaching of the cathode deposit or the electrolyte, which contains  $\text{Na}_2\text{WO}_4$  and  $\text{Li}_2\text{WO}_4$ , is concentrated by evaporation, and  $\text{Li}_2\text{CO}_3$  is deposited as sodium carbonate:



As a consequence of its low solubility in the water (not more than 7.3 g/l at  $T = 100\text{ }^{\circ}\text{C}$ ), lithium carbonate separates out into the deposit and passes readily through a filter. Following repeated washing in heated distilled water,  $\text{Li}_2\text{CO}_3$  is dried and repeatedly reused. 54% of the lithium contained in the salt phase of the cathode deposit is recovered. More complete deposition of  $\text{Li}_2\text{CO}_3$  requires multistage concentration by evaporation of the filtrate and sedimentation, which is not cost-effective.

Following separation of  $\text{Li}_2\text{CO}_3$  from the solution, tungsten is isolated in the form of tungstic acid. After leaching of the cathode deposit, the filtrate contains 60–80 g/l tungsten. Prior to deposition, the solution is concentrated by evaporation to 100 g/l W. Hydrochloric acid is used to produce the deposit. The nature of the deposit thus obtained depends on the concentration of the initial solution and the method of deposition employed. Poorly filtered deposits of white tungstic acid, i.e., hydrated tungsten trioxide, are obtained from cold and dilute solutions. To obtain easily filtered yellow tungstic acid ( $\text{H}_2\text{WO}_4$ ) heated to  $T = 60\text{--}80\text{ }^\circ\text{C}$ , a concentrated solution of tungstates is poured into a boiling HCl solution (1:1) to which a small quantity of  $\text{HNO}_3$  is added to prevent partial reduction of the tungsten. The quantity of hydrochloric acid is calculated on the basis of the fact that the concentration of free HCl in the final solution must be in the range 7–10%. After the entire solution has been mixed together, the pulp is poured through a filter. The  $\text{H}_2\text{WO}_4$  deposit is washed in a filter in a 2%  $\text{HNO}_3$  solution until it produces a negative reaction to chlorine ions.

The washed  $\text{H}_2\text{WO}_4$  deposit is dried and calcined to a constant mass at  $T = 500\text{ }^\circ\text{C}$ . At this temperature, tungstic acid completely loses all water in the course of being turned into tungstic acid anhydride:



The yield of  $\text{WO}_3$  amounts to 97–98% of the computed quantity in the electrolyte or bulb. Recycled lithium carbonate and tungsten trioxide are employed as reusable reagents for preparing adjusting addition agents.

## 19.4 Conclusions

1. It is established that free alkali  $\text{Li}_2\text{O}$ , a product of thermal decomposition of lithium carbonate, accumulates in the course of isothermal heating in a  $\text{Na}_2\text{WO}_4\text{-Li}_2\text{WO}_4\text{-Li}_2\text{CO}_3$  melt.
2. In lengthy electrolysis of tungstate-carbonate melts for the purpose of producing carbide with the stoichiometry of tungsten carbide, a constant concentration of the carbonate in the melt must be maintained.
3. It is shown that the phase composition of the cathode deposit is determined largely by the content of lithium carbonate in the melt.
4. Methods were developed in the study for use in washing cathode deposits and in recovery of tungsten and lithium from spent electrolyte and carbide-salt deposits.

**Acknowledgments** Authors of the present paper acknowledge support of all the Ecole Polytechnique and the University “Ukraine” staff in conducting scientific researches and writing this paper.

**Competing Interests** Authors of the present paper have no competing interests.

**Authors’ Contributions** Authors of the present paper have made equal contributions in conducting scientific researches and writing this paper.

**Funding** Authors of the present paper have not used any external sources of funding in addition to regular financing for scientific investigations provided by CNRS and the University “Ukraine.”

## References

1. Malyshev V, Shakhnin D, Gab A, Gaune-Escard M, Astrelin I (2014) Galvanic coatings of molybdenum and tungsten carbides from oxide melts: electrodeposition and initial stages of nucleation. In: Gaune-Escard M, Haarberg GM (eds) *Molten salts chemistry and technology*. Wiley, Chichester, pp 303–317
2. Malyshev VV, Soloviev VV, Chernenko LA, Rozhko VN (2015) Management of composition cathodic products in the electrolysis of molybdenum-, tungsten- and carbon-bearing halogenide-oxide and oxide melts. *Mater Werkst* 45:67–72
3. Almiyashev VI, Gusarov VV (1999) *Termicheskiye metody analiza* (Thermal methods of analysis). Saint-Petersburg State Electrotechnical University “LETT”, St. Petersburg
4. Shatalova TB, Shliakhtin OA, Veriaieva E (2011) *Metody termicheskogo analiza* (Methods of thermal analysis). Moscow State University, Moscow
5. Kharitonov YY, Dzhabarov DN, Grigorieva VY (2012) *Analiticheskaya khimiya* (Analytical chemistry). GEOTAR-Media, Moscow
6. Welz B, Sperling M (1999) *Atomic absorption spectrometry*, 3rd edn. Wiley-VCH, Weinheim
7. Malyshev VV, Novoselova IA, Gab AI, Shakhnin DB, Astrelin IM, Gaune-Escard M (2016) Tungsten carbide: high temperature electrochemical synthesis from ionic melts, technologies of obtaining and regeneration. In: Taylor JC (ed) *Advances in chemistry research*, vol 33. Nova Science Pub. Inc., New York, pp 71–124
8. Shapoval VI, Novoselova IA, Malyshev VV (2000) Properties of electrolytic dispersed powders of tungsten and molybdenum carbides. *Mater Sci* 36:111–117
9. Upadhyaya GS (1998) *Cemented tungsten carbides: production, properties, and testing*. Noyes Publications, Westwood
10. Malyshev VV, Gab AI, Uskova NN, Soloviev VV (2003) Structure and electrochemistry of tungsten-containing ionic melts. In: *Proceedings of the international symposium of ionic liquids in honour of Marcelle Gaune-Escard, Carry le Rouet, 26–28 June 2003*
11. Malyshev VV, Gab AI (2011) High-temperature electrometallurgical synthesis of molybdenum and tungsten carbides. *Russ J Non-Ferrous Met* 52:262–265



# Chapter 20

## Magnetic Memory of Antitumor Magneto-sensitive Nanocomplex



V. Orel, A. Shevchenko, O. Rykhalskyi, A. Romanov, A. Burlaka, and S. Lukin

### 20.1 Introduction

Drug delivery and release are important to improve the therapeutic effects of drugs and reduce toxic side effects during cancer chemotherapy [1]. Drug release and delivery into tumor can be improved using nanotechnology based on the utilization of the antitumor magneto-sensitive nanocomplex (AMNC) with magnetic memory effect. The magnetic memory effect is the ability of magnetic material (e.g., AMNC) to remember the magnetic field strength at which its shape was mechanically deformed [2].

Iron oxide nanoparticles (NPs) with spinel structure such as magnetite ( $\text{Fe}_3\text{O}_4$ ) are often used in antitumor treatment as AMNC placed in biocompatible magnetic fluids since they have a low toxicity and peculiar magnetic properties [3]. In recent years, a hybrid method of combined ultrahigh-field magnetic resonance imaging (MRI) with controlled and localized radio-frequency heating in the tumor has been

---

V. Orel (✉) · O. Rykhalskyi  
National Cancer Institute, Kyiv, Ukraine

National Technical University of Ukraine “Igor Sikorsky Kyiv Polytechnic Institute”, Kyiv, Ukraine

A. Shevchenko  
G.V. Kurdyumov Institute for Metal Physics of the National Academy of Sciences of Ukraine, Kyiv, Ukraine

A. Romanov  
National Cancer Institute, Kyiv, Ukraine

A. Burlaka · S. Lukin  
R.E. Kavetsky Institute of Experimental Pathology, Oncology and Radiobiology of the National Academy of Sciences of Ukraine, Kyiv, Ukraine

proposed. However, this type of therapy requires a sufficient tumor area to be covered by the NPs for successful treatment. But this can be difficult to achieve in real clinical practice. Also, hematogenous dissemination of metastatic tumors is also the one of the challenges for treatment by magnetic NPs [4, 5].

In order to overcome the above issues, we have proposed the magnetic resonance nanotherapy with magneto-mechano-chemically synthesized AMNC that have a magnetic memory effect. In our previous studies [6], it was shown that the treatment by AMNC consisted of iron oxide  $\text{Fe}_3\text{O}_4$  NPs and antitumor drug doxorubicin (DOXO) with simultaneous electromagnetic radiation using the magnetic resonance effect during moderate hyperthermia of Lewis lung carcinoma had the highest antitumor effect compared to the conventional DOXO or AMNC without electromagnetic radiation. This opens new prospects for development of personalized and individually optimized nanotechnology-based treatment protocols to be implemented in clinics for cancer patients at higher risks of tumor dissemination.

Furthermore, personalized synthesis of AMNC with manageable magnetic properties is a key component in the nanotechnology approach. It was earlier shown that the radio-frequency electromagnetic radiation in shortwave range and constant magnetic fields impact on magnetic memory (the magnetic properties) of magneto-mechano-chemically synthesized AMNC [7, 8].

In view of the previously found correlation between mechanical stress and magnetic properties in nanometer Fe films [9], this paper sheds new light on understanding the nonlinear interactions of mechanical and electromagnetic phenomena in AMNC. Therefore, we have studied the influence of mechanical vibration and electromagnetic irradiation on the AMNC magnetic properties during magneto-mechano-chemical synthesis.

## 20.2 Materials and Methods

### 20.2.1 Magneto-Mechano-Chemical Synthesis

$\text{Fe}_3\text{O}_4$  NPs (International Center for Electron Beam Technologies of E.O. Paton Electric Welding Institute, Ukraine) with diameters in the range of 20–40 nm and DOXO (Actavis, Romania) were processed in a high-precision magneto-mechanical milling chamber (NCI, Ukraine), which was designed according to a typical scheme for the magnetic resonance apparatus. The samples of  $\text{Fe}_3\text{O}_4$  and DOXO were placed in the diamagnetic chamber together with metallic balls. Mechanical processing was performed by vertical vibrations of the chamber at frequencies 15, 20, 25, 30, and 35 Hz and an amplitude of 9 mm for 5 min. Simultaneously, ER with frequency 42 MHz and output power of 2 W for 5 min in combination with constant magnetic field with induction 8 mT was applied. In addition, we have investigated the magnetic properties of magneto-mechano-chemically activated iron oxide NPs (without DOXO), mechano-chemically synthesized AMNC without electromagnetic radiation, and a mixture of DOXO and  $\text{Fe}_3\text{O}_4$  NPs without any influence.

### 20.2.2 Magnetic Studies

The magnetic properties were studied through magnetometry using the “Vibrating Magnetometer 7404 VSM” (Lake Shore Cryotronics Inc., USA) with magnetic fields up to 13 kOe. The magnetometer’s sensitivity was  $10^{-7}$  emu which allowed measuring the magnetic moment of samples weighing milligrams. The mass was determined by the electronic microbalance AB135-S/FACT with auto-identification (Mettler Toledo, Switzerland) which had a sensitivity of  $10^{-5}$  g.

### 20.2.3 Electron Spin Resonance (ESR) Spectroscopy

ESR spectra were recorded with the spectrometer RE1307 at liquid nitrogen temperatures (77 K) in a cylinder resonator with the mode  $H_{011}$  and frequency 9.15 GHz. The power of microwave radiation was 40 mW, and the magnetic field modulation frequency was 100 kHz. The samples were placed in a quartz Dewar flask with an inner diameter of 4.5 mm.

## 20.3 Experimental Results

### 20.3.1 Magnetic Studies of $Fe_3O_4$ Nanoparticles

The results of magnetic studies of magneto-mechano-chemically activated  $Fe_3O_4$  NPs are shown on Fig. 20.1 and Table 20.1.

The data analysis testifies that parameters of the samples exposed to various vibration frequencies had a significant quantitative difference in comparison to the sample exposed to ER only and the sample without any influence. The studies found a negative correlation ( $r = -0.63$ ) between the saturation magnetic moment  $m_s$  and vibration frequency  $f$ . It is known that the coercivity  $H_c$  is the intensity of an applied magnetic field required to reduce the magnetization of the material to 0 after the magnetization of the sample had been driven to saturation. Thus, coercivity measures the resistance of a ferromagnetic material to demagnetization. The greater the coercivity, the higher the specific absorption rate (SAR) of electromagnetic field is detected [10]. In our experiments, all samples had low coercivity  $H_c$  and a small area of the hysteresis loop  $S$  that can be classified as soft magnetic materials. The changes of coercivity  $H_c$  and area of the hysteresis loop  $S$  in NPs after magneto-mechano-chemically activation did not have any correlation with vibration frequencies.

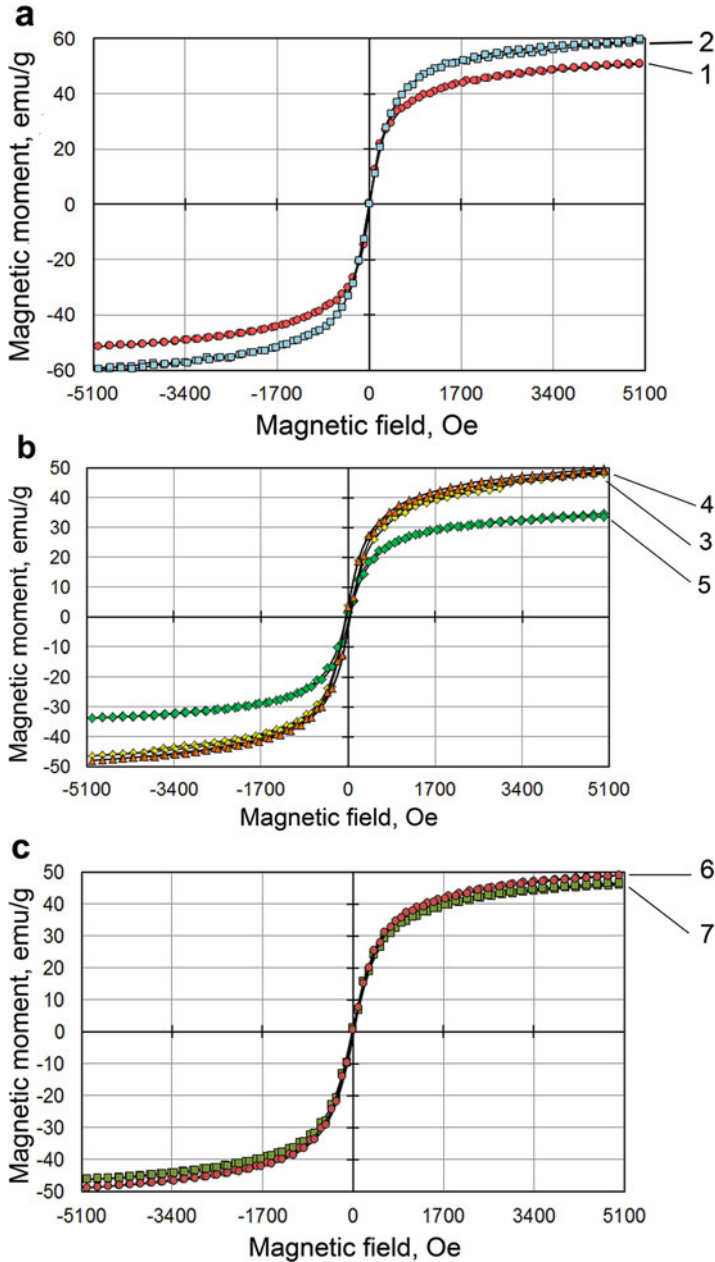


**Fig. 20.1** The hysteresis loops of magneto-mechano-chemically activated  $\text{Fe}_3\text{O}_4$  NPs at 300 K: (a) 1, without influence; 2, ER. (b) 3, mechanical vibration 15 Hz and ER; 4, mechanical vibration 20 Hz and ER; 5, mechanical vibration 25 Hz and ER. (c) 6, mechanical vibration 30 Hz and ER; 7, mechanical vibration 35 Hz and ER. ER in all experiments: 42 MHz and induction of constant magnetic field 8mT

**Table 20.1** Magnetic properties of magneto-mechano-chemically activated Fe<sub>3</sub>O<sub>4</sub> NPs.  $T = 300$  K

Sample	Vibration frequency, $f$ , Hz	Saturation magnetic moment $m_s$ , emu/g	Coercivity $H_c$ , G	Area of the hysteresis loop $S$ , erg/g
1	Without influence	51.30	6.12	3721
2	ER	59.70	4.29	1008
3	15	48.42	45.69	23,544
4	20	49.49	34.40	23,671
5	25	34.16	22.90	5653
6	30	48.89	9.02	4742
7	35	46.44	17.42	3821
Pearson correlation coefficient $r$ (samples 2–7) with vibration frequency		−0.63	0.04	−0.09

### 20.3.2 Magnetic Studies and ESR Spectroscopy of AMNC

The magnetic studies and ESR spectroscopy of AMNC are given in Figs. 20.2 and 20.3 and Table.20.2.

The analysis of the presented data reveals that all investigated properties of samples 3–7 after synthesis under the influence of fixed vibration frequencies and ER differed from the values of similar magnetic properties in control samples 1 and 2. The saturation magnetic moment  $m_s$  and area of the hysteresis loops  $S$  were found to have larger values in magneto-mechano-chemically synthesized AMNC. The saturation magnetic moment  $m_s$  had a positive correlation ( $r = 0.8$ ) with vibration frequencies. The coercivity  $H_c$  on the contrary showed smaller values in magneto-mechano-chemically synthesized AMNC with a negative correlation ( $r = -0.87$ ) with vibration frequencies. A relative intensity ESR of magneto-mechano-chemically synthesized AMNC had a positive correlation ( $r = 0.63$ ) with vibration frequencies.

## 20.4 Discussion

The saturation magnetic moments  $m_s$  of the iron oxide NP samples were higher than in corresponding AMNC samples. However, Pearson correlation coefficient of this parameter with the vibration frequency was negative ( $r = -0.63$ ) for NPs and positive ( $r = 0.8$ ) for AMNC. On contrary, coercivity  $H_c$  in AMNC had a negative correlation ( $r = -0.87$ ) with the vibration frequency. The AMNC had a smaller area of the hysteresis loop  $S$  than the NPs.

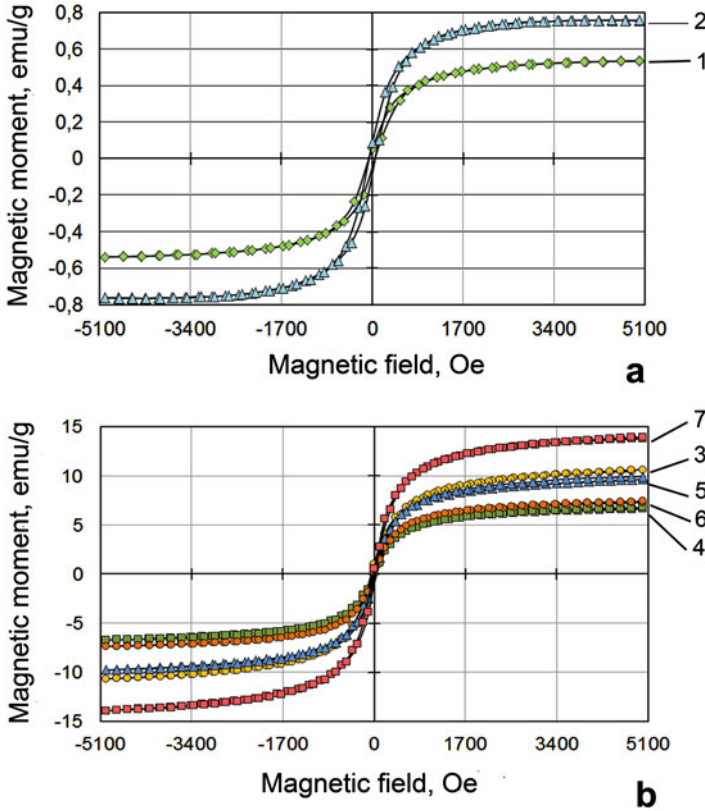


**Fig. 20.2** The hysteresis loops of magneto-mechano-chemically synthesized AMNC of  $\text{Fe}_3\text{O}_4$  NPs and DOXO at 300 K: (a) 1, without influence; 2, ER. (b) 3, mechanical vibration 15 Hz and ER; 4, mechanical vibration 20 Hz and ER; 5, mechanical vibration 25 Hz and ER; 6, mechanical vibration 30 Hz and ER; 7, mechanical vibration 35 Hz and ER. ER in all experiments: 42 MHz and induction of constant magnetic field 8mT

Thus, a logical question arose: Why did the iron oxide NPs and antitumor drug doxorubicin cause such changes compared to the conventional NPs in our experiments?

The obtained results can be explained by Villari (the magnetoelastic) effect and the influence of magnetic fields on physicochemical reactions. Villari effect can be observed as a result of the change in magnetic field strength achieved within the nanocrystalline core of the iron oxide NPs due to mechanical stress. According to Hooke's law, the stress tensor is described by the following equation:

$$\sigma_{ij} = dF_{ij}/dS_{ij}, \quad (1)$$

where  $F_{ij}$  is the surface force and  $S_{ij}$  is the surface area.

**Fig. 20.3** The ESR spectrum of magneto-mechano-chemically synthesized AMNC at 300 K: 1, mechanical vibration 15 Hz and ER; 2, mechanical vibration 20 Hz and ER; 3, mechanical vibration 25 Hz and ER; 4, mechanical vibration 30 Hz and ER; 5, mechanical vibration 35 Hz and ER; 6, without influence; 7, ER. ER in all experiments 42 MHz and induction of constant magnetic field 8mT

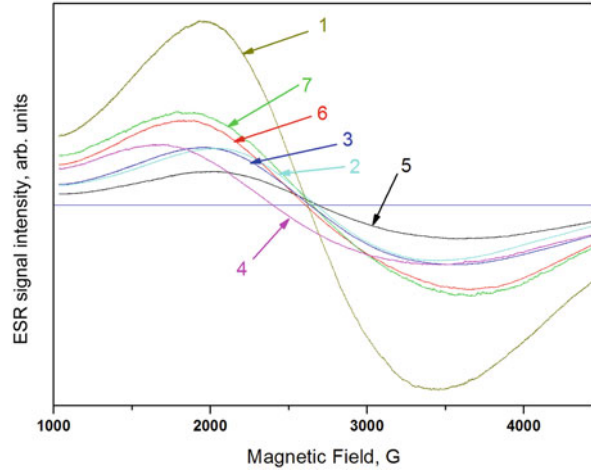


**Table 20.2** Magnetic properties of AMNC ( $\text{Fe}_3\text{O}_4$  NPs and DOXO) after MMCS

Sample	Vibration frequency, Hz	Saturation magnetic moment $m_s$ , emu/g	Coercivity $H_c$ , G	Area of the hysteresis loop $S$ , erg/g	Relative intensity ESR, arb. units	$g$ -factor
1	Without influence	0.54	55.94	148	1.67	2.47
2	ER	0.76	57.96	189	0.49	2.42
3	15	10.67	51.22	2058	0.57	2.46
4	20	6.75	16.65	372	0.64	2.70
5	25	9.85	21.88	201	0.33	2.41
6	30	7.39	9.99	455	0.93	2.48
7	35	13.94	18.17	1777	1	2.45
Pearson correlation coefficient $r$ (samples 2–7) with vibration frequency		0.8	-0.87	0.26	0.63	-

In paper [11] it was theoretically shown the mechanical interaction between the electromagnetic field and the nanoscopic thin film near electronic resonance by calculation of Maxwell's stress tensor. The expression of the Maxwell stress tensor illustrates that the electric and magnetic fields have quite a different behavior under mechanical deformation, although they are both vector fields:

$$\sigma_{ij} = \varepsilon_0 E_i E_j + \frac{1}{\mu_0} B_i B_j - \frac{1}{2} \left( \varepsilon_0 E^2 + \frac{1}{\mu_0} B^2 \right) \delta_{ij}, \quad (2)$$

where  $\varepsilon_0$  is the electric constant and  $\mu_0$  is the magnetic constant,  $E$  is the electric field,  $B$  is the magnetic field, and  $\delta_{ij}$  is Kronecker's delta.

In our experiments under fixed frequency vibration during magneto-mechano-chemical synthesis, we had differences in the magnetic memory response for conventional iron oxide NPs ( $\text{Fe}_3\text{O}_4$ ) and nanocomplex from the core ( $\text{Fe}_3\text{O}_4$ ) – shell (oxide film and DOXO). It may be assumed that the difference in the magnetic memory response is related to the spin-dependent radical pair states on the surface layers of conventional iron oxide NPs and NPs loaded with DOXO. The magnetic memory effect originates from the interaction of a magnetically ordered layer in the magnetite shell and the spins located at the interface  $\text{Fe}_3\text{O}_4/\text{DOXO}$ .

This can be explained with well-known effect of the Zeeman spectral line splitting on several components for paramagnetic centers (free radicals) in the presence of a constant magnetic field. Then a resonant radio-frequency irradiation under fixed vibration frequency can cause the transition from one electron spin state to another switching between a spin forbidden, nonreactive triplet spin state of a radical pair and a spin-allowed, chemically reactive singlet state [12, 13]. These phenomena are based on the magnetic nuclear and electron spin resonance [14].

The probability of a transition between singlet and all three triplet states of the radical pair under the influence of an electromagnetic field  $H_i(\tau)$ , associated with electronic transitions during resonance, could be determined by modified equation [15]:

$$P = \frac{1}{2} \left( \frac{g\beta}{\hbar} \right)^2 \frac{H_1^2(\tau)}{1 + (g\beta/\hbar)^2 (H_0 - H_0^{\text{res}})^2}, \quad (3)$$

where  $g$  is Lande  $g$ -factor,  $\beta$  is the Bohr magneton,  $H_0$  is the external constant magnetic field strength,  $H_0$  is the external resonance constant magnetic field strength,  $H_i$  is the external resonance electromagnetic field strength,  $\tau$  is the lifetime of a radicals pair, and  $\hbar$  is the reduced Planck constant.

Ability to control the concentration of paramagnetic centers via mechanical, magnetic, and electromagnetic can help to increase the activity, concentration, and lifetime of paramagnetic centers (free radicals), which might cause oxidative stress, genetic mutation, and/or apoptosis of tumor cells [16].

## 20.5 Conclusion and Future Perspectives

This paper shows the impact of combined mechanical vibration and electromagnetic irradiation on the magnetic memory effect during the magneto-mechano-chemical synthesis of the AMNC. This research opens the future way for remote control of redox reactions within the tumor based on the magnetic memory effect in AMNC without changing standard treatment doses for widely used chemotherapeutic agents. Furthermore, limitation side effects of magnetic nanoparticle hyperthermia [17] associated with high temperature may be avoided in clinical practices due to decreased upper temperatures reached by the proposed approach in the treatment of deep-seated malignant tumors.



## References

1. Liang XJ, Chen C, Zhao Y et al (2010) Circumventing tumor resistance to chemotherapy by nanotechnology. *Methods Mol Biol* 596:467–488
2. Yasar Razaq M, Behl M, Lendlein A (2012) Magnetic memory effect of nanocomposites. *Adv Funct Mater* 22(1):184–191. <https://doi.org/10.1002/adfm.201101590>
3. Gobbo OL, Sjaastad K, Radomski MW et al (2015) Magnetic nanoparticles in cancer theranostics (review). *Theranostics* 5(11):1249–1263. <https://doi.org/10.7150/thno.11544>
4. Maier-Hauff K, Ulrich F, Nestler D et al (2011) Efficacy and safety of intratumoral thermotherapy using magnetic iron-oxide nanoparticles combined with external beam radiotherapy on patients with recurrent glioblastoma multiforme. *J Neuro-Oncol* 103:317–324. <https://doi.org/10.1007/s11060-010-0389-0>
5. Winter L, Oezerdem C, Hoffmann W et al (2015) Thermal magnetic resonance: physics considerations and electromagnetic field simulations up to 23.5 Tesla (1GHz). *Radiat Oncol* 10:201
6. Orel V, Shevchenko A, Romanov A et al (2015) Magnetic properties and antitumor effect of nanocomplexes of iron oxide and doxorubicin. *Nanomedicine* 11:47–55
7. Orel VE, Shevchenko AD, Rykhalskiy OY et al (2015) Investigation of nonlinear magnetic properties magneto-mechano-chemical synthesized nanocomplex from magnetite and antitumor antibiotic doxorubicin. In: Fesenko O, Yatsenko L (eds) *Nanocomposites, nanophotonics, nanobiotechnology and applications*, vol 156. Springer Proceedings in Physics, pp 103–110. [https://doi.org/10.1007/978-3-319-06611-0\\_8](https://doi.org/10.1007/978-3-319-06611-0_8)
8. Orel V, Shevchenko A, Rykhalskiy O et al (2017) Influence of radio frequency electromagnetic irradiation on magnetic properties of magneto-mechano-chemically synthesized antitumor nanocomplex. In: Fesenko O, Yatsenko I (eds) *Nanocomposites, nanophotonics, nanobiotechnology and applications*, vol 195. Springer Proceedings in Physics, pp 813–826. [https://doi.org/10.1007/978-3-319-56422-7\\_62](https://doi.org/10.1007/978-3-319-56422-7_62)
9. Sander D, Skomski R, Enders A et al (1998) The correlation between mechanical stress and magnetic properties of ultrathin films. *J Phys D Appl Phys* 31:663–670
10. Tumanski S (2011) *Handbook of magnetic measurements*. CRC Press, Boca Raton
11. Iida T, Ishihara H (2002) Study of the mechanical interaction between an electromagnetic field and a nanoscopic thin film near electronic resonance. *Opt Lett* 27:754–756
12. Woodward JR, Jackson RJ, Timmel CR (1997) Resonant radiofrequency magnetic field effects on a chemical reaction. *Chem Phys Lett* 272:376–382
13. Buchachenko AL, Berdinsky VL (2002) Electron spin catalysis. *Chem Rev* 102:603–612. <https://doi.org/10.1021/cr010370l>
14. Barnes FS, Greenebaum B (2015) The effects of weak magnetic fields on radical pairs. *Bioelectromagnetics* 36:45–54. <https://doi.org/10.1002/bem.21883>
15. Zel'dovich YB, Buchachenko AL, Frankevich EL (1988) Magnetic-spin effects in chemistry and molecular physics. *Sov Phys Usp* 31:385–408
16. Ghodbane S, Lahbib A, Sakly M et al (2013) Bioeffects of static magnetic fields: oxidative stress, genotoxic effects, and Cancer studies. *Biomed Res Int* 2013:1. <https://doi.org/10.1155/2013/602987>
17. Johannsen M, Thiesen B, Wust P et al (2010) Magnetic nanoparticle hyperthermia for prostate cancer. *Int J Hyperther* 26(8):790–795. <https://doi.org/10.3109/02656731003745740>

# Chapter 21

## Nonlinear Optical Properties of Polymer Nanocomposites with a Random and Periodic Distribution of Silver Nanoparticles

T. N. Smirnova, V. I. Rudenko, and V. O. Hryn

### 21.1 Introduction

Nanocomposites based on optically transparent matrices with embedded noble metal nanoparticles (NPs) have become an important research subject for the development of new materials for photonics, since these materials possess unique optical and electronic properties. Their specific properties are mainly attributed to the quantum and dielectric confinement effects and excitation of local surface plasmons in the metal NPs [1–4] that is accompanied by the appearance of plasmon absorption bands in the optical region of the spectrum.

Irradiation of composites with high-power light pulses at frequencies close to plasmon resonance leads to a significant enhancement of local electric field near the surface of metallic NPs that is the main cause of the giant nonlinear response of metal-containing nanocomposites. The high values of nonlinearity and velocity of nonlinear response of nanocomposites make them promising materials for the creation of high-speed nonlinear devices, for example, optical limiters and ultrafast optical switches [5–7].

Doped-glass and polymer-based nanocomposites, being the most widely used optical materials, exhibit particularly promising features for the application in linear and nonlinear optics, laser physics, and optoelectronics [2, 3]. In addition to the high flexibility of their structure and properties, polymers are relatively cheap and simple to manufacture as compared to glasses. Polymers can also act as effective stabilizers of metallic NPs, preventing their aggregation. And finally, the use of

---

T. N. Smirnova (✉) · V. I. Rudenko · V. O. Hryn  
Institute of Physics, National Academy of Sciences of Ukraine, Kyiv, Ukraine  
e-mail: [smirnova@iop.kiev.ua](mailto:smirnova@iop.kiev.ua); [val@iop.kiev.ua](mailto:val@iop.kiev.ua); [vohryn@iop.kiev.ua](mailto:vohryn@iop.kiev.ua)

photopolymerizable composites opens the possibility to create periodic distribution of NPs in polymer matrix by a simple one-step holographic polymerization method [8, 9].

Due to the limited size of NPs, their electron dynamics differs substantially from the case of bulk medium and is governed by the laws determined by both the properties of individual metallic nanoparticles and their spatial organization and the properties of the dielectric matrix [10–14]. This opens up the possibility to control the nonlinear properties of nanocomposites, which is easier to implement when using polymer matrices.

One of the ways to control the plasmon properties of nanocomposites is sub-micrometer scale structuring [15, 16]. Ordered structures with a submicron period can be used for the creation of optical memory and neural networks [17], as sensors [18], diffraction elements of a new type with ultrahigh spectral dispersion [19, 20], or distributed feedback cavities of waveguide lasers [21].

Nowadays, nonlinear properties of NPs of various sizes and shapes are being investigated, starting from metal clusters comprising several atoms to nanoparticles consisting of tens of thousands of atoms. Theoretical description of the properties of systems of different sizes requires different approaches and does not always allow to explain and even more so to predict the results of the experiment.

Thus, despite many years of research of metal-doped nanocomposites, this direction remains relevant both from the point of view of further development of theory of nonlinear processes and seeking technologically simple and economically expedient methods to create structures with required properties.

Nanocomposites are most often created using silver, gold, and copper nanoparticles. Silver NPs are of particular interest, because their absorption bands in the optical spectral region are characterized by higher oscillator strength than that of Au and Cu NPs [22] and references in it. Thus higher nonlinear absorption coefficients can be expected for Ag nanoparticles compared to Au and Cu NPs under equal conditions. In addition the overlapping of plasmon and interband absorption bands is less pronounced for Ag nanoparticles. For them, the energy of interband transition is of about 4 eV (the energy of plasmon resonance is approximately 2.8 eV), whereas for Au and Cu NPs, the interband transition energy is 2.3 and 2.6 eV, respectively. This allows investigating nonlinear optical processes caused solely by surface plasmons at moderate excitation intensities.

A large number of works are devoted to the study of Ag-doped nanocomposites, for example, [22–39], and references therein. An exhaustive bibliography of researches performed before 2004 is given in [26]. The nonlinear properties of Ag NP colloidal solutions [26, 27, 29], layers of Ag NPs applied to various substrates [25], or nanoparticles incorporated in various inorganic matrices [22–24, 28, 30] and polymers [31–38] are explored.

While earlier studies paid more attention to nonlinear properties of nanocomposites based on “neutral” matrices, characterized by extremely low nonlinear response, recent works concentrate on the development and study of multicomponent composites, where metal NPs are used to further enhance the nonlinear response, luminescence efficiency, and other properties. As mentioned above, polymers open

up great possibilities for varying the composition of nanocomposite. The rare earth-doped borate nanocrystallites embedded in polyvinyl alcohol polymer matrices with Ag NPs [35], polydiacetylene–silver nanocomposite [36], and liquid crystalline elastomer nanocomposite with embedded Ag NPs [37] can serve as examples. The introduction of Ag NPs in azobenzene polymer film does not only significantly enhance the nonlinear response of the composite but also increases the reorientation rate of azo polymer [38].

The distribution of Ag NPs in the matrix was random in all the abovementioned nanocomposites. In our work we investigated the influence of Ag NPs ordering in a polymer matrix on the nonlinear properties of a nanocomposite. We used the photopolymer composite developed by us, which allows producing periodic Ag NPs–polymer structures by holographic lithography method. The nonlinear optical properties of the random and ordered structures were measured by the Z-scan method using radiation with a wavelength ( $\lambda_{\text{ex}}$ ) of 532 nm and a pulse duration ( $\tau$ ) of 20 ns, as well as radiation with  $\lambda_{\text{ex}} = 800$  nm and  $\tau = 180$  fs.

## 21.2 Experimental Details

Nonlinear optical characteristics of the composites were measured by Z-scan technique using the nanosecond and femtosecond lasers. The basic experimental scheme is shown in Fig. 21.1. In a nanosecond time range, measurements were performed at the wavelength of the second harmonic of a pulsed Nd:YAG laser with the following output characteristics: pulse duration  $\tau = 20$  ns, wavelength  $\lambda_{\text{ex}} = 532$  nm, and repetition rate  $f = 0.5$  Hz. The parameters of the measurement scheme were the lens focal length, 10 cm; the aperture diaphragm diameter, 1 mm; the aperture transmittance  $S = 0.14$ ; and the beam diameter in focal plane,  $68 \mu\text{m}$ . The intensity of the laser beam in focus was  $I_0 = 5 \text{ MW/cm}^2$ .

In the femtosecond experiment, the titanium–sapphire laser Mira 900F with a wavelength  $\lambda_{\text{ex}} = 800$  nm was used; the pulse duration was 180 fs, and repetition rate was of about 75 kHz. The laser beam was focused by a lens with a focal length

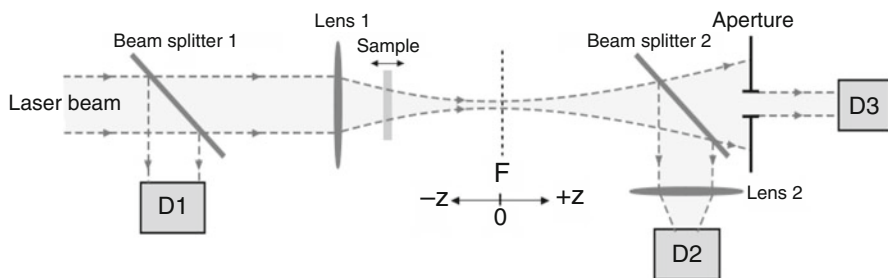


Fig. 21.1 Scheme of the Z-scan setup (D1, D2, D3 – photodetectors)

of 35 cm. The diameter of the beam in the focus was 58  $\mu\text{m}$ ; aperture transmittance was 0.36. The intensity of the laser beam in the focus was  $I_0 = 0.14 \text{ GW/cm}^2$ .

The real (Re) and imaginary (Im) parts of the complex third-order susceptibility  $\chi^{(3)}$ , the nonlinear absorption coefficient  $\beta$ , and the nonlinear refractive index  $n_2$  were calculated by the method proposed by Sheik-Bahae et al. [40].

The mentioned laser radiation parameters were chosen to avoid the influence of thermal accumulative effect on experimental results. The measurements were repeated several times to ensure the reproducibility of the results. In our experiments, there were no irreversible changes in the transmission. The repetition of measurements for a pure matrix showed an absence of nonlinear response under the same conditions.

## 21.3 Results and Discussion

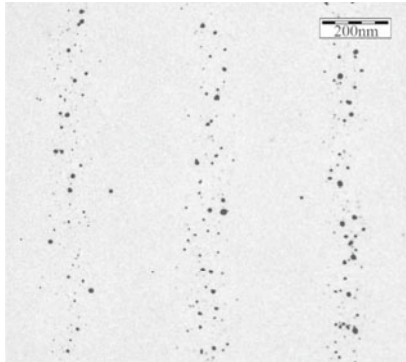
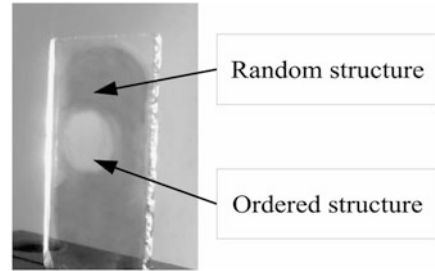
### 21.3.1 Production and Characterization of the Samples

Previously, we proposed so-called in situ method for the formation of periodic polymer–metal NP structures [41]. The initial composite for holographic patterning is a homogeneous mixture containing monomers, photoinitiator of polymerization, and metal precursor solution. During the first step – photopolymerization in the interference pattern – a stable volume grating polymer–metal precursor is formed. Reduction of the precursor and formation of metal NPs occur mainly during the second stage of photo- or thermo-processing. The optimal proposed composition includes two copolymerized monomers, which form a cross-linked polymer network and solution of  $\text{AgNO}_3$  in acetonitrile as an Ag NP precursor. Michler's ketone and camphorquinone were used as the components of the photoinitiating system for photo-induced radical polymerization of monomers. Camphorquinone provides the sensitivity of the composition in the range of 440–500 nm. A standard two-beam interference scheme based on the Ar-ion laser, operating at  $\lambda_{\text{rec}} = 488 \text{ nm}$ , was used for the holographic recording.

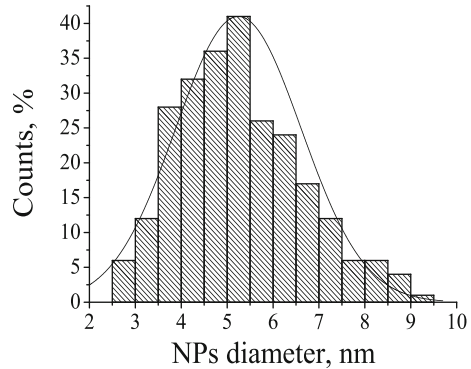
The reactive samples for the holographic patterning were prepared by sandwiching a drop of the initially liquid composites between two glass slides separated by spacers with a thickness of about 10  $\mu\text{m}$ . Then a half the sample surface was exposed to an interference pattern. UV flood exposure of the sample after holographic illumination was carried out to provide curing of residual monomers and formation of a random structure in the film area outside the grating (Fig. 21.2).

The mechanism of the grating formation was discussed in [41]. It was established that during photopolymerization in the periodic light pattern, both main components, the monomer and the metal precursor solution, take part in the irreversible photo-induced mass transfer, providing the stability of the resulting structure. The

**Fig. 21.2** Photo of sample with random and ordered NP distribution ( $d = 10 \mu\text{m}$ ,  $\Lambda = 380 \text{ nm}$ )



(a)



(b)

**Fig. 21.3** TEM image of the 1D structure of NPs (a) and size distribution of NPs in polymer layer ( $d_{\text{avg}} = 5 \text{ nm}$ ,  $(\text{sd})^2 = 1.9$ ) (b)

precursor solution is forced out from the forming polymer network and located mostly in the fringes of the grating corresponded to the low-intensity areas of the interference pattern. Full polymerization of the composite provides a formation of high-efficient volume structure consisted from the periodicity of polymer and metal precursor-containing regions. A subsequent thermo-treatment of the grating causes the solvent evaporation and reduction of silver salt to Ag nanoparticles selectively in the areas of the film containing metal precursor.

The periodic distribution of NPs in the polymer matrix was directly confirmed by TEM measurements of a 1D grating. It can be seen that the spherical NPs with an average particle diameter of about 5 nm are located in the fringes of the grating (Fig. 21.3). The formation of Ag NPs is also confirmed by the changes in absorption spectra of the gratings. Figure 21.4 shows stationary absorption spectra of a random and a periodic structure. The band with a maximum of 450 nm corresponds to the excitation of local surface plasmons in the Ag NPs. The band at 360 nm corresponds to Michler's ketone absorption.

**Fig. 21.4** Absorption spectra of polymer nanocomposite containing Ag NPs with random (1) and 1D ordered (2) structure. The upward arrows indicate excitation wavelengths: dashed arrow corresponds to  $\lambda = 532$  nm,  $h\nu = 2.33$  eV; solid arrows correspond to  $\lambda = 800$  nm,  $h\nu = 1.55$  eV

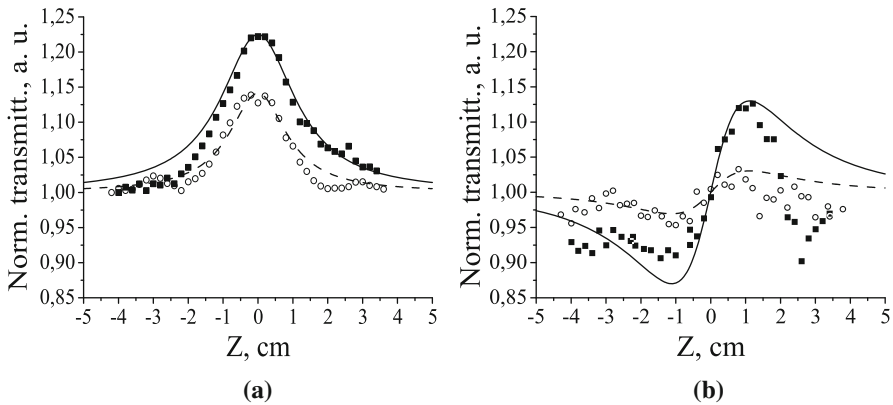
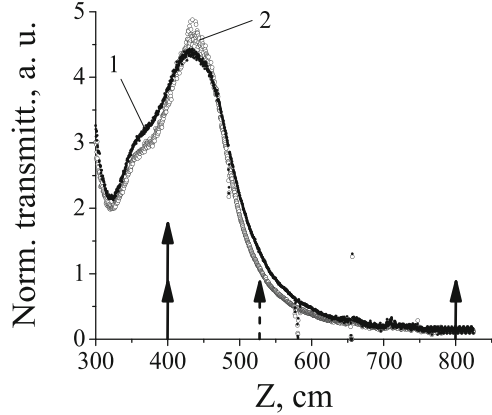


**Fig. 21.5** Nonlinear response of Ag nanocomposite at 532 nm excitation ( $\tau = 20$  ns,  $f = 0.5$  Hz,  $I_0 = 5.11$  MW/cm<sup>2</sup>): open-aperture (a) and closed-aperture (CA/OA) (b) Z-scan results for random (open circles) and ordered (black squares) structures. The lines are the theoretical fits

### 21.3.2 Nonlinear Optical Properties of the Nanocomposites

Open-aperture Z-scan transmittance curves measured at  $I_0 = 5.11$  MW/cm<sup>2</sup> are shown in Fig. 21.5a. The normalized transmission increases in the focal point ( $z = 0$  mm) indicating the nonlinear saturation of absorbance for both random and ordered structures. The decrease in absorption under strong optical radiation corresponds to the negative values of  $\text{Im } \chi^{(3)}$  and  $\beta$  for the stated  $I_0$  of radiation.

Transmittance curves reflecting a pure nonlinear refractive effect are shown in Fig. 21.5b. They are obtained with the closed-aperture Z-scan scheme. The character of the curves indicates the self-focusing of laser radiation in the layer of Ag-doped polymer nanocomposite, i.e., the positive value of nonlinear refractive index.

The observed asymmetry of Z-scan transmittance curves may be the result of a large nonlinear phase shift induced by a pulsed laser [42] that requires additional analysis and verification.

Under femtosecond excitation at a wavelength of 800 nm, the nonlinear absorption is absent in the random structure and decreases in the ordered one (Fig. 21.6a). Unlike the nanosecond experiment, the sign of  $\text{Im } \chi^{(3)}$  changes from negative to positive under femtosecond excitation of ordered structures. This transformation reveals that another nonlinear effect such as reverse saturated absorption or two-photon absorption determines the nonlinear response of the nanocomposite. Transmittance curves reflecting a purely nonlinear refractive effect indicate a negative value of the nonlinear refractive index in both chaotic and ordered structures (Fig. 21.6b).

By using the mentioned fitting [40], we calculated the values of  $\text{Im } \chi^{(3)}$ ,  $\text{Re } \chi^{(3)}$ , nonlinear absorption coefficient  $\beta$ , and nonlinear refractive index  $n_2$  for random and ordered structure. They are given in Tables 21.1 and 21.2. In both cases of nanosecond and femtosecond excitation, we found a significant increase in transmission, absorption, and nonlinear refraction for ordered structures compared to disordered ones.

We have compared the values of nonlinear parameters of the proposed nanocomposite with the results obtained by other authors under similar experimental

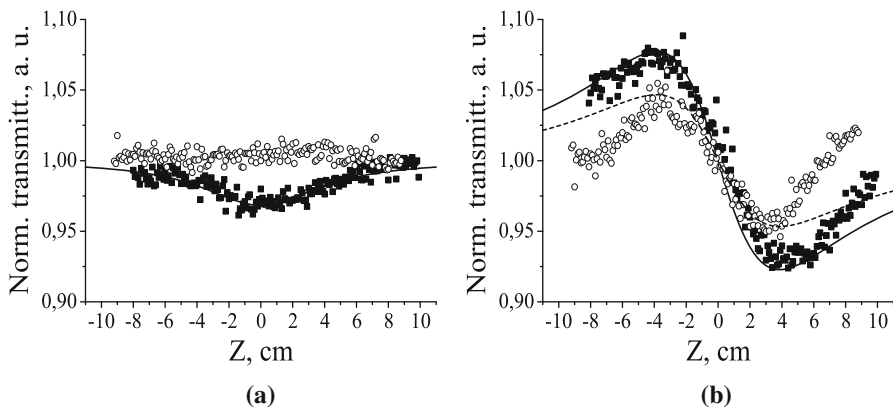


**Fig. 21.6** Nonlinear response of Ag nanocomposite at 800 nm excitation ( $\tau = 180$  fs,  $f = 75$  kHz,  $I_0 = 0.142$  GW/cm<sup>2</sup>): open-aperture (a) and closed-aperture (CA/OA) (b) Z-scan results for random (open circles) and ordered (black squares) structures. The lines are the theoretical fits

**Table 21.1** Nonlinear parameters calculated for random and ordered structure ( $\lambda_{\text{ex}} = 532$  nm,  $\tau = 20$  ns,  $f = 0.5$  Hz)

Structure type	$\alpha$ , cm <sup>-1</sup>	$I_0$ , MW/cm <sup>2</sup>	$n_2$ , cm <sup>2</sup> /W	$\beta$ , cm/W	$\text{Re } \chi^{(3)}$ , esu	$\text{Im } \chi^{(3)}$ , esu	$ \chi^{(3)} $ , esu
Random	1381	5.11	$3 \times 10^{-10}$	$-1.13 \times 10^{-4}$	$1.36 \times 10^{-8}$	$-2.88 \times 10^{-8}$	$3.19 \times 10^{-8}$
Ordered	1381	5.11	$1.14 \times 10^{-9}$	$-1.77 \times 10^{-4}$	$5.17 \times 10^{-8}$	$-4.52 \times 10^{-8}$	$6.87 \times 10^{-8}$



**Table 21.2** Nonlinear parameters calculated for random and ordered structure ( $\lambda_{\text{ex}} = 800$  nm,  $\tau = 180$  fs,  $f = 75$  kHz)

Structure type	$\alpha$ , $\text{cm}^{-1}$	$I_0$ , $\text{GW}/\text{cm}^2$	$n_2$ , $\text{cm}^2/\text{W}$	$\beta$ , $\text{cm}/\text{W}$	$\text{Re } \chi^{(3)}$ , esu	$\text{Im } \chi^{(3)}$ , esu	$ \chi^{(3)} $ , esu
Random	50	0.14	$-3.57 \times 10^{-11}$	–	$-1.6 \times 10^{-9}$	–	–
Ordered	50	0.14	$-4.08 \times 10^{-11}$	$6.5 \times 10^{-7}$	$-1.8 \times 10^{-9}$	$2.42 \times 10^{-10}$	$1.8 \times 10^{-9}$

conditions. The comparison showed that the values given in the tables coincide in order of magnitude [23, 24, 31] and in some cases [25, 26, 32, 33] exceed by one or two orders of magnitude the nonlinear characteristics obtained in the works cited above.

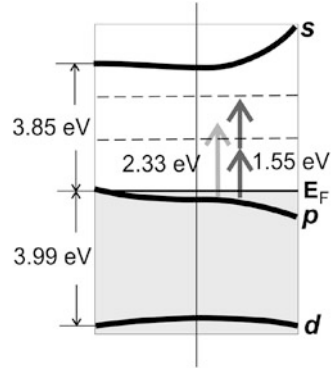
It should be noted that the ordering of nanoparticles in the matrix does not only enhance the nonlinear response but also affects the dynamics of electronic excitations in the structure. Previously we found out that sub-wavelength ordering of Ag NPs significantly influences the values of induced changes of intensity and shape of plasmonic band as well as relaxation times of electron subsystem [43]. The relaxation times in the vicinity of induced absorption increase significantly as the symmetry varies from 1D to 2D tetragonal and 2D hexagonal structures. For example,  $\tau_1 \cong 1.1$  ps and  $\tau_2 \cong 12$  ps for random and 1D structure with  $\Lambda = 900$  nm;  $\tau_1 \cong 1.8$  ps,  $\tau_2 \cong 16$  ps for 1D structure with  $\Lambda = 380$  nm; and  $\tau_1 \cong 2.7$  ps,  $\tau_2 \cong 131$  ps for 2D structure with square grating ( $\Lambda = 370$  nm).

Thus, the correlation of changes of the nonlinear response and the electron dynamics indicates that the ordering of Ag NPs in nanocomposites substantially affects their properties. In the studied structures, Ag NPs are synthesized from metal precursor in the matrix after structure formation. Change of the size and symmetry of regions where precursor is localized may alter the conditions of NP formation and, respectively, alter their size and concentration, thus strongly influencing the nonlinear response of a nanocomposite. It can be also assumed that the decrease of size of Ag NP location zones stimulates the occurrence of collective effects upon excitation of the electron subsystem by powerful laser radiation. Our further research will be aimed at confirmation of the stated assumptions.

We can explain the mechanism of nanocomposite optical nonlinearity from the point of view of electronic transitions in Ag NPs. The energy level diagram proposed in [44] is shown in Fig. 21.7. Noble metals possess a valence band formed by fully populated  $d$  states and a conduction band formed by the  $s$ - $p$  states and populated up to the Fermi level. For Ag NPs, the interband transition energy is of about 3.99 eV (310 nm), and  $p \rightarrow s$  distance between the occupied  $p$ -states and unoccupied  $s$ -states is of about 3.85 eV (322 nm). The plasmon band of metal NPs is determined by dipolar oscillations of free electrons in the conduction band that occupy energy states near the Fermi level. The plasmon resonance energy of our nanocomposite is 2.87 eV.

In our Z-scan experiment, the excitation energies were 2.33 eV (532 nm) and 1.55 eV (800 nm) that are obviously smaller than the energies of interband and  $p \rightarrow s$  transitions. Thus, under used experimental conditions, the nonlinear response of

**Fig. 21.7** Energy level diagram explaining the mechanism of Ag nanocomposite optical nonlinearity



the studied structures is the result of an intraband transition with the local surface plasmon excitation. The wavelength of 532 nm, shown in Fig. 21.4 with a dashed arrow, lies near the plasmon resonance. Therefore, one-photon excitation of hot electrons at a wavelength of 532 nm causes the saturated absorption. The latter is confirmed by the measurement of differential absorption spectra of 1D and 2D Ag-doped structures with “pump–probe” method [43]. At femtosecond excitation, the wavelength of 800 nm was located far from plasmon resonance (solid arrows in Fig. 21.4). The nonlinear absorption in this case can be attributed to the two-photon excitation of free electrons in conduction band.

## 21.4 Conclusions

Under nanosecond excitation at a wavelength of 532 nm, the nonlinear response of the nanocomposite is determined by the saturated absorption. The nonlinear refractive index has a positive sign that causes self-focusing of laser radiation in the nanocomposite layer.

Under femtosecond excitation at a wavelength of 800 nm, nonlinear absorption increases with the increase of laser radiation intensity indicating the contribution of two-photon absorption to the nonlinear response of the nanocomposite. The sign of the nonlinear refraction index, unlike in the nanosecond experiment, is negative that leads to self-defocusing of laser radiation.

The analysis of nature of nonlinear response in Ag NP-doped photopolymer matrix reveals that the main mechanism of nonlinearity at 532 and 800 nm is related to the local electric field enhancement due to one- and two-photon electron excitation in a conduction band.

In both cases of nanosecond and femtosecond excitation, the values of nonlinear characteristics of ordered structures exceed the values obtained for disordered structures. This indicates the influence of the nanocomposite ordering on the size, shape, or concentration of Ag NPs, which are formed in a composite from a periodically or randomly distributed precursor of the metal. This assumption requires further investigation and confirmation.

**Acknowledgements** This work was supported by the grant of the Target Comprehensive Program of Fundamental Research of National Academy of Science of Ukraine “The Fundamental Problems of Creation of New Nanomaterials and Nanotechnologies” (Project 3/17-H).

## References

1. Kreibig U, Vollmer M (eds) (1995) Optical properties of metal clusters. Springer, Berlin/Heidelberg
2. Nicolais L, Carotenuto G (eds) (2005) Metal–polymer nanocomposites. Wiley, Hoboken
3. Gonela F, Mazzoldi P (2000) Metal nanocluster composite glasses. In: Nalwa HS (ed) Handbook of nanostructured materials and nanotechnology, vol 4. Academic Press, San Diego, pp 81–158
4. Kelly KL, Coronado E, Zhao LL, Schatz GC (2003) The optical properties of metal nanoparticles: the influence of size, shape, and dielectric environment. *J Phys Chem B* 107:668–677
5. Inouye H, Tanaka K, Tanahashi I, Hattori T, Nakatsuka H (2000) Ultrafast optical switching in a silver nanoparticle system. *Jpn J Appl Phys* 39:5132–5133
6. Porel S, Venkatram N, Rao DN, Radhakrishnan TP (2007) Optical power limiting in the femtosecond regime by silver nanoparticle–embedded polymer film. *J Appl Phys* 102:033107
7. Qu S, Gao Y, Jiang X, Zeng H, Song Y, Qiu J, Zhu C, Hirao K (2003) Nonlinear absorption and optical limiting in gold-precipitated glasses induced by a femtosecond laser. *Opt Commun* 224:321–327
8. Vaia RA, Dennis CL, Natarajan LV, Tondiglia VP, Tomlin DW, Bunning TJ (2001) One-step, micrometer-scale organization of nano- and mesoparticles using holographic photopolymerization: a generic technique. *Adv Mater* 13:1570–1574
9. Sakhno OV, Goldenberg LM, Stumpe J, Smirnova TN (2007) Surface modified ZrO<sub>2</sub> and TiO<sub>2</sub> nanoparticles embedded in organic photopolymers for highly effective and UV-stable volume holograms. *Nanotechnology* 18:105704
10. Bigot J-Y, Halté V, Merle J-C, Daunois A (2000) Electron dynamics in metallic nanoparticles. *Chem Phys* 251:181–203
11. Link S, El-Sayed MA (2003) Optical properties and ultrafast dynamics of metallic nanocrystals. *Annu Rev Phys Chem* 54:331–366
12. Eah S-K, Jaeger HM, Scherer NF, Lin X-M, Wiederrecht GP (2004) Femtosecond transient absorption dynamics of close-packed gold nanocrystal monolayer arrays. *Chem Phys Lett* 386:390–395
13. Sönnichsen C, Franzl T, Wilk T, von Plessen G, Feldmann J, Wilson O, Mulvaney P (2002) Drastic reduction of plasmon damping in gold nanorods. *Phys Rev Lett* 88:077402
14. Blonskyy IV (2009) Femtooptics of films and nanoparticles of noble metals. *Ukr J Phys* 5:170–202
15. Lamprecht B, Schider G, Lechner RT, Dittbacher H, Krenn JR, Leitner A, Aussenegg FR (2000) Metal nanoparticle gratings: influence of dipolar particle interaction on the plasmon resonance. *Phys Rev Lett* 84:4721
16. Ponyavina AN, Kachan SM (2011) Plasmonic spectroscopy of 2D densely packed and layered metallic nanostructures. In: Mishchenko M, Yatskiv Y, Rosenbush V, Videen G (eds) Polarimetric detection, characterization and remote sensing. NATO science for peace and security series C: environmental security. Springer, Dordrecht, pp 383–408
17. Dyachenko PV, Miklyaev YuV (2007) One-dimensional photonic crystal based on nanocomposite of metal nanoparticles and dielectric. *Opt Mem Neural Netw* 16:198–203
18. Hanisch C, Kulkarni A, Zaporozhchenko V, Faupel F (2008) Polymer-metal nanocomposites with 2-dimensional Au nanoparticle arrays for sensoric applications. *J Phys Conf Ser* 100:052043

19. Ditlbacher H, Krenn JR, Schider G, Leitner A, Aussenegg FR (2002) Two-dimensional optics with surface plasmon polaritons. *Appl Phys Lett* 81:1762
20. Mikhailov V, Wurtz GA, Elliott J, Bayvel P, Zayats AV (2007) Dispersing light with surface plasmon polaritonic crystals. *Phys Rev Lett* 99:083901
21. Stehr J, Grewett J, Shindler F, Sperling R, Von Plessen G, Lemmer U, Lupton JM, Klar TA, Feldman J, Holleitner AW, Forster M, Scherf U (2003) A low threshold polymer laser based on metallic nanoparticle gratings. *Adv Mater* 15:1726–1729
22. Mai HH, Kaydashev VE, Tikhomirov VK, Janssens E, Shestakov MV, Meledina M, Turner S, Van Tendeloo G, Moshchalkov VV, Lievens P (2014) Nonlinear optical properties of Ag nanoclusters and nanoparticles dispersed in a glass host. *J Phys Chem C* 118:15995–16002
23. Hamanaka Y, Nakamura A, Hayashi N, Omi S (2003) Dispersion curves of complex third-order optical susceptibilities around the surface plasmon resonance in Ag nanocrystal–glass composites. *J Opt Soc Am B* 20:1227–1232
24. Ganeev RA, Rysanyansky AI, Stepanov AL, Usmanov T (2004) Saturated absorption and nonlinear refraction of silicate glasses doped with silver nanoparticles at 532 nm. *Opt Quantum Electron* 36:949–960
25. Gurudas U, Brooks E, Bubb DM, Heiroth S, Lippert T, Wokaun A (2008) Saturable and reverse saturable absorption in silver nanodots at 532 nm using picosecond laser pulses. *J Appl Phys* 104:073107
26. Rativa D, de Araujo RE, Gomes ASL (2008) One photon nonresonant high-order nonlinear optical properties of silver nanoparticles in aqueous solution. *Opt Expr* 16:19244–19252
27. Guang-Hua F, Shi-Liang Q, Zhong-Yi G, Qiang W, Zhong-Guo L (2012) Size-dependent nonlinear absorption and refraction of Ag nanoparticles excited by femtosecond lasers. *Chin Phys B* 21:047804
28. Sato R, Ohnuma M, Oyoshi K, Takeda Y (2014) Experimental investigation of nonlinear optical properties of Ag nanoparticles: effects of size quantization. *Phys Rev B* 90:125417
29. Alesnikov A, Pilipavičius J, Beganskienė A, Sirutkaitis R, Sirutkaitis V (2015) Nonlinear properties of silver nanoparticles explored by a femtosecond Z-scan technique. *Lith J Phys* 55:100–109
30. Li R, Dong N, Cheng C, Ren F, Hübner R, Wang J, Zhou S, Chen F (2017) Giant enhancement of nonlinear optical response in Nd:YAG single crystals by embedded silver nanoparticles. *ACS Omega* 2:1279–1286
31. Zeng R, Wang SF, Liang HC, Rong MZ, Zhang MQ, Zeng HM, Gong QH (2002) Nanostructured silver/polystyrene composite film: preparation and ultrafast third-order optical nonlinearity. *Poly Poly Comp* 10:291–298
32. Lee GJ, Lee Y-P, Yoon CS (2008) Microstructures and linear/nonlinear optical properties of monolayered silver nanoparticles. *J Kor Phys Soc* 53:3818–3822
33. Krishnan PMG, Sobha A, Balakrishnan MP, Sumangala R (2014) Synthesis and characterization of Ag/PVP nanocomposites by reduction method. *Open Access Library J* 1:e519
34. Ghanipour M, Dorranian D (2015) Nonlinear optical characterization of the Ag nanoparticles doped in polyvinyl alcohol films. *Opt Spectrosc* 118:949–954
35. Fuks-Janczarek I, Miedziński R, Chrulik M, Majchrowski A, Kobayashi K, Chen XM, Oyama M, Jaroszewicz LR, Pępczyńska M, Wojciechowski A (2015)  $\delta$ -BiB<sub>3</sub>O<sub>6</sub>:Pr<sup>3+</sup>: polymer nanocomposites deposited on substrates with silver nanoparticles for nonlinear optics. *J Mater Sci Mater Electron* 26:7134–7139
36. Bhushan B, Stalwar S, Kundu T, Singh BP (2016) Synthesis, characterization and third-order nonlinear optical properties of polydiacetylene nanostructures, silver nanoparticles and polydiacetylene–silver nanocomposites. *Pramana J Phys* 87:56
37. Bi M, Shao Y, Wang Y, Zhang J, Niu H, Gao Y, Wang B, Lishow C (2017) Liquid crystalline elastomer doped with silver nanoparticles: fabrication and nonlinear absorption properties. *Mol Cryst Liq Cryst* 652:41–50
38. Yan D, Jing S (2010) Photoinduced reorientation process and nonlinear optical properties of Ag nanoparticle doped azo polymer films. *Chin Phys Lett* 27:024204

39. Zhang Y, Wang Y (2017) Nonlinear optical properties of metal nanoparticles: a review. *RSC Adv* 7:45129–45144
40. Sheik-Bahae M, Said AA, Wei TH, Hagan DJ, Van Stryland EV (1990) Sensitive measurement of optical nonlinearities using a single beam. *IEEE J Quantum Electron* 26:760–769
41. Smirnova TN, Kokhtych LM, Kutsenko AS, Sakhno OV, Stumpe J (2009) Fabrication of periodic polymer/silver nanoparticles structures: in situ reduction of silver nanoparticles from precursor spatially distributed in polymer using holographic exposure. *Nanotechnology* 20:405301
42. Chen S-Q, Liu Z-B, Zang W-P, Tian J-G, Zhou W-Y, Song F, Zhang C-P (2005) Study on Z-scan characteristics for a large nonlinear phase shift. *J Opt Soc Am B* 22:1911–1916
43. Smirnova TN, Yezhov PV, Tikhomirov SA, Buganov OV, Ponyavina AN (2016) Time-dependent absorption spectra of 1D, 2D plasmonic structures obtained by the ordering of Ag nanoparticles in polymer matrix. In: Fesenko O, Yatsenko L (eds) *Nanophysics, nanophotonics, surface studies, and applications*. Springer proceedings in physics, vol 183. Springer, Cham, pp 131–141
44. Rosei R, Culp CH, Weavert JH (1974) Temperature modulation of the optical transitions involving the Fermi surface in Ag: experimental. *Phys Rev B* 10:484–488

# Chapter 22

## The Nanocomposite Diffusion Coating of Details Prepared of Boriding



Andrew Stetsko

### 22.1 Introduction

It is advisable to change the sample surface areas for a large number of parts. For this purpose a promising technology is developed with strengthening boriding backcoat (local boriding), which takes place between the interim boriding of powders and melts.

Boriding is used to increase the durability of plugs oil pump, exhaust, bending and forming dies, parts, and machines for injection molding, heavy duty friction hinge, and etc. The stability of these parts after boriding increases by two to ten times.

*Objective:* Create a new economic method for strengthening steel surfaces of friction pairs by diffusion boriding that provides selective strengthening of them (in the areas of load) and simultaneously is economically feasible to manufacture or restore relevant details.

### 22.2 Materials and Methods

As you know, boriding is called chemical-thermal treatment, which is a diffusion saturation of the surface layer of boron steel by heating in an appropriate environment [1]. Like other treatments involving diffusion, the treated substrate must be in contact with a boronaceous substance in the form of a solid powder, paste, liquid,

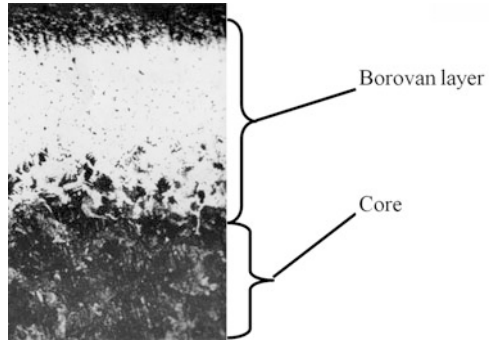
---

A. Stetsko (✉)

Faculty of computer engineering printing, Ukraine Academy of Printing, Pidgolosko Str., 19,  
Lviv-79020, Ukraine

e-mail: [andrew73@ukr.net](mailto:andrew73@ukr.net)

**Fig. 22.1** Borovan layer on the steel (1%C) obtained by diffusion boriding gas at 950 °C for 3 h.



or gas and held at high temperatures (700–1200 °C). Under these conditions, boron atoms diffuse from the surface into the metal lattice, forming borides with the atoms of the substrate and alloying elements, promoting the formation of the borided layer. Fluidized bed techniques can also be used for boriding. Other means to promote boride layer deposition without using thermochemical activation are plasma vapor deposition (PVD), ion implantation, and plasma spray.

The thickness of the diffusion layer is 100–200 microns (Fig. 22.1). Borovan layer has high hardness HV 1800–2000 (18000–20,000 MPa), durability (mainly abrasive), corrosion resistance, cinder resistance (to 800 °C), and heat resistance.

The same as many other surface treatments, hard boride layers with attractive physical and chemical properties can be developed on most metals and engineering alloys.

In the study, AISI P20, H13, and D2 steels were pack borided at 900 and 950 °C for retention times of 2, 4, and 6 h [2]. The boride layer thickness values changed depending on the chemical composition of the steels. The hardness values of borides that formed on the surface of AISI P20, AISI H13, and AISI D2 steels were 1897 HV(50 g), 1989 HV(50 g), and 1916 HV(50 g), respectively. On the other hand, the Vickers hardness values of the untreated steels were 532 HV(50 g), 485 HV(50 g), and 408 HV(50 g), respectively. According to the adhesion and wear test results, the adhesion and wear resistance of the boride layer decreased with the increase in the boriding temperature and time.

Other authors [3] apply ultrafast surface hardening of low carbon steel that is introduced via the application powder-pack boriding process in a hot isostatic pressing special fixture. Boriding (boronizing) powder consisting of boric acid and borax mixture is utilized in 50 wt. % boric acid and 50 wt. % of borax. Low carbon steel sample packed with boric acid and borax is heated at 1050 °C for 30 min and then tempered at 900 °C for 30 min in a special fixture sealed with a 10 ton pressure. The surface boride layer as FeB and Fe<sub>2</sub>B phase with the hardness about ~1800 HV and depth of 130–180 μm is achieved and compared to untreated base metal of 123 HV. Alloy segregation along with delocalized zone of interest is achieved with different boron content 1.77 wt. % along grain boundaries, 3.93 wt. % leading phase, and 7.86 wt. % trailing phase at the sample surface. This process provides high performance and high thickness of coatings and can be used fast

and economically if compared to traditional processes with less emission. From economic and environmental points of view, it is highly desirable to develop and implement novel surface treatment technologies that are quick, cheap, clean, and energy efficient.

In this [4] study, new results about the practical adhesion resistance of boride coating/substrate system formed at the surface of AISI 316 L steel and improved by means of a diffusion annealing process are received. First, the boriding of AISI 316 L steel was performed by the powder-pack method at 1173 K with different exposure times (4–8 h). The diffusion annealing process was conducted on the borided steels at 1273 K with 2 h of exposure using a diluent atmosphere of boron powder mixture. The mechanical behavior of the boride coating/substrate system developed by both treatments was established using Vickers and Berkovich tests along the depth of the boride coatings, respectively. Finally, for the entire set of experimental conditions, the scratch tests were performed with a continuously increasing normal force, in which the practical adhesion resistance of the boride coating/substrate system was represented by the critical load. The failure mechanisms developed over the surface of the scratch tracks were analyzed; the FeB-Fe<sub>2</sub>B/substrate system exhibited an adhesive mode, while the Fe<sub>2</sub>B/substrate system obtained by the diffusion annealing process showed predominantly a cohesive failure mode.

In work [5], a kinetic model was suggested to evaluate the boron diffusion coefficient in the Fe<sub>2</sub>B layers grown on the Armco iron substrate by the powder-pack boriding. This thermochemical treatment was carried out in the temperature range of 1123–1273 K for treatment times ranging from 2 to 8 h. The boron diffusion coefficient in the Fe<sub>2</sub>B layers was estimated by solving the mass balance equation at the (Fe<sub>2</sub>B/substrate) interface with an inclusion of boride incubation time. To validate the present model, the simulated value of Fe<sub>2</sub>B layer thickness was compared with the experimental value obtained at 1253 K for a treatment time of 5 h. The morphology of Fe<sub>2</sub>B layers was observed by SEM and optical microscopy. Metallographic studies showed that the boride layer has a sawtooth morphology in all the samples.

In work [6], the EN-GJS-400-15 cast iron was pack-borided in a powder mixture composed of 5% B<sub>4</sub>C, 5% NaBF<sub>4</sub>, and 90% SiC at the three temperatures: 900, 950, and 1000 °C for 2, 4, and 6 h, respectively. The pack-borided EN-GJS-400-15 cast iron was characterized by the following experimental techniques: optical microscopy, XRD analysis, and microhardness Vickers tester. The growth kinetics of boride layers was also investigated. As a consequence, the boron activation energy was found to be 212.28 kJ mol<sup>-1</sup> for the EN-GJS-400-15 cast iron.

In study [7] the behavior of the borided 316 L stainless steel and 1018 steel is evaluated under micro-abrasion wear. The boriding was carried out at 1223 K over 6 h of exposure time, resulting in a biphasic layer composed of FeB/Fe<sub>2</sub>B phases. In order to evaluate Fe<sub>2</sub>B phase with no influence from FeB phase, AISI 1018 steel samples were borided at 1273 K for over 20 min and then diffusion annealed at 1273 K over 2 h to obtain a Fe<sub>2</sub>B monophase layer. The obtained wear rates for FeB and Fe<sub>2</sub>B phases and for the 316 L stainless steel were compared. Wear resistance of 316 L stainless steel increases after boriding.



The study [8] reports on the kinetics of borided Nickel 201 alloy. The thermochemical treatment of boronizing was carried out in a solid medium consisting of  $B_4C$  and  $KBF_4$  powders mixture at 1123, 1173, and 1223 K for 2, 4, and 6 h, respectively. The boride layer was characterized by optical microscopy, X-ray diffraction technique, and microhardness Vickers tester. X-ray diffraction analysis revealed the existence of  $NiB$ ,  $Ni_2B$ ,  $Ni_3B$ , and  $Ni_4B_3$  compounds at the surface of borided Nickel 201 alloy. The thickness of the boride layer increased with an increase in the boriding time and the temperature. The hardness of the nickel borides formed on the surface of the nickel substrate ranged from 1642 to 1854  $HV_{0.05}$ , whereas the Vickers hardness value of the untreated nickel was 185  $HV_{0.05}$ .

Pack boronizing and rare-earth (RE)-borosulphurizing of high-carbon steel (T8) were conducted at 950 °C for 6 h [9]. Different from the BL layer, the RBSL layer is compact, continuous, and flat. The formation of  $FeS$ ,  $Fe_2B$ , and  $FeB$  phases on the substrates was confirmed by Auger electron spectroscopy analysis. The wear resistance test indicated that within a certain range, the abrasion resistance of the RBSL layer is better than that of the BL layer, especially under high-load conditions. The corrosion resistance test using the weight loss method has shown that the corrosion resistance of the RBSL layer is better but decreases faster with time extension than that of the BL layer.

From the analyzed work, we can draw the following conclusions.

The surface layers are covered by hard phase-type borides, nitrides, etc. It is very difficult to provide high efficiency across a large number of defects that cause significant stress concentration. In addition, boride surface layer has a small thickness, which is not enough for abrasion wear. So, there is a need to use new method of hardening machines, which would give an opportunity to get hardened layers of increased thickness were quite plastic, in the process of strengthening economic, and allowed to re-recovery of such parts.

## 22.3 Discussion

It is suggested to apply borage with paste.

In study [10], the AISI 440C steel was plasma paste borided in a gas mixture of 70% $H_2$ –30% $Ar$  using borax paste as a boron source. This thermochemical treatment was carried out at three temperatures of 700, 750, and 800 °C for 3, 5, and 7 h. The morphology of the formed boride layers was studied by scanning electron microscope. An identification of iron borides was performed using an X-ray microanalyzer, equipped with energy-dispersive X-ray spectroscopy. The phases present in the boride layer were identified by means of X-ray diffraction analysis. In addition, the glow discharge optical spectroscopy analysis was performed in order to determine the concentration profiles of elements. The wear resistance of plasma paste-borided AISI 440 C steel (at 800 °C for 3 h) was also investigated. As a result, the value of boron activation energy for the AISI 440C steel was found to be equal to 134.62  $kJ\ mol^{-1}$  on the basis of our experimental results.

In the study [11], AISI 8620 steel was plasma paste borided by using various  $B_2O_3$  paste mixture. The plasma paste boriding process was carried out in a dc plasma system at temperatures of 973, 1023, and 1073 K for 2, 5, and 7 h in a gas mixture of 70%  $H_2$ –30% Ar under a constant pressure of 10 mbar. The properties of the boride layer were evaluated by optical microscopy, X-ray diffraction, Vickers microhardness tester, and the growth kinetics of the boride layers. X-ray diffraction analysis of boride layers on the surface of the steel revealed FeB and  $Fe_2B$  phases. Depending on temperature and layer thickness, the activation energies of boron in steel were found to be 124.7 kJ/mol for 100%  $B_2O_3$ .

In the study [12], AISI 8620 steel was plasma paste boronized by using various borax paste mixtures. The plasma paste boronizing process was carried out in a dc plasma system at a temperature of 973, 1023, and 1073 K for 2, 5, and 7 h, respectively, in a gas mixture of 70%  $H_2$ –30% Ar under a constant pressure of 10 mbar. The properties of the boride layer were evaluated by optical microscopy, X-ray diffraction, the microhardness Vickers tester, and the growth kinetics of the boride layers. The thickness of the boride layers varied from 14 to 91  $\mu m$  depending on the boronizing time and temperature. X-ray diffraction analysis of boride layers on the surface of the steel revealed the formation of FeB and  $Fe_2B$  phases.

Technology hardening of paste (coating) involves the following operations:

Before the pouring process, the chemical coating of the Ni-Co-P of different ten recipes is applied to the parts of Tables 22.1 and 22.2. The main components of the paste (Table 22.3.) are thoroughly mixed in a special mixer and diluted with binder component to the desired consistency (Fig. 22.2). As a binding material, hydrolyzed ethyl silicate, liquid glass, sulfite-alcohol bard, a solution of glue BF-2 in acetone, glue, etc. are used. The consistency of the paste is mainly determined by the selected technology application in its detail: spraying, brush, or diving.

The thickness of the coating should be at 1.5–2.5 mm, which, if necessary, can be applied to multiple coating steps.

**Table 22.1** Elements of chemical Ni-Co-P sedimentation and diffusion boriding

Chemical element	#1	#2	#3	#4	#5
$CoCl_2$ (g/l)	–	15	15	30	–
$NiCl_2$ (g/l)	–	30	30	30	–
$Na_3C_6H_5O_7$ (g/l)	84	100	100	80	–
$NaH_2PO_2$ (g/l)	30	20	60	10	25
$NH_4Cl$ (g/l)	–	50	50	50	50
$CoCO_3$ (g/l)	7	–	–	–	–
$CoSO_4$ (g/l)	–	–	–	–	30
$NiSO_4$ (g/l)	15	–	–	–	30
$CH_3COONa$ (g/l)	–	–	–	–	100
$H_2SO_4$ (g/l)	15	–	–	–	–
$NH_4OH$ (ml)	90	60	60	60	50

**Table 22.2** Elements of chemical Ni-Co-P sedimentation and diffusion boriding

Chemical element	#6	#7	#8	#9	#10
CoCl <sub>2</sub> (g/l)	15	30	–	–	–
NiCl <sub>2</sub> (g/l)	30	30	–	–	–
Na <sub>3</sub> C <sub>6</sub> H <sub>5</sub> O <sub>7</sub> (g/l)	90	–	–	–	–
NaH <sub>2</sub> PO <sub>2</sub> (g/l)	25	25	25	30	–
K <sub>2</sub> H <sub>2</sub> PO <sub>2</sub> (g/l)	–	–	–	–	30
NH <sub>4</sub> Cl (g/l)	–	50	50	45	–
CoCO <sub>3</sub> (g/l)	–	–	–	15	–
NiCO <sub>3</sub> (g/l)	–	–	–	30	–
CoSO <sub>4</sub> (g/l)	–	–	20	–	–
NiSO <sub>4</sub> (g/l)	–	–	30	–	–
Co(NO <sub>3</sub> ) <sub>2</sub> (g/l)	–	–	–	–	18
Ni(NO <sub>3</sub> ) <sub>2</sub> (g/l)	–	–	–	–	30
CH <sub>3</sub> COONa (g/l)	–	90	–	90	–
(CHCOONa) <sub>2</sub> (g/l)	–	–	90	–	–
C <sub>4</sub> H <sub>6</sub> O <sub>6</sub> (g/l)	15	–	–	–	–
CH <sub>2</sub> NH <sub>2</sub> COOH (g/l)	25	–	–	–	–
Na <sub>2</sub> C <sub>4</sub> H <sub>4</sub> O <sub>4</sub> (g/l)	–	–	–	–	100
NH <sub>4</sub> OH (ml)	50	50	50	50	60

**Table 22.3** Elements of paste for boriding

#3	#2	#1	# Backcoat
55–60	65–75	45 to –51	Boron carbide
		15 to –18	Cryolite
15–20		3–6	Iron oxide
1–3	7–9	2–5	Sodium fluoride
		5–15	Liquid glass
	7–9		Graphite
	1 to –3		Copper
8–12			Charcoal
8–10			Glue BF
3–5			Acetone
	10–14	5–30	Solution 90% glue BF and 10% acetone
1150–1200	1100–1200	1100–1200	Temperature, °C
20–25	25–35	30–40	Dwell time, s
200	180	160	Thickness, microns
10000	9000	8000	Microhardness layer, MPa
70	80	100	Continuity of coverage, %

Acetone-based coating is characterized by high evaporation rate, so it should be dried at room temperature. In case of saturation for the implementation of other bonding materials, use a drying cabinet.

The case of studies to strengthen the samples of boron coating technology with heating by high-frequency current is investigated [13–16]. Strengthening of steel

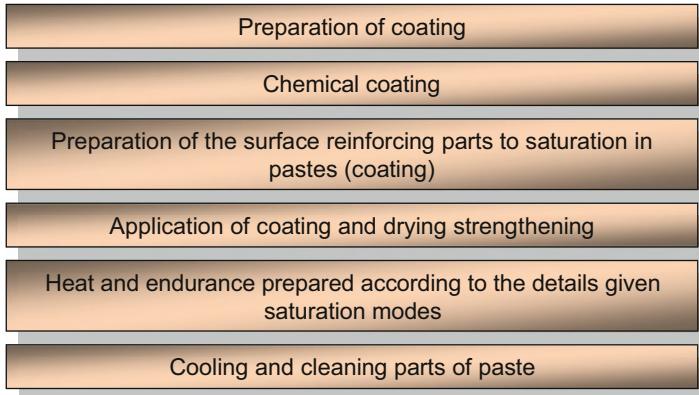


**Fig. 22.2** Operations of boriding

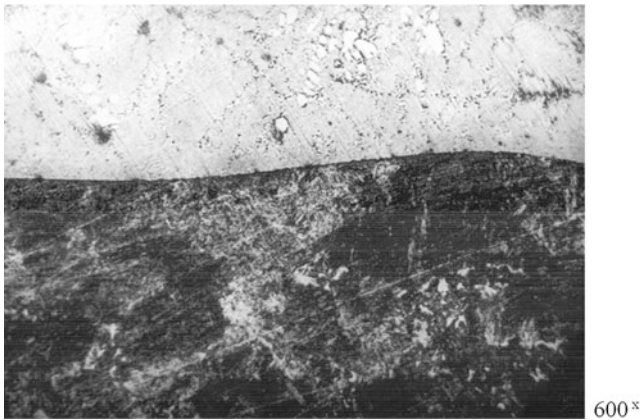


**Fig. 22.3** Consolidated borovan layer obtained is an economical way to strengthen steel (0.45%C)

(0.45%C) is carried out by drawing on previously cleaned and degreased surface coating and drying by air. Then strengthening detail with image coating is heated at a temperature of 1150–1200 °C by high frequency.

The existing structure is reinforced with white layers containing borides and has a thickness of 160 microns and microhardness of 9000 MPa (Fig. 22.3).

Boriding for coating consists of basic parts and connections. Experiments have shown that the using of hydrolyzed ethyl silicate is not always justified, as the temperature increases this connection “swells” blown away and detached from the surface of the sample, or at high power settings microwave, baked on its surface. Therefore, the studies used glue BF-2 and acetone as the communication solution.

In preparation for the strengthening of surfaces, it is needed first to determine their shape and configuration. As the gap between the fixing piece and the inductor should be at a certain value, the inductor configuration is repeated reinforcing

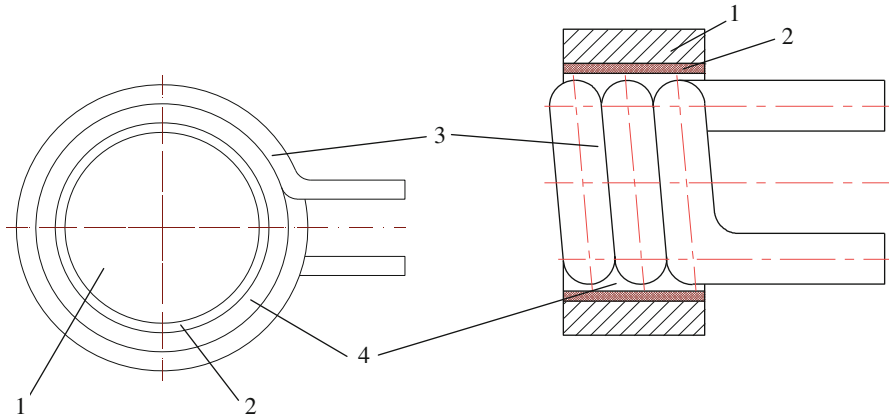
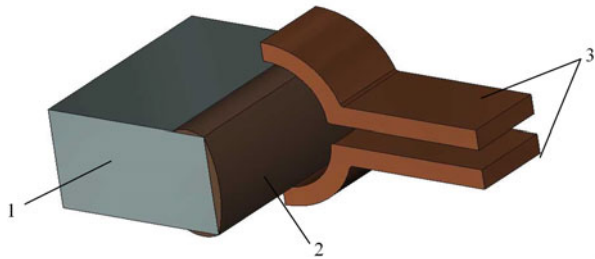


**Fig. 22.4** Scheme boriding diffusion of pastes and backcoat microwave by heating parts of bodies of rotation 1, strengthened detail; 2, coating; 3, inductor; 4, the gap between the workpiece and inductor

**Fig. 22.5** Scheme boriding diffusion of pastes and microwave backcoat when heated flat parts 1, strengthened detail; 2, coating; 3, inductor



surface configuration details. Often, reinforcing surface is divided into three groups: surface rotation, planar surfaces, and surfaces of complex configuration (shaped). The inductor should be chosen for each type of strengthened surface for repeating its profile.

Often changing rotation surface (Fig. 22.4) and planar surface (Fig. 22.5), this surface friction pairs “shaft-hub” or “slide-guide.”

For surfaces with complex configurations that are much rarer, inducers should be made according to their profile and size. In the manufacture of inducers (Figs. 22.4 and 22.5), it should be taken into account the condition that this method of strengthening is often used to enhance surface details not all but only its working surfaces (work surfaces). Also it is important to note the inductor type fastened to the microwave installation and the amount and type of coolant given through the cavities of the inductor.

Strengthening of the research sample (Fig. 22.6) made of steel (0.45%C) is made by drawing on previously cleaned and degreased surface coating, comprising (wt.%) boron carbide, 48; cryolite, 16; iron oxide, 4; sodium fluoride, 4; liquid glass, 8; and solution of 90% glue BF and 10% acetone, 20 of coating, and drying it by air.

**Fig. 22.6** Sample steel (0.45%C), reinforced diffusion boriding with heating microwave: 1, sleeve; 2, contains boron coating; 3, skirting

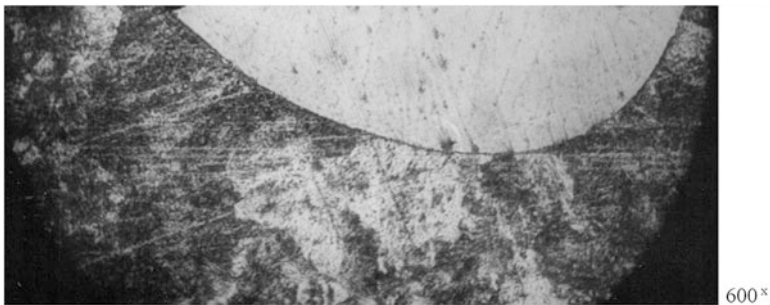
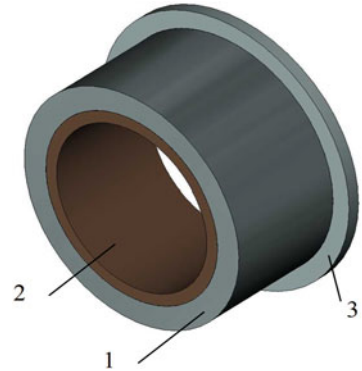


**Fig. 22.7** Structure borides hardened layer obtained in steel (0.45%C)

Then the strengthened detail with the covered coating is set in the rotational installation centers of microwave and heat at 1150 °C during 35 s by the high-frequency power 100 kW and frequency 0.066 MHz.

The finished hardened bushing is fixed in the hole of the hub of a renewable detail. If necessary, the finishing processing of the work surface assembled parts is performed.

Formed reinforced layer (Fig. 22.7) has a structure of white layers and contains borides and has a thickness of 200 microns and microhardness of at least 9000 MPa.

In the study of the morphology of hardened covering, the diffusion of individual boriding backcoat with heating by high-frequency current was revealed that coverage is not continuously strengthened across the whole surface. The structure of the coating was not solid but “spotted.” Borides strengthen the coverage of about 90–95% of the surface. This structure of hardened layers speaks about the selective saturation of backcoat adopted by modes. This may be a slight blowing of coating during the heating by high frequency and, therefore, lack of source diffusion element in these places.

This hardened layer structure during conjugate machine parts will be realized by the random wearing on the work surface – softer the hardness areas. Formed worn areas will serve as reservoirs for oil and also for product wear collecting. Such an

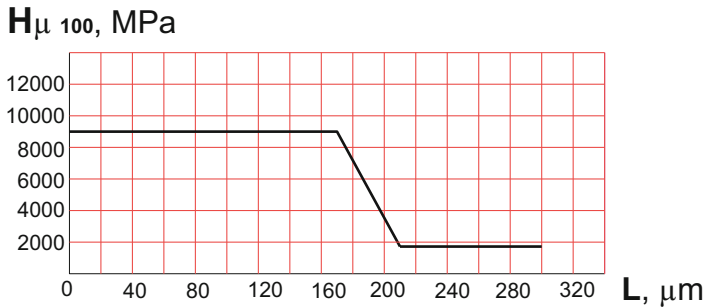


Fig. 22.8 Microhardness boron hardened layer obtained in steel (0.45%C)

implementation scheme is similar to wear composite material, which is currently the most promising.

Boron refers to the elements with a small atomic radius (0,91 Å), which contributes the diffusion of boron in to steel. The small atomic radius (0,91 Å) of Boron is playing important role in the boron diffusion into steel. Researchers are inclined to think that the boron solution forms a substitution of  $\alpha$ -iron and appearance solution of  $\gamma$ -iron.

The solubility of boron in  $\alpha$ -iron and  $\gamma$ -iron is low. After saturation of iron by boron, the reaction of diffusion layer zone is seen under microscope (zone borides). In the system B-Fe reaction diffusion is carried out mainly by diffusion of boron through the borides layer to the main front of the reaction, which are posted on the phase boundaries between iron-Fe<sub>2</sub>B borides and boride Fe<sub>2</sub>B-boride FeB. Obviously, boron diffuses through the lattice borides in the form of positive ions.

Microhardness of the hardened layer (Fig. 22.8), received on steel (0.45%C), is at least 9000 MPa. The thickness of the diffusion hardened layer is 200 microns. The roughness is 1,6–1,25 microns.

These figures show hardened layer obtained by boriding from coating and heating by high-frequency current are sufficient to strengthen the overwhelming amount of machine details wearing and as a result their, reliability and durability of parts, reinforced by this way.

The thickness of the resulting hardened layer can be used to the method of repair sizes significantly which simplifies and reduces the cost of repeated restoration and repairment.

## 22.4 Conclusions

1. Use of boriding diffusion in coating with heating by high-frequency current due to physical and chemical properties of the boron element is a promising method of surface hardening of machines.

2. Application of connection: 90% of glue BF and 10% acetone in almost all cases give a positive effect. Using other recipes connection causes coating sticking to strengthening backcoat surface, or vice versa, by blowing them off on the stage of heating by high-frequency current.
3. Being activators is the important role played by the following components of the primary coating. Experiments have shown that they significantly affect the thickness of boron layer. The most effective was NaF. Activators NaCl and Al<sub>2</sub>O<sub>3</sub> do not give the desired effect.
4. Use of high-frequency settings gives a positive result. This reduces the duration of boriding to tens of seconds. This significantly increases the speed of heating, providing fine-grained structure of steel of austenite. This structure increases the penetration of boron diffusion in to the core metal and its strength as a whole. Accelerating of heating rate and therefore heating exposure time allows to raise the temperature of heating to 150–200 °C without the threat of metal structure change.
5. The greatest effect is achieved in unalloyed carbon steel that gives reduced cost of parts, significantly improving their basic characteristics.
6. By adjusting the heating mode, it is possible to get nonsolid (“spotted”) boron hardened layer that will work well in heavy wear (thickness of 200 microns and microhardness of at least 9000 MPa). Wearing of the soft surface phase will be more intensive that will create worn niches where grease and food deterioration will be accumulated.
7. This method of strengthening makes it possible to strengthen when necessary only the separate working surfaces of details, including the large parts.
8. The method is economical because the use of microwave heating provides fast (tens of seconds) heating without requiring special training of details from previous coating for protection against oxidation.

## References

1. Casteletti LC, Lombardi AN, Totten GE (2013) Encyclopedia of tribology. Springer, New York, pp 249–255
2. Kara R, Çolak F, Kayali Y (2016) Investigation of wear and adhesion behaviors of borided steels. *Trans Indian Inst Metals* 69:1169. <https://doi.org/10.1007/s12666-015-0698-2>
3. Rabeeh BM (2015) Ultra-fast boriding and surface hardening of low carbon steel. In: The Minerals, Metals & Materials Society (eds) TMS 2015 144th annual meeting & exhibition, Springer, Cham
4. Campos-Silva I, Bernabé-Molina S, Bravo-Bárceñas D et al (2016) Improving the adhesion resistance of the boride coatings to AISI 316L steel substrate by diffusion annealing. *J Mater Eng Perform* 25:3852. <https://doi.org/10.1007/s11665-016-2201-6>
5. Elias-Espinosa M, Ortiz-Domínguez M, Keddám M et al (2014) Growth kinetics of the Fe<sub>2</sub>B layers and adhesion on Armco iron substrate. *J Mater Eng Perform* 23:2943. <https://doi.org/10.1007/s11665-014-1052-2>
6. Azouani O, Keddám M, Allaoui O et al (2017) Characterization of boride coatings on a ductile cast iron. *Prot Met Phys Chem Surf* 53:306. <https://doi.org/10.1134/S207020511702006X>



7. Reséndiz-Calderon CD, Rodríguez-Castro GA, Meneses-Amador A et al (2017) Micro-abrasion wear resistance of borided 316L stainless steel and AISI 1018 steel. *J Mater Eng Perform* 26:5599. <https://doi.org/10.1007/s11665-017-3004-0>
8. Gunes I, Keddad M, Chegroune R et al (2015) Growth kinetics of boride layers formed on 99.0% purity nickel. *Bull Mater Sci* 38:1113. <https://doi.org/10.1007/s12034-015-0931-y>
9. Wang D, Zhang X, Zhao H et al (2013) Surface property enhancement by RE-borosulphurizing on high-carbon steel. *Appl Phys A* 113:115. <https://doi.org/10.1007/s00339-013-7714-3>
10. Keddad M, Chegroune R, Kulka M et al (2017) Characterization and diffusion kinetics of the plasma paste borided AISI 440C steel. *Trans Indian Inst Metals* 70:1377. <https://doi.org/10.1007/s12666-016-0934-4>
11. Gunes I, Taktak I, Bindal C et al (2013) Investigation of diffusion kinetics of plasma paste borided AISI 8620 steel using a mixture of B<sub>2</sub>O<sub>3</sub> paste and B<sub>4</sub>C/SiC. *Sadhana* 38:513. <https://doi.org/10.1007/s12046-013-0136-2>
12. Gunes I, Ulker S, Taktak S (2013) Kinetics of plasma paste boronized AISI 8620 steel in borax paste mixtures. *Prot Met Phys Chem Surf* 49:567. <https://doi.org/10.1134/S2070205113050122>
13. UA 93744, C23C 10/12, C23C 10/02, C23C 10/00, C23C 12/00, 10 March 2011
14. UA 93811, C23C 10/02, C23C 12/00, C23C 10/00, B05D 1/00, 10 March 2011
15. UA 102035, C23C 8/68, C23C 8/70(2006.01), C23C 10/02, C23C 22/02, 27 May 2013
16. UA 109096, C23C 8/68, C23C 20/08, 10 July 2015



# Chapter 23

## Ni Addition Induced Changes in Structural, Magnetic, and Cationic Distribution of $\text{Zn}_{0.75-x}\text{Ni}_x\text{Mg}_{0.15}$ $\text{Cu}_{0.1}\text{Fe}_2\text{O}_4$ Nano-ferrite

Manvi Satalkar, Shashank Narayan Kane, Tetiana Tatarchuk,  
and João Pedro Araújo

### 23.1 Introduction

Nano-magnetic material with spinel structure containing two sub-lattices, tetrahedral A and octahedral B site, has become an important matter of study because of its variety of industrial and biomedical applications [1–8]. Spinel ferrites (SF) have turned into a prominent material of research mainly for addressing the basic correlation between the spinel crystal structure and magnetic properties. This basic relation between structural and magnetic properties can be studied via cationic distribution at A and B site [9, 10]. Distribution of cations on A and B site depends on the valency, ionic radii, presence of different cations ( $\text{Zn}^{2+}$ ,  $\text{Ni}^{2+}$ ,  $\text{Mn}^{2+}$ ,  $\text{Co}^{2+}$ ,  $\text{Fe}^{3+}$ ), synthesis method, synthesis parameters [11], etc., which plays a decisive role in determining structural and magnetic properties [12] of SF.

Cationic distribution can be effectively used in tuning the magnetic properties of SF. The magnetization behavior of SF can be elucidated either by Néel's collinear two-sub-lattice model or by Yafet-Kittel three-sub-lattice model. According to Néel's model, the cationic magnetic moments on A and B sites are allied antiparallel

---

M. Satalkar · S. N. Kane (✉)  
Magnetic Materials Laboratory, School of Physics, D. A. University, Indore, India

T. Tatarchuk  
Department of Pure and Applied Chemistry, Vasyl Stefanyk Precarpathian National University,  
Ivano-Frankivsk, Ukraine

Educational and Scientific Center of Chemical Materials Science and Nanotechnology, Vasyl  
Stefanyk Precarpathian National University, Ivano-Frankivsk, Ukraine

J. P. Araújo  
IFIMUP and IN-Institute of Nanoscience and Nanotechnology, Department of Physics and  
Astronomy, Faculty of Sciences, University of Porto, Porto, Portugal  
e-mail: [jearaujo@fc.up.pt](mailto:jearaujo@fc.up.pt)

to each other forming a collinear structure [13, 14] with certain resultant magnetization  $M = M_B - M_A$ , where  $M_A$  and  $M_B$  are, respectively, magnetic moment of A and B site. But, according to Yafet-Kittel (Y-K) model, B sub-lattice can be divided into two sub-lattices,  $B_1$  and  $B_2$ , having equal magnitude of magnetic moments, each canted oppositely at identical angle,  $\alpha_{Y-K}$ . In this way, two sub-lattices  $B_1$  and  $B_2$  have triangular spin arrangement which becomes more significant with changing concentration and cationic redistribution.

Among other SF, most of the literature reports electromagnetic properties of Ni-Zn-Mg-Cu ferrite [15–19], but the magnetic properties of Zn-Ni-Mg-Cu spinel ferrite are less explored [16, 19–24]. Sujatha et al. [16] investigated Mg substituted ann. (powder, 500 °C/3 h.; pellets, 950 °C/1 h.) Ni-Cu-Zn ferrite. The results depict enhanced permeability, decrease in saturation magnetization ( $M_s$ ), and dielectric losses at higher frequencies with Mg substitution in  $Ni_{0.5-x}Mg_xCu_{0.05}Zn_{0.45}Fe_2O_4$  ( $x = 0.1, 0.2, 0.3, 0.4$ ). Coercivity ( $H_c$ ) and anisotropy constant ( $K_1$ ) increase up to  $x = 0.2$  and then reduce with increasing Mg content. Maximum initial permeability ( $\mu_i$ ) was obtained for  $x = 0.1$ . Abdullah Dar et al. [19] examined  $Ni_{0.5-x}Cu_{0.2}Zn_{0.3}Mg_xFe_2O_4$  ( $x = 0.0-0.4$ ) (900 °C/5 h) ferrite system, synthesized by sol-gel method. Results showed increased electrical resistivity, reduced  $H_c$ , and dielectric losses with Mg substitution. Mg doping leads to increase in  $M_s$  up to  $x = 0.2$ , and thereafter it starts to decrease with increase in Mg content. Sujatha et al. [20] explored Mg substituted ann. (powder, 500 °C/3 h.; pellets, 950 °C/1 h.)  $Ni_{0.5}Cu_{0.05}Mg_xZn_{0.45-x}Fe_2O_4$  ( $x = 0.09, 0.18, 0.27, 0.36, 0.45$ ). Results reveal decrease in  $M_s$ ,  $\mu_i$  and increase in  $H_c$ ,  $K_1$ , Curie temperature ( $T_c$ ) with increasing Mg content. Sujatha et al. [21] studied co-substitution effect of Mg, Zn of ann. (powder, 500 °C/3 h.; pellets, 950 °C/2 h.)  $Ni_{0.5-2x}Mg_xCu_{0.05}Zn_{0.45+x}Fe_2O_4$  ( $x = 0.0, 0.04, 0.08, 0.12, 0.16$ ) ferrite. Results demonstrate gradual decrease of  $M_s$ ,  $H_c$ ,  $K_1$ , dielectric constant, dielectric loss factor, improved permeability, and enhanced resistance of samples. Satalkar et al. [22] studied the synthesis, structural and soft magnetic properties, and cation distribution of as-burnt  $Zn_{0.8-x}Ni_xMg_{0.1}Cu_{0.1}Fe_2O_4$  ( $x = 0.0-0.8$ ) ferrites prepared by sol-gel auto-combustion method. The paper reports increase in 50 Hz and quasi-static coercivity and anisotropy constant values with nickel content. Best magnetization value of 25.04 emu/g was obtained for  $x = 0.60$ . Kane et al. [23] demonstrate the correlation between magnetic properties and cationic distribution of ann. (500 °C/3 h)  $Zn_{0.85-x}Ni_xMg_{0.05}Cu_{0.1}Fe_2O_4$  ( $x = 0.0-0.8$ ). The paper depicts decrease in experimental, theoretical lattice constant ( $a_{exp.}$ ,  $a_{th.}$ ), specific surface area ( $S$ ), and the distances between cations (Me-Me) (b, c, d, e, f) with increase in Ni doping.  $H_c$  and  $M_s$  of Zn-Ni-Mg-Cu ferrite ranges between 0.97–167.5 Oe and 47.63–136.93 Am<sup>2</sup>kg<sup>-1</sup>, respectively, signifying the soft character of annealed samples. The paper shows similar trend of  $M_s$ , Néel/experimental magnetic moment ( $n_B^N$ ,  $n_B^e$ ) with Ni content ( $x$ ) which establishes the Néel's two-sub-lattice model of ferrimagnetism in ann. (500 °C/3 h)  $Zn_{0.7-x}Ni_xMg_{0.2}Cu_{0.1}Fe_2O_4$  nano-ferrite. Furthermore the role of cationic distribution in determining magnetic properties

of  $\text{Zn}_{0.7-x}\text{Ni}_x\text{Mg}_{0.2}\text{Cu}_{0.1}\text{Fe}_2\text{O}_4$  ( $x = 0.0\text{--}0.7$ ) nano-ferrite is presented in [24]. The magnetic properties  $M_s$  (43.2–69.9  $\text{Am}^2/\text{kg}$ ) and  $n_B^N$  (1.74–2.86  $\mu_B$ ) increase up to  $x = 0.42$ , but at higher values of Ni content ( $0.42 < x \leq 0.70$ )  $M_s$  and  $n_B^N$  decrease, but coercivity (16.3–131.1 Oe) increases constantly with increasing Ni content. Zero values of Yafet-Kittel angle ( $\alpha_{Y-K}$ ) suggest the presence of Néel-type magnetic ordering in  $\text{Zn}_{0.7-x}\text{Ni}_x\text{Mg}_{0.2}\text{Cu}_{0.1}\text{Fe}_2\text{O}_4$ .

The above available literature [16, 19–24] on Zn-/Mg-doped mixed Zn-Ni-Mg-Cu SF explains the variation of magnetization with the doping content on the basis of Néel's two-sub-lattice model of ferrimagnetism, but up till now no literature on Ni-doped Zn-Mg-Cu SF is available which shows the presence of Yafet-Kittel three-sub-lattice model. Some reports are available [25–30] which shows the presence of Y-K type of magnetic ordering for high doping content. Thus, magnetic ordering also depends on the effect of doping concentration of the cation as also observed in [25–30]. Hence, it becomes important to study the effect of dopant on the structural, magnetic properties of SF.

Therefore, the aim of the present work is to look into the effect of Ni content on structural, magnetic properties of  $\text{Zn}_{0.75-x}\text{Ni}_x\text{Mg}_{0.15}\text{Cu}_{0.1}\text{Fe}_2\text{O}_4$  ferrite, synthesized by sol-gel auto-combustion.

## 23.2 Materials and Methods

### 23.2.1 Materials

AR-grade zinc nitrate,  $\text{Zn}(\text{NO}_3)_2 \cdot 6\text{H}_2\text{O}$ ; nickel acetate,  $\text{Ni}(\text{CH}_3\text{COO})_2 \cdot 4\text{H}_2\text{O}$ ; magnesium acetate,  $\text{Mg}(\text{CH}_3\text{COO})_2 \cdot 4\text{H}_2\text{O}$ ; copper nitrate,  $\text{Cu}(\text{NO}_3)_2 \cdot 3\text{H}_2\text{O}$ ; and ferric nitrate,  $\text{Fe}(\text{NO}_3)_3 \cdot 9\text{H}_2\text{O}$ , were used for the synthesis of  $\text{Zn}_{0.75-x}\text{Ni}_x\text{Mg}_{0.15}\text{Cu}_{0.1}\text{Fe}_2\text{O}_4$  ( $x = 0.00, 0.15, 0.30, 0.45, 0.60, \text{ and } 0.75$ ) spinel ferrite.

### 23.2.2 Material Synthesis

$\text{Zn}_{0.75-x}\text{Ni}_x\text{Mg}_{0.15}\text{Cu}_{0.1}\text{Fe}_2\text{O}_4$  ferrites were synthesized by sol-gel auto-combustion method. Stoichiometric amounts of citrate-nitrate/acetate precursors were mixed with citric acid (in the molar ratio 1:1). Citric acid has a dual function: *initially it acts as a chelator and then as a fuel* [31]. Synthesis was done by dissolving all the precursors in stoichiometric ratio in deionized water, and then ammonia solution ( $\text{NH}_4\text{OH}$ ) was added to maintain the pH at 7 by continuous stirring. Now the solution was heated at 120 °C in air till the loose powder (fluffy) was formed called as “dry gel or as-burnt powder” which was then annealed at 500 °C for 3 h in air.

### 23.2.3 Characterizations

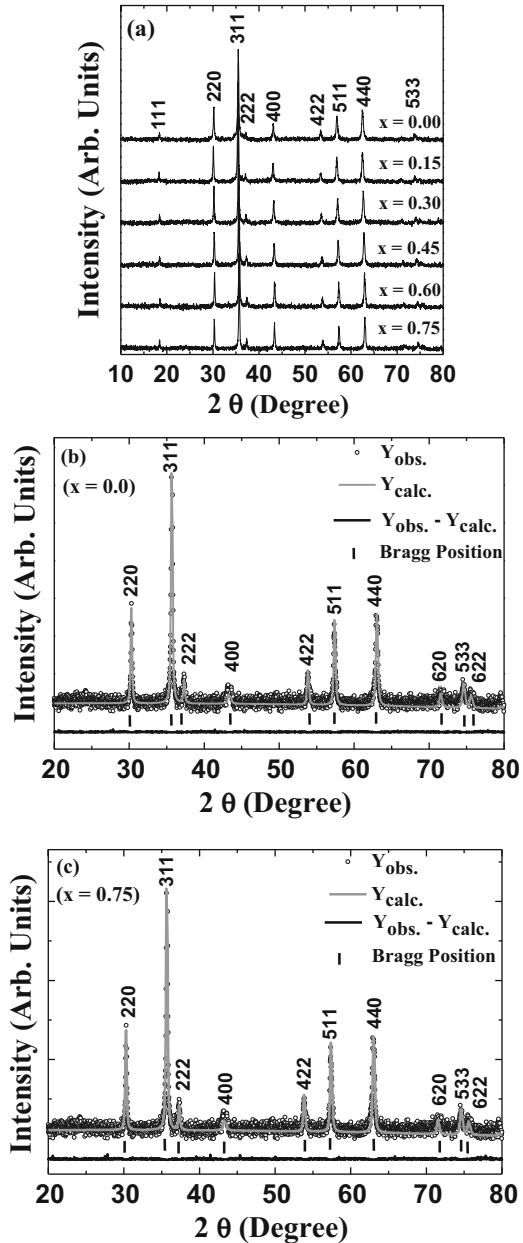
Room temperature structural properties of annealed powders were examined by X-ray diffraction (XRD) using Cu-K $\alpha$  radiation (wavelength ' $\lambda$ ' = 0.1540562 nm) in  $\theta$ - $2\theta$  configuration (step size of 0.019° and a scanning rate of 1.14 degree/minute), equipped by a fast counting Bruker LynxEye detector, with silicon strip technology. Elemental, quantitative analysis of surface morphology of Zn-Ni-Mg-Cu ferrite samples was performed by energy-dispersive X-ray analysis (EDAX, INCA-OXFORD) and scanning electron microscope (SEM, JEOL JSM-6390LV). Room temperature magnetization studies were done via SQUID magnetometer (Quantum Design MPMS-5S) with a maximum applied field ( $H_{\max}$ ) of  $\pm 5$  tesla. The magnetic properties, saturation magnetization ( $M_s$ ), squareness ratio/reduced magnetization ( $M_r/M_s$ ), and coercivity ( $H_c$ ), have been elucidated from hysteresis loops.

## 23.3 Results and Discussions

### 23.3.1 Structural Properties

X-ray diffraction (XRD) patterns of Ni<sup>2+</sup>-doped annealed 500 °C/3 h Zn<sub>0.75-x</sub>Ni<sub>x</sub>Mg<sub>0.15</sub>Cu<sub>0.1</sub>Fe<sub>2</sub>O<sub>4</sub> ( $x = 0.00$ – $0.75$ ) ferrite system is depicted in Fig. 23.1a. Figure 23.1b, c, respectively, illustrates the Rietveld refinement for the composition  $x = 0.00$  and  $x = 0.75$ , done via MAUD (Material Analysis Using Diffraction) software [32]. XRD confirms the single-phase spinel structure (JCPDS card No. 08-0234), signifying the cations solubility within their individual lattice sites. Structural parameters, experimental lattice parameter ( $a_{\text{exp}}$ ), Scherrer's grain diameter ( $D$ ), hopping length at A ( $L_A$ ) and B ( $L_B$ ) site, and specific surface area ( $S$ ) of the studied samples, were calculated as described in [22, 33] and are specified in Table 23.1. Observed changes in  $a_{\text{exp}}$ ,  $L_A$  and  $L_B$  can be accredited to difference in ionic radii of Zn<sup>2+</sup> (0.060 nm) and Ni<sup>2+</sup> (0.055 nm) ion. Lattice parameter of Zn<sub>0.75-x</sub>Ni<sub>x</sub>Mg<sub>0.15</sub>Cu<sub>0.1</sub>Fe<sub>2</sub>O<sub>4</sub> ferrite system initially increases for  $x = 0.15$  and decreases up to  $x = 0.60$  and again increases for  $x = 0.75$ . The value should decrease with the substitution of larger Zn<sup>2+</sup> (0.060 nm) ion by smaller Ni<sup>2+</sup> (0.055 nm) ion. But in present system,  $a_{\text{exp}}$  of Ni<sup>2+</sup> substituted Zn-Mg-Cu ferrite shows a non-monotonic behavior (common in systems which are not entirely normal or inverse [34, 35]) with increasing Ni<sup>2+</sup> content, violating Vegard's law [36]. Scherrer's grain diameter ( $D$ ) of the nano-phase synthesized particles initially increases for  $x = 0.15$ , decreases up to  $x = 0.45$ , and thereafter again increases up to  $x = 0.75$ . Though the synthesis was done under same conditions, the observed grain size is not same for all Ni<sup>2+</sup>-doped samples. Such non-monotonic behavior of  $D$  with increasing Ni concentration may be due to reaction condition, which initially favored the particle growth, and when Ni content is increased further, the creation of new nuclei occurs without any increase in particle size. At higher Ni content ( $0.45 < x \leq 0.75$ ),

**Fig. 23.1** (a) XRD pattern of annealed  $\text{Zn}_{0.75-x}\text{Ni}_x\text{Mg}_{0.15}\text{Cu}_{0.1}\text{Fe}_2\text{O}_4$  system. Representative Rietveld refinement for (b)  $x = 0.00$  and (c)  $x = 0.75$



again the reaction condition favors the particle growth, attributed to different dry gel formation time. High specific surface areas ( $S$ ) of particles are tremendously important for assorted catalytic processes. In general, high surface areas suggest small particle sizes. The smaller the particle size, the larger the surface area.  $S$

**Table 23.1** Lattice parameter ( $a_{\text{exp.}}$ ), hopping length for A site ( $L_A$ ) and B site ( $L_B$ ), Scherrer's grain diameter ( $D$ ), specific surface area ( $S$ ), and uniform strain ( $\varepsilon_u$ ) with Ni content ( $x$ ) of ann. 500 °C/3 h  $\text{Zn}_{0.75-x}\text{Ni}_x\text{Mg}_{0.15}\text{Cu}_{0.1}\text{Fe}_2\text{O}_4$  spinel ferrite

$x$	$a$ (nm)	$L_A$ (nm)	$L_B$ (nm)	$D$ (nm)	$S$ (m <sup>2</sup> /g)	$\varepsilon_u \times 10^{-3}$
0.00	0.8380	0.3629	0.2963	41.40	27.35	–
0.15	0.8397	0.3636	0.2969	50.89	22.48	1.9786
0.30	0.8385	0.3631	0.2965	49.67	23.04	3.9573
0.45	0.8349	0.3615	0.2952	47.09	24.09	–3.9573
0.60	0.8328	0.3606	0.2944	54.99	20.56	–6.3316
0.75	0.8336	0.3610	0.2947	56.73	20.08	–5.5402

of Zn-Ni-Mg-Cu ferrite system initially decreases for  $x = 0.15$ , increases up to  $x = 0.45$ , and again decreases thereafter. Increase and decrease in  $S$  can be ascribed to decrease and increase of  $D$ , respectively. Annealed particles are less suitable for catalytic application than the as-burnt particles (without any thermal/sintering treatment) because of their larger grain size. The uniform strain ( $\varepsilon_u$ ) for the studied samples was calculated using the expression [37]. Table 23.1 depicts the presence of compressive and tensile strain in the annealed Zn-Ni-Mg-Cu ferrite. The variation in the strain value can be attributed to the crystallinity of the synthesized samples.

### 23.3.2 Cationic Distribution

Cationic distribution of all the studied samples was determined by analyzing the XRD pattern, employing Bertaut method [38–41]. Cationic distribution of such mixed ferrite determined from the XRD intensities is also reported earlier in many reports [22–24, 42–46]. XRD intensity depends on the atomic position in spinel unit cell, whereas XRD peak position relies on size and shape of unit cell. This method uses a pair of reflections, 400/422 and 220/400, according to expression:

$$\frac{I_{\text{hkl}}^{\text{obs}}}{I_{\text{h'k'l'}}^{\text{obs}}} = \frac{I_{\text{hkl}}^{\text{cal}}}{I_{\text{h'k'l'}}^{\text{cal}}}$$

where  $I_{\text{hkl}}^{\text{obs}}$  and  $I_{\text{hkl}}^{\text{cal}}$  are, respectively, the observed and calculated intensities for the reflection (hkl). These ratios were evaluated for several combinations of cationic distribution at A and B sites as described in [41]. The finest cationic distribution among A and B sites for which theoretical and experimental ratios agree clearly was taken. Cationic distribution of  $\text{Zn}_{0.75-x}\text{Ni}_x\text{Mg}_{0.15}\text{Cu}_{0.1}\text{Fe}_2\text{O}_4$  spinel ferrite and calculated, observed intensity ratio for the planes, 400/422 and 220/400, are given in Table 23.2. Close matching of observed and calculated intensity ratio of 400/422 and 220/400 suggests an appropriate distribution of cations among A and B site. Table 23.2 also summarizes the occupation of  $\text{Zn}^{2+}$ ,  $\text{Ni}^{2+}$ ,  $\text{Mg}^{2+}$ ,  $\text{Cu}^{2+}$ , and  $\text{Fe}^{3+}$  ions on A and B site. Cationic distribution of  $\text{Mg}^{2+}$  ions on A and B site is independent of Ni doping.  $\text{Cu}^{2+}$  ions are present only at B site for all values of  $x$ , but, for  $x = 0.00$ ,  $\text{Cu}^{2+}$  ions are equally distributed at A and B site.  $\text{Ni}^{2+}$  ions

**Table 23.2** Cation distribution (for A and B site) and observed, calculated intensity ratios for  $I_{400/422}$ ,  $I_{220/400}$  of  $\text{Zn}_{0.75-x}\text{Ni}_x\text{Mg}_{0.15}\text{Cu}_{0.1}\text{Fe}_2\text{O}_4$  as a function of Ni content ( $x$ )

$x$	Cation distribution	$I_{400/422}$		$I_{220/400}$		$r_A$ (nm)	$r_B$ (nm)
		Cal.	Obs.	Cal.	Obs.		
0.00	$(\text{Zn}^{2+}_{0.07}\text{Cu}^{2+}_{0.05}\text{Fe}^{3+}_{0.88})_A$ $[\text{Zn}^{2+}_{0.68}\text{Mg}^{2+}_{0.15}\text{Cu}_{0.05}\text{Fe}^{3+}_{1.12}]_B$	1.70	1.72	1.61	1.60	0.0502	0.0685
0.15	$(\text{Zn}^{2+}_{0.1}\text{Ni}^{2+}_{0.15}\text{Fe}^{3+}_{0.75})_A$ $[\text{Zn}^{2+}_{0.5}\text{Mg}^{2+}_{0.15}\text{Cu}_{0.1}\text{Fe}^{3+}_{1.25}]_B$	1.44	1.41	1.67	1.65	0.0510	0.0679
0.30	$(\text{Zn}^{2+}_{0.06}\text{Ni}^{2+}_{0.2}\text{Fe}^{3+}_{0.74})_A$ $[\text{Zn}^{2+}_{0.39}\text{Ni}^{2+}_{0.1}\text{Mg}^{2+}_{0.15}\text{Cu}^{2+}_{0.1}\text{Fe}^{3+}_{1.26}]_B$	1.59	1.59	1.78	1.73	0.0509	0.0676
0.45	$(\text{Ni}^{2+}_{0.33}\text{Fe}^{3+}_{0.67})_A$ $[\text{Zn}^{2+}_{0.3}\text{Ni}^{2+}_{0.12}\text{Mg}^{2+}_{0.15}\text{Cu}_{0.1}\text{Fe}^{3+}_{1.33}]_B$	1.65	1.63	1.79	1.76	0.0510	0.0672
0.60	$(\text{Ni}^{2+}_{0.25}\text{Fe}^{3+}_{0.75})_A$ $[\text{Zn}^{2+}_{0.15}\text{Ni}^{2+}_{0.35}\text{Mg}^{2+}_{0.15}\text{Cu}_{0.1}\text{Fe}^{3+}_{1.25}]_B$	1.69	1.68	1.65	1.63	0.0505	0.0669
0.75	$(\text{Ni}^{2+}_{0.05}\text{Fe}^{3+}_{0.95})_A$ $[\text{Ni}^{2+}_{0.7}\text{Mg}^{2+}_{0.15}\text{Cu}^{2+}_{0.1}\text{Fe}^{3+}_{1.05}]_B$	1.74	1.75	1.71	1.71	0.0493	0.0671

occupy only A site for  $x = 0.15$ , but, with further increase in doping content ( $x$ ),  $\text{Ni}^{2+}$  ions occupy both A and B site. Also the concentration of  $\text{Ni}^{2+}$  ions increases on A site with  $x$ ; however, for  $x = 0.60$ – $0.75$ ,  $\text{Ni}^{2+}$  ions decrease. Ni doping also decreases  $\text{Zn}^{2+}$  ions on B site.  $\text{Zn}^{2+}$  ions are present both at A and B site, except for higher values of Ni content ( $0.45 \leq x \leq 0.75$ ) where  $\text{Zn}^{2+}$  ions are completely migrated to B site. Ni doping also decreases  $\text{Fe}^{3+}$  ions on A and increases on B site up to  $x = 0.45$  and then increases for A and decreases for B site thereafter. The cationic distribution in the present system shows the same trend as observed earlier [22–24, 47–50]. Using the obtained cation distribution, A and B site ionic radii ( $r_A$ ,  $r_B$ ) were calculated using the relation given in [41]. Ni content dependence of A ( $r_A$ ) and B ( $r_B$ ) site ionic radii is depicted in Table 23.2. Not much change is observed in the values of  $r_A$  except for  $x = 0.15$  which can be accredited to the sudden increase in larger  $\text{Zn}^{2+}$  ion (0.06 nm) by a large amount and decrease of smaller  $\text{Fe}^{3+}$  (0.049 nm) ions on A site. But the values of  $r_B$  show considerable changes with Ni content ( $x$ ). Observed decreases in  $r_B$  with  $x$  are due to continuous decrease in larger  $\text{Zn}^{2+}$  ion (0.074 nm) and increase of smaller  $\text{Ni}^{2+}$  ion (0.069 nm) on B site.

For a better understanding of Zn-Ni-Mg-Cu ferrite, spinel structure tetrahedral and octahedral bond length ( $R_A$ ,  $R_B$ ), oxygen parameter ( $u^{43m}$ ), shared tetrahedral edge length ( $d_{AE}$ ), and shared and unshared octahedral edge length ( $d_{BE}$ ,  $d_{BEu}$ ) were also calculated and are given in Table 23.3. Oxygen positional parameter or anion parameter ( $u^{43m}$ ) is calculated using  $r_A$  and  $a_{\text{exp}}$  values via the expression [43]. Oxygen parameter represents the movement of  $\text{O}^{2-}$  ion due to substitution of  $\text{Ni}^{2+}$  cation at A site.  $u$  parameter reflects modification of the spinel structure to adjust differences in the radius ratio of the cation in A and B sites. Values of  $u^{43m}$  parameter calculated for different compositions specified in Table 23.3 show an increase with  $x$



**Table 23.3** Ni content dependence of oxygen positional parameter ( $u^{43m}$ ), shared tetrahedral edge length ( $d_{AE}$ ), shared ( $d_{BE}$ ) and unshared octahedral edge length ( $d_{BEu}$ ), and tetrahedral ( $R_A$ ) and octahedral bond length ( $R_B$ ) for ann. (500 °C/3 h)  $Zn_{0.75-x}Ni_xMg_{0.15}Cu_{0.1}Fe_2O_4$  system

$x$	$u^{43m}$	$d_{AE}$ (nm)	$d_{BE}$ (nm)	$d_{BEu}$ (nm)	$R_A$ (nm)	$R_B$ (nm)
0.00	0.3796	0.3073	0.2853	0.2964	0.1882	0.2056
0.15	0.3799	0.3086	0.2851	0.2970	0.1890	0.2058
0.30	0.3800	0.3084	0.2845	0.2966	0.1889	0.2054
0.45	0.3807	0.3086	0.2818	0.2953	0.1890	0.2040
0.60	0.3806	0.3078	0.2811	0.2946	0.1885	0.2035
0.75	0.3797	0.3058	0.2835	0.2949	0.1873	0.2045

up to  $x = 0.45$  and reduces for  $0.45 < x \leq 0.75$ . For ideal cubic closed packed spinel structure,  $u_{ideal}^{43m} = 0.375$  [43]. The calculated  $u$  parameter values are greater than the ideal value ( $u_{ideal}^{43m} = 0.375$ ) for entire  $Zn_{0.75-x}Ni_xMg_{0.15}Cu_{0.1}Fe_2O_4$  nano-ferrite revealing distortion in the spinel structure.  $u^{43m}$  and  $a_{exp}$  values were also utilized in the calculation of other cation distribution parameters, demonstrated in Table 23.3:  $d_{AE}$ ,  $d_{BE}$ ,  $d_{BEu}$ ,  $R_A$ , and  $R_B$  using the relations [51]. The observed variation in tetrahedral bond length ( $R_A$ ) and shared tetrahedral edge ( $d_{AE}$ ) is in accordance with the changes in the ionic radii of A site ( $r_A$ ) with Ni content ( $x$ ). Decrease in octahedral bond length ( $R_B$ ) and shared and unshared octahedral edge ( $d_{BE}$ ,  $d_{BEu}$ ) with Ni doping is accredited to the replacement of larger ion ( $Zn^{2+}$ ) by smaller ion ( $Ni^{2+}$ ).

### 23.3.3 SEM, EDAX

Representative low-magnification (LM) and high-magnification (HM) SEM images for the composition  $x = 0.00$  and  $x = 0.45$  shown in Fig. 23.2 depict difference in surface morphology, porosity, and particle agglomeration with diverse shapes and sizes. This difference signifies that presence or absence of Ni ion in Zn-Mg-Cu ferrite plays an imperative role in microstructure of prepared spinel ferrite. The encircled area of SEM images represents the magnified region of the image. The non-connected spherical pores are noticeably visible in the LM and HM SEM images of  $x = 0.00$  with dissimilar pore sizes (555.70, 768.37, and 1.30  $\mu m$ ), which are missing for  $x = 0.45$ . The HM SEM image of the sample with  $x = 0.45$  shows large particle clusters with a planar and homogeneous surface. Pores present in sample,  $x = 0.00$ , are accredited to the liberation of large quantity of gases during combustion process [52], which would also get influenced by different amounts of nitrate/acetate salts of Zn, Ni, Mg, Cu, and Fe ions and citric acid used for synthesizing the studied samples [53], leading to changes in the pore sizes. Pores affect saturation magnetization ( $M_s$ ), grain size ( $D$ ), and surface area ( $S$ ) of the

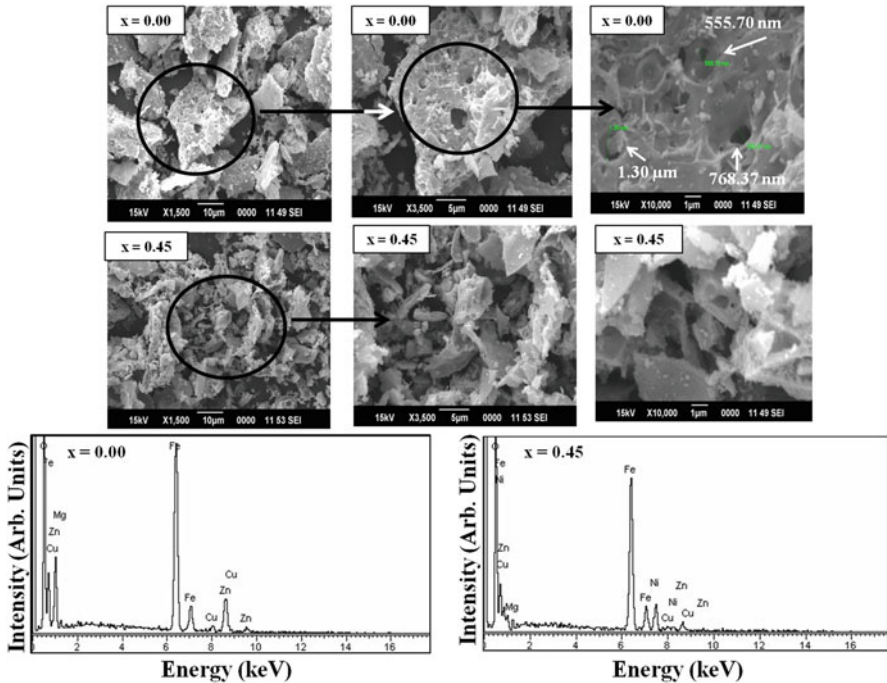


**Fig. 23.2** SEM microstructures and EDAX of  $\text{Zn}_{0.75-x}\text{Ni}_x\text{Mg}_{0.15}\text{Cu}_{0.1}\text{Fe}_2\text{O}_4$  system for  $x = 0.00$  and  $0.45$

sample [54, 55]. The sample with  $x = 0.00$  shows the lowest value of  $M_s$  ( $27.22 \text{ Am}^2/\text{kg}$ ), and the sample with  $x = 0.45$  exhibits the highest  $M_s$  ( $69.78 \text{ Am}^2/\text{kg}$ ). Pores operate as pinning core for electron spins and work as a demagnetizing field generator and, hence, reduce  $M_s$  as reported in earlier studies [54]. Occurrence of pores in the sample:  $x = 0.00$  decreases  $D$  and increases  $S$  of the particles as compared with that of the sample:  $x = 0.45$  (which is clearly seen in Table 23.1). Low value of  $D$  (for  $x = 0.00$  than for  $x = 0.45$ ) is due to the presence of pores which neutralizes the driving force for grain boundary movement and increases thickness of the grain boundary, and, hence,  $D$  decreases and  $S$  increases. Such porous structure with large surface area can be used in catalytic applications and as adsorbents [54, 56].

Elemental and quantitative analysis of the composition with  $x = 0.00$  and  $x = 0.45$  has been done using EDAX technique. EDAX spectra represented in Fig. 23.2 confirm the existence of all elements (Zn, Ni, Mg, Cu, Fe, O) in samples. The EDAX results distinctly indicate that all the precursors are very well reacted with each other to finally form the desired ferrite composition. The quantitative analysis of elements obtained from EDAX spectrum shows atomic and weight percentages of Zn, Ni, Mg, Cu, Fe, and O in Table 23.4. The close values of

**Table 23.4** Weight %, atomic %, experimental Me/Fe molar ratio  $(\text{Me/Fe})^{\text{exp}}$ , and theoretical Me/Fe molar ratio  $(\text{Me/Fe})^{\text{th}}$  of the elements Zn, Ni, Mg, Cu, Fe, and O present in  $\text{Zn}_{0.75-x}\text{Ni}_x\text{Mg}_{0.15}\text{Cu}_{0.1}\text{Fe}_2\text{O}_4$  ( $x = 0.00, 0.45$ ) system obtained from EDS analysis

Element	Weight %	Atomic %	$(\text{Me/Fe})^{\text{exp}}$	$(\text{Me/Fe})^{\text{th}}$
$x = 0.0$				
O	27.90	56.64	–	–
Mg	1.54	2.43	0.08	0.08
Fe	47.52	28.94	1	1
Zn	20.28	10.60	0.37	0.38
Cu	2.76	1.39	0.05	0.05
<b>Total</b>	<b>100.00</b>	<b>100.00</b>		
$x = 0.45$				
O	28.61	57.13	–	–
Mg	1.56	2.03	0.07	0.08
Fe	48.12	28.70	1	1
Ni	11.18	6.25	0.22	0.23
Cu	2.26	1.54	0.05	0.05
Zn	8.27	4.35	0.15	0.15
<b>Total</b>	<b>100.00</b>	<b>100.00</b>		

experimental and theoretical Me/Fe molar ratio (shown in Table 23.4) further confirm the homogeneous distribution of all the elements in the sample.

### 23.3.4 Magnetic Properties

Figure 23.3 shows room temperature hysteresis loops of the studied samples. Saturation magnetization ( $M_s$ ) of Zn-Ni-Mg-Cu spinel ferrite is determined from M-H curve. But  $M_s$  for  $x = 0.00$  and  $0.15$  is obtained by plotting M versus  $1/H$  curve and extrapolating the data to  $1/H = 0$  [11] as samples are not saturated even at  $H_{\text{max}}$  of 5 tesla. The superparamagnetic behavior observed for  $x = 0.00$  and  $0.15$  samples signifies that the magneto-crystalline anisotropy energy has been overcome by thermal energy. The samples are able to sustain magnetic ordering and show soft ferrimagnetic behavior due to enhancement of the magneto-crystalline anisotropy by the substitution of soft magnetic  $\text{Ni}^{2+}$  ions. Similar soft magnetic behavior in Zn-Ni-Mg-Cu ferrites has also been reported in literature [23, 24].

The magnetic parameters, Néel and experimental magnetic moment ( $n^e_N$ ,  $n^e_B$ )  $\mu_B$ , saturation magnetization ( $M_s$ ), and Yafet-Kittle angle ( $\alpha_{YK}$ ), are illustrated in Table 23.5. Magnetization is influenced by both extrinsic and inherent parameters such as magneto-crystalline anisotropy constant, grain size, A-B exchange interactions, and site occupancy of cations [57]. Fluctuation in grain size also influences the magnetization due to domain wall movement under the action of magnetic field. The overall value of magnetization obtained is a result of the contribution of all the factors depending upon ferrite composition.

**Fig. 23.3** Variation of room temperature magnetization with applied magnetic field

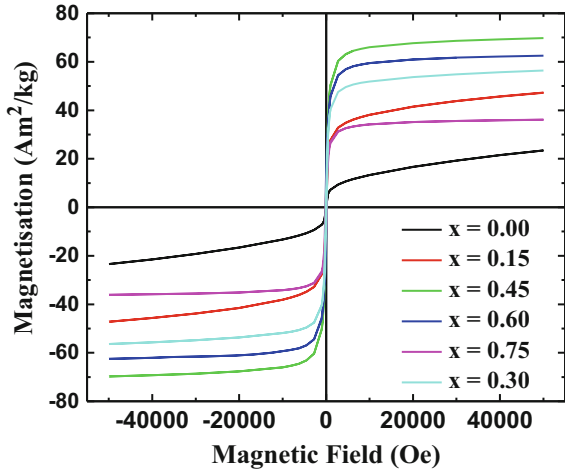
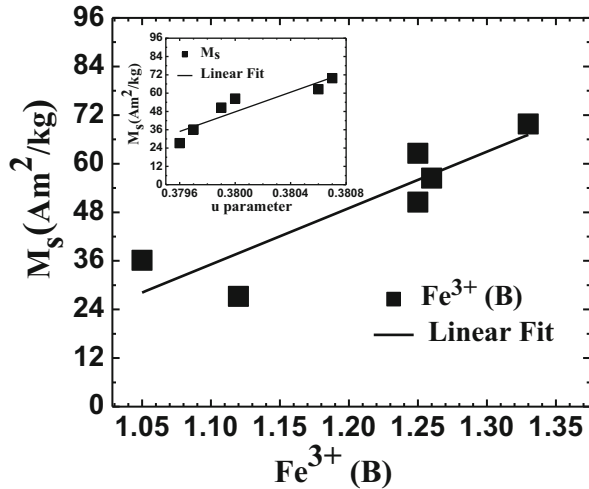


**Table 23.5** Variation of magnetic parameters: Néel and experimental magnetic moment ( $n^e_N$ ,  $n^e_B$ )  $\mu_B$ , saturation magnetization ( $M_s$ ), and Yafet-Kittel angle ( $\alpha_{Y-K}$ ) with Ni content ( $x$ ) for  $Zn_{0.75-x}Ni_xMg_{0.15}Cu_{0.1}Fe_2O_4$  (ann. 500 °C/3 h) system

$x$	$n^e_N$ ( $\mu_B$ )	$n^e_B$ ( $\mu_B$ )	$M_s$ ( $Am^2/Kg$ )	$\alpha_{Y-K}$ (degree)
0.00	1.20	1.14	27.22	7.48
0.15	2.30	2.11	50.49	13.38
0.30	2.50	2.35	56.41	11.52
0.45	2.98	2.90	69.78	7.78
0.60	2.80	2.58	62.55	13.60
0.75	1.90	1.49	36.11	19.93

Perusal of Table 23.5 shows that Néel and experimental magnetic moment (calculated by using the expression [13]) and saturation magnetization initially enhance with Ni content up to  $x = 0.45$  and then decrease for  $0.45 < x \leq 0.75$ , accredited to the occupation of cations as also explained earlier in [22–24, 51]. Magnetization of Zn-Ni-Mg-Cu ferrite mainly resides on the  $Ni^{2+}$  ( $2\mu_B$ ) and  $Fe^{3+}$  ( $5\mu_B$ ) ions because  $Zn^{2+}$  and  $Mg^{2+}$  ions are diamagnetic with 0 magnetic moment, and the percentage of occupied  $Cu^{2+}$  ( $1\mu_B$ ) ions is constant at B site as the dopant ( $Ni(x)$ ) is introduced in the spinel structure. With increasing Ni, up to  $x = 0.45$ ,  $Ni^{2+}$  ions force  $Fe^{3+}$  ions to migrate from A to B site; thus,  $Fe^{3+}$  ions on B site increase which in turn increase B site magnetic moment ( $M_B$ ) and decrease A site magnetic moment ( $M_A$ ), and therefore, the magnetization increases. Thus the saturation magnetization of Zn-Ni-Mg-Cu ferrite linearly depends on the content of  $Fe^{3+}$  ions on B site (shown in Fig. 23.4). Highest value of magnetization (69.78  $Am^2/kg$ ) is obtained for  $x = 0.45$ . When  $Zn^{2+}$  are completely substituted by  $Ni^{2+}$  ions (for  $x = 0.75$ ),  $Ni^{2+}$  ions push  $Fe^{3+}$  ions from B to A site, resulting in decrease of  $M_s$  of the system.

**Fig. 23.4** Variation of saturation magnetization ( $M_s$ ) with  $\text{Fe}^{3+}$  ions on B site ( $\text{Fe}^{3+}(\text{B})$ ). Inset: variation of  $M_s$  with oxygen parameter ( $u^{43m}$ )



The magnetization behavior with different Ni concentration can also be explained by Yafet-Kittel three-sub-lattice model. The non-zero Y-K angles for  $\text{Zn}_{0.75-x}\text{Ni}_x\text{Mg}_{0.15}\text{Cu}_{0.1}\text{Fe}_2\text{O}_4$  ferrite given in Table 23.5 suggest the presence of non-collinear spin structure on B site, i.e., existence of Yafet-Kittel model [58]. According to Yafet-Kittel model, the octahedral lattice (B) of spinel can be separated into two sub-lattices,  $B_1$  and  $B_2$ , with equal magnitude of magnetic moments, canted oppositely at the identical angle  $\alpha_{\text{Y-K}}$ , known as Y-K angle and calculated as given in [26]. In this way, two sub-lattices,  $B_1$  and  $B_2$ , have the triangular spin arrangement. Non-collinear magnetic ordering is also reported earlier for different systems [25–30].  $\alpha_{\text{Y-K}}$  initially increases for  $x = 0.15$ , decreases up to  $x = 0.45$ , and then finally increases for  $0.45 < x \leq 0.75$  with increase in Ni content ( $x$ ). Decrease in Y-K angle signifies decrease in spin canting at B site because of increase in A-B super exchange interaction, and increase of Y-K angle suggests increases of B-B interaction due to increase in spin canting at B site.

Observed linear variation (represented in Fig. 23.4 inset) of  $M_s$  with  $u^{43m}$  can also be attributed due to changes in  $u^{43m}$  values. Based on the linear variation between  $M_s$  and  $u^{43m}$ , one can propose the following empirical relations:  $M_s = Au^{43m} + B$  [59], where A and B are fitting constants with values, respectively, 12,186 and  $-32,193$ . This variation noticeably illustrates that  $u^{43m}$  also contributes resolutely in determining  $M_s$  of the studied Zn-Ni-Mg-Cu ferrite. It is worth noting that increase of  $M_s$  with  $u^{43m}$  is ascribed to higher distortion in the spinel structure, expected to affect the magnetization.

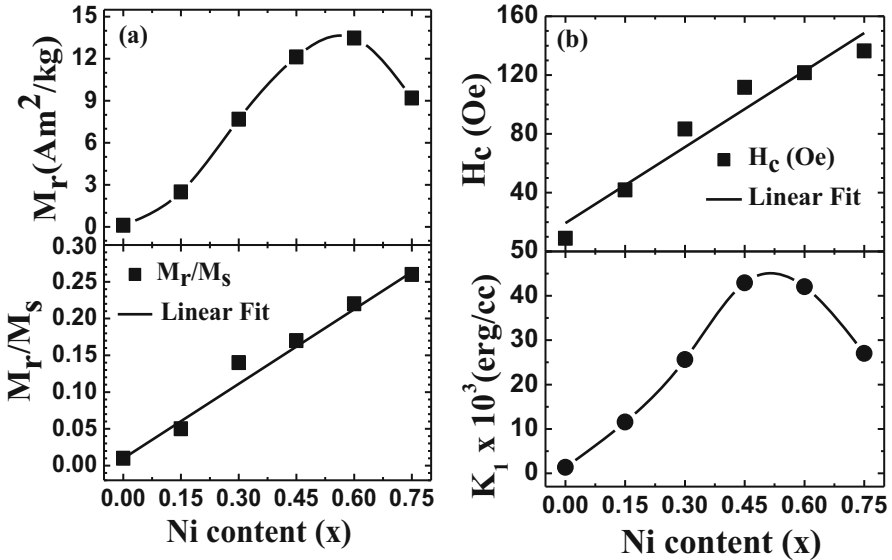


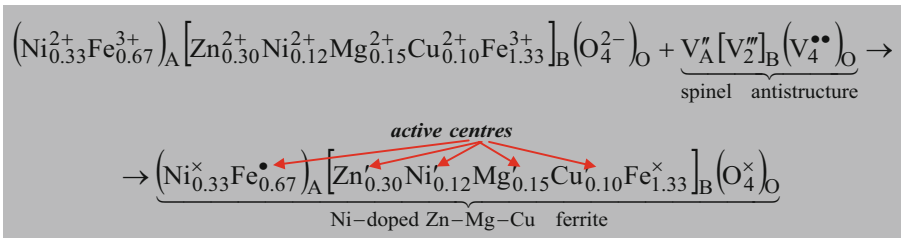
Fig. 23.5 (a) Ni content dependence of remanent magnetization ( $M_R$ ) and squareness ratio ( $M_R/M_S$ ). (b) Ni content dependence of coercivity ( $H_c$ ) and magneto-crystalline anisotropy constant ( $K_1$ ) for  $\text{Zn}_{0.75-x}\text{Ni}_x\text{Mg}_{0.15}\text{Cu}_{0.1}\text{Fe}_2\text{O}_4$

Variation of squareness ratio or reduced remanent magnetization ( $M_R/M_S$ ) and remanent magnetization ( $M_R$ ) with Ni content is specified in Fig. 23.5a.  $M_R/M_S$  and  $M_R$  values, respectively, range between 0.01–0.26 and 0.11–13.47  $\text{Am}^2/\text{kg}$ .  $M_R/M_S$  values increase continuously with Ni content.  $M_R$  increases up to  $x = 0.45$  and decreases thereafter. The variation in  $M_R$  is attributed to the changes in magnetization of the system [52], and it can be explained on the basis of cationic redistribution among A and B site [60] (as described for  $M_S$ ). Variation of magnetic parameters, magneto-crystalline anisotropy constant ( $K_1$ ) and coercivity ( $H_c$ ), is given in Fig. 23.5b. The coercivity of polycrystalline ferrite depends on  $K_1$ . When  $\text{Zn}^{2+}$  ions are replaced by  $\text{Ni}^{2+}$  ions, magneto-crystalline anisotropy increases because the anisotropy constant value of Ni-ferrite is greater than Zn ferrite [13], and hence,  $H_c$  increases. Since  $K_1$  of  $\text{NiFe}_2\text{O}_4$  is greater than  $\text{ZnFe}_2\text{O}_4$  [13] and when  $\text{Zn}^{2+}$  ions are replaced by  $\text{Ni}^{2+}$  ions, increase in  $K_1$  is observed (clearly seen in Fig. 23.5b). But for  $0.45 < x \leq 0.75$ ,  $K_1$  decreases, which can be elucidated by single-ion anisotropy model [52]. According to this model,  $\text{Fe}^{3+}$  ions on A and B site contribute to anisotropy energy.  $K_1$  value is then given by comparative combination A site  $\text{Fe}^{3+}$  ions with positive anisotropy which is compensated by B site  $\text{Fe}^{3+}$  ions with negative anisotropy. For  $0.45 < x \leq 0.75$ , negative contribution of B site  $\text{Fe}^{3+}$  ions increases, and positive contribution of A site  $\text{Fe}^{3+}$  ions decreases, which in turn decreases  $K_1$ .

### 23.3.5 Antistructural Modeling

Antistructural modeling is a new approach, which lets us predict the nature of the active surface centers. It is based on the superposition of the crystal structure with spinel antistructure  $V''_A[V''_B]_B(V_4^{\bullet\bullet})_O$ , where  $V''_A$  is negatively charged tetrahedral cationic vacancy,  $V''_B$  is negatively charged octahedral cationic vacancy, and  $V_4^{\bullet\bullet}$  is positively charged oxygen vacancy. The markings  $''$ ,  $'''$  (negative charge) and  $\bullet\bullet$  (positive charge) correspond to the electronic charge of the species as regards the sites in the spinel lattice. So each cation from A site interacts with tetrahedral cationic vacancy  $V''_A$ , each cation from B site interacts with octahedral cationic vacancy  $V''_B$ , and oxygen anions interact with oxygen vacancy  $V_4^{\bullet\bullet}$ . Antistructural modeling can be used for describing solid-solid interactions [61–63], for explanations of the defects in the ferrites system irradiated by  $\gamma$ -rays [64], for catalysts [65, 66], etc.

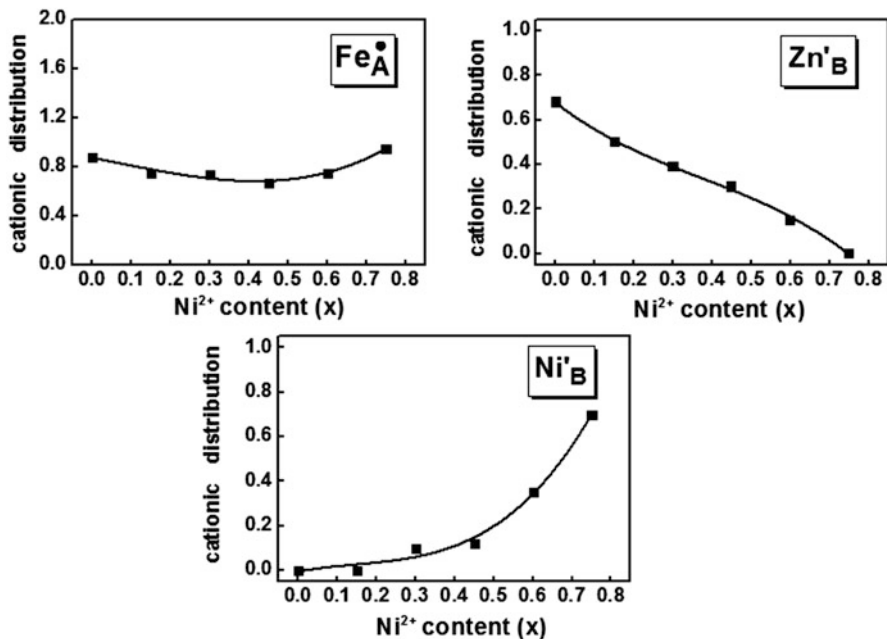
Detail explanation of the interaction between metal cations, oxygen anions, and spinel vacancies, respectively, can be written as  $Me^{2+} + V''_A \rightarrow Me^{\times}_A$ ;  $Me^{3+} + V''_A \rightarrow Me^{\bullet}_A$ ;  $Me^{2+} + V'''_B \rightarrow Me'_B$ ;  $Me^{3+} + V'''_B \rightarrow Me^{\times}_B$ ;  $O^{2-} + V_4^{\bullet\bullet} \rightarrow O^{\times}_O$ , where  $\times$  is an effective zero charge. The positive effective charges for electron neutrality reason must be balanced by the equivalent concentration of negative effective charges. In our case, the antistructural modeling, for example, for Ni-doped Mg-Zn-Cu ferrite with  $x = 0.45$  can be written as follows:



The antistructural modeling for Ni-doped zinc-magnesium-copper ferrites shown in Table 23.6 gives us new information about the active centers on the ferrite surface. As can be seen from Fig. 23.6, the concentration of positively charged ferric ions in tetrahedral A sites  $Fe^{\bullet}_A$  versus nickel ions content first decreases and then increases; the concentration of  $Zn'_B$  decreases, while the  $Ni'_B$  increases with the Ni content. Antistructural modeling provides us new information about surface-active centers (Table 23.6):  $Fe_A^{3+}$ ,  $Zn_B^{2+}$ ,  $Mg_B^{2+}$ ,  $Ni_B^{2+}$ , and  $Cu_B^{2+}$  will be active centers in any chemical processes, while  $Zn_A^{2+}$ ,  $Cu_A^{2+}$ ,  $Ni_A^{2+}$ , and  $Fe_B^{3+}$  cations will not be active centers due to their effective zero charge in the crystal lattice.

**Table 23.6** Donor and acceptor active centers on the surface of the  $\text{Zn}_{0.75-x}\text{Ni}_x\text{Mg}_{0.15}\text{Cu}_{0.1}\text{Fe}_2\text{O}_4$  system

Ni (x)	Chemical formulae	Crystalloquasichemical composition
0.00	$\text{Zn}_{0.75}^{2+}\text{Mg}_{0.15}^{2+}\text{Cu}_{0.10}^{2+}\text{Fe}_{2.0}^{3+}\text{O}_4^{2-}$	$(\text{Zn}_{0.07}^{\times}\text{Cu}_{0.05}^{\times}\text{Fe}_{0.88}^{\bullet})_{\text{A}}[\text{Zn}'_{0.68}\text{Mg}'_{0.15}\text{Cu}'_{0.05}\text{Fe}_{1.12}^{\times}]_{\text{B}}(\text{O}_4^{\times})_{\text{O}}$
0.15	$\text{Zn}_{0.60}^{2+}\text{Ni}_{0.15}^{2+}\text{Mg}_{0.15}^{2+}\text{Cu}_{0.10}^{2+}\text{Fe}_{2.0}^{3+}\text{O}_4^{2-}$	$(\text{Zn}_{0.10}^{\times}\text{Ni}_{0.15}^{\times}\text{Fe}_{0.75}^{\bullet})_{\text{A}}[\text{Zn}'_{0.50}\text{Mg}'_{0.15}\text{Cu}'_{0.10}\text{Fe}_{1.25}^{\times}]_{\text{B}}(\text{O}_4^{\times})_{\text{O}}$
0.30	$\text{Zn}_{0.45}^{2+}\text{Ni}_{0.30}^{2+}\text{Mg}_{0.15}^{2+}\text{Cu}_{0.10}^{2+}\text{Fe}_{2.0}^{3+}\text{O}_4^{2-}$	$(\text{Zn}_{0.06}^{\times}\text{Ni}_{0.20}^{\times}\text{Fe}_{0.74}^{\bullet})_{\text{A}}[\text{Zn}'_{0.39}\text{Ni}'_{0.1}\text{Mg}'_{0.15}\text{Cu}'_{0.10}\text{Fe}_{1.26}^{\times}]_{\text{B}}(\text{O}_4^{\times})_{\text{O}}$
0.45	$\text{Zn}_{0.30}^{2+}\text{Ni}_{0.45}^{2+}\text{Mg}_{0.15}^{2+}\text{Cu}_{0.10}^{2+}\text{Fe}_{2.0}^{3+}\text{O}_4^{2-}$	$(\text{Ni}_{0.33}^{\times}\text{Fe}_{0.67}^{\bullet})_{\text{A}}[\text{Zn}'_{0.30}\text{Ni}'_{0.12}\text{Mg}'_{0.15}\text{Cu}'_{0.10}\text{Fe}_{1.33}^{\times}]_{\text{B}}(\text{O}_4^{\times})_{\text{O}}$
0.60	$\text{Zn}_{0.15}^{2+}\text{Ni}_{0.60}^{2+}\text{Mg}_{0.15}^{2+}\text{Cu}_{0.10}^{2+}\text{Fe}_{2.0}^{3+}\text{O}_4^{2-}$	$(\text{Ni}_{0.25}^{\times}\text{Fe}_{0.75}^{\bullet})_{\text{A}}[\text{Zn}'_{0.15}\text{Ni}'_{0.35}\text{Mg}'_{0.15}\text{Cu}'_{0.10}\text{Fe}_{1.25}^{\times}]_{\text{B}}(\text{O}_4^{\times})_{\text{O}}$
0.75	$\text{Ni}_{0.75}^{2+}\text{Mg}_{0.15}^{2+}\text{Cu}_{0.10}^{2+}\text{Fe}_{2.0}^{3+}\text{O}_4^{2-}$	$(\text{Ni}_{0.05}^{\times}\text{Fe}_{0.95}^{\bullet})_{\text{A}}[\text{Ni}'_{0.70}\text{Mg}'_{0.15}\text{Cu}'_{0.10}\text{Fe}_{1.05}^{\times}]_{\text{B}}(\text{O}_4^{\times})_{\text{O}}$

**Fig. 23.6** Concentration of active surface centers in tetrahedral A sites (Fe) and octahedral B sites (Zn, Ni) as a function of the  $\text{Ni}^{2+}$  content (x) for  $\text{Zn}_{0.75-x}\text{Ni}_x\text{Mg}_{0.15}\text{Cu}_{0.1}\text{Fe}_2\text{O}_4$  samples

## 23.4 Conclusions

Ni addition induced changes in structural, magnetic properties, morphology, and cationic distribution of ann. Zn-Ni-Mg-Cu ferrite is studied in this paper. X-ray diffraction pattern of annealed (500 °C/3 h)  $\text{Zn}_{0.75-x}\text{Ni}_x\text{Mg}_{0.15}\text{Cu}_{0.1}\text{Fe}_2\text{O}_4$  ferrite with  $x = 0.0, 0.15, 0.30, 0.45, 0.60,$  and  $0.75$  synthesized by sol-gel auto-combustion



technique gives a clear indication of formation of cubic spinel phase with Scherrer's grain diameter ( $D$ ) ranging: 41.40–56.73 nm. Lattice parameter ( $a_{\text{exp}}$ ) and hopping length for A and B site ( $L_A$ ,  $L_B$ ) decrease with Ni addition, accredited to the replacement of  $\text{Zn}^{2+}$  by  $\text{Ni}^{2+}$  ions. Ni addition induced variation in tetrahedral bond length ( $R_A$ ) and is in agreement with changes in the ionic radii of A site ( $r_A$ ). Decrease in octahedral bond length ( $R_B$ ) and shared and unshared octahedral edge ( $d_{\text{BE}}$ ,  $d_{\text{BEu}}$ ) with Ni addition is accredited to the replacement of larger ion ( $\text{Zn}^{2+}$ ) by smaller ion ( $\text{Ni}^{2+}$ ). SEM images clearly show porous structure of the sample:  $x = 0.00$ . With Ni addition, coercivity ( $H_c$ ) and squareness ratio ( $M_r/M_s$ ) increase. The magnetic parameters, Néel and experimental magnetic moment ( $n^e_N$ ,  $n^e_B$ )  $\mu_B$ , saturation magnetization ( $M_s$ ), and magneto-crystalline anisotropy constant ( $K_1$ ), increase for lower Ni content ( $0.00 \leq x \leq 0.45$ ) and reduce for higher Ni content ( $0.45 < x \leq 0.75$ ). Non-zero Yafet-Kittel angle ( $\alpha_{\text{Y-K}}$ ) suggests presence of Yafet-Kittel type of magnetic ordering in  $\text{Zn}_{0.75-x}\text{Ni}_x\text{Mg}_{0.15}\text{Cu}_{0.1}\text{Fe}_2\text{O}_4$  (ann. 500 °C/3 h) system. A new antistructural modeling for describing active surface centers for Ni-doped zinc-magnesium-copper ferrites system is discussed for the first time.

**Acknowledgments** This work is supported by projects 783/CST/R & D/Phy and, Engg Sc, CSR-IC/CRS-74/2014-15/2104. Authors thank Dr. Mukul Gupta and Mr. L. Behra, UGC-DAE Consortium for Scientific Research, Indore, for performing XRD measurements. Authors express their gratitude to Dr. Shibu. M. Eapen, scientist-in-charge, STIC, Kochi (India), for providing SEM measurements.

## References

1. Zhang H, Ma Z, Zhou J et al (2000) Preparation and investigation of  $(\text{Ni}_{0.15}\text{Cu}_{0.25}\text{Zn}_{0.60})\text{Fe}_{1.96}\text{O}_4$  ferrite with very high initial permeability from self-propagated powders. *J Magn Magn Mater* 213:304–308
2. Reddy MP, Madhuri W, Ramana MV et al (2010) Effect of sintering temperature on structural and magnetic properties of NiCuZn and MgCuZn ferrites. *J Magn Magn Mater* 322:2819–2823
3. Reddy MP, Madhuri W, Balakrishnaiah G et al (2011) Microwave sintering of iron deficient Ni–Cu–Zn ferrites for multilayer chip inductors. *Curr Appl Phys* 11:191–198
4. Costa ACFM, Lula RT, Kiminami RHGA et al (2006) Preparation of nanostructured  $\text{NiFe}_2\text{O}_4$  catalysts by combustion reaction. *J Mater Sci* 41:4871–4875
5. Dey C, Baishya K, Ghosh A et al (2017) Improvement of drug delivery by hyperthermia treatment using magnetic cubic cobalt ferrite nanoparticles. *J Magn Magn Mater* 427:168–174. <https://doi.org/10.1016/j.jmmm.2016.11.024>
6. Tartaj P, Morales MP, Verdaguer SV et al (2003) The preparation of magnetic nanoparticles for applications in biomedicine. *J Phys D Appl Phys* 36:R182–R197
7. Azad AM, Hedayati A, Rydn M et al (2013) Examining the Cu–Mn–O spinel system as an oxygen carrier in chemical looping combustion. *Energy Technol* 1:59–69
8. Reddy DHK, Yun Y-S (2016) Spinel ferrite magnetic adsorbents: alternative future materials for water purification? *Coord Chem Rev* 315:90–111
9. Ehrhardt H, Campbell SJ, Hofmann M (2002) Structural evolution of ball-milled  $\text{ZnFe}_2\text{O}_4$ . *J Alloys Compd* 339:255–260
10. Sepelak V, Baabe D, Mienert D et al (2003) Evolution of structure and magnetic properties with annealing temperature in nanoscale high-energy-milled nickel ferrite. *J Magn Magn Mater* 257:377–386

11. Ammar S, Jouini N, Fiévet F et al (2004) Influence of the synthesis parameters on the cationic distribution of ZnFe<sub>2</sub>O<sub>4</sub> nanoparticles obtained by forced hydrolysis in polyol medium. *J Non-Cryst Solids* 345:658–662
12. Willard MA, Nakamura Y, Laughlin DE et al (1999) Magnetic properties of ordered and disordered spinel-phase ferrimagnets. *J Am Ceram Soc* 82:3342–3346
13. Smit J, Wijn HPJ (1959) Ferrites. Philips' Technical Library, Eindhoven-Netherlands, pp 148–149, 157
14. Chikazumi S (1997) Physics of ferromagnetism. Oxford University Press, Oxford, pp 502–504
15. Roy PK, Bera J (2006) Effect of Mg substitution on electromagnetic properties of (Ni<sub>0.25</sub>Cu<sub>0.20</sub>Zn<sub>0.55</sub>) Fe<sub>2</sub>O<sub>4</sub> ferrite prepared by auto combustion method. *J Magn Magn Mater* 298:38–42
16. Sujatha C, Reddy KV, Babu KS et al (2013) Effect of Mg substitution on electromagnetic properties of NiCuZn ferrite. *J Magn Magn Mater* 340:38–45
17. Akther Hossain AKM, Biswas TS, Yanagida T et al (2010) Investigation of structural and magnetic properties of polycrystalline Ni<sub>0.50</sub>Zn<sub>0.50-x</sub>Mg<sub>x</sub>Fe<sub>2</sub>O<sub>4</sub> spinel ferrites. *Mater Chem Phys* 120:461–467
18. Varalaxmi N, Reddy NR, Ramana MV et al (2008) Stress sensitivity of inductance in NiMgCuZn ferrites and development of a stress insensitive ferrite composition for micro inductors. *J Mater Sci Mater Electron* 19:399–405
19. Dar MA, Verma V, Gairola SP et al (2012) Low dielectric loss of Mg doped Ni–Cu–Zn nanoferrites for power applications. *Appl Surf Sci* 258:5342–5347
20. Sujatha C, Reddy KV, Babu KS et al (2012) Structural and magnetic properties of Mg substituted NiCuZn nano ferrites. *Physica B* 407:1232–1237
21. Sujatha C, Reddy KV, Babu KS et al (2013) Effect of co substitution of Mg and Zn on electromagnetic properties of NiCuZn ferrites. *J Phys Chem Solids* 74:917–923
22. Satakar M, Kane SN, Ghosh A et al (2014) Synthesis and soft magnetic properties of Zn<sub>0.8-x</sub>Ni<sub>x</sub>Mg<sub>0.1</sub>Cu<sub>0.1</sub>Fe<sub>2</sub>O<sub>4</sub> (x = 0.0–0.8) ferrites prepared by sol-gel auto-combustion method. *J Alloys Compd* 615:S313–S316
23. Kane SN, Satakar M (2017) Correlation between magnetic properties and cationic distribution of Zn<sub>0.85-x</sub>Ni<sub>x</sub>Mg<sub>0.05</sub>Cu<sub>0.1</sub>Fe<sub>2</sub>O<sub>4</sub> nano spinel ferrite: effect of Ni doping. *J Mater Sci* 52:3467–3477
24. Satakar M, Kane SN, Kumaresavanji M et al (2017) On the role of cationic distribution in determining magnetic properties of Zn<sub>0.7-x</sub>Ni<sub>x</sub>Mg<sub>0.2</sub>Cu<sub>0.1</sub>Fe<sub>2</sub>O<sub>4</sub> nano ferrite. *Mater Res Bull* 91:14–21. <https://doi.org/10.1016/j.materresbull.2017.03.021>
25. Rana MU, Misbah-ul-Islam, Abbas T (2003) Magnetic interactions in Cu-substituted manganese ferrites. *Solid State Commun* 126:129–133
26. Topkaya R, Baykal A, Demir A (2013) Yafet–Kittel-type magnetic order in Zn-substituted cobalt ferrite nanoparticles with uniaxial anisotropy. *J Nanopart Res* 15:1359–1376
27. Bamzai KK, Kour G, Kaur B et al (2014) Preparation, and structural and magnetic properties of Ca substituted magnesium ferrite with composition MgCa<sub>x</sub>Fe<sub>2-x</sub>O<sub>4</sub> (x = 0.00, 0.01, 0.03, 0.05, 0.07). *J Mater* 2014:1–8
28. Mazen SA, Abu-Elsaad NI (2006) Structural and some magnetic properties of manganese-substituted lithium ferrites. *J Magn Magn Mater* 298:38–42
29. Gadhari AB, Shinde TJ, Vasambekar PN (2010) Magnetic properties of rare earth ion (Sm<sup>3+</sup>) added nanocrystalline Mg–Cd ferrites, prepared by oxalate co-precipitation method. *J Magn Magn Mater* 322:3823–3827
30. Jadhav SA (2001) Magnetic properties of Zn-substituted Li–Cu ferrites. *J Magn Magn Mater* 224:167–172
31. Kapse VD, Ghosh SA, Raghuvanshi FC et al (2009) Nanocrystalline spinel Ni<sub>0.6</sub>Zn<sub>0.4</sub>Fe<sub>2</sub>O<sub>4</sub>: A novel material for H<sub>2</sub>S sensing. *Mater Chem Phys* 113:638–644
32. Lutterotti L, Scardi P (1990) Simultaneous structure and size-strain refinement by the Rietveld method. *J Appl Crystallogr* 23:246–252
33. Qi X, Zhou J, Yue Z et al (2003) Permeability and microstructure of manganese modified lithium ferrite prepared by sol–gel auto-combustion method. *Mater Sci Eng B* 99:278–281

34. Mohammed KA, Al-Rawas AD, Gismelseed AM et al (2012) Infrared and structural studies of  $Mg_{1-x}Zn_xFe_2O_4$  ferrites. *Physica B* 407:795–804
35. Alone ST, Shirsath SE, Kadam RH et al (2011) Chemical synthesis, structural and magnetic properties of nano-structured Co–Zn–Fe–Cr ferrite. *J Alloys Compd* 509:5055–5060
36. Vegard L (1921) The constitution of mixed crystals and the space occupied by atoms. *Z Phys* 5:17–26
37. Sharma R, Thakur P, Sharma P et al (2017) Ferrimagnetic  $Ni^{2+}$  doped Mg–Zn spinel ferrite nanoparticles for high density information storage. *J Alloys Compd* 704:7–17
38. Weil L, Bertaut EF, Bochirol L (1950) Propriétés magnétiques et structure de la phase quadratique du ferrite de cuivre. *J Phys Radium* 11:208–212
39. Eloska E, Wolski W (1992) The evidence of  $Cd_x^{2+}Fe_{1-x}^{3+}[Ni^{2+}_{1-x}Fe^{3+}_{1+x}]O_4$  cation distribution based on X-ray and mossbauer data. *Phys Status Solidi (A)* 132:K51–K56
40. Cervinka L, Simsa Z (1970) Distribution of copper ions in some copper-manganese ferrites. *J Phys B (Czechoslovakia)* 20:470–474
41. Tanna AR, Joshi HH (2013) Computer aided X-ray diffraction intensity analysis for spinels: hands-on computing experience. *World Acad Sci Eng Technol* 75:334–341
42. Pandit AA, More SS, Dorik RG et al (2003) Structural and magnetic properties of  $Co_{1+y}Sn_yFe_{2-2y-x}Cr_xO_4$  ferrite system. *Bull Mater Sci* 26:517–521
43. Al-Hilli MF, Li S, Kassim KS (2012) Structural analysis, magnetic and electrical properties of samarium substituted lithium–nickel mixed ferrites. *J Magn Magn Mater* 324:873–879
44. Alimuddin MH, Shirsath SE, Meena SS et al (2013) Investigation of structural, dielectric, magnetic and antibacterial activity of Cu–Cd–Ni–FeO<sub>4</sub> nanoparticles. *J Magn Magn Mater* 341:148–157
45. Hashim M, Meena SS, Kotnala RK et al (2014) Exploring the structural, Mössbauer and dielectric properties of  $Co^{2+}$  incorporated  $Mg_{0.5}Zn_{0.5-x}Co_xFe_2O_4$  nanocrystalline ferrite. *J Magn Magn Mater* 360:21–33
46. Mustafa G, Islam MU, Zhang W et al (2015) Influence of the divalent and trivalent ions substitution on the structural and magnetic properties of  $Mg_{0.5-x}Cd_xCo_{0.5}Cr_{0.04}Tb_yFe_{1.96-y}O_4$  ferrites prepared by sol–gel method. *J Magn Magn Mater* 387:147–154
47. Mohamed MB, Wahba AM, Heiba ZK (2015) Effect of Zn substitution on structural, magnetic, and electric properties of  $Ni_{1-x}Zn_xFe_{1.78}Al_{0.2}Gd_{0.02}O_4$  nanoparticles. *J Supercond Nov Magn* 28:3675–3683
48. Sathishkumar G, Venkataraju C, Sivakumar K (2013) Magnetic and dielectric properties of cadmium substituted nickel cobalt nanoferrites. *J Mater Sci Mater Electron* 24:1057–1062
49. Najmoddin N, Beitollahi A, Kavas H et al (2014) XRD cation distribution and magnetic properties of mesoporous Zn-substituted  $CuFe_2O_4$ . *Ceram Int* 40:3619–3625
50. Jadhav J, Biswas S, Yadav AK et al (2017) Structural and magnetic properties of nanocrystalline Ni–Zn ferrites: in the context of cationic distribution. *J Alloys Compd* 696:28–41
51. Kurmude DV, Barkule RS, Raut AV et al (2014) X-ray diffraction and cation distribution studies in zinc-substituted nickel ferrite nanoparticles. *J Supercond Nov Magn* 27:547–553
52. Tholkappian R, Vishista K (2015) Combustion synthesis of Mg–Er ferrite nanoparticles: cation distribution and structural, optical, and magnetic properties. *Mater Sci Semicond Process* 40:631–642
53. Sutka A, Meziniskis G (2012) Sol–gel auto-combustion synthesis of spinel-type ferrite nanomaterials. *Front Mater Sci* 6:128–141
54. Sun Y, Ji G, Zheng M et al (2010) Synthesis and magnetic properties of crystalline mesoporous  $CoFe_2O_4$  with large specific surface area. *J Mater Chem* 20:945–952
55. Rikukawa H (1982) Relationship between microstructures and magnetic properties of ferrites containing closed pores. *IEEE Trans Magn* 18:1535–1537
56. Gao Z, Cui F, Zeng S et al (2010) A high surface area superparamagnetic mesoporous spinel ferrite synthesized by a template-free approach and its adsorptive property. *Microporous Mesoporous Mater* 132:188–195

57. Verma A, Chatterjee R (2006) Effect of zinc concentration on the structural, electrical and magnetic properties of mixed Mn–Zn and Ni–Zn ferrites synthesized by the citrate precursor technique. *J Magn Magn Mater* 306:313–320
58. Yafet Y, Kittel C (1952) Antiferromagnetic arrangements in ferrites. *Phys Rev* 87:290–294
59. Raghuvanshi S, Mazaleyrat F, Kane SN (2018)  $Mg_{1-x}Zn_xFe_2O_4$  nanoparticles: interplay between cation distribution and magnetic properties. *AIP Adv* 8:047804–047810
60. Faraz A, Maqsood A (2012) Synthesis, structural, electrical, magnetic Curie temperature and Y–K angle studies of Mn–Cu–Ni mixed spinel nanoferrites. *J Supercond Nov Magn* 25:509–517
61. Tatarchuk TR, Paliychuk ND, Bououdina M et al (2018) Effect of cobalt substitution on structural, elastic, magnetic and optical properties of zinc ferrite nanoparticles. *J Alloys Compd* 731:1256–1266. <https://doi.org/10.1016/j.jallcom.2017.10.103>
62. Tatarchuk T, Bououdina M, Macyk W et al (2017) Structural, optical, and magnetic properties of Zn-doped  $CoFe_2O_4$  nanoparticles. *Nanoscale Res Lett* 12(1):141–151. <https://doi.org/10.1186/s11671-017-1899-x>
63. Tatarchuk T, Bououdina M, Paliychuk N et al (2017) Structural characterization and antistructure modeling of cobalt-substituted zinc ferrites. *J Alloys Compd* 694:777–791. <https://doi.org/10.1016/j.jallcom.2016.10.067>
64. Ahmed MA, Hassan HE, Eltabey MM et al (2018) Mössbauer spectroscopy of  $Mg_xCu_{0.5-x}Zn_{0.5}Fe_2O_4$  ( $x=0.0, 0.2$  and  $0.5$ ) ferrites system irradiated by  $\gamma$ -rays. *Phys B Condens Matter* 530:195–200. <https://doi.org/10.1016/j.physb.2017.10.125>
65. Kurta SA, Mykytyn IM, Tatarchuk TR (2014) Structure and the catalysis mechanism of oxidative chlorination in nanostructural layers of a surface of alumina. *Nanoscale Res Lett* 9(1):357–365. <https://doi.org/10.1186/1556-276X-9-357>
66. Tatarchuk T, Bououdina M, Vijaya JJ et al (2017) Spinel ferrite nanoparticles: synthesis, crystal structure, properties, and perspective applications. In: Fesenko O, Yat-senko L (eds) *Nanophysics, nanomaterials, interface studies, and applications*. NANO 2016. Springer Proceedings in Physics, vol 195. Springer, Cham, pp 305–325. [https://doi.org/10.1007/978-3-319-56422-7\\_22](https://doi.org/10.1007/978-3-319-56422-7_22)

# Chapter 24

## Dielectric Properties and AC Conductivity of Epoxy/Hybrid Nanocarbon Filler Composites



Ludmila L. Vovchenko, Ludmila Yu. Matzui, Yulia S. Perets,  
and Yurii S. Milovanov

### 24.1 Introduction

Discovery of nanoscaled carbon materials such as carbon nanotubes (CNTs), graphite nanoplatelets (GNPs), and graphene and the development of nanocarbon-based polymer composites open new era in material science and technology [1]. Nanoscaled carbon fillers exhibit a range of remarkable properties, such as exceptional Young's modulus, high tensile strength, excellent thermal and electrical conductivity, and high surface area [2, 3]. Graphene, which consists of several stacked graphene sheets, shows many extraordinary properties such as high carrier mobility, mechanic stiffness, and fascinating electromagnetic response [4, 5]. Compared with graphene, GNPs exhibit good mechanical and electrical properties [6] and have much lower production cost and better stability. Due to these outstanding properties, nanocarbon materials are the most promising fillers to improve mechanical and physical properties of composites. In particular, the incorporation of highly conductive nanocarbon particles into different polymers (epoxy, polypropylene, poly(vinylidene fluoride), polystyrene, etc.) [6–8] allows to create the new nanocomposites with tunable electrical properties. The most important feature of reported composites is very low percolation threshold in electrical conductivity due to high aspect ratio of carbon nanoparticles and easy formation of conductive network in composite. Furthermore, nanocarbon-based polymer composites are very perspective for applications in electromagnetic shielding and high-energy-density capacitors, owing to unique property of dramatic increase in their dielectric constants near the percolation threshold.

---

L. L. Vovchenko (✉) · L. Y. Matzui · Y. S. Perets · Y. S. Milovanov  
Departments of Physics and Institute of High Technologies, Taras Shevchenko National  
University of Kyiv, Kyiv, Ukraine  
e-mail: [vovch@univ.kiev.ua](mailto:vovch@univ.kiev.ua)

Nanocomposites are heterostructures with a large number of interphase boundaries of carbon nanotubes/polymers with a certain spatial distribution of the disperse phase (1D or 2D nanocarbon particles) in the polymer matrix; both the microstructure of such composites and their properties are significantly dependent on the content of nanofillers. So, as it was shown in [9] at studies of graphene/poly(vinylidene fluoride) composites, there are still some challenges in development of nanocarbon/polymer composites. First, it is difficult to tailor the dielectric properties of the composites by changing the volume fraction of nanocarbon, since a small change in the conductive filler content would cause a dramatic variation of percolation network near the percolation threshold. Second, the dielectric loss in the conductive filler/polymer composites always appears to be very large due to the leakage current in composites after percolation threshold. Third, poor compatibility between the nanocarbon and polymers prevents the formation of a homogeneous composite that leads to the harmful agglomeration of nanocarbon particles. To solve these problems, it is obvious that the controllable dispersibility of nanocarbon particles in polymer matrix should be primarily realized since the nanofiller dispersion is decisive to the electrical, mechanical, thermal, and other properties of nanocomposites.

The electrical transport and propagation of electromagnetic waves in composite heterostructures is a field of great fundamental importance in diverse applications, with potential in aeronautics, space, and telecommunications [4, 10]. Achieving an understanding of the properties and behavior of a wide range of composite heterostructures has therefore become one of the main themes in material research. Inhomogeneity and boundary conditions in heterogeneous media strongly influence on effective properties of composite such as electrical conductivity, dielectric permittivity, and magnetic permeability. As it was noted in [4, 11] at modeling and calculation of physical properties of mentioned composites, it is necessary to take into account the collective effects that are operative at high concentrations of filler particles and consider the complicated microstructures of real composite materials for obtaining of predictive values of effective parameters of composites [12].

In recent years in many studies [13–16], it was shown that multicomponent composites have advantages in mechanical property and electrical and thermal conductivities. Multiphase composites with several different fillers in the matrix are very interesting in order to find the so-called synergy effect. Often, the distribution of different fillers within the polymer matrix can be favorable, and electrical transport can occur in different filler networks together. When this occurs, the percolation threshold can decrease dramatically. Many investigations of synergy effects were performed in CNT/CB composites, and a significant decrease in the percolation threshold, in comparison with CB composites, was observed [17, 18].

However, it is not clear whether multicomponent composites also have the advantage in preparing materials with high tunable dielectric permittivity, because dielectric property and conductivity have a fundamental difference. Specifically, the dielectric property reflects the ability to store and consume electrostatic energy in an alternating electric field of a material, while the electric conductivity of a material refers to the ability of transporting electric charges. For a conductor/polymer

composite, when a perfect conductive network is formed, continuously increasing the content of electric conductors will lead to increased electric conductivity, declined dielectric constant, and significantly increased dielectric loss. Therefore, it is interesting and necessary to reveal the origin of the dielectric properties of the multicomponent composites. So, in [15] at study of broadband dielectric/electric properties of composites filled with 12 wt.% of CNT, onion-like carbon (OLC), and mixed CNT/OLC composites, it was demonstrated that the dielectric and electric properties with OLC inclusions can be substantially improved with the addition of CNT.

The aim of this study is to investigate the influence of hybrid nanocarbon filler on dielectric properties and AC conductivity of epoxy-based composites in the frequency range 1 kHz–2 MHz and reveal the peculiarities of the electrical transport in these composites.

## 24.2 Experimental

Multiwalled carbon nanotubes (CNTs) and graphite nanoplatelets (GNPs) were used as filler in polymer composites. CNTs (average outer diameter 10–30 nm, length 10–30  $\mu\text{m}$ , purity >90.0%) were purchased from Cheap tubes Inc., USA. Graphite nanoplatelets (diameter 0.2–30  $\mu\text{m}$ , thickness 5–65 nm) were prepared according to a scheme described in [19]. Figure 24.1 presents the electron microscopy images of carbon filler particles, and Table 24.1 summarizes the data on the size and morphology of filler particles.

Epoxy resin Larite 285 with low viscosity (600  $\div$  900 mPa·s at 25  $^{\circ}\text{C}$ ) was used as polymer matrix at composite fabrication. 0–7 wt.% GNP- and GNP/CNT/L285 composite samples were fabricated by ultrasound mixing of the components. Namely, mixture of L285 epoxy resin and nanocarbon component of the filler was

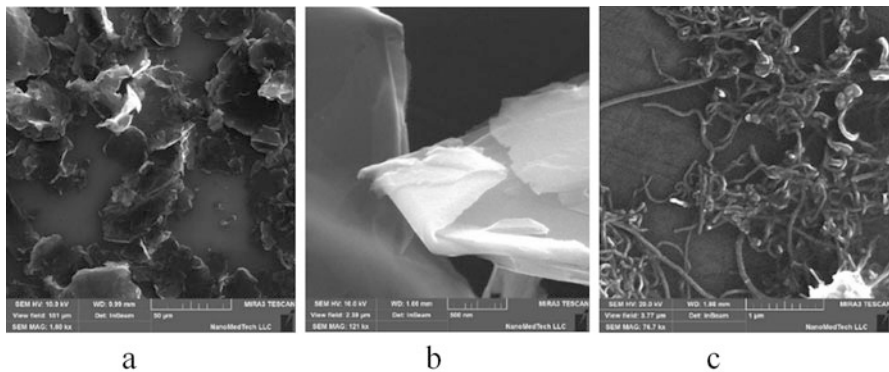


Fig. 24.1 SEM images of nanocarbon fillers: (a, b) graphite nanoplatelets, (c) carbon nanotubes

**Table 24.1** Morphology of the polymer composite fillers

	GNPs	CNTs
Shape of particles	Plates	Cylinders
Length of particles		10–30 $\mu\text{m}$
Diameter	0.2–30 $\mu\text{m}$	10–30 nm
Thickness	5–65 nm	
Aspect ratio AR	40–460	1000
Packing factor $F$	0.05	0.06

**Table 24.2** Phase composition of epoxy composites

Type of composite nanocarbon/L285	Total content of filler, wt. %
GNP:CNT 1:0	1; 2; 4; 6; 7
GNP:CNT 3:1	1; 2; 3; 4
GNP:CNT 1:1	0,3; 2; 3; 4

subjected to ultrasound action (in BAKU 9050 ultrasonic cleaner, 40 kHz, 50 W), for 15 min in the case of GNP filler and for 45 min in the case of MWCNT filler. After H285 hardener (based on polyamine) was added to the liquid composite mixture of 0–7 wt.%, GNP- or GNP/CNT/L285 and carefully mixed and then poured into a mold made of a nonmagnetic polymer material. The curing of the composite was performed in two stages: under normal conditions in air during a day with next final drying of cured composite sample at stepwise increasing temperature from 40 to 80 °C during 5 h.

Table 24.2 presents the composition of carbon filler in fabricated epoxy composites.

Scanning electron microscopy (SEM) images were performed by using Mira3 TESCAN technique.

The electrical properties of epoxy composites were studied by measuring impedance spectra at room temperature using Z-2000 impedance meter at ac current mode in the frequency range from 1 kHz to 2 MHz.

## 24.3 Results and Discussion

### 24.3.1 Microstructure of Nanocarbon/Epoxy Composites

It is obvious that the microstructure of developed composites strongly depends on the content and structure/morphology of filler particles. Figure 24.2 schematically presents the spatial distribution of nanocarbon filler particles in epoxy matrix before and after percolation threshold.

As it is seen, GNP particles become uniformly distributed in the bulk of the epoxy matrix (Fig. 24.2a), and great quantity of contacts between graphite particles through polymer interlayer appears in the infinite cluster form of GNP particles



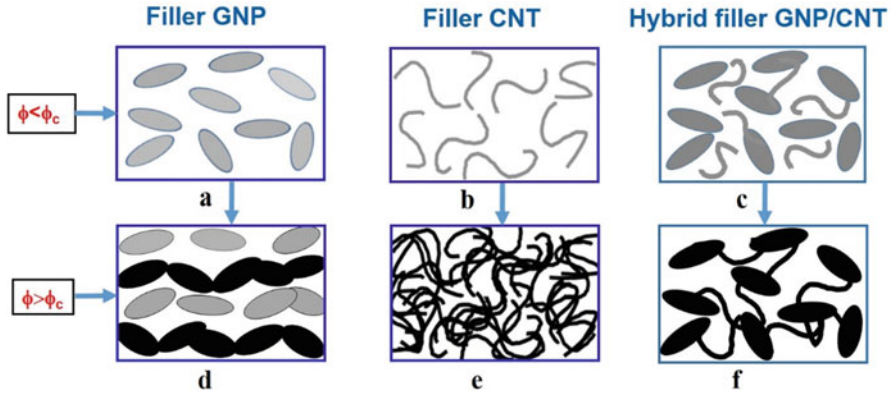


**Fig. 24.2** Schematic presentation of nanocarbon-filled epoxy composites: (a, d) GNP filler, (b, e) CNT filler, (c, f) hybrid GNP/CNT filler

at GNP content increase (Fig. 24.2d). Volume distribution of CNT constituent in CMs is nonuniform due to both high CNT aspect ratio and high level of CNT agglomeration (see Fig. 24.2b, e), because the ultrasonic dispersion is insufficient to separate strongly twisted CNTs in such materials. Such structure of CNTs is favorable for the formation of CNT infinite cluster (grid) even at low concentrations in the epoxy CM. In a case of hybrid filler CNT/GNP after the percolation threshold, the additional noncontinuous chains of agglomerates of CNTs and GNPs are formed that lead to increase of electrical conductivity (Fig. 24.2f).

### 24.3.2 Impedance Analysis for CMs GNP/CNT/L285

Figures 24.3, 24.4, and 24.5 show the Nyquist diagram for complex impedance  $Z^*$  of CMs filled with single GNP and hybrid GNP/CNT fillers. Complex impedance can be presented as [20]:

$$Z^* = Z' - i \cdot Z'', \quad (24.1)$$

where  $Z'$  and  $Z''$  are real and imaginary parts of impedance.

The measured impedance decreases as the carbon filler concentration increases. The decrease in impedance indicates that the composite material becomes more conductive. Also, when the frequency was high enough, some gaps in the nanocarbon chains became conductive, and the carbon chains with small gaps became conductive. The conductive modes include tunneling or hopping.

Electron conduction in the carbon-filled composites occurred along carbon particles contacting each other or carbon nanoparticles particles separated by very small gaps in the composites. The gaps could be considered as potential barriers for

**Fig. 24.3** Nyquist diagram for complex impedance  $Z^*$  of CMs filled with 1 wt.% of hybrid GNP/CNT filler at various weight ratios between GNP and CNT

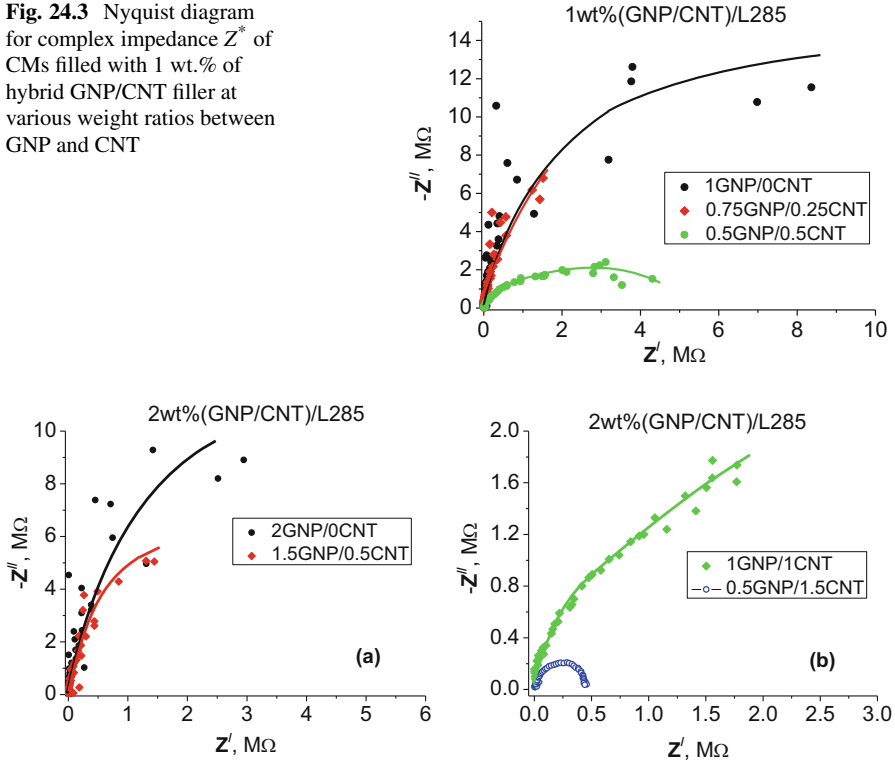
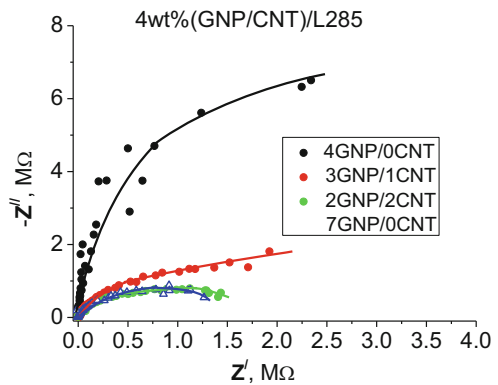


**Fig. 24.4** Nyquist diagram for complex impedance  $Z^*$  of CMs filled with 2 wt.% of hybrid GNP/CNT filler at various weight ratio between GNP and CNT

**Fig. 24.5** Nyquist diagram for complex impedance  $Z^*$  of CMs filled with 2 wt.% of hybrid GNP/CNT filler at various weight ratios between GNP and CNT



electrons to hop by the tunneling effect. Reducing the numbers or widths of gaps in the nanocarbon chains could enhance the free flow electrons and decrease the macroscopic electrical volume resistivity.

The Nyquist diagram exhibits a semicircle for CMs with single GNPs only at GNP content in 7 wt.%, while in a case of CMs with hybrid filler, GNP/CNT semicircle dependence  $Z''(Z')$  appears for the lower content of carbon filler and means that conductive pathways have been formed, and there are currents and polarization among conductors [21]. Such difference in Nyquist diagram behavior for GNP- and GNP/CNT/L285 composites is explained by lower percolation threshold for CMs filled with CNTs and CNT content in 1–2 wt.% and is sufficiently bigger than the  $C_{cr}$  for CNT/L285 CMs. Data on  $\sigma_{DC}$  for these composites were presented in our previous paper [22]. Because of the large aspect ratio, CNTs are easy to curl and form coil structures and thus producing an inductance. As the content of CNTs increases, CNTs tend toward aggregate, resulting in increase of the inductance [23].

In order to obtain more detail information about properties of the developed composites, different circuits are considered for analysis of actual complex impedance spectra [23, 24]. All composites have microcapacitor structures, and thus a capacitor exists in their equivalent circuits. In addition, at high content of conductive filler, equivalent circuit of composite has an inductance. However, it is worth pointing out that CMs with various content and type of filler have greatly different values of equivalent circuit elements because of different spatial distribution and dispersion of GNP and CNTs in composite. Figure 24.6 shows the variation of the imaginary part ( $Z''$ ) of the impedance as a function of frequency for some specimens with various types of filler and its content.

It was found that for the majority of investigated samples of nanocarbon/L285, there is an absence of any relaxation peak in the measured frequency range. Only for CM with 7 wt.% GNPs and for CMs with hybrid filler GNP/CNT where CNT content-rich 1–2 wt.%  $Z''$  values reach a maximum peak ( $Z''_{max}$ ) and then decrease with increasing frequency indicating the presence of dipolar relaxation in these nanocomposites [25].

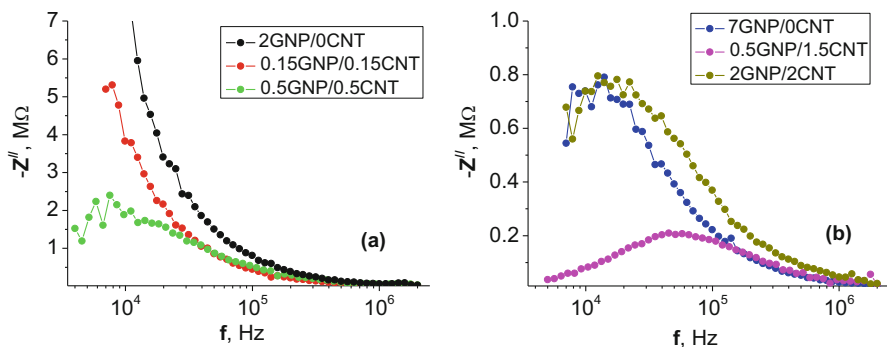


**Fig. 24.6** Imaginary part  $Z''$  of the complex impedance for different GNP and GNP/CNT concentrations in epoxy-based composites

### 24.3.3 Dielectric Properties of CMs GNP/CNT/L285

The dielectric constant  $\varepsilon_r'$  is a measure of the amount of energy stored, and the dielectric loss  $\varepsilon_r''$  is a measure of the amount of energy dissipated in the dielectric material under an applied electric field, and complex dielectric constant can be presented as  $\varepsilon_r^* = \varepsilon_r' - i \cdot \varepsilon_r''$  [20].

Using the data of impedance spectroscopy, we determined the real and imaginary parts of permittivity and AC electrical conductivity using the following relations:

$$\begin{aligned}\varepsilon_r' &= \frac{-Z''}{2\pi f \varepsilon_0 [(Z')^2 + (Z'')^2]} \cdot \frac{l}{A} \\ \varepsilon_r'' &= \frac{Z'}{2\pi f \varepsilon_0 [(Z')^2 + (Z'')^2]} \cdot \frac{l}{A}\end{aligned}\quad (24.2)$$

where  $f$  is the frequency of AC current,  $\varepsilon_0$  is the permittivity of free space, and  $l$  and  $A$  are sample thickness and sample cross section, relatively.

Dissipation factor determined as:

$$\tan \delta = \varepsilon_r'' / \varepsilon_r' \quad (24.3)$$

Electrical conductivity related with frequency and dielectric loss by following expression:

$$\sigma_{AC} = 2\pi f \varepsilon_0 \varepsilon_r'' \quad (24.4)$$

The variations of the real and imaginary parts of permittivity with frequency and filler content for L285 epoxy-based composites with hybrid filler GNP/CNT at various weight ratios between GNP and CNT are shown in Figs. 24.7, 24.8, and 24.9.

A common feature that can be seen in all figures is that the addition of GNPs or GNP/CNT increases the dielectric permittivity of epoxy resin. The carbon is a conductive material and does not work as dielectrics by itself. If it is covered with insulation materials, however, it shows a dielectric property by generating the space charge polarization at the interfaces. The promotion in dielectric permittivity can be mainly attributed to a gradual formation of microcapacitor networks in the epoxy matrix as the volume fraction of conductive nanofiller increases. The local microcapacitors consist of GNP or CNT particles separated by a thin insulating epoxy layer. This gives rise to a substantial increase in the intensity of local electric field around the fillers GNP and CNT, which subsequently promotes the charge carriers to migrate and accumulate at the interface of electrodes. This leads to the strong Maxwell-Wagner-Sillars (MWS) polarization (due to large difference of dielectric constant and in Fermi levels or chemical potential between the insulator

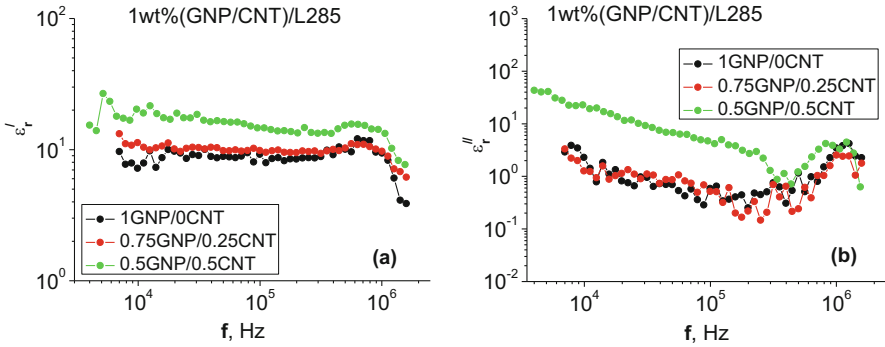


**Fig. 24.7** Real (a) and imaginary (b) parts of dielectric permittivity and dielectric loss tangent  $\tan\delta$  (c) of epoxy composites 1 wt.% nanocarbon/L285 versus frequency

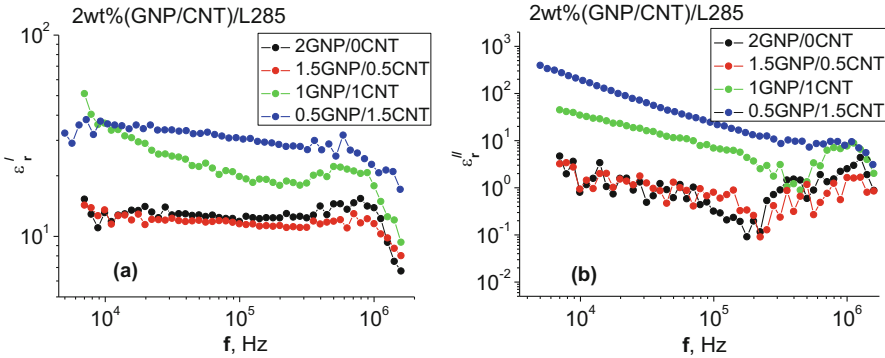


**Fig. 24.8** Real (a) and imaginary (b) parts of dielectric permittivity and dielectric loss tangent  $\tan\delta$  of epoxy composites 2 wt.% nanocarbon/L285 versus frequency

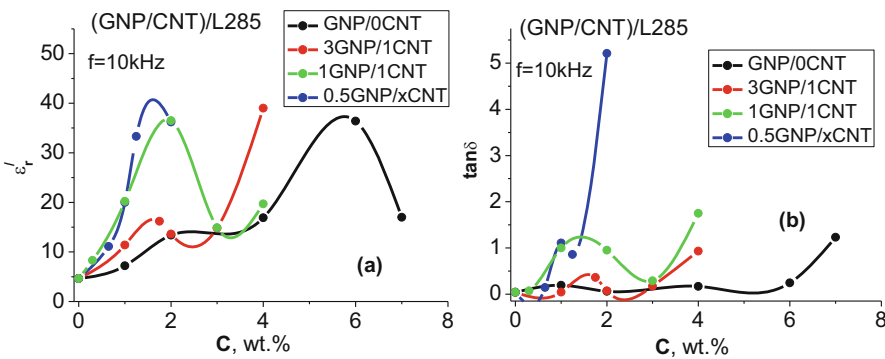


**Fig. 24.9** Real part of permittivity (a) and dielectric tangent loss (b) of epoxy composites nanocarbon/L285 at frequency 10 kHz versus hybrid nanocarbon filler content

polymer matrix and conductive filler) [26] and thus causes the increase in the dielectric constant, especially in low-frequency range [26, 27].

Furthermore, a thin insulating layer of epoxy resin is combined with the GNP or CNT particles to form a nanoscale structure in the polymer nanocomposites. This structure can fully realize the advantages of GNPs and CNTs (i.e., large specific surface area and high aspect ratio) and result in a huge interfacial area between nanocarbon filler and epoxy in the nanocomposite [28]. This provides a large number of sites for this interfacial polarization and significantly enhances MWS effect.

For the composites filled with conductive fillers, the percolation theory depicts that the variations of dielectric constant with frequency follow a power law as the filler content approaches percolation threshold [29]:

$$\varepsilon_{\text{eff}} = \varepsilon_m \cdot (\phi_c - \phi)^{-s} \quad (24.5)$$

where  $\varepsilon_{\text{eff}}$  is dielectric constant of composite;  $\varepsilon_i$  and  $\varepsilon_m$  are dielectric constants of nanocarbon filler and epoxy matrix, accordingly;  $\phi$  is volume fraction of filler; and  $s$  is critical index.

Initially, when small amount of fillers are incorporated into the matrix, i.e., at dilute concentration, the distance between fillers is large, and there is a little possibility for tunneling activity and also for the formation of microcapacitors. With increase of nanocarbon content in the polymer matrix, the distance between neighboring fillers is continuously reduced, resulting in a network of virtual microcapacitors to be slowly built up throughout the nanocomposite. However, near the percolation threshold, the distance between the nanocarbon fillers is greatly reduced. As a consequence, the capacitance of microcapacitors undergoes a sharp increase, and the tunneling activity also will become intense. Above the  $\phi_c$ , the distance between the fillers gets closer, so that even some fillers get in direct contact with each other due to their high aspect ratio.

Accordingly, new microcapacitor structures with high virtual capacitance are formed by those GNP or CNT fillers which are not yet in contact with each other. Meanwhile, the electron tunneling still takes place between neighboring fillers and clusters. In view of that, after the percolation threshold, the tunneling activity and microcapacitor effects will continue to be at high level.

The formation of microscale capacitors can be modeled as an additional contribution to interfacial permittivity of fillers, through the observation that the charge carriers accumulate at the fillers' interface due to abovementioned microcapacitor effect. According to (24.5) a divergence of the permittivity seemed to occur below the threshold as revealed by a sharp increase for filler content near percolation threshold  $C_{\text{cr}}$ . Above  $C_{\text{cr}}$ , however, a decrease of permittivity to an asymptotic value was expected. Instead, permittivity kept on increasing with increased filler content higher than the percolation concentration for these CMs. Similar results have been described in polymers filled with carbon black and carbon nanotubes [30, 31]. The one of the reasons of such behavior of  $\varepsilon'_r(C)$  dependence as proposed in [31] is related to presence of polymer layers between carbon fillers that promotes

the creation of microcapacitors which prevail over structural formation of the filler network. In other words, the percolating network also induces a capacitive effect that is stronger than the loss of capacitance associated with the reduction of the correlation length. In addition, the part of filler clusters is not directly integrated to the percolation network and is likely to participate in the permittivity of the composite [29].

So, near the percolation threshold, conductive GNP or CNT particles are almost touching each other but still remain isolated due to the existence of epoxy space layer. That is why we observed the broad maximum on  $\varepsilon'_r(C)$  dependence around percolation threshold and slight decrease of dielectric permittivity with increase of nanocarbon content. It is important to note that the position of maximum on  $\varepsilon'_r(C)$  dependence (see Fig. 24.9a) fully correlates with the percolation threshold in  $\sigma_{dc}$  conductivity for these composites (the percolation threshold  $C_{cr}$  for each series of nanocarbon/L285 composites is indicated in Fig. 24.11 by dashed lines).

The dielectric constant of the composites decreases with increasing frequency. The decrease of relative permittivity with frequency could be attributed to the insufficient time for dipoles to align before the field changes direction; in other words incapability of the dipole to follow the field variations at high frequency and the displacement or orientation of bound charge carriers may also play a role in this dispersion. At low frequency, the energy gap is wider than at high frequency; thus, the capacitance at low frequency is higher than at high frequency. The smaller is the distance between conductive particles, the lower is the frequency for the conduction. Therefore, with the increase of frequency, the capacitive resistance will greatly decrease, and some microcapacitors even become conductive, leading to decreased dielectric constant.

Apparently, the dielectric permittivity of CMs with higher content of carbon filler shows an even more serious frequency dependence behavior, suggesting that there should be a stronger MWS polarization.

With regard to a conductor/polymer composite, its dielectric loss mainly consists of the loss of electric conduction, dipolar loss, and the loss of interfacial polarization [32]. As the volume fraction of nanocarbon filler increases, the number of conductive paths will increase, leading to increased loss of electric conduction; therefore, the dielectric loss of GNP- and GNP/CNT/L285 composites increases as the content of nanocarbon increases. On the other hand, at relatively low frequency, the loss of electric conduction makes more contribution to dielectric loss than that of interfacial polarization, so the dielectric loss of composites decreases with the increase of frequency as shown in Figs. 24.7 and 24.8. As we can see from Fig. 24.9, the increase of CNT in hybrid filler promotes the high increase of dielectric permittivity and dissipation factor  $\tan\delta$  (compare samples of series 1:0; 3:1; 1:1; 0.5:x with hybrid filler content) and, accordingly, shift of the maximum of permittivity and dielectric loss into lower concentration of filler. So, maximum dielectric loss was observed for CMs series 0.5:x with 0.5wt.%GNP/1.5wt.%CNT, while the dielectric permittivity for this composite is the same as for samples filled with 1wt.%GNP/1wt.%CNT, 3wt.%GNP/1wt.%CNT, and 6wt.%GNP with much lower values of dielectric loss. Such behavior agreed with lower percolation threshold for CNT-based CMs related

to higher aspect ratio of CNT compared with GNPs and better ability to form carbon network in epoxy matrix. The presence of GNP in hybrid filler GNP/CNT expands the filler concentration range before percolation for increasing of the number of carbon filler particles acting as “artificial dipoles” and leading to increased dielectric permittivity. In addition, GNP particles with the large diameter/thickness ratio make it difficult for CNT on one side to bypass the graphite sheet and tangle with another CNT on the other side, consequently blocking the aggregation of CNTs [33]. This may improve the dispersion of CNTs promoting their de-agglomeration that also leads to increase of the number of formed microcapacitors and enhances dielectric permittivity. The presence of aggregates and agglomerates with shape irregularities in random packing causes the number of contacts to increase with increasing inclusions concentration and will eventually affect the conduction threshold. As it was shown in [34], ternary composites expanded graphite–carbon nanotube/cyanate ester (EG–MWCNT/CE) with very small contents of conductors can simultaneously have remarkably higher dielectric constant and lower dielectric loss, indicating that the weight ratio between EG and MWCNT is an important factor of determining the dielectric properties of the ternary composites. This is attractive for practical application of these composites for storing energy and homogenizing electric field. In our case it may be concluded that optimal ratio between GNP and CNT in hybrid is 3:1, when material is characterized by relatively high value of permittivity and low dielectric loss.

#### 24.3.4 AC Conductivity of CMs GNP/CNT/L285

Figure 24.10 displays the frequency dependence of alternating current (AC) conductivity of developed nanocomposites GNP- and GNP/CNT/L285 with filler contents 1 and 2 wt.% at various GNP:CNT ratios. As expected, the variation of AC conductivity with frequency is the reverse of dielectric constant  $\epsilon'_r$ . Figure 24.11 depicts the data on AC conductivity versus nanocarbon content at the frequency 10 kHz. It can be clearly seen that all composite systems show typical percolation transition as CNT content in CMs increases. For GNP/L285 nanocomposites, the conductivity shows dependence on frequency at 1 wt.% content owing to the insulating nature.

The conductivity of CMs with increased content of CNT in hybrid GNP/CNT displays a conducting characteristic which remains nearly frequency-independent (up to onset frequency  $f_c$ ) when the GNP/CNT loading exceeds the percolation threshold (see Figs. 24.9a and 24.10b, sample 0.5GNP/1.5CNT). So, in this case DC electrical conductivity is large, and overall conductivity  $\sigma(f)$  may be expressed as [15]:

$$\sigma(f) = \sigma_{DC} + \sigma_{AC} = \sigma_{DC} + A \cdot \omega^u \quad (24.6)$$



**Fig. 24.10** AC conductivity of epoxy composites with 1 (a) and 2 (b) wt.% of hybrid nanocarbon filler versus frequency for various ratio GNP/CNT

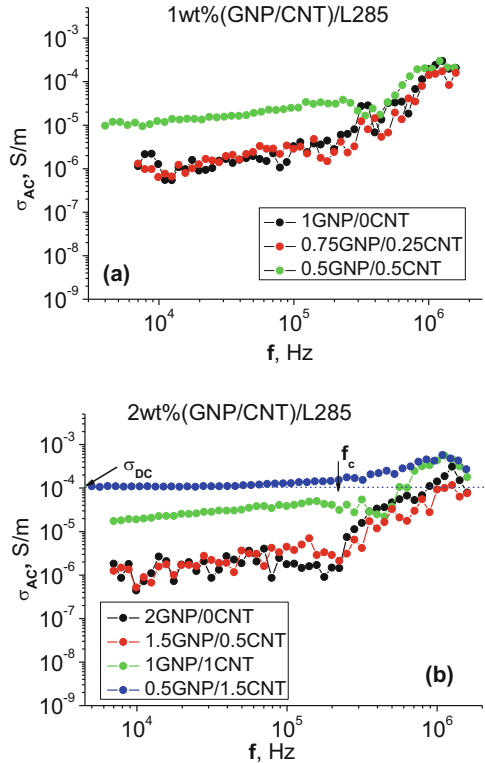
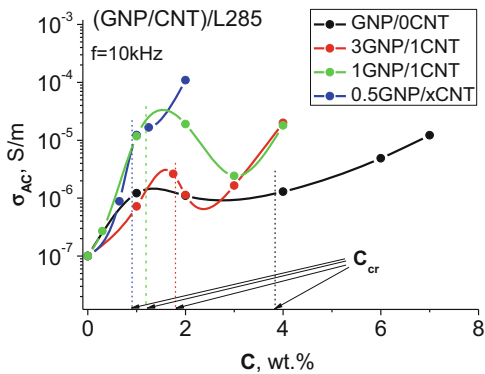


**Fig. 24.11** AC conductivity of epoxy composites nanocarbon/L285 at frequency 10 kHz versus hybrid nanocarbon filler content. Vertical dashed lines indicate the percolation threshold for each series of nanocarbon/L285 composites



where  $\omega = 2\pi f$  is angular frequency and  $A$  is a filler content and temperature-dependent constant.

Therefore, AC conductivity can be recognized as the combined effect of DC conductivity ( $f = 0$  Hz) caused by migrating charge carriers and frequency-induced dielectric dispersion. In this case, a large DC conductivity caused by formation of conducting pathways significantly dominates the transport behavior in a broad

frequency range (up to  $1.5 \times 10^5$  Hz) as seen the plateau region in Fig. 24.10b for the sample 0.5wt.%GNP/1.5wt.%CNT/L285.

The frequency-independent conductivity is commonly regarded as direct current DC conductivity. As it was mentioned above, electron conduction in the nanocarbon-filled composites occurred via two mechanisms: along carbon particles contacting each other (leakage current) or carbon particles separated by very small gaps in the composites (tunneling current) [35]. The gaps could be considered as potential barriers for electrons to hop by the tunneling effect. Generally, being higher the leakage current makes more contribution to conductivity than tunneling current. Hence for the leakage current, the content of filler should be high so that a network is formed in the matrix. Thus, the conduction mechanism of the composites is closely related to both the dispersion and the content of conductors. Specifically, when the content of GNP and CNT is very small, that is, the content of nanocarbon particles in the composites is not sufficient to make the connecting networks, hence, their conduction mechanisms are due to the tunneling of electron. In the frequency range higher onset frequency  $f_c$ , electrical conductivity increased since the frequency was high enough, and some gaps in carbon pathways became conductive, and the nanocarbon chains with small gaps became conductive first. The smaller is the distance between conductors, the lower is the frequency for the conduction. Therefore, with the increase of frequency, the capacitive resistance will greatly decrease, and some microcapacitors (formed between conducting particles or clusters) even become conductive, leading to decreased dielectric constant and increased electrical conductivity.

## 24.4 Conclusion

It was found that dielectric permittivity and electrical conductivity increase with increasing content of hybrid carbon filler and are characterized by percolative behavior. In composites with high nanocarbon content, the Nyquist diagram exhibits a semicircle dependence  $Z''(Z')$  indicating that conductive pathways have been formed and there are currents and polarization among conductive filler particles.

It was shown that substitution of GNP particles by carbon nanotubes promotes the shift of percolation threshold into lower filler content and enhances the electrical conductivity, permittivity, and dielectric loss ( $\tan\delta$ ) of these CMs compared with CMs filled only with GNPs. The increase of dielectric permittivity can be mainly attributed to a gradual formation of microcapacitor networks in the epoxy matrix as the volume fraction of conductive nanofiller increases. The microcapacitor network is an additional contribution to interfacial permittivity of fillers, due to charge carrier accumulation at the fillers' interface. It was shown that dependence of dielectric permittivity versus nanocarbon filler content  $\varepsilon'_r(C)$  exhibits the broad maximum around percolation threshold, and its position fully correlates with the percolation

threshold in  $\sigma_{dc}$  conductivity for these composites. It was found that the increase of CNT in hybrid filler promotes the high increase of dielectric permittivity and dissipation factor  $\tan\delta$  and, accordingly, shift of the maximum of permittivity and dielectric loss into lower concentration of filler. It was concluded that the presence of GNP in hybrid filler GNP/CNT expands the filler concentration range before percolation and blocks the aggregation of CNTs that leads to increase of the number of formed microcapacitors and enhances dielectric permittivity.

The mechanism of electrical conductivity in these CMs is electron tunneling between neighboring fillers and/or clusters. The increase of CNT content in CMs increases the electrical conductivity and weakens its dependence on frequency (related to electron tunneling transport process in CMs) due to more effective formation of a continuous carbon network and turning of diffusive electron transport.

## References

1. Stankovich S, Dikin DA, Dommett GHB, Kohlhaas KM, Zimney EJ, Stach EA, Piner RD, Nguyen ST, Ruoff RS (2006) Graphene composite materials. *Nature* 442:282–286
2. Lee CG, Wei XD, Kysar JW, Hone J (2008) Measurement of the elastic properties and intrinsic strength of monolayer graphene. *Science* 321:385–388
3. Balandin AA, Ghosh S, Bao W, Calizo I, Teweldebrhan D, Miao F, Lau C-N (2008) Superior thermal conductivity of single-layer graphene. *Nano Lett* 8(3):902–907
4. Wang Z, Luo J, Zhao G-L (2014) Dielectric and microwave attenuation properties of graphene nanoplatelet-epoxy composites. *AIP Adv* 4:017139
5. Zhang H-B, Yan Q, Zheng W-G, He Z, Zhong-Zhen Y (2011) Tough graphene-polymer microcellular foams for electromagnetic interference shielding. *ACS Appl Mater Interfaces* 3(3):918–924
6. Zhang HB, Zheng WG, Yan Q, Yang Y, Wang J, Lu ZH, Ji G-Y, Yu Z-Z (2010) Electrically conductive polyethylene terephthalate/graphene nanocomposites prepared by melt compounding. *Polymer* 51:1191–1196
7. He L, Tjong SC (2013) Low percolation threshold of graphene/polymer composites prepared by solvothermal reduction of graphene oxide in the polymer solution. *Nanoscale Res Lett* 8:132
8. Mansour SA, Al-ghoury ME, Shalaan E, El Eraki MHI, Abdel-Bary EM (2011) Dielectric dispersion and AC conductivity of acrylonitrile butadiene rubber-poly(vinyl chloride)/graphite composite. *J Appl Polym Sci* 122(2):1226–1235
9. Wang D, Bao Y, Zha J-W, Zhao J, Dang Z-M, Hu G-H (2012) Improved dielectric properties of nanocomposites based on poly(vinylidene fluoride) and poly(vinyl alcohol)-functionalized graphene. *ACS Appl Mater Interfaces* 4:6273–6279
10. Brosseau C, Beroual A (2001) Effective permittivity of composites with stratified particles. *J Phys D Appl Phys* 34:704–710
11. Hashemi R, Weng GJ (2016) A theoretical treatment of graphene nanocomposites with percolation threshold, tunneling-assisted conductivity and microcapacitor effect in AC and DC electrical settings. *Carbon* 96:474–490
12. El Bouazzaoui S, Achour ME, Brosseau C (2011) Microwave effective permittivity of carbon black filled polymers: comparison of mixing law and effective medium equation predictions. *J Appl Phys* 110:074105

13. Bilotti E, Zhang H, Deng H, Zhang R, Fu Q, Peijs T (2013) Controlling the dynamic percolation of carbon nanotube based conductive polymer composites by addition of secondary nanofillers: the effect on electrical conductivity and tuneable sensing behaviour. *Compos Sci Technol* 74:85–90
14. Sumfleth J, Adroher XC, Shulte K (2009) Synergistic effects in network formation and electrical properties of hybrid epoxy nanocomposites containing multi-wall carbon nanotubes and carbon black. *J Mater Sci* 44:3241–3247
15. Kranauskaitė I, Banys J, Talik E, Kuznetsov V, Nunn N, Shenderova O (2015) Electric/dielectric properties of composites filled with onion-like carbon and multiwalled carbon nanotubes. *Lith J Phys* 55(2):126–131
16. Raza MA, Westwood A, Stirling C (2012) Carbon black/graphite nanoplatelet/rubbery epoxy hybrid composites for thermal interface applications. *J Mater Sci* 47:1059–1070
17. Agnelli S, Cipolletti V, Musto S, Coombs M, Conzatti L, Pandini S, Riccò T, Galimberti M (2014) Interactive effects between carbon allotrope fillers on the mechanical reinforcement of polyisoprene based nanocomposites. *Express Polym Lett* 8:436–449
18. Patsidis AC, Kalaitzidou K, Anastassopoulos DL, Vradis AA, Psarras GC (2014) Graphite nanoplatelets and/or barium titanate/polymer nanocomposites: fabrication, thermomechanical properties, dielectric response and energy storage. *J Chin Adv Mater Soc* 2:207–221
19. Lazarenko O, Vovchenko L, Matzui L, Perets Y (2011) The electronic transport properties of the composites with nanosized carbon fillers. *Mol Cryst Liq Cryst* 536:72/[304]–80/[312]
20. Elimat ZM (2015) AC-impedance and dielectric properties of hybrid polymer composites. *J Compos Mater* 49(1):3–15
21. Qiang Z, Liang G, Aijuan G, Li Y (2014) The dielectric behavior and origin of high-k composites with very low percolation threshold based on unique multi-branched polyaniline/carbon nanotube hybrids and epoxy resin. *Compos Part A* 64:1–10
22. Perets Y, Aleksandrovych L, Melnychenko M, Lazarenko O, Vovchenko L, Matzui L (2017) The electrical properties of hybrid composites based on multiwall carbon nanotubes with graphite nanoplatelets. *Nanoscale Res Lett* 12(406):406
23. Chang J, Liang G, Gu A, Cai S, Yuan L (2012) The production of carbon nanotube/epoxy composites with a very high dielectric constant and low dielectric loss by microwave curing. *Carbon* 50:689–698
24. Samir Z, Merabet YEL, Grasa MPF, Soreto Teixeira S, Achour ME, Costa LC (2016) Complex impedance study of carbon nanotubes/polyester polymer composites. In: *Dielectric Materials and Applications: ISyDMA'2016 Materials Research Forum LLC Materials Research Proceedings* 1:13–16. <https://doi.org/10.21741/2474-395X/1/4>
25. Banerjee S, Kumar A (2012) Relaxation and charge transport phenomena in polyaniline nanofibers: swift heavy ion irradiation effects. *J Non-Cryst Solids* 358:2990–2998
26. Prateek, Thakur VK, Gupta RK (2016) Recent progress on ferroelectric polymer-based nanocomposites for high energy density capacitors: synthesis, dielectric properties, and future aspects. *Chem Rev* 116:4260–4317
27. Wang F, Wang J-W, Li S-q, Xiao J (2009) Dielectric properties of epoxy composites with modified multiwalled carbon nanotubes. *Polym Bull* 63:101–110
28. Yuan J-K, Yao S-H, Dang Z-M, Sylvestre A, Genestoux M, Bai J (2011) Giant dielectric permittivity Nanocomposites: realizing true potential of pristine carbon nanotubes in polyvinylidene fluoride matrix through an enhanced interfacial interaction. *J Phys Chem C* 115:5515–5552
29. Mathieu B, Anthony C, Arnaud A, Lionel F (2015) CNT aggregation mechanisms probed by electrical and dielectric measurements. *J Mater Chem C* 3:5769
30. Shi S-L, Liang J (2006) Effect of multiwall carbon nanotubes on electrical and dielectric properties of yttria-stabilized zirconia ceramic. *J Am Ceram Soc* 89:3533–3535
31. Lorenz H, Fritzsche J, Das A, Stueckelhuber K, Jurk R, Heinrich G, Klueppel M (2009) Advanced elastomer nano-composites based on CNT-hybrid filler systems. *Compos Sci Technol* 69:2135–2143

32. Wu C, Huang X, Wang G, Wu X, Yang K, Lib S, Jiang P (2012) Hyperbranched-polymer functionalization of graphene sheets for enhanced mechanical and dielectric properties of polyurethane composites. *J Mater Chem* 22:7010
33. Liu L, Grunlan JC (2007) Clay assisted dispersion of carbon nanotubes in conductive epoxy nanocomposites. *Adv Funct Mater* 17(14):2343–2348
34. Zhang X, Liang G, Chang J, Gu A, Li Y, Zhang W (2012) The origin of the electric and dielectric behavior of expanded graphite–carbon nanotube/cyanate ester composites with very high dielectric constant and low dielectric loss. *Carbon* 50:4995–5007
35. Trihotri M, Dwivedi UK, Malik MM, Khan FH, Qureshi MS (2016) Study of low weight percentage filler on dielectric properties of MWCNT-epoxy nanocomposites. *J Adv Dielectr* 6(3):1650024 (9 pages)



# Chapter 25

## Obtaining of the Modified $\text{NH}_4\text{NO}_3$ Granules with 3-D Nanoporous Structure: Impact of Humidifier Type on the Granule's Structure

A. E. Artyukhov, J. Gabrusenoks, and P. C. Rossi

### 25.1 Introduction

Ammonium nitrate with advanced porous surface, so-called porous ammonium nitrate (PAN), is a necessary component of simplest industrial explosives. A promising method of PAN producing is combination of heat treatment method and hydration of granules in small vortex granulators [1, 2].

Hydrodynamic conditions of continuous and dispersed phases motion in the vortex granulator workspace were described in detail in [3, 4], while the model of moisture removal process from the granule to form a porous surface layer was described in studies [5, 6].

Estimation of granulated porous ammonium nitrate (PAN) quality, which is generated for mining industry, is carried out by the following factors [7–10]:

1. Absorptivity – amount of diesel fuel distillate (in percentage terms from granule's total weight), which is absorbed by PAN after humidification with the diesel fuel distillate

---

A. E. Artyukhov (✉)

Processes and Equipment of Chemical and Petroleum Refinery Department, Sumy State University, Sumy, Ukraine

e-mail: [artyukhov@pohnp.sumdu.edu.ua](mailto:artyukhov@pohnp.sumdu.edu.ua)

J. Gabrusenoks

Institute of Solid State Physics, University of Latvia, Riga, Latvia

e-mail: [jg14078@lu.lv](mailto:jg14078@lu.lv)

P. C. Rossi

Department of Chemical Technology, National University of Río Cuarto, Río Cuarto, Córdoba, Argentina

e-mail: [prossi@ing.unrc.edu.ar](mailto:prossi@ing.unrc.edu.ar)

© Springer International Publishing AG, part of Springer Nature 2018

O. Fesenko, L. Yatsenko (eds.), *Nanochemistry, Biotechnology, Nanomaterials, and Their Applications*, Springer Proceedings in Physics 214,

[https://doi.org/10.1007/978-3-319-92567-7\\_25](https://doi.org/10.1007/978-3-319-92567-7_25)

2. Retentivity – amount of diesel fuel distillate (in percentage terms from granule's total weight) which remains in the granule after its transportation and surplus runoff
3. PAN granule firmness

Absorptivity is defined by the total volume of pores (their form and nature are not taken into account; the decisive factor is their size) and by the developed nanoporous surface structure, which mostly consists of macropores (size is over 50 nm). The retentivity normative indicator is provided by the internal “modification” nanoporous structure. This structure includes mainly wavy mesopores (size 2–50 nm). Firmness of the granule is defined by the core destruction degree (or integrality). Low firmness of the granule has a negative impact on the production ecological indicators (great deal of dust) and leads to the granules sealing. Thus, a nanoporous structure must be developed on the granule surface and in its near-surface layers.

Results of previous studies [11, 12] have shown that modification of ammonium nitrate granules by humidification and subsequent heat treatment leads to changes in the parameters of crystal lattice of samples. The porous surface of granules in this case consists primarily of macropores, the presence of which allows to open access to internal mesopores (which were also formed during the modification process).

The main objective of the work is to study the impact of humidifier type and the number of humidification cycles on the surface and internal structure of PAN granule nanopores and its quality indicators (holding and absorption capacity).

## 25.2 Description of Object and Methods of Research

As humidifier in research, of such variants were used:

- Water
- Aqueous urea solution
- Aqueous ammonium nitrate solution

The following samples were prepared to study nanoporous structure of PAN granules and humidifier's impact on the granule structure:

1. Granules of ammonium nitrate moistened with water and dried at a temperature of 230–240 °F to a moisture content of 0.002 kg of moisture/kg of material
2. Granules of ammonium nitrate moistened with urea solution and dried at a temperature of 230–240 °F to a moisture content of 0.002 kg of moisture/kg material (composition of the humidifier solution – 50% of carbamide and 50% of water)
3. Granules of ammonium nitrate moistened with a solution of ammonium nitrate and dried at a temperature of 230–240 °F to moisture content of 0.002 kg of moisture/kg of material (the composition of the humidifier solution is 40% of ammonium nitrate and 60% of water)

At the first stage of the experiment, the moistened granules of ammonium nitrate underwent heat treatment after humidification with various solutions. After this, an analysis of their nanoporous structure was carried out.

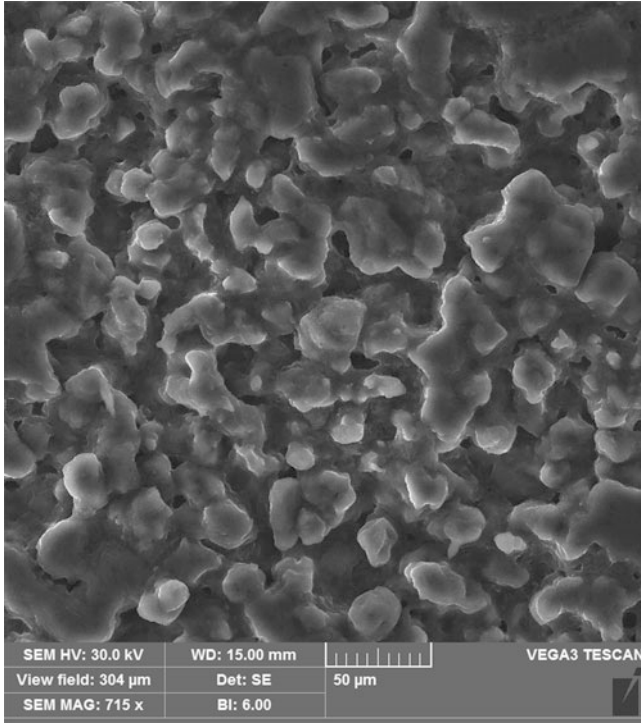


**Fig. 25.1** Ammonium nitrate original granules (from original packing)

Tools and facilities:

- Thermoanemometer TES-1340 – to define hydrodynamic peculiarities of flow motion
- Thermocouple instrument TC10-C – to measure temperature in calorifer, potentiometer recorder-controller KCH-3
- Thermal viewer Fluke Ti25, pyrometer Victor 305B – to measure temperature in the working area of granulator
- Multimeter DT-838 – to measure moisture of granule and air
- Microscope KONUSPIX-450X KONUS, scanning electronic microscope SEM – 100 U and X-ray spectrometer with energy dispersion, to study microstructure of granules

### 25.3 Visualization of Results and Discussion

The granules were exposed to single humidification and were dried in previously defined [5] optimum thermodynamic conditions.

Analysis of experiments results (Figs. 25.1, 25.2, 25.3, and 25.4) has shown that various types of humidifiers can form various kinds of pores after drying according to the classification [8]:



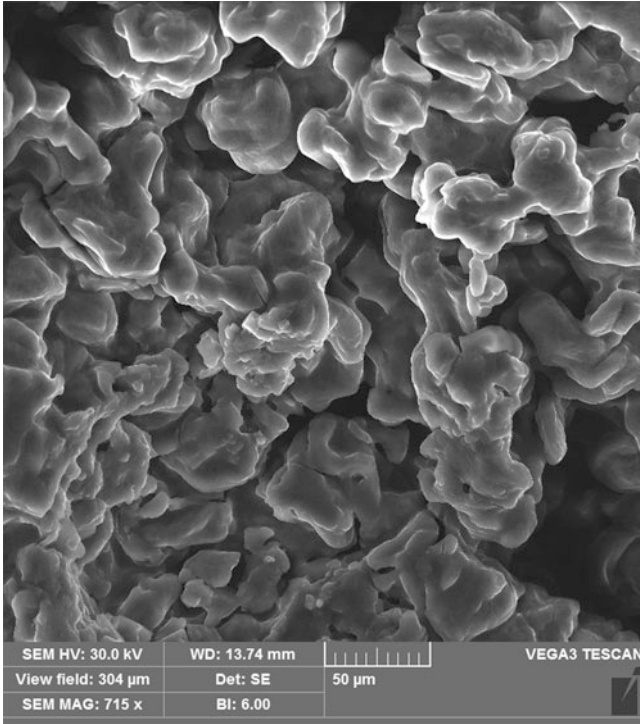


Fig. 25.2 Sample 1

- Cracks, chips, and cavities – “mechanical” pores
- Channels of various shapes – “modification” pores (micro-, meso-, and macropores)

Some of these pores were formed as a result of thermal stresses and inadequate core strength of initial granule (“mechanical” pores), some directly into granules during the drying process after humidification (“modification” pores).

After humidification with water, the granule is characterized mostly by linear shallow macropores.

After humidification with ammonium nitrate solution, deep wavy meso- and micropores are mostly formed.

After humidification with carbamide solution, surface and near-surface layers of granules are characterized with mesopores, configuration of which practically in equal parts has a form of linear and wavy pores.

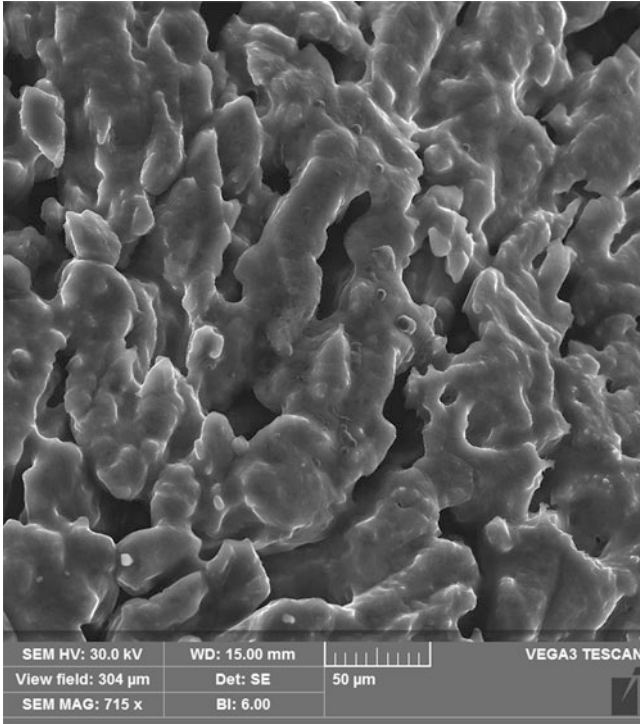


**Fig. 25.3** Sample 2

The results, presented in Figs. 25.5, 25.6, 25.7, 25.8, and 25.9, led us to make the following conclusions:

- Number of pores in the original sample depth is reduced.
- After humidification with all solution types, micropores are mostly formed on the granule surface; however, their number depends on humidifier type.
- Humidification with water is reasonable to implement for the granule surface. In this case, formed linear meso- and macropores enable free penetration of diesel fuel distillate into the granule.
- Humidification with ammonium nitrate solution lets us receive a number of wavy micropores in the near-surface layers of the granule. As a result, diesel fuel distillate is kept in the granule and does not flow out during its transportation.

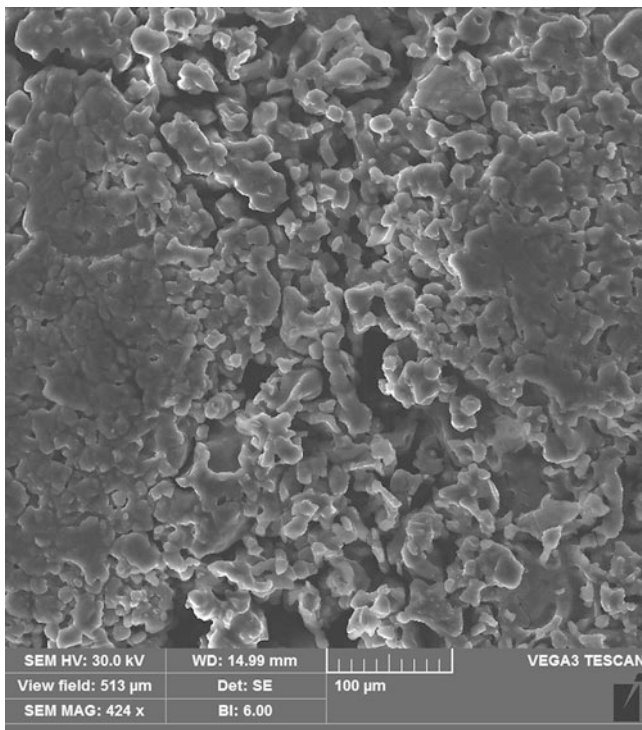


Fig. 25.4 Sample 3

## 25.4 Conclusions

Various types of humidifiers also have significant effect on the ratio of values of “mechanical” and “modification” pores.

The obtained results allow to select the optimal humidifier composition, which promotes the formation of significant amount of macropores on surface and mesopores of near-surface areas.

The task of further research is to study PAN quality under conditions of repeated humidification with various solutions (generation of multilayer granules with fixed structure of every layer).

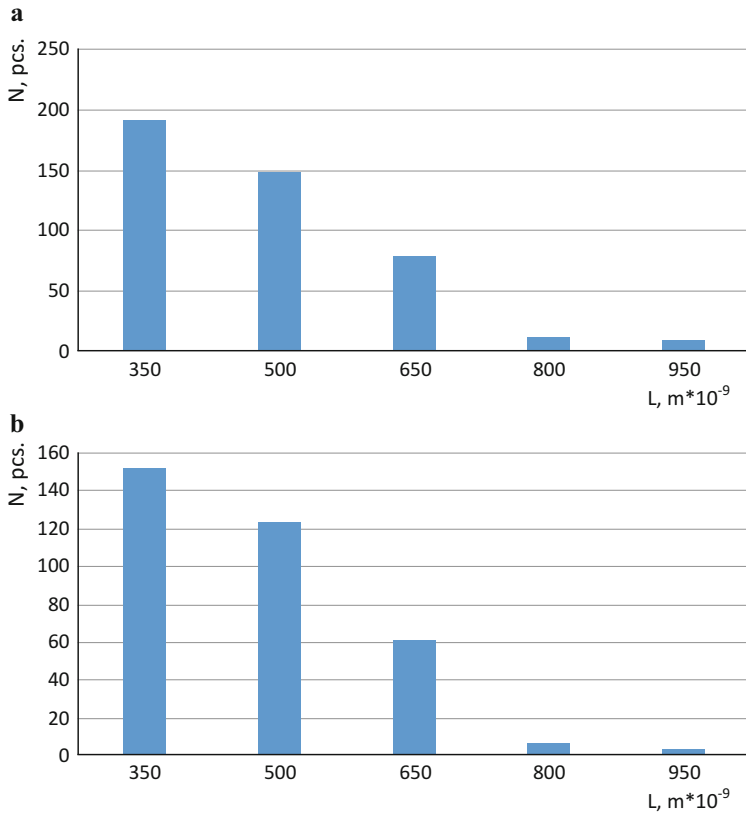


**Fig. 25.5** Number and size of pores per surface square unit. Original granules (from package): (a) surface; (b) near-surface layers

**Acknowledgments** This work was carried out under the project “Improving the efficiency of granulators and dryers with active hydrodynamic regimes for obtaining, modification, and encapsulation of fertilizers,” state registration No. 0116 U006812. The authors thank researchers of Processes and Equipment of Chemical and Petroleum-Refining Industries Department, Sumy State University; Institute of Solid State Physics, University of Latvia; and Department of Chemical Technology, National University of Río Cuarto, Argentina, for their valuable comments during the article preparation.

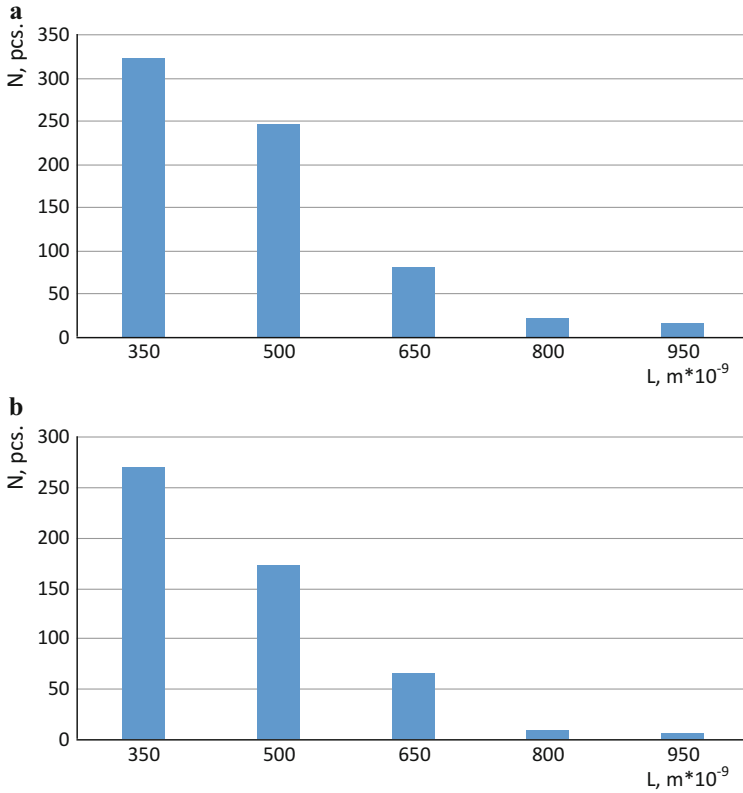


**Fig. 25.6** Number and size of pores per surface square unit. Granule, which is moistened with water: (a) surface; (b) near-surface layers

## References

1. Artyukhov AE, Sklabinskiy VI (2013) Experimental and industrial implementation of porous ammonium nitrate producing process in vortex granulators. *Nauk Visnyk Nats Hirnychoho Univ* 6:42–48
2. Artyukhov AE, Sklabinskiy VI (2016) Thermodynamic conditions for obtaining 3D nanostructured porous surface layer on the granules of ammonium nitrate. *J Nano Electron Phys* 8(4):04083-1-04083-5

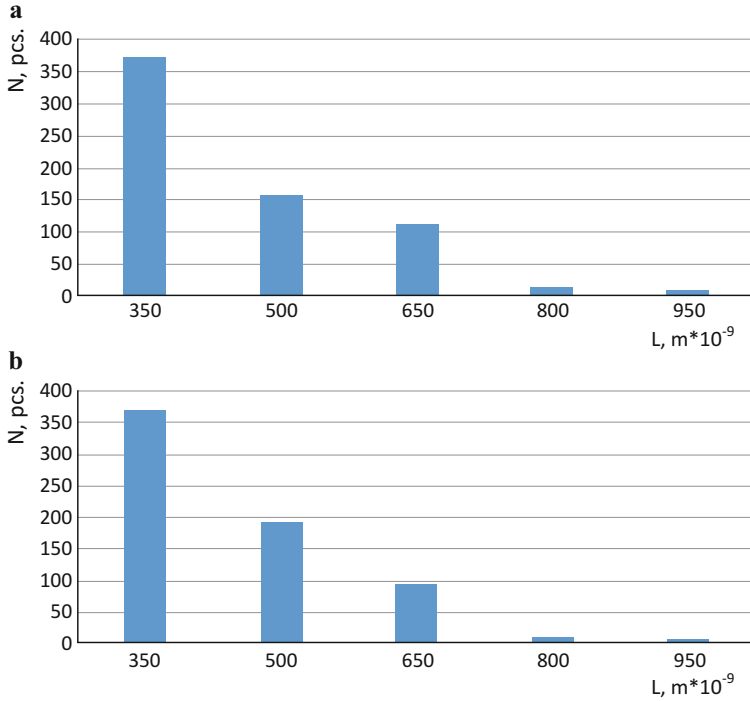


**Fig. 25.7** Number and size of pores per surface square unit Granule, moistened with ammonium nitrate solution: **(a)** surface; **(b)** near-surface layers

3. Artyukhov AE, Sklabinskyi VI (2015) Theoretical analysis of granules movement hydrodynamics in the vortex granulators of ammonium nitrate and carbamide production. *Chem Chem Technol* 9(2):175–180
4. Artyukhov AE, Sklabinskyi VI (2015) Hydrodynamics of gas flow in small-sized vortex granulators in the production of nitrogen fertilizers. *Chem Chem Technol* 9(3):337–342
5. Artyukhov AE, Voznyi AA (2016) Thermodynamics of the vortex granulator's workspace: the impact on the structure of porous ammonium nitrate. In: 6th international conference nanomaterials: application & properties (NAP-2016), vol 5, No 2, p 02NEA01

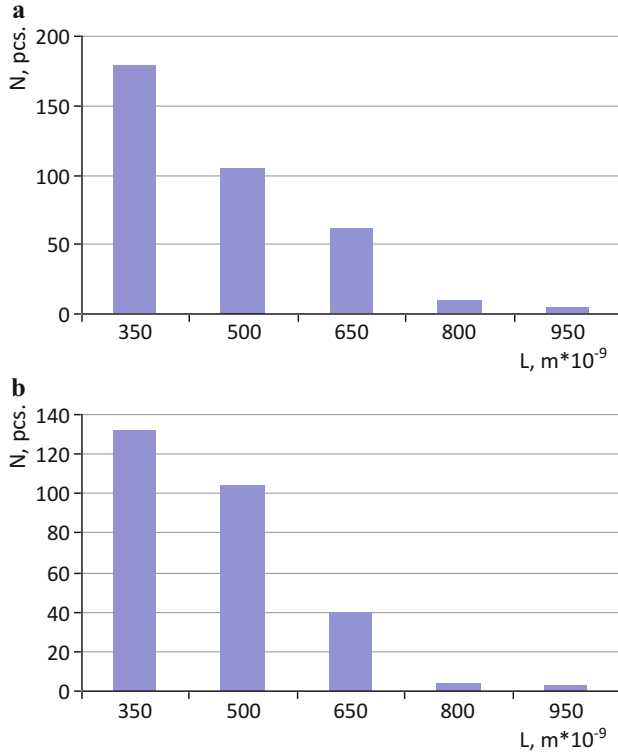


**Fig. 25.8** Number and size of pores per surface square unit. Granule, moistened with carbamide solution: (a) surface; (b) near-surface layers

- Artyukhov AE (2016) Kinetics of heating and drying of porous ammonium nitrate granules in the vortex granulator. In: 6th international conference nanomaterials: application & properties (NAP-2016), vol 5, No 2, p 02NEA02
- Weber PW, Millage KK, Crepeau JE, Happ HJ, Gitterman Y, Needham CE (2015) Numerical simulation of a 100-ton ANFO detonation. *Shock Waves* 25(2):127–140
- Lipinska K, Lipinski M, Maranda A (2005) Demilitarized propellants as ingredients in commercial explosives. In: European Federation of Explosives Engineers: Brighton conference proceedings, Brighton, pp 493–498
- Short M, Quirk JJ, Kiyanda CB, Jackson SI, Briggs ME, Shinas MA (2010) Simulation of detonation of ammonium nitrate fuel oil mixture confined by aluminum: edge angles for DSD. In: Proceedings of the 14th international detonation symposium, Office of Naval Research, Idaho, pp 769–778

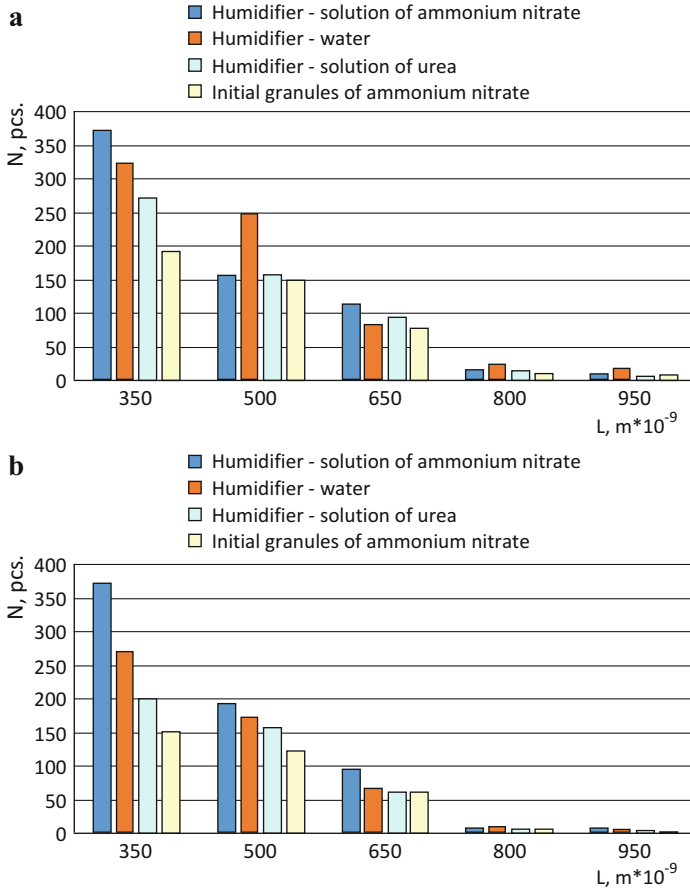


**Fig. 25.9** Number and size of pores per surface square unit. Comparing description of samples: (a) surface; (b) near-surface layers

10. Zygmunt B, Buczkowski D (2007) Influence of ammonium nitrate Prills' properties on detonation velocity of ANFO. *Propellants Explos Pyrotech* 32(5):411–414
11. Artyukhov AE, Sklabinskyi VI (2017) Investigation of the temperature field of coolant in the installations for obtaining 3d nanostructured porous surface layer on the granules of ammonium nitrate. *J Nano Electron Phys* 9(1):01015-1-01015-4
12. Artyukhov AE, Sklabinskyi VI (2016) 3D nanostructured porous layer of ammonium nitrate: influence of the moisturizing method on the layer's structure. *J Nano Electron Phys* 8(4):04051-1-04051-5



# Chapter 26

## Bifunctional Silicas with Immobilized Lignin



**Yulia Bolbukh, Stanislav Sevostianov, Beata Podkoscielna, Dariusz Sternik, Panagiotis Klonos, Polycarpos Pissis, Barbara Gawdzik, and Valentin Tertykh**

### 26.1 Introduction

In the recent time, most interest takes renewable sources as raw materials for many practical applications. Lignin is a multi-tonal waste of pulp production. This natural polymer determines the mechanical strength of wood. Softwood contains it in 18–25 wt% and hardwood in 27–33 wt% [1]. Lignin is not an individual substance, but a mixture of biopolymers with different structures is typical for different types of wood. Generally, it is composed of three basic units: *p*-coumaryl alcohol, coniferyl alcohol, and sinapyl alcohol [2]. It is an irregular network biopolymer that was made up of oxidative coupling of the three major units linked by ether and carbon–carbon bonds. Today, most of lignin is utilized as solid fuel for power plants, heating boilers, fireplaces, etc. Meanwhile, lignin is a valuable chemical raw material used to produce functional biopolymers, dispersants [3], sorbents [4, 5], and biologically active additives. Unfortunately, the widespread uses of lignin as an available raw material for the industry are limited by the properties of this polymer. Different from most other natural polymers (such as cellulose and hemicellulose), lignin is difficult to use for the preparation of composite materials without additional processing due to its bond types and irregular linked ways.

---

Y. Bolbukh (✉) · S. Sevostianov · V. Tertykh  
Chuiiko Institute of Surface Chemistry, National Academy of Sciences of Ukraine, Kyiv, Ukraine

B. Podkoscielna · D. Sternik · B. Gawdzik  
Faculty of Chemistry, Maria Curie-Skłodowska University, Lublin, Poland  
e-mail: [sternik@hektor.umcs.lublin.pl](mailto:sternik@hektor.umcs.lublin.pl); [barbara.gawdzik@poczta.umcs.lublin.pl](mailto:barbara.gawdzik@poczta.umcs.lublin.pl)

P. Klonos · P. Pissis  
Department of Physics, National Technical University of Athens, Athens, Greece  
e-mail: [ppissis@central.ntua.gr](mailto:ppissis@central.ntua.gr)

As lignin has different functional groups in its structure, it has become an interesting material with prospects of application in many areas, including adsorption of heavy metals [6], as a substrate for the synthesis of low molecular organic compounds [7] and, in particular, as an active component of biocomposites [8, 9]. Moreover, lignin strongly participates in water economy and helps with water and nutrient transport. The presence of various functional groups (aliphatic and aromatic OH groups) makes lignin a suitable substance for chemical syntheses. The amounts of functional groups depend on the source of the lignin, the process used to extract it, and/or posttreatment. Kraft lignin is a by-product of kraft pulping of wood. Kraft lignin contains a greater amount of phenolic groups, due to the extensive cleavage of *b*-aryl bonds during kraft pulping, some biphenyl units, as well as other condensed structures as a result of the severe cooking conditions [10]. The phenolic and aliphatic hydroxyl groups present in the lignin structure can be used for chemical modifications. Based on the reaction parameters and the reactants used, esterification is one of the easiest methods of the chemical modification of lignin. Depending on the type of new introduced groups, the properties of lignin, such as hydrophobicity, solubility, and thermal behavior, can be significantly changed. Esterification reactions have also been applied to increase lignin reactivity by introducing new active sites into the lignin macromolecule that are able to copolymerize with other monomers [11]. The lignin derivatives with acrylic functionality and containing reactive vinyl groups through esterification reactions have been successfully copolymerized with styrene (St) and divinylbenzene (DVB) to produce functional porous microspheres for use as specific sorbents in solid-phase extraction [12].

With an esterification reaction when a carboxylic acid is treated with an alcohol and an acid catalyst, an ester is formed (along with water). However, this reaction can be used not only to introduce new active sites into the polymer structure but also to immobilize the polymer on the inorganic carrier. Organic/inorganic hybrid materials combine most applicable properties for practical using. One of the most popular inorganic components for such materials is silica. There are a lot of studies for lignin/silica hybrid materials, but it used few main methods to obtain the samples, such as sol-gel synthesis with tetraethoxysilane (TEOS) [13–15] and precipitation in a nonpolar or polar medium using sodium silicate [16]. An advanced functional silica/lignin material was obtained when silica was initially modified with N-2-(aminoethyl)-3-aminopropyltrimethoxysilane [5] to activate the carrier surface. In order to activate the lignin, an oxidation process was carried out using sodium iodate. The activation of lignin and initial functionalization of silica made possible the chemical combination of the precursors to produce a functional SiO<sub>2</sub>/lignin sorbent. In [17] the silica/lignin interaction was achieved due to silica surface functionalization with aminosilane and then modified with kraft lignin preliminary activated with sodium periodate solution. In other work the key parameter of silica/lignin interaction was lignin modification with periodate [18].

So, the production of novel inorganic/organic composites with specific application possibilities has recently become a pressing need. The use of organic products of natural origin, including biomass in the broad sense of the word, is of particular

interest. The successful combination of silica with a natural biopolymer, such as lignin, can provide new products with unique dispersive, morphological, and physicochemical properties. In this connection it is important to study the interaction of polymer carrier at the interface and their mutual effect on properties of the composite. In our study as an inorganic matrix, we used pyrogenic silica with attached amino, silicon hydride, or methyl groups in mono- or bifunctional (methyl-hydride, methyl-amino, amino-hydride) layer. Modification of silica surface was carried out to impart different hydrophobic/hydrophilic properties and chemical activity of the surface. Impregnation of water-soluble lignin on silica bearing various functional groups was carried out to study the effect of the functionalized silica surface on structure and properties of lignin.

## 26.2 Experimental Section

### 26.2.1 Materials

Fumed silica with a specific surface area of 300 m<sup>2</sup>/g (Kalush, Ukraine) was used as initial hydrophilic filler. 3-Aminopropyltriethoxysilane (APTES), triethoxysilane (TES), and hexamethyldisilazane (HMDS) (Sigma-Aldrich) were used without additional treating. The water-soluble commercially available kraft lignin from softwood was obtained from Sigma-Aldrich.

### 26.2.2 Silica Surface Modification

Modification of silica surface was carried out on a well-known standard method liquid-phase processing using appropriate organosilane in toluene solution [19]. Briefly, modification of silica surface with 3-aminopropyltriethoxysilane (A300-NH<sub>2</sub>) and triethoxysilane (A300-SiH) was performed by liquid-phase process. Toluene solution of alkoxy silane-required concentration was added to silica. The mixture was kept in the thermostat for 24 h at 60 or 80 °C for amino or silicon hydride group attaching, respectively. Then, modified silica was washed and dried at low pressure and heating. The modification with hexamethyldisilazane (A300-CH<sub>3</sub>) was performed by the gas-phase process at room temperature using a leak-proof reactor with stirring at 25 °C for 24 h. After modification the methyl-containing silica was heated at 150 °C for 30 min. Silica with grafted methylsilyl and silicon hydride groups (methyl-hydride-containing silica) as well as methylsilyl and aminopropyl groups (methyl-amino-containing silica) was prepared by interaction of the methyl-containing silica with triethoxysilane or 3-aminopropyltriethoxysilane in toluene at 80 °C for 24 h. The modification degree for all types of silicas was 30 and 100%. The concentration of the attached groups in the bifunctional

layer was maintained at 30% of each type of group. The degree of substitution of isolated silanols on the silica surface with functional groups was controlled by IR spectroscopy.

### 26.2.3 Preparation of Silica/Lignin Composites

For the silica impregnation, the water-soluble lignin (150 mg) was dissolved in deionized water (20 ml) and then mixed with dry powder (500 mg) at room temperature. Obtained paste was left without disturbing overnight and dried at 80 °C for 12–17 h. The polymer content in organic/inorganic composite was 20 wt%. The sample description is presented in Table 26.1.

### 26.2.4 Analytic Technique

Fourier transform infrared (FTIR) spectroscopy (Thermo Nicolet Nexus FTIR) has been used to characterize the silica surface. The dispersed samples were mixed with KBr (1:100). The FTIR spectra were obtained by recording 50 scans between 4000 and 400  $\text{cm}^{-1}$  with a resolution of 8  $\text{cm}^{-1}$ .

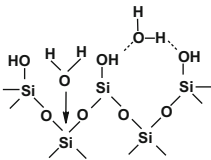
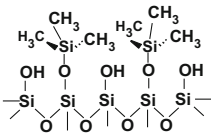
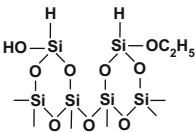
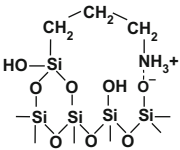
The UV–vis absorption measurements were performed with a UV–vis spectrophotometer Cary 4000 (Varian, Australia). Deionized water was scanned at the same wavelength as a baseline.

Infrared spectra ATR was carried out on a STA 449 Jupiter F1, NETZSCH (Germany). Spectra were recorded in the spectral range of 600–4000  $\text{cm}^{-1}$  with 16 scans per spectrum at a resolution of 4  $\text{cm}^{-1}$  and have been used to characterize the silica/lignin composites.

Thermal properties and stability of the surface layer were studied using differential scanning calorimetry (DSC) that was performed under nitrogen atmosphere in the temperature range from 20 up to 480 °C using a NETZSCH DSC 204F1 Phoenix instrument (Germany). Samples of ~8–16 mg in mass were closed in standard Tzero aluminum pans. Cooling and heating rates were 10 °C/min. During the first heating scan, the samples stayed at 120 °C for 5 min (isothermally) and during the second heating scan, at 20 °C for 3 min in order to stabilize the materials.

Relaxation process and phase transitions in the polymer immobilized on the silica surface were investigated in nitrogen atmosphere in the temperature range from –50 to 350 °C using a Perkin Elmer Pyris 6 DSC instrument, calibrated with indium for temperature and enthalpy. Samples of 8 mg in mass were closed in aluminum pans. Cooling and heating rates were fixed to 20 K/min. A first heating scan (heating 1) from room temperature (30 °C) to 150 °C was performed for evaporating water and remaining solvents. Then the sample was cooled to –50 °C, and then, the second DSC scan (heating 2) up to 350 °C was performed. For pure lignin additional scans were performed (up to 150 to 250 and to 350 °C) on a second fresh sample.

**Table 26.1** Lignin-containing sample description and acronyms

N <sup>o</sup>	Sample name	Description	Structure of silicas' surface layer
1	LigA1	Lignin + SiO <sub>2</sub> (A-300)	Pristine silica 
2	LigA2	Lignin + SiO <sub>2</sub> -CH <sub>3</sub> (100%)	Methylated silica 
3	LigA3	Lignin + SiO <sub>2</sub> -CH <sub>3</sub> (30%)	Hydride silica 
4	LigA4	Lignin + SiO <sub>2</sub> -H (100%)	
5	LigA5	Lignin + SiO <sub>2</sub> -NH <sub>2</sub> (100%)	Aminated silica 
6	LigA6	Lignin + SiO <sub>2</sub> -CH <sub>3</sub> (30%)-NH <sub>2</sub> (30%)	Combination of different groups including OH
7	LigA7	Lignin + SiO <sub>2</sub> -CH <sub>3</sub> (30%)-H (30%)	
8	LigA8	Lignin + SiO <sub>2</sub> -NH <sub>2</sub> (30%)-H (30%)	
9	LigA9	Lignin + SiO <sub>2</sub> -H (30%)	Combination of silicon hydride groups and OH
10	LigA10	Lignin + SiO <sub>2</sub> -NH <sub>2</sub> (30%)	Combination of amino groups and OH

## 26.3 Results and Discussion

Ensuring interaction between the silica surface and the polymer is a main task when creating organic/inorganic materials. In spite of the presence of different types of functional groups, lignin is a low reactive polymer, and providing interaction with the matter introduced has some difficulties. As was mentioned above, lignin

is a complex molecular structure containing cross-linked polymers of phenolic monomers especially *p*-coumaryl alcohol, coniferyl alcohol, and sinapyl alcohol. It is well known that amino-silica-based stationary phase is widely utilized to carbohydrate separation. The interaction is primarily due to the reactivity of amino group and can be implemented via hydroxyl groups of the polymer. In the presence of carboxyl or carbonyl groups, the reaction with amino groups proceeds under mild conditions to form silica/polymer bonds. The choice of the silicon hydride group is primarily due to the possibility of chemically grafting the polymer as a result of the reaction of the silicon hydride group with the C=C groupings of the polymer. In addition, at a pH above 7, the hydrogen of the silicon hydride group is cleaved to form an active site on silicon atom. The presence of methyl groups provides a change in the hydrophobic/hydrophilic characteristics of the surface, which in turn provides a change in the structure of the surface layer of the polymer and the orientation of the macromolecules near the surface and inside the layer. The combination of amino and hydride groups, along with a change in the hydrophobic/hydrophilic characteristics of the filler surface, was expected to allow the chemical immobilization of lignin under mild conditions.

So, silica surface chemistry (Table 26.1) can determine the structure of the composite material. Interaction of the polymer with functional groups on the silica surface determines the mechanism of macromolecule immobilization, namely, physical adsorption or chemisorption as well as structure of polymer layer due to influence on a macromolecule orientation relative to each other and to the silica particles.

The infrared spectra (FTIR) of silica with the relatively chemically inert or with chemically active groups in the surface layer are represented in Fig. 26.1a. Pristine (unmodified) silica contains on surface isolated hydroxyl groups ( $3745\text{ cm}^{-1}$ , stretching vibrations of O–H in silanol groups), the OH groups perturbed with hydrogen bonds ( $3660\text{ cm}^{-1}$ ), as well as physically adsorbed and strongly bound water with a broadband with maximum absorption at  $3450\text{ cm}^{-1}$ . The presence of adsorbed water is additionally evidenced by the band at  $1639\text{ cm}^{-1}$ . The bands at  $1126$  and  $820\text{ cm}^{-1}$  are assigned to the stretching symmetric ( $\nu_s$ ) and asymmetric ( $\nu_{as}$ ) vibrations of Si–O–Si grouping, band  $980\text{ cm}^{-1}$  is attributed to the stretching symmetric vibrations of Si–OH, and absorption at  $474\text{ cm}^{-1}$  is attributed to the bending vibrations ( $\delta$ ) of Si–O bonds. For the silica with substitution of surface silanols with trimethylsilyl groups ( $\text{SiO}_2\text{ CH}_3$ ), the band of hydroxyl group at  $3745\text{ cm}^{-1}$  disappeared, and bands of stretching vibrations of methyl groups at  $2970$  and  $2935\text{ cm}^{-1}$  are present (Fig. 26.1a, spectrum 2). The presence of silicon hydride groups on the silica surface is confirmed by the band of the stretching vibrations of Si–H bonds at  $2250\text{ cm}^{-1}$  (Fig. 26.1a, spectrum 3). For the silica with bifunctional surface layer ( $\text{SiO}_2\text{ CH}_3\text{ SiH}$ ), the spectra revealed the presence of methylsilyl and silicon hydride groupings (Fig. 26.1a, spectrum 4). As known, grafted aminopropyl radicals can form bridge-like structures via interaction of amine groups with protons of surface hydroxyl groups or adsorbed water molecules. Because of this the surface layer of aminosilica ( $\text{SiO}_2\text{ NH}_2$ ) contains  $\text{NH}_2$  groups with different protonation degrees ( $1643$  and  $1560\text{ cm}^{-1}$ ).

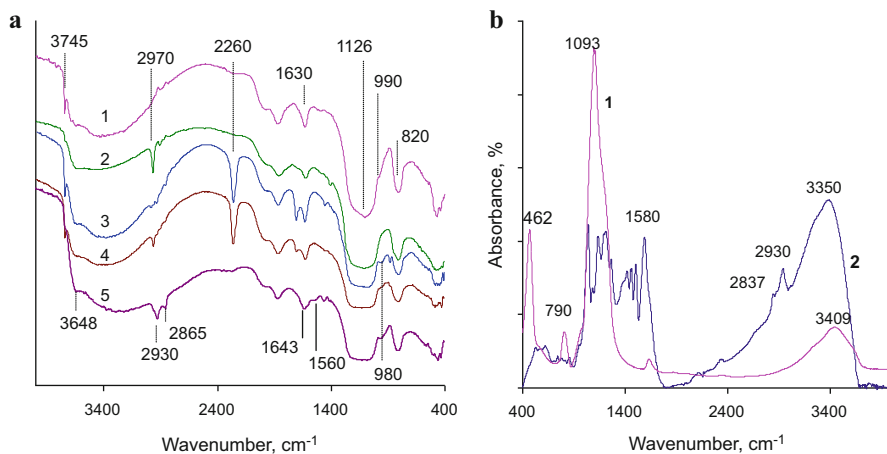


**Fig. 26.1** (a) FTIR and (b) ATR spectra of silicas. The illustrations *a* show the spectra of pristine silica (1); silica with attached trimethylsilyl  $-\text{CH}_3$  (2) and silicon hydride  $\equiv \text{Si}-\text{H}$  (3) or amino groups  $-\text{NH}_2$  with modification degree 100% (4); and silica with bifunctional methyl-hydride modified layer (a4) with both group contents of 30% (5). Figure *b* presented ATR spectra of pristine silica (1) and pure lignin (2)

IR analysis using the spectrometer equipped with an attenuated total reflection (ATR) attachment was carried out to verify the composite preparation and to identify the characteristic groups present in the structure of silica, lignin, and  $\text{SiO}_2/\text{lignin}$  biocomposites. The disturbances at 2200–1900  $\text{cm}^{-1}$  in the spectra were assigned to the presence of a diamond in the ATR attachment [15]. The IR spectrum of kraft lignin [18] (Fig. 26.1b) shows the following bands: O–H stretching vibrations (phenolic  $-\text{OH}$  and aliphatic  $-\text{OH}$ ) in the range 3600–3200  $\text{cm}^{-1}$  and C–H stretching vibrations at 2930  $\text{cm}^{-1}$  ( $\text{CH}_3$  and  $\text{CH}_2$ ), 2837  $\text{cm}^{-1}$  ( $\text{OCH}_3$ ) and low intensity band at 3008  $\text{cm}^{-1}$ . Bands in the range 1760–1300  $\text{cm}^{-1}$  correspond to overlapping of the stretching vibrations C–C of the aromatic skeleton at 1580, 1500, and 1450  $\text{cm}^{-1}$  and the deformation vibration of the nonconjugated group C=O. In the spectrum of lignin, there are also bands at 1363, 1261, and 1210  $\text{cm}^{-1}$ , attributed to stretching vibrations of C–O, C–O(H), and C–O(Ar) of phenol groups and ether bonds, which are an important type of bonds in lignin. The presence of the ether bonds C–O–C is also indicated by the band corresponding to the stretching vibrations C–O at 1040 and 1080  $\text{cm}^{-1}$ . The other band characteristics of lignin correspond to in-plane deformation  $\delta_{\text{ip}}$  Ar C–H at 1134  $\text{cm}^{-1}$  and out-of-plane deformation  $\delta_{\text{op}}$  Ar C–H, appearing at 850 and 780  $\text{cm}^{-1}$  [18] (Fig. 26.1b, spectrum 2). The ATR spectrum of unmodified silica shows a broadband at 3430  $\text{cm}^{-1}$  ( $\nu_{\text{O-H}}$ ,  $\text{H}_2\text{O}$ ) and 1620  $\text{cm}^{-1}$  ( $\delta_{\text{H-OH}}$ ) and bands corresponding to typical vibrations of silica, Si–O–Si ( $\nu_{\text{s}}$ , 1093  $\text{cm}^{-1}$ ;  $\nu_{\text{as}}$ , 800  $\text{cm}^{-1}$ ), Si–OH ( $\nu$  960  $\text{cm}^{-1}$ ), and Si–O ( $\delta$ , 790 and 462  $\text{cm}^{-1}$ ). As can be seen, there is overlapping of the characteristic bands in the regions 3670–2400  $\text{cm}^{-1}$  and 1250–860  $\text{cm}^{-1}$ .

Figure 26.2 presents the ATR spectra of the silica/lignin biocomposites obtained, evidencing the presence of band characteristics of appropriate functional groups both silica and lignin. Taking into account equal content of the polymer in samples, the increasing (or decreasing) intensity of bands with changing of surface chemistry of the silica matrix confirms different structure of the polymeric immobilized layer. A band appearing in the spectra of samples with lignin in the range  $950\text{--}720\text{ cm}^{-1}$  can be attributed to structure-sensitive one.

For the sample Lig-A1 with totally methylated silica, the bands  $835$  and  $750\text{ cm}^{-1}$  appeared in spectra. These bands are characteristic for pure lignin and attributed to guaiacyl units [20]. This means that on the hydrophobic surface, the structure of the adsorbed layer is identical to the polymer structure in volume. For samples Lig-A4 and Lig-A8 based on hydride- and amino-hydride-containing silicas, respectively, the bands of stretching vibrations of C–H bonds intensified, while the band at  $940\text{ cm}^{-1}$  became more intensive in spectrum for the sample Lig-A9 (contains 30% of silicon hydride groups), where the bands of stretching vibrations of C–H bonds are less visible. Preliminarily, it can be concluded that the silicon hydride groups on the silica surface have the greatest effect on the structure of the immobilized polymer layer.

The UV–vis absorption spectra of dispersed samples at pH 7 are represented in Fig. 26.3. The absorption bands located at 240 and 280 nm are assigned to K- and B-bands of  $\pi\text{--}\pi^*$  transitions of the aromatic rings in lignin linked by ionized phenolic hydroxyls and carboxylic groups [21]. After immobilization on silica, the K-band disappears and the B-band shifts to 285 nm with decreased absorption intensity. It is a result of change in protonation of phenolic hydroxyls. Exceptions are samples Lig-A3, Lig-A5, and Lig-A10. Combining the results of UV analysis and IR spectroscopy, one can conclude that a dense polymeric layer with a low degree of freedom of  $\text{--CH}_3$  ( $\text{CH}_2$ ) groups (weak intensity of the bands in the region of  $3000\text{--}2800\text{ cm}^{-1}$ ) and a changed protonation degree of phenyl groups (Fig. 26.3, Lig-A1) is formed on the hydrated surface of pristine silica; with a fully methylated surface (Lig-A2), the interaction is carried out through the benzene rings of the polymer, which changes the energy state of the phenolic groups, whereas the deformation vibrations of the  $\text{CH}_3$  ( $\text{CH}_2$ ) groups are not hindered (Fig. 26.2, spectrum 2); on a partially methylated surface ( $\text{SiO}_2\text{ CH}_3$  30%), phenolic groups are not involved in the interaction, which indicates a change in the orientation of macromolecules depending on the degree of methylation of the silica surface.

The spectra of samples Lig-A5 and Lig-A10 (Fig. 26.3) indicate the presence of K- and B-bands at 235 and 288 but with a significant decrease in intensity, which indicates the interaction of the amino groups of silica with the acidic phenolic groups of the polymer. In addition, for sample Lig-A5, relative intensification of the

---

**Fig. 26.2** (continued) and aminated silica with modification degree 100% (5, Lig-A5); silica with bifunctional amino-methyl (6, Lig-A6), hydride-methyl (7, Lig-A7), and hydride-amino surface layer (8, Lig-A8); and silica with modification degree 30% with silicon hydride (9, Lig-A9) and amino groups (10, Lig-A10). Sample description is present in Table 26.1



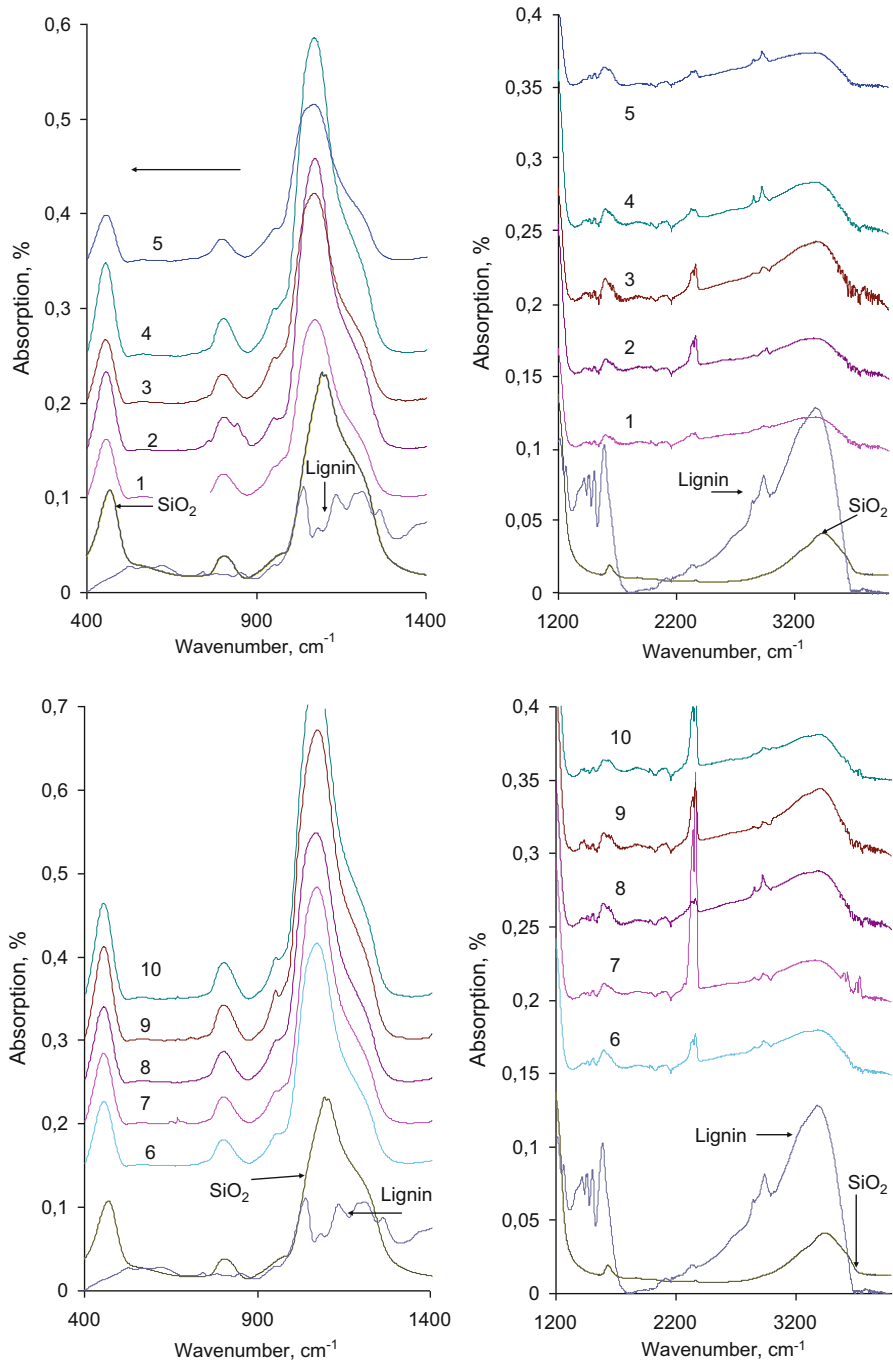


**Fig. 26.2** ATR spectra of silica/lignin composites. Figures represent ATR spectra of the pristine silica, lignin, and composites with lignin based on pristine silica (1, Lig-A1); methylated silica with modification degree 100 (2, Lig-A2) and 30% (3, Lig-A3); hydride-contained silica (4, Lig-A4)

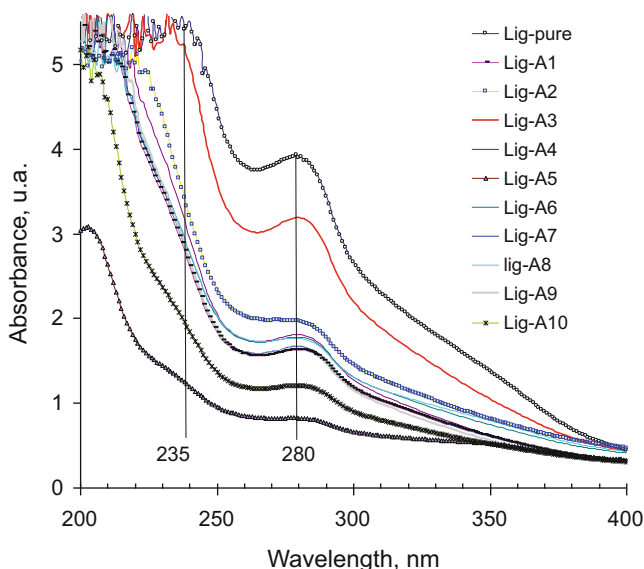


**Fig. 26.3** The UV–vis absorption spectra of lignin and silica/lignin composites (see Table 26.1). Illustration shows changes in the UV–vis absorption of the lignin (Lig-pure) after immobilization on the pristine silica (Lig-A1) and methylated silica with modification degree 100 (Lig-A2) and 30% (Lig-A3); on the hydride-contained silica (Lig-A4) and aminated silica with modification degree 100% (Lig-A5); on silica with bifunctional amino-methyl (Lig-A6), hydride-methyl (Lig-A7), and hydride-amino surface layer (Lig-A8); and on the silica with modification degree 30% with hydride (Lig-A9) and amino groups (Lig-A10)

bands is observed in the valence vibration region of  $\text{CH}_3$  ( $\text{CH}_2$ ). In other words, as the degree of surface modification increases, the intensity of interaction with phenolic groups increases ensuring the definite orientation of the macromolecules in the surface layer, predominantly, loosening of the polymer layer.

For analysis of thermal behavior of immobilized lignite, several DSC techniques were applied: for degradation and relaxation processes' investigation.

From results of DSC analysis (Figs. 26.4 and 26.5), after first heating circle (first heat) carried out for the evaporation of water (Fig. 26.4a, b), we can see that all the curves were initiated with endothermic regions due to the required heat for evaporation of residual or internal moisture before the heat flows turned from endothermic to exothermic. Analysis of DCS curves at first heating circle (Fig. 26.4a, b) shows water evaporation temperature ( $T_{\text{ev}}$ ) decreases in general by 10–15 °C. This could have been caused by a change in the macromolecule's packing density. The greatest decrease in  $T_{\text{ev}}$  was noted for the sample Lig-A2 based on completely methylated silica ( $\text{SiO}_2 \text{ CH}_3$  100%). It indicates a weakening of interaction between absorbed water and immobilized lignin in the silica surface layer.

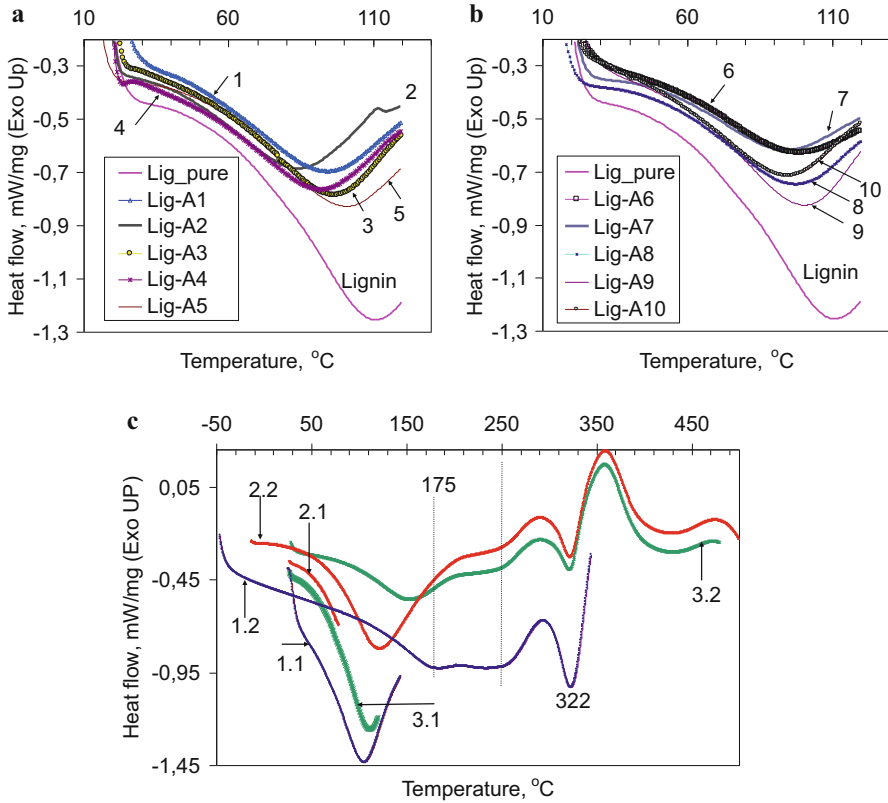


**Fig. 26.4** The DSC curves for composites based on modified silica and lignin. Illustration demonstrates the heat behavior of the lignin (Lig-pure) and composites silica/lignin (see Table 26.1) at the first heating run from 20 to 120 °C (a, b) and DSC curves for pure lignin (c) obtained at the different heating regimes: 1.1, first heat from 20 to 140 °C, and 1.2, second heat from -50 to 350 °C; 2.1, first heat from 20 to 100 °C, and 2.2, second heat from -20 to 500 °C; 3.1, first heat from 20 to 120 °C, and 3.2, second heat from 20 to 480 °C

In order to confirm the attribution of a first endotherm, the study of pristine lignin at the different DSC analysis conditions was carried out. In this context, it may be regarded that moisture elimination was most complete when first heat circle was carried out from 20 to 140 °C. When the final temperature on the first heat was lower, the residual moisture caused the shifting of the endotherm's extremum in the interval 20–200 °C to low temperatures. In addition, the endotherms with maxima at 175 and 250 °C have the same intensity, which was not observed on DSC curves obtained under other regimes.

According to literature data [22], lignin is slowly decomposed in a wider temperature range starting from 180 °C, that can be explained by the fact that lignin contains many aromatic rings with various branches, and the activity of the chemical bonds and functional groups in lignin covers an extremely wide temperature range.

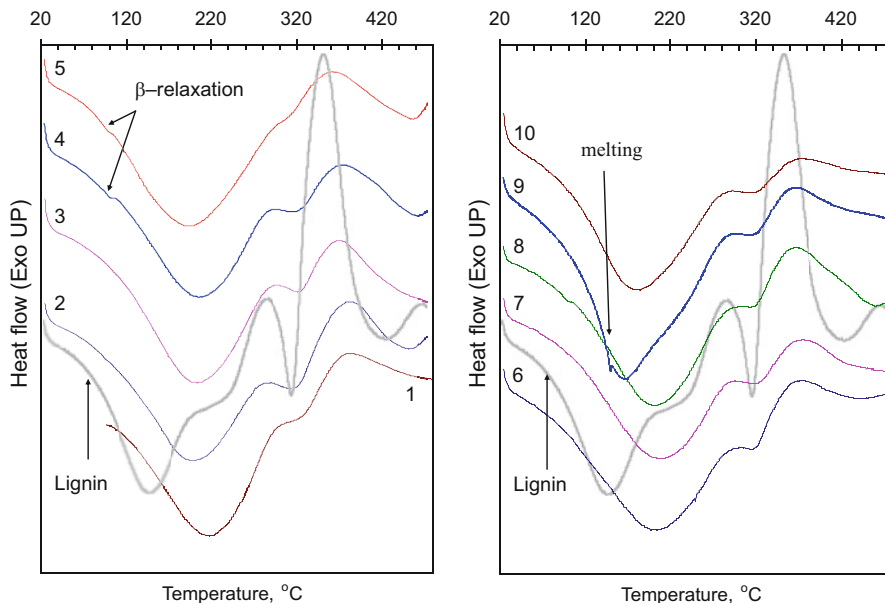


**Fig. 26.5** DSC curves of silica/lignin composites. Figures represent DSC curves of the composites with lignin immobilized on pristine silica (1, Lig-A1); methylated silica with modification degree 100 (2, Lig-A2) and 30% (3, Lig-A3); hydride-contained silica (4, Lig-A4) and aminated silica with modification degree 100% (5, Lig-A5); silica with bifunctional amino-methyl (6, Lig-A6), hydride-methyl (7, Lig-A7), and hydride-amino surface layer (8, Lig-A8); and silica with modification degree 30% with silicon hydride (9, Lig-A9) and amino groups (10, Lig-A10). Sample description is present in Table 26.1

In [23], it was shown that the major pyrolysis occurred between 200 and 450 °C, and in the temperature range from 290 °C to about 430 °C, the lignin has a higher thermal degradation rate with extremum at 360 °C. In this interval mass loss is related to the complex thermal decomposition of lignin, involving the formation of new bonds as a consequence of cross-linking reactions.

On DSC curve for lignin under study (Fig. 26.4c), endothermic events take place at 155, 247 and 322 °C up to 350 °C; above the curve exhibits an exothermic character followed by an exo-/endothermic transition and an endotherm at 427 °C. According to [24] lignin decomposition was associated with exothermic heat flow. The authors consider the interval on DSC curve of 320–480 °C as an exothermic event and linked it to the viscosity due to the inner frictions in the structure. They explain the exothermic effect (closely to 360 °C) by pyrolysis of lignin with the formation of plastic phase by crazing, which releases, during its damage, all the heat necessary to its formation and to its development. Also, authors indicate the different phases of the pyrolysis of lignin. Other explanation of exothermal character of DSC curve is the effect appearing at 320–460 °C is related to either the decomposition of bridge linkages with evolution of the CO<sub>2</sub> that can promote the thermooxidation process or the condensation of the aromatic rings.

Considering all extrema as endothermic ones, we can correlate them with the following processes: the effect appearing at 427 °C is related to degradation of the aromatic ring; the peaks near 150 and 250 °C can correspond to destruction of different links in macromolecules. Namely, the syringyl, as well as the guaiacyl units, is built into the lignin macromolecule mainly by ether bonds, and the ether bonds between syringyl units are easier to split than those between guaiacyl units [23]. Moreover, the guaiacyl units easily undergo condensation and coupling reactions. The thermal effect at 320 °C occurred due to destruction of main lignin chain. It should be noted that the highest degradation rate of lignin is observed over the temperature range from 290 to 430 °C where the DSC curve has both the endo and the exo direction [24]. And the endo-/exothermal transitions with extrema at 427 and 473 °C can be attributed to lignin carbonization (Fig. 26.4c).

The differences in the inherent structures of lignin could account for the diversities of thermal degradation behaviors. For lignin immobilized on silica, the curves differ significantly from the curve of the initial polymer: only two intense peaks of about 200 and 320 °C were detected (Fig. 26.5). It is known that the destruction of the cross-links in the lignin structure leads to a displacement of the basic extrema to the lower temperatures, which allows us to assume the inverse effect will be observed at formation of additional bonds. The DSC data obtained were accumulated in Table 26.2. As can be seen, the first endotherm of the decomposition is broadened, while the endothermic process at 320 °C passes with the same enthalpy. A general tendency is violated by samples based on silicon hydride-containing silica. The DSC curve for Lig-A4 demonstrates  $\beta$ -relaxation at 114 °C appeared during sample heating. This conformation transition ( $\beta$ -relaxation) is the local rotational motion of the segments of the flexible macromolecules in the interlayer between lamellar phases. At the stronger macromolecules, bending this transition is more significant and appears at the lower temperature. For composites under study,  $\beta$ -relaxation was found also for sample Lig-A8 but less apparent and at the lower temperature, 107 °C. In the absence of local tension, this transition was not observed, the endotherm being narrower. For the Lig-A10 the narrow endothermal peak at 156 °C occurred which can be corresponded to the melting process. Moreover, the endotherm has extremum at the lowest temperature and includes two overlapped bands which can be caused by degradation of new bonds formed in the polymer or with the silica surface. The endotherm's broadening usually occurs when polymer structure becomes loose. In this case we can assume that the polymeric surface layer is structured. A possible explanation is that the less homogeneous structure of the sample was caused by different orientation of macromolecules near the particle surface and in the bulk. This leads to discreteness of the thermodynamic and thermokinetic parameters of structure.

In order to investigate self-organized structures on the silica surface, the DSC study was carried out in the interval  $-50$ – $350$  °C with the different heating regimes. When the components of the lignin sample are amorphous or semicrystalline polymers during the degradation process, the melting point at 250 °C depression is indicative of favored breakage interactions between the polymer chains. The lower  $\Delta H$  and  $T_{\text{endo}}$  values may also be associated with the breakup of aromatic polymers

**Table 26.2** Thermal behavior parameters and characteristics of silica/lignin composites from DSC measurements: temperature of water evaporation ( $T_{ev}$ , °C) on first heat stage and interval ( $T_s - T_f$ ) and temperature ( $T_{endo}$ ) and heat of endo-effects ( $\Delta H$ , J/g) and heat of endo-effects ( $\Delta H$ , J/g) on the second heat curve

Samples	$T_{ev}$ , °C	$T_s - T_f$	$T_{endo}$ , °C	$\Delta H$ , J/g	$T_s - T_f$	$T_{endo}$ , °C	$\Delta H$ , J/g	$T_s - T_f$	$T_{endo}$ , °C	$\Delta H$ , J/g
Lignin	110	100-208	153	56.10	210-291	245	40.20	291-330	321	16.79
Lig-A1	95	100-306	220	94.77				318-378	324	30.28
Lig-A2	85	100-288	205	86.98				291-385	324	35.36
Lig-A3	98	100-302	208	103.32				309-375	329	15.75
Lig-A4	91	117-296	212	70.23				266-380	323	17.81
Lig-A5	101	110-300	200	72.62				278-364	308	18.71
Lig-A6	99	110-300	209	67.29				299-377	322	17.47
Lig-A7	94	125-298	214	61.39				270-381	327	14.60
Lig-A8	97	112-305	210	76.62				280-371	325	18.20
Lig-A9	100	100-200	176	-	100-300	240	123.44	299-376	327	16.77
Lig-A10	94	184	108-297	80.73				270-377	325	11.62

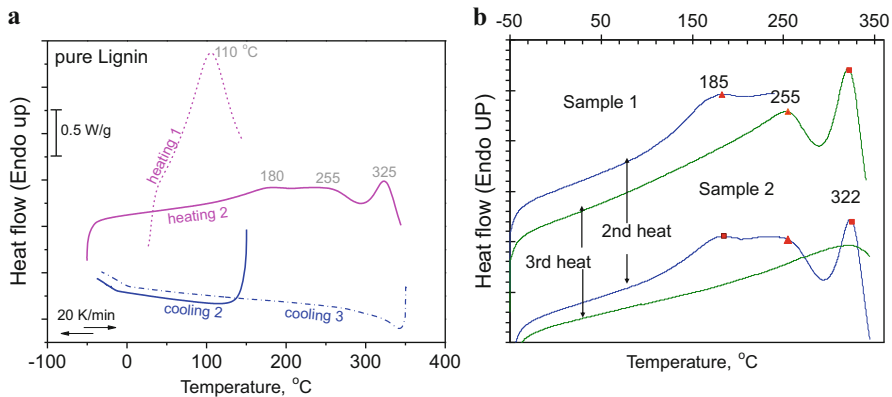


**Fig. 26.6** DSC curves of lignin. Figures (a) represent the common heating-cooling program with two runs that was applied for lignin microstructure investigation. Figure (b) demonstrates DSC curve of lignin on second and third heating runs: *Sample 1*, first heat, 20–150 °C; second heat, –50–250 °C; and third heat, –50–350 °C. *Sample 2*, first heat, 20–150 °C; second heat, –50–350 °C; and third heat, –50–350 °C

chains [25]. The three heating-cooling runs confirm the degradation nature of all endothermic processes (Fig. 26.6a, b). Namely, when after first cooling, the second heating run was from –50 to 250 °C, on DSC curve of the third heating, endotherms at 255 and 322 °C that are not affected by the presence of water were detected. In turn the water contents are controlled by temperature on the first heating run (Fig. 26.4c) and have strong influence on the first (closely to 180 °C) endotherm's position. After heating of the lignin to 350 °C on next cycle DSC curve, all bands were absent. A comparison of the DSC results at different temperature on the first heat and results obtained at stable temperature on first heat allows to conclude that the first heat to 150 °C promotes not only the removal of water bonded on the lignin surface but also ether links inside the macromolecules.

At heating to 250 °C on the second run (Fig. 26.6b), on the curve of the third run, the endotherm at this temperature is fixed, which may indicate the presence of pseudocrystalline structures in the material. It should be noted a decrease in the intensity of this peak; the degradation of the propanoid side chain can also occur at this temperature. The peak at 325 °C that related to the complex thermal decomposition of lignin (especially the  $\beta$ - $\beta$  and C-C bonds between lignin basic units) [20], involving the formation of new bonds as a consequence of cross-linking reactions, does not change.

Analysis of silica/lignin composite DSC curves (Fig. 26.7) shows that functional groups of silica surface promote formation of polymeric layer with different structure that reflects the intensity and position of endotherm in the interval 180–300 °C. For materials based on pristine and totally methylated silicas, the lowest endotherm was observed. The lowering of the endotherm intensity for composite based on pristine silica (Lig-A1) can be caused by polymer amorphization. From

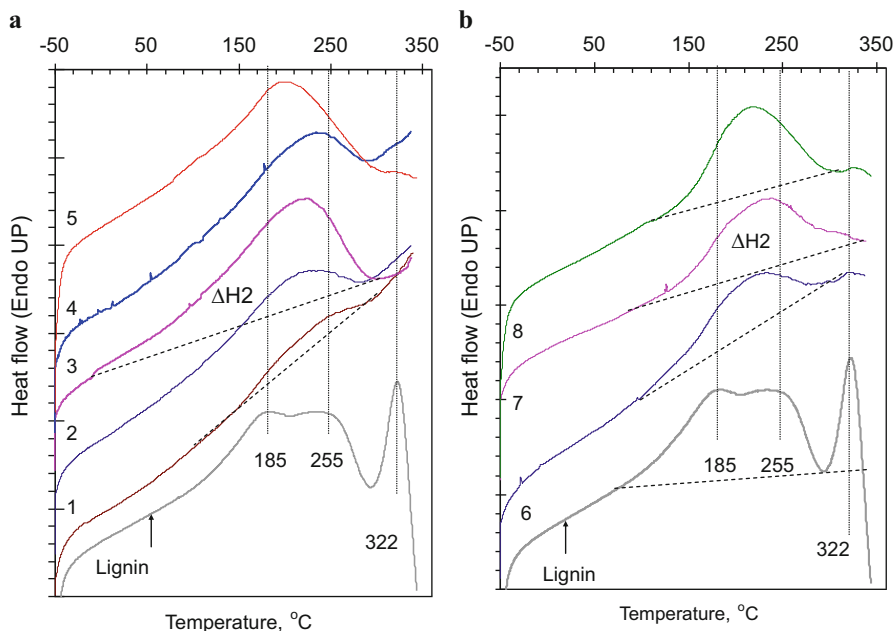


**Fig. 26.7** DSC curves of silica/lignin composites. Figures represent DSC curves of the second heat run obtained in two cycles of heating/cooling measurement at temperatures  $-50$ – $350$ °C. The first heating run (not presented) was conducted at  $T = 20$ – $150$ °C. Illustration shows the thermal behavior of lignin immobilized on pristine silica (1, Lig-A1); methylated silica with modification degree 100% (2, Lig-A2) and 30% (3, Lig-A3); hydride-contained silica (4, Lig-A4) and aminated silica with modification degree 100% (5, Lig-A5); and silica with bifunctional amino-methyl (6, Lig-A6), hydride-methyl (7, Lig-A7), and hydride-amino surface layer (8, Lig-A8). Sample description is represent in Table 26.1

the other side, 30% of the methyl groups on silica surface promotes increase of enthalpy of process at  $227$  °C (Table 26.3). A more intensive endotherm and highest value of the enthalpy ( $\Delta H_2$ ) were marked for samples based on aminated silica (Lig-A5). It should be noted that the presence of silicon hydride groups on silica surface reflected endotherm narrowing that indicates the compressing of polymer layer near the surface. For bifunctional silicas, more structured layer was obtained on amino-silicon hydride-containing surface.

The enthalpy of endothermic process (Table 26.3) during degradation of polymer layers on totally methylated silica (Lig-A2) is significantly lower than for samples with silicon hydride (Lig-A4) or amino groups (Lig-A5) with the same modification degree. Obviously, the hydrophobicity of the silica surface has a significant effect on the structure of the polymer layer formed. If a fully hydrophilic surface of the pristine silica contributes to the amorphization of the polymeric layer structure, a reverse effect from a completely hydrophobic surface (methylated silica with modification degree 100%) should be expected. However, the highest enthalpy



**Table 26.3** Thermal behavior parameters and characteristics of silica/lignin composites from DSC measurements at two heating/cooling cycles in interval  $-50$ – $350^\circ\text{C}$ : temperature of water evaporation ( $T_{\text{ev}}$ ,  $^\circ\text{C}$ ) on the first heat stage and interval ( $T_s - T_f$ ); temperature ( $T_{\text{endo}}$ ) and heat of endo-effects ( $\Delta H$ ,  $\text{J/g}$ ) on the second heat curve; and results on hydration for selected samples for ambient (40 rh%) and very high (98 rh%) relative humidities (rh)

Sample	First heating			Second heating			Hydration, on dry basis	
	$T_{\text{ev}}$ , $^\circ\text{C}$	$T_s - T_f$	$\Delta H_1$ , $\text{J g}^{-1}$ ( $\pm 10 \text{ J/g}$ )	$T_{\text{ev}}$ , $^\circ\text{C}$	$T_s - T_f$	$\Delta H_2$ , $\text{J g}^{-1}$ ( $\pm 5 \text{ J/g}$ )	rh 40%	rh 98%
Lignin (sample 1)	115	40–150	199	180/250/325	50–340	175	0.08	0.84
Lignin (sample 2)	106	40–150	164	180/250/325	50–340	116		
Lig-A1	99	30–150	112	244	150–300	15	0.06	0.30
Lig-A2	95	30–150	77	227	130–286	38	0.05	0.26
Lig-A3	97	30–150	123	227	60–290	90		
Lig-A4	91	30–150	100	245	70–290	52		
Lig-A5	99	30–150	127	200	35–325	97		
Lig-A6	89	30–150	160	222	100–296	51		
Lig-A7	84	30–150	82	235	130–303	58		
Lig-A8	92	30–150	103	216	122–301	76		
Pristine silica	100	30–150	89	–	–	–	0.07	0.60

was found for endothermic process on the partially methylated surface (methylated silica with modification degree 30%) and for composite based on aminated silica with a modification degree of 100% (Table 26.3). Both these samples are partially hydrophobic. And taking into account that on the methyl-aminated surface the enthalpy of endo-effect decreases, it can be assumed that there is a certain optimum of the hydrophilicity degree, which ensures the structuring of the polymer layer.

## 26.4 Conclusion

In general, the results characterizing the silica/lignin composites indicate that formation of the adsorbed polymer layer can be controlled by functionality of the carrier surface. It was found that characteristics of the lignin immobilized on silica surface are differing from lignin in volume. The parameters of degradation, relaxation, and phase transitions are determined by structure and functionality of the silica surface layer. Silica with silicon hydride groups promotes a structuration and compression of the polymer layer; on the other hand, amino groups caused the layer loosening. Analysis of DSC data using the different techniques confirms the strong influence of moisture inside lignin and water on the silica surface on the structure of immobilized polymer, especially on hydrated silica surface and methylated silicas. The presence of functional groups that can chemically react with lignin has great impact on degradation process that can be used in the future for elaboration of the.

**Acknowledgments** The research leading to these results has received funding from the People Programme (Marie Curie Actions) of the European Union's Seventh Framework Programme FP7/2007-2013 under REA grant agreement no. PIRSES-GA-2013-612484.

**Competing Interest** The authors declare that they have no competing interests.

## References

1. Calvo-Flores FG, Dobado JA, Isac-García J, Martín-Martínez FJ (2015) Lignin and Lignans as renewable raw materials. Chemistry. Technology and applications. Wiley, Hoboken
2. Lee HV, Hamid SBA, Zain SK (2014) Conversion of lignocellulosic biomass to nanocellulose: structure and chemical process. *Sci World J.* <https://doi.org/10.1155/2014/631013>
3. Qin Y, Mo W, Yu L, Yang D, Qiu X (2016) A light-colored hydroxypropyl sulfonated alkali lignin for utilization as a dye dispersant. *Holzforschung* 70:109–116
4. Albadarin AB, Al-Muhtaseb AH, Al-laqtah NA, Walker GM, Allen SJ, Ahmad MNM (2011) Biosorption of toxic chromium from aqueous phase by lignin: mechanism, effect of other metal ions and salts. *Chem Eng J* 169:20–30
5. Klapiszewski Ł, Bartczak P, Wysokowski M, Jankowska M, Kabat K, Jesionowski T (2015) Silica conjugated with kraft lignin and its use as a novel 'green' sorbent for hazardous metal ions removal. *Chem Eng J* 260:684–693
6. Mohan D, Pittman CU, Steele PH (2006) Pyrolysis of wood/biomass for bio-oil: a critical review. *Energy Fuel* 20(3):848–889

7. Ahmad M, Taylor CR, Pink D, Burton K, Eastwood D, Bending GD, Bugg TD (2010) Development of novel assays for lignin degradation: comparative analysis of bacterial and fungal lignin degraders. *Mol BioSyst* 6:815–825
8. Klapiszewski Ł, Nowacka M, Milczarek G, Jesionowski T (2013) Physicochemical and electrokinetic properties of silica/lignin biocomposites. *Carbohydr Polym* 94:345–355
9. Milczarek G, Inganäs O (2012) Renewable cathode materials from biopolymer/conjugated polymer interpenetrating networks. *Science* 335:1468–1471
10. Podkościelna B, Goliszka M, Sevastyanova O (2016) New approach in the application of lignin for the synthesis of hybrid materials. *Pure Appl Chem*. <https://doi.org/10.1515/pac-2016-1009>
11. Hilburg SL, Elder AN, Chung H, Ferebee RL, Bockstaller MR, Washburn NR (2014) A universal route towards thermoplastic lignin composites with improved mechanical properties. *Polymer* 55:995–1003
12. Podkościelna B, Sobiesiak M, Gawdzik B, Zhao Y, Sevastyanova O (2015) Lignin vinyl esters and their co-polymers with styrene, divinylbenzene and triethoxyvinylsilane. *Holzforchung* 69:769
13. Qu Y, Tian Y, Zou B, Zhang J, Zheng Y, Wang L, Li Y, Rong C, Wang Z (2010) A novel mesoporous lignin/silica hybrid from rice husk produced by a sol–gel method. *Bioresour Technol* 101:8402–8405
14. Saad R, Hawari J (2013) Grafting of lignin onto nanostructured silica SBA-15: preparation and characterization. *J Porous Mater* 20:227–233
15. Klapiszewski Ł, Królak M, Jesionowski T (2014) Silica synthesis by the sol-gel method and its use in the preparation of multifunctional biocomposites. *Cent Eur J Chem* 12:173–184
16. Xiong W, Yang D, Zhong R, Li Y, Zhou H, Qiu X (2015) Preparation of lignin-based silica composite submicron particles from alkali lignin and sodium silicate in aqueous solution using a direct precipitation method. *Ind Crop Prod* 74:285–292
17. Klapiszewski Ł, Madrawska M, Jesionowski T (2012) Preparation and characterisation of hydrated silica/lignin biocomposites. *Physicochem Probl Miner Process* 48(2):463–473
18. Jesionowski T, Klapiszewski Ł, Milczarek G (2014) Kraft lignin and silica as precursors of advanced composite materials and electroactive blends. *J Mater Sci* 49:1376–1385
19. Bolbukh YN, Tertykh VA, Gawdzik B (2006) TGA and DSC studies of filled porous copolymers. *J Therm Anal Calorim* 86:125–132
20. Strzemiecka B, Klapiszewski Ł, Jamrozik A, Szalaty TJ, Matykiewicz D, Sterzynski T, Voelkel A, Jesionowski T (2016) Physicochemical characterization of functional lignin–silica hybrid fillers for potential application in abrasive tools. *Materials* 9:517–530
21. Jiang C, He H, Jiang H, Ma L, Jia DM (2013) Nano-lignin filled natural rubber composites: preparation and characterization. *Express Polym Lett* 7(5):480–493
22. Liu Y, Hu T, Wu Z, Zeng G, Huang D, Shen Y, He X, Lai M, He Y (2014) Study on biodegradation process of lignin by FTIR and DSC. *Environ Sci Pollut Res* 21:14004–14013
23. Wang S, Wang K, Liu Q, Gu Y, Luo Z, Cen K, Fransson T (2009) Comparison of the pyrolysis behavior of lignins from different tree species. *Biotechnol Adv* 27:562–567
24. Kifani-Sahban F, Kifani A, Belkbir L, Zoulalian A, Arauzo J, Cardero T (1997) A physical approach in the understanding of the phenomena accompanying the thermal treatment of lignin. *Thermochim Acta* 298:199–204
25. Mousavioun P, Halley PJ, Doherty WOS (2013) Thermophysical properties and rheology of PHB/lignin blends. *Ind Crop Prod* 50:270–275

# Chapter 27

## Cooperative Phenomena in Spin-Crossover Molecular Crystals

Iurii Gudyma, Artur Maksymov, and Kateryna Polonska

### 27.1 Introduction

Spin-crossover (SCO) systems are relatively rare class of transition metal complexes that display molecular magnetic bistability and interconverted reversibility upon external stimuli. Under normal conditions, these complexes can exhibit spin crossover, that is, the entropy-driven thermal transition from a low-spin (LS) state, populated at low temperatures, to a high-spin (HS) state, populated at higher temperatures. The observed spin state depends on the balance between maximizing the number of parallel spins/unpaired electrons (Hund's rule of maximum multiplicity) and having the lowest electronic energy by populating the lowest energy orbitals. For a free atom or ion, or ionic compound, the normal spin state is that of maximum multiplicity, in accordance to the first Hund's rule; however, for sufficiently large ligand field, one obtains a low-spin ground state. By the influence of external physical field (light irradiation, temperature, pressure, and others), it is possible to bring into the system additional energy that could increase spin-pairing repulsion of the electrons. Due to equalization between spin-pairing energy and ligand field splitting energy, the favorable conditions for transition are established. Besides the changes of magnetic moment of the molecule, the spin transition is also accompanied by the changes in the molecular volume for different states. For spin-crossover materials are found a great variety of spin transition curves that were characterized as follows: sharp transitions often accompanied by hysteresis, more or less gradual transitions, and sometimes incomplete transitions with residual

---

Iu. Gudyma (✉) · K. Polonska  
Department of General Physics, Technical and Computer Sciences, Yuriy Fedkovych Chernivtsi National University, Chernivtsi, Ukraine

A. Maksymov  
Marian Smoluchowski Institute of Physics, Jagiellonian University, Kraków, Poland

dia- or paramagnetism. The cooperative behavior of the spin transition in the solid spin-crossover materials demands an interaction between their molecules. The largest class of SCO complexes are the Fe(II) SCO complexes. In octahedral symmetry  $O_h$ , the ferrous iron molecular complexes can be converted between diamagnetic LS ( $e_g^0 t_{2g}^6$ ) and paramagnetic HS ( $e_g^2 t_{2g}^4$ ) states, which leads to a significant change in the metal-ligand bond length. SCO materials are known to have potential applications such as reversible high-density memories, ultrafast switches (at the nanoscale), sensors of temperature and pressure, fundamental elements in display technologies, etc. Consequently SCO systems have been studied extensively both theoretically and experimentally. We will not here recall all the properties of the SCO systems, since extensive literature exists on the subject (see, e.g., [1–5]).

If solids shrink to the nanoscale, the surface-to-volume ratio increases, and the surface-environment interaction becomes a major factor for affecting material behavior. The control over functionalities at the nanoscale (in nanoparticles, nanopatterns, thin films, and, ultimately, single molecules) appears as a cornerstone in the elaboration of advanced materials for many very important above technologies. The individual nanoparticles possessing an abrupt transition with a thermal hysteresis loop are appealing because they can be used for information storage at the nanometric level. Such effects are ambiguous or beneficial, depending on environmental conditions and material application. These properties are very sensitive to changes in external environment. The surface exhibits some disorganized fluctuations which usually are ascribed to environmental randomness [6]. However the rational control of the behavior of these materials on a nanometric scale is highly required, especially when they are integrated into functional devices. The investigation of surface-environment effects can be realized by modern experiments with a comprehensive suite of surface-sensitive spectroscopy and microscopy tools [7]. One of the major challenges of modern technology is to stabilize the nanoparticles and the surface in order to minimize its interaction with the environment. It is obvious that surface-environment distribution can be neglected in the thermodynamic limit, but on the other hand, a molecule must always be viewed as part of its environment [8].

The current review addresses mainly the role of surface-environment effects of spin-crossover nanocrystals in the occurrence of phase transition in the material. The important issue is to understand the interplay of cooperativity of the system and the fluctuations of its environment. It is almost obvious that molecules on surfaces have different SCO properties than the inner molecules [6, 9]. This may influence the properties of the whole particle in this very low size range [10]. The transition metal ions can be seriously altered at the surface of the particle. It is very likely, particularly in the case of small particles with high specific surface areas, that these Fe(II) ions “feel” considerable differences in bond strength or even suffer from coordinative defects and consequently do not exhibit SCO [11]. We are interested in phenomena that are associated with the emergence of disorganized random fluctuations in the state of the system under influence of surrounding environment. This chapter is organized as follows: In Sect. 27.2, we outline the Hamiltonian and its application to the Ising-like model of spin-crossover nanocrystal interacting with the surroundings; in Sect. 27.3, we discuss the results; and finally, in Sect. 27.4, we present our conclusions.

## 27.2 Ising-Like Model of Spin-Crossover Nanocrystal Interacting with the Surroundings

With the achievement of nanoscopic sizes of spin-crossover nanocrystals, the dynamics of surface molecules becomes relevant and can influence the phase stability and transformation kinetics of entire solids. Despite the variety of the models that are able to describe the physical processes at microscopic space and time scales, there is a lack of descriptions which account for linkage between the surface of the crystal and its volume. Since the sizes of solid nanocrystals decrease, the increase in surface area-to-volume ratio makes the surface-environment effects become more pronounced. Therefore the importance of theoretical model that could explain the role of surface of separate spin-crossover nanocrystal is evident. Phenomenologically, the interactions between any spin-crossover nanoparticles located into the lattice can be modeled in a simplest way by the Ising-like Hamiltonian

$$\mathcal{H} = - \sum_{\langle ij \rangle}^b J_{ij}^b s_i s_j - \sum_{\langle ij \rangle}^s J_{ij}^s s_i s_j - \sum_{\langle ij \rangle}^{s-b} J_{ij}^{s-b} s_i s_j - h_0 \sum_i s_i - \sum_i^s h_i(t) s_i. \quad (27.1)$$

Here  $s_i$  is a fictitious spin (pseudospin) operator which has two eigenvalues  $\pm 1$ , corresponding to the HS and LS states of respective  $i$ -s molecule, and  $\langle ij \rangle$  denotes the summation over all nearest neighboring spin pairs. The Ising-like Hamiltonian describes the elastic interaction between spin states via the near-neighbor coupling of two-level units. We based our study on 3D crystal lattice with open boundary conditions. In this case it is obvious that depending whether the particle is located on the surface or inside the crystal, the number of bonds associated to it is different. In framework of mean field approximation, it means that the interacting force between the sites on the surface and inside the volume is not the same. The intersite short-range coupling constants  $J_{ij}^\alpha$ , measured in energy units, are parameters of the theory, where an index  $\alpha = b, s, b - s$  corresponds to occupied pairs of bulk sites, surface sites, and bulk surface sites. The schematic illustration of the model composed of a bulk sites which are surrounded by a surface of one site thick is shown in Fig. 27.1. In this figure are displayed only two kinds of bonds: one for surface sites and another one for bulk sites since the interaction between the surface sites and bulk sites is considered the same as for the sites inside the lattice, i.e., the  $b - s = b$  which leads to the decomposition of the Hamiltonian into bulk and surface parts [6].

The effective external field describing the result of surrounding action of crystal on single molecular magnet is

$$h_0 = -\frac{1}{2}(\Delta - k_B T \ln g), \quad (27.2)$$

where  $\Delta$  stands for the energy difference between HS and LS states (the enthalpy change associated with the LS  $\rightarrow$  HS conversion) for an individual spin-crossover

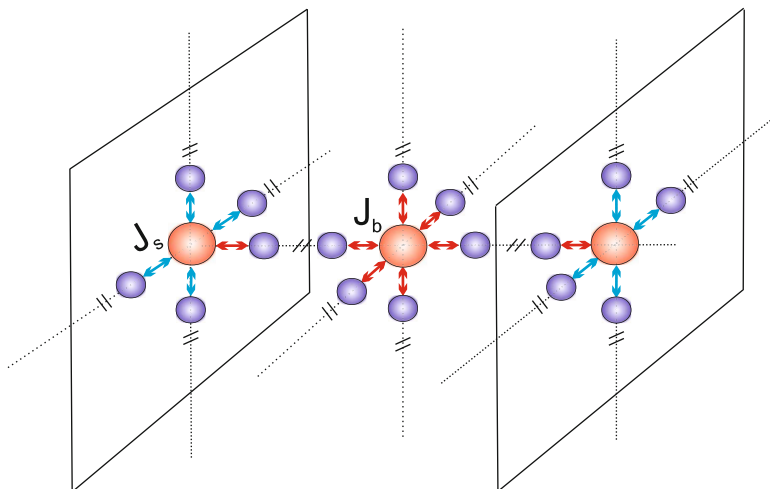


**Fig. 27.1** The spatial configuration of a three-dimensional SCO system where the difference is shown between the interactions of magnetic molecules situated on the surface and inside the lattice

molecule,  $g = g_{HS}/g_{LS}$  is the degeneracy ratio between HS and LS energy levels, and  $k_B$  is Boltzmann's constant. It is considered that the value  $\Delta$  is fully formed by the ligand environment of the transition metal ion; this is why it is called the ligand field. In this version the external field is homogeneous but it depends on temperature. Thus in noninteracting system, the equilibrium temperature  $T_{eq}^0$  at which mole fractions of the LS and HS states are equal corresponds to a zero effective field, and consequently  $T_{eq}^0 = \Delta/(k_B \ln g)$ . It is important to note for our study that  $T_{eq}^0$  coincides with the transition temperature in the bulk material. The Hamiltonian (27.1) describes in a convenient way the behavior of spin-crossover system where the control parameter is a temperature  $T$ . If the critical temperature in purely Ising model is smaller than the equilibrium temperature in noninteracting model, then a gradual spin transition from LS to HS takes place by increasing the temperature. Otherwise, the spin transition is discontinuous and is associated to a first-order phase transition. In turn,  $h_i(t)$  is seen to correspond to the randomly fluctuating ligand field. The  $h_i(t)$  is the random field only at site  $i$  on the ideal (sharp) surface of the bulk material. Indeed, the ligand field as function of the molecule positions in the lattice is the key point of examination of surface effects leading to unusual size dependence of the thermal hysteresis behavior in spin-crossover nanoparticles [12]. Linares et al. [12] included the interaction between the edge molecules and the environment as a negative (but nonuniform) pressure on the system through the interaction of surface atoms with their nearest neighboring atoms situated inside the lattice. The local pressure acting on the edge spin-crossover molecules from the matrix side during transition from HS to LS states was considered in paper [13]. This idea arises from the mechanoelastic model where local pressure changes at the edge molecules are taken into account by missing springs [14]. The same idea

was used by Tissot et al. [15] to explain the experiments of control of the thermal hysteresis of the prototypical spin transition in  $Fe^{II}(phen)_2(NCS)_2$  compound via the microcrystallite environment. Muraoka et al. [16] considered the edge molecules as inactive HS ones, whereas all inside molecules are active in the framework of the Ising-like model. We proceed somewhat differently. Since a Gaussian stochastic process is archetypical for contact with thermal surrounding system, we use the statistical characteristic of the fluctuating external field as follows:

$$\langle h_i(t) \rangle = 0, \quad (27.3)$$

$$\langle h_i(t)h_j(t') \rangle = \varepsilon^2 \delta(t - t'). \quad (27.4)$$

Here  $\langle \dots \rangle$  represents an ensemble average over all realizations of the fluctuating field. Besides  $\varepsilon$  is a measure of the strength of random surface fields, and  $\delta_{ij}$  is the Kronecker delta symbol. The basic idea behind Langevin approach is to assume that the fluctuations on each atomic site can be represented by a Gaussian white noise term. Stronger fluctuations lead to increasing the width of the Gaussian distribution.

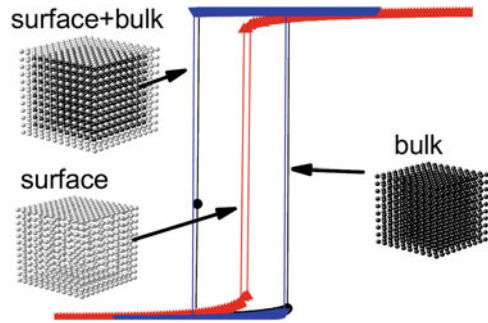
In the usual consideration, each molecule on surface is assumed to be instantaneous coupled to a thermal reservoir, and heat currents may arise between the reservoirs in the stationary state scenario. The surface itself provides a new intrinsically low-symmetry environment that can trigger structural distortions and modify the ligand field. Thus the order parameter is sensitive to the stochastic environment process with respond to the system, acting as a disorder force. In fact, the surrounding environment is the main factor governing the spin transition behavior of spin-crossover materials. Inasmuch as spin crossover is an inherently ligand field problem that this coupling is through random variations of the field.

### 27.3 Monte Carlo Simulation of Magnetic Behavior in Spin-Crossover Nanocrystals

For the spin-crossover system described by the Hamiltonian (27.1), we have provided a series of three-dimensional (3D) Monte Carlo (MC) simulations based on the Metropolis algorithm. The MC Metropolis algorithm provides a natural way to simulate temperature effects where dynamics are not required due to the rapid convergence to equilibrium and relatively simple implementation. In order to reproduce the experimental situations, we have used for simulations 3D cubic lattice with size  $L^3$ , where  $L$  is the length of each side, and open boundary conditions. For simulations the following parameters of the system were fixed: The intersite interaction of inside molecules is chosen at  $J^b = 85$ , the degenerating ratio is  $g = 150$ , and the energy gap is  $\Delta = 900$ . In this way we characterize the behavior of temperature transition curves which are the main characteristic for this type of Ising-like model. The numerical solutions of Hamiltonian (27.1) were obtained for 5000 MC steps assuming that the coupling of bulk sites with the surface ones is the same like for the bulk sites, i.e.,  $J_{ij}^{bs} = J_{ij}^b$ .



**Fig. 27.2** The schematic representation of the analysis of magnetization dynamics for the molecules on the surface and inside the crystal



In our study we are interested on how much the magnetization dynamics of entire crystal depends on surface effects. For this reason, the degree of changes in the intermolecular interaction on the surface with respect to the bulk one was fixed by relationship which describes the weakening of cooperativeness as  $J^s = \eta J^b$ , where  $0 < \eta \leq 1$ . In order to understand the impact of molecules from the surface on magnetization behavior of entire solid, we analyzed separately the temperature transition curves of the surface of one molecule thick and of the remaining (bulk) part of the crystal. The way we interpreted the entire solid as the two subsystems, the surface of the crystal and its bulk part, illustratively is shown in Fig. 27.2. The resulting magnetization has been averaged over last 3000 MC steps after reaching by the system its steady state at certain temperature. For the simulation of the thermal transition, we start at high temperature where all the molecules are in the HS state, i.e., the HS configuration has been used as the initial state of the cooling branch of the hysteresis loop.

In Fig. 27.3 are shown the several transition curves for various interactions of magnetic molecules on surface sites (its values are indicated in the caption of the figure) obtained for SC molecules from entire 3D lattice (which are displayed in Fig. 27.3a) and for bulk and surface sites separately (which are plotted in Fig. 27.3b, respectively). The lattice side of the system was chosen to be  $L = 12$ .

At this step the randomness of fields on surface has been omitted; therefore the Hamiltonian (27.1) is considered without fluctuations in ligand field, i.e.,  $h_i(t) = 0$  for all surface sites. The results from Fig. 27.3 demonstrate the contributions of the coupling of surface spins into resulting bistability of spin-crossover system. The narrowing of hysteresis with decrease of surface spin coupling which is shown in Fig. 27.3a is probably related to the reduction of their degree of cooperativity. But this effect is observed only for a certain range of surface interaction. In the case when  $J^s < 0.5J^b$ , no longer changes of hysteresis width take place, which happens because of too weak influence of surface effects on magnetization behavior of the lattice of this size. However, it is quite remarkable that the hysteresis loop area decreases. This is due to the increase in the residual magnetization and the degree of incompleteness of spin transition. However such movement is limited since with decreasing of the coupling of surface molecules, the hysteresis gradually becomes controlled by the molecules inside the lattice. Figure 27.3a shows the

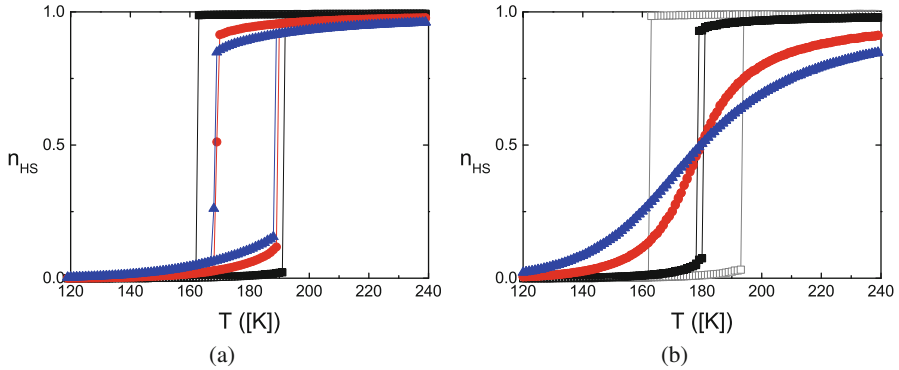


**Fig. 27.3** The simulated temperature-induced hysteresis for several values of intermolecular interaction on the surface:  $J^s = J^b$  (black [squared] curves),  $J^s = 0.5J^b$  (red [circled] curves), and  $J^s = 0.25J^b$  (blue [triangled] curves) (a). The transition curves calculated only for magnetic molecules inside the lattice (gray [open squared] curve) and only for molecules on the surface are shown in (b). The values of intermolecular interaction and the marking of transition curves for molecules on the surface are the same like in (a)

relationship between the state of the molecules on the surface of solid nanoparticles and processes which take place in the entire crystal matrix. It is obvious that with the weakening of the surface intermolecular interaction, the saturation point of hysteresis loop moves slowly to the equilibrium point. Figure 27.3b is plotted for surface spins with several fixed values of coupling:  $J^s = J^b$  (black [squared] curve),  $J^s = 0.5J^b$  (red [circled] curve), and  $J^s = 0.25J^b$  (blue [triangled up] curve). The number of lattice sites belonging to different regions is  $N = 1000$  for bulk sites and  $N = 728$  for surface ones. The hysteresis only for molecules inside the lattice is additionally plotted (gray [open square] curve). As it is observed from Fig. 27.3b, the decreasing of surface coupling shifts the surface magnetization of the lattice toward non-hysteretic transition; therefore the competition between the hysteretic behavior of molecules inside the lattice and non-hysteretic ones of molecules on the surface appears. This is the main reason for the narrowing of hysteresis of entire lattice with decreasing of surface coupling which is displayed in Fig. 27.3a. Here we are not especially interested in the dependence of system behavior on its size, but the effects of size which lead to narrowing of hysteresis are reported in [9, 10, 17, 18], the ones which give the residual magnetization are reported in [9, 10, 17], and the ones leading to shifting of transitions temperature are reported in [10, 17, 18].

In an effort to understand how the transition process occurs in the lattice, the spin configurations at several points on cooling branch of temperature transition curve have been examined. In this calculation we have analyzed the spin configurations of the system starting from ordered HS state and finishing with the spin configuration at equilibrium temperature  $T_{eq}$  of cooling regime which corresponds to  $n_{HS} = 0.5$ . Such range has been chosen because it gives principal variants of spin configurations. This part of cooling branch of temperature transition curve

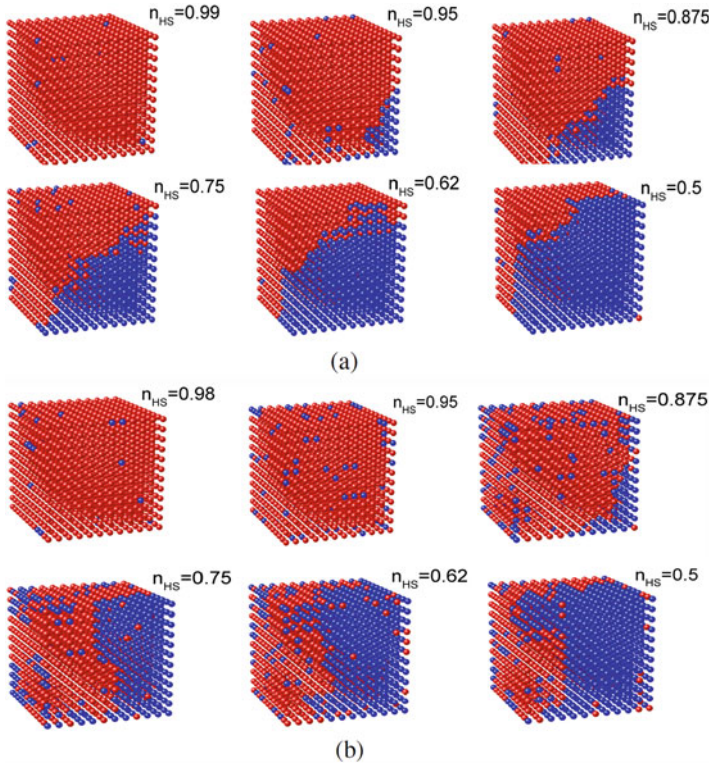


**Fig. 27.4** The spin configurations of the lattice at indicated values of high-spin fraction  $n_{HS}$  for two values of surface coupling  $J^s = J^b$  (a) and  $J^s = 0.5J^b$  (b). The red circles indicate the molecules with HS configuration, whereas the blue ones correspond to LS configuration

represents decay of HS phase states. In our simulations we assumed that physical picture is symmetrical for LS and HS states; however in more rigorous approach, some asymmetry could be observed. Several spin configurations for the first half of cooling branch are displayed in Fig. 27.4 for  $J^s = J^b$  (Fig. 27.4a) and  $J^s = 0.5J^b$  (Fig. 27.4b). As in previous figures, this analysis is provided for lattice side  $L = 12$  which gives 1000 bulk sites and 728 surface sites, respectively.

As we can see from the figure, the transformation from one state to another (here from HS to LS state) is initiated on the surface and is propagating inside the lattice. The similar propagation effect is observed in 2D mechanoelastic models where the spin transition starts at the corners and is propagating inside the lattice [5, 19] in contrast to classic Ising models in which clusters start from anywhere inside the lattice. In order to have a better understanding how switching occurs, for each spin configuration in Fig. 27.4 we have quantitatively analyzed the number of molecules on the surface and inside the lattice that remain in HS state and are contributed to the total magnetization of the system. It is worth to remind that for the chosen Fe(II) SCO systems, the HS molecule is characterized by the total spin number  $S = 2$ ,

whereas the LS configuration is not magnetic ( $S = 0$ ). Therefore, such analysis also sheds light on the system's magnetization and its variation during transition. For the temperature at which the molecules inside the lattice are almost completely switched, the switching of molecules on the surface is incomplete which is related to smaller surface coupling and is the main reason of residual magnetization. The spin configurations for  $n_{HS} = 0.99$  and  $n_{HS} = 0.98$  in Fig. 27.4a, b, respectively, are obtained at relatively high temperature  $T = 240$  which ideally should provide the ordered HS configuration over entire lattice. However, only 1713 molecules for  $J^s = J^b$  and 1697 molecules for  $J^s = 0.5J^b$  from total number of 1728 sites are in HS state. Since the HS molecules are characterized by a magnetic moment, these numbers of HS sites contribute to the total fictitious magnetization of studied Ising-like model  $m$ , and therefore the mentioned values of HS fraction ( $n_{HS} \approx 0.99$  and  $n_{HS} \approx 0.98$ ) are obtained according to the relations  $m = 2n_{HS} - 1$ . For this certain case, the number of HS molecules inside the lattice is 993 for  $J^s = J^b$  and 998 for  $J^s = 0.5J^b$ ; therefore one can conclude that the main difference between the magnetization of analyzed configurations is provided by molecules from the surface.

The smaller surface coupling also provides different starting points for the switching (here from HS to LS state). From displayed spin configurations, one can see that for  $n_{HS} \approx 0.95$  at which the switching for the spin-crossover lattice with  $J^s = 0.5J^b$  is just starting (see Fig. 27.4b at  $n_{HS} \approx 0.95$ ), the switching for the lattice with  $J^s = J^b$  has already begun and is propagating inside (see Fig. 27.4a at the same value of  $n_{HS}$ ). The corresponding numbers of HS molecules from the surface and inside the lattice which provide the value of HS fraction  $n_{HS} = 0.95$  in Fig. 27.4 are 670 and 985 for Fig. 27.4a vs 650 and 997, respectively, for Fig. 27.4b. For  $J^s = 0.5J^b$  the number of HS molecules inside the lattice for two consequent spin configuration (at  $n_{HS} \approx 0.99$  and  $n_{HS} \approx 0.95$  in Fig. 27.4a) is almost unchanged, whereas the bulk HS sites for  $J^s = 0.5J^b$  and the same spin configuration (at  $n_{HS} \approx 0.98$  and  $n_{HS} \approx 0.95$  in Fig. 27.4b) are changed more pronounced. The next spin configurations in Fig. 27.4a, b are obtained for the same values of HS fractions; therefore in order to understand what molecules contribute to the HS states, we just enumerate the pair of molecules on the surface and inside the lattice in the form (number of surface sites; number of bulk sites) for both surface coupling indicated in the caption of Fig. 27.4. For  $J^s = J^b$  the numbers of HS molecules on the surface and inside the lattice are (615; 905), (530; 762), (463; 613), and (365; 497) for spin configurations at  $n_{HS} \approx 0.875$ ,  $n_{HS} \approx 0.75$ ,  $n_{HS} \approx 0.62$ , and  $n_{HS} \approx 0.5$  in Fig. 27.4a, respectively. For  $J^s = 0.5J^b$  the numbers of HS molecules on the surface and inside the lattice are (532; 979), (464; 837), (404; 679), and (342; 523) for spin configurations at the same values of HS fraction in Fig. 27.4b. For smaller intermolecular interaction, the magnetization which corresponds to HS fractions  $n_{HS}$  is determined mostly by the molecules inside the lattice (the number of HS molecules in this case is greater for all-spin configurations), whereas for the homogeneous intermolecular interaction over entire lattice (like in Fig. 27.4a), there are no prevailed contributions into total magnetization from molecules on the surface and inside the lattice.

Additional important information about the evolution of magnetization can be extracted from the analysis of the Monte Carlo trajectories. From entire range of temperature for which the transition curves have been calculated, we have checked the evolution of the system magnetization at three most relevant values of temperatures: the magnetization dynamics at transition temperature and at temperatures where the system magnetization becomes saturated which correspond to HS and LS ordered states. In Fig. 27.5 are shown the trajectories that describe the evolution of magnetization at indicated values of temperatures on cooling branch of transition curve separately for bulk and surface sites. Notice that the surface sites form the surface magnetization of spin-crossover nanocrystal. We analyzed only the cooling branch of transition curve since due to the symmetry reason, the dynamics for cooling and heating physically is similar with only difference that it occurs in opposite direction so the opposite physical processes can be observed (e.g., instead of relaxation, one can see the excitation and so on). As it is observed from the comparison of Fig. 27.5a, b which are calculated for bulk and surface sites only with  $J^s = J^b$ , the relaxation of HS fractions on the surface takes place with lower rate than the one for the HS molecules inside the crystal. It can serve additional argument about smaller degree of cooperativity of surface sites. As it is shown in Fig. 27.3b, the decrease of coupling of surface molecules shifts the surface magnetization into non-hysteretic region with the gradual transition between the states. The MC trajectories that correspond to that cases do not show the relaxation dynamics but evolves around the value of magnetization which corresponds to certain temperature (see Fig. 27.5c, d). However the smaller values of coupling of surface molecules decrease the saturated magnetization of the surface which is clearly seen from Fig. 27.5d where additionally the mean values of magnetization of HS and LS states obtained at the same temperature for  $J^s = 0.5J^b$  (green dashed lines) and  $J^s = 0.25J^b$  (yellow dashed lines) are indicated, respectively.

In more rigorous approach, we should consider the contact of the system with environment. Usually this is made by the accounting of the random disordering of effective field on system's surface [18, 20, 21] (see also Sect. 27.2). In order to analyze the system's behavior for fluctuating effective ligand field, we have followed its description given by Eq. (27.2) with condition (27.4). We have confined to the description with fluctuating ligand field only for molecules on the surface, since these molecules directly interact with environment including the control field which here is temperature. For the next molecules inside the lattice, we assumed that fluctuations caused by the external environment are completely vanished. The comparison of temperature transition curves for fluctuationless lattice and the system with fluctuations with different strengths is given in Fig. 27.6.

Due to fluctuating behavior manifested only in the case of surface coupling, we have analyzed separately the temperature transition curves of molecules on the surface from Fig. 27.3b for several fixed values of fluctuation strength. The increase of the random field on the surface enlarges the hysteresis of 3D spin-crossover lattice, despite the fact that only surface molecules fluctuate. It is important to notice that the thermal hysteresis loop progressively increases similar to the results of the work of [12], but the equilibrium temperature does not undergo a shift. It shows

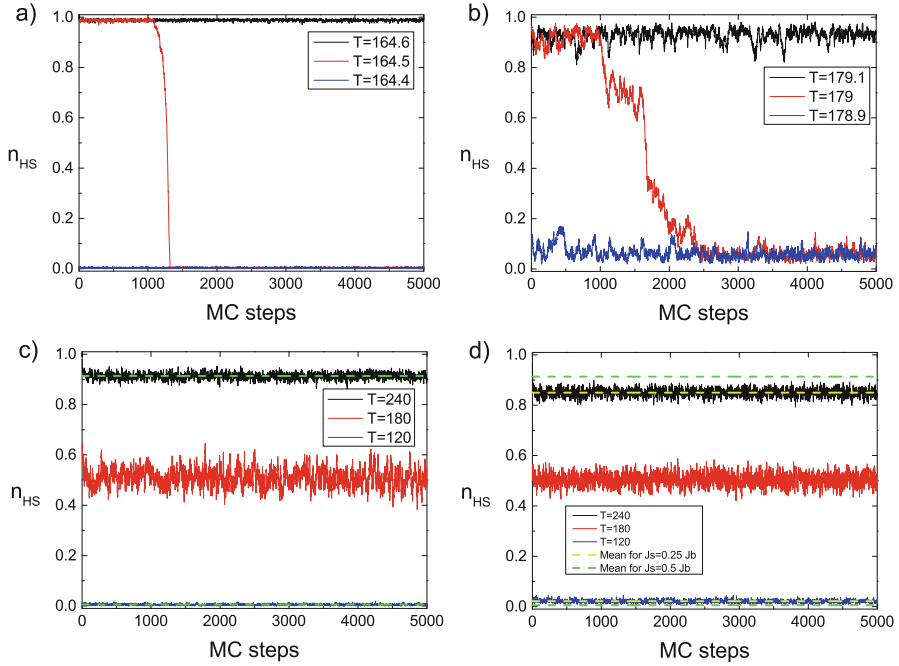


**Fig. 27.5** The evolution of magnetization in ordered HS and LS states and at transition temperature for surface and bulk sites. The trajectories are obtained for cooling branch of temperature transition curve which corresponds to the bulk sites only (a) and surface sites only with  $J^b = J^s$  (b),  $J^b = 0.5J^s$  (c), and  $J^b = 0.25J^s$  (d). Other parameters are the same like for Fig. 27.3b

both similarities and differences in these two approaches. On the other hand, this behavior contrasts with the classical behavior of the thermal hysteresis with particle size, where indeed it monotonously vanishes at small sizes. In Fig. 27.6a is analyzed the entire 3D spin-crossover lattice without fluctuations (black [squared] curve) and for the following fixed values of fluctuation strength:  $\varepsilon = 100$  (red [circled] curves),  $\varepsilon = 200$  (blue [triangled up] curve), and  $\varepsilon = 300$  (magenta [triangled down] curve). For the same fluctuation strength, the behavior of surface magnetization for intersite coupling  $J^s = J^b$ ,  $J^s = 0.5J^b$ , and  $J^s = 0.25J^b$  is displayed in Fig. 27.6b–d, respectively. As we can see from the figure, the presence of fluctuations is able to shift the surface magnetization from non-hysteretic phase to hysteretic one and to contribute to reach the saturated magnetization which corresponds to completed transition to HS and LS states. As a consequence, the hysteresis loop area as the main characteristic of first-order phase transition increases. In other words, despite that the fluctuations are present only in surface molecules, they anyway tend to shift the system toward first-order phase transition with complete interconversion of system's sites.

Similar to the detailed analysis of magnetization dynamics of lattice sites for the fluctuationless system displayed in Fig. 27.4, we provided the spin configurations

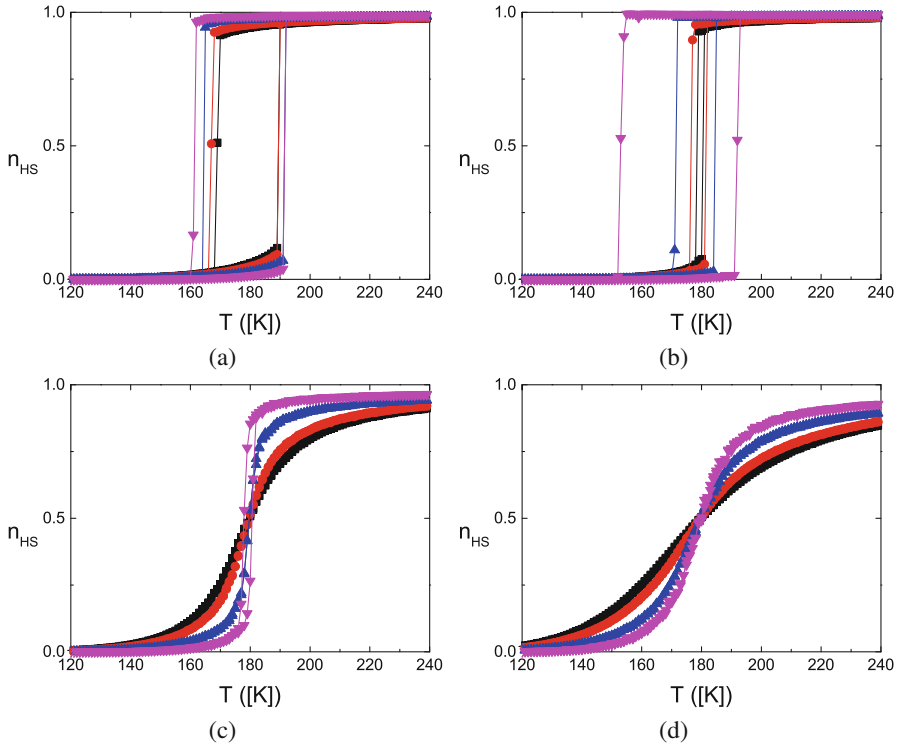


**Fig. 27.6** The behavior of temperature-induced hysteresis for fluctuationless spin-crossover system and system with fluctuations for entire lattice with  $J^s = 0.5J^b$  (a) and for surface molecules only with surface coupling  $J^s = J^b$  (b),  $J^s = 0.5J^b$  (c), and  $J^s = 0.25J^b$  (d). For all cases the black [squared] curve is for fluctuationless system, and the red [circled] curve, the blue [triangled up] curve, and the magenta [triangled down] curve are for the values of fluctuation strengths  $\varepsilon = 100$ ,  $\varepsilon = 200$ , and  $\varepsilon = 300$ , respectively. The interaction of molecules inside the lattice is fixed at the value  $J^b = 85$

for the case with nonzero fluctuations of ligand field for surface sites at three points on the first half of cooling branch of temperature transition curve for  $J^s = 0.5J^b$  shown in Fig. 27.6a. The spin configurations for the values of HS fractions which correspond to the chosen points are shown in Fig. 27.7. In comparison to the fluctuationless case, now there is no evident border dividing the regions with HS and LS molecules, and switching between HS and LS states takes place randomly over all lattice. However by comparing Figs. 27.7 and 27.4, it is observed that the total spin of the molecules from the surface is not strongly ordered but rather randomly oriented which one can suppose that for the system with fluctuations, the residual magnetization is also contributed by the molecules from the surface. The value of residual magnetization in this case is bigger in comparison to the fluctuationless system not only due to the weaker bounding of molecules on the surface but also due to the disorder induced by the fluctuations of the external field.

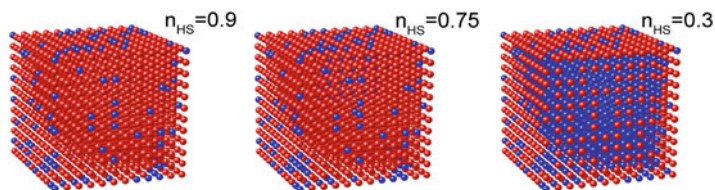


**Fig. 27.7** The spin configurations of the lattice at indicated values of high-spin fraction  $n_{HS}$  for the value of surface coupling  $J^s = 0.5J^b$  and fluctuation strength  $\varepsilon = 100$ . The red and blue circles indicate the molecules in HS and LS states, respectively

As was mentioned, for our analysis, we have considered the system with fixed size; however the role of fluctuations in magnetization behavior for open finite system is highly impacted by its size. For the system far from thermodynamic limit which takes place for small number of its sites (e.g., for  $N < 40$  as is shown in [20]), the variation of ratio between system size and fluctuation strength may scale the system's properties in the nonlinear manner, which sometimes are very different from the fluctuationless case. The analysis of magnetization behavior of small finite-sized Ising-like system of general form on noise strength is partially shown in the work of [22], where the noise strength is contributed by decreasing of system size. In mentioned work it was shown that the presence of fluctuations in the system can be a reason for residual magnetization, which is in agreement with the results obtained in current work. The detailed explanation of the impact of system's size on the dynamics of surface magnetization in presence of fluctuations and different couplings for the sites inside the lattice and on the surface is still under consideration.

## 27.4 Conclusion

We have presented a study of thermal reversal properties of the spin-crossover solids related to the surface-environment effects using Monte Carlo method. The modified Ising-like model of spin-crossover solids with the ligand field as function of the molecule positions and random component on surface was used.

The investigation shows that the decreasing of surface coupling, as a consequence of the destruction of molecular bonds at the surface, leads to narrowing of the temperature hysteresis and is the main reason of residual magnetization. As it is seen from spin configurations for smaller surface coupling, the magnetization of molecules inside the lattice is prevailed in comparison to the ones from the surface. Apparently this effect is related to the weakening of cooperativity of surface sites in comparison to the bulk ones.

The shapes of the loops and the loop area depend on the values of surface intermolecular interaction as well as on the strength of ligand field fluctuations of spin-crossover particle. The interplay between the surface random ligand field



variation and the cooperativity explains the enhancement of the width of the thermal hysteresis loop. The randomness of ligand field shifts the system toward hysteretic phase and decreases the residual magnetization of the system. Surface effects are becoming also increasingly important at reduced scales.

**Acknowledgements** The research of AM was partly supported by Project No. 2015/19/B/ST2/01028 financed by the National Science Centre (Poland).

## References

1. Gütllich P, Goodwin HA (eds) (2004) Spin crossover in transition metal compounds I. Springer, Berlin
2. Gütllich P, Goodwin HA (eds) (2004) Spin crossover in transition metal compounds II. Springer, Berlin
3. Gütllich P, Goodwin HA (eds) (2004) Spin crossover in transition metal compounds III. Springer, Berlin
4. Halcrow MA (ed) (2013) Spin-crossover materials: properties and applications. Wiley, Chichester
5. Gudyma Iu, Enachescu C, Maksymov A (2015) Kinetics of nonequilibrium transition in spin-crossover compounds. In: Fesenko O, Yatsenko L (eds) Nanocomposites, nanophotonics, nanobiotechnology, and applications. Springer, Cham, pp 375–401
6. Gudyma Iu, Maksymov A (2017) Surface-environment effects in spin crossover solids. *Appl Surf Sci* 407:93–98
7. Beniwal S, Zhang X, Mu S, Naim A, Rosa P, Chastanet G, Létard J-F, Liu J, Sterbinsky GE, Arena A, Dowben PA, Enders A (2016) Surface-induced spin state locking of the  $[Fe(H_2B(pz)_2)_2(bipy)]$  spin crossover complex. *J Phys Condens Matter* 28:206002
8. Gaspar AB, Weber B (2016) Spin crossover phenomenon in coordination compounds. In: Sieklucka B, Pinkowicz D (eds) Molecular magnetic materials: concepts and applications. Wiley, Weinheim, pp 231–252
9. Gudyma Iu, Ivashko V, Bobák A (2017) Surface and size effects in spin-crossover nanocrystals. *Nanoscale Res Lett* 12:101
10. Félix G, Nicolazzi W, Salmon L, Molnár G, Perrier M, Maurin G, Larionova J, Long J, Guari Y, Bousseksou A (2013) Enhanced cooperative interactions at the nanoscale in spin-crossover materials with a first-order phase transition. *Phys Rev Lett* 110:235701
11. Boldog I, Gaspar AB, Martínez V, Pardo-Ibañez P, Ksenofontov V, Bhattacharjee A, Gütllich, Real JA (2008) Spin-crossover nanocrystals with magnetic, optical, and structural bistability near room temperature. *Angew Chem Int Ed* 120:6533–6537
12. Linares J, Jureschi CM, Boukheddaden K (2016) Surface effects leading to unusual size dependence of the thermal hysteresis behavior in spin-crossover nanoparticles. *Magnetochemistry* 2:24
13. Enachescu C, Tanasa R, Stancu A, Tissot A, Laisney J, Boillot M-L (2016) Matrix-assisted relaxation in  $Fe(phen)_2(NCS)_2$  spin-crossover microparticles, experimental and theoretical investigations. *Appl Phys Lett* 109:031908
14. Stoleriu L, Chakraborty P, Hauser A, Stancu A, Enachescu C (2011) Thermal hysteresis in spin-crossover compounds studied within the mechanoelastic model and its potential application to nanoparticles. *Phys Rev B* 84:134102
15. Tissot A, Enachescu C, Boillot M-L (2012) Control of the thermal hysteresis of the prototypical spin-transition  $Fe^{II}(phen)_2(NCS)_2$  compound via the microcrystallites environment: experiments and mechanoelastic model. *J Mater Chem* 22:20451

16. Muraoka A, Boukheddaden K, Linares J, Varret F (2011) Two-dimensional Ising-like model with specific edge effects for spin-crossover nanoparticles: a Monte Carlo study. *Phys Rev B* 84:054119
17. Atitoaie A, Tanasa R, Enachescu C (2012) Size dependent thermal hysteresis in spin crossover nanoparticles reflected within a Monte Carlo based Ising-like model. *J Magn Magn Mater* 324:1596–1600
18. Gudyma Iu, Maksymov A, Spinu L (2015) Size effects in spin-crossover nanoparticles in framework of 2D and 3D Ising-like breathing crystal field model. *Appl Surf Sci* 352:60–65
19. Enachescu C, Nishino M, Miyashita S, Hauser A, Stancu A, Stoleriu L (2010) Cluster evolution in spin crossover systems observed in the frame of a mechano-elastic model. *Europhys Lett* 91:27003
20. Gudyma Iu, Maksymov A, Enachescu C (2014) Phase transition in spin-crossover compounds in the breathing crystal field model. *Phys Rev B* 89:224412
21. Gudyma Iu, Maksymov A, Ivashko VV (2014) Study of pressure influence on thermal transition in spin-crossover nanomaterials. *Nanoscale Res Lett* 9:691
22. Gudyma Iu, Maksymov A, Miyashita S (2011) Noise effects in a finite-size Ising-like model. *Phys Rev E* 84:031126

# Chapter 28

## Copper Nucleation on Nickel from Pyrophosphate-Based Polyligand Electrolyte

Antonnia Maizelis and Boris Bairachniy

### 28.1 Introduction

The copper nucleation on foreign substrates is a subject of great technological interest. The process of copper thin film deposition has been widely used in electronic industry for interconnects, manufacturing of printed circuit boards, and multilayer sandwiches of GMR read heads for hard disk. It is also used as commercial catalysts in fuel cells and in hydrogenation process [1]. The electrodeposition of thin metal films is a viable alternative to vacuum-based deposition processes, such as sputtering, plasma deposition, or chemical vapor deposition [2]. The major advantages offered by the electrodeposition among several deposition techniques are their simplicity, compatibility of the processing at room temperature, and controllability of the thin film properties [3]. One-dimensional (1D) nanostructured metallic materials (e.g., nanowires, nanorods, nanotubes, and nanocones) [4], nanoparticles incorporated in conducting polymer films [5] and the ones deposited on foreign substrates [3, 6], have attracted great attention, due to their unique properties and potential applications in microelectronic interconnection, electrocatalysts, transparent electrodes, nanoprobe, solar cells [7], etc. As a sensing material for electrochemical detection, copper nanostructures have many unique properties such as the enhanced mass-transport rate, high surface-to-volume ratio, and improved signal-to-noise ratio in electroanalytical measurements [8]. Managing the process of copper nucleation and growth is important in through-hole electrodeposition, such as that used by LIGA (lithographie, galvanoformung, abformtechnik) microfabrication [9]. The kinetics of crystal formation and growth is one of the determining factors in the formation of copper, copper-containing

---

A. Maizelis (✉) · B. Bairachniy  
National Technical University “Kharkiv Polytechnic Institute”, Kharkiv, Ukraine

alloys, and multilayer coatings of high quality. Even though the deposition time for a commercial copper electrowinning circuit is around 1 week, it is critically important to control the nucleation, growth, and nature of the initial deposit [10, 11].

The nucleation and growth of copper nuclei were studied for different substrates: Au [12–14], Pt [15], Ru [16], Pd [17], Ni [18, 19], W [20], Ta [21], RuTa seeded substrate [22], Ti [23], TiN [24], stainless steel [10, 25], passivated chromium [26], anodized thin-film aluminum [9], titanium oxide films [27], Si [28–30], immiscible liquid-liquid interface [31], and various forms of carbons used as electrodes including glassy carbon [2, 7], pencil graphite [32], graphene [33], boron-doped diamond [3], and conductive polymers [34]. We chose nickel substrate because it is important for the micro-component industry, in multilayer coating formation. Moreover, nickel is used in industry as an underlayer before copper layer deposition.

Copper nucleation was studied in different electrolytes, both nonaqueous [19] and aqueous electrolytes, such as sulfate [8, 10, 15, 25], chloride [35], perchlorate [3, 36, 37], tetrafluoroborate [38], methanesulfonate [39], as well as complex, EDTA [40], glycinate [18], tartrate [41], pyrophosphate [9, 42, 43], and ammonia [2]. The nucleation processes in polyligand electrolytes [20, 44], which are an active instrument to influence the coating properties [45–47], have been studied a little.

In this chapter we analyze the process of copper nucleation and growth in additive-free polyligand pyrophosphate-ammonia electrolyte. Pyrophosphate-ammonia copper-containing component was used in the development of electrolyte for copper-nickel multilayer coating formation. Such polyligand electrolyte has high buffer capacity, good throwing power, and the ability to deposit on an electronegative substrate and produce coatings that simultaneously possess high mechanical and anticorrosive properties [48, 49].

## 28.2 Experimental

All solutions were prepared from analytical grade chemicals and distilled water without further treatment. Pyrophosphate-ammonia polyligand electrolyte for the copper deposition contained  $0.1 \text{ mol L}^{-1} \text{ CuSO}_4 \cdot 5\text{H}_2\text{O}$ ,  $0.22 \text{ mol L}^{-1} \text{ K}_4\text{P}_2\text{O}_7$ , and  $0.77 \text{ mol L}^{-1} \text{ NH}_3(\text{NH}_4^+)$ . The pH of solution was adjusted to 9.25 by  $\text{H}_2\text{SO}_4$  and KOH solutions.

Electrochemical measurements were carried out in the three-electrode cell using a potentiostat PI-50.1. The results were transferred from analogue form to digital by means of the two-channel voltmeter and TeleMax program for PC (100 signals per second). Cyclic voltammograms (CVA) were obtained at a potential scan rate of  $50 \text{ mV s}^{-1}$ . The working electrodes were made of nickel. Before each measurement, the electrode surface was updated by the treatment with carbide-silicone paper (500, 1000, 2000, and 3000 grit, sequentially), cleaned by sonication in distilled water and cathodically polarized to obtain reproducible results in the range of the potentials corresponding to the surface oxide reduction process. The Pt electrode

was used as counter electrode. Saturated Ag/AgCl reference electrode was used in the measurements, and all the potentials are given in the reference to this electrode.

## 28.3 Experimental Results and Discussion

### 28.3.1 Cyclic Voltammetry Study

Cyclic voltammetry study was performed in the potential range from  $-0.2$  to  $-1.5$  V on Ni electrode from weak alkaline electrolyte, containing ammonia and pyrophosphate ions as ligands. The potential scan was initiated in the negative direction from the open circuit potential ( $E_{OCP}$ ) to different switching potentials  $E_\lambda$ . In forward scanning copper deposition on nickel begins at a potential of  $-0.55$  V (Fig. 28.1a). At a potential of  $-0.7$  V, the cathode process speed begins to be substantially limited by the lack of discharging copper ions in the near-electrode layer. The current rise at the cathode branch at a potential of  $-1$  V is due to beginning of simultaneous hydrogen evolution and copper deposition. The copper ion reduction in the process of backward scanning occurs at a slower rate. However, on the layer of deposited copper, they continue reduction at potentials greater than  $-0.55$  V too. Two crossovers ( $E_{CO}$  and  $E_N$ ) are observed on CVA, a feature that is characteristic of a new phase formation. The crossover  $E_N$  at the potential of  $-0.65$  V is just a crossover potential at which nucleation and growth take place with a measurable rate [43]. The crossover  $E_{CO}$  at the potential of  $-0.3$  V is associated with potential of reversible metal/ion reaction, if it does not change position with shifting the scan border [50]. As it is shown in Fig. 28.1a, the value of  $E_{CO}$  and  $E_N$  is independent of the  $E_\lambda$  value. It is possible to estimate the nucleation overvoltage out of the difference between the  $E_N$  and  $E_{CO}$  potentials [18, 19], which is  $0.35$  V in this case. At the anodic branch of the CVA, the deposited copper layer dissolves; therefore, in the second cycle, the cathode branch is reproduced. Shifting the cathode border of the potential scan to the negative side up to  $-1.2$  V leads to the change in the ratio of the anode peak height. This may be due to a change in the structure of the copper layer deposited at different potential values. When the scan direction was reversed in the switching potential  $E_\lambda = -1.5$  V (Fig. 28.1b), the copper deposit accumulates on nickel electrode during the first cycle. It does not have time to dissolve during the anode part of the cycle. Therefore the copper deposition on the second cycle starts on the surface of oxidized deposit at a larger potential. In the case of obtaining CVA only in the cathode region (Fig. 28.1c), the deposition in the second cycle also starts not on nickel but on the surface of copper deposit from the  $E_{CO}$  potential.

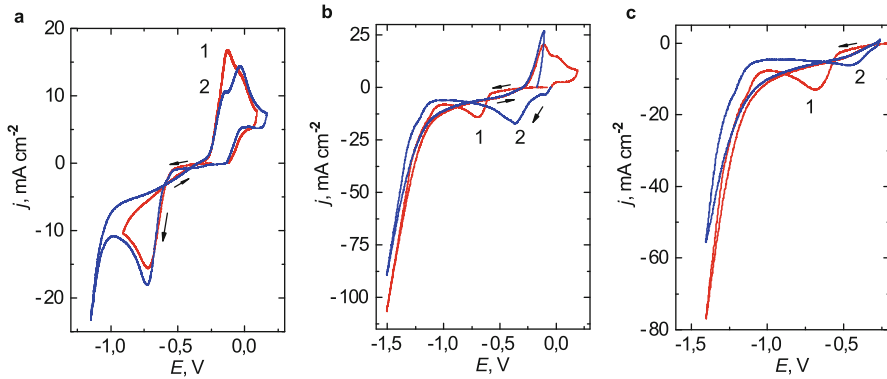


**Fig. 28.1** CVA on nickel substrate in pyrophosphate-ammonia electrolyte: 1, first cycle; 2, second cycle

### 28.3.2 Chronoamperometry Study

The nucleation kinetics and growth of copper onto Ni electrode were studied with the chronoamperometry technique. This technique gives an idea of the possible mechanism of nucleation and growth by interpreting “current transients,” the dependence of current density on time when the potential step from a stationary value to a given value, in different coordinates.

Figure 28.2 shows a set of potentiostatic current transients recorded during the electrochemical deposition of copper in the wide potential range that corresponds to both deposition of copper from  $-0.5$  to  $-0.75$  V and formation of alloys with electronegative metals, e.g., nickel and zinc (cathodic potential large than  $-0.75$  V). The potentiostatic transients, except the one obtained at  $-0.5$  V, have maximum whose intensity ( $j_{\max}$ ) increases with the potential step, whereas the corresponding maximum time ( $t_{\max}$ ) decreases. The formation of copper nuclei begins at potential of  $-0.6$  V. The current transient obtained at  $-0.6$  V has two maxima, which suggests electrocrystallization by two mechanisms. The maximum, which is associated with crystal nucleation and growth processes, is followed by a decaying in the cathodic current, converging to the limiting current. The shape of transients is similar to that observed for nucleation with diffusion controlled growth. The transient obtained at  $-1.2$  V has higher value of the limiting current too, since it also contains a fraction of the current for simultaneous hydrogen evolution.

Diffusion-limited current obeys Cottrell equation:

$$j(t) = \frac{nFD^{1/2}c_0}{\pi^{1/2}t^{1/2}}, \quad (28.1)$$

where  $n$  is ion charge;  $F$  is Faraday constant, As mol $^{-1}$ ;  $c_0$  is bulk concentration of discharging ions, mol cm $^{-3}$ ; and  $t$  is time, s.

**Fig. 28.2** Current transients obtained at potentials from  $-0.5$  to  $-1.2$  V

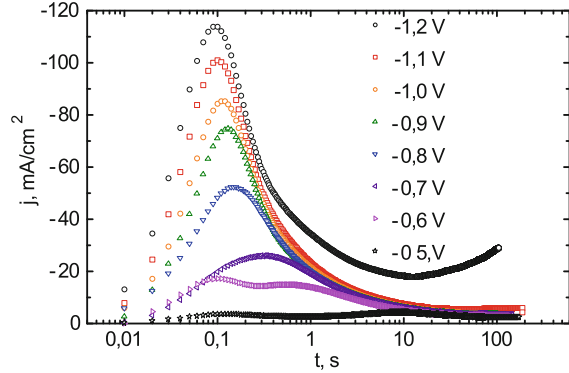


**Fig. 28.3** Cottrell plots corresponding data from related chronoamperograms of Fig. 28.2

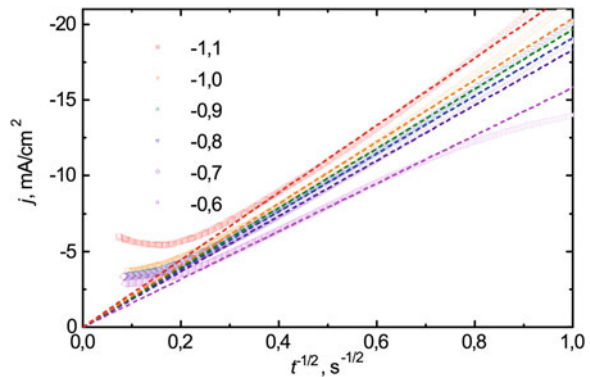
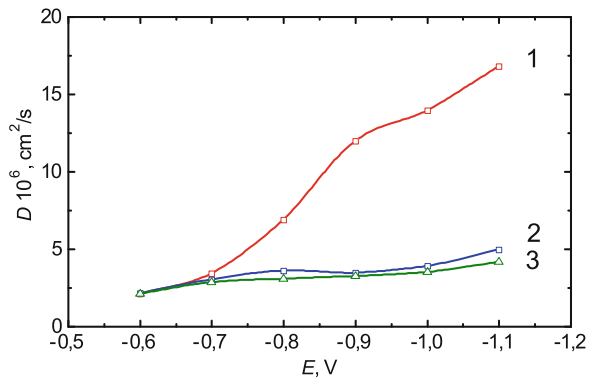


**Fig. 28.4** Dependencies of copper ion diffusion coefficient on copper deposition potential: 1, using Eq. (28.4) for 3DI nucleation model; 2, using Eq. (28.4) for 2DI+3DI nucleation model; 3, using Eq. (28.1)



Current transients obtained at potentials from  $-0.6$  to  $-1.1$  V are linearized in  $j-t^{-0.5}$  coordinates (Fig. 28.3). This indicates that nucleation process is limited by diffusion. The diffusion coefficients of discharging ions for each electrode potential calculated out of the slope of the dependencies in the Cottrell coordinates are shown in Fig. 28.4, curve 3).

Analysis of the transients was performed by comparing the experimental transients to the dimensionless theoretical curves for instantaneous and progressive 3D nucleation and growth with diffusion control proposed by B. Scharifker and G. Hills [51], in order to determine the nucleation mechanism. The models for instantaneous and progressive nucleation are given by Eqs. (28.2) and (28.3), respectively [50]:

$$\frac{j^2}{j_{\max}^2} = \frac{1.9542}{t/t_{\max}} \{1 - \exp[-1, 2564(t/t_{\max})]\}^2, \quad (28.2)$$

$$\frac{j^2}{j_{\max}^2} = \frac{1.2254}{t/t_{\max}} \{1 - \exp[-2, 3367(t/t_{\max})^2]\}^2, \quad (28.3)$$

where  $j$  and  $j_{\max}$  are the current density at current time and maximum current density on the current transients, mA/cm<sup>2</sup>, and  $t$  and  $t_{\max}$  are the current time and the time corresponding to the current maximum, s. The current transients from Fig. 28.2 were plotted along with the theoretical current transients to identify the 3D nucleation mode (Fig. 28.5).

Diffusion coefficients [51] were calculated out of Eq. (28.4)

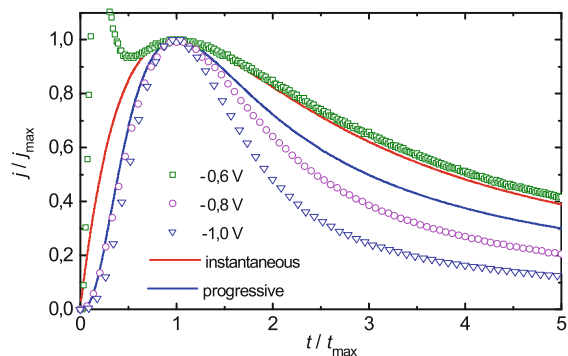
$$D = \frac{j_{\max}^2 t_{\max}}{0.1629(zFc_0)^2}, \quad (28.4)$$

and are presented in Fig. 28.4, curve 1.

Comparison between the curves obtained, for example, under potential of  $-0.6$ ,  $-0.8$ , and  $-1.0$  V and the Scharifker and Hills theoretical transients is valid only for the curve obtained under  $-0.6$  V after the maximum value. This transient partially corresponds to the mechanism of instantaneous nucleation of 3D crystals.

The initial section of the current transient obtained at  $-0.6$  V has a sharp peak, i.e., the process quickly (in less than 0.2 s) begins, reaches its maximum, and decays. Such a shape of the curve allows one to assume the 2D nucleation and growth. First,

**Fig. 28.5** Nondimensional current transients in comparison with Scharifker's Eqs. (28.2) and (28.3)





the current rises sharply due to the rapid increase in the area of nuclei, which grow only parallel to the substrate. Then the current drastically decreases and becomes zero when the entire electrode surface is covered by a monolayer of deposited metal. For nucleation and growth of 2D crystals, the dependencies  $j/j_{\max}$  on  $t/t_{\max}$  (dimensionless coordinates) are proposed:

instantaneous

$$\frac{j}{j_{\max}} = \left(\frac{t}{t_{\max}}\right) \exp\left[-\frac{1}{2}\left(\frac{t^2 - t_{\max}^2}{t_{\max}^2}\right)\right], \quad (28.5)$$

and progressive

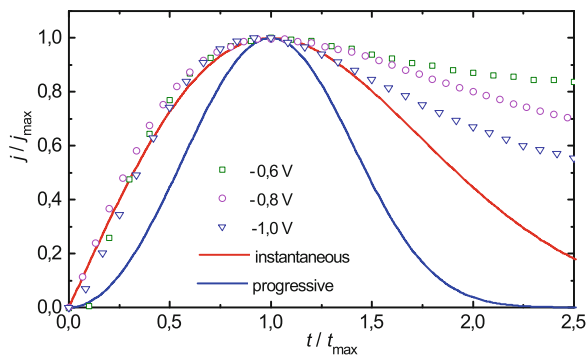
$$\frac{j}{j_{\max}} = \left(\frac{t}{t_{\max}}\right)^2 \exp\left[-\frac{2}{3}\left(\frac{t^3 - t_{\max}^3}{t_{\max}^3}\right)\right] \quad (28.6)$$

mechanism as cited in [52].

The current transients for copper deposition from pyrophosphate-ammonia electrolyte in dimensionless coordinates for 2D nucleation are shown in Fig. 28.6. The initial sections correspond quite accurately to the theoretically predicted dependencies for mechanism of instantaneous 2D nucleation.

The deviation of the experimental dependencies from the theoretical ones with nucleation time increase is obviously connected with overlap of the process of 3D crystal formation and an increase in the working surface of electrode. That is, the theoretical models for 2D and 3D nucleation separately are not applicable to these curves as the experimental transients reflect the behavior of parallel processes. Therefore, the mechanism of copper nucleation and growth on nickel substrate from pyrophosphate-ammonia electrolyte is not of Volmer-Weber mechanism, formation of three-dimensional (3D) and Frank-van der Merwe mechanism, and formation of epitaxial two-dimensional (2D) layers. It is a Stranski-Krastanov mechanism, according to which the formation of one or several 2D layers and further nucleation and growth of 3D crystallites occur [53].

**Fig. 28.6** Comparison of theoretical dependencies according to Eqs. (28.4) and (28.5) and experimental data from Fig. 28.2 in dimensionless coordinates for 2D nucleation



### 28.3.3 Modeling the Current Transients

Theoretical transients and the experimental data were compared using a nonlinear fitting approach, and the contribution of the different processes involved was determined. The best fit for all the transients studied was obtained on using Eq. (28.7):

$$j = j_{2DI} + j_{3DI}, \quad (28.7)$$

This equation includes the  $j_{2DI}$  summand describing the instantaneous nucleation and 2D growth (the rate-determining step is incorporation of atoms or molecules at the expanding periphery of the centers [37], as predicted from the BFT theory [54]):

$$j_{2DI} = k_{2D_1} t \exp(-k_{2D_2} t^2), \quad (28.8)$$

and the  $j_{3DI}$  summand describing the instantaneous 3D nucleation with diffusion control [51]:

$$j_{3DI} = k_{3D_1} t^{-1/2} [1 - \exp(-k_{3D_2} t)], \quad (28.9)$$

where  $k_{2D_1}$ ,  $k_{2D_2}$ ,  $k_{3D_1}$ , and  $k_{3D_2}$  are the coefficients obtained out of the fitting.

Fitted current transients obtained from Eqs. (28.7), (28.8), and (28.9) with contributions of different processes are represented in Fig. 28.7:

For 2DI process the fitting parameters [55]

$$k_{2D_1} = \frac{2\pi z F M h_{2D} k_{\text{disk}}^2 N_0}{\rho}, \quad (28.10)$$

$$k_{2D_2} = \frac{-\pi M^2 k_{\text{disk}}^2 N_0}{\rho} \quad (28.11)$$

where  $F$  is Faraday constant,  $A \text{ s mol}^{-1}$ ;  $M$  is the atomic mass of the deposited metal (copper),  $\text{g mol}^{-1}$ ;  $h_{2D}$  is the height of the deposited layer (disk),  $\text{cm}$ ;  $k_{\text{disk}}$  is the constant of horizontal growth,  $\text{mol cm}^{-2} \text{ s}^{-1}$ ;  $N_0$  is the number of the active site density,  $\text{cm}^{-2}$ ; and  $\rho$  is metal density,  $\text{g cm}^{-3}$ . The obtained parameters  $k_{2D_1}$  and  $k_{2D_2}$  are presented in Table 28.1.

The calculated values of the charge spent for the copper layer deposition  $Q_{2D}$  and kinetic parameter  $k_{\text{disk}}^2 N_0$  using fitting parameters  $k_{2D_1}$  and  $k_{2D_2}$  are presented in Table 28.1. The height  $h_{2D}$  of nuclei in the form of disk is shown in Fig. 28.8. The average height of 2D crystals is greater than the copper monolayer height in the entire potential range. That is, the surface of the nickel electrode is completely covered by 2D layer of copper nuclei.

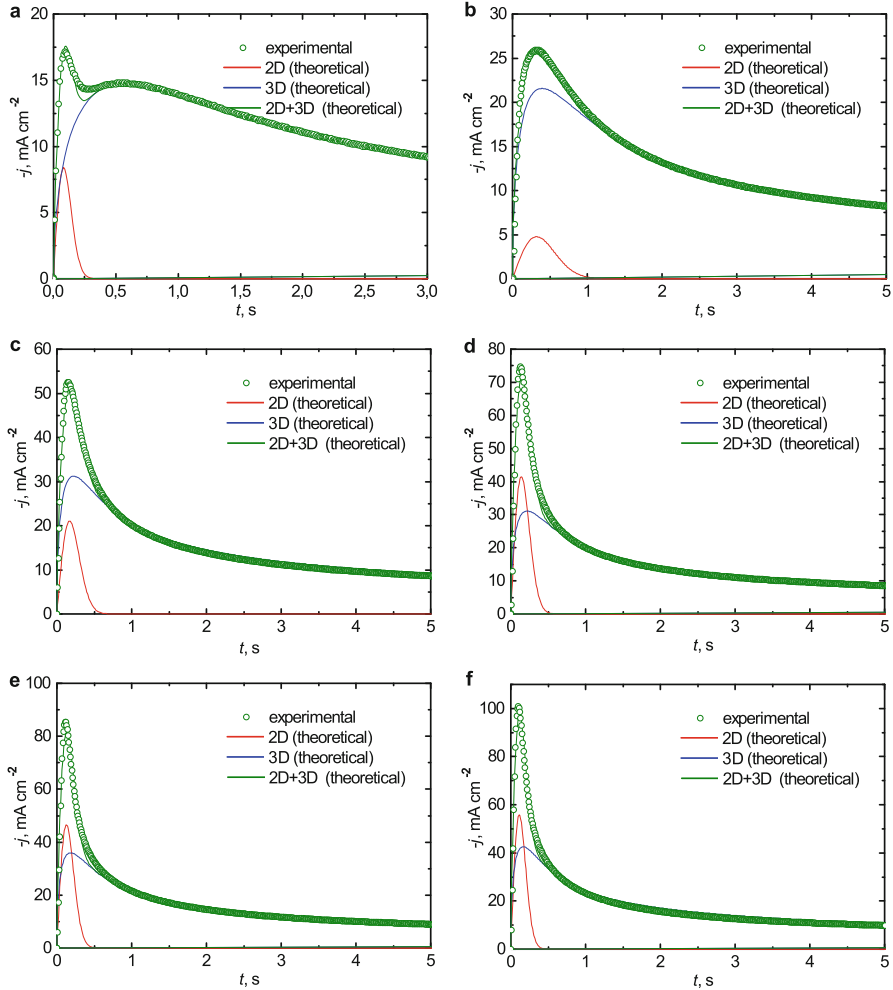


**Fig. 28.7** Numerical fit line calculated according to Eqs. (28.7), (28.8), and (28.9) of the experimental current transients (dots) recorded at  $-0.6$  V (a),  $-0.7$  V (b),  $-0.8$  V (c),  $-0.9$  V (d),  $-1.0$  V (e), and  $-1.1$  V (f)

**Table 28.1** Parameters of 2DI copper nucleation and growth

E, V	$k_{2D_1}$ mAcm <sup>-2</sup> s <sup>-1</sup>	$k_{2D_2}$ s <sup>-2</sup>	$Q_{2D}$ mC cm <sup>-2</sup>	$k_{\text{disk}}^2 N_0$ mol <sup>2</sup> cm <sup>-6</sup> s <sup>-2</sup>
-0.6	172	77.21	1.11	0.485
-0.7	24.3	4.81	2.51	0.030
-0.8	205.2	17.48	5.87	0.110
-0.9	487.4	25.38	9.60	0.159
-1	606	31.14	9.73	0.196
-1.1	521	39.88	6.53	0.251

For 3DI process the fitting parameters [56]

$$k_{3d1} = \frac{zFD^{1/2}c}{\pi^{1/2}}, \quad (28.12)$$

$$k_{3d2} = N_0\pi\left(\frac{8\pi cM}{\rho}\right)^{1/2} \quad (28.13)$$

are presented in Table 28.2.

Values of the diffusion coefficients calculated using the fitting parameters according to Eq. (28.4) are shown in Fig. 28.4, curve 2. These values of the diffusion coefficients are close to those obtained using the slopes of the current transients in Cottrell coordinates (curve 3). Besides that, these values are between the known ones for ammonia [2, 57, 58] and pyrophosphate [9, 42, 43] electrolytes (taking into account the difference in the copper ion concentrations and pH of these electrolytes).

The semilogarithmic dependence of nuclei number on deposition potential is shown in Fig. 28.9. Increase in the polarization up to deposition potential of  $-0.8$  V leads to the sharp increase in nuclei number. Since the height of 2D copper nuclei layer increases at the same time (Fig. 28.8), the continuous copper films form at the

**Table 28.2** The fitting parameters of 3DI copper nucleation and growth

E, V	$k_{3D1}$ , mAc $m^{-2}s^{1/2}$	$k_{3D2}$ , s $^{-1}$
-0.6	15.9	2.14
-0.7	18.9	3.18
-0.8	20.6	5.66
-0.9	20.3	5.75
-1.0	21.5	6.87
-1.1	24.2	7.60

**Fig. 28.8** Copper layer height dependence on deposition potential

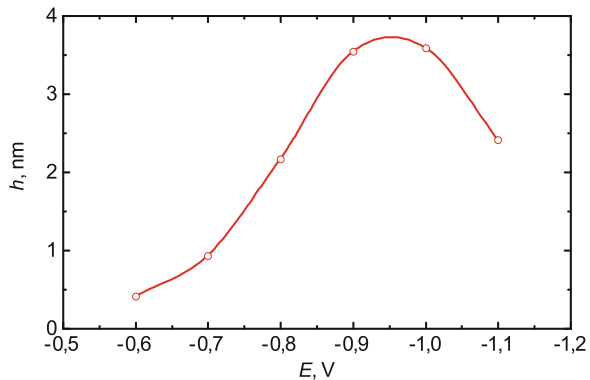
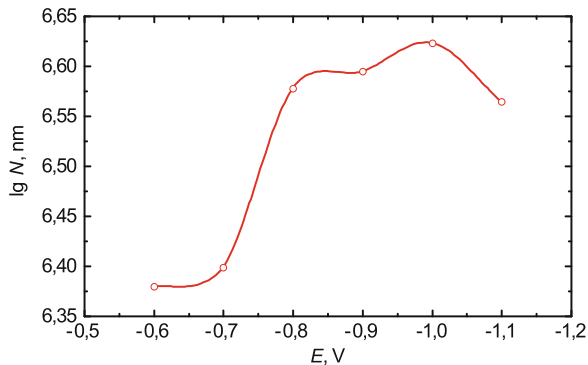


**Fig. 28.9** Dependence of density of copper nuclei sites on the deposition potential



minimum thickness. The nuclei number decreases at potential of  $-1.1 \text{ V}$ , and the deposit growth at the limiting current is due to increase in the copper crystal size, which is accompanied by loosening of the surface.

## 28.4 Conclusions

The Stranski-Krastanov mechanism of copper nucleation and growth on nickel substrate from pyrophosphate-ammonia electrolyte is realized. In the potential range from  $-0.6$  to  $-1.1 \text{ V}$ , the two-dimensional copper nuclei are instantaneously formed simultaneously with the instantaneous nucleation of the three-dimensional nuclei on the surface of the nickel electrode when the current is switched on. The parameters of formation and growth nuclei determined from the mathematical model indicate a change in the conditions of copper film formation with the change in electrode potential. When the cathode potential is increased above  $-0.8 \text{ V}$ , the height of the 2D layer of copper nuclei and the number of simultaneously formed 3D nuclei increase substantially, which leads to the formation of continuous copper films of minimal thickness. This is especially important in the process of formation of multilayer coating containing not only copper layers but also layers of copper alloys with more electronegative metals.

**Acknowledgements** The publication contains the results of studies conducted by presidents of Ukraine grant for competitive projects No. F70/18701 of the State Fund for Fundamental Research and by project of the Ministry of Education and Science of Ukraine.

## References

1. Rout S, Mallik A, Ray BC (2010) Electrochemical synthesis of Cu thin films under ultrasonic irradiation: the effect on ex-situ growth behavior. In: International conference on recent trends in materials and characterization, Suratkal, 14–15 Feb

2. Grujicic D, Pesic B (2005) Reaction and nucleation mechanisms of copper electrodeposition from ammoniacal solutions on vitreous carbon. *Electrochim Acta* 50(22):4426–4443. <https://doi.org/10.1016/j.electacta.2005.02.012>
3. Matsushima JT, Santos LCD, Couto AB, Baldan MR, Ferreira NG (2012) Electrodeposition of Cu nanoparticles on BDD electrodes: reactions and nucleation mechanism. *J Electrochem Soc* 159(4):D246–D252. <https://doi.org/10.1149/2.093204jes>
4. Deng Y, Ling H, Feng X, Hang T, Li M (2015) Electrodeposition and characterization of copper nanocone structures. *Cryst Eng Commun* 17(4):868–876. <https://doi.org/10.1039/C4CE01993H>
5. Tsakova V, Borissov D, Rangelov B, Stromberg C, Schultze JW (2001) Electrochemical incorporation of copper in polyaniline layers. *Electrochim Acta* 46(26):4213–4222. [https://doi.org/10.1016/S0013-4686\(01\)00705-8](https://doi.org/10.1016/S0013-4686(01)00705-8)
6. Lai SC, Lazenby RA, Kirkman PM, Unwin PR (2015) Nucleation, aggregative growth and detachment of metal nanoparticles during electrodeposition at electrode surfaces. *Chem Sci* 6(2):1126–1138. <https://doi.org/10.1039/C4SC02792B>
7. Simkunaite D, Valsiunas I, Jasulaitiene V, Selskis A (2015) The initial stages of copper deposition onto glassy carbon electrode modified with selenium compounds. *Chemija* 26(4):229–237
8. Li Y, Sun JZ, Bian C, Tong JH, Dong HP, Zhang H, Xia SH (2015) Copper nano-clusters prepared by one-step electrodeposition and its application on nitrate sensing. *AIP Adv* 5(4):041312. <https://doi.org/10.1063/1.4905712>
9. Losey MW, Griffiths SK, Hachman JT (2006) Nucleation and adhesion of electrodeposited copper on anodized thin-film aluminum for LIGA microfabrication. *J Electrochem Soc* 153(12):D177–D186. <https://doi.org/10.1149/1.2354453>
10. Luyima A, Cui W, Heckman C, Moats MS (2016) Examination of copper electrowinning smoothing agents. Part IV: nucleation and growth of copper on stainless steel. *Miner Metall Proc* 33(1):39–46
11. Aromaa J, Kekki A, Stefanova A, Forsen O (2012) Copper nucleation and growth patterns on stainless steel cathode blanks in copper electrorefining. *J Solid State Electr* 16(11):3529–3537. <https://doi.org/10.1007/s10008-012-1898-x>
12. Palomar-Pardave M, Garfias-Garcia E, Romero-Romo M, Ramirez-Silva MT, Batina N (2011) Influence of the substrate's surface structure on the mechanism and kinetics of the electrochemical UPD formation of a copper monolayer on gold. *Electrochim Acta* 56(27):10083–10092. <https://doi.org/10.1016/j.electacta.2011.08.105>
13. Willis M, Alkire R (2009) Additive-assisted nucleation and growth by electrodeposition I. Experimental studies with copper seed arrays on gold films. *J Electrochem Soc* 156(10):D377–D384. <https://doi.org/10.1149/1.3183502>
14. Garfias-Garcia E, Palomar-Pardave M, Romero-Romo M, Ramirez-Silva MT, Batina N (2007) Kinetics mechanism of copper UPD nucleation and growth on mono and polycrystalline gold. *ECS Trans* 3(34):35–43. <https://doi.org/10.1149/1.2795610>
15. Molodkina EB, Ehrenburg MR, Danilov AI, Feliu JM (2016) Two-dimensional Cu deposition on Pt(100) and stepped surfaces of platinum single crystals. *Electrochim Acta* 194: 385–394. <https://doi.org/10.1016/j.electacta.2016.02.082>
16. Emekli U, West AC (2009) Effect of additives and pulse plating on copper nucleation onto Ru. *Electrochim Acta* 54(4):1177–1183. <https://doi.org/10.1016/j.electacta.2008.08.065>
17. Rigano PM, Mayer C, Chierchie T (1988) Electrochemical nucleation and growth of copper on polycrystalline palladium. *J Electroanal Chem Interfacial Electrochem* 248(1):219–228. [https://doi.org/10.1016/0022-0728\(88\)85163-5](https://doi.org/10.1016/0022-0728(88)85163-5)
18. Ballesteros JC, Chainet E, Ozil P, Trejo G, Meas Y (2010) Initial stages of the electrocrystallization of copper from non-cyanide alkaline bath containing glycine. *J Electroanal Chem* 645(2):94–102. <https://doi.org/10.1016/j.jelechem.2010.05.002>
19. Zhang QB, Hua YX (2014) Electrochemical synthesis of copper nanoparticles using cuprous oxide as a precursor in choline chloride/urea deep eutectic solvent: nucleation and growth mechanism. *Phys Chem Chem Phys* 16(48):27088–27095. <https://doi.org/10.1039/C4CP03041A>

20. Im B, Kim S (2014) Nucleation and growth of Cu electrodeposited directly on W diffusion barrier in neutral electrolyte. *Electrochim Acta* 130:52–59. <https://doi.org/10.1016/j.electacta.2014.02.154>
21. Zheng M, Kelly JJ, Deligianni H (2007) Electrodeposition of Cu on Ta-based layers I. Electrodeposition on Ta. *J Electrochem Soc* 154(8):D400–D405. <https://doi.org/10.1149/1.2744153>
22. Nagar M, Radisic A, Strubbe K, Vereecken PM (2014) The effect of polyether suppressors on the nucleation and growth of copper on RuTa seeded substrate for direct copper plating. *Electrochim Acta* 127:315–326. <https://doi.org/10.1016/j.electacta.2014.02.052>
23. Dutra AJB, O'keefe TJ (1999) Copper nucleation on titanium for thin film applications. *J Appl Electrochem* 29(10):1217–1227. <https://doi.org/10.1023/A:1003537318303>
24. Kim S, Duquette DJ (2006) Nucleation characteristics of directly electrodeposited copper on TiN. *J Electrochem Soc* 153(9):C673–C676. <https://doi.org/10.1149/1.2219712>
25. Schrebler Arratia R, Aros Meneses H, Schrebler Guzman R, Carlesi Jara C (2012) Use of polyethylene glycol as organic additive in copper electrodeposition over stainless steel cathodes. *Lat Am Appl Res* 42(4):371–376
26. Mascaro LH, Pereira EC (2000) Deposition of copper on passivated chromium. *J Electroanal Chem* 485(1):81–85. [https://doi.org/10.1016/S0022-0728\(00\)00076-0](https://doi.org/10.1016/S0022-0728(00)00076-0)
27. Chang HK, Choe BH, Lee JK (2005) Influence of titanium oxide films on copper nucleation during electrodeposition. *Mater Sci Eng A* 409(1):317–328. <https://doi.org/10.1016/j.msea.2005.03.114>
28. Argañaraz MBQ, Vázquez CI, Lacconi GI (2010) Copper electrodeposition onto hydrogenated Si (1 1 1) surfaces: Influence of thiourea. *J Electroanal Chem* 639(1–2):95–101
29. Khelladi MR, Mentar L, Azizi A, Sahari A, Kahoul A (2009) Electrochemical nucleation and growth of copper deposition onto FTO and n-Si (100) electrodes. *Mater Chem Phys* 115(1):385–390. <https://doi.org/10.1016/j.matchemphys.2008.12.017>
30. Ivanou DK, Ivanova YA, Kulak AI, Streltsov EA (2012) Photoinduced selective copper electrodeposition on p-Si (111). *Electrochem Commun* 17:38–40. <https://doi.org/10.1016/j.elecom.2012.01.015>
31. Zhu XR (2014) The nucleation and growth kinetics of copper nanoparticles electrodeposited at water-immiscible interface of castor oiled graphite-epoxy solid electrodes by cyclic voltammetry. *Appl Mech Mater* 510:86–90. <https://doi.org/10.4028/www.scientific.net/AMM.510.86>
32. Majidi MR, Asadpour-Zeynali K, Hafezi B (2009) Reaction and nucleation mechanisms of copper electrodeposition on disposable pencil graphite electrode. *Electrochim Acta* 54(3):1119–1126. <https://doi.org/10.1016/j.electacta.2008.08.035>
33. Wu S, Yin Z, He Q, Lu G, Yan Q, Zhang H (2011) Nucleation mechanism of electrochemical deposition of Cu on reduced graphene oxide electrodes. *J Phys Chem C* 115(32):15973–15979. <https://doi.org/10.1021/jp201667p>
34. Nichols RJ, Schroer D, Meyer H (1995) An in situ scanning probe microscopy study of copper electrodeposition on conductive polypyrrole. *Electrochim Acta* 40(10):1479–1485. [https://doi.org/10.1016/0013-4686\(95\)00051-F](https://doi.org/10.1016/0013-4686(95)00051-F)
35. Polewska W, Behm RJ, Magnussen OM (2003) In-situ video-STM studies of Cu electrodeposition on Cu (100) in HCl solution. *Electrochim Acta* 48(20):2915–2921. [https://doi.org/10.1016/S0013-4686\(03\)00356-6](https://doi.org/10.1016/S0013-4686(03)00356-6)
36. Garcia-Rodriguez DE, Mendoza-Huizar LH, Rios-Reyes CH, Alatorre-Ordaz MA (2012) Copper electrodeposition on glassy carbon and highly oriented pyrolytic graphite substrates from perchlorate solutions. *Quim Nova* 35(4):699–704. <https://doi.org/10.1590/S0100-40422012000400008>
37. Guascito MR, Malitesta C, Sabbatini L (2012) Nucleation and growth of copper particles on Pt and Pt/poly-3-methylthiophene modified electrode in presence of Cl<sup>-</sup> complexing agent. *Mater Chem Phys* 131(3):719–727. <https://doi.org/10.1016/j.matchemphys.2011.10.041>
38. Oskam G, Vereecken PM, Searson PC (1999) Electrochemical deposition of copper on n-Si/TiN. *J Electrochem Soc* 146(4):1436–1441. <https://doi.org/10.1149/1.1391782>

39. Hasan M, Rohan JF (2010) Cu electrodeposition from methanesulfonate electrolytes for ULSI and MEMS applications. *J Electrochem Soc* 157(5):D278–D282. <https://doi.org/10.1149/1.3332729>
40. Paunovic M (1985) Potentiostatic high overpotential studies of copper deposition from electrodeless copper solutions. *Sci Technol* 132(5):1155–1157
41. Ballesteros JC, Chainet E, Ozil P, Meas Y, Trejo G (2011) Electrodeposition of copper from non-cyanide alkaline solution containing tartrate. *Int J Electrochem Sci* 6:2632–2651
42. Radisic A, Long JG, Hoffmann PM, Searson PC (2001) Nucleation and growth of copper on TiN from pyrophosphate solution. *J Electrochem Soc* 148(1):C41–C46. <https://doi.org/10.1149/1.1344539>
43. Hoffmann PM, Radisic A, Searson PC (2000) Growth kinetics for copper deposition on Si (100) from pyrophosphate solution. *J Electrochem Soc* 147(7):2576–2580. <https://doi.org/10.1149/1.1393571>
44. Shaw MJ, Grunow S, Duquette DJ (2001) “Seedless” electrochemical deposition of copper on physical vapor deposition-W2N liner materials for ultra large scale integration (ULSI) devices. *J Electron Mater* 30(12):1602
45. Maizelis A, Bairachniy B (2017) Voltammetric analysis of phase composition of Zn-Ni alloy thin films electrodeposited from weak alkaline polyligand electrolyte. *J Nano Electron Phys* 9(5):1–7. [https://doi.org/10.21272/jnep.9\(5\).05010](https://doi.org/10.21272/jnep.9(5).05010)
46. Maizelis A, Bairachniy B (2017) Electrochemical formation of multilayer  $SnO_2 - Sb_xO_y$  coating in complex electrolyte. *Nanoscale Res Lett* 12(1):119. <https://doi.org/10.1186/s11671-017-1902-6>
47. Maizelis AA, Tul'skii GG, Bairachnyi VB, Trubnikova LV (2017) The effect of ligands on contact exchange in the  $NdFeB-Cu^{2+}-P_2O_7^{4-}-NH_4^+$  system. *Russ J Electrochem* 53(4):417–423. <https://doi.org/10.1134/S1023193517040085>
48. Maizelis A, Bairachniy B (2016) Electrochemical formation of multilayer metal and metal oxide coatings in complex electrolytes. In: International conference on nanotechnology and nanomaterials. Springer, Cham, pp 557–572. [https://doi.org/10.1007/978-3-319-56422-7\\_41](https://doi.org/10.1007/978-3-319-56422-7_41)
49. Majzelis AA, Bairachniy BI, Trubnikova LV, Savitsky BA (2012) The effect of architecture of the Cu/(Ni-Cu) multilayer coatings on their microhardness. *Funct Mater* 19(2):238–244
50. Fletcher S, Halliday CS, Gates D, Westcott M, Lwin T, Nelson G (1983) The response of some nucleation/growth processes to triangular scans of potential. *J Electroanal Chem Interfacial Electrochem* 159(2):267–285. [https://doi.org/10.1016/S0022-0728\(83\)80627--5](https://doi.org/10.1016/S0022-0728(83)80627--5)
51. Scharifker B, Hills G (1983) Theoretical and experimental studies of multiple nucleation. *Electrochim Acta* 28(7):879–889. [https://doi.org/10.1016/0013-4686\(83\)85163-9](https://doi.org/10.1016/0013-4686(83)85163-9)
52. Palomar-Pardave M, Miranda-Hernandez M, Gonzalez I, Batina N (1998) Detailed characterization of potentiostatic current transients with 2D-2D and 2D-3D nucleation transitions. *Surf Sci* 399(1):80–95. [https://doi.org/10.1016/S0039-6028\(97\)00813-3](https://doi.org/10.1016/S0039-6028(97)00813-3)
53. Milchev A (2002) Electrocrystallization. Fundamentals of nucleation and growth. Kluwer Academic, Boston
54. Bewick A, Fleischmann M, Thirsk HR (1962) Kinetics of the electrocrystallization of thin films of calomel. *Trans Faraday Soc* 58:2200–2216. <https://doi.org/10.1039/TF9625802200>
55. Gonzalez Garcia J, Gallud Martinez F, Iniesta Valcarcel J, Montiel Leguey V, Aldaz Riera A, Lasia A (2001) Kinetics of electrocrystallization of  $PbO_2$  on glassy carbon electrodes: influence of electrode rotation. *Electroanalysis* 13(15):1258–1264. [https://doi.org/10.1002/1521-4109\(200110\)13:15](https://doi.org/10.1002/1521-4109(200110)13:15)
56. Miranda-Hernandez M, Palomar-Pardave M, Batina N, Gonzalez I (1998) Identification of different silver nucleation processes on vitreous carbon surfaces from an ammonia electrolytic bath. *J Electroanal Chem* 443(1):81–93. [https://doi.org/10.1016/S0022-0728\(97\)00487-7](https://doi.org/10.1016/S0022-0728(97)00487-7)
57. Graham L, Steinbruchel C, Duquette DJ (2002) Nucleation and growth of electrochemically deposited copper on TiN and copper from a  $Cu NH_3$  bath. *J Electrochem Soc* 149(8):C390–C395. <https://doi.org/10.1149/1.1487836>



58. Vazquez-Arenas J, Cruz R, Mendoza-Huizar LH (2006) The role of temperature in copper electrocrystallization in ammonia-chloride solutions. *Electrochim Acta* 52(3):892–903. <https://doi.org/10.1016/j.electacta.2006.06.022>
59. Radisic A, Long JG, Hoffmann PM, Searson PC (2001) Nucleation and growth of copper on TiN from pyrophosphate solution. *J Electrochem Soc* 148(1):C41–C46. <https://doi.org/10.1149/1.1344539>
60. Hoffmann PM, Radisic A, Searson PC (2000) Growth kinetics for copper deposition on Si (100) from pyrophosphate solution. *J Electrochem Soc* 147(7):2576–2580. <https://doi.org/10.1149/1.1393571>



# Chapter 29

## Structural Study of the Modified $\text{Cu}_{0.4}\text{Co}_{0.4}\text{Ni}_{0.4}\text{Mn}_{1.8}\text{O}_4$ and $\text{Cu}_{0.1}\text{Ni}_{0.8}\text{Co}_{0.2}\text{Mn}_{1.9}\text{O}_4$ Ceramics Using Combined Methods

H. Klym, I. Hadzaman, A. Ingram, O. Shpotyuk, I. Karbovnyk, Yu. Kostiv,  
I. Vasylyshyn, and D. Chalyy

### 29.1 Introduction

Temperature-sensitive spinel ceramics based on transition metal manganites with topologically disordered structures is one of the perspective materials for temperature sensors and other practical applications [1–3]. The main structural elements in these materials are grain, grain boundaries, and pores depending on technological procedure of ceramic sintering [4, 5]. Understanding of correlation between grain-porous and free-void structures as well as physical properties of such materials is still in focus of scientific and commercial interests for scientists across the globe [6, 7].

In ceramics, depending on the sintering temperature, shrinkage of the atomic structure occurs, eventually leading to more or less complex pore topology [8–10].

---

H. Klym (✉) · Y. Kostiv · I. Vasylyshyn  
Lviv Polytechnic National University, Lviv, Ukraine  
e-mail: [halyna.i.klym@lpnu.ua](mailto:halyna.i.klym@lpnu.ua)

I. Hadzaman  
Drohobych State Pedagogical University, Drohobych, Ukraine

A. Ingram  
Opole University of Technology, Opole, Poland

O. Shpotyuk  
Vlokh Institute of Physical Optics, Lviv, Ukraine

Jan Dlugosz University in Czestochowa, Czestochowa, Poland

I. Karbovnyk  
Ivan Franko National University of Lviv, Lviv, Ukraine

D. Chalyy  
Lviv State University of Life Safety, Lviv, Ukraine

These pores along with specific vacancy-type defects within individual crystalline grains and grain boundaries represent free-volume structure of ceramics. In addition, previous investigations have shown that in temperature-sensitive spinel-type ceramics, the quantity of the additional phase and its distribution in bulk and on the surface of ceramic samples are essentially influenced by temperature-time sintering regimes [5, 11].

But technological modification of spinel ceramics results in stabilization of functional properties of ceramics. So, in  $\text{Cu}_{0.1}\text{Ni}_{0.8}\text{Co}_{0.2}\text{Mn}_{1.9}\text{O}_4$  ceramics, metallic additives located in intergranular regions closely to grain boundaries diminish thermally activated aging phenomena owing by stabilizing the cationic distribution within individual ceramic grains. As a result, the chemically modified ceramics show higher stability in comparison with non-modified ones [4, 12].

Because of significant complications in the structure of spinel-type ceramics revealed at the levels of individual grains, grain boundaries, and pores [13], the further progress in this field is dependent to a great extent on the development of new characterization techniques, which can be used in addition to traditional ones (scanning/tunneling electron microscopy, porosimetry methods, etc.). This concerns, in part, the positron annihilation lifetime (PAL) spectroscopy, the alternative method only recently applied to fine-grained powders, nanostructured glasses, and ceramics [14, 15]. In general, the PAL reflects a so-called free-volume distribution within structural network of solids.

It was shown previously [16–18] that in the case of ceramics, PAL data are determined mainly by crystallographic features of individual grains, while structural disturbances due to grain contacts inside ceramics were a subject for additional complications. This is why the measured positron lifetime spectra for sintered ceramics can be adequately explained within a unified positron annihilation model involving discrete positron trapping and ortho-positronium (*o-Ps*) decay modes, the best fitting being achieved using at least three independent components in the resolved lifetime spectra (two for positron trapping and one for *o-Ps* decaying) [11, 16–19]. In terms of this model, the second positron trapping component with lifetime  $\tau_2$  is attributed to free-volume defects such as neutral or negatively charged vacancies especially near grain boundaries. The shortest component named the reduced bulk positron lifetime  $\tau_1$  is mainly due to annihilation in defect-free bulk with small mixing from other positron trapping channels. The largest component at the level of a few nanoseconds is responsible for a so-called *o-Ps* “pick-off” annihilation [18, 20].

The main aim of this work is structural study of the technologically modified  $\text{Cu}_{0.4}\text{Co}_{0.4}\text{Ni}_{0.4}\text{Mn}_{1.8}\text{O}_4$  and  $\text{Cu}_{0.1}\text{Ni}_{0.8}\text{Co}_{0.2}\text{Mn}_{1.9}\text{O}_4$  ceramics using alternative PAL technique in comparison with scanning electron microscopy (SEM) and porosimetry methods [8, 21].

## 29.2 Preparation of Modified Ceramics

Macro- and micro-modified  $\text{Cu}_{0.4}\text{Co}_{0.4}\text{Ni}_{0.4}\text{Mn}_{1.8}\text{O}_4$  ceramics was obtained via traditional ceramic technology as was described in greater details elsewhere [4, 12, 16, 20, 22]. Equal molar amounts of initial powders were mixed in a planetary ball mill for 96 h in an environment with acetone to obtain mixture. The aqueous solution of polyvinyl alcohol was used for obtaining of the molding powder. Bilateral compression was performed in steel molds. After pressing these samples were sintered in a furnace at maximal temperature ( $T_s$ ) 1100 °C for 2 h. To validate PAL investigations performed, we divided the  $\text{Cu}_{0.4}\text{Co}_{0.4}\text{Ni}_{0.4}\text{Mn}_{1.8}\text{O}_4$  ceramics into two groups presumably not affecting lifetime spectra – the  $\text{Cu}_{0.4}\text{Co}_{0.4}\text{Ni}_{0.4}\text{Mn}_{1.8}\text{O}_4$ -micro- and  $\text{Cu}_{0.4}\text{Co}_{0.4}\text{Ni}_{0.4}\text{Mn}_{1.8}\text{O}_4$ -macro-modified ceramics prepared by preliminary sifting of powder through fine (with 0.1 mm pores) and more rough sieve (0.5 mm pores). In both cases, the sizes of intrinsic pores are too large to change significantly positron annihilation spectra [20].

To preparation of  $\text{Cu}_{0.1}\text{Ni}_{0.8}\text{Co}_{0.2}\text{Mn}_{1.9}\text{O}_4$  ceramics, the precise amounts of high purity and previously tested carbonate salts were weighted and wet mixed. This mixture was thermally decomposed in the air at  $700 \pm 5^\circ\text{C}$  for 4 h [12, 16]. Then the obtained powders were milled, blended with organic binder, and pressed into the disks of approximately 10 mm in diameter and 1 mm in thickness. The prepared four batches of blanks were sintered in the air in respect to the time-temperature regimes (see Fig. 29.1).

It should be noted the sintering route of ceramics was performed to ensure all necessary conditions for inhibition effect in degradation [23], the content of additional NiO phase with NaCl-type structure having decisive role in the final ceramic structure. In fact, we deal with Ni-deficient ceramics in respect to stoichiometric  $\text{Cu}_{0.1}\text{Ni}_{0.8}\text{Co}_{0.2}\text{Mn}_{1.9}\text{O}_4$  composition taken as start one in disproportionality

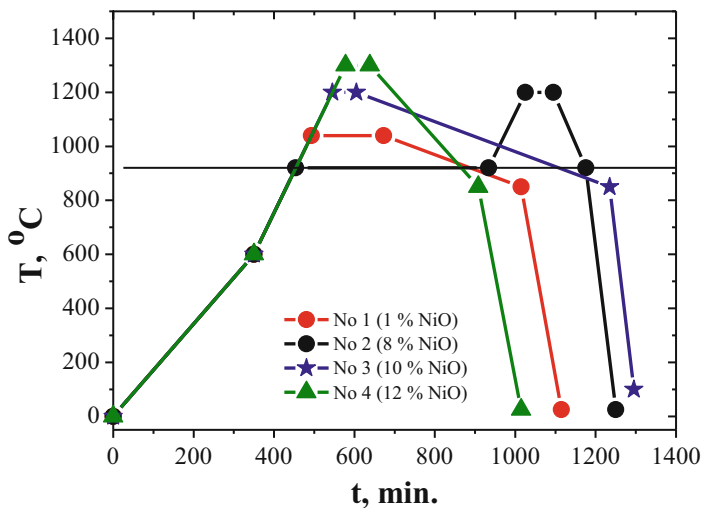


Fig. 29.1 Time-temperature sintering regime for  $\text{Cu}_{0.1}\text{Ni}_{0.8}\text{Co}_{0.2}\text{Mn}_{1.9}\text{O}_4$  ceramics [16]

calculations. Four batches of  $\text{Cu}_{0.1}\text{Ni}_{0.8}\text{Co}_{0.2}\text{Mn}_{1.9}\text{O}_4$  ceramics with 1–12% of NiO phase were prepared owing to different amounts of thermal energy transferred during the sintering (batch No. 1–1% NiO, batch No. 2–8% NiO, batch No. 3–10% NiO, batch No. 4–12% NiO). The latter was numerically determined as square value restricted by temperature-time curve above straight line corresponding to 920 °C, which is the temperature of monophasic  $\text{Cu}_{0.1}\text{Ni}_{0.8}\text{Co}_{0.2}\text{Mn}_{1.9}\text{O}_4$  ceramic formation [16, 23].

### 29.3 Experimental Details

Structures of grains, grain boundaries, and pores for micro- and macro-modified  $\text{Cu}_{0.4}\text{Co}_{0.4}\text{Ni}_{0.4}\text{Mn}_{1.8}\text{O}_4$  ceramics were studied using LEO 982 microscope [20, 24]. Pore size distribution in the region from 2 to 300 nm was investigated with Hg-porosimetry (POROSIMETR 4000) [11, 20, 21].

Microstructure of the  $\text{Cu}_{0.1}\text{Ni}_{0.8}\text{Co}_{0.2}\text{Mn}_{1.9}\text{O}_4$  ceramics was probed using electron microscope JSM-6700F, cross sections morphology of the samples being tested near surface (0–70  $\mu\text{m}$  depth) and chip centers.

PAL measurements for all samples of ceramics were performed using ORTEC spectrometer at temperature of 20 °C and relative humidity of ~35% [11, 16–18, 25]. The isotope  $^{22}\text{Na}$  was used as positron source. The two identical samples of ceramics were placed in the both sides of the source. The PAL spectra were treated by LT computer program [26]. For each pair of ceramic samples, we used three measured positron annihilation spectra. The best results were obtained at three-component fitting procedure with parameters of each components  $(\tau_1, I_1)$ ,  $(\tau_2, I_2)$ , and  $(\tau_3, I_3)$  for micro- and macro-modified  $\text{Cu}_{0.4}\text{Co}_{0.4}\text{Ni}_{0.4}\text{Mn}_{1.8}\text{O}_4$  ceramics and two-component component fitting procedure with parameters  $(\tau_1, I_1)$ ,  $(\tau_2, I_2)$ . Such parameters as average positron lifetimes  $\tau_{\text{av}}$ , positron lifetime in defect-free bulk  $\tau_{\text{b}}$ , and positron trapping rate in defects  $\kappa_{\text{d}}$  were calculated using two-state positron trapping model [26, 27]. The difference  $(\tau_2 - \tau_{\text{b}})$  can be accepted as a size measure of extended defects where positrons are trapped, and the  $\tau_2/\tau_{\text{b}}$  ratio represents the nature of these defects [28].

### 29.4 Results and Discussion

#### 29.4.1 Micro- and Macro-modified $\text{Cu}_{0.4}\text{Co}_{0.4}\text{Ni}_{0.4}\text{Mn}_{1.8}\text{O}_4$ Ceramics

According to our X-ray diffraction investigations, the micro- and macro-modified  $\text{Cu}_{0.4}\text{Co}_{0.4}\text{Ni}_{0.4}\text{Mn}_{1.8}\text{O}_4$  ceramics are preferentially of single spinel phase with lattice parameter of  $a = 8.365 \text{ \AA}$  [4, 20]. The XRD patterns for the micro- and macro-modified  $\text{Cu}_{0.4}\text{Co}_{0.4}\text{Ni}_{0.4}\text{Mn}_{1.8}\text{O}_4$  ceramics are shown in Figs. 29.2 and 29.3.

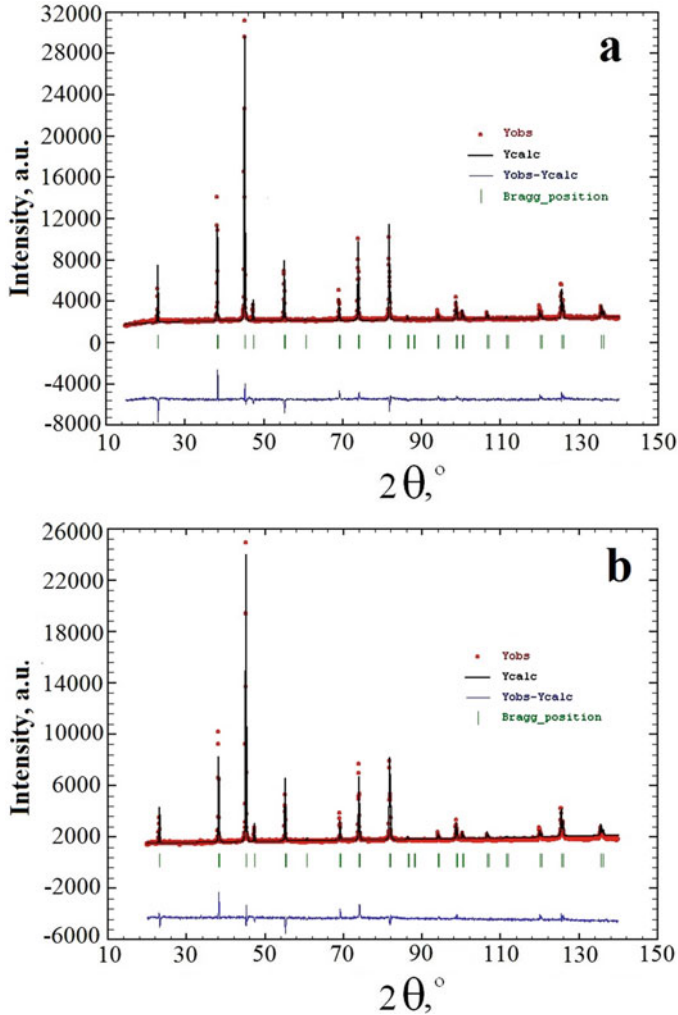


**Fig. 29.2** Experimental (rings), theoretical (line), and difference XRD pattern (down) for micro- (a) and macro-modified (b)  $\text{Cu}_{0.4}\text{Co}_{0.4}\text{Ni}_{0.4}\text{Mn}_{1.8}\text{O}_4$  ceramics (row of reflexes is the basic spinel phase)

In respect to SEM investigations, the  $\text{Cu}_{0.4}\text{Co}_{0.4}\text{Ni}_{0.4}\text{Mn}_{1.8}\text{O}_4$  ceramics contained large grains ( $\sim 10$  mm) as well as relatively sharp grain boundaries. So-called “closed” pores have a spherical form and are located mainly near grain boundaries. As it is obvious from electron micrographs (Fig. 29.4), micro- and macro-modified  $\text{Cu}_{0.4}\text{Co}_{0.4}\text{Ni}_{0.4}\text{Mn}_{1.8}\text{O}_4$  ceramics differ only by pores [20]. The neatly shaping grains with comparatively tiny pores ( $\sim 1$  mm) are characteristic for micro-modified  $\text{Cu}_{0.4}\text{Co}_{0.4}\text{Ni}_{0.4}\text{Mn}_{1.8}\text{O}_4$  samples, while macro-modified  $\text{Cu}_{0.4}\text{Co}_{0.4}\text{Ni}_{0.4}\text{Mn}_{1.8}\text{O}_4$  ceramics contain similar crystalline grains with larger pores (reaching in size up to  $\sim 10$  mm).

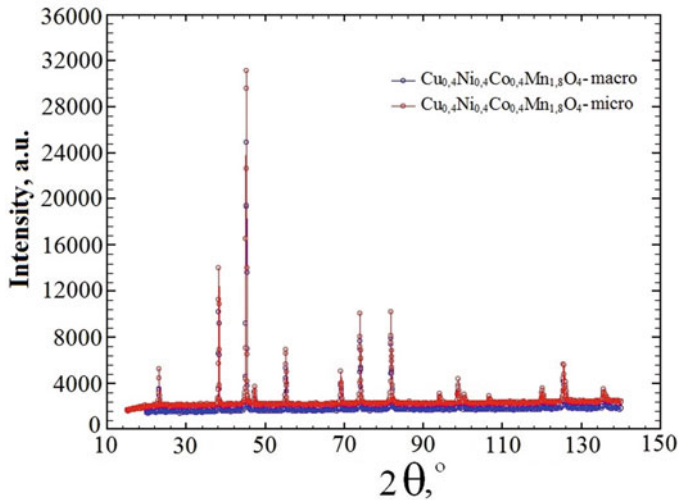


**Fig. 29.3** Comparison of experimental XRD patterns for crystalline phase of micro- (a) and macro-modified (b)  $\text{Cu}_{0.4}\text{Co}_{0.4}\text{Ni}_{0.4}\text{Mn}_{1.8}\text{O}_4$  ceramics

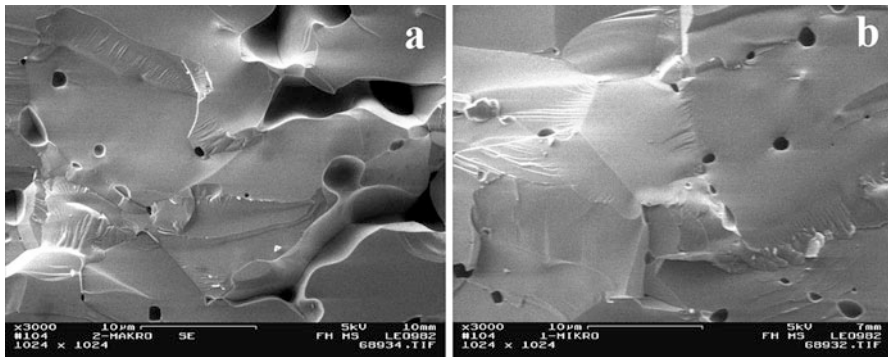


**Fig. 29.4** Scanning electron micrographs for micro- (a) and macro-modified (b)  $\text{Cu}_{0.4}\text{Co}_{0.4}\text{Ni}_{0.4}\text{Mn}_{1.8}\text{O}_4$  ceramics

Open pore size distributions for micro- and macro-modified  $\text{Cu}_{0.4}\text{Co}_{0.4}\text{Ni}_{0.4}\text{Mn}_{1.8}\text{O}_4$  ceramics are shown in Fig. 29.5. Such distributions cover significant amount of charge-transferring nanopores depending on sintering procedure and small amount of communication mesopores [11, 20]. In contrast to humidity-sensitive  $\text{MgAl}_2\text{O}_4$  ceramics, temperature-sensitive  $\text{Cu}_{0.4}\text{Co}_{0.4}\text{Ni}_{0.4}\text{Mn}_{1.8}\text{O}_4$  ceramics practically do not possess outside-delivering macropores depending on specific surface area of initial powder [5]. Thus,  $\text{Cu}_{0.4}\text{Co}_{0.4}\text{Ni}_{0.4}\text{Mn}_{1.8}\text{O}_4$  ceramics prepared at 1100 °C exhibit so-called one-modal pore size distribution with maximum position near 2 nm and double-maximum near 2.3 and 5.5 nm for

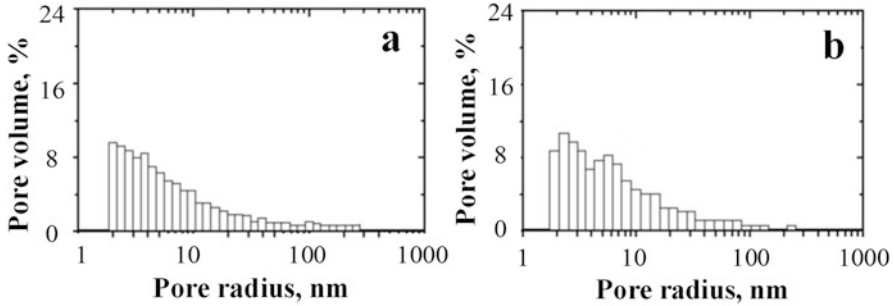


**Fig. 29.5** Pore size distributions of micro- (a) and macro-modified (b)  $\text{Cu}_{0.4}\text{Co}_{0.4}\text{Ni}_{0.4}\text{Mn}_{1.8}\text{O}_4$  ceramics

micro- and macro-modified  $\text{Cu}_{0.4}\text{Co}_{0.4}\text{Ni}_{0.4}\text{Mn}_{1.8}\text{O}_4$  ceramics, respectively (Fig. 29.5).

Let's try to discuss the results (Table 29.1) obtained within positron trapping model by accepting that structural peculiarities of spinel ceramics are associated mainly in the first PAL component ( $\tau_1, I_1$ ). The second component ( $\tau_2, I_2$ ) corresponds directly to free-volume positron traps (voids in the form of vacancy-like clusters, agglomerates, etc.) located near grain boundaries [11, 16, 20]. It means that input of the first component in the PAL spectra will be, in part, a determinant of the average electron density distribution reflected structural compactness of the testes network. The  $\tau_2$  lifetime is associated with the size of voids and the intensity  $I_2$  is proportional to the amount of voids in the case of the same defect-free bulk annihilation lifetime [16, 20]. The third component ( $\tau_3, I_3$ ) corresponds to *o-Ps* annihilation in nanopores. In spite of small value of  $I_3$  intensity (2%), this component cannot be removed without losses in the quality of the fitting procedure. The similar component was detected in many porous materials with different structural type [16, 29]. In addition, the third component can be related with *o-Ps* "pick-off" annihilation in water absorbed by materials [29]. We don't exclude the meaning of other positron annihilation channels in this PAL component too, such as para-positronium (*p-Ps*) decaying with character lifetime of 0.125 ns [14]. But their influence is negligibly small, if the above requirement on close positron affinity will be more or less kept within a whole positron trapping medium [30].

As it was shown in Tables 29.1 and 29.2, micro- and macro-modification of  $\text{Cu}_{0.4}\text{Co}_{0.4}\text{Ni}_{0.4}\text{Mn}_{1.8}\text{O}_4$  ceramics during preparation does not influence their fitting parameters. As a result, such positron trapping modes as positron lifetime  $\tau_b$ , average positron lifetime  $\tau_{av.}$ , positron trapping rate of defect  $\kappa_d$ , size of extended defects, where positrons are trapped ( $\tau_2 - \tau_b$ ), and ratio represents the nature of these defects ( $\tau_2/\tau_b$ ) [14, 21] remain unchanged. Obviously, pores of large examination by SEM and Hg-porosimetry do not modify significantly the measured positron lifetime spectra, testifying in a favor of correctness of the performed measuring and fitting procedures.



**Table 29.1** Fitting parameters of LT computer program describing positron annihilation in the micro- and macro-modified  $\text{Cu}_{0.4}\text{Co}_{0.4}\text{Ni}_{0.4}\text{Mn}_{1.8}\text{O}_4$  ceramics

Sample	Fitting parameters						Component input		
	$\tau_1$ , ns	$I_1$ , a.u.	$\tau_2$ , ns	$I_2$ , a.u.	$\tau_3$ , ns	$I_3$ , a.u.	$\tau_1 I_1$ , ns	$\tau_2 I_2$ , ns	$\tau_3 I_3$ , ns
$\text{Cu}_{0.4}\text{Co}_{0.4}\text{Ni}_{0.4}\text{Mn}_{1.8}\text{O}_4$ (macro)	0.21	0.78	0.37	0.20	1.85	0.02	0.16	0.07	0.04
$\text{Cu}_{0.4}\text{Co}_{0.4}\text{Ni}_{0.4}\text{Mn}_{1.8}\text{O}_4$ (micro)	0.22	0.77	0.38	0.21	1.83	0.02	0.17	0.08	0.04

**Table 29.2** Positron trapping modes in the micro- and macro-modified  $\text{Cu}_{0.4}\text{Co}_{0.4}\text{Ni}_{0.4}\text{Mn}_{1.8}\text{O}_4$  ceramics calculated within two-state positron trapping model and free-volume characteristics

Sample	Free-volume characteristics			Positron trapping modes				
	$R_{\text{octa}}$ , Å	$R_{\text{tetra}}$ , Å	$R$ (Tao-Eldrup), nm	$\tau_{\text{av}}$ , ns	$\tau_{\text{b}}$ , ns	$\kappa_{\text{d}}$ , ns <sup>-1</sup>	$\tau_2 - \tau_{\text{b}}$ , ns	$\tau_2/\tau_{\text{b}}$
$\text{Cu}_{0.4}\text{Co}_{0.4}\text{Ni}_{0.4}\text{Mn}_{1.8}\text{O}_4$ (macro)	0.69	0.64	2.74	0.24	0.23	0.4	0.14	1.6
$\text{Cu}_{0.4}\text{Co}_{0.4}\text{Ni}_{0.4}\text{Mn}_{1.8}\text{O}_4$ (micro)			2.72	0.25	0.24	0.4	0.14	1.6

As was shown early in [20], the potential positron traps in functional spinel-type ceramics are tetrahedral and octahedral cation vacancies. The average volume of these tetrahedrons  $V_{\text{tetra}}$  and octants  $V_{\text{octa}}$  can be selected as free-volume parameters for spinel-structured ceramics.

The radii of tetrahedral and octahedral sites in a spinel structure can be calculated using lattice parameter  $a$  [20]:

$$R_{\text{tetra}} = \sqrt{3} \left( u - \frac{1}{4} \right) a - R_0, \quad (29.1)$$

$$R_{\text{octa}} = \left( \frac{5}{8} - u \right) a - R_0 \quad (29.2)$$

where  $u$  is oxygen parameter and  $R_0$  is oxygen atom with radius of 1.32 Å.

The oxygen parameter  $u$  in oxide spinels is near 0.385 and insignificantly depends on cation type [4, 16]. The radius of tetrahedral vacancies in  $\text{Cu}_{0.4}\text{Co}_{0.4}\text{Ni}_{0.4}\text{Mn}_{1.8}\text{O}_4$  ceramics is 0.64 Å, which gives  $V_{\text{tetra}}$  in spherical approximation  $\sim 1.10 \text{ \AA}^3$ . The volume of octahedral vacancies  $V_{\text{octa}}$  is  $\sim 1.37 \text{ \AA}^3$ .

As it was noted [20], positrons have a preference to annihilate in octahedral vacancy sites as it follows from charge density distribution in partially inverted spinel structures. But the calculated ratio between the first component inputs in the PAL spectra for previously studied  $\text{MgAl}_2\text{O}_4$  ceramics [20, 31] and  $\text{Cu}_{0.4}\text{Co}_{0.4}\text{Ni}_{0.4}\text{Mn}_{1.8}\text{O}_4$  ceramics (0.78) is closer to the ratio between corresponding volumes of tetrahedral vacancies (0.76) rather than octahedral ones (0.69). Consequently, in the studied  $\text{Cu}_{0.4}\text{Co}_{0.4}\text{Ni}_{0.4}\text{Mn}_{1.8}\text{O}_4$  ceramics in contrast to nanocrystalline ferrites [14], positron trapping in tetrahedral vacancies predominates in the first PAL component. The positron trapping in octahedral vacancies is character to inverse spinel structure.

It is evident that octahedral monovacancies themselves do not play a decisive role in the second component of PAL spectra. This component is associated with more extended agglomerates such as vacancy-like clusters and nanovoids. They appear, as a rule, near grain boundaries, where ceramic structure is more defective. The characteristic volumes of these clusters are larger in ceramics with a more stretched pore structure. In seats where ceramics are composed of very small grains with divaricated grain boundaries and tiny pores, the positrons are prepped more effective.

Recently, PAL spectroscopy started to be used as an alternative porosimetry technique to characterize the local free volumes first of all in both open and closed nanopores [14, 32, 33–35]. The PAL method is particularly effective when  $P_s$  is formed. In disordered solids,  $P_s$  is usually organized in two ground states ( $p$ - $P_s$  and  $o$ - $P_s$ ) and localized in the pores and free volumes [33–35]. Usually, quantification is based on the analysis of  $o$ - $P_s$  lifetime (the lifetimes of the third component  $\tau_3$  in  $\text{Cu}_{0.4}\text{Co}_{0.4}\text{Ni}_{0.4}\text{Mn}_{1.8}\text{O}_4$  ceramics correspond to  $o$ - $P_s$  lifetime). The  $o$ - $P_s$  “pick-off” annihilation depends on the size of holes and gives additional important information on the void structure of the materials [35]. Despite small  $I_3$  intensity for  $\text{Cu}_{0.4}\text{Co}_{0.4}\text{Ni}_{0.4}\text{Mn}_{1.8}\text{O}_4$  ceramics, it is possible to estimate the average nanopore size from  $o$ - $P_s$  lifetime in a given material [51]. Assuming approximately spherical shape of the free volume, the  $o$ - $P_s$  lifetime ( $\tau_{o-P_s}$ ) in oxide materials can be related to the average radius of pores ( $R$ ) by semiempirical Tao-Eldrup equation [36, 37]:

$$\tau_{o-P_s} = \left[ 2 \left( 1 - \frac{R}{R + \Delta R} + \frac{1}{2\pi} \sin \left( \frac{2\pi R}{R + \Delta R} \right) \right) + 0.007 \right]^{-1}, \quad (29.3)$$

where  $\Delta R$  is the empirically determined parameter (in the classical case  $\Delta R \approx 0.1656$  nm), describing effective thickness of the electron layer responsible for the “pick-off” annihilation of  $o$ - $P_s$  in the pore [36, 37].

In functional  $\text{Cu}_{0.4}\text{Co}_{0.4}\text{Ni}_{0.4}\text{Mn}_{1.8}\text{O}_4$  ceramics, there is one  $o$ - $P_s$  PAL component with small intensity (2%). Therefore,  $\tau_3$  lifetime can be related to corresponding pores via Tao-Eldrup model. The  $\tau_{o-P_s}$  value of around  $\sim 1.8$  ns ( $\tau_3$  in Table 29.1) corresponds to nanopores with radius ( $R$ ) distribution centered near  $\sim 0.27$  nm. This result is addition to Hg-porosimetry measurements. In addition, it should be noted that porosimetry methods are limited to open pores, which should have an

access to the environment to be determined. On the other hand, PAL spectroscopy can probe both open and closed pores in functional oxide ceramics of sizes ranging from atomic scale to several tens of nanometers.

### 29.4.2 Technologically Modified $\text{Cu}_{0.1}\text{Ni}_{0.8}\text{Co}_{0.2}\text{Mn}_{1.9}\text{O}_4$ Ceramics

In respect to the results of microstructure characterization with X-ray diffractometry method, the lattice constant of the main spinel was slightly grown from 8.38 до 8.41 Å without significant changes in the parameter of additional NiO phase (at the level of 4.17–4.19 Å) despite increase in the content of this phase from 1 to 12% [16].

To explain the above phenomena, microstructure of the prepared ceramics was studied. As it follows from Fig. 29.6, the prepared ceramic samples differ significantly by their grain-pore microstructure.

The samples of batch No. 1 (Fig. 29.6a) are characterized by fine 1–3 μm grains. The numerous intergranular pores are small enough in these samples, their sizes not exceeding 1–2 μm. White film, which can be attributed to additional NiO phase extractions, weakly appears in these ceramics mainly near intergrain boundaries; sometimes it partially fills of pores. The samples of batch No. 2 (Fig. 29.6a) are characterized by larger grains with sizes near 5–7 μm, some of them achieving 10 μm. The white NiO film appears in these ceramics only in the regions of grain boundaries. The grain structure of the samples of batch No. 3 (Fig. 29.6c) gradually changes. The corresponding chip structure of these ceramics is more monolithic, it being characterized only by separate pores with 1–3 μm in sizes. White NiO film appears as bright layer of 10 μm thickness on the grain surface of these samples. In contrast, the grain structure of the samples of batch No. 4 (Fig. 29.6d) attains fully monolithic shape. Only some individual pores of relatively large sizes (near 3–5 μm) are observed in these ceramics, the NiO appearing as uniform layer on the whole ceramic surface. The observed additional NiO phase is nonuniformly distributed within ceramic bulk, being more clearly pronounced near grain boundaries. These phase extractions serve as specific trapping centers for positrons penetrating ceramics.

Investigation of element composition of grain for  $\text{Cu}_{0.1}\text{Ni}_{0.8}\text{Co}_{0.2}\text{Mn}_{1.9}\text{O}_4$  ceramics specifies on their stoichiometry (Fig. 29.7). However basic influence on the structural processes in material open and closed pores formed by modification on the stage of sintering is realized.

By accepting two-state positron trapping model [27, 28], for spinel-type ceramic materials, the first component of spectra was connected with main spinel structure and the second one – with extended defects located near grain boundaries in the vicinity of additional extracted phases. The intensity  $I_1$  corresponds to the amounts

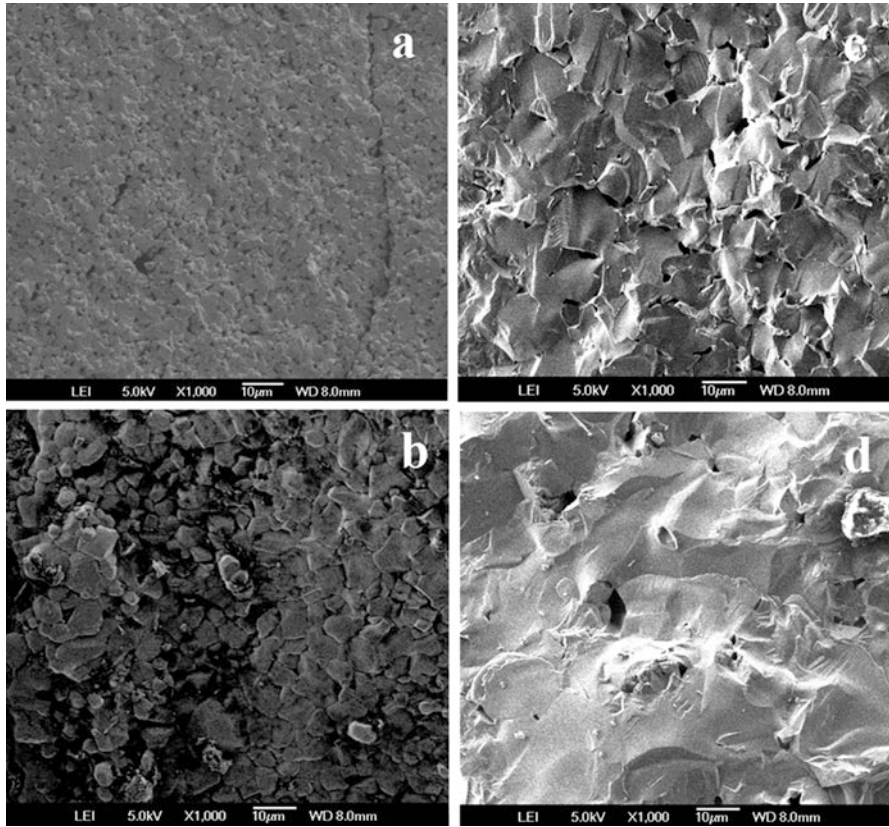


**Fig. 29.6** Microstructure of modified  $\text{Cu}_{0.1}\text{Ni}_{0.8}\text{Co}_{0.2}\text{Mn}_{1.9}\text{O}_4$  ceramics: (a) batch No 1 (1 % NiO), (b) batch No 2 (8 % NiO), (c) batch No 3 (10 % NiO), (d) batch No 4 (12 % NiO)

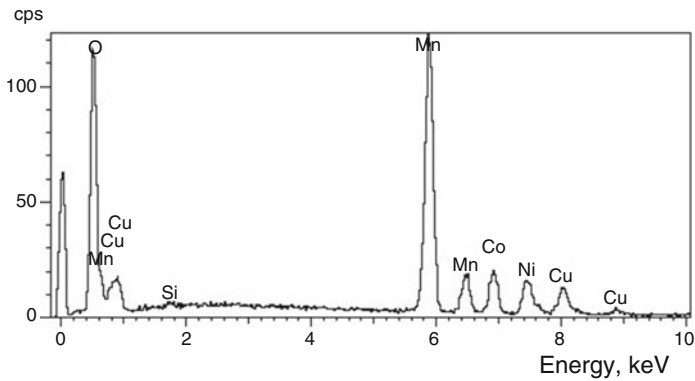


**Fig. 29.7** Elemental composition of grain for  $\text{Cu}_{0.1}\text{Ni}_{0.8}\text{Co}_{0.2}\text{Mn}_{1.9}\text{O}_4$  ceramics

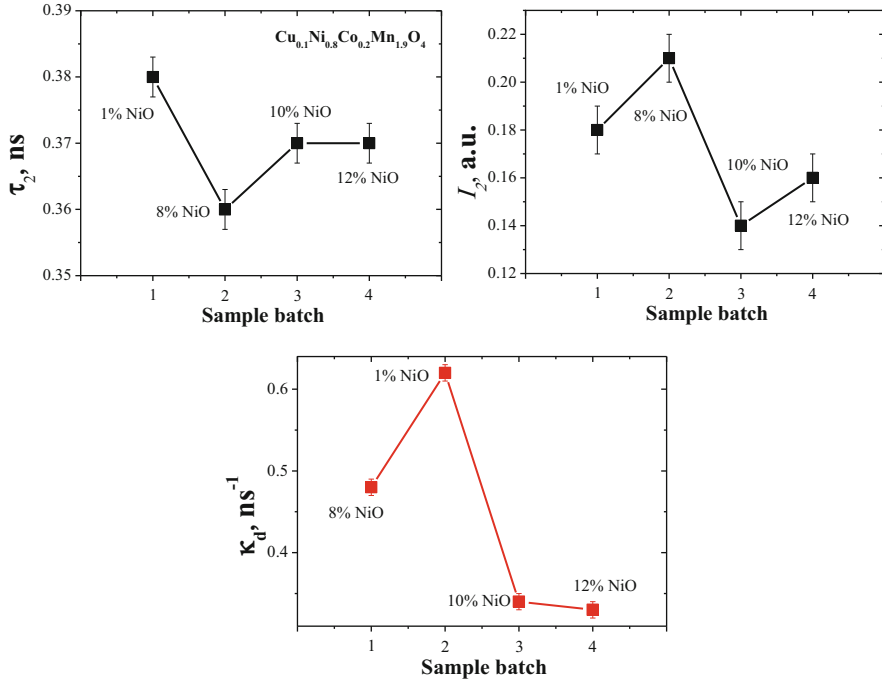


**Fig. 29.8** Defect-related component and positron trapping rate in defects as a function of amount of NiO in the studied  $\text{Cu}_{0.1}\text{Ni}_{0.8}\text{Co}_{0.2}\text{Mn}_{1.9}\text{O}_4$  ceramics

of the main spinel phase, while the  $I_2$  intensity to the amount of addition NiO phase near grain boundaries.

The lifetime of the first and second components for  $\text{Cu}_{0.1}\text{Ni}_{0.8}\text{Co}_{0.2}\text{Mn}_{1.9}\text{O}_4$  ceramics is typically for spinel-structured materials and equals  $\sim 0.37$  and  $0.20$  ns, accordingly (Table 29.3). The lower  $\tau_1$  value in the batch No. 2 ( $0.17$  ns) will be correlated with Ni content in different crystallographic positions. Since the amount of grain/pores in the sample of batch No. 2 was greater, the process of positron trapping in these ceramics was more intensive (the positron trapping rate of defects increased from  $0.48$  to  $0.62$   $\text{ns}^{-1}$ ).

The intensity of the second component for samples of batch No. 1 is 18% (Table 29.3, Fig. 29.8), although amount of additional NiO phase in this batch is small (1%). This additional phase is localized near grain boundaries and partly fills pores. In samples of batch No. 2, the intensity  $I_2$  increases to 21% correspondingly to amount of NiO phase.

In batch No. 3 ceramics, the grain-pore structure was not developed because of occurred monolithization process accompanied by surface extraction of additional NiO phase. The same was character for batch No. 4 ceramic samples.

**Table 29.3** PAL characteristics of  $\text{Cu}_{0.4}\text{Co}_{0.4}\text{Ni}_{0.4}\text{Mn}_{1.8}\text{O}_4$  ceramic mathematical treatment within two-component fitting procedure

Sample batch	Fitting parameters			Component input			Positron trapping modes				
	$\tau_1$ , ns	$I_1$ , a.u.	$\tau_2$ , ns	$I_2$ , a.u.	$\tau_{av.}^1$ , ns	$\tau_{av.}^2$ , ns	$\tau_{av.}$ , ns	$\tau_b$ , ns	$\kappa_d$ , ns <sup>-1</sup>	$\tau_2 - \tau_b$ , ns	$\tau_2/\tau_b$
No. 1	0.19	0.82	0.38	0.18	0.16	0.07	0.23	0.21	0.48	0.17	1.8
No. 2	0.17	0.79	0.36	0.21	0.14	0.07	0.21	0.19	0.62	0.17	1.9
No. 3	0.20	0.86	0.37	0.14	0.17	0.05	0.22	0.21	0.34	0.16	1.7
No. 4	0.21	0.84	0.37	0.16	0.18	0.06	0.23	0.22	0.33	0.15	1.7

These transformations were in good agreement with positron trapping rate in defects (Table 29.3, Fig. 29.8). Nevertheless, there were no significant changes in  $\tau_{av}$ ,  $\tau_b$ ,  $\tau_2/\tau_b$ , and  $(\tau_2 - \tau_b)$ . In all cases, the same type of positron trapping center is formed. The character size of these extended positron traps near grain boundaries estimated due to  $(\tau_2 - \tau_b)$  difference is close to single-double atomic vacancies [16].

## 29.5 Conclusions

Structural peculiarities of temperature-sensitive  $\text{Cu}_{0.4}\text{Co}_{0.4}\text{Ni}_{0.4}\text{Mn}_{1.8}\text{O}_4$  ceramics caused by micro- and macro-modifications as well as  $\text{Cu}_{0.1}\text{Ni}_{0.8}\text{Co}_{0.2}\text{Mn}_{1.9}\text{O}_4$  ceramics related with monolithization processes were studied using traditional structural methods in comparison with PAL technique. It is shown that adequate characterization methodology for free-volume defects in the modified spinel ceramics can be developed in terms of positron trapping model. The first component on the positron lifetime spectra has shown microstructure specificity of the spinel ceramics with octahedral and tetrahedral cation vacancies. The extended defects near grain boundaries (voids) are reflected by the second component. The small third component is due to “pick-off” annihilation of *o-Pos* in the intergranular nanopores. The observed *o-Pos* lifetime  $\sim 1.8$  ns is related to the nanopores with radius of  $\sim 2.7$  nm based on classic Tao-Eldrup equation. The reported data gives additional information to Hg-porosimetry and SEM results.

In the case of  $\text{Cu}_{0.1}\text{Ni}_{0.8}\text{Co}_{0.2}\text{Mn}_{1.9}\text{O}_4$  ceramics, the results of PAL measurements confirm the interphase mass transfer processes caused by monolithization processes in ceramics during technological modification and owing to optimal content of additional NiO phase. Obtained results are in well agreement with microstructural X-ray diffractometry and electron microscopy data, confirming the structural changes in these ceramics caused by their technological modification.

**Acknowledgments** H. Klym thanks the Ministry of Education and Science of Ukraine for support (grant No 0116 U004411).

## References

1. Salomao R, Bôas MOV, Pandolfelli VC (2011) Porous alumina-spinel ceramics for high temperature applications. *Ceram Int* 37(4):1393–1399 <https://doi.org/10.1016/j.ceramint.2011.01.012>
2. Feltz A, Pözl W (2000) Spinel forming ceramics of the system  $\text{Fe}_x\text{Ni}_y\text{Mn}_{3-x-y}\text{O}_4$  for high temperature NTC thermistor applications. *J Eur Ceram Soc* 20(14):2353–2366 [https://doi.org/10.1016/S0955-2219\(00\)00140-0](https://doi.org/10.1016/S0955-2219(00)00140-0)
3. Feteira A (2009) Negative temperature coefficient resistance (NTCR) ceramic thermistors: an industrial perspective. *J Am Ceram Soc* 92(5):967–983. <https://doi.org/10.1111/j.1551-2916.2009.02990.x>

4. Shpotyuk O, Balitska V, Brunner M, Hadzaman I, Klym H (2015) Thermally-induced electronic relaxation in structurally-modified  $\text{Cu}_{0.1}\text{Ni}_{0.8}\text{Co}_{0.2}\text{Mn}_{1.9}\text{O}_4$  spinel ceramics. *Phys B Condens Matter* 459:116–121 <https://doi.org/10.1016/j.physb.2014.11.023>
5. Klym H, Hadzaman I, Shpotyuk O (2015) Influence of sintering temperature on pore structure and electrical properties of technologically modified  $\text{MgO-Al}_2\text{O}_3$  ceramics. *Mater Sci* 21(1):92–95 <https://doi.org/10.5755/j01.ms.21.1.5189>
6. Setter N (2001) Electroceramics: looking ahead. *J Eur Ceram Soc* 21(10):1279–1293. [https://doi.org/10.1016/S0955-2219\(01\)00217-5](https://doi.org/10.1016/S0955-2219(01)00217-5)
7. Rousset A, Tenaillieu C, Dufour P, Bordeneuve H, Pasquet I, Guillemet-Fritsch S, Schuurman S (2013) Electrical properties of  $\text{Mn}_{3-x}\text{Co}_x\text{O}_4$  ( $0 \leq x \leq 3$ ) ceramics: an interesting system for negative temperature coefficient thermistors. *Int J Appl Ceram Technol* 10(1):175–185. <https://doi.org/10.1111/j.1744-7402.2011.02723.x>
8. Bondarchuk A, Shpotyuk O, Glot A, Klym H (2012) Current saturation in  $\text{In}_2\text{O}_3$ -SrO ceramics: a role of oxidizing atmosphere. *Revista mexicana de física* 58(4):313–316 <http://www.scielo.org.mx/pdf/rmf/v58n4/v58n4a5.pdf>
9. Deng ZY, Fukasawa T, Ando M, Zhang GJ, Ohji T (2001) Microstructure and mechanical properties of porous alumina ceramics fabricated by the decomposition of aluminum hydroxide. *J Am Ceram Soc* 84(11):2638–2644. <https://doi.org/10.1111/j.1151-2916.2001.tb01065.x>
10. Ohji T, Fukushima M (2012) Macro-porous ceramics: processing and properties. *Int Mater Rev* 57(2):115–131 <https://doi.org/10.1179/1743280411Y.0000000006>
11. Klym H, Ingram A, Shpotyuk O, Hadzaman I, Hotra O, Kostiv Y (2016) Nanostructural free-volume effects in humidity-sensitive  $\text{MgO-Al}_2\text{O}_3$  ceramics for sensor applications. *J Mater Eng Perform* 25(3):866–873. <https://doi.org/10.1007/s11665-016-1931-9>
12. Shpotyuk O, Brunner M, Hadzaman I, Balitska V, Klym H (2016) Analytical description of degradation-relaxation transformations in nanoinhomogeneous spinel ceramics. *Nanoscale Res Lett* 11(1):499. <https://doi.org/10.1186/s11671-016-1722-0>
13. Klym H, Balitska V, Shpotyuk O, Hadzaman I (2014) Degradation transformation in spinel-type functional thick-film ceramic materials. *Microelectron Reliab* 54(12):2843–2848 <https://doi.org/10.1016/j.microrel.2014.07.137>
14. Krause-Rehberg R, Leipner HS (1999) Positron annihilation in semiconductors. *Defect studies*. Springer-Verlag, Berlin/Heidelberg/New York, p 378
15. Shpotyuk O, Filipecki J (2003) Free volume in vitreous chalcogenide semiconductors: possibilities of positron annihilation lifetime study. *Wyd-wo WSP w Czesochowie, Czesochowa*
16. Klym H, Ingram A, Shpotyuk O, Filipecki J, Hadzaman I (2011) Structural studies of spinel manganite ceramics with positron annihilation lifetime spectroscopy. *J Phys Conf Ser* 289(1):012010 <http://iopscience.iop.org/article/10.1088/1742-6596/289/1/012010/meta>
17. Klym H, Ingram A, Shpotyuk O, Filipecki J (2010) PALS as characterization tool in application to humidity-sensitive electroceramics. In: 27th international conference on microelectronics proceedings (MIEL), pp 239–242. <https://doi.org/10.1109/MIEL.2010.5490492>
18. Klym H, Ingram A, Shpotyuk O, Hadzaman I, Solntsev V (2016) Water-vapor sorption processes in nanoporous  $\text{MgO-Al}_2\text{O}_3$  ceramics: the PAL spectroscopy study. *Nanoscale Res Lett* 11(1):1. <https://doi.org/10.1186/s11671-016-1352-6>
19. Shpotyuk O, Filipecki J, Ingram A, Golovchak R, Vakiv M, Klym H, Balitska V, Shpotyuk M, Kozdras A (2015) Positronics of subnanometer atomistic imperfections in solids as a high-informative structure characterization tool. *Nanoscale Res Lett* 10(1):1–5. <https://doi.org/10.1186/s11671-015-0764-z>
20. Klym H, Ingram A, Shpotyuk O, Hadzaman I, Solntsev V, Hotra O, Popov AI (2016) Positron annihilation characterization of free volume in micro-and macro-modified  $\text{Cu}_{0.4}\text{Co}_{0.4}\text{Ni}_{0.4}\text{Mn}_{1.8}\text{O}_4$  ceramics. *Low Temp Phys* 42(7):601–605 <https://doi.org/10.1063/1.4959021>
21. Karbovnyk I, Bolesta I, Rovetskii I, Velgosh S, Klym H (2014) Studies of  $\text{CdI}_2$ - $\text{Bi}_3$  microstructures with optical methods, atomic force microscopy and positron annihilation spectroscopy. *Mater Sci Poland* 32(3):391–395. <https://doi.org/10.2478/s13536-014-0215-z>



22. Hadzaman I, Klym H, Shpotyuk O (2014) Nanostructured oxyspinel multilayers for novel high-efficient conversion and control. *Int J Nanotechnol* 11(9–10–11):843–853 <https://doi.org/10.1504/IJNT.2014.063793>
23. Bodak O, Akselrud L, Demchenko P, Kotur B, Mrooz O, Hadzaman I, Shpotyuk O, Aldinger L, Seifert H, Volkov S, Pekhnyo V (2002) Crystal structure and electrical properties of  $\text{Cu}_{0.8}\text{Ni}_{0.1}\text{Co}_{0.2}\text{Mn}_{1.9}\text{O}_4$  electroceramics. *J. Alloys Compd* 347:14–23 [https://doi.org/10.1016/S0925-8388\(02\)00675-8](https://doi.org/10.1016/S0925-8388(02)00675-8)
24. Klym H, Shpotyuk O, Ingram A, Calvez L, Hadzaman I, Yu K, Ivanusa A, Chalyy D (2017) Influence of free volumes on functional properties of modified chalcogenide glasses and oxide ceramics. *Springer Proc Phys* 195:479–493 [https://doi.org/10.1007/978-3-319-56422-7\\_36](https://doi.org/10.1007/978-3-319-56422-7_36)
25. Klym HI, Ivanusa AI, Kostiv YM, Chalyy DO, Tkachuk TI, Dunets RB, Vasylyshyn II (2017) Methodology and algorithm of multicomponent analysis of positron annihilation spectra for nanostructured functional materials. *J Nano Electron Phys* 9(3):03037-1-6. [https://doi.org/10.21272/jnep.9\(3\).03037](https://doi.org/10.21272/jnep.9(3).03037)
26. Kansy J (1996) Microcomputer program for analysis of positron annihilation lifetime spectra. *Nucl Instrum Methods Phys Res, Sect A* 374(2):235–244 [https://doi.org/10.1016/0168-9002\(96\)00075-7](https://doi.org/10.1016/0168-9002(96)00075-7)
27. Klym H, Ingram A (2007) Unified model of multichannel positron annihilation in nanoporous magnesium aluminate ceramics. *J Phys Conf Ser* 79(1):012014 <https://doi.org/10.1088/1742-6596/79/1/012014>
28. Nambissan PMG, Upadhyay C, Verma HC (2003) Positron lifetime spectroscopic studies of nanocrystalline  $\text{ZnFe}_2\text{O}_4$ . *J Appl Phys* 93:6320 <https://doi.org/10.1063/1.1569973>
29. Filipecki J, Ingram A, Klym H, Shpotyuk O, Vakiv M (2007) Water-sensitive positron-trapping modes in nanoporous magnesium aluminate ceramics. *J Phys Conf Ser* 79(1):012015. <https://doi.org/10.1088/1742-6596/79/1/012015>
30. Hassan HE, Sharshar T, Hessien MM, Hemeda OM (2013) Effect of  $\gamma$ -rays irradiation on Mn–Ni ferrites: structure, magnetic properties and positron annihilation studies. *Nucl Instrum Methods Phys Res, Sect B* 304:72–79. <https://doi.org/10.1016/j.nimb.2013.03.053>
31. Klym H, Ingram A, Shpotyuk O, Filipecki J, Hadzaman I (2010) Extended defects in insulating  $\text{MgAl}_2\text{O}_4$  ceramic materials studied by PALS methods. *IOP Conf Ser Mater Sci Eng* 15(1):012044. <https://doi.org/10.1088/1757-899X/15/1/012044>
32. Jean YC, Mallon PE, Schrader DM (2003) Principles and application of positron and positronium chemistry. Word Scientific, Singapore
33. Mogensen OE (1995) Positron annihilation in chemistry. Springer, Berlin
34. Nakanishi H, Jean YC, Schrader DM, Jean YC (1998) In positron and positronium chemistry. Elsevier, Amsterdam
35. Dlubek G, Sen Gupta A, Pionteck J, Hassler R, Krause-Rehberg R, Kaspar H, Lochhaas KH (2005) High-pressure dependence of the free volume in fluoroelastomers from positron lifetime and PVT experiments. *Macromolecules* 38(2):429–437. <https://doi.org/10.1021/ma048310f>
36. Tao SJ (1972) Positronium annihilation in molecular substance. *J Chem Phys* 56(11):5499–5510 <https://doi.org/10.1063/1.1677067>
37. Eldrup M, Lightbody D, Sherwood JN (1981) The temperature dependence of positron lifetimes in solid pivalic acid. *Chem Phys* 63:51–58 [https://doi.org/10.1016/0301-0104\(81\)80307-2](https://doi.org/10.1016/0301-0104(81)80307-2)

# Chapter 30

## Effect of a Hydrogen Sulfide-Containing Atmosphere on the Physical and Mechanical Properties of Solid Oxide Fuel Cell Materials



B. D. Vasyliv, V. Ya. Podhurska, O. P. Ostash, and V. V. Vira

### 30.1 Introduction

Fuel cells are electrochemical devices that transform the chemical energy of fuel into electric energy or heat without intermediate stage of combustion. They have much higher efficiency than the energy-transforming systems and a much lower level of emission than internal combustion engines. Therefore, fuel cells are ideal energy sources for transport, stationary power plants, and mobile power plants. At present, solid oxide fuel cells (SOFCs), due to their versatility (they use all known types of fuel and are only slightly affected by the purity of fuel), reveal high economic indices. The problems of degradation of the properties of individual elements of a SOFC and optimization of their structure as layered macrocomposites still remain the key problems whose solution is urgently required [1, 2]. To improve the efficiency of a SOFC, it is necessary to reduce its operating temperature down to 550–600 °C and increase the electrochemical (electrical conductivity) and mechanical (strength and a lifetime) characteristics of materials [3–7].

The poisoning effect of sulfur by chemisorption on Ni catalysts is well known [8]. It is reversible, and a temperature-dependent threshold exists below which no effect is observed [9]. At 700 °C the threshold is about 1 ppm, and at 1000 °C the extrapolated value is of the order of 50 ppm. Poisoning by sulfur has been investigated on YSZ–Ni cermet anodes in  $\text{H}_2 + 3\% \text{H}_2\text{O}$  by several groups [10–12]. In amounts from 5 to 105 ppm, an increase of about a factor of 2 in polarization resistance has been observed. The effect at 5 ppm  $\text{H}_2\text{S}$  [11] is in contradiction with

---

B. D. Vasyliv (✉) · V. Y. Podhurska · O. P. Ostash  
Karpenko Physico-Mechanical Institute of the National Academy of Sciences of Ukraine, Lviv, Ukraine

V. V. Vira  
Lviv Polytechnic National University, Lviv, Ukraine

the reported limit for degradation of Ni catalysts' performance, and no additional effect is seen applying 105 ppm. At 35 ppm the effect was found to be reversible and to be constant with temperature from 700 to 1000 °C, with or without passing anodic current and equal for low-performance porous Ni anodes and high-performance YSZ–Ni cermets [10]. The effect was found not to be reversible at 105 ppm [12].

Assuming that sulfur chemisorbs exclusively to the Ni surface, the data indicate that the Ni surface is either the location of rate-limiting reactions or that it provides a limiting species to the rate-determining reaction. It would appear that the role of the Ni surface is fairly constant with temperature and passing of current under the given circumstances.

Considering the impedance of a full SOFC at 1000 °C, the effect of 69 ppm sulfur is about 5% on the cell voltage, and at 800 °C 10 ppm, sulfur causes about 2% reduction of the cell voltage [11]. These observations are partially affected by the anode usually not being the most significant limitation for well-performing SOFC. The fuel cells with YSZ–Ni cermet anodes have been operated with up to 2000 ppm sulfur at 950 °C, maintaining output stability [10].

The aim of this work is to study the effect of hydrogen sulfide content in a hydrogenous atmosphere on the structure, physical, and mechanical properties of SOFC anode materials.

## 30.2 Materials and Methods

In order to investigate the effect of hydrogen sulfide content in a hydrogenous atmosphere on the structure, physical, and mechanical properties of SOFC anode materials, and based on our experience of studying such materials in atmospheres with water vapor admixtures [13], a special experimental stand has been developed (Fig. 30.1).

A ceramic disk or prismatic specimen (Fig. 30.1) is fixed by the holder in the working space of a cylindrical quartz chamber, which passes through a cylindrical furnace. The chamber allows reaching the gas pressure up to 0.5 MPa at a temperature of 600 °C. The temperature control and support are carried out thanks to the heating system, which contains a heating unit connected to the furnace and a thermocouple that comes in contact with the specimen. The gas supply system contains gas cylinders (hydrogen of 99.99% purity, Ar-5 vol% H<sub>2</sub>, argon), a vacuum pump for degassing, and a Kipp generator for the production of hydrogen sulfide. A flask filled with water is provided for recycling of exhaust gas. The indicated parts of the experimental stand are connected to the network by plastic tubes with corresponding one- and three-way taps. A general view of the experimental stand is given in the photo (Fig. 30.2).

We prepared a quartz chamber, providing a pressure of 0.0133 Pa with a vacuum pump, and then ran hydrogen sulfide and additional gas in the required proportions. Exhaust gas was disposed by passing it through a flask with water. The quartz

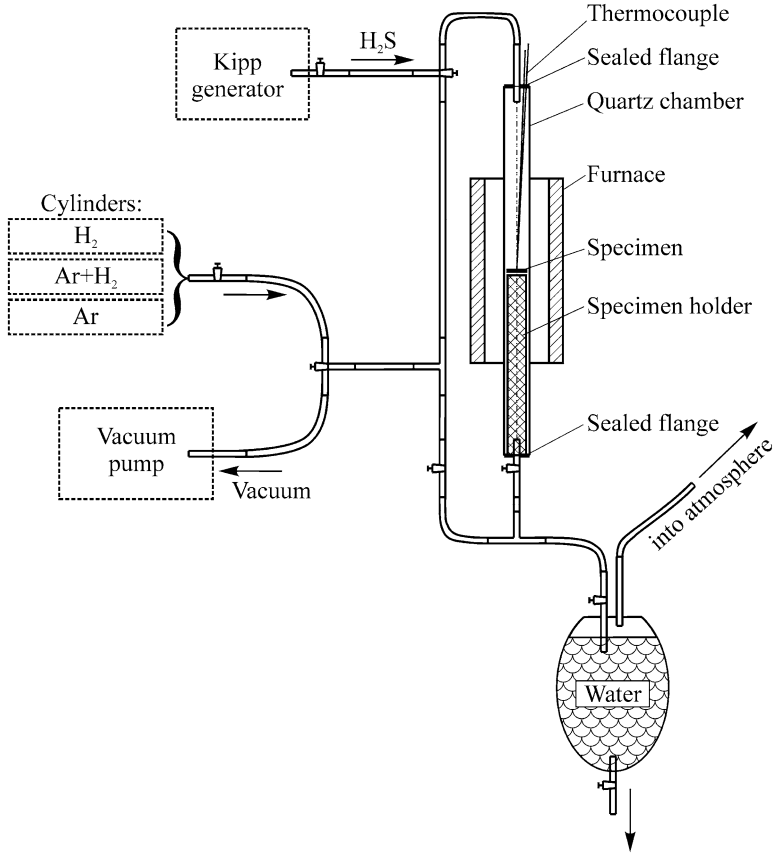


**Fig. 30.1** A diagram of the experimental stand with supplementary equipment

chamber and the network were purified from the residue of the working gas mixture, by blowing with argon at a pressure of 0.1 MPa.

The technique was worked out on 10Sc1CeSZ-50NiO ceramics in a mixture of argon with hydrogen (Ar-5 vol% H<sub>2</sub>) at a temperature of 600 °C. The physical and mechanical characteristics of the material obtained after processing in this atmosphere coincided satisfactorily with the set of characteristics for the same material, obtained earlier [3–6].

Anode materials for SOFCs have been investigated. In order to study a pure effect of an environment on nickel-containing anode materials, we used porous metallic Ni as a model material. The porosity of the material was 1.6%. We also studied the behavior of the YSZ–NiO anode ceramics (ZrO<sub>2</sub> stabilized by 8 mol% Y<sub>2</sub>O<sub>3</sub> with the addition of 50 wt% NiO) prepared by sintering at the temperature 1450 °C. The resulting grain size of the ceramics was in the range of 1–2 μm, and the porosity was 29%.

**Fig. 30.2** A general view of the experimental stand

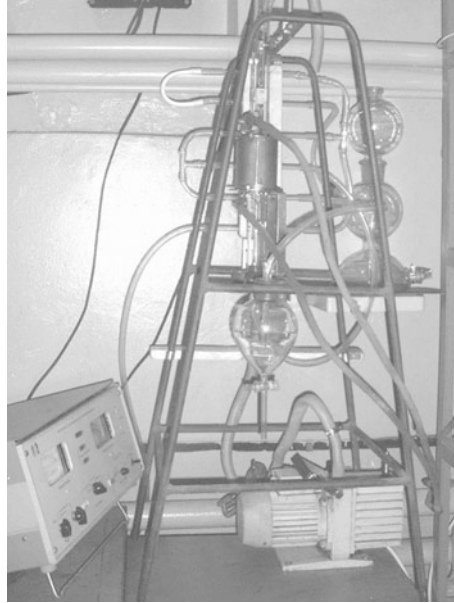
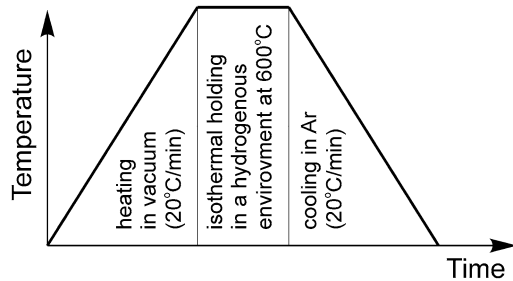


**Fig. 30.3** The scheme of the one-time reduction of materials in a hydrogenous environment



A series of specimens of porous metallic Ni and YSZ–NiO ceramics of  $1.5 \times 5 \times 25$  mm in size were prepared. In order to obtain the corresponding YSZ–Ni cermet structure, specimens of the YSZ–NiO anode ceramics were singly reduced in hydrogenous atmosphere (either Ar–5 vol% H<sub>2</sub> mixture or hydrogen of 99.99 vol% H<sub>2</sub> purity) for 4 h at 600 °C under the pressure of 0.15 MPa (Fig. 30.3). A part of the specimens of each series was then aged in “hydrogen sulfide in Ar–5 vol% H<sub>2</sub> mixture” atmosphere for 4 h at 600 °C under the pressure of 0.15 MPa. According to a test mode, the atmosphere contained 7 or 18 vol% H<sub>2</sub>S. In order to reach the pressure of 0.15 MPa, the test chamber was degassed and filled with hydrogen sulfide of certain volume and then filled up to the pressure of 0.15 MPa with Ar–5 vol% H<sub>2</sub> mixture.

The mechanical properties of the material were studied in air at 20 °C under three-point bending of beam specimens (Fig. 30.4).

**Fig. 30.4** Geometry of the specimens tested and the loading mode

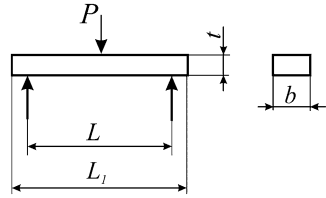
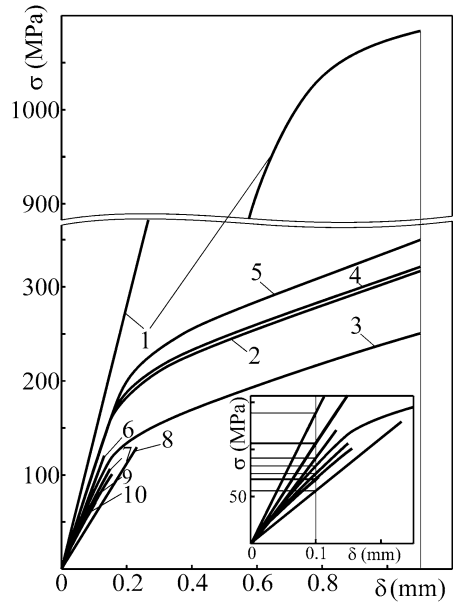


**Fig. 30.5** The “stress–flexure” diagrams for the materials in modes 1–10 (see Table 30.1). The magnified initial part of the graph contains horizontal lines indicating stress levels at a certain flexure, for estimation of the values of a relative stiffness  $E/E_0$



The fracture stresses were determined from the “stress–flexure” diagrams at  $P = P_{\max}$  for the materials in the initial state ( $\sigma_{f0}$ ) and after the corresponding treatments ( $\sigma_f$ ) by the relation

$$\sigma_f = \frac{1.5 \cdot P_{\max} \cdot L}{b \cdot t^2},$$

where  $P_{\max}$  is the load, N;  $L$  is the span between two supporting rollers, mm; and  $b$  and  $t$  are the specimen width and thickness, mm. In case of a significant plasticization of material, we used for this purpose the parameter of ultimate elastic stress which corresponds to the end of a linear domain of a “stress–flexure” diagram (Fig. 30.5).

Five samples of each series were used to define the average values of the fracture stresses. The error margins were about  $\pm 5\%$  of the corresponding values.

The relative stiffness  $E/E_0$ , where  $E$  is Young’s modulus, was estimated by the ratio between tangents of the slopes of linear domains of the corresponding “stress–flexure” diagrams for the material after treatment and in the initial state (see magnified initial part of the graph in Fig. 30.5).

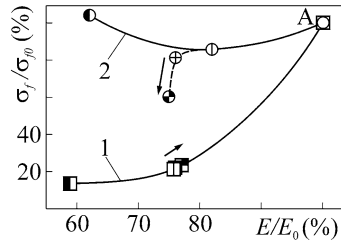


**Fig. 30.6** Dependences of the relative strength on the relative stiffness for the investigated materials: (1) porous Ni, (2) YSZ–Ni cermet, (A) as-received materials. The coordinates of the points correspond to the data in Table 30.1. The arrows show the tendencies of change of the characteristics while hydrogen sulfide content increases

Based on the obtained data of the relative strength and relative stiffness of materials in modes 1–10 (Table 30.1), certain features of changes in their mechanical behavior were studied.

The specific electrical conductivity  $\sigma$  was determined in air at 20 °C by the four-point scheme [14]. For the microstructural and quantitative analysis of element distribution, we applied a Carl Zeiss EVO-40XVP scanning electron microscope (SEM) with an INCA Energy 350 system for energy-dispersive X-ray (EDX) microanalysis.

### 30.3 Results and Discussion

A significant plasticization of specimens of porous Ni after their exposition in hydrogenous environments at 600 °C has been revealed. The “stress–flexure” diagrams displayed a drastic drop of the elasticity modulus along with the ultimate elastic stress for the material treated (Fig. 30.5). It was stated that the higher is a content of hydrogen in a gaseous atmosphere, the lower are these characteristics and the higher is the hydrogen-assisted plasticization of nickel in general.

Based on the characteristics of relative stiffness and strength, it was revealed that hydrogen sulfide does not do any discernible influence on mechanical behavior of porous Ni (Fig. 30.6). Neither 7 nor 18 vol% H<sub>2</sub>S affects plasticity and strength of the material. It can be suggested that only a content of hydrogen in a gaseous atmosphere, at the same treatment mode, i.e., holding at the temperature 600 °C and pressure 0.15 MPa for 4 h, affects these characteristics. The estimated values were in the ranges of 21.1–13.9% (relative strength) and 76–59% (relative stiffness), while a content of hydrogen in a gaseous atmosphere was changed in the range of 5–99.99 vol % (see Table 30.1). A general tendency of change of these characteristics, while hydrogen sulfide content increases, is indicated by the arrow along curve 1 (see Fig. 30.6).

**Table 30.1** Influence of material treatment mode on the physical and mechanical properties

Material	Mode marking	Mode	Preconditioning	Aging	Mean values of the characteristics		
					$\sigma_f / \sigma_{f0}$ %	$E/E_0$	$\sigma$ (S/m)
Ni	1	As-received			100	100	$1.4 \cdot 10^7$
	2	Processing in Ar-5 vol% H <sub>2</sub> at 600 °C for 4 h		-	21.1	76	$1.4 \cdot 10^7$
	3	Processing in 99.99 vol% H <sub>2</sub> at 600 °C for 4 h		-	13.9	59	$1.4 \cdot 10^7$
	4	Processing in Ar-5 vol% H <sub>2</sub> at 600 °C for 4 h		Aging in Ar-5 vol% H <sub>2</sub> with 7 vol% H <sub>2</sub> S at 600 °C for 4 h	21.7	76	$1.4 \cdot 10^7$
	5	Processing in Ar-5 vol% H <sub>2</sub> at 600 °C for 4 h		Aging in Ar-5 vol% H <sub>2</sub> with 18 vol% H <sub>2</sub> S at 600 °C for 4 h	23.3	77	$1.4 \cdot 10^7$
YSZ-NiO	6	As-received			100	100 (*)	
	7	Processing in Ar-5 vol% H <sub>2</sub> at 600 °C for 4 h		-	86	82	$(5.5-6.5) \cdot 10^5$
	8	Processing in 99.99 vol% H <sub>2</sub> at 600 °C for 4 h		-	105	62	$(2.1-2.7) \cdot 10^6$
	9	Processing in Ar-5 vol% H <sub>2</sub> at 600 °C for 4 h		Aging in Ar-5 vol% H <sub>2</sub> with 7 vol% H <sub>2</sub> S at 600 °C for 4 h	82	76	$(5.5-6.5) \cdot 10^5$
	10	Processing in Ar-5 vol% H <sub>2</sub> at 600 °C for 4 h		Aging in Ar-5 vol% H <sub>2</sub> with 18 vol% H <sub>2</sub> S at 600 °C for 4 h	61	75	$(5.5-6.5) \cdot 10^5$

Comment: (\*) Electrical conductivity is absent



No changes in the electrical conductivity of porous Ni were found for all the treatment modes (see Table 30.1). Even a relatively high concentration of hydrogen sulfide (18 vol%) in a hydrogenous environment did not cause a formation of a protective surface layer which could decrease surface conductivity of the material.

The YSZ–NiO anode ceramics, depending on a content of hydrogen in a gaseous atmosphere, displayed quite different mechanical behavior as compared to porous Ni (Fig. 30.5). Based on previously obtained data [5, 7], it was stated that after a single exposure of the YSZ–NiO ceramics in Ar–5 vol% H<sub>2</sub> gas mixture, only the surface layers of the particles of nickel oxide are reduced, and after exposure in hydrogen, the particles are reduced completely what causes the substantial growth of electrical conductivity of the material (up to  $(2.1\text{--}2.7)\cdot 10^6$  S/m).

As a result of complete reduction of the nickel phase in pure hydrogen followed by a significant plasticization of reduced Ni, the relative stiffness decreased to 62%.

The local EDX analysis (with dispersion of energy, *W*) of the zirconium and nickel phases of the YSZ–Ni cermet after aging in hydrogenous atmospheres containing 7 and 18 vol% H<sub>2</sub>S did not detect sulfur in both these phases and within their boundaries (see spectra No. 1–6 in Tables 30.2 and 30.3). However, during the EDX analysis of the entire areas on the cross-sectional surfaces of the aged specimens, from 0.12 to 0.27 wt%, sulfur was found (see Tables 30.2 and 30.3). In the core of all specimens, its content did not exceed 0.12 wt%.

However, in near-surface layers (Fig. 30.7a, b), the sulfur content depended on the concentration of hydrogen sulfide admixture and was, respectively, 0.14 wt% (at a concentration of 7 vol% H<sub>2</sub>S) and 0.27 wt% (18 vol% H<sub>2</sub>S).

**Table 30.2** The data of the EDX spectra of the YSZ–Ni cermet specimen after aging in Ar–5 vol% H<sub>2</sub> gas atmosphere with an admixture of 7 vol% H<sub>2</sub>S

Chemical element and X-ray series	Spectrum 1 (Ni-phase)		Spectrum 2 (Zr-phase)		Spectrum 3 (boundary)		Specimen surface layer		Specimen core	
	wt%	at%	wt%	at%	wt%	at%	wt%	at%	wt%	at%
O K	25.62	55.82	28.06	68.39	24.09	60.63	19.20	51.04	14.41	42.71
S K	–	–	–	–	–	–	0.14	0.18	0.12	0.18
Ni K	74.38	44.18	3.25	2.15	23.67	16.24	43.08	31.21	43.88	35.43
Y L	–	–	8.29	3.64	5.75	2.61	3.92	1.88	4.50	2.40
Zr L	–	–	60.40	25.82	46.49	20.52	33.66	15.69	37.09	19.28

**Table 30.3** The data of the EDX spectra of the YSZ–Ni cermet specimen after aging in Ar–5 vol% H<sub>2</sub> gas atmosphere with an admixture of 18 vol% H<sub>2</sub>S

Chemical element and X-ray series	Spectrum 4 (Ni-phase)		Spectrum 5 (Zr-phase)		Spectrum 6 (boundary)		Specimen surface layer		Specimen core	
	wt%	at%	wt%	at%	wt%	at%	wt%	at%	wt%	at%
O K	25.96	56.26	28.71	69.11	26.02	64.35	17.14	47.53	14.49	42.82
S K	–	–	–	–	–	–	0.27	0.37	0.12	0.18
Ni K	74.04	43.74	3.03	1.99	20.33	11.36	44.15	33.36	44.24	35.62
Y L	–	–	7.99	3.46	6.81	3.24	4.07	2.03	4.24	2.25
Zr L	–	–	60.27	25.44	46.84	21.05	34.37	16.71	36.91	19.13

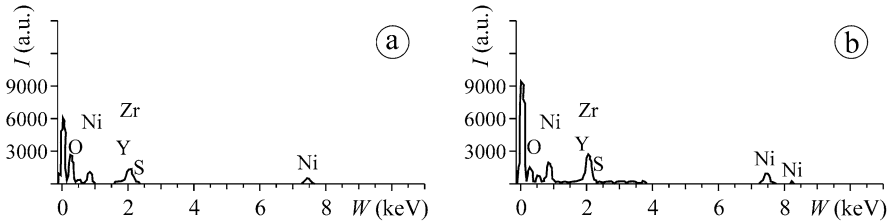


**Fig. 30.7** The EDX spectra of surface layers of YSZ–Ni cermet specimens after aging in Ar–5 vol% H<sub>2</sub> gas atmosphere with an admixture of 7 vol% H<sub>2</sub>S (a) and 18 vol% H<sub>2</sub>S (b) (see Tables 30.2 and 30.3)

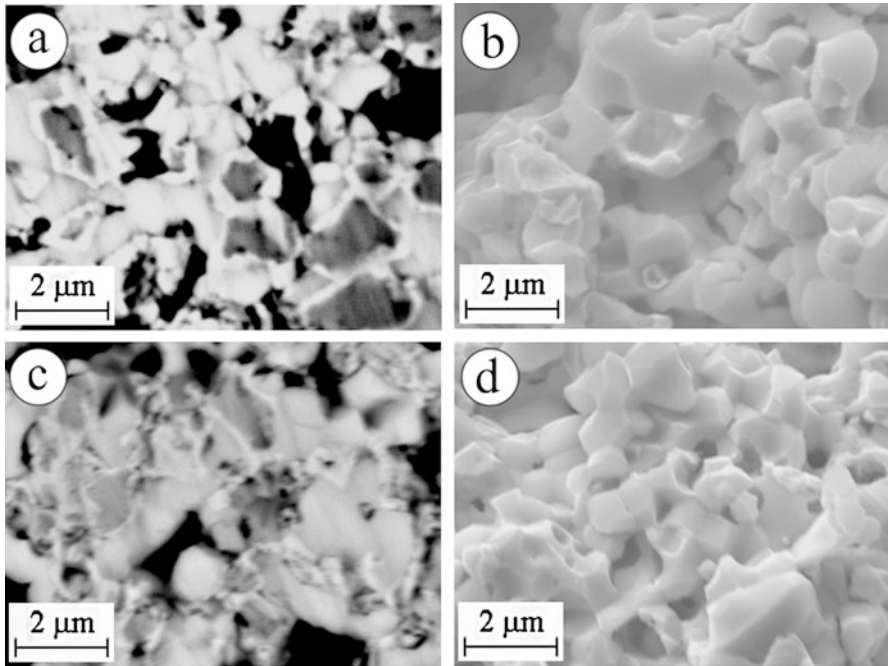


**Fig. 30.8** SEM images of the microstructures (a, c) and microfractograms (b, d) of YSZ–Ni cermet specimens after aging in Ar–5 vol% H<sub>2</sub> gas atmosphere with an admixture of 7 vol% H<sub>2</sub>S (a, b) and 18 vol% H<sub>2</sub>S (c, d)

On the basis of microstructural analysis of the YSZ–Ni cermet specimens after aging in hydrogenous atmospheres containing 7 and 18 vol% H<sub>2</sub>S, certain features of changes in their structure and fracture micromechanisms were revealed (Fig. 30.8). Taking into account the abovementioned peculiarities of the distribution of sulfur in the volume of treated samples and its insignificant content, even in near-surface layers of specimens, it can be assumed that the material degrades mainly due to the action of high-temperature H<sub>2</sub>S gas, which reacts with reduced nickel.

The observed tendency to reduce the amount of oxygen in the near-surface layers indicates that hydrogen sulfide, at its high concentration, improves the reduction of the nickel phase. It is likely that both of these processes (more active reduction and interaction of nickel with high-temperature hydrogen sulfide gas) occur mainly on the three-phase boundaries (pores–nickel phase–zirconium phase), resulting in the concentration of sulfur as a product of the reaction in these places, i.e., in the pores and near them.

First of all, the degradation of the structure is manifested through the discontinuity of the “zirconium phase–nickel phase” and “nickel phase–nickel phase” bonds. This does not violate the integrity of the YSZ ceramic skeleton in the cermet at concentrations up to 7 vol%  $\text{H}_2\text{S}$ . With the increase of the hydrogen sulfide concentration followed by the improvement of the nickel phase reduction, a larger amount of completely reduced small nickel particles is formed (Fig. 30.8c as compared to Fig. 30.8a). These particles interact actively with hydrogen sulfide and weaken their bonds with the particles of the zirconium phase. Such structural transformations are followed by a change of fracture micromechanisms prevailing in a cermet: from the mixed one containing both the elements of the cleavage and intergranular fracture along the cracked boundaries (Fig. 30.8b) to completely intergranular fracture (Fig. 30.8d). As a result, the cermet strength is reduced to 61% of the initial state (Table 30.1).

The arrow along the deviated branch of curve 2 (see Fig. 30.6) indicates a general tendency of change of the relative strength and stiffness of the YSZ–Ni anode cermet while hydrogen sulfide content in high-temperature hydrogenous atmosphere increases. It can be marked that the arrow direction differs from that for porous Ni.

Unlike mechanical behavior, the electrical conductivity of YSZ–Ni cermet after aging in a hydrogenous atmosphere at a concentration of 7 and 18 vol%  $\text{H}_2\text{S}$  is  $(5.5\text{--}6.5)\cdot 10^5$  S/m, which does not differ from the value for one-time reduced cermet (Table 30.1). Thus, the YSZ–Ni anode material is not sensitive to high-temperature hydrogenous atmosphere with an admixture of 7 vol%  $\text{H}_2\text{S}$ . The little drop of the relative stiffness (see Fig. 30.6) is probably connected with a slight improvement of the reduction of the nickel phase by hydrogen sulfide, as compared to pure Ar–5 vol%  $\text{H}_2$  atmosphere. This concentration of hydrogen sulfide in the SOFC operating environment does not lead to a significant decrease in its strength at a stable high electrical conductivity.

## 30.4 Conclusions

The certain features of changes in the structure and physical and mechanical properties of porous nickel and the YSZ–Ni anode cermet caused by high-temperature hydrogenous atmospheres with and without an admixture of  $\text{H}_2\text{S}$ , were revealed. It was found that exposition of porous Ni for 4 h in a hydrogenous atmosphere at the temperature 600 °C causes its significant plasticization. The relative strength and stiffness of the material decrease with increasing hydrogen concentration and

can reach 13.9 and 59%, respectively, after the treatment in pure hydrogen. Neither 7 nor 18 vol% H<sub>2</sub>S in a hydrogenous atmosphere affects plasticity, strength, and electrical conductivity of the material.

The hydrogenous atmosphere containing up to 7 vol% H<sub>2</sub>S does not affect the strength and electrical conductivity of the YSZ–Ni cermet. Increased content of H<sub>2</sub>S (18 vol%) causes some changes in the YSZ–Ni cermet structure due to improvement of the reduction process and formation of a large number of fully reduced tiny nickel particles which react with hydrogen sulfide. Multiple breaking of the zirconia–nickel bonds occurs that results in reduced strength of the cermet (by 39% as compared to as-received YSZ–NiO ceramics).

## References

1. Sarantaridis D, Atkinson A (2007) Redox cycling of Ni-based solid oxide fuel cell anodes: a review. *Fuel Cells* 3:246–258
2. Ettler M, Timmermann H, Malzbender J et al (2010) Durability of Ni anodes during reoxidation cycles. *J Power Sources* 195:5452–5467
3. Vasylyv BD (2009) A procedure for the investigation of mechanical and physical properties of ceramics under the conditions of biaxial bending of a disk specimen according to the ring–ring scheme. *Mater Sci* 45(4):571–575
4. Vasylyv BD, Ostash OP, Podhurs'ka VY et al (2013) Method of treatment of NiO-containing anodes of a solid oxide fuel cell [in Ukrainian]. Patent of Ukraine No. 78992. Published on 10.04.13, Bulletin No. 7
5. Vasylyv BD, Podhurs'ka VY, Ostash OP et al (2013) Influence of reducing and oxidizing media on the physicomechanical properties of ScCeSZ–NiO and YSZ–NiO ceramics. *Mater Sci* 49(2):135–144
6. Podhurs'ka VY, Vasylyv BD, Ostash OP et al (2014) Structural transformations in the NiO-containing anode of ceramic fuel cells in the course of its reduction and oxidation. *Mater Sci* 49(6):805–811
7. Podhurska V, Vasylyv B, Ostash O et al (2016) Influence of treatment temperature on microstructure and properties of YSZ–NiO anode materials. *Nanoscale Res Lett* 11:93. <https://doi.org/10.1186/s11671-016-1306-z>
8. Alstrup I, Rostrup-Nielsen JR, Roen S (1981) High temperature hydrogen sulfide chemisorption on nickel catalysts. *Appl Catal* 1:303–314
9. Twigg MV (1996) *Catalyst handbook*, 2nd edn. Manson Publishing, Ltd, London
10. Primdahl S (1999) Nickel/yttria-stabilised zirconia cermet anodes for solid oxide fuel cells. Dissertation, University of Twente, Faculty of Chemical Technology, The Netherlands, and Risø National Laboratory, Materials Research Department, Denmark
11. Norheim A, Wærnhus I, Broström M et al (2007) Experimental studies on the influence of H<sub>2</sub>S on solid oxide fuel cell performance at 800 °C. *Energy Fuel* 21(2):1098–1101
12. Dees DW, Balachandran U, Dorris SE et al (1989) Interfacial effects in monolithic solid oxide fuel cells. In: *SOFC I: the electrochemical society proceedings series*, Pennington, pp 317–321
13. Vasylyv B, Podhurska V, Ostash O (2017) Preconditioning of the YSZ–NiO fuel cell anode in hydrogenous atmospheres containing water vapor. *Nanoscale Res Lett* 12:265. <https://doi.org/10.1186/s11671-017-2038-4>
14. Van der Pauw L (1958) A method of measuring specific resistivity and hall effect of discs of arbitrary shape. *Philips Res Rep* 13(1):1–9

# Chapter 31

## Influence of Annealing in Vacuum on Dispersion Kinetics of Titanium and Zirconium Nanofilms Deposited onto Oxide Materials



Y. V. Naidich, I. I. Gab, T. V. Stetsyuk, B. D. Kostyuk, O. M. Fesenko, and D. B. Shakhnin

### 31.1 Introduction

Joining ceramics and other nonmetal materials with metals using solder and metal deformable gaskets is widely used in modern technology. For such joints making, thin metal films are often used as they are widely applicable in various fields of science and technology.

The thickness of films deposited onto metallic and nonmetallic materials may be within a wide range: from a few nanometers till tens of microns. For technological purposes, metal films are often used with different thicknesses deposited by various methods (plasma sputtering, magnetron sputtering, chemical and electrochemical methods, electron-beam sputtering, etc.) onto nonmetallic parts to join them with each other or with metals by brazing or pressure welding [1–6].

A special role in joining such different materials is played by adhesively active metals including titanium, zirconium, niobium, hafnium, and others. These metals are either added to metallic solders composition or used as coatings, particularly in the form of thin films at the surfaces of joined materials; and using pressure welding joints of different materials may be obtained through deformable gaskets made of these metals. These metals have good adhesion to both nonmetallic and metallic

---

Y. V. Naidich · I. I. Gab (✉) · T. V. Stetsyuk · B. D. Kostyuk  
Frantsevich Institute for Problems of Materials Science of National Academy Sciences of Ukraine, Kyiv, Ukraine  
e-mail: [gab@ipms.kiev.ua](mailto:gab@ipms.kiev.ua)

O. M. Fesenko  
Institute of Physics of National Academy Sciences of Ukraine, Kyiv, Ukraine

D. B. Shakhnin  
V.I. Vernadsky Institute of General and Inorganic Chemistry of National Academy Sciences of Ukraine, Kyiv, Ukraine

materials and provide good spreading of metal solders and their interaction at the interface “solder – hard surface to be joined.”

Since, during the process of brazing or pressure welding, metalized nonmetallic parts must be heated to very high temperatures (1300–1600 °C), studying processes of fragmentation-coagulation occurring during the annealing of these metal nanofilms is not only of cognitive interest but also of practical importance for the development of technological modes of joining nonmetallic materials.

We have previously studied the kinetics of the fragmentation during annealing in vacuum of niobium and hafnium nanofilms deposited onto oxide and non-oxide nonmetallic materials such as sapphire, ceramics based on ZrO<sub>2</sub>, and others [7, 8].

The aim of this work was to study the kinetics of fragmentation during the annealing of titanium nanofilms deposited onto some oxide and non-oxide materials.

## 31.2 Materials and Experimental Methods

Titanium and zirconium nanofilms 100 nm thick were deposited onto nonmetallic substrates 4 × 4 × 1 mm made of leucosapphire (single crystal alumina) and zirconium dioxide by electron-beam sputtering method [9]. Substrates were made of materials which are either the most widely used in industry, particularly leucosapphire, or the matrix of high-temperature ceramics. Metallic films were deposited onto polished surfaces of substrates. The parameter of surface roughness  $R_z$  was equal to 0,03 ÷ 0,05 microns.

The polished substrate surfaces were degreased by acetone and ethanol, after which they were annealed in air at 1200 °C for 2 h, and then these substrates were annealed in vacuum not worse than  $2 \times 10^{-3}$  Pa at the same temperature for 1 h. The 100 nm thickness of the metal nanofilms was chosen taking into account the fact that such films are solid, completely covering the oxide surface, have good adhesion to it, and provide good solder spreading [10]. Thicker films have the ability to exfoliate due to the presence in them of residual stresses as a result of growth tensions occurrence during the multilayer deposition and because of the large difference between thermal coefficients of linear expansion (TCLE) of film metal and substrate material. Films were deposited during 10–15 min onto the substrates whose temperature was about 100 °C, and the films' thickness was determined using a special device with a quartz sensor.

Films were deposited onto all substrates under the same conditions, and their quality was monitored by metallographic microscope XJL-17.

Annealing of nonmetallic samples coated by metal films was performed in a vacuum chamber during various time periods from 2 up to 20 min at different temperatures (1200 ÷ 1600 °C) in vacuum not worse than  $2 \times 10^{-3}$  Pa.

Annealed samples were examined using scanning electron microscopes JCM-6700 and JCM-5000 and an atomic force microscope Nanoscope III A with micrograph recording. The Raman spectra of titanium and zirconium nanofilms were obtained using a Renishaw inVia Raman microscope (Renishaw plc, Wotton-under-Edge, UK) at an excitation wavelength of 633 nm.

Using these micrographs, the area of substrate surface coated with metal film islands was calculated by planimetric weighting method, i.e., by weighting of metal-coated sample parts images cut from micrographs [2]. The data obtained by this method were analyzed as the dependence of sample surface area covered with metal film fragments after annealing on annealing parameters (annealing temperature and time).

### 31.3 Results and Discussion

Original titanium and zirconium films on both substrates were solid, without any significant defects, and micrographs obtained using electronic scanning microscopes show only the uniform dark gray field.

During annealing of titanium film on the leucosapphire surface, at first, minor signs of changes in the structure of the film appeared only as a result of its 2-min heating up to 1300 °C. As a result of further exposition at this temperature for 5 min, film began to blister in part without losing its integrity, and the process rate is slightly increased after a 10-min annealing (Fig. 31.1a), but the film still remained solid. With increased exposition time up to 20 min at 1300 °C, the film is rapidly disintegrated into large pieces. The similar pattern was observed with increase of annealing temperature up to 1400 °C: the film is partially started to blister after the 2-min exposition without losing its integrity; after a 5-min annealing, process greatly intensified, and the film even started to crack (Fig. 31.1b). With further exposition at this temperature for 10 min, quite long and wide cracks appear in the film; and, finally, after a 20-min annealing, film completely disintegrated into large fragments between which significant parts of free leucosapphire surface appear. Annealing at 1500 °C has speeded up significantly the process of the titanium film disintegration. Thus, after the 2-min annealing, film blistered intensively and lost its integrity; after the 5-min exposition, it is cracked significantly; during further exposition time increase of up to 10 min, film disintegrated into large fragments (Fig. 31.1c); and after 2-min annealing at this temperature, there were only some film fragments on the leucosapphire surface covering no more than 40% of it (Fig. 31.1d). With the annealing temperature increase up to 1600 °C, the film began to disintegrate already after a 2-min exposure (Fig. 31.2); further increase of annealing time up to 5 min led to a complete decomposition of the film covering only about 10% of the leucosapphire surface which was almost completely free after 10-min annealing.

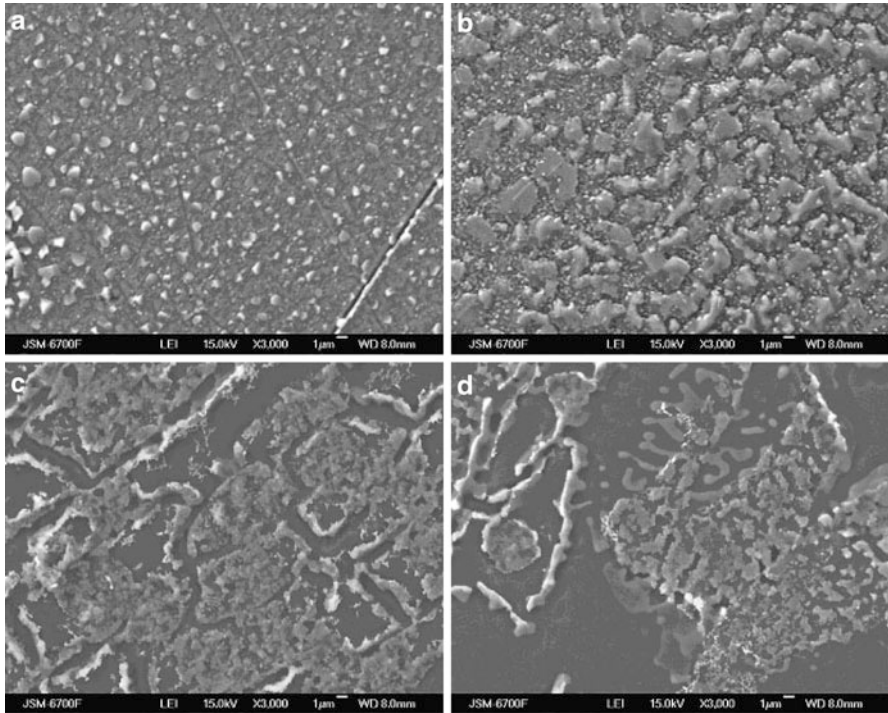


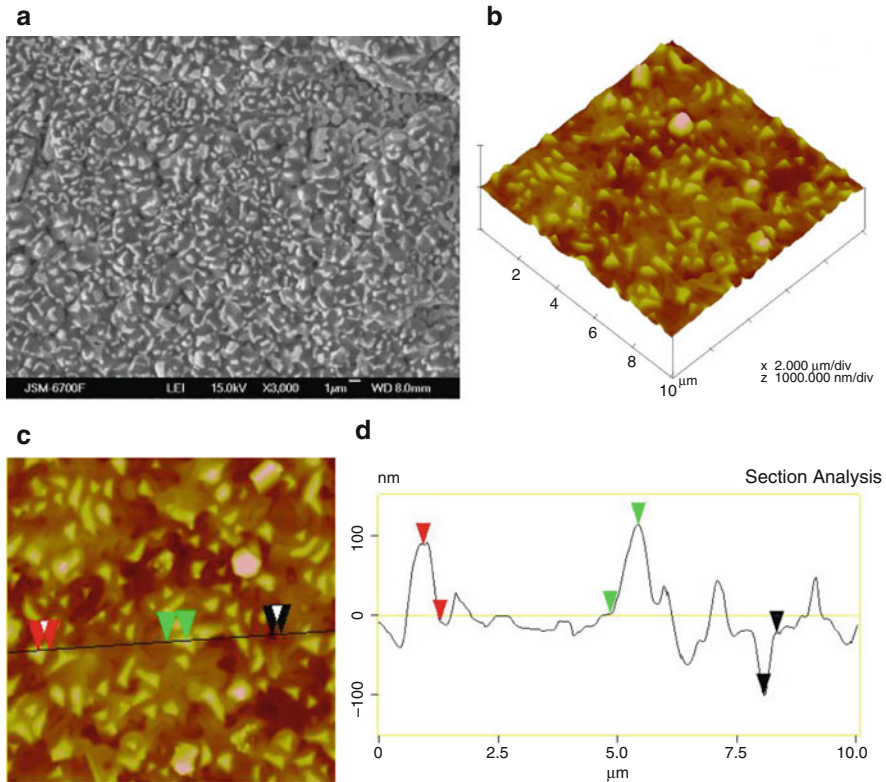
**Fig. 31.1** SEM image titanium film 100 nm thickness onto leucosapphire which was annealed in vacuum,  $\times 3000$ : (a)  $1300\text{ }^{\circ}\text{C}$ , 10 min; (b)  $1400\text{ }^{\circ}\text{C}$ , 5 min; (c)  $1500\text{ }^{\circ}\text{C}$ , 10 min; (d)  $1500\text{ }^{\circ}\text{C}$ , 20 min

It should be noted that, at all stages of annealing, rounded remains of films were not found which was observed by us earlier for disintegration on oxide substrates of metal films which, unlike titanium, are not adhesively active metals and does not wet the surface of the nonmetallic substrate.

Figure 31.3 shows diagrams for kinetics of disintegration of titanium film on the leucosapphire surface during its annealing at different temperatures ( $1300 \div 1600\text{ }^{\circ}\text{C}$ ) with exposition at each temperature from 2 up to 20 min.

Continuous titanium film at the zirconium dioxide surface was more refractory than the same film on leucosapphire and remained unchanged even after a 20-min annealing at  $1300\text{ }^{\circ}\text{C}$ . Two-minute annealing at  $1400\text{ }^{\circ}\text{C}$  caused also no change in the structure of the film, and only after the 5-min exposure, the first cracks were observed in it. With increase of annealing time up to 10, and especially up to 20 min, the film shows significant changes and starts to lose its integrity (Fig. 31.4a).

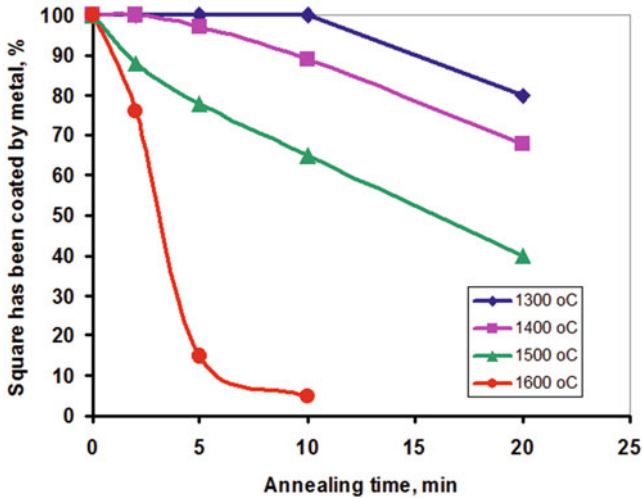




**Fig. 31.2** Titanium film 100 nm thickness onto leucosapphire which was annealed up to 1600 °C during 2 min in vacuum: (a) SEM image,  $\times 3000$ ; (b) three-dimensional AFM images; (c) AFM images of intersections on which the film profilogram was measured; (d) the film profilogram

Two-minute annealing at 1500 °C caused significant blistering of the film without losing its integrity; with a further exposition prolongation up to 5 min, the film began to crack and to fragment into pieces; after 10-min annealing, the film is rapidly divided into large fragments, which in turn were fragmented into smaller particles (Fig. 31.4b). As a result of a 20-min annealing, only a small number of pieces of the film of different sizes and irregular shapes remained.

As a result of annealing at 1600 °C, already after the 2-min exposition, all the film was blistered and began to crack (Fig. 31.4c). After 5- and 10-min exposure at 1600 °C, the film was completely disintegrated into small fragments of irregular shape forming conglomerates of various sizes (Fig. 31.4d); and after a 20-min annealing, only some crystals remained (Fig. 31.4e) which were apparently formed as a result of titanium film particles recrystallization at a temperature equal to 96% of the melting point of titanium.



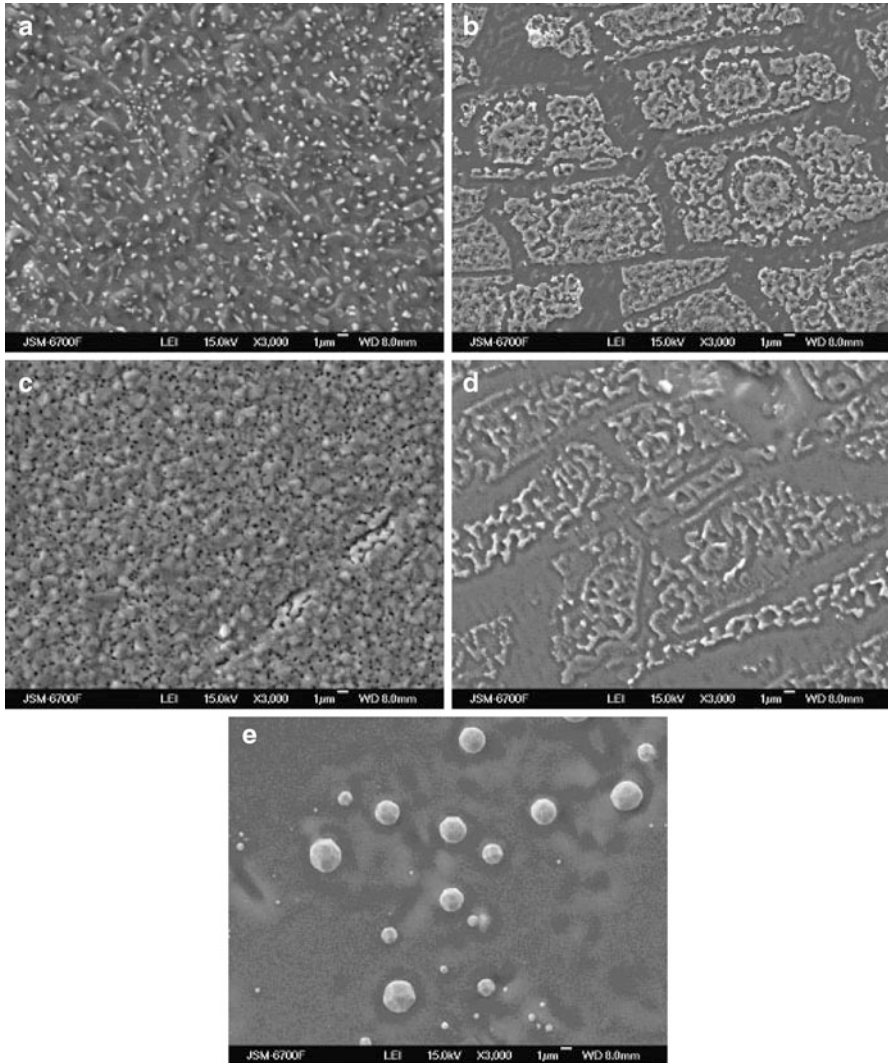
**Fig. 31.3** Leucosapphire area covered by titanium film dependence on annealing time at various temperatures (1300–1600 °C)

Figure 31.5 shows diagrams for kinetics of disintegration of titanium film deposited onto zirconium dioxide surface during its annealing at different temperatures within 1400 ÷ 1600 °C range with exposition at each temperature from 2 to 20 min.

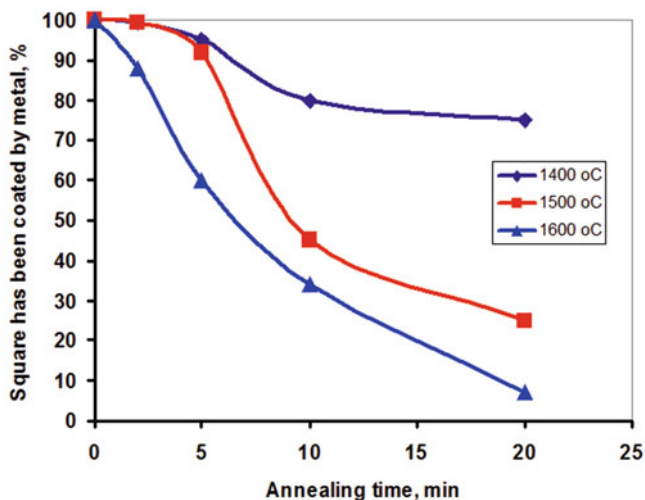
During the annealing of a zirconium film at a leucosapphire surface, the first changes in the structure of the film in the form of small cracks appeared only after 5-min annealing at 1400 °C. The number of cracks increased after 10 min of exposure at that temperature, and, after 20-min annealing, the zirconium film was already noticeably dispersed (Fig. 31.6a). After 2-h annealing at 1500 °C, the film began to disperse, and, at the same time, long but not wide cracks appeared in it. A further increase of the annealing time at this temperature up to 5 and 10 min intensified the process of cracking and dispersion of the nanofilm which significantly intensified after a 20-min exposure (Fig. 31.6b). As a result of annealing at 1600 °C, the film began to be dispersed vigorously from the first minutes of annealing, i.e., from 2 to 5 min of exposure. After 10 min of annealing at 1600 °C, the film was dispersed almost completely (Fig. 31.6c), and the process of its decomposition after 20-min exposure was completed when the film residues covered only about 20% of the surface of the leucosapphire (Fig. 31.7).

Figure 31.7 shows diagrams for kinetics of disintegration of zirconium film on the leucosapphire surface during its annealing at different temperatures (1400 ÷ 1600 °C) with exposition at each temperature from 2 up to 20 min.

The initial zirconium film at the zirconium dioxide (single crystal) surface remained solid up to 5-min annealing at 1400 °C, with only isolated cracks in it apparently due to the difference in the thermal coefficients of the linear expansion



**Fig. 31.4** SEM image titanium film 100 nm thickness onto zirconia which was annealed in vacuum,  $\times 3000$ : (a) 1400 °C, 20 min; (b) 1500 °C, 10 min; (c) 1600 °C, 2 min; (d) 1600 °C, 10 min; (e) 1600 °C, 20 min



**Fig. 31.5** Zirconia area covered by titanium film dependence on annealing time at various temperatures (1400–1600 °C)

of the zirconium ( $5 \times 10^{-6} \text{ l}^\circ\text{C}$ ) and of the single crystal of zirconium dioxide ( $11 \times 10^{-6} \text{ l}^\circ\text{C}$ ). After 10 min of annealing at 1400 °C, certain changes appeared in the nanofilm structure, and it began partially to blister and crack. After 20-min exposure, the entire film began to be dispersed (Fig. 31.8a).

Already during the first minutes of annealing of the film at 1500 °C, the beginning of its dispersion was discovered. This process was intensified with a further increase in the exposure time up to 10 min. After 20-min annealing, the film was substantially dispersed, but it covered still about 83% of the surface of the single crystal of zirconia (Fig. 31.8b).

Changes in the structure of the film were also detected after 2-h annealing at 1600 °C. After a 5-min exposure, the film was largely blistered and began to crack. After 10 min of annealing, the film began to intensively disperse (Fig. 31.8c). A 20-min exposure resulted in a strong disintegration of the film, with its elements appearing to some extent interconnected, and not completely isolated, covering about 68% of the surface of the single crystal of zirconia (Fig. 31.9). It was shown that changes in the structure of titanium and zirconium nanofilms are correlated with changes in Raman spectra of these nanofilms.

Figure 31.9 shows diagrams for kinetics of disintegration of titanium film deposited onto monocrystal zirconium dioxide surface during its annealing at different temperatures within  $1400 \div 1600 \text{ }^\circ\text{C}$  range with exposition at each temperature from 2 to 20 min.

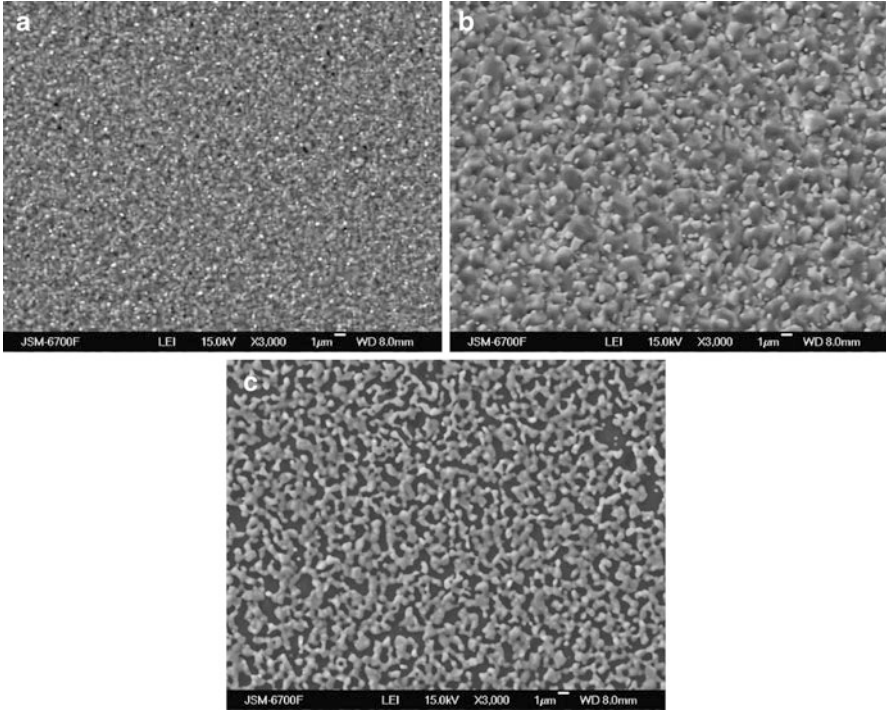


**Fig. 31.6** SEM image zirconium film 100 nm thickness onto leucosapphire which was annealed in vacuum,  $\times 3000$ : (a)  $1400^{\circ}\text{C}$ , 5 min; (b)  $1500^{\circ}\text{C}$ , 20 min; (c)  $1600^{\circ}\text{C}$ , 10 min

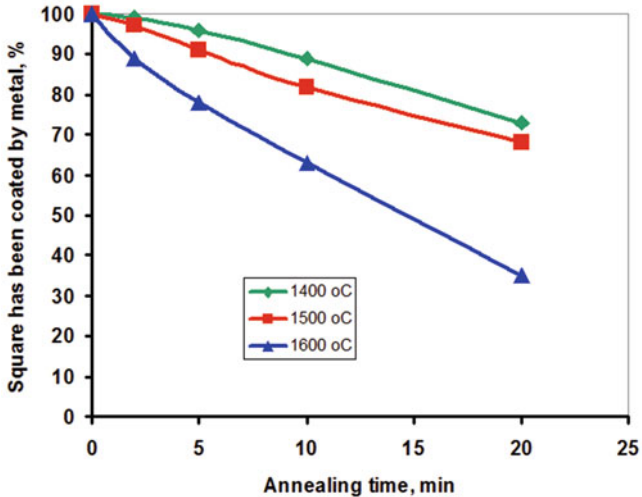


**Fig. 31.7** Leucosapphire area covered by zirconium film dependence on annealing time at various temperatures ( $1300\text{--}1600^{\circ}\text{C}$ )

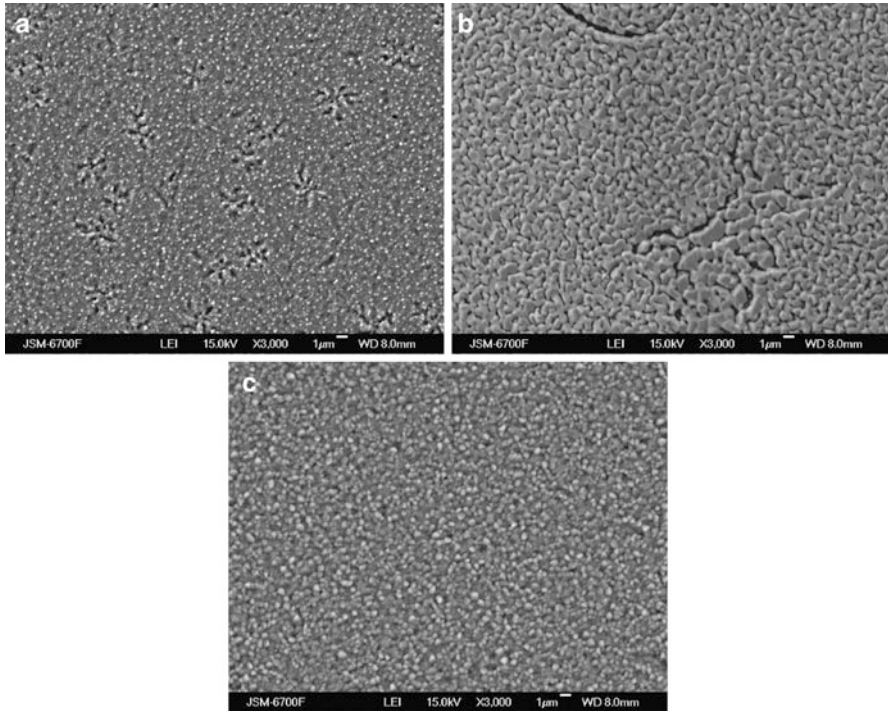


**Fig. 31.8** SEM image zirconium film 100 nm thickness onto zirconia which was annealed in vacuum,  $\times 3000$ : (a) 1400 °C, 20 min; (b) 1500 °C, 20 min; (c) 1600 °C, 10 min

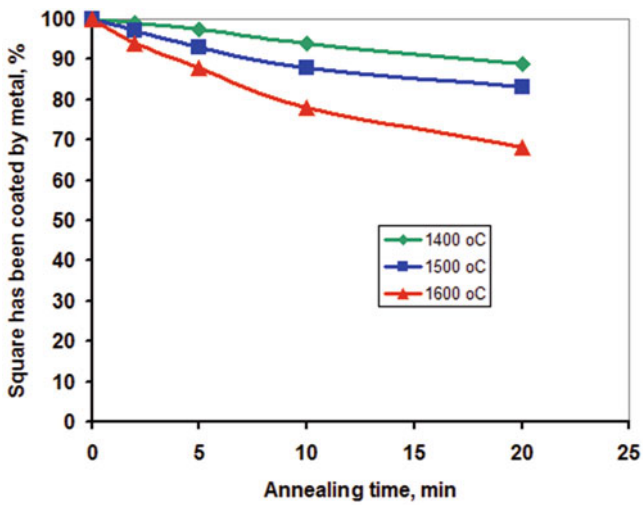


**Fig. 31.9** Zirconia area covered by zirconium film dependence on annealing time at various temperatures (1400–1600 °C)

## 31.4 Conclusions

It was found that fragmentation of 100 nm thick titanium nanofilms deposited onto leucosapphire and zirconium dioxide surfaces is characterized by approximately the same course: during short-time annealing (2–5 min) at 1400 °C, they are still almost continuous; with increase of annealing time at this temperature film, disintegration process is intensified although the film fragments cover more than 70% of the substrate surface even after a 20-min exposition; and, thus, under these conditions, the film is quite suitable for use in high-temperature brazing of these oxides. With increase of the annealing temperature up to 1600 °C, the film fragmentation rate is growing rapidly. The film disintegrates completely after a 10-min exposition at this temperature; therefore, it is not suitable for brazing.

During the study of kinetics of dispersion of zirconium nanofilms 100 nm thick at the surface of leucosapphire and single crystals of zirconium dioxide, it was determined that, up to 1400 °C, with short-term annealing (2–5 min), the film is still practically continuous.

Besides, it was found that the process of dispersion of zirconium nanofilms at the surface of leucosapphire and zirconium dioxide is intensified with increase of the annealing time at 1400 °C, but, even after a 20-min annealing, films were still covering a significant part of the surface of oxides. Approximately the same results were obtained for annealing of films at both oxides' surface at 1500 °C which makes it possible to use zirconium coatings on these materials for further soldering of them at temperatures up to 1500 °C. With annealing temperature increase up to 1600 °C, the films begin to disperse intensively from the first minutes of annealing, and this dispersion process is rapidly activated with an increase of the annealing time, which makes it impossible to solder these oxides at the temperature.

Thus, using all the obtained data in graphic representation, it becomes possible to find the necessary parameters (temperature and time) of the soldering process for the studied nonmetallic materials metallized with zirconium nanofilms.

## References

1. Hafakeyama F, Sukanuma K (1986) Solid-state bonding of alumina to austenitic stainless steel. *J Mater Sci* 21(7):2455
2. Naydich YV, Gab II, Kostyuk BD, Stetsyuk TV, Kurkova DI, Dukarov SV (2007) Investigation of the ceramic materials connection processes (soldering) using metal nanofilms. *J Rep Natl Acad Sci Ukr* 35:97 (in Ukrainian)
3. Naydich YV, Gab II, Kostyuk BD, Stetsyuk TV, Kurkova DI, Dukarov SV, Kulikovskyy VY, Onoprienko AA (2005) Effect of the thickness of metal nanofilms deposited on oxide and carbide materials for their subsequent welding and soldering, on the structural and capillary properties of films and on the strength of welded and welded joints. *Adheziya Rasplavov i Paika Materialov* 38:69 (in Ukrainian)

4. Elssner G, Diem W, Wallace JS (1981) Microstructure and mechanical properties of metal-to-ceramic and ceramic-to-ceramic joints. In: Proceedings of (17 Univ. Conf. Ceram. "Surfaces and Interfaces Ceram. and Ceram.–Metal Syst." Berkeley, Calif., July 28–August 1, 1980). New-York/London, p 629
5. Pan WX, Okamoto T, Ning XS (1994) Joining of Al-plasma-sprayed Si<sub>3</sub>N<sub>4</sub> ceramics. *J Mater Sci* 29(6):1436
6. Dalgleish BJ, Tomsia AP, Nakashima K et al (1994) Temperature routes to joining ceramics for high temperature applications (2nd Int workshop interfaces, Santiago, Sept 27–29, 1993). *Scr Met Et Mater* 31(8):1043
7. Naydich YV, Gab II, Stetsyuk TV, Kostyuk BD, Kuzmenko EF (2012) Kinetics of dispersion in annealing in vacuum of niobium and hafnium nanofilms deposited onto non-oxide materials. *Adheziya Rasplavov i Paika Materialov* 45:71 (in Ukrainian)
8. Naydich YV, Gab II, Stetsyuk TV, Kostyuk BD, Lytvin OS (2013) Dispersing kinetics during annealing in vacuum of niobium and hafnium nanofilms deposited onto oxide materials. *Svarochnoe proizvodstvo* 12:21 (in Russian)
9. Metfessel S (1963) Tonkie plenki, sh szgotovlenie I izmerenie .Gosenergoizdat, Moscow-Leningrad (in Russian)
10. Eremenko VN editors (1975) *Fizicheskaya himiya kondesirovannyh faz, sverhtverdyh materialov i ih granits razdela*. Naukova Dumka, Kiev (in Ukrainian)



# Chapter 32

## Grain Porous Structure and Exploitation Properties of Humidity-Sensitive Magnesium Aluminate Spinel-Type Ceramics



H. Klym, I. Hadzaman, O. Shpotyuk, and A. Ingram

### 32.1 Introduction

Nanostructured functional spinel-based  $\text{MgAl}_2\text{O}_4$  ceramics is considered very interesting material when it comes to applications as active elements for humidity sensors [1–3]. It is established that sensing functionality of these materials is determined largely by the microstructure of ceramics grains, grain boundaries, and pores [4]. These elements are strongly dependent on ceramics sintering route [5]. Therefore, the correlation between sintering temperature of the abovementioned ceramics, its porous structure, and exploitation properties should be carefully taken into account.

The microstructure of ceramics is typically probed with conventional X-ray diffractometry (XRD) and scanning electron microscopy (SEM) and using porosimetry methods [6, 7]. In order to obtain more information on sintering effects in  $\text{MgAl}_2\text{O}_4$  ceramics, the approach should be extended based on new methods of structural characterization. Those include the techniques that yield independent data on phase composition of ceramics bulk and small (1–2 nm) pores corresponding

---

H. Klym (✉)

Lviv Polytechnic National University, Lviv, Ukraine

e-mail: [halyna.i.klym@lpnu.ua](mailto:halyna.i.klym@lpnu.ua)

I. Hadzaman

Drohobych State Pedagogical University, Drohobych, Ukraine

O. Shpotyuk

Vlokh Institute of Physical Optics, Lviv, Ukraine

Jan Dlugosz University in Czestochowa, Czestochowa, Poland

A. Ingram

Opole University of Technology, Opole, Poland

© Springer International Publishing AG, part of Springer Nature 2018

O. Fesenko, L. Yatsenko (eds.), *Nanochemistry, Biotechnology, Nanomaterials, and Their Applications*, Springer Proceedings in Physics 214,

[https://doi.org/10.1007/978-3-319-92567-7\\_32](https://doi.org/10.1007/978-3-319-92567-7_32)

to capillary condensation processes in ceramics. One of such methods is called positron annihilation lifetime (PAL) spectroscopy [8, 9]. This is an experimental technique used to study extended defects and nanosized free-volume entities in solids despite their structural hierarchy [10].

It is well known that exploitation electrical properties of humidity-sensitive elements based on  $\text{MgAl}_2\text{O}_4$  ceramics depend on sorption processes of active materials [11]. Therefore, the actual task appears in relation to modification of porous materials with controlled microstructure, firstly, with large specific surface area, high open porosity, and controlled and optimal pore size distribution [12, 13].

In this work, we present an attempt to investigate grain porous structure of humidity-sensitive  $\text{MgAl}_2\text{O}_4$  and modified  $\text{MgO-Al}_2\text{O}_3$  ceramics using combined XRD, Hg-porosimetry, and SEM with PAL methods and influence of technological modification on exploitation properties of the studied ceramics.

## 32.2 Preparation of Magnesium Aluminate Ceramics

The traditional ceramic technology was used for preparation of spinel  $\text{MgAl}_2\text{O}_4$  and  $\text{MgO-Al}_2\text{O}_3$  ceramics, as was described in greater details elsewhere [14–18]. The samples of ceramics under study were prepared at maximum sintering temperatures  $T_s$  of 1200, 1300, and 1400 °C. Total treatment duration was 2 h. For preparation of  $\text{MgAl}_2\text{O}_4$  ceramics, initial fine-dispersed powders of  $\text{Al}_2\text{O}_3$  with specific surface area of 12.4 m<sup>2</sup>/g and MgO with specific surface area of 10.7 m<sup>2</sup>/g were used as starting components in conventional ceramics technology route [14].

For preparation of modified  $\text{MgO-Al}_2\text{O}_3$  ceramics, equimolar amounts of initial powders ( $\text{Al}_2\text{O}_3$  with specific surface area of 67 m<sup>2</sup>/g and  $4\text{MgCO}_3 \cdot \text{Mg}(\text{OH})_2 \cdot 5\text{H}_2\text{O}$  with specific surface area of 12.8 m<sup>2</sup>/g) were mixed in a planetary ball mill for 96 h in an environment with acetone to obtain mixture. The aqueous solution of polyvinyl alcohol was used for obtaining of the molding powder. Bilateral compression was performed in steel molds. After pressing, the samples were sintered also in a furnace at 1200, 1300, and 1400 °C for 2 h [16, 17].

Electrical contacts on the planar surface of all ceramics were formed by screen printing using Ru-contained paste and Pt contacts [19, 20]. Pre-dried layers of paste were sintered at 850 °C with an exposure of 10 min [21, 22].

## 32.3 Experimental Details

The phase composition of the studied ceramics was determined by XRD method. The XRD patterns were recorded at room temperature using HZG-4a powder diffractometer with  $\text{CuK}\alpha$  radiation. This equipment was calibrated with NIST SRM-1976 and Si standards. The measurements were carried out with the  $2\theta$  step of 0.05° with variable scanning rate, depending on the sample quality. The profile

analyses were performed using X-ray reflections approximation method by pseudo-Voigt function. The lattice parameters and crystal structures of phases were refined using the Rietveld method [23] and WinPLOTR software [24, 25].

The grain porous structure of ceramics was studied using scanning electron microscopy (SEM) with LEO 982 field emission microscope [14, 16, 17]. The pore size distribution of  $\text{MgAl}_2\text{O}_4$  ceramics in the region from 2 to 1000 nm was studied using Hg-porosimetry (Porosimetr 4000, Carlo Erba Strumentazione) [26, 27].

The PAL measurements with a full width at half maximum of 270 ps were performed with the ORTEC spectrometer using  $^{22}\text{Na}$  source placed between two sandwiched samples as it was described in more details elsewhere [14, 16, 28–34]. In order to study the influence of the sintering temperature on the size of nanopores in ceramic bulk, the PALS investigations were performed at 22 °C and RH = 35% after 7 days of exposure in water (vapor in desiccator at RH = 100%) and further drying in vacuum at 120 °C during 4 h. The obtained spectra were analyzed with LT 9.0 computer program [35, 36], and the best fitting results were obtained using four-component fitting procedures. Each of these spectra was processed multiple times owing to slight changes in the number of final channels, annihilation background, and the time shift of the spectrum. Then, the variance of statistically weighted least-squares deviations between experimental points and theoretical curve was taken into account to compare the obtained results. Only the results having deviations close to 1.0 (the optimal deviation typically ranges from 0.95 to  $\sim 1.1$ –1.2 [37]) were selected for further consideration. In such a manner, we obtained numerical PAL parameters (positron lifetimes  $\tau_1$ ,  $\tau_2$ ,  $\tau_3$ , and  $\tau_4$  and intensities  $I_1$ ,  $I_2$ ,  $I_3$ , and  $I_4$ ) which correspond to annihilation of positrons in the samples of interest [14, 16, 34].

The positron trapping modes in the studied ceramics were calculated using a known formalism for two-state positron trapping model [9, 38]:

$$\tau_{\text{av.}} = \frac{\tau_1 I_1 + \tau_2 I_2}{I_1 + I_2}, \tau_{\text{b}} = \frac{I_1 + I_2}{\frac{I_1}{\tau_1} + \frac{I_2}{\tau_2}}, \kappa_{\text{d}} = \frac{I_2}{I_1} \left( \frac{1}{\tau_{\text{b}}} - \frac{1}{\tau_2} \right) \quad (32.1)$$

where  $\tau_{\text{b}}$  is positron lifetime in defect-free bulk,  $\tau_{\text{av.}}$  is average positron lifetime, and  $\kappa_{\text{d}}$  is positron trapping rate of defect. In addition, the  $(\tau_2 - \tau_{\text{b}})$  difference was accepted as a size measure for extended free-volume defects where positrons are trapped (in terms of equivalent number of monovacancies), and the  $\tau_2/\tau_{\text{b}}$  ratio was taken in a direct correlation to the nature of these defects [39].

Assuming approximately spherical shape of the free volume, the *o-Ps* lifetime ( $\tau_3$  and  $\tau_4$ ) in oxide materials can be related to the average radius of pores ( $R$ ) by semiempirical Tao-Eldrup equation [40, 41]:

$$\tau_{\text{o-Ps}} = \left[ 2 \left( 1 - \frac{R}{R + \Delta R} + \frac{1}{2\pi} \sin \left( \frac{2\pi R}{R + \Delta R} \right) \right) + 0.007 \right]^{-1}, \quad (32.2)$$

where  $\Delta R$  is the empirically determined parameter (in the classical case  $\Delta R \approx 0.1656$  nm), describing effective thickness of the electron layer responsible for the “pick-off” annihilation of *o*-Ps in the hole [40].

The humidity sensitivity of ceramics was determined by measuring the dependence of electrical resistance  $R$  on relative humidity RH of environment. The electrical resistance of the studied ceramics was measured in the heat and humidity chamber PR-3E “TABAI” at 20 °C in the region of RH = 20–99%. The electrodes were attached to the connecting cables of M-Ohmmeter. Electrical measurements were made at fixed frequency of 500 Hz to avoid of polarization of adsorbed water molecules. The maximal overall uncertainties in the electrical measurements did not exceed approximately  $\pm(0.02\text{--}0.04)$  M-Ohm in electrical resistance. The confidence interval in RH measuring bar restricted by equipment accuracy was no worse than  $\pm 1\%$ . In addition, the degradation transformation at 40 °C and RH = 95% for 240 h was induced in samples in order to study their stability in time [14, 16, 17].

## 32.4 Results and Discussion

### 32.4.1 Spinel $\text{MgAl}_2\text{O}_4$ Ceramics

With respect to our XRD measurements, the ceramics sintered at 1200 °C has a three-phase composition with the lattice parameter  $a = 8.07996(3)$  Å (see Fig. 32.1).

In contrast, the ceramics sintered at 1300 °C contains only two phases, the main spinel-type (lattice parameter  $a = 8.0822(2)$  Å) and MgO phases (the remainders of  $\alpha\text{-Al}_2\text{O}_3$  phase disappear). The ceramics sintered at  $T_s = 1400$  °C in addition to the main spinel phase with lattice parameter  $a = 8.0828(1)$  Å has a small quantity of MgO phase as compared to the ceramics sintered at  $T_s = 1300$  °C (corresponding contents of MgO phase in the above ceramics are 3.48% and 1.54%, respectively) [14]. Thus, it can be concluded that there is a different amount of additional MgO/ $\text{Al}_2\text{O}_3$  phases in the studied  $\text{MgAl}_2\text{O}_4$  ceramics (see Fig. 32.1 and Table 32.1).

The obtained trimodal pore size distributions of spinel  $\text{MgAl}_2\text{O}_4$  ceramics sintered at 1200, 1300, and 1400 °C are shown in Fig. 32.2. These distributions describe the charge-transferring micropores with radius  $r_1$  depending on sintering conditions, water-exchange inside-delivering or communication mesopores ( $r_2$ ), and water-exchange outside-delivering macropores ( $r_3$ ) depending on specific surface area of milled MgO- $\text{Al}_2\text{O}_3$  powder [14, 26]. Maximum peak positions ( $r_1$ ,  $r_2$ , and  $r_3$ ) and intensities ( $I_{r1}$ ,  $I_{r2}$ , and  $I_{r3}$ ) of the pore size distribution for studied ceramics are summarized in Table 32.2. The obtained results indicate that the sintering temperature influences the porous structure of ceramics. It is shown that the radius of micropores  $r_1$  in  $\text{MgAl}_2\text{O}_4$  ceramics slightly increases from 3.2 nm for samples sintered at 1200 °C to 3.5 nm for ceramics obtained at 1300 °C. Position of the first peak  $I_{r1}$  decreases from 5% to 3% for ceramics sintered at 1100–1200 °C and is stabilized at that level in ceramics obtained at 1300–1400 °C (Fig. 32.2b, c).

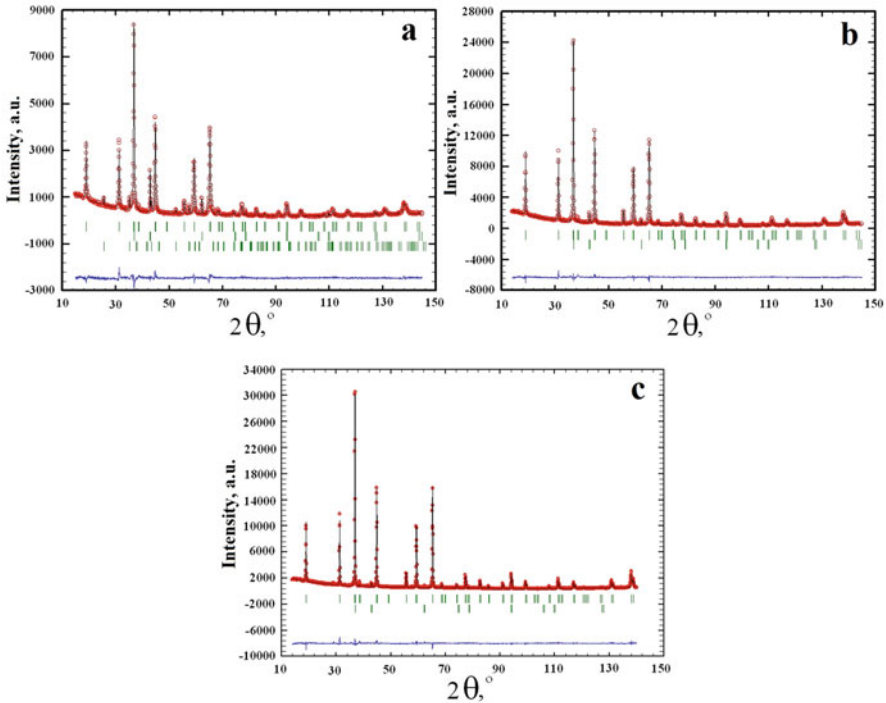


**Fig. 32.1** Experimental (rings), theoretical (line), and difference XRD pattern (down) for  $\text{MgAl}_2\text{O}_4$  ceramics sintered at 1200 °C (a), 1300 °C (b), and 1400 °C (c) (row of reflexes is the basic spinel phase)

**Table 32.1** Phase compositions of  $\text{MgAl}_2\text{O}_4$  ceramics obtained by XRD method [14]

$T_s$ , °C	Phase composition/space group					
	$\text{MgAl}_2\text{O}_4/Fd\bar{3}m$		$\alpha\text{-Al}_2\text{O}_3/R\bar{3}c$		$\text{MgO}/Fm\bar{3}m$	
	Lattice parameter, Å	Weight fraction, %	Lattice parameter, Å	Weight fraction, %	Lattice parameter, Å	Weight fraction, %
1200	$a = 8.0796(3)$	88.12	$a = 4.7585(5)$ , $c = 12.991(2)$	6.06	$a = 4.2112(2)$	5.82
1300	$a = 8.0822(2)$	96.52	–	–	$a = 4.2114(3)$	3.48
1400	$a = 8.0828(1)$	98.46	–	–	$a = 4.2117(7)$	1.54

The radius  $r_2$  substantially rises from 28 to 97 nm with increasing  $T_s$ . The peak width narrows and the intensity  $I_{r2}$  is near 2.5–4%. At the same time, the second peak is shifted toward the third peak. Obviously, such changes can be attributed to the expanding of the contact area between grains during the initial stage of sintering. Spherical pores are transformed into cylindrical. Subsequent confluence of these pores is accompanied by diminishing of their surface and volume. There is an intensive growth of grains and forming of a small number of large pores. The radius  $r_3$  slightly rises from 310 to 400 nm with increasing  $T_s$ . The intensity of the third peak  $I_{r3}$  increases from 11% to 23% [14].

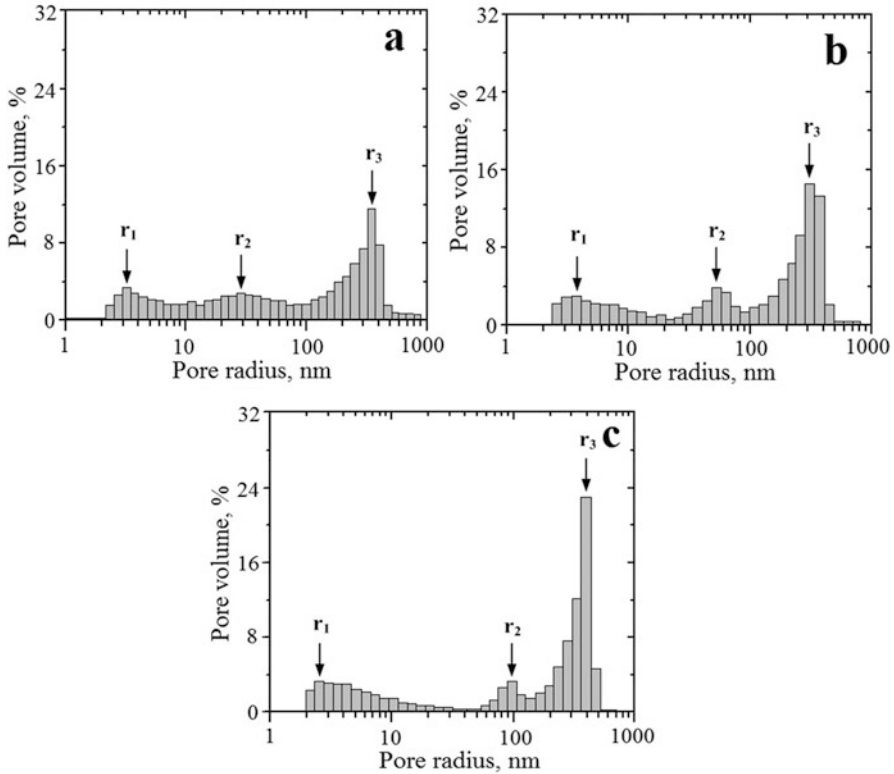


**Fig. 32.2** Pore size distributions of  $\text{MgAl}_2\text{O}_4$  ceramics sintered at 1200 °C (a), 1300 °C (b), and 1400 °C (c) [14]

**Table 32.2** Peak positions of the pore size distribution for  $\text{MgAl}_2\text{O}_4$  ceramics sintered at 1200–1400 °C [14]

$T_c$ , °C	$r_1$ , nm	$I_{r1}$ , %	$r_2$ , nm	$I_{r2}$ , %	$r_3$ , nm	$I_{r3}$ , %
1200	3.2	3	28	2.5	310	11
1300	3.5	3	43	4	320	15
1400	3.0	3	97	3	400	23

As it follows from visual examination of SEM images shown in Fig. 32.3, the structure of grains in ceramics sintered at 1200 °C is incomplete (Fig. 32.3a). Average grain size is nearly 200 nm. In ceramics sintered at 1300 °C and 1400 °C, the contact region between grains is increased (Fig. 32.3b, c). At that, the grains are integrated into agglomerates. Pores tend to shape into spherical and then cylindrical forms and locate near grain boundaries. Average grain size for these ceramic samples increases to ~300–500 nm. At the same time, the so-called “closed” porosity (not involved in absorption-desorption processes) is formed.

According to Kelvin equation [42, 43], cylindrical pores with radii between 1 and 20 nm are required for capillary condensation of humidity in ceramics at room temperature in the investigated range of RH (20–99%). Such a region includes a

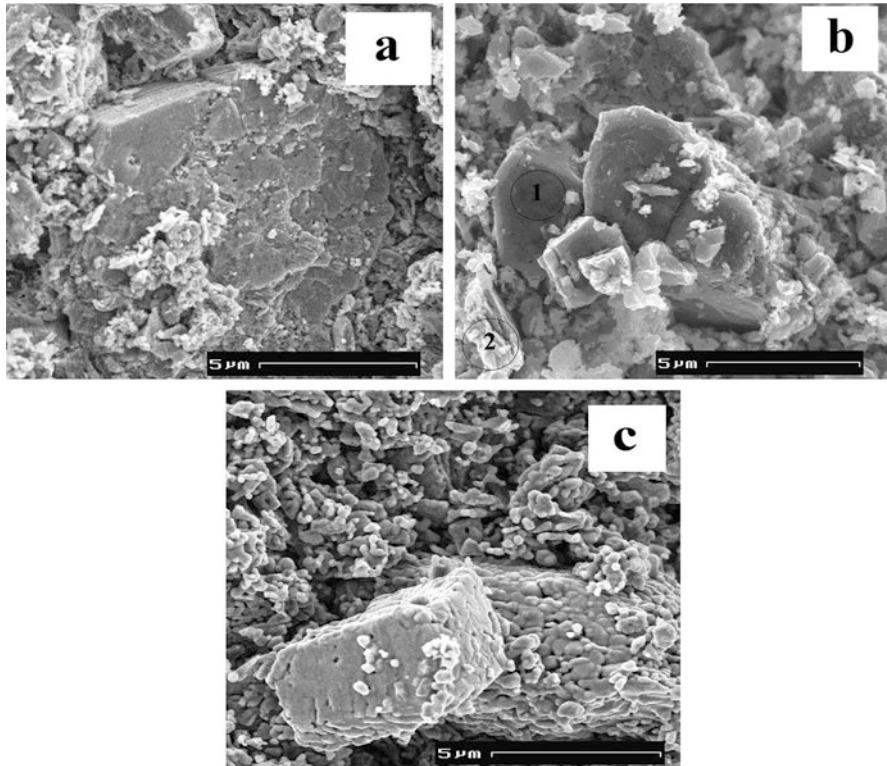


**Fig. 32.3** Scanning electron micrographs of  $\text{MgAl}_2\text{O}_4$  ceramics sintered at 1200 °C (a), 1300 °C (b), and 1400 °C (c) [14]

pore distribution peak at  $r_1$  and a secondary peak at  $r_2$ . Meso- and macropores with larger radius ( $>20$  nm, the second and the third peak) are not involved in the capillary condensation process, but they ensure the effective transfer of water into ceramic bulk. However, by using traditional porosimetry equipment, we were not able to obtain the information about pores that are smaller than 1–2 nm and other free-volume entities in ceramics. Therefore, alternative methods, such as PAL technique, are needed for the deeper understanding of adsorption/desorption processes in porous materials.

It should be noted that PAL is especially sensitive to tiny intrinsic nanopores and small free-volume entities with geometrical sizes less than  $\leq 20$  Å [8] because of the small size of  $P_s$ . Moreover, a possibility of the  $P_s$  formation should be taken into account, as it was demonstrated previously for some other kinds of glass-like [44–47] powders and fine-grained porous materials [31, 39]. As confirmed by SEM, a variety of positron trapping sites, such as grain boundaries, intrinsic surfaces of pores, incomplete contacts between some grains with pores of different geometrical sizes and shapes, etc., exist in ceramic samples.

**Table 32.3** Fitting parameters for MgAl<sub>2</sub>O<sub>4</sub> ceramics obtained according to four-component fitting procedure [14]

$T_s$ , °C	$\tau_1$ , ns	$I_1$ , a.u.	$\tau_2$ , ns	$I_2$ , a.u.	$\tau_3$ , ns	$I_3$ , a.u.	$\tau_4$ , ns	$I_4$ , a.u.
1200	0.164	0.73	0.443	0.24	2.347	0.011	70.51	0.020
1300	0.155	0.82	0.414	0.16	2.426	0.008	68.74	0.014
1400	0.152	0.88	0.388	0.11	2.504	0.007	62.32	0.008

According to SEM data, the observed phases are nonuniformly distributed within ceramics bulk, being more clearly pronounced near grain boundaries (see Fig. 32.3). These phase extractions serve as specific trapping centers for positrons penetrating ceramics. By using PAL technique in addition to XRD and porosimetry methods, we have made an attempt to study more carefully the chemical characteristics of these extracted phases in MgAl<sub>2</sub>O<sub>4</sub> ceramics sintered at different  $T_s$ . We aim also to estimate the size of nanopores in ceramics bulk, where capillary condensation processes occur.

It has been shown already that for MgAl<sub>2</sub>O<sub>4</sub> ceramics two of positron annihilation channels should be considered – the positron trapping with shortest  $\tau_1$  and middle  $\tau_2$  lifetimes and *o*-*Ps* decaying (“pick-off” annihilation) with the longest  $\tau_3$  and  $\tau_4$  lifetimes [14, 16].

Assuming the two-state positron trapping model for spinel ceramics [8, 9, 38], four components in the fit of the experimental PAL spectra can be associated with the microstructure peculiarities of the spinel. This microstructure exhibits characteristic octahedral and tetrahedral cation vacancies ( $\tau_1$ ,  $I_1$ ), positron trapping extended defects located near grain boundaries, and positron traps in the free-volume entities ( $\tau_2$ ,  $I_2$ ). *O*-*Ps* decay in the water-filled nanopores of ceramics is described by  $\tau_3$ ,  $I_3$  and  $\tau_4$ ,  $I_4$ . Within the formalism of this model, the open volume entities free of the electron density are treated as “defects,” while hypothetical structure without these entities is treated as the “defect-free” bulk (represented by  $\tau_b$  value).

It is shown (see Table 32.3) that the lifetime  $\tau_1$  of this first component decreases with  $T_s$ , while the intensity  $I_1$  increases in accordance with the amount of the main spinel phase. Smaller  $\tau_1$  lifetime reflects more perfect ceramics structure prepared at higher  $T_s$ . The second component with  $\tau_2$  lifetime is directly related to size of free-volume entity (trapping center) and extended defects near grain boundaries. The intensity  $I_2$  is proportional to the number of such “defects.”

Positrons are trapped more strongly in the spinel-type ceramics obtained at lower  $T_s$ , as reflected in the values of the middle component of the lifetime spectra. As it follows from Table 32.3, the fitting parameters of this lifetime component ( $\tau_2$  and  $I_2$ ) significantly decrease with  $T_s$ . Consequently, the corresponding positron trapping modes of extended defects near grain boundaries will also change (see Table 32.4). Indeed, the values of such parameters as  $\tau_{av}$ ,  $\tau_b$ , and ( $\tau_2 - \tau_b$ ) decrease with  $T_s$  in good accordance with the amount of MgO/Al<sub>2</sub>O<sub>3</sub> phases in



**Table 32.4** Positron trapping modes and calculated free volume for MgAl<sub>2</sub>O<sub>4</sub> ceramics

$T_s, ^\circ\text{C}$	Positron trapping modes			Free-volume (nanopores) radius	
	$\tau_{av}, \text{ns}$	$\tau_b, \text{ns}$	$\kappa_d, \text{ns}^{-1}$	$R_3, \text{Å}$	$R_4, \text{Å}$
1200	0.232	0.19	0.94	3.19	18.52
1300	0.197	0.17	0.66	3.25	18.18
1400	0.178	0.16	0.44	3.31	17.01

ceramics. Thus, the size and the number of free-volume entity and extended defects near grain boundaries in MgAl<sub>2</sub>O<sub>4</sub> ceramics decrease with sintering temperature. The characteristic size of these extended positron traps is close to that of single-double atomic vacancies. Hence, the obtained PAL results agree well with phase composition study of MgAl<sub>2</sub>O<sub>4</sub> ceramics by XRD method.

The third and the fourth longest components in lifetime spectra are due to the “pick-off” annihilation of *o*-Ps atoms in nanopores. Despite small  $I_3$  intensity, these components cannot be eliminated without significant losses in the quality of the fitting procedure. Similar components were detected in different porous substances with different structural type [39, 48]. It can be surmised that these components are related to predominant *o*-Ps “pick-off” decay in nanopores. The  $\tau_3$  lifetime of the third component increases with  $T_s$ . At the same time its intensity  $I_3$  decreases. These changes correspond to increased nanopore size and smaller amount of nanopores. But size and amount of smaller nanopores in ceramics bulk decrease with  $T_s$  which is manifested in changes of  $\tau_4$  lifetime and  $I_4$  intensity.

The radius of free volumes of nanopores in MgAl<sub>2</sub>O<sub>4</sub> ceramics was calculated using Tao-Eldrup model [40, 41] considering *o*-Ps “pick-off” lifetimes of the third and fourth components with lifetimes  $\tau_3$  and  $\tau_4$ . With increasing of ceramics sintering temperature, the free-volume radius  $R_3$  increases from 3.19 to 3.31 Å and  $R_4$  decreases from ~18.5 Å to 17 Å (Table 32.4). Thus, the MgAl<sub>2</sub>O<sub>4</sub> ceramics with more perfect structure is characterized by larger nanopores needed for effective capillary condensation process.

Changes caused by different pore size distribution and amount of these pores in all regions were reflected in humidity sensitivity of the studied MgAl<sub>2</sub>O<sub>4</sub> ceramics. In spite of small amount of transporting pores, ceramics sintered at 1200–1300 °C are characterized by a short linear dependence of electrical resistance  $R$  vs. RH with an noticeable hysteresis in absorption-desorption cycles ( $T_s = 1200$ – $1300$  °C). However, after the degradation transformation, these ceramic samples show linear dependences in the region of RH = 30–95% (Fig. 32.4a, b). After 240 h at 40 °C and RH = 95%, the profiles of these dependences are changed and shifted. In ceramics sintered at 1400 °C with optimal pore size distribution and necessary number of nanopores tested by PAL method, the dependence  $R$  vs. RH is practically linear in all studied RH regions without hysteresis before and after the degradation transformation [14].

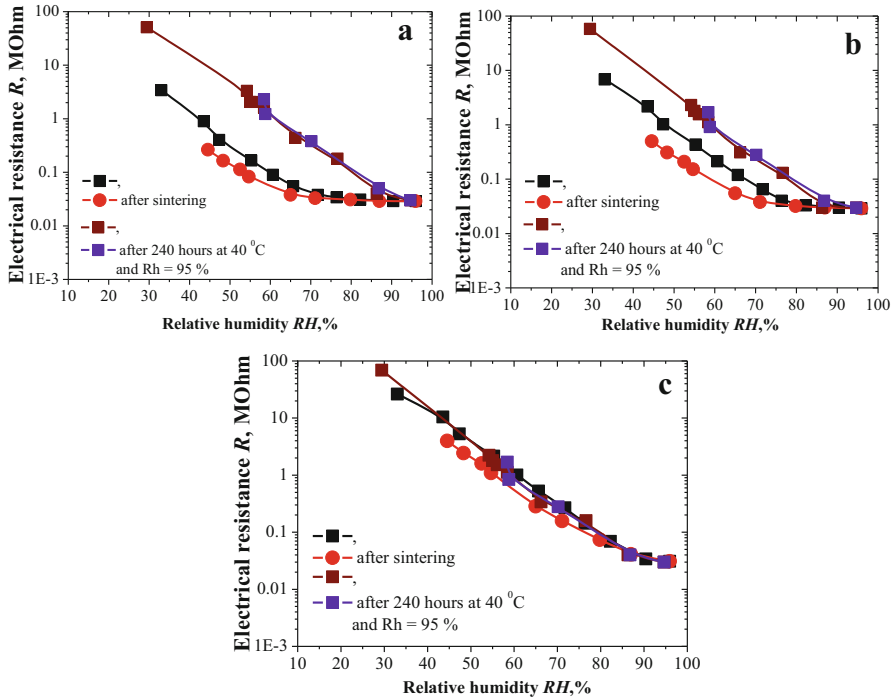


Fig. 32.4 Exploitation properties of  $\text{MgAl}_2\text{O}_4$  ceramics sintered at 1200 °C (a), 1300 °C (b), and 1400 °C (c) [14]

### 32.4.2 Modified $\text{MgO-Al}_2\text{O}_3$ Ceramics

Our results obtained with XRD method testify that ceramics sintered  $T_s = 1200\text{--}1400$  °C contain two phases: the main spinel-type  $\text{MgAl}_2\text{O}_4$  phase (space group  $Fd\bar{3}m$ ) and some additives of additional  $\text{MgO}$  (space group  $Fm\bar{3}m$ ) (see Fig. 32.5). The phase composition and lattice parameter values of  $\text{MgO-Al}_2\text{O}_3$  ceramics obtained with XRD method are shown in Table 32.5.

Thus, increase in the sintering temperature from 1200 to 1400 °C leads to the formation of spinel phase; the corresponding lattice parameter slightly increases within this process being at the level of 8.08 Å (see Table 32.5). So, we can conclude that in magnesium aluminate ceramics, the same spinel-type phase is formed regardless of  $T_s$  like in [14].

The pore size distributions of technologically modified  $\text{MgO-Al}_2\text{O}_3$  ceramics obtained at 1200, 1300, and 1400 °C are shown in Fig. 32.6. Such distribution covers the charge-transferring nanopores with  $r_1$  radius depending on sintering conditions, water-exchange inside-delivering or communication mesopores ( $r_2$  radius), and water-exchange outside-delivering macropores ( $r_3$  radius) depending on specific surface area of milled  $\text{MgO-Al}_2\text{O}_3$  powder. Maximum peak positions ( $r_1$ ,  $r_2$ , and

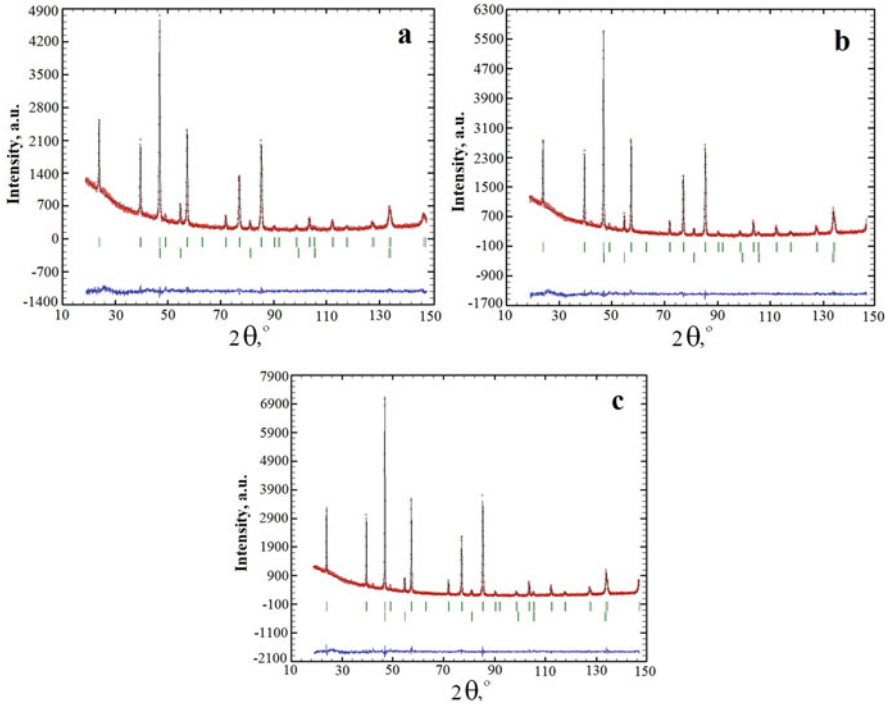


**Fig. 32.5** Observed and calculated XRD profiles for MgO-Al<sub>2</sub>O<sub>3</sub> ceramics sintered at 1200 °C (a), 1300 °C (b), and 1400 °C (c); the overhead row of reflexes is spinel phase; the lower row of reflexes is MgO phase [16]

**Table 32.5** Phase composition of the modified MgO-Al<sub>2</sub>O<sub>3</sub> ceramics [16, 17]

$T_c$ , °C	Main MgAl <sub>2</sub> O <sub>4</sub> phase		Additional MgO phase	
	Lattice parameter, Å	Weight fraction, %	Lattice parameter, Å	Weight fraction, %
1200	8.0809(2)	93.63(0.78)	4.2124(4)	6.37(0.27)
1300	8.0812(2)	94.12(0.80)	4.2145(4)	5.88(0.30)
1400	8.0808(1)	94.05(0.78)	4.2169(4)	5.95(0.34)

$r_3$ ) and intensities ( $I_{r1}$ ,  $I_{r2}$ , and  $I_{r3}$ ) of pore size distribution for studied ceramics prepared at 1200, 1300, and 1400 °C are shown in Table 32.6.

Ceramics sintered at 1200 °C exhibit trimodal pore size distribution with maximum position of  $r_1$ ,  $r_2$ , and  $r_3$  near 2.3, 35, and 160 nm, respectively (Table 32.6 and Fig. 32.6a). It is established that large open pores with size near 100–300 nm correspond to open surface pores in ceramics. They are involved in absorption-desorption process of water from environment. Pores centered near 35 nm are so-called transporting pores providing the effective passing of water into ceramic body [14, 17].

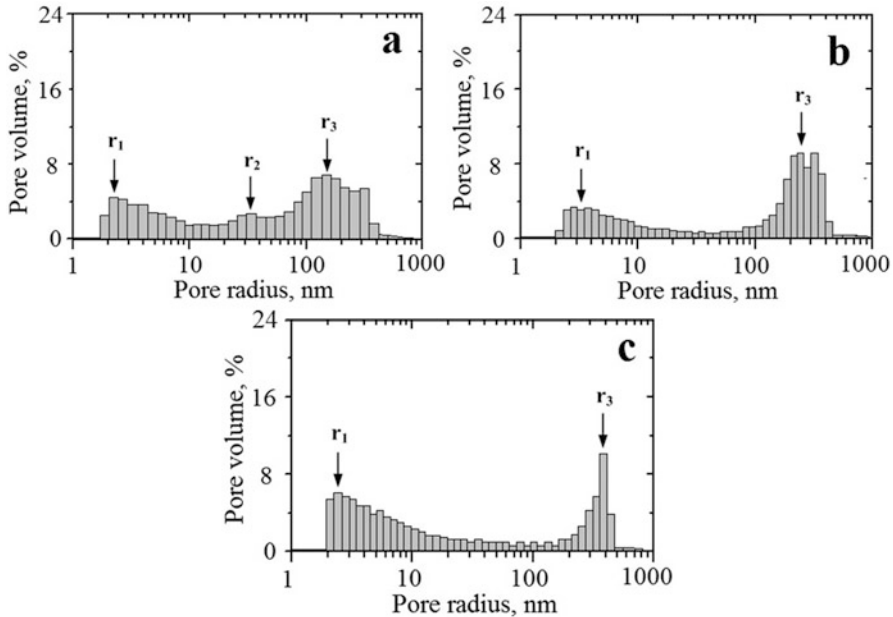


**Fig. 32.6** Pore size distributions of MgO-Al<sub>2</sub>O<sub>3</sub> ceramics sintered at 1200 °C (a), 1300 °C (b), and 1400 °C (c) [16, 17]

**Table 32.6** Peak position of pore size distribution for modified MgO-Al<sub>2</sub>O<sub>3</sub> ceramics sintered at 1200–1400 °C

$T_c$ , °C	$r_1$ , nm	$I_{r_1}$ , %	$r_2$ , nm	$I_{r_2}$ , %	$r_3$ , nm	$I_{r_3}$ , %
1200	2.3	4.5	35	3.4	160	6.9
1300	2.9	3.2	–	–	270	9.1
1400	2.5	6.0	–	–	380	10.3

According to Kelvin equation [40, 41], the open cylindrical nanopores with a radius from smaller 1 nm to 20 nm are required for capillary condensation processes of humidity in ceramics at room temperature in the range of relative humidity of 30–98%. Such region includes peak with radius  $r_1$  and partly peak with radius  $r_2$ . Meso- and macropores with radius more than 20 nm (the second and the third peak) are not involved in capillary condensation process, but they are needed for effective passing of water into ceramic body.

The obtained results indicate that the sintering temperature influences the porous structure of ceramics. It is shown that radius of nanopores  $r_1$  in studied ceramics slightly increases from 2.3 nm for samples sintered at 1200 °C to 2.9 nm for ceramics obtained at 1300 °C (Fig. 32.6a, b). Intensity of the first peak  $I_{r_1}$  changes from 4.5% to 3.2% for ceramics sintered at 1200–1300 °C with further growth to 6% in ceramics obtained at 1400 °C (Fig. 32.6c). The position of the second peak with radius  $r_2$  is observed in ceramics sintered at 1200 °C. At the same time, it is shown that this peak is shifted in the direction of the third peak. In ceramics sintered at 1300 and 1400 °C, the clear peak position corresponding to

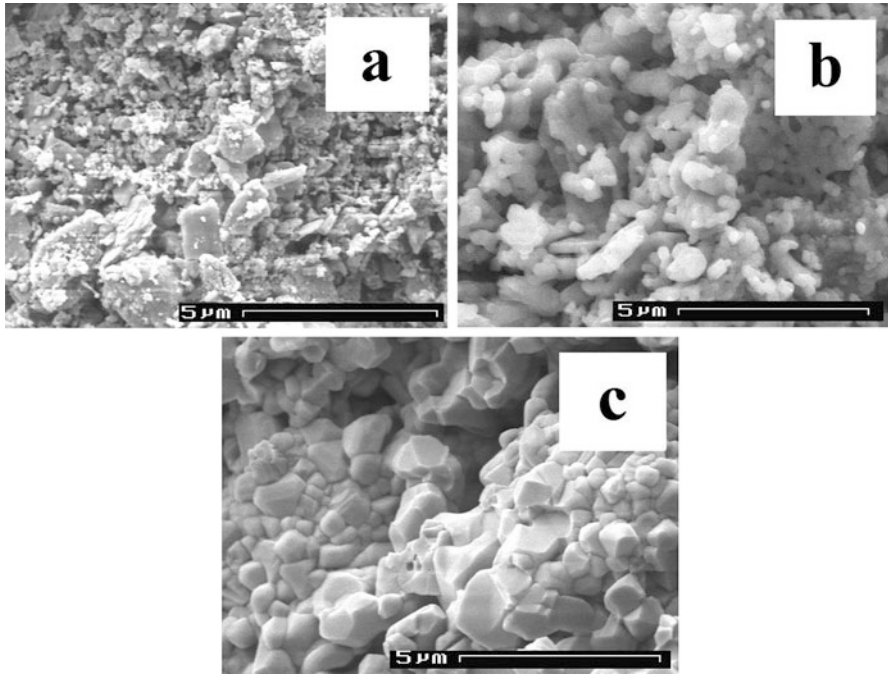


**Fig. 32.7** SEM micrograph of the modified MgO-Al<sub>2</sub>O<sub>3</sub> ceramics sintered at 1200 °C (a), 1300 °C (b), and 1400 °C (c) [16, 17]

radius  $r_2$  cannot be resolved. But some amount of open mesopores still remains. Thus, trimodal pore size distribution is transformed into bimodal, similarly to [26]. Obviously, such changes can be attributed to the growth of grains during sintering at high temperature with future decreasing of size and amount of pores. Subsequent confluence of pores is accompanied by diminishing of their surface and volume. There occurs an intensive growth of grains and forming of large pores. As a result, the pore size distribution is translocated to macropores region (Fig. 32.6b). Radius  $r_3$  substantially rises from 160 to 380 nm with  $T_s$  of ceramics obtained from 1200 to 1400 °C. The intensity  $I_{r_3}$  of the third peak increases from 6.9% to 10.3% (Table 32.2 and Fig. 32.6b, c).

Evolution of porous structure is confirmed by the results of SEM investigations. It is shown that structure grains and pores in ceramics sintered at 1200 °C are not well formed. Average grain size is about 200 nm. Additional MgO phase is unevenly distributed in the volume of studied ceramics and mostly located near grain boundaries bordering the pores (Fig. 32.7a). With increasing of sintering temperature to 1300 °C, the contact area between grains grows, specific surface area increases, the grains are combined into agglomerates, and the amount of open pores increases. Such pores adopt initially spherical and then cylindrical shapes being located on the grain boundaries (Fig. 32.7b). Average grain size increases to 300–

**Table 32.7** Fitting parameters of modified MgO-Al<sub>2</sub>O<sub>3</sub> ceramics mathematically treated with four-component fitting procedure

$T_c$ , °C	$\tau_1$ , ns	$I_1$ , a.u.	$\tau_2$ , ns	$I_2$ , a.u.	$\tau_3$ , ns	$I_3$ , a.u.	$\tau_4$ , ns	$I_4$ , a.u.
1200	0.16	0.65	0.38	0.33	2.03	0.010	48.4	0.011
1300	0.15	0.67	0.35	0.32	1.98	0.007	40.8	0.005
1400	0.15	0.67	0.35	0.31	1.94	0.008	42.4	0.005

500 nm. These ceramic samples have better developed porosity. Along with this, closed porosity is formed due to the growth of small pores. These closed pores are not involved in the sorption processes in the studied ceramics [17]. In ceramics sintered at 1400 °C, the grain structure continues to take shape showing their intense coagulation. The average size of the grains is near 600–3000 nm. However, the porous structure is modified mainly due to increasing of closed porosity and reduction of channel transport pores (Fig. 32.7c).

As it follows from XRD measurements, the studied MgO-Al<sub>2</sub>O<sub>3</sub> ceramics have a different amount of additional MgO phase. In accordance with SEM data, the observed additional phases are nonuniformly distributed within the ceramics bulk, being more clearly pronounced near grain boundaries (see Fig. 32.7). These phase extractions serve as specific trapping centers for positrons penetrating the ceramics. So, by using PAL method, we shall try to study more carefully chemical characteristics of these extracted phases and nanosize free-volume entities (nanopores) in MgO-Al<sub>2</sub>O<sub>3</sub> ceramics sintered at different  $T_s$ .

As it was shown early, in the case of MgAl<sub>2</sub>O<sub>4</sub> ceramics, two independent channels of positron annihilation should be considered – the positron trapping with short  $\tau_1$  and  $\tau_2$  lifetimes and *o*-Ps decaying with longer  $\tau_3$  and  $\tau_4$  lifetimes.

Taking into account the model described in [8, 9, 38], the shortest lifetime component (the first channel of positron annihilation) in the studied ceramics reflects mainly the microstructure specificity of the spinel with characteristic octahedral and tetrahedral cation vacancies. It is shown (see Table 32.7) that the lifetime  $\tau_1$  of this first component slightly decreases with  $T_s$ , while the intensity  $I_1$  increases in accordance with the amount of the main spinel phase (see Tables 32.5 and 32.7). Apparently, the decreasing of  $\tau_1$  lifetime reflects more perfect ceramics structure prepared at higher  $T_s$ . By accepting two-state positron trapping model [38], the longer  $\tau_2$  lifetime can be treated as defect-related one, these positron trapping defects being located near grain boundaries [16]. According to our XRD measurements, in the studied MgO-Al<sub>2</sub>O<sub>3</sub> ceramics, the amount of additional phases is dependent on  $T_s$  (see Table 32.5). Thus, the positrons are trapped more strongly in the spinel-type ceramics obtained at lower  $T_s$ , which is reflected in the middle component of lifetime spectra. As it follows from Table 32.3, the fitting parameters of this lifetime component ( $\tau_2$  and  $I_2$ ) significantly decrease with  $T_s$ . Consequently, the corresponding positron trapping modes of extended defects near grain boundaries will be changed as well.

Indeed, the values of such parameters as  $\tau_{av}$ ,  $\tau_b$ ,  $\tau_d$ , and  $(\tau_2 - \tau_b)$  decrease with  $T_s$  in good accordance with the amount of additional MgO phase in the studied

**Table 32.8** Positron trapping modes and free-volume radius in the modified MgO-Al<sub>2</sub>O<sub>3</sub> ceramics

$T_c, ^\circ\text{C}$	Free-volume (nanopores) radius		Positron trapping modes				
	$R_3, \text{nm}$	$R_4, \text{nm}$	$\tau_{av}, \text{ns}$	$\tau_b, \text{ns}$	$\kappa_d, \text{ns}^{-1}$	$\tau_2 - \tau_b, \text{ns}$	$\tau_2/\tau_b$
1200	0.291	1.459	0.24	0.20	1.07	0.18	1.89
1300	0.286	1.328	0.22	0.19	0.85	0.20	2.03
1400	0.282	1.357	0.22	0.19	0.81	0.21	2.10

ceramics (see Table 32.8). But in all cases, the same type of positron trapping center is formed since  $\tau_2/\tau_b$  values are near 2.0. The characteristic size of these extended positron traps near grain boundaries estimated from  $(\tau_2 - \tau_b)$  difference is close to single-double atomic vacancies [14].

The third and the fourth longest components in the resolved lifetime spectra are due to “pick-off” annihilation of *o*-*Ps* atoms in the intergranular pores. It can be surmised that these components are owing to predominant *o*-*Ps* “pick-off” decaying. The  $\tau_3$  and  $\tau_4$  lifetimes of these components decrease with  $T_s$ . These changes are connected with more branched structure of the open pores of the ceramics sintered at higher  $T_s$  (1300 and 1400 °C). With  $T_s$  increased, the *o*-*Ps* “pick-off” decaying occurs preferentially in the nanopores filled by absorbed water, while the ceramic samples sintered at relatively low  $T_s$  (1200 °C) show this process in both water-filled and water-free nanopores.

Recently, PAL spectroscopy started to be used as an alternative porosimetry technique to characterize the local free volumes, first of all in both open and closed nanopores. The PAL method is particularly effective when *Ps* is formed. In disordered solids, *Ps* is usually organized in two ground state (*p*-*Ps* and *o*-*Ps*) and localized in the pores and free volumes. Usually, quantification is based on the analysis of *o*-*Ps* lifetime (the lifetimes of the third and fourth components  $\tau_3$  and  $\tau_4$  in MgO-Al<sub>2</sub>O<sub>3</sub> ceramics corresponds to *o*-*Ps* lifetime). The *o*-*Ps* “pick-off” annihilation depends on the size of pores and gives additional important information on the void structure of the materials. Despite small  $I_3$  and  $I_4$  intensities for MgO-Al<sub>2</sub>O<sub>3</sub> ceramics, it is possible to estimate the average nanopores size from *o*-*Ps* lifetime in a given material.

In MgO-Al<sub>2</sub>O<sub>3</sub> ceramics, there are two *o*-*Ps*-related PAL components. Therefore,  $\tau_3$  and  $\tau_4$  lifetimes can be related to corresponding pores via Tao-Eldrup model. The nanopores radii  $R_3$  and  $R_4$  calculated using corresponded  $\tau_{o-Ps}$  values are shown in Table 32.8. The  $\tau_{o-Ps}$  value of around  $\sim 40 \div 48$  ns corresponds to nanopores with radius ( $R_4$ ) distribution centered near  $\sim 1.3 \div 1.5$  nm. Most probably, these pores correspond to the empty volumes associated with mismatches in the packing of extended atomic group (clusters, fractals, etc.). The similar lifetime  $\tau_3 \approx 2$  ns was also observed in MgO-Al<sub>2</sub>O<sub>3</sub> ceramics, and its origin was associated with fine pores of  $R_3 \sim 0.3$  nm. Fraction of nanopores associated with *o*-*Ps* lifetimes can be estimated by the intensities of corresponding long-lived components ( $I_3$  and  $I_4$ ). However, contrary to the short-lifetime components, annihilating almost entirely via two-quantum annihilation, substantial part of *o*-*Ps* annihilates also

via three-quantum process, which is completed by the “pick-off” annihilation process [49–51]. Different efficiency of the registration for two- and three-quantum processes can distort the proportion between observed  $o$ - $P_s$  annihilation intensities ( $I_3$  and  $I_4$ ) introducing uncertainty into the estimation of the number of pores. In addition, it should be noted that porosimetry methods are limited to open pores, which should have an access to the environment to be determined. These PAL results are complementary data to Hg-porosimetry measurements. On the other hand, PAL spectroscopy can probe both open and closed pores in functional humidity-sensitive ceramics of sizes ranging from atomic scale to several tens of nanometers.

Changes caused by sintering temperature on pore size distribution were reflected in humidity sensitivity of MgO- $\text{Al}_2\text{O}_3$  ceramics. Hence, ceramics sintered at low temperature (1200 °C) has enough of open pores in all regions. Such behavior of pore size distribution is manifested in electrical properties of ceramic samples. They have good sensitivity (changes of electrical resistance  $\sim 4$  orders) between average values of relative humidity (33–95%) and minimal hysteresis of resistance dependence in adsorption-desorption cycles (Fig. 32.8a).

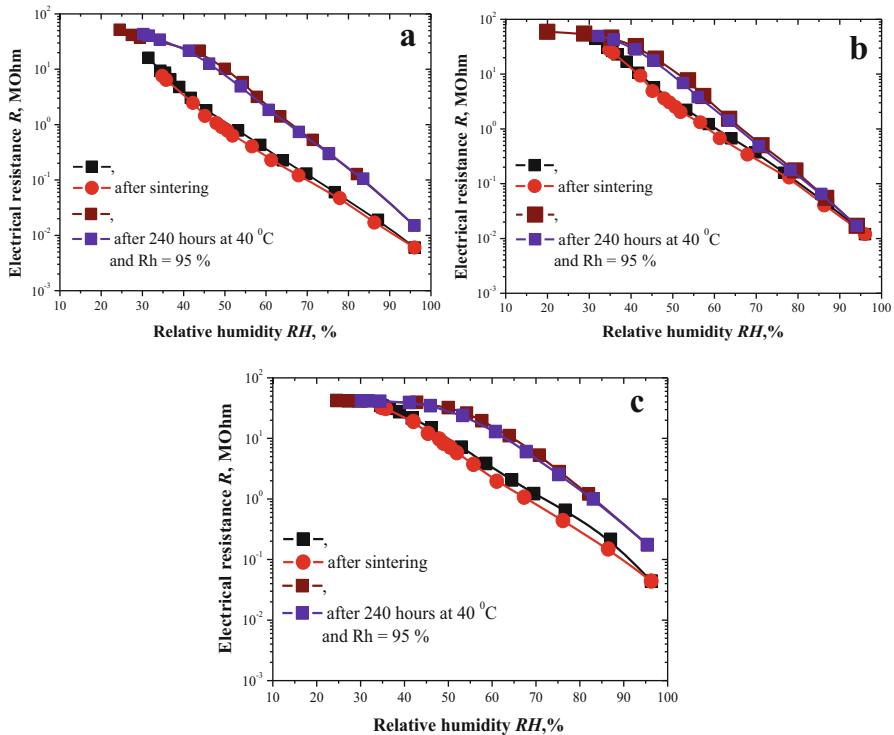


**Fig. 32.8** Exploitation properties of the modified MgO- $\text{Al}_2\text{O}_3$  ceramics sintered at 1200 °C (a), 1300 °C (b), and 1400 °C (c) [16]



In spite of a small amount of transporting pores, ceramics sintered at 1300 °C are characterized by linear dependence of electrical resistance  $R$  vs. RH in the entire studied region without significant hysteresis in absorption-desorption cycles (Fig. 32.8b). But after degradation tests there is a drop in sensitivity down to 35%. However, studied characteristics before and after degradation does not change substantially.

In contrast to other ceramic samples, ceramics sintered at 1400 °C have a small amount of macropores centered near  $r_3 = 380$  nm. Humidity sensitivity of these ceramics is characterized by linearity but with appreciable hysteresis (Fig. 32.8c).

Thus, humidity sensitivity in ceramics sintered at low 1200 °C and recoverability of electrical characteristic in adsorption-desorption cycles are obviously connected with sufficient amount of open pores with different size from all pore size distribution region. Increasing of humidity sensitivity and stability of ceramics sintered at 1300°C results in increased amount of open water-exchange outside-delivering macropores. They provide efficient sorption processes of water through small amount of communication mesopores [16, 17].

Bimodal pore size distribution of ceramics sintered at 1400°C continues to be modified. Capillary condensation processes effectively occur due to increasing of amount of transferring nanopores. Hysteresis in absorption-desorption cycles becomes larger due to the reduction of pores with radius  $r_3$ .

## 32.5 Conclusions

It is shown that the structure of humidity-sensitive spinel  $\text{MgAl}_2\text{O}_4$  ceramics is improved with the increase of the sintering temperature, which mainly results in the transformation of the pore size distribution and decreasing of amount of  $\text{MgO}/\text{Al}_2\text{O}_3$  phases located near grain boundaries. Positrons are trapped more intensively in the spinel ceramics obtained at lower temperature. This is reflected in the second component of the lifetime spectra. The third and the fourth longest components of the spectra are due to “pick-off” annihilation of  $o$ - $Ps$  atoms in nanopores. Tao-Eldrup model can be applied in order to calculate of nanopore size in ceramic materials.

It is established that the sintering temperature allows to change the porous structure of ceramic materials. Evolution of pore size distribution in humidity-sensitive spinel  $\text{MgAl}_2\text{O}_4$  ceramics leads to corresponding changes in water-sorption processes in these materials. Degradation transformations at 40 °C and RH = 95% result in the increased humidity sensitivity of ceramics in all studied regions with minimal hysteresis. Such changes confirm the active work of transporting pores after the full saturation of some nanopores by water is reached.

The sintered temperatures allow to refine the most significant changes in free-volume (porous) structure of modified  $\text{MgO}-\text{Al}_2\text{O}_3$  ceramics and to decrease the amount of additional phases located near grain boundaries. Evolution of pore size distribution from tri- to bimodal in the studied ceramics leads to corresponding

changes in pore-related water-sorption processes. The increase of humidity sensitivity in ceramics sintered at 1300 °C is related to the fact that close to optimal pore size distribution is achieved. It is shown that in all sintered samples there are pores with radii larger than 10–20 nm, which do not participate in the processes of capillary condensation, although their presence is needed to support fast response of humidity-sensitive elements to the change of relative humidity. Positrons are trapped more strongly in the spinel-type ceramics obtained at lower temperature, and this is reflected in the second component of lifetime spectra. The third and the fourth longest components in the resolved lifetime spectra are due to “pick-off” annihilation of *o*-*Ps* atoms in the intergranular pores. The observed *o*-*Ps* lifetimes are related to the nanopores with radius of  $\sim 0.3$  and  $\sim 1.3 \div 1.5$  nm based on classic Tao-Eldrup equation. The reported data were confirmed by Hg-porosimetry and SEM results.

**Acknowledgment** H. Klym thanks the Ministry of Education and Science of Ukraine for its support (grant no. 0116 U004411).

## References

1. Zhi C, Chi L (2005) Humidity sensors: a review of materials and mechanisms. *Sens Lett* 3(4):274–295. <https://doi.org/10.1166/sl.2005.045>
2. Kulwicki BM (1991) Humidity sensors. *J Am Ceram Soc* 74(4):697–708. <https://doi.org/10.1111/j.1151-2916.1991.tb06911.x>
3. Li Y, Fu ZY, Su BL (2012) Hierarchically structured porous materials for energy conversion and storage. *Adv Funct Mater* 22(22):4634–4667. <https://doi.org/10.1002/adfm.201200591>
4. Gusmano G, Montesperelli G, Traversa E (1993) Microstructure and electrical properties of  $\text{MgAl}_2\text{O}_4$  thin film for humidity sensors. *J Am Ceram Soc* 76:743–750. <https://doi.org/10.1111/j.1151-2916.1993.tb03669.x>
5. Farahani H, Wagiran R, Hamidon MN (2014) Humidity sensors principle, mechanism, and fabrication technologies: a comprehensive review. *Sensors* 14(5):7881–7939. <https://doi.org/10.3390/s140507881>
6. Asami K, Mitani S, Fujimori H, Ohnuma S, Masumoto T (1999) Characterization of Co-Al-O magnetic thin films by combined use of XPS, XRD and EPMA *Surf Interface Anal* 28:250–253. [https://doi.org/10.1002/\(SICI\)1096-9918\(199908\)28:1<250::AID-SIA587>3.0.CO;2-T](https://doi.org/10.1002/(SICI)1096-9918(199908)28:1<250::AID-SIA587>3.0.CO;2-T)
7. Asami K, Ohnuma T (1998) Masumoto XPS and X-ray diffraction characterization of thin Co-Al-N alloy films prepared by reactive sputtering deposition. *Surf Interface Anal* 26:659–666. [https://doi.org/10.1002/\(SICI\)1096-9918\(199808\)26:9<659::AID-SIA412>3.0.CO;2-Z](https://doi.org/10.1002/(SICI)1096-9918(199808)26:9<659::AID-SIA412>3.0.CO;2-Z)
8. Krause-Rehberg R, Leipner HS (1999) Positron annihilation in semiconductors. In: *Defect studies*. Springer, Berlin/Heidelberg/New York, p 378
9. Shpotyuk O, Filipecki J (2003) Free volume in vitreous chalcogenide semiconductors: possibilities of positron annihilation lifetime study. *Wyd-wo WSP w Czestochowie, Czestochowa*
10. Hübner C, Staab T, Krause-Rehberg R (1995) On the interpretation of positron-annihilation data in powders and fine-grained materials. *Appl Phys A* 61(2):203–206. <https://doi.org/10.1007/BF01538390>
11. Weaver PM, Cain MG, Stewart M, Anson A, Franks J, Lipscomb IP, McBride JP, Zheng D, Swingler J (2012) The effects of porosity, electrode and barrier materials on the conductivity of piezoelectric ceramics in high humidity and dc electric field smart materials and structures. *Smart Mater Struct* 21(4):045012. <https://doi.org/10.1088/0964-1726/21/4/045012>

12. Armatas GS, Salmas CE, Louludi MG, Androutopoulos P, Pomonis PJ (2003) Relationships among pore size, connectivity, dimensionality of capillary condensation, and pore structure tortuosity of functionalized mesoporous silica. *Langmuir* 19:3128–3136. <https://doi.org/10.1021/la020261h>
13. Kashi MA, Ramazani A, Abbasian H, Khayyatian A (2012) Capacitive humidity sensors based on large diameter porous alumina prepared by high current anodization. *Sensors Actuators A* 174:69–74. <https://doi.org/10.1016/j.sna.2011.11.033>
14. Klym H, Ingram A, Hadzaman I, Shpotyuk O (2014) Evolution of porous structure and free-volume entities in magnesium aluminate spinel ceramics. *Ceram Int* 40(6):8561–8567. <https://doi.org/10.1016/j.ceramint.2014.01.070>
15. Klym H, Ingram A, Shpotyuk O, Hadzaman I, Solntsev V (2016) Water-vapor sorption processes in nanoporous MgO-Al<sub>2</sub>O<sub>3</sub> ceramics: the PAL spectroscopy study. *Nanoscale Res Lett* 11(1):1. <https://doi.org/10.1186/s11671-016-1352-6>
16. Klym H, Ingram A, Shpotyuk O, Hadzaman I, Hotra O, Kostiv Y (2016) Nanostructural free-volume effects in humidity-sensitive MgO-Al<sub>2</sub>O<sub>3</sub> ceramics for sensor applications. *J Mater Eng Perform* 25(3):866–873. <https://doi.org/10.1007/s11665-016-1931-9>
17. Klym H, Hadzaman I, Shpotyuk O (2015) Influence of sintering temperature on pore structure and electrical properties of technologically modified MgO-Al<sub>2</sub>O<sub>3</sub> ceramics. *Mater Sci* 21(1):92–95 <https://doi.org/10.5755/j01.ms.21.1.5189>
18. Klym H, Shpotyuk O, Ingram A, Calvez L, Hadzaman I, Yu K, Ivanusa A, Chalyy D (2017) Influence of free volumes on functional properties of modified chalcogenide glasses and oxide ceramics. *Springer Proc Phys* 195:479–493. [https://doi.org/10.1007/978-3-319-56422-7\\_36](https://doi.org/10.1007/978-3-319-56422-7_36)
19. Shpotyuk O, Balitska V, Brunner M, Hadzaman I, Klym H (2015) Thermally-induced electronic relaxation in structurally-modified Cu<sub>0.1</sub>Ni<sub>0.8</sub>Co<sub>0.2</sub>Mn<sub>1.9</sub>O<sub>4</sub> spinel ceramics. *Phys B Condens Matter* 459:116–121 <https://doi.org/10.1016/j.physb.2014.11.023>
20. Shpotyuk O, Brunner M, Hadzaman I, Balitska V, Klym H (2016) Analytical description of degradation-relaxation transformations in nanoinhomogeneous spinel ceramics. *Nanoscale Res Lett* 11(1):499. <https://doi.org/10.1186/s11671-016-1722-0>
21. Klym H, Balitska V, Shpotyuk O, Hadzaman I (2014) Degradation transformation in spinel-type functional thick-film ceramic materials. *Microelectron Reliab* 54(12):2843–2848 <https://doi.org/10.1016/j.microrel.2014.07.137>
22. Hadzaman I, Klym H, Shpotyuk O (2014) Nanostructured oxyspinel multilayers for novel high-efficient conversion and control. *Int J Nanotechnol* 11(9–10-11):843–853. <https://doi.org/10.1504/IJNT.2014.063793>
23. Rodriguez-Carvajal J (2001) Recent developments of the program FULLPROF, Commission on Powder Diffraction (IUCr). *Newsletter* 26:12–19
24. Roisnel T, Rodriguez-Carvajal J (2000) WinPLOTR: a windows tool for powder diffraction patterns analysis, materials, science forum. In: *Proceedings of the seventh European powder diffraction conference, Barcelona*
25. Hill RJ, Howard CJ (1987) Quantitative phase analysis from neutron powder diffraction data using the Rietveld method. *J Appl Crystallogr* 20:467–474. <https://doi.org/10.1107/S0021889887086199>
26. Bondarchuk A, Shpotyuk O, Glot A, Klym H (2012) Current saturation in In<sub>2</sub>O<sub>3</sub>-SrO ceramics: a role of oxidizing atmosphere. *Revista mexicana de física* 58(4):313–316. <http://www.scielo.org.mx/pdf/rmf/v58n4/v58n4a5.pdf>
27. Karbovnyk I, Bolesta I, Rovetskii I, Velgosh S, Klym H (2014) Studies of CdI<sub>2</sub>-Bi<sub>3</sub> microstructures with optical methods, atomic force microscopy and positron annihilation spectroscopy. *Mater Sci Pol* 32(3):391–395. <https://doi.org/10.2478/s13536-014-0215-z>
28. Klym H, Ingram A, Shpotyuk O, Filipecki J, Hadzaman I (2011) Structural studies of spinel manganite ceramics with positron annihilation lifetime spectroscopy. *J Phys Conf Ser* 289(1):012010 <http://iopscience.iop.org/article/10.1088/1742-6596/289/1/012010/meta>
29. Klym H, Ingram A, Shpotyuk O, Filipecki J (2010) PALS as characterization tool in application to humidity-sensitive electroceramics. In: *27th International Conference on Microelectronics Proceedings (MIEL)*, pp 239–242. <https://doi.org/10.1109/MIEL.2010.5490492>

30. Shpotyuk O, Filipecki J, Ingram A, Golovchak R, Vakiv M, Klym H, Balitska V, Shpotyuk M, Kozdras A (2015) Positronics of subnanometer atomistic imperfections in solids as a high-informative structure characterization tool. *Nanoscale Res Lett* 10(1):1–5. <https://doi.org/10.1186/s11671-015-0764-z>
31. Klym H, Ingram A, Shpotyuk O, Hadzaman I, Solntsev V, Hotra O, Popov AI (2016) Positron annihilation characterization of free volume in micro- and macro-modified  $\text{Cu}_{0.4}\text{Co}_{0.4}\text{Ni}_{0.4}\text{Mn}_{1.8}\text{O}_4$  ceramics. *Low Temp Phys* 42(7):601–605. <https://doi.org/10.1063/1.4959021>
32. Filipecki J, Ingram A, Klym H, Shpotyuk O, Vakiv M (2007) Water-sensitive positron-trapping modes in nanoporous magnesium aluminate ceramics. *J Phys Conf Ser* 79(1):012015. <https://doi.org/10.1088/1742-6596/79/1/012015>
33. Klym H, Ingram A, Shpotyuk O, Filipecki J, Hadzaman I (2010) Extended defects in insulating  $\text{MgAl}_2\text{O}_4$  ceramic materials studied by PALS methods. *IOP Conference Series: Mater Sci Eng* 15(1):012044. <https://doi.org/10.1088/1757-899X/15/1/012044>
34. Klym H, Karbovnyk I, Vasylyshyn I (2016) Multicomponent positronium lifetime modes to nanoporous study of  $\text{MgO-Al}_2\text{O}_3$  ceramics. In: 13th international conference on modern problems of radio engineering, Telecommunications and computer science (TCSET), pp 406–408. <https://doi.org/10.1109/TCSET.2016.7452071>
35. Kansy J (2000) Positronium trapping in free volume of polymers. *Rad Phys Chem* 58:427–431. [https://doi.org/10.1016/S0969-806X\(00\)00195-X](https://doi.org/10.1016/S0969-806X(00)00195-X)
36. Kansy J (1996) Microcomputer program for analysis of positron annihilation lifetime spectra. *Nucl Instrum Methods Phys Res, Sect A* 374(2):235–244. [https://doi.org/10.1016/0168-9002\(96\)00075-7](https://doi.org/10.1016/0168-9002(96)00075-7)
37. Klym HI, Ivanusa AI, Kostiv YM, Chalyy DO, Tkachuk TI, Dunets RB, Vasylyshyn I (2017) Methodology and algorithm of multicomponent analysis of positron annihilation spectra for nanostructured functional materials. *J Nano- Electron Phys* 9(3):03037-1-6. [https://doi.org/10.21272/jnep.9\(3\).03037](https://doi.org/10.21272/jnep.9(3).03037)
38. Klym H, Ingram A (2007) Unified model of multichannel positron annihilation in nanoporous magnesium aluminate ceramics. *J Phys Conf Ser* 79(1):012014. <https://doi.org/10.1088/1742-6596/79/1/012014>
39. Nambissan PMG, Upadhyay C, Verma HC (2003) Positron lifetime spectroscopic studies of nanocrystalline  $\text{ZnFe}_2\text{O}_4$ . *J Appl Phys* 93:6320. <https://doi.org/10.1063/1.1569973>
40. Tao SJ (1972) Positronium annihilation in molecular substance. *J Chem Phys* 56(11):5499–5510. <https://doi.org/10.1063/1.1677067>
41. Eldrup M, Lightbody D, Sherwood JN (1981) The temperature dependence of positron lifetimes in solid pivalic acid. *Chem Phys* 63:51–58. [https://doi.org/10.1016/0301-0104\(81\)80307-2](https://doi.org/10.1016/0301-0104(81)80307-2)
42. Traversa E (1995) Ceramic sensors for humidity detection: the state-of-the-art and future developments. *Sensors Actuators* 23:135–156. [https://doi.org/10.1016/0925-4005\(94\)01268-M](https://doi.org/10.1016/0925-4005(94)01268-M)
43. Gusmano G, Montesperelli G, Nunziante P, Traversa E (1993) Microstructure and electrical properties of  $\text{MgAl}_2\text{O}_4$  and  $\text{MgFe}_2\text{O}_4$  spinel porous compacts for use in humidity sensors. *Br Ceram Trans* 92(3):104–108
44. Klym H, Ingram A, Shpotyuk O (2016) Free-volume nanostructural transformation in crystallized  $\text{GeS}_2\text{-Ga}_2\text{S}_3\text{-CsCl}$  glasses. *Mater Werkst* 47(2–3):198–202. <https://doi.org/10.1002/mawe.201600476>
45. Klym H, Ingram A, Shpotyuk O, Calvez L, Petracovschi E, Kulyk B, Serkiz R, Szatanik R (2015) 'Cold' crystallization in nanostructured 80 $\text{GeS}_2\text{-}20\text{Ga}_2\text{S}_3$  glass. *Nanoscale Res Lett* 10(1):1–8. <https://doi.org/10.1186/s11671-015-0775-9>
46. Klym H, Ingram A, Shpotyuk O, Karbovnyk I (2016) Influence of CsCl addition on the nanostructured voids and optical properties of 80 $\text{GeS}_2\text{-}20\text{Ga}_2\text{S}_3$  glasses. *Opt Mater* 59:39–42. <https://doi.org/10.1016/j.optmat.2016.03.004>
47. Klym H, Ingram A, Shpotyuk O, Hotra O, Popov AI (2016) Positron trapping defects in free-volume investigation of  $\text{Ge-Ga-S-CsCl}$  glasses. *Radiat Meas* 90:117–121. <https://doi.org/10.1016/j.radmeas.2016.01.023>

- 32 Grain Porous Structure and Exploitation Properties of Humidity-Sensitive. . . 519
48. Ghosh S, Nambissan PMG, Bhattacharya R (2004) Positron annihilation and Mössbauer spectroscopic studies of  $\text{in}^{3+}$  substitution effects in bulk and nanocrystalline  $\text{MgMn}_{0.1}\text{Fe}_{1.9-x}\text{O}_4$ . *Phys Lett A* 325:301–308 doi: <https://doi.org/10.1016/j.physleta.2004.03.062>. Get rights and content
49. Jean YC, Mallon PE, Schrader DM (2003) Principles and application of positron and positronium chemistry. Word Scientific, Singapore
50. Mogensen OE (1995) Positron annihilation in chemistry. Springer, Berlin
51. Nakanishi H, Jean YC, Schrader DM, Jean YC (1998) Positron and positronium chemistry. Elsevier, Amsterdam

# Index

## A

- Abramov, M.V., 35–45  
 Absorption, 50, 58, 65, 85, 99, 100, 110, 111, 153, 156, 157, 189–193, 240, 252–255, 269, 277, 312, 313, 315, 325, 333, 334, 336–341, 396, 410, 412, 414, 416  
 Alloys, 3–12, 14–22, 25–31, 36, 165–175, 346, 348, 355, 444, 446, 453  
 Amorphous  
   alloys, 25  
   composite, 105, 157  
   phase, 253, 263  
 Annealing, 24, 319, 347, 487–497  
 Antimicrobial properties, 50, 57–61  
 Antistructural modeling, 370–372  
 Antitumor magneto-sensitive nanocomplex, 323–330  
 Antsibor, V., 165–175  
 Araújo, J.P., 357–372  
 Artyukhov, A.E., 395–402  
 Astrelin, I., 233–244  
 Atomic force microscopy (AFM), 7, 10–12, 17, 21, 23, 121, 127–129, 250, 491

## B

- Bairachniy, B., 443–453  
 Bershtein, V.A., 115–146  
 Bifunctional layer, 409, 412, 416, 418  
 Bio-ethanol, 304  
 Bolbukh, Y., 149–163, 407–424  
 Boriding, 345–355  
 Budnyak, T.M., 35–45  
 Burlaka, A., 323–330

## C

- Cancer nanotechnology, 324  
 Carbides, 167, 311, 317, 319  
 Catalyst, 3, 30, 31, 102, 104, 193, 297, 299, 304, 306, 307, 370, 408, 443, 475, 476  
 Catalytic activity, 4, 11, 24, 29–31, 99, 306  
 Cation distribution, 82, 358, 363, 364  
 CeO<sub>2</sub>-MoO<sub>3</sub> system, 297–308  
 Ceramics, 248, 459–472, 477, 478, 482, 485, 488, 499–515  
 Chalyy, D., 459–472  
 Chemical heat treatment, 395  
 Chitosan, 150–152, 156, 157, 160, 162  
 Coagulation, 226, 228, 488, 512  
 Cobalt, 6–10, 12, 14–16, 18, 26, 30, 31, 79–85, 102, 165–175  
 Colloid, 36, 215, 220, 225, 226, 228  
 Composite, 58, 63, 64, 102, 116, 117, 120, 124, 136, 139–142, 145, 149–163, 177–182, 187, 192–199, 233, 247–260, 262–264, 267–271, 297–308, 335–337, 353, 377–391, 408–410, 412, 413, 415–424  
 Controlled release system, 149–163  
 Coordinative complexes, 198  
 Corrosion resistance, 3, 4, 11, 346, 348  
 Creep resistance, 122  
 Crystallization, 53, 84, 116, 157, 159, 212, 213  
 Crystal structure, 102, 105, 357, 370, 501  
 Current, 3–25, 29, 30, 43, 49, 63, 105, 111, 166, 168, 169, 173–175, 206, 225, 240, 247, 261, 313, 315, 316, 350, 353–355, 378, 380, 383, 384, 388, 390, 428, 431, 439, 445–453

**D**

- Dar, M.A., 358  
 Deformation, 122, 154, 157, 209, 227, 236,  
 300, 302, 303, 308, 329, 413, 414  
 Demchenko, V., 49–61  
 Demchenko, V.L., 177–199  
 Dendzik, Z., 289–294  
 Dielectric permittivity, 264, 271, 378, 384,  
 385, 387, 390, 391  
 Differential scanning calorimetry (DSC), 152,  
 158, 159, 180, 181, 207, 212–213, 261,  
 265, 266, 410, 416–424  
 Diffusion, 27, 58, 66, 69, 91–96, 153, 155, 156,  
 160, 161, 163, 166, 168, 169, 171, 174,  
 175, 189, 345–355, 446–448, 450, 452  
 Dispersion, 106, 115, 119, 126, 127, 129–130,  
 136–139, 225, 249, 253, 261, 334, 378,  
 381, 383, 387–390, 397, 482, 487–497  
 Diyuk, O.A., 297–308  
 Dontsova, T., 99–111, 233–244  
 Doxorubicin, 35, 38, 39, 41, 42, 44, 324, 328  
 Dyes, 63, 65–73, 104, 109, 297, 299, 300, 307,  
 308  
 Dzyazko, Y., 63–74

**E**

- Elastic module, 207, 210  
 Electrical conductivity, 116, 117, 183, 188,  
 233, 377, 378, 381, 384, 388, 390, 391,  
 475, 480–482, 484, 485  
 Electrodeposition, 6, 19, 166, 167, 174, 443  
 Electron  
 beams, 7, 206, 207, 213, 224, 487, 488  
 spectrum, 192, 252  
 Electron spin resonance spectra, 325  
 Emission of light, 250  
 Enoxil, 149–164  
 Epoxy resin, 179, 188, 189, 379, 384, 386  
 External field, 429–431

**F**

- Fedenko, Y., 99–111  
 Ferrites, 79–86, 357–359, 366, 370, 372, 467  
 Ferromagnetic semiconductor, 36  
 Fesenko, O.M., 487–497  
 Free volume, 139, 460, 465–467, 500, 501,  
 505–507, 512, 513  
 Frolova, L.A., 79–86  
 Fumed and modified silicas, 151, 154, 162, 409  
 Functionalized MWCNT, 116, 117

**G**

- Gab, A., 311–320  
 Gab, I.I., 487–497  
 Gabrusenoks, J., 395–402  
 Gaune-Escard, M., 311–320  
 Gawdzik, B., 407–424  
 Gburski, Z., 89–96, 277–285  
 Gelatin, 6, 150–152, 156, 157, 160, 162  
 Glass transition temperature, 138, 157, 159,  
 178, 180–182, 207  
 Goncharenko, L., 49–61  
 Gorbyk, P.P., 35–45  
 Górný, K., 289–294  
 Grain boundaries, 346, 459, 460, 462, 463,  
 465, 467, 468, 470, 472, 499, 504–507,  
 511–513, 515  
 Grains, 9–11, 16, 21, 25, 65, 67, 68, 172–174,  
 261, 346, 355, 360, 362, 364–366, 372,  
 459, 460, 462, 463, 465, 467–470, 472,  
 477, 499–516  
 Gudyma, Iu., 427–440

**H**

- Hadzaman, I., 459–472, 499–516  
 High-temperature electrochemical synthesis,  
 165–175, 311–321  
 High temperature stability, 169  
 Hryn, V.O., 333–341  
 Humidifier, 395–405  
 Hydrogel, 152, 205–213  
 Hydroxyethyl methacrylate (HEMA),  
 150–153, 156–162

**I**

- Impedance, 8, 27, 185, 187, 380–384, 476  
 Impedance spectroscopy (IS), 27, 384  
 Ingram, A., 459–472, 499–516  
 Injected electron, 37  
 Inkjet printing, 500  
 Intermetallides, 11, 18, 24, 165–176  
 Interpolyelectrolyte complexes (IPEC), 50–61  
 Interpolyelectrolyte–metal complexes (IMC),  
 50, 53–61  
 Ion-conductive polymers, 444  
 Ionic melts, 311–321  
 Iron oxide, 323, 327, 328, 330, 352  
 Ishtvanik, O., 311–320  
 Iurzhenko, M.V., 177–199  
 Ivanenko, I., 99–111

**K**

Kane, S.N., 357–372  
 Karabanova, L.V., 115–146  
 Karbovnyk, I., 459–472  
 Kinetic, 27, 31, 37, 44, 109, 150, 152, 153,  
 155–156, 161–162, 166, 167, 220,  
 347–349, 355, 419, 429, 443, 446, 450,  
 487–497  
 equation, 31, 161, 349, 446  
 Klym, H., 459–472, 499–516  
 Kobylinskiy, S., 49–61  
 Kolotilov, S.V., 297–308  
 Kostiv, V., 459–472  
 Kostyuk, B.D., 487–497  
 Kovzun, I.G., 215–229  
 Kozakevych, R., 149–163  
 Kuan, H.-C., 144  
 Kushnerov, O.A., 79–86  
 Kutsevol, N., 205–213  
 Kwon, J.-Y., 117

**L**

Laser radiation, 250, 256, 336, 338, 340,  
 341  
 Linearly-dependent effective mass, 183  
 Lithium perchlorate, 177–200  
 Lloyd, A.W., 115–146  
 Lukashenko, T., 165–175, 311–320  
 Lukin, S., 323–330  
 Lupascu, L., 149–163  
 Lupascu, T., 149–163

**M**

Magnetometry, 325  
 Maizelis, A., 443–453  
 Makiela, D., 89–96  
 Maksymov, A., 427–440  
 Malyshev, V., 165–175, 311–320  
 Mamunya, Y.P., 177–199  
 Matkovska, L.K., 177–199  
 Matzui, L.Y., 377–391  
 McClory, C., 117, 144  
 Mechanical  
 properties, 50, 115, 116, 121, 139,  
 141–146, 179, 206, 208, 209, 213, 251,  
 258, 475–485  
 vibration, 324, 326, 328–330  
 Metal, 3–31, 35, 49–51, 53, 56–61, 64, 69, 73,  
 85, 99–111, 118, 149, 166, 167, 171,  
 173, 178, 189, 192, 233, 240, 248, 249,  
 256, 324, 333, 334, 336, 337, 340, 346,

355, 370, 408, 427, 428, 430, 443, 445,  
 446, 449, 450, 453, 459, 460, 487–490  
 ions, 35, 73, 178, 256, 428, 430, 445  
 Mikhailovsky, S.V., 115–146  
 Milovanov, Y.S., 377–391  
 Mixed oxides, 260  
 Modified silica, 155, 409, 412, 413, 417  
 Molybdenum, 12, 14–21, 24, 27, 28, 31, 104,  
 105, 107, 111, 165–176, 297, 298, 308,  
 319

**N**

Nadtoka, O., 205–213  
 Nahirniak, S., 233–244  
 Naidich, Y.V., 487–497  
 Nanocarbon, 378–391  
 Nanocomposites, 35–45, 49–61, 66–69, 71–73,  
 115–146, 247–271, 298, 333–342,  
 345–355, 377, 378, 383, 386, 388  
 Nanofilm, 487–497  
 Nanoparticle, 36, 37, 49–57, 59–61, 63–74,  
 80, 222, 223, 225–228, 234, 247, 248,  
 250–252, 259–270, 298, 303, 325–327,  
 330, 333–342, 377, 381, 428–430, 433,  
 443  
 Nanoporous structure, 396  
 Nanopowders, 80, 252, 258, 311, 321  
 Nanosized oxides, 260, 297–308  
 Nanostructure, 3–31, 35, 36, 44, 127, 165–175,  
 216, 225, 228, 233–244, 277–342, 405,  
 443, 460, 499  
 coatings, 165–175  
 Nedilko, S.G., 247–271  
 Néel magnetic moment, 357  
 Nenastina, T.A., 3–31  
 Nickel, 102, 121, 166–175, 319, 348, 358, 359,  
 370, 443–453, 480, 482–485  
 Nikipelova, O.M., 215–229

**O**

Oliinyk, V.O., 215–229  
 Onanko, A., 205–213  
 Orel, V., 323–330  
 Ostash, O.P., 475–485  
 Oxide, 5, 7, 8, 19, 20, 24, 26, 27, 30, 31, 84,  
 99, 100, 121, 166, 167, 169–171, 173,  
 174, 178, 179, 190, 193, 216, 220, 227,  
 228, 233–244, 248–270, 297–308, 312,  
 317, 323, 324, 327, 328, 330, 350, 352,  
 444, 466–468, 475–485, 488–497,  
 501



**P**

- Pabiszczak, M., 277–285  
 Panko, A.V., 215–229  
 Perets, Y.S., 377–391  
 Petranovska, A.L., 35–45  
 Phase composition, 4, 81, 172–174, 311, 314–318, 320, 499, 500, 503, 508, 509  
 Photoluminescence, 251, 253, 254, 257, 261, 267, 277  
 Pivovarov, O.A., 79–86  
 Plasmon resonance, 333, 334, 340, 341  
 Podhurska, V.Y., 475–485  
 Podkoscielna, B., 407–424  
 Polarization resistance, 7, 27  
 Polonska, K., 427–440  
 Polyacids, 206  
 Polyalcohols, 206  
 Polymer/silica interaction, 126, 132  
 Polyurethane matrix, 115–146  
 Ponomarova, V., 63–74  
 Pores, 21, 64, 66–69, 73, 109, 218, 225, 235, 364, 365, 396–405, 459–463, 465, 467, 468, 470, 484, 499, 501–505, 507–516  
 Porous ammonium nitrate (PAN), 395, 396, 400, 403, 404  
 Positronium decaying, 460  
 Positron trapping, 460, 462, 465–468, 470–472, 501, 505–507, 512, 513  
 Prokopenko, V.A., 215–229  
 Protein molecule, 277  
 Pylypchuk, Ie.V., 35–45

**Q**

- Quantum well, 33, 99

**R**

- Raczyńska, V., 289–294  
 Raczyński, P., 89–96, 277–285, 289–294  
 Radio frequency, 323, 324, 330  
 Raja, M., 117  
 Refractory metals, 10, 11, 15, 19  
 Riabov, S., 49–61  
 Romanov, A., 323–330  
 Rossi, P.C., 395–402  
 Rybalchenko, N., 49–61  
 Rykhalskyi, O., 323–330

**S**

- Sachuk, O.V., 297–308  
 Sakhnenko, N.D., 3–31

- Satakar, M., 357–372  
 Sawlowicz, Z., 297–308  
 Scanning electron microscope (SEM), 7, 121, 129–130, 181, 195, 197, 207–209, 216, 224, 250, 260–262, 302, 303, 360, 364, 365, 372, 379, 380, 397, 460, 463, 465, 472, 480, 483, 490, 491, 493, 495, 496, 499–501, 504–506, 511, 512, 516  
 Segmental dynamics, 140, 145  
 Sevostianov, S., 407–424  
 Shakhnin, D., 165–175, 311–320  
 Shakhnin, D.B., 487–497  
 Shcherbakov, S.M., 297–308  
 Shpotyuk, O., 459–472, 499–516  
 Silica/lignin biocomposites, 413, 414  
 Silver-containing nanocomposite, 50, 59  
 Silver nanoparticles, 36, 49, 60  
 Sintering, 362, 459–462, 464, 468, 477, 499–503, 507, 508, 510, 511, 514, 515  
 Smirnova, T.N., 333–341  
 Soft magnetic films, 3  
 Sonochemical activation, 298  
 Sosenkin, V., 63–74  
 Starchevskyy, V.L., 297–308  
 Sternik, D., 407–424  
 Stetsko, A.E., 345–355  
 Stetsyuk, T.V., 487–497  
 Structure, 4, 10, 16, 18, 19, 21, 24, 25, 43, 50–54, 57–61, 63–74, 79–86, 91, 100–102, 105–107, 109–111, 115–117, 124–128, 134, 147, 149, 157, 162, 171, 172, 174, 175, 177–199, 205, 207–209, 211, 213, 219, 220, 226, 228, 233–236, 239, 240, 242, 244, 248–250, 253, 256, 258–260, 263, 267, 277, 289, 290, 293, 294, 300, 303, 304, 323, 333, 338–341, 351, 353, 355, 357, 358, 360, 363–365, 367, 368, 372, 380, 381, 383, 386, 395–400, 403, 405, 408, 409, 412–414, 418, 419, 421, 422, 424, 445, 459–462, 466–468, 470, 475, 478, 483–485, 489, 490, 492, 494, 499–515  
 Substrate, 4, 10–12, 17, 18, 22, 24–27, 31, 102, 166, 167, 171, 172, 174, 175, 179, 253, 255, 289, 293, 294, 334, 345–347, 408, 443, 444, 446, 449, 453, 488–490, 497  
 Sujatha, C., 358  
 Surface plasmon polariton, 333  
 Synthesis, 3, 4, 35–38, 42, 43, 64–65, 79, 80, 86, 102, 117, 119, 124, 165–176, 179, 180, 195, 198, 206, 213, 233–244, 249, 258, 260, 297, 298, 308, 311–321, 324, 327, 330, 357, 359–360, 408

**T**

- Tatarchuk, T., 357–372  
Temperature, 5, 8, 24, 31, 51, 56–60, 65, 80–91, 94, 99, 105, 107, 116–118, 121–123, 136–141, 150–152, 157, 159, 172, 174, 175, 177, 178, 180–188, 196, 198, 206, 207, 210, 212, 233, 234, 239–241, 244, 255, 260, 261, 264–267, 278, 289, 290, 298, 299, 304–308, 312, 313, 317, 319, 325, 330, 346–351, 355, 360, 366, 367, 380, 389, 396, 397, 409, 410, 416–423, 427, 428, 430–433, 435–438, 459–462, 475–477, 480, 484, 488–492, 494, 496, 497, 499, 500, 502, 504, 507, 508, 510, 514–516  
Temperature quenching of luminescence, 260, 267  
Ternary alloys, 20, 26–29, 31  
Tertykh, V., 149–163, 407–424  
Thermal properties, 206, 410  
Thermodynamic miscibility, 145  
Thermogravimetric analysis (TGA), 207, 210, 213, 261, 265  
Thermomechanical properties, 50–57, 247  
Titanium, 99, 100, 102, 111, 335, 444, 487–497  
Tolstopalova, N.M., 79–86  
Transmission coefficient, 91  
Transmission electron microscopy (TEM), 65, 66, 121, 127, 129–130, 235–237, 258, 299, 302–304, 337  
Tsyganovich, O.A., 215–229  
Tungsten, 4, 8–10, 165–175, 311–320  
Turanksa, S.P., 35–45

**U**

- Upward diffusion, 338  
Uskova, N., 165–175  
Ustundag, Z., 165–175

**V**

- Vacuum, 65, 81, 120, 131, 180, 187, 207, 443, 476, 487–497, 501  
Vasylchyshyn, I., 459–472  
Vasyliv, B.D., 475–485  
Ved, M.V., 3–31  
Vira, V.V., 475–485  
Volfkovich, Y., 63–74  
Vortex granulator, 395, 402, 403  
Vovchenko, L.L., 377–391

**W**

- Wang, X., 144  
Whitby, R.L., 115–146  
Wound dressing, 205, 213

**Y**

- Yafet-Kittel angle, 359, 367, 372  
Yakushev, P.N., 115–146  
Yermolenko, I.Y., 3–31

**Z**

- Zakutevskyy, O.I., 297–308  
Zazhigalov, V.A., 297–308  
Zirconium, 20, 27, 28, 31, 64, 66, 67, 102, 256, 482, 484, 487–497